Proceedings of the

8th International Conference on

Flow Processes in Composite Materials

(FPCM-8)

11-13 July 2006

Ecole des Mines de Douai

France

Proceedings of the 8th International Conference on

Flow Processes in Composite Materials

(FPCM-8)

11-13 July 2006

Ecole des Mines de Douai

France

Edited by :

Christophe BINETRUY
Professor
Department of Polymers and Composites Technology & Mechanical Engineering
Ecole des Mines de Douai
France

Published by :

Ecole des Mines de Douai
941 Rue Charles Bourseul
BP 10838
F-59508 DOUAI, France

Telephone : +33 (0)3 27 71 22 22
Fax : +33 (0)3 27 71 25 25
e-mail : mines@ensm-douai.fr
Website: **http://www.ensm-douai.fr**

First published, June 2006 at Ecole des Mines de Douai, France

Cover design realised by Michèle Delcambre, Ecole des Mines de Douai.
Printed by Ecole des Mines de Douai.

Organising committee

C. Binétruy	Ecole des Mines de Douai, France
C. Canivet	Ecole des Mines de Douai, France
S. Comas Cardona	Ecole des Mines de Douai, France
M. Deléglise	Ecole des Mines de Douai, France
P. Krawczak	Ecole des Mines de Douai, France

International Advisory Board Members FPCM

SG Advani	University of Delaware, USA
S Bickerton	University of Auckland, New Zealand
C Binétruy	Ecole des Mines de Douai, France
RJ Crawford	University of Waikato, New Zealand
I Crivelli-Visconti	University di Napoli, Italy
K. Friedrich	IVW Kaiserslautern, Germany
RB Gebart	Lulea University of Technology, Sweden
AC Loos	Michigan State University, USA
JA Mänson	Ecole Polytechnique Federale de Lausanne, Switzerland
PJ Mallon	Univeristy of Limerick, Ireland
CM O Bradaigh	University College of Galway, Ireland
R Parnas	University of Connecticut, USA
RB Pipes	Purdue University, USA
C Rudd	University of Nottingham, England
J Summerscales	University of Plymouth, England
F Trochu	Ecole Polytechnique Montreal, Canada
K Walters	University of Wales,Wales

Foreword

This publication contains the written versions of the papers presented at the 8th International Conference on Flow Processes in Composite Materials (FPCM8), held on July 11th-13th 2006 at the Ecole des Mines de Douai, France. This was the first meeting in France. The previous FPCM conferences in this series took place at the Brunel University, England, in 1988; the University of Limerick, Ireland, in 1991; the University of Galway, Ireland, in 1994; the University College of Wales, Aberystwyth, Wales, in 1996; the University of Plymouth, England, in 1999 ; the University of Auckland, New Zealand, in 2001. The 7th conference was held at the University of Delaware, USA, in 2004.

The general purpose of this conference is to provide a forum for the presentation and discussion of the latest research and technology on all aspects of flow processes in composite materials. The topics addressed in this publication span the entire spectrum of research to applications for composite manufacturing processes.
Papers are grouped into several broad areas, including permeability prediction, experimental analysis, modeling, forming, material characterization, applications, simulation, monitoring and control. Flow processes in stationary fiber beds are predominant. The topic of hydraulic permeability of fibrous preform continues to give rise to fundamental and applied researches. References to the pioneer work of the French Engineer Henry G. P. Darcy are numerous in this volume. This conference coincides with the 150th anniversary of the publication of “Les Fontaines Publiques de la Ville de Dijon" with the famous Appendix D, where Darcy's Law for flow in porous media was stated. A mini-exhibition in honor of H. G.P. Darcy was held during this meeting.

I want to thank J. C. Duriez, Director of the Ecole des Mines de Douai, and Prof. P. Krawczak, head of the Department of Polymers and Composites Technology & Mechanical Engineering, for their support to this conference. I want to thank the JEC Group for the endorsement of the conference. We especially thank the City of Dijon and Mme E. Lochot for supplying us with Henry G. P. Darcy’s documents exhibited during this conference. We are grateful to Prof. E. Glenn Brown, Oklahoma State University, and Henry Darcy for providing the biographical material published in this volume.

I am grateful to the scientific advisory board for reviewing the abstracts of these manuscripts.
I would like to acknowledge the contributions of the members of the organising committee and of the sponsors towards the success of FPCM8. The local organiser Catherine Canivet contributed with her professionalism in tracking any details, in designing the website, collecting abstracts and papers and preparing the published proceedings, was indispensable during the organization of FPCM8. Thanks are also due to the accounting, computer science, media and catering departments for all necessary arrangements for the meeting.

I hope that you will enjoy the excellent work of our many authors and this volume brings you some new ideas and understanding of the magical composites manufacturing world.

Christophe BINETRUY
Chairman of the FPCM8 Conference
June 6th, 2006

The Environmental and Water Resource Institute of the American Society of Civil Engineering held a one day symposium in honor of Henry G. P. Darcy's 200th birthday. The Symposium was part of the larger, World Water and Environmental Resource Congress held in Philadelphia, PA, June 23 -26, 2003.

The following biography by Henry Darcy was first published in :

> Brown, G. O., J. D. Garbrecht, and W. H. Hager (eds), 2003, Henry P. G. Darcy and Other Pioneers in Hydraulics: Contributions in Celebration of the 200th Birthday of Henry Philibert Gaspard Darcy, ASCE, Reston, VA, 320 pg., ISBN 0-7844-0683-9. http://biosystems.okstate.edu/Darcy/index.htm

In addition to it, each conference delegate received a copy of the book “HENRY DARCY le bicentenaire 1803 – 2003” published by the city of Dijon, France.

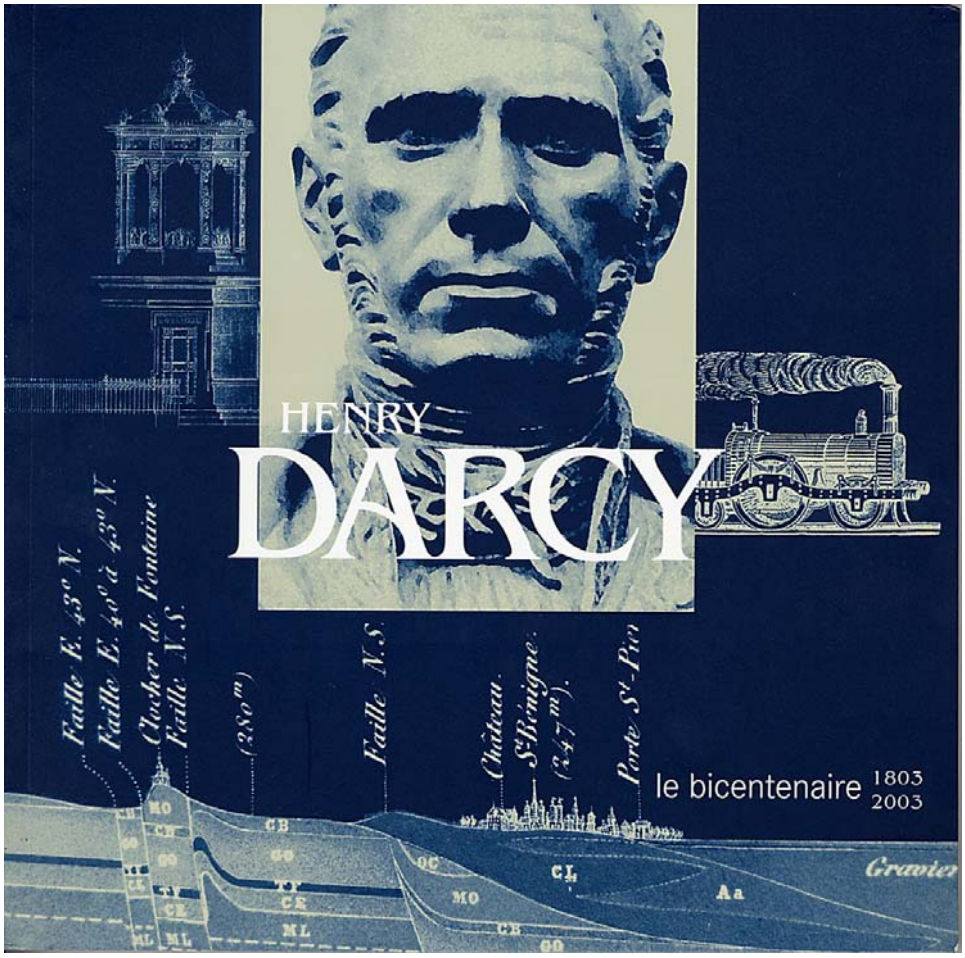

HENRY DARCY le bicentenaire 1803 –2003 - ISBN 2-915-128-12-X

Henry Darcy: Inspecteur général des ponts et chaussées

Henry Darcy[1]

Abstract

Henry P. G. Darcy is known for his achievements in engineering and contributions to his birthplace of Dijon, France. His descendant, Henry Darcy, the fifth person to carry the name, provides a family perceptive of his illustrious relative. In addition to biographical material, each of the other Henry's is described. Finally, excerpts from several letters from Darcy to Henry Bazin are used to show Darcy's modesty, humor and finesse. The complete paper is presented in both French and an English translation.

Figure 1. Henry Darcy at Ecole Polytechnique, circa 1821. (P. Darcy, 1957)

[1] Ingénieur civil des mines, Paris, France.

Introduction

L'importance de l'oeuvre scientifique et technique laissée par l'ingénieur Henry Philibert Gaspard Darcy justifie l'intérêt, voire l'engouement, que sa personnalité suscite aujourd'hui dans la communauté scientifique mondiale. Cet engouement se porte sur son oeuvre, bien sûr, mais également sur sa personnalité, sa vie et cette extraordinaire énergie qui lui permis en si peu de temps de faire autant de choses. Le « Darcy Memorial Symposium on the History of Hydraulics » est un signe de cet intérêt.

Les rédacteurs de ce volume ont souhaité qu'un témoignage familial soit apporté à ce séminaire. Notre famille a été très honorée de cette demande et c'est bien volontiers que j'apporterai ma contribution qui sera modeste compte tenu de l'abondance des informations disponibles aujourd'hui grâce au réseau internet dont les sites consacrés à mon illustre parent sont nombreux et actifs. Je vous proposerai donc un rapide rappel biographique de ce que fut la vie de l'ingénieur Darcy et je tenterai d'analyser ses principaux traits de caractères d'après ce qu'en rapporte la tradition familiale.

Héritage

Henry Philibert Gaspard Darcy est né à Dijon, capitale historique de la Bourgogne, le 10 juin 1803. Le nom de Darcy est ancien en Bourgogne puisqu'une lignée continue d'ecclésiastiques de haut rang le porte au XIII et XIV siècle en particulier dans la région d'Autun. Cette famille semble avoir été ruinée et dispersée lors des guerres de religion du XVI siècle au

Translation by Glenn O. Brown[2]

Introduction

The importance of the scientific and technical work left by the engineer Henry Darcy justifies the interest, even the passion, which his celebrity creates today in the world scientific community. This passion is based on his work of course, but also on his personality, life and extraordinary energy, which permitted great accomplishments in a short time. The "Darcy Memorial Symposium on the History of Hydraulics" is a sign of this interest.

The editors of this volume wished that our family's perspective be presented to the seminar, and we are greatly honored by this request. Thus, it is well that I contribute my share today, which will be modest taking into account the abundance of information available on the Internet, where many sites are devoted to my famous ancestor. Thus, I offer to you a small biographical note on the life of engineer Darcy. In it, I will examine his principal qualities according to our family tradition.

Heritage

Henry Philibert Gaspard Darcy was born in Dijon, historic capital of Burgundy, on June 10, 1803. Darcy is an old name in Burgundy. In particular, a continuous lineage of high-ranking clergymen carried it in the XIII and XIV century in the Autun region. The family appeared to be ruined and dispersed during the Wars of Religion in the XVI century. At that time, the family made the choice to reform as attested by old portraits of Luther and Calvin still appearing in the

[2] Professor, Biosystems and Agricultural Engineering, Oklahoma State University, Stillwater, OK 74078; gbrown@okstate.edu

cours desquelles elle fit le choix de la réforme comme en attestent d'anciens portraits de Luther et Calvin figurant encore dans le patrimoine familial au début du XIX siècle. L'ancêtre avéré et direct d'Henry Darcy, est le capitaine Pierre d'Arcy, son quart aïeul, né en 1618 et mort à Epinac en 1686. La famille s'était installée à Dijon au début du XVIII siècle et c'est là que naît en 1776 Jacques Lazare Gaspard d'Arcy, père du futur ingénieur. En 1794, c'est, en France, l'époque de la tourmente révolutionnaire. Lazare Gaspard s'enrôle dans le troisième bataillon des volontaires de la Cote d'Or; il participe aux combats historiques de Jemmapes et de Fleurus. C'est un « soldat de l'an II ». Comme l'écrivait un siècle plus tard son petit-fils,il appartenait à cette génération dont le rêve fut « La Révolution, la Grande Nation, la Grande Armée, la Liberté, la Dignité, la Félicité du genre humain par la France.» Le 28 Mai 1802, Lazare Gaspard d'Arcy épouse Agathe Angélique Serdet ; ils auront deux enfants : Henry, l'ingénieur, et Hugues Iéna, le préfet, mon quart aïeul.

Agathe Serdet était d'un milieu très modeste ; S'exprimant à propos de cette femme admirable qu'il avait bien connue puisqu'elle mourût en 1870 à 92 ans, mon trisaïeul, Henry II, son petit-fils, parvenu au soir d'une vie qui lui avait permis de côtoyer au Conseil d'Etat, dans la Préfectorale, et au sein du Patronat français tout ce que la France de l'époque comptait d'élites, n'en tirait aucune vanité et écrivait :

« A-t-il jamais passé du sang noble ou quart de noble par nos veines, je n'en sais rien ; mais pour sûr, souvenez vous-en mes enfants, il y a du sang de peuple, de ce bon peuple de France, de ce tout petit monde, point artiste ni compliqué, mais attaché en simplicité aux devoirs

family inheritance at the beginning of the XIX century. The direct ancestor of Henry Darcy was Captain Pierre d'Arcy, his grandfather fourth removed. He was born in 1618 and died in Epinac in 1686. The family settled in Dijon by the beginning of the XVIII century, and it is there that Jacques Lazare Gaspard d'Arcy, father of the future engineer, was born in 1776. In 1794 in France, revolution was stirring, and Lazare Gaspard enlisted in the Third Volunteer Battalion of the Cote d'Or. He took part in the historical battles at Jemmapes and Fleurus, and was a "soldier of the second year" [of the revolution]. One century later, his grandson wrote that Lazare Gaspard's generation's dream was "the Revolution, the Grand Nation, the Grand Army, Freedom, Dignity, and the Bliss of mankind through France." On May 28th, 1802, Lazare Gaspard d'Arcy married Agathe Angélique Serdet. They had two children, Henry the engineer, and Hugues Iéna the prefect, my grandfather, fourth removed.

Agathe Serdet had a very modest middle class background. He wrote about this admirable woman that he had known even though she was born in the previous century, since she died in 1870 at age 92. My great-great-grandfather, the second Henry, her grandson reached the end of a life where he dealt with the Council of State in the Prefecture, and within the French Council of Employers and gained everything that France of the time considered elite, but despite all this he was not vain.

"If ever passed noble blood or quarter of noble in our veins, I know nothing of it, but remember for certain my children, there is the blood of the good people of France. Not complicated artists, but simple people of a very small world devoted to daily duties, yet none the less

quotidiens ; non sans une pointe d'idéal cependant qui, aux heures bénies, parfume les destinées nationales, race de labour, mais travaillant comme chante l'alouette, gardant sous le hâle du jour toutes les sensibilités du coeur, secourable autant qu'économe, et en toutes choses, au naturel et sans pompe, amassant sou à sou le trésor matériel et moral du pays, et comblant sans jamais désespérer, les trous faits par les coquins, les dilettantes ou les sots. »

C'est à cette femme du « tout petit monde » qu'Henry et Hugues Iéna devront leur éducation et leur remarquable réussite. « Cette mère fut une éducatrice admirable. Elle était, elle est restée jusqu'à sa dernière heure débordante de tendresse vigilante, efficiente et désintéressée ; mais elle avait en même temps la volonté du but, le culte de l'effort et de la règle. Ce but qui est que, débiteur de tout ce qu'on vaut, on doit rendre tout ce qu'on peut. » Ces valeurs essentielles du travail, de l'effort et de la recherche du bien commun sont exactement celles que traduiront la vie et l'oeuvre de son fils Henry dont tous ses biographes ont souligné l'absence totale de recherche d'intérêt personnel, lui qui refusa toute rétribution particulière pour les services qu'il avait rendus, n'acceptant de la ville de Dijon que l'eau courante gratuite sa vie durant et une concession au cimetière municipal.

Lorsque Henry naît, en 1803, la France est en pleine épopée Napoléonienne et nul doute que sa famille suive avec passion l'actualité de l'époque : mon quart-aieul, né en 1807, se voit attribué le prénom de « Hugues Iéna » pour fêter la victoire que l'empereur a remporté sur les prussiens l'année précédente. Lazare Gaspard, étant fonctionnaire, on ne peut exclure totalement qu'un peu d'opportunisme

with ideals. Thus, at the proper time, they sense the national destiny and work hard but happily, keeping unto themselves all the sensitivities of the heart. In all things they are like a treasurer. With good nature and no conceit, they pile up penny upon penny, the material and moral treasure of the country. They fill without despairing, the holes made by the rascals, the dilettantes and the foolish."

It is to this woman of the "very small world" that Henry and Hugues Iéna will owe their education and their remarkable success. "This mother was an admirable teacher. She was and remained until her last hour, vigilant, efficient and unselfish in her tenderness. However, at the same time she had the will to reach a goal, with drive and determination. She was devoted to the belief that one owes all that she is worth, and one must return all one can." These essential work ethics, duty and the pursuit of the common good, are exactly those that her son Henry would translate into his own life and work. His biographers underlined the total absence of self-interested pursuits. He refused all commissions for the services that he rendered, and accepted from Dijon only free water service during his life and a concession in the municipal cemetery.

When Henry was born in 1803, France was in the Napoleonic era, and there is little doubt that his family passionately followed the popular movement of the time. My direct ancestor, born in 1807, saw himself given the first name "Hugues Iéna" to celebrate the emperor's victory over the Prussians the previous year. One cannot totally rule out that Lazare Gaspard, being a civil servant slipped a little political opportunism into the choice of the name. Under these conditions, one

politique se soit glissé dans le choix de ce prénom et on peut s'étonner dans ces conditions que Henry, né en 1803, ne se soit pas appelé Henry Marengo en l'honneur de la campagne d'Italie au cours de laquelle son oncle Jean d'Arcy avait été tué.

En 1817, Lazare Gaspard d'Arcy meurt en laissant une veuve et deux jeunes garçons dans une situation financière très précaire. Henry n'a que quatorze ans mais il se comporte alors comme un adulte responsable. Le soir de l'enterrement de son père, il prend à part son cadet Hugues Iéna, âgé de 10 ans, et lui dit « C'est notre père qui nous faisait vivre. Je ne t'abandonnerai jamais. Je serai le père. Aide moi en travaillant comme je travaillerai pour que, le plus tôt possible, nous gagnions notre pain et celui de notre mère avec honneur. (Darcy, 1957) »

Dès lors une exceptionnelle affection liera toute leur vie Agathe et ses deux fils. Dans une lettre écrite en 1823, Henry écrit à sa mère : « ne fondons notre bonheur que sur notre triple amitié » Ils resteront unis tous les trois toute leur vie et formeront ensemble, comme l'écrit Henry, une véritable « trinité ».

Ces deux enfants tinrent parole puisque le premier devint l'ingénieur que nous connaissons, et le second, mon quartaieul, devint un préfet important (Nîmes, Metz, Lyon) puis sous-secrétaire d'Etat à l'intérieur sous la seconde république (Forstenzer, 1981), avant de se reconvertir dans l'industrie en fondant la compagnie des forges de Châtillon et Commentry.

Agathe d'Arcy, n'ayant pas les moyens de financer les études de ses fils demanda et obtint des bourses de la ville de Dijon et un prêt de son beau-frère, par ailleurs tuteur des deux enfants : en

can wonder why Henry, who was born in 1803, was not called Henry Marengo in honor of the region in Italy where his Uncle Jean d'Arcy had been killed.

In 1817, Lazare Gaspard d'Arcy died and left his widow and two young boys in a very precarious financial situation. Henry was only fourteen years old, but he behaved like a responsible adult. The evening of his father's burial, he took his 10 year old sibling, Hugues Iéna, aside and said, "Our father supported us. I will never give up on you. I will be the father. Help me by working as I will, so that as soon as possible, we can earn our bread and that of our mother with honor (Darcy, 1957)".

Consequently, an exceptional affection bound Agathe and her two sons all their lives. In an 1823 letter, Henry writes to his mother, "lets found our happiness only on our triple friendship." All three remained united throughout their lives, and formed, as Henry wrote a true "trinity".

These two children kept their word, since the first became the engineer whom we know. The second, my ancestor, became an important Prefect (Nimes, Metz and Lyon) and then Under-Secretary of the Interior in the Second Republic (Forstenzer, 1981). He then changed occupations and founded the Forging Company of Châtillon and Commentry.

Agathe d'Arcy, not having the means to finance her sons' studies, asked for and obtained a scholarship from the city of Dijon and a loan from her brother-in-law, who was also a tutor for the two children. This republican brute advised the children to give up the particle and to transform d'Arcy into Darcy, which they did. Since that time, our family has chosen to preserve this corrected orthography because it is in this form that

contre partie, celui-ci, républicain farouche, conseilla aux enfants d'abandonner la particule et de transformer d'Arcy en Darcy, ce qu'ils firent. Notre famille a depuis lors choisi de conserver cette orthographe corrigée puisque c'est sous cette forme que notre nom a été illustré.

Descendants

De même le « y » du prénom Henry tel que le portait l'ingénieur s'est transmis de génération en génération et je suis moi-même le 5ème Henry Darcy depuis l'ingénieur.

La Lignée de Henry Darcy

***I*:** Henry P. G. (1803-1858), l'ingénieur.

***II*:** (1840-1926), mon trisaïeul était le fils de Hugues Iéna. Il fit, comme son père, une carrière remarquable dans l'administration d'abord (préfet d'Epinal, d'Arras puis de Nice) puis dans l'industrie lourde (Charbonnages et Métallurgie) où il fonda et présida pendant quarante ans le Comité Central des Houillères de France (Isambert, 1965).

***III*:** (1895-1916): Frère de mon grand-père, est mort pour la France à 20 ans.

***IV*:** (1930-1953), cousin germain de mon père était officier dans l'aéronavale et est mort en service commandé à 23ans.

***V*:** (1954 -), moi-même, mais revenons à l'ingénieur.

La Vie de Henry Darcy

En 1821, âgé de 18ans, il entre à l'école polytechnique qui était, et qui reste la plus prestigieuse des écoles d'ingénieurs

our name was distinguished.

In the same way, the Henry first name carried by the engineer has been transmitted from generation to generation. I am the fifth Henry Darcy. [The later Henry's are not in a direct line and did not use middle names. They are denoted here by II, III, etc.]

The Henry Darcy Lineage

***I*:** Henry P. G. (1803-1858), the engineer.

***II*:** (1840-1926), My great-great-grandfather was the son of Hugues Iéna. Like his father, he had a remarkable career in administration. He was initially Prefect in Epinal, Arras and Nice. He then moved into heavy industry, (coal and metallurgy) where he founded and chaired for 40 years the Central Committee of the Collieries of France (Isambert, 1965).

***III*:** (1895-1916) brother of my grandfather, died for France at age 20.

***IV*:** (1930-1953), the first cousin of my father was a Naval Aviator who died in service at age 23.

***V*:** (1954 -), myself, but let us return to the engineer.

Henry Darcy's Life

At age 18 in 1821, he entered the Ecole Polytechnique, which was and remains the most prestigious school of engineering in France (Figure 1). In 1823 he continued his education at the Ecole des Ponts et Chaussées (School of Bridges and Roads). At that time, he was described as having. "fire in his piercing eyes, and a fascinating smile." [The French is much more passionate.]

françaises (Figure 1). En 1823 il complète sa formation à l'école des ponts et chaussées. A cette époque, il est décrit comme ayant « des yeux roux qui lançaient des flammes, ou s'enveloppaient dans un nuage farouche, quand ils ne s'éclairaient pas du plus vif,du plus affectueux et du plus prenant des sourires ».

En 1826 il rentre dans la vie professionnelle et, après un stage dans le Jura, est rapidement nommé à Dijon. En 1828, il épouse une anglaise de Guernesey, Henriette Carey, dont les parents habitent à Dijon, le bel hôtel Vogüe . De ce mariage, semble-t-il parfois difficile, ne naîtra malheureusement aucun enfant.

Puis viennent les trente années de vie professionnelles passionnantes et harassantes à la fois au cours desquelles Henry Darcy va littéralement brûler sa santé. Cette carrière est jalonnée de réalisations techniques et de découvertes scientifiques majeures.

Septembre 1840 **:** Alimentation en eau de la ville de Dijon qui devient, avec cent quarante bornes-fontaines réparties dans toute la ville, la ville d'Europe la mieux alimentée en eau après Rome, et bien avant Paris.

Juillet 1845 **:** Adoption par la chambre des députés du projet de tracer Darcy pour la ligne de chemin de fer de Paris à Lyon via Dijon. Ce tracé comporte le percement de tunnel de Blaisy (4,6 Km), ouvrage considérable pour l'époque.

1850-1852 **:** Mission à Londres pour l'étude de l'emploi du Macadam pour le revêtement des chaussées en remplacement du pavage, et à Bruxelles pour y étudier le projet d'alimentation en eau de la ville.

In 1826 he began his professional life, and after a training course in Jura, he was quickly posted to Dijon. He married Henriette Carey in 1828, who was from the English island of Guernsey. Her parents lived in Dijon, at the beautiful Vogüe Hotel. It appears that the marriage was difficult, and unfortunately no children where produced.

Then came the 30 years of professional service that was both enthralling and difficult, during which Henry Darcy literally ruined his health. The career was marked by technical achievements and major scientific discoveries.

September 1840**:** Water supply of the city of Dijon is completed. With 140 public fountains, distributed throughout the city, it was the best water supply in Europe after Rome, but well before Paris.

July 1845**:** Darcy's plan for the Paris to Lyon railroad alignment through Dijon was adopted by the House of Commons. His design included the 4.6 km tunnel at Blaisy, a remarkable work for the time.

1850-1852**:** Mission to London to study the use of Macadamizing on roads [a graded stone foundation and pavement system]. He also traveled to Brussels to consult on the water supply of that city.

1856**:** Publication of *Les Fontaines Publiques de la ville de Dijon* [*The Public Fountains of Dijon*]. That publication contains "Darcy's law" for the permeability of porous media.

1857**:** Publication of *Recherches expérimentales relatives au mouvement de l'eau dans les tuyaux* [*Experimental research relating to the movement of water in pipes*], which provided the

1856 **:** Publication de *« Les Fontaines Publiques de la ville de Dijon »* avec l'énoncé de la *« loi de Darcy »* relative à la perméabilité des milieux poreux.

1857 **:** Publication de *« Recherches expérimentales relatives au mouvement de l'eau dans les tuyaux ».* Equation de Darcy-Weisbach.

2 Janvier 1858 **:** Henry Darcy meurt à Paris d'une pneumonie. Sa dépouille est transférée à Dijon par la voie ferrée qu'il avait dessinée ; à la gare, la troupe rend les honneurs et il reçoit l'hommage de toute la ville. Le lendemain, le conseil municipal de Dijon prend à l'unanimité la décision de donner son nom à l'actuelle Place Darcy qui marque l'entrée à Dijon des eaux de la source du Rosoir que Darcy avait canalisées.

Lettres à Bazin

L'ingénieur Darcy a entretenu une correspondance importante avec son jeune condisciple au Corps des Ponts et Chaussées, Henry Bazin ; ces lettres ne sont pas datées mais elles ont été numérotées de 1 à 25 par Bazin et sont très instructives quand au caractère de Darcy : elles sont empreintes de modestie, d'humour et de finesse.

Lettre n1**:** « Et sur ce, je vous sers cordialement la main : On m'a écrit que vous aviez bu récemment à ma santé ; je crains que cette obligation ne vous soit longtemps encore imposée : mais le vin de Bourgogne est bon et je vous plains un peu moins de ce dévouement que de celui dont vous aurez besoin pour la lecture de ces épreuves. »
Lettre n7**:** « Ce n'est pas dans un temps où l'on se joue si bien des principes, que je tiendrai, vous le pesez bien, à ma [experimental] basis for the Darcy-Weisbach Equation.

January 2, 1858**:** Henry Darcy died in Paris of pneumonia. His body was returned to Dijon by the railway that he had designed. An honor guard met the train at the station, and he received the homage of the entire city. The following day, the Dijon municipal council unanimously decided to give his name to the current Place Darcy, which marks the entry terminal to Dijon of the Rosoir spring water that Darcy had developed.

Letters to Bazin

Engineer Darcy maintained a significant correspondence with his younger colleague from the Ponts et Chaussées, Henry Bazin. These letters are not dated but were numbered from 1 to 25 by Bazin. They are very instructive on Darcy's character, and are full of modesty, humor and finesse.

Letter 1**:** "And on this, I extend my hand cordially to you. It was written to me that you had toasted recently to my health. I fear that this obligation will be imposed on you for a long time, but the wine of Burgundy is good and I feel a little less sorry for this devotion than the one you will need to read these proofs."

Letter 7**:** "It is not in this time when people make light of the many principles, that I will hold on to it. But, weigh well my small law: $a = \alpha + \beta/R$ [Darcy's relation for friction coefficient in cast-iron pipe.], it is so simple and so convenient that I would like to see you make a final good effort in its favor "

Letter 8**:** "Finally you found my $\varepsilon = 0.00175$, which is about what I found

petite loi : $a = \alpha + \beta/R$ mais elle est si simple et si commode que je voudrais bien vous voir tenter un dernier effort en sa faveur. »

Lettre n8**:** « Enfin vous retrouvez mon $\varepsilon = 0.00175$; c'est à peu près ce que j'ai rencontré dans les tuyaux, peut-être trouverons-nous quelques procédés pour arriver à la valeur exacte ! Mais j'avoue en ce qui concerne ε que la foi est difficile, l'espérance est difficile, nous réclamerons donc de nos lecteurs, s'ils sont chrétiens, la troisième vertu théologiale. »

Lettre n15**:** « Je vous enverrai quand il les aura recopiées mes élucubrations sur la formule,

$$\varepsilon R^2(dv/d2) = ri/2$$

La raison de la chose m'échappe toujours, j'ai donc pris le parti d'affirmer qu'elle était vrai sur le blason de mon père. J'en ferai une affaire personnelle, et je trouverai bien quelques Durandal pour soutenir ma conviction : dans le temps où ma pauvre santé florissait, j'avais fait un pèlerinage à Rocamadour pour contempler cette glorieuse épée du neveu de Charlemagne. J'ai consacré, sans les regretter, 8 jours de ma tournée à la mémoire du gigantesque Roland : je préférerai cela à la lecture des livres de comptabilité et des livres de cantonniers. »

Le dévouement sans limites de l'ingénieur Darcy au bien public s'est clairement traduit par le sacrifice de sa santé. Il s'est, au sens propre, tué au travail. En 1855, il ne demande à être mis à disponibilité pour des raisons de santé que pour mieux se consacrer à ses recherches scientifiques et à ses publications capitales de 1856 et 1857. Il devait être déjà bien tard pour lui puisque la mort le prend dès Janvier 1858. Là in pipes. Perhaps we will find some way to arrive at the exact value! However in this, I acknowledge that the faith is difficult and the hope is difficult. We will thus ask our readers, if they are Christian, the third theological virtue [charity]."

Letter 15**:** "I will send you when it is copied my considerable discussion on the formula,

$$\varepsilon R^2(dv/d2) = ri/2$$

The justification of the thing [the formula] always escapes me. I have thus decided to affirm on the coat of arms of my father that it is true. I will make a personal quest of it, and I will find some Durandal [a famous sword's name] to support my conviction. In the time when my poor health flowered, I made a pilgrimage to Rocamadour to contemplate this glorious sword of Charlemagne's nephew. I devoted, without regretting them, eight days of my tour to the memory of the great Roland. I would prefer that to the reading of books on accountancy and road repair."

The unlimited devotion of Darcy to the public well being clearly resulted in the sacrifice of his health. He killed himself with work. In 1855, due to heath reasons, he asked to be relieved of duties to better devote himself to his scientific research and his major publications of 1856 and 1857. It may have already been too late, since death took him in January 1858. A Bazin letter illustrates his physical courage and brute energy.

Letter 21**:** "Night before last, I had nervous pains [in his body] so cruel that I screamed for 8 or 10 hours like a man under torture. Yesterday, the fatigue of the previous night gave me a violent migraine. Today, I am calm, but weak. Thursday, I hope to come and see you."

encore, une lettre de Bazin illustre ce courage physique et cette énergie farouche.

Lettre n21**:** « J'ai eu l'avant dernière nuit des douleurs nerveuses si cruelles que j'ai crié pendant 8 ou 10 heures comme un homme à la torture : hier la fatigue de la nuit précédente m'a donné une violente migraine. Je suis calme aujourd'hui, mais faible. Jeudi, j'espère aller vous trouver. »

Remarques de Conclusion

Le plus grand écrivain et poète français du 19ème siècle, Victor Hugo, né en 1802, était d'un an l'aîné de Henry Darcy. Les deux hommes partageaient sans doute un certain nombre d'idées, ils avaient de surcroît une référence commune: l'île anglo-normande de Guernesey: Henry avait épousé Henriette Carey dont la famille était originaire de l'île, Victor Hugo y fut exilé de 1851 à 1870. L'île est très petite et on peut rêver, rêver qu'à l'occasion d'une visite à son beau-frère qui y résidait, l'ingénieur et le poète se soient rencontrés et qu'ensemble ils aient marché le long de la grève et évoqués les grands sujets qui leur tenaient à coeur.

« J'ai bien souvent et bien sombrement rêvé » écrit Darcy à Bazin « dans mes longs jours et mes longues nuits de souffrances à ces mystérieuses causes finales dont Dieu seul s'est réservé la clef, et malgré mon horreur du doute, j'en suis réduit à douter encore. »

Références Bibliographiques

Darcy, P. (1957). *Henry Darcy, inspecteur général des ponts et chaussées*. Imprimerie Darantière, Dijon.

Concluding Remarks

Victor Hugo, the great French writer and poet of the 19th century, was born in 1802 and was one year older than Henry Darcy. The two men undoubtedly shared a number of ideals and they had a common connection to the Anglo-Norman island of Guernsey. Henry had married Henriette Carey whose family originated from the island, while Victor Hugo was exiled there from 1851 to 1870. The island is very small and one can dream that at the time of a visit with his brother-in-law, the engineer and the poet met. Together they may have walked along the shore and evoked the great subjects of their hearts.

"I very often have gloomily dreamed" Darcy wrote to Bazin "in my long days and long nights of sufferings to the mysterious final questions, who God alone reserves the key, and despite my aversion to uncertainty, I have little choice but to doubt still".

Forstenzer, T. R. (1981). *French Provincial Police and the Fall of the Second Republic.* Princeton University Press, Princeton, New Jersey.

Guyot, J. (1944). "L'Académie de Dijon et les ponts et chaussées". *Mémoires* de l'Académie des Sciences, Arts et Belles-Lettres de Dijon, 109:119-136.

"In memoriam". (1914). Bibliothèque Municipale, Dijon. [The anonymous author was a Darcy family member.]

Isambert, Y. (1965), "Darcy". *Dictionnaire de biographie française*, 10, 166-167, d'Amat, R. and Limouzin-Lamothe, R. (eds). Letouzey, Paris.

Jobert, P. (1991). *Les patrons du second empire*, Picard-Cénomane, Paris.

TABLE OF CONTENTS

KEYNOTE PAPERS

MULTI-SCALE MODELING IN LIQUID COMPOSITE MOLDING

Suresh G. Advani, Nina Barnett, FuPing Zhou and Pavel Simacek

Department of Mechanical Engineering and Center for Composite Materials
University of Delaware, Newark, DE 19711

ABSTRACT:

In Liquid Composite Molding (LCM), fibrous preform is placed within a mold and injected with liquid resin. Once the preform is saturated, the resin cures and the finished component is de-molded. There are many variations of the process, most important being Resin Transfer Molding (RTM) in which the two-sided mold is rigid and resin is injected under positive pressure. Second widely used variation is the Vacuum Assisted Resin Transfer Molding (VARTM) in which the mold is one sided, preform is covered with a flexible bag and vacuum is drawn. The resin is drawn into the preform due to the pressure gradient. In this case, highly permeable distribution media is placed on one face of the perform to speed the injection. In all these processes, it is imperative that the preform is sufficiently saturated during the resin injection. Otherwise, the resulting part will contain inadmissible void content. To ensure successful filling, numerical analysis of the flow process has been widely applied.

The complication arises from the internal structure of textile reinforcement generally used in LCM. Preforms usually consist of woven or braided fiber tows. Under this "macrostructure" there is the underlying "microstructure" of fiber tows, consisting of aligned fibers. On both levels of its structure the reinforcement acts as porous medium. As the scale of the pores between the fiber tows (macro-pores) is several orders of magnitude larger than that of pores within the fiber tows (micro-pores) it creates a dual scale porous medium. The result of dual-scale structure is that the resin flow progresses at different rates within the macro- and micro-pores. The flow-front advances through the macro-pores but micro-pores remain unsaturated in the region behind this "macro" or "unsaturated" flow-front up to the "saturated" flowfront.

Usual numerical modeling of the flow cannot capture this effect as it utilizes the concept of homogenous porous media and, therefore, a single flow-front. Depending on the structure of the reinforcement, this approach might prove sufficient, but it cannot capture some effects observed experimentally, and, most importantly, predict the fiber tow saturation whenever there is a significant lag between the saturated and unsaturated flow-fronts.

The dual scale flow can be modeled by using Darcy's law to describe flow through porous medium and mass conservation for the flow within the larger pores and representing the smaller pores can be included within these equations as a sink term. Alternatively, in this paper, we present the standard finite element/control volume approach and model the "internal" sink term by appending extra one-dimensional elements to control volumes associated with the control volumes of discretized part geometry to represent the resin sink. This approach allows one to solve the problem efficiently using existing simulation package for RTM filling simulation.

To model the single scale flow through porous medium one requires only limited description of the porous medium: its porosity and its permeability. The mutil scale model is more accurate, but it requires additional material parameters to characterize not just the "macro" properties but also the effective "micro" properties of the fiber tows. In this paper, we analyze the material properties necessary to characterize the dual-scale flow and we present the approach to determine these values from simple 1-D, constant flow-rate injection experiment and show examples of experimental characterization.

The dual-scale model can be used to provide more accurate information about the resin flow in macro-pores, but most importantly it allows one to predict the degree of saturation of micro-pores within fiber tows. For example, this allows one to determine the necessary "bleeding" time after the macro-flow reaches the vent to saturate the fiber tows. In this paper we present optimization of the bleeding time and application of flow resistance at the vent location to achieve satisfactory fiber tow saturation and compare the numerical results with the experimental data. Finally, we demonstrate how to model the saturation of fiber tows in VARTM process with distribution media, where the resin flow from collapsing distribution media continues to saturate fiber tows even after the injection is terminated.

COMPOSITE MATERIAL PARTS IN RENAULT CARS : THE PAST, THE PRESENT AND THE FUTURE

Alain Giocosa – Renault
General Manager of Polymers Engineering Department
Material Engineering Department

In this presentation, I would like to present some applications for composite materials (thermoplastic and thermoset) in Renault cars, especially for large series vehicles.

My proposed outline is as follows:

- First of all, I would like to make some comments on **customer perception**, based on an ESTEL survey conducted of 400 new-car buyers and to give an overview of composite materials used in Renault cars.

- Then, I would like to spend some time explaining why composite materials have been used and where these materials have been used : that is to say the **past situation since over 30 years.**

- Next, I will give several examples of what Renault is using nowadays : **the present and current uses and developments going on.**

- Lastly, I will try to explain what will be **the future of composite materials** and what we need to increase new applications.

- **Customer perception** : During the ESTEL survey 4 main questions were asked to customers :

1. "What score, on a scale of 1 to 10, would you give to plastics for different characteristics ?" (safety, reliability, corrosion …).
2. The same question for the same characteristics, but comparing steel, aluminum and plastic.
3. "Did exterior materials influence your choice of model ?"
4. "In the future, which materials do you think will be increasingly used for car exteriors ?"

The answers show that the customer perception of different materials is quite reasonable, that materials are not the decisive factor to choose one car among another and that plastic is overwhelmingly seen as the material of the future, aluminum and especially steel are left far behind.

- **Overview of composite materials in Renault cars** : a breakdown of the different materials used in a car will give an idea of the weight ratio of ferrous, non ferrous, mineral and organic materials used in an average car.

- **Why composite materials have been used since 30 years ?**
  The main reasons are : weight saving to reduce gas emissions and fuel consumption, safety, cost reduction and customer's needs.

- **Where composite materials have been used since 30 years ?**
  Some examples of applications since 30 years will be described.

- **The present and current uses and developments going on.**
  A breakdown will show the main functions where composite materials are used today in a car and some examples will be outlined and explained.
  The current developments in composite materials will be discussed, especially the trend to go from current semi structural applications to structural applications : we need new composite materials, new composite manufacturing technologies and new composite design developments. An example of the development of a "high speed" RTM process will be given through the TECABS project.

- **The future of composite materials** : to increase the use of composite materials the part manufacturers will have to increase part quality, to have a better knowledge on composite material behavior, to improve manufacturing processes and to develop accurate calculation tools. On the other hand car manufacturers will have to work on how to introduce composite parts in the manufacturing car process and to develop joining technologies compatible with multi-material cars.
  Both we will have to work on recycling and waste management solutions.

In the conclusion, I will outline that the use of composite materials has increased by 200 % over 30 years, a strong potential still exists for structural parts but metallic materials, aluminum and magnesium, are severe competitors and that we have to overcome two main drawbacks of composite parts : recycling and cost.

Summary

- Custumer perception of materials
- Overview of composite materials in Renault cars
- Why composite materials have been used since 30 years ?
- Where and how composite materials have been used since 30 years ?
- Main functions where composite materials are used today
- Current developments going on
- The future of composite materials : how to increase their use ?
- Conclusion

CUSTOMER PERCEPTION OF MATERIALS

Which mark would you give to plastics related to …?

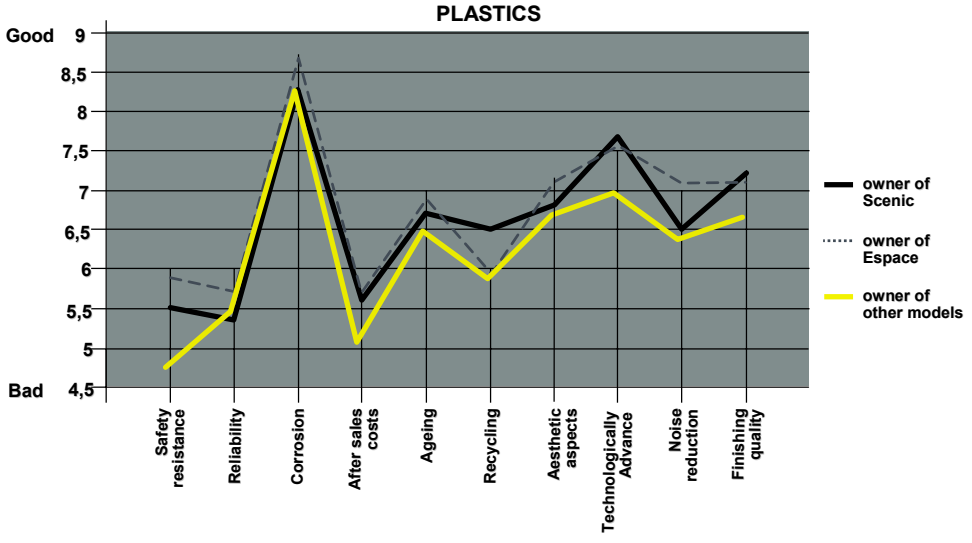

DREAM – DIMat – A. GIOCOSA – 11/13 Juillet 2006 P / 3

CUSTOMER PERCEPTION OF MATERIALS

Which mark would you give to steel, aluminium, plastics related to …?

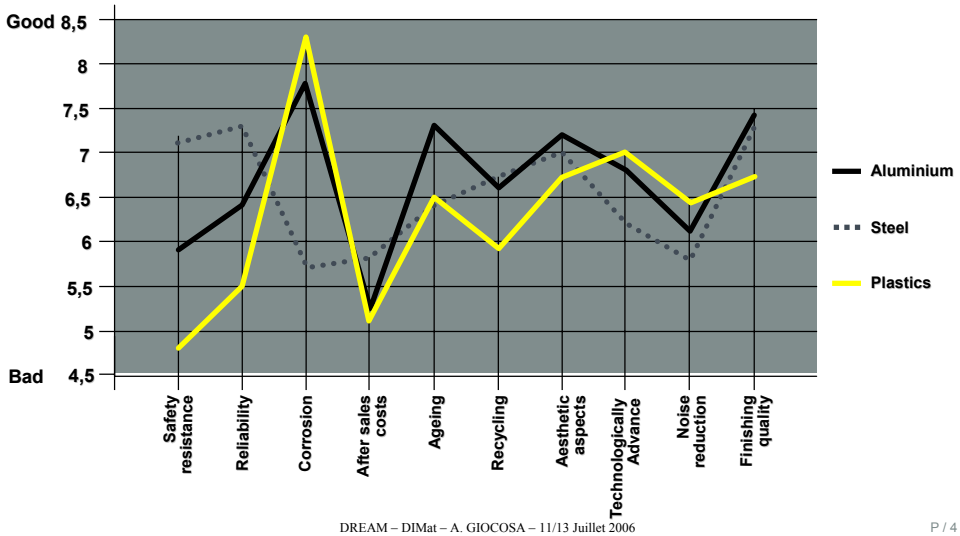

DREAM – DIMat – A. GIOCOSA – 11/13 Juillet 2006 P / 4

CUSTOMER PERCEPTION OF MATERIALS

DID EXTERIOR MATERIALS INFLUENCE YOUR CHOICE OF MODEL ?

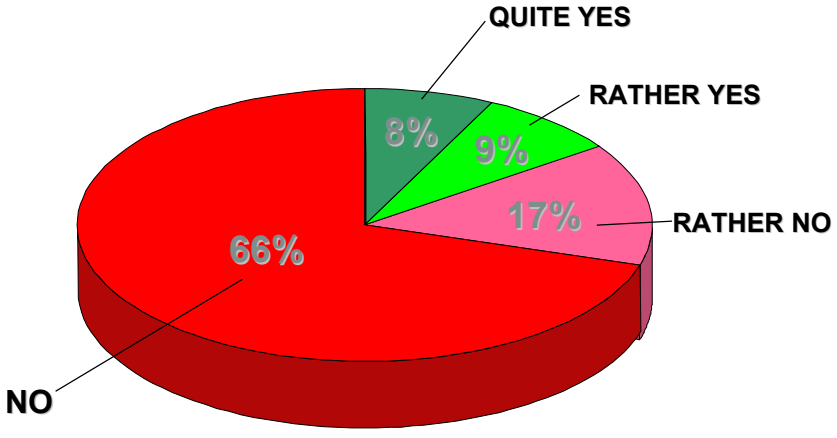

DREAM – DIMat – A. GIOCOSA – 11/13 Juillet 2006 P / 5

CUSTOMER PERCEPTION OF MATERIALS

IN THE FUTURE, WHICH MATERIALS DO YOU THINK WILL BE INCREASINGLY USED FOR CAR EXTERIORS ?

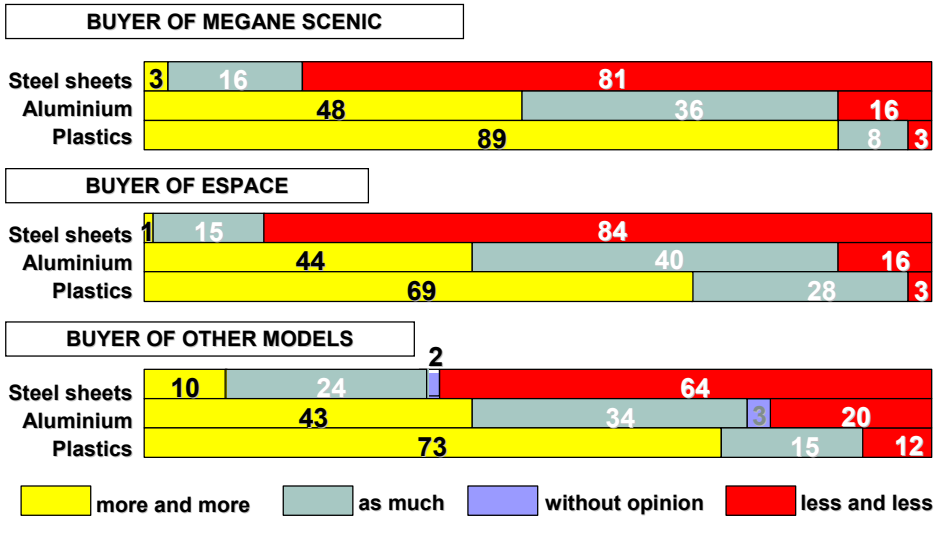

DREAM – DIMat – A. GIOCOSA – 11/13 Juillet 2006 P / 6

Overview of composite materials in Renault cars

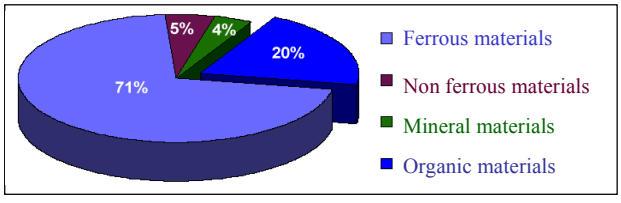

Weight ratio of materials in a car

Weight ratio of organic materials in a car

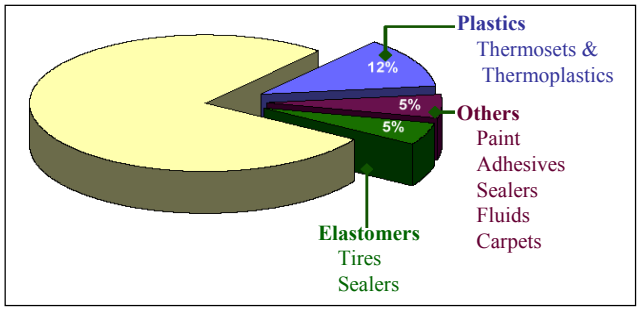

Why composite materials have been used since 30 years ?

- **Reduction of gaz emissions - Fuel consumption**
  - ***Reduction of CO_2 emissions (CAFE)***

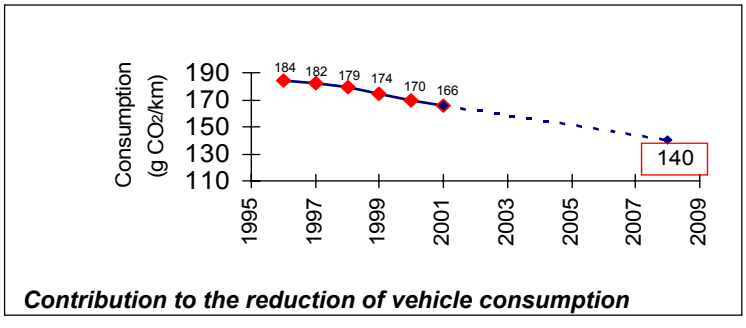

Contribution to the reduction of vehicle consumption

Source ACEA

Gain of composite materials = Reduction of vehicle weight
100kg saved = Decrease of 0.4 l/100km (stabilized speed)

Why composite materials have been used since 30 years ?

◆**Vehicle safety**

– ***No damage at low speed crash (4km/h)***

– ***New regulation concerning pedestrian impact***
Low pedestrian damage during crash

– ***Low repairing costs***

Removable crash area

Energy absorption curve of a SMC/BMC Material

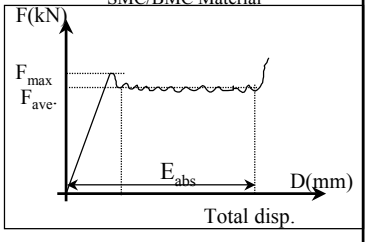

Why composite materials have been used since 30 years ?

◆ **Cost Reductions**

– ***Increase of version number per vehicle model***

New Renault Megane : 5 different rear floor pans for 7 models

➡ *Reduction of the production volumes per model*

– ***Low tooling cost (for low to medium production volumes)***

– ***Simplification of manufacturing processes***
No machining processes
Multifunctionnal parts

Why composite materials have been used since 30 years ?

- **Customer's needs**
  - ***Low cost in use***
  - ***Safety, Comfort, Reliability***
    Increase of constructor warranty (2 years --> 12 years)
    Fatigue properties increased with composite materials
  - ***Image and new services***

Vel Satis tailgate

Renault Kangoo : under roof boxes

Where and how composite materials have been used since 30 years ?

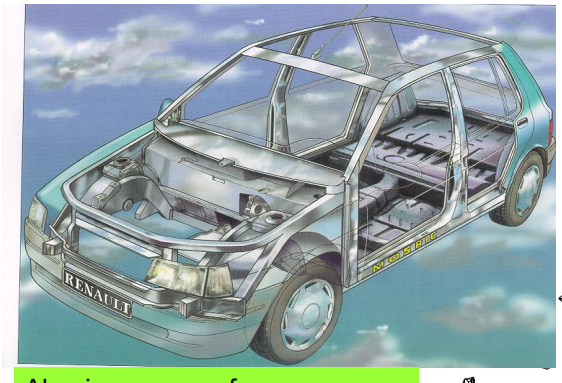

MOSAIC Project 1994

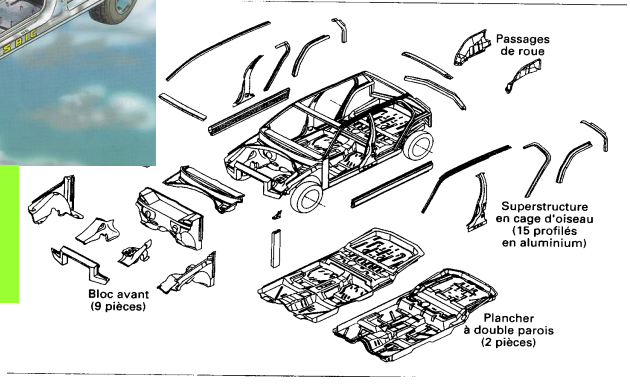

Aluminum space frame
Extrusion and cast node
Composites Integrated panels
Riveting + Adhesive bonding

Weight saving 20%
Overcost 20-40%

Where and how composite materials have been used since 30 years ?

◆ **SMC bumpers evolution**


R5, bumpers & trims


R15, bumper


R14, bumpers


Fuego, bumper


R25, bumpers & trims

Where and how composite materials have been used since 30 years ?

◆ **SMC body panels painted at low temperature**


Alpine A610


Espace 2


Espace 3 (except bonnet)


Avantime

Where and how composite materials have been used since 30 years ?

- **SMC/BMC components evolution**

1972 - Bumpers & trim unpainted part

1983 - SMC body panels Painted at low temperature

2000 - SMC tail gate Painted off line

2001 - SMC fenders Painted on line

Where and how composite materials have been used since 30 years ?

Trafic rear spring leaf :
- Weight saving : from 15 to 20 kg,
- Same cost / double steel spring leafs
- pre-preg epoxy glass LF (50/50 vol).

New transversal front suspension :
- epoxy – glass fabric,
- “High speed” RTM.

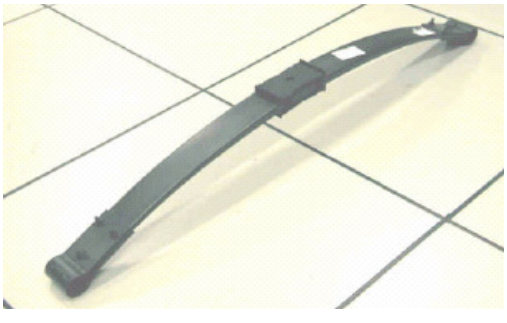

Main functions where composite materials are used today

◆ **Today's distribution of composite materials in a car**

• Interior accessories	50%
• External accessories	20%
• Under hood applications	15%
• External body panels	10 - 15%
• Structural applications	0 - 5%

Main functions where composite materials are used today

◆ **Composite materials for interior applications**

Clutch pedal
PA +GF

Roof panel
PP + Nat. Fib. or GF

Dash board structure
TP + fillers or GF

Door panel
TP + Wood

Main functions where composite materials are used today

◆ **Composite materials for exterior applications : SMC and TP fenders**

SMC fenders
Medium production volume cars

ThermoPlastic fenders
High production volume cars

Main functions where composite materials are used today

◆ **Thermoplastic fenders across the range**

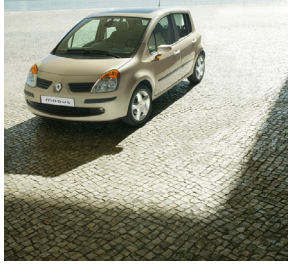

Main functions where composite materials are used today

◆ **Composite materials for exterior applications : SMC / BMC tailgates**

DREAM – DIMat – A. GIOCOSA – 11/13 Juillet 2006 P / 21

Main functions where composite materials are used today

◆ **Composite materials for exterior applications : Scénic RX4 hybrid tailgate**

DREAM – DIMat – A. GIOCOSA – 11/13 Juillet 2006 P / 22

Main functions where composite materials are used today

◆ **Composite materials for exterior applications : Modus split tailgate**

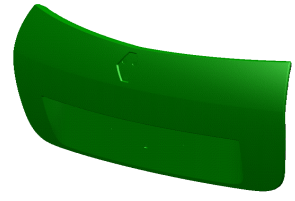

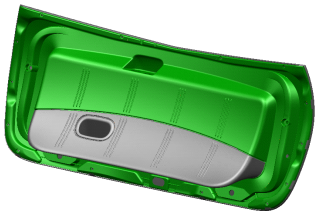

- **Skin panel painted Polypropylene (same as bumper)**
- **Inner panel GF reinforced PP – grained and bulk colored**
- **Additional element PP – grained and bulk colored (same as interior panels).**

Main functions where composite materials are used today

◆ **Composite materials for under the hood parts**

Under engine protection
PP + GF

Air filter
PA+GF

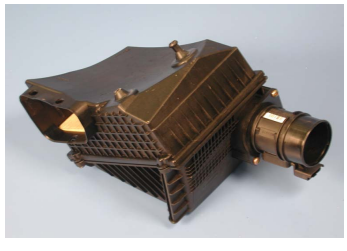

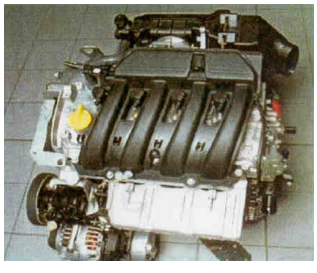

Intake manifold
PA + GF
Cost reduction : 30%
Weight reduction : 30%

Main functions where composite materials are used today

◆ **Composite materials for structural parts**

Rear floor pan (Mégane 2)
Low density SMC

Technical front end (Mégane 2)
PA+GF
+ Steel structure

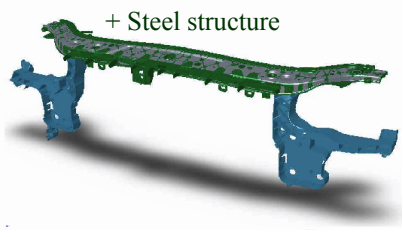

DREAM – DIMat – A. GIOCOSA – 11/13 Juillet 2006 P / 25

Main functions where composite materials are used today

◆ **Rear floor pan modularity (Mégane 2)**

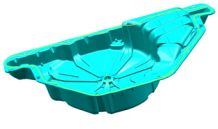

BC84

Rear overhang : 742mm

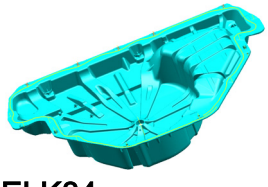

ELK84

Rear overhang : 970 to 991mm

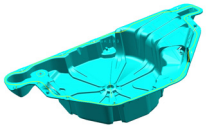

J84

Rear overhang : 723mm

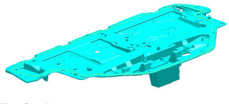

R84

Rear overhang : 906mm

Steel reinforced

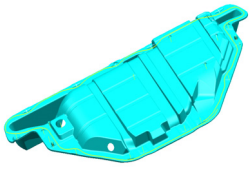

B84 LPG

DREAM – DIMat – A. GIOCOSA – 11/13 Juillet 2006 P / 26

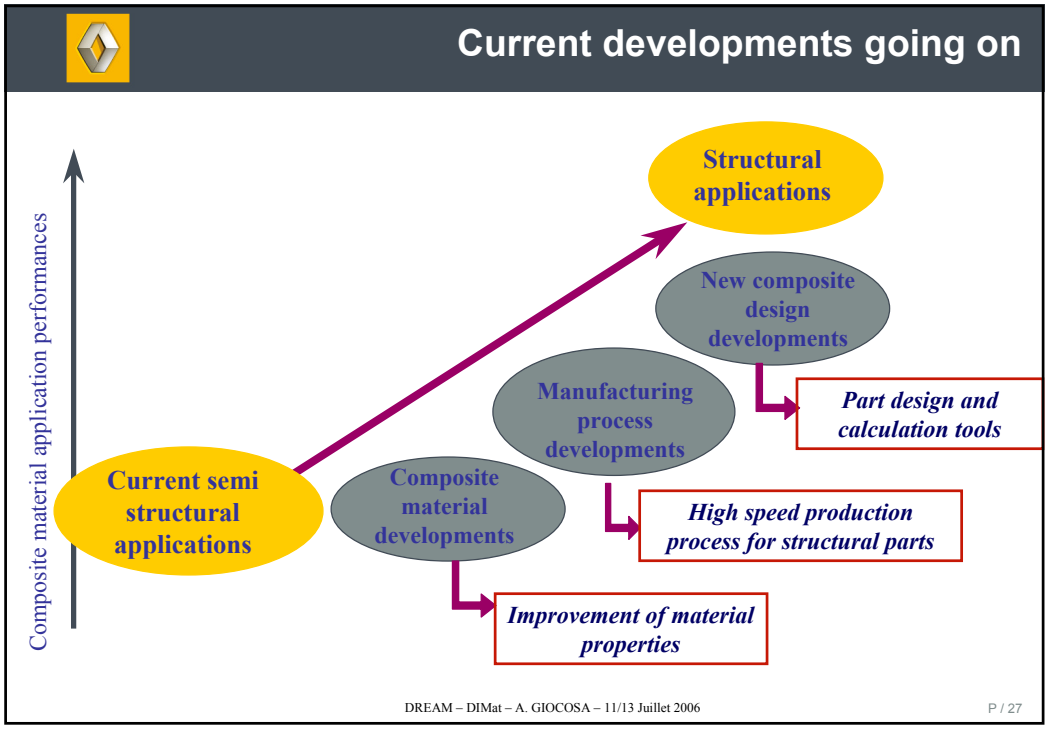
Current developments going on
Composite material application performances
Structural applications
New composite design developments
Manufacturing process developments
Part design and calculation tools
Current semi structural applications
Composite material developments
High speed production process for structural parts
Improvement of material properties
DREAM – DIMat – A. GIOCOSA – 11/13 Juillet 2006
P / 27

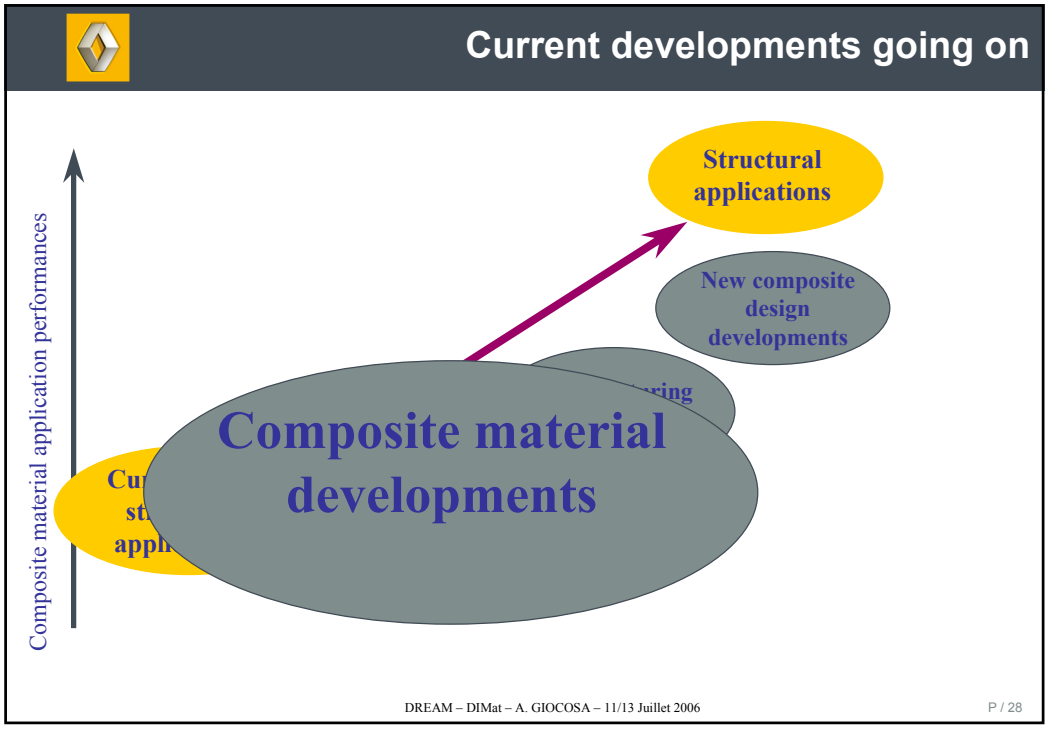
Current developments going on
Composite material application performances
Structural applications
New composite design developments
Composite material developments
DREAM – DIMat – A. GIOCOSA – 11/13 Juillet 2006
P / 28

Current developments going on

◆ **New composite materials : Targets**

- ***Costs effective parts***
- ***Improvement of composite part properties***
- ***Introduction of composite parts in the car manufacturing process***

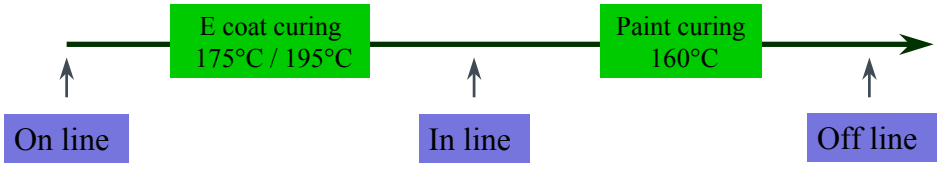

Current developments going on

◆ **New composite materials : Some examples**

- ***Composite materials reinforced with nano fillers***
  Introduction of mineral nano fillers or carbon nano tubes in TP matrix
  Semi structural applications (body panels, under the hood parts)
- ***Composite materials reinforced with natural fibers***
  Introduction of natural fibres (Hemp, flax ...) in TP and thermoset matrix
  Semi structural applications (Interior applications)
- ***Composite materials reinforced with carbon fibers***
  Introduction of short carbon fibres, or carbon fibre fabrics
  Structural parts (floor pans, cross beams, Body In White parts …)
  Semi structural parts (openings)

Current developments going on

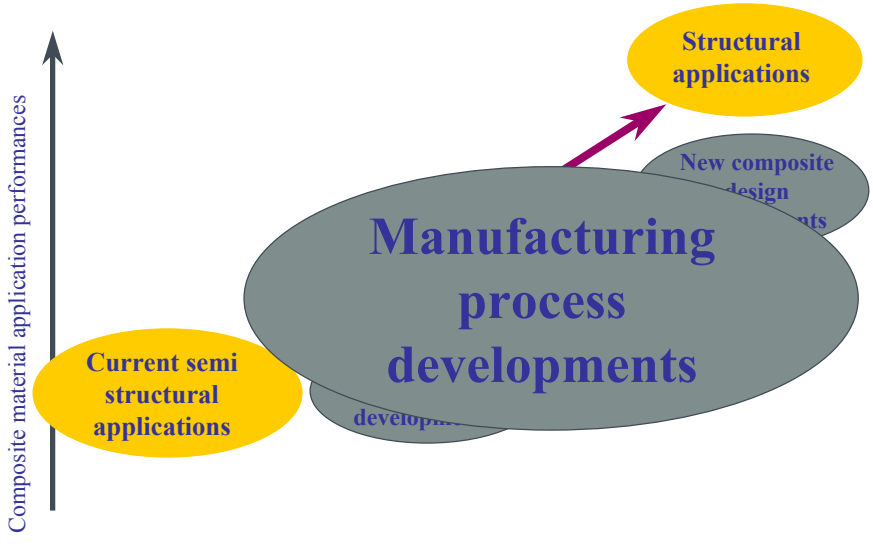

Current developments going on

- **New composite manufacturing technologies : Targets**
  - ***Cost effective process***
    Integration of functions
    Waste reduction
  - ***Production of structural composite parts***
    Use of long fibre reinforcements and fabrics
  - ***At least medium production volumes (100 - 700 parts / day)***
  - ***Production of high quality composite parts***

Current developments going on

- **New composite manufacturing technologies : Research area**
  - ***Manufacturing process***
    New manufacturing tools
    Improvement of process parameters
  - ***Process calculation tools***
    Selection of the best manufacturing strategy
    Reduction of development duration
    Reduction of prototyping step
  - ***Improvement of material processability***
    Resin reactivity
    Fabric drapability

Current developments going on

- **New composite manufacturing technologies : Development of a «High Speed» RTM process**
  - ***High fibre ratio (up to 50%)***
  - ***Use of carbon fibre reinforcements***
  - ***Complex shape : part with hollow cores***
  - ***Improvement of injection step***
  - ***Improvement of resin curing***
  - ***Production time < 10 min***

Part developed in the TECABS project

Current developments going on

- **New composite manufacturing technologies : Process calculation tools**
  - ***Material behavior description***
    Definition of local material properties
  - ***Strong impact of part structure***
    Geometrical singularities
    Structural singularities (sandwich structures ...)
  - ***Influence of material properties evolutions***
    Viscosity,
    Fibres / matrix segregation (SMC)

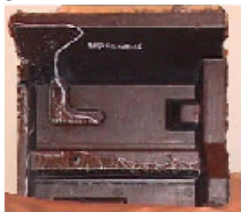

From TECABS project

DREAM – DIMat – A. GIOCOSA – 11/13 Juillet 2006 P / 35

Current developments going on

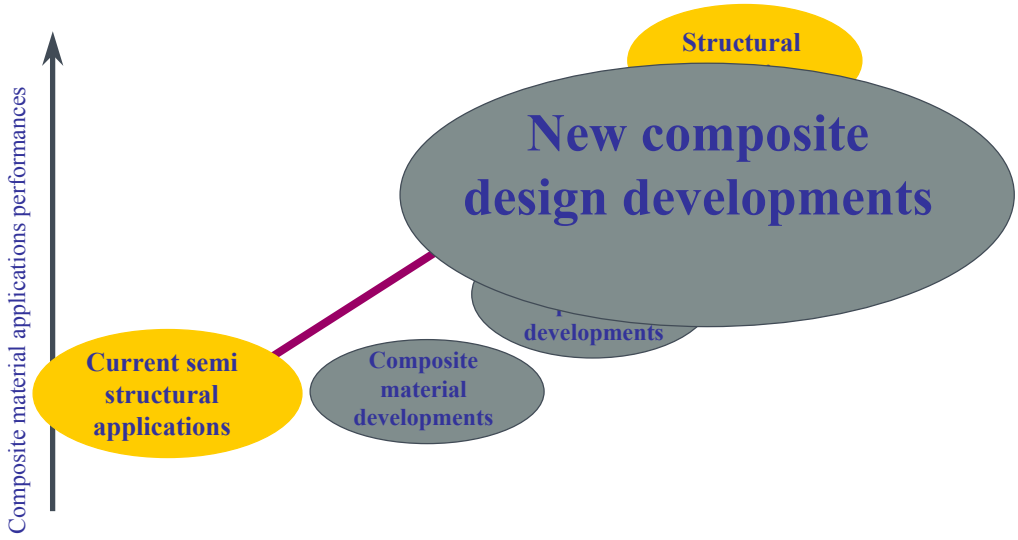

DREAM – DIMat – A. GIOCOSA – 11/13 Juillet 2006 P / 36

Current developments going on

◆ **New composite design developments : Targets**

- *Lightweight innovative composite parts*
- *Increase performance part versus metallic solution*
- *Improvement of calculation tools for designing composite parts*

Current developments going on

◆ **New composite design developments :**

- **Tailgate with carbon fibre reinforced materials**

	Weight saving (%)
Steel version	Ref
SMC reinforced GF version	15%
SMC reinforced CF version	25%

- **Structural rear floor pan**

	Weight saving (%)	Cost
Steel version	Ref	1
Metal / composite version	15%	1
Composite reinforced GF version	38%	1.2
Composite reinforced CF version	47%	2.2

Current developments going on

- **New composite design developments : calculation tools**
  - ***Virtual validation of composite part behavior***
    Static behavior
    Dynamic behavior

Ex : Composite LPG tank

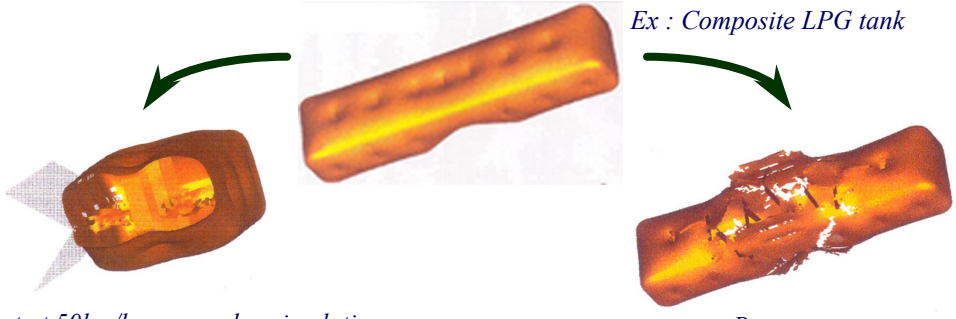

Impact at 50km/h on an edge simulation

Burst test

DREAM – DIMat – A. GIOCOSA – 11/13 Juillet 2006 P / 39

The future of composite materials

- **Trend of composite materials evolution in the automotives**

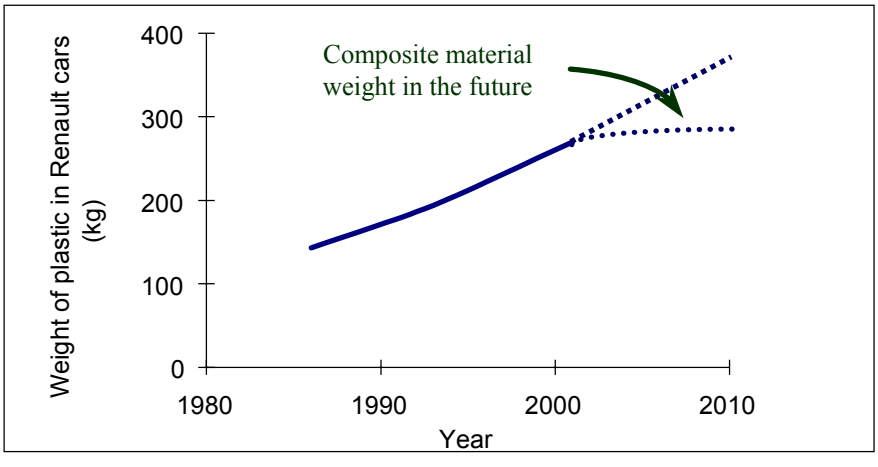

DREAM – DIMat – A. GIOCOSA – 11/13 Juillet 2006 P / 40

The future of composite materials

◆ **How to increase the use of composite materials ?**

- **Improvement of part quality**
  Improvement of surface aspect for body panels applications
  (SMC parts)
- **Better knowledge on composite material behavior**
  Dynamic behavior
  Durability
- **Manufacturing processes**
  Reliable manufacturing process
  Good part quality
- **Accurate calculation tools**
  Overall trend : increase of virtual prototypes

The future of composite materials

◆ **How to increase the use of composite materials ?**

- **Introduction of composite part in the manufacturing car process**
  No influence on the manufacturing car process
- **Development of multi-material joining**
  Strong joining for structural applications
  Removable assembling techniques (After Market ...)
- **Reduction of material costs**
  Case of High Tow Carbon Fibres
  Today : 12 - 17 Euros / kg
  Future : 8 - 10 Euros / kg ??

The future of composite materials

◆ **How to increase the use of composite materials ?**

- **Recycling Aspects**
  - ***End of Life Vehicle (ELV) European directive for 2015***
    - 95% of the vehicle by weight should be re-used or recovered
    - 5% of vehicle by weight could go to landfill
    - 10% of vehicle by weight could be incinerated
  - ***Development of recycling and waste management solutions***
    Cost effective recycled materials
    Cost effective waste treatments

Conclusion

- **The use of composite materials has increased by 200% over 30 years.**
- **A strong potential still exists for structural parts but the introduction of composite materials is difficult.**
- **The introduction of composite materials in a new vehicle project is long : complete development needs 10 years.**
- **Steel, Aluminum, Magnesium, are severe competitors of composites.**
- **The choice of a car manufacturer takes into account the part requirements and costs and NOT the material.**

Session 1

PERMEABILITY PREDICTION – I

FINITE POINTSET METHOD (FPM): A MESHFREE APPROACH FOR INCOMPRESSIBLE FLOW SIMULATIONS APPLIED TO COMPOSITE MATERIALS

Alain Trameçon[1], Patrick de Luca[1], Christophe Binetruy[2] and Jörg Kuhnert[3]

[1] *ESI-GROUP*
Parc d'affaire SILIC, 99 Rue des Solets, BP 80112 F-94513 RUNGIS, FRANCE:
atr@esi-group.com

[2] *Polymers and Composites Technology & Mechanical Engineering Department*
Ecole des Mines de Douai, 941 Rue Charles Bourseul, F-59508 DOUAI, France :
binetruy@ensm-douai.fr

[3] *Fraunhofer Institute for Industrial Mathematics (ITWM)*
Gottlieb-Daimler-Straße, D-67663 KAISERSLAUTERN, GERMANY:
kuhnert@itwm.fhg.de

ABSTRACT: A meshfree particle method is used to simulate resin flow through a complex network of fibers. Flows are modeled by the incompressible Navier-Stokes equations. The particle projection method is used to solve the Navier-Stokes equations. The spatial derivatives are approximated by the weighted least squares method (WLS). One application is presented regarding the application of the method to numerical permeability prediction, related to LCM processes.

KEYWORDS: Mesh-free method, incompressible Navier-Stokes equations, least squares (LSQ) approximation, LCM, permeability prediction

INTRODUCTION

Meshfree techniques

In this paper we present a mesh-free method called FPM (Finite Point Method) for simulations of resin transfer moulding through a complex network of fibers. This method was developed by Dr Jorg Kuhnert at ITWM in Germany. A fluid domain is first replaced by a discrete number of points, which are referred to as particles. Each particle carries all fluid information, like density, velocity, temperature etc. and moves with fluid velocity. Therefore, particles themselves can be considered as geometrical grids of the fluid domain. This method has some advantages over grid based techniques, for example, it can handle fluid domains, which change naturally, whereas grid based techniques require additional computational effort. Or they are able to simulate the flow in very complicated domains, which would be impossible or difficult to mesh.

A classical grid free Lagrangian method is Smoothed Particle Hydrodynamics (SPH), which was originally introduced to solve problems in astrophysics (Lucy 1977, Gingold et al. 1977). It has since been extended to simulate the compressible Euler equations in fluid dynamics and applied to a wide range of problems, see (Monaghan 92, Monaghan et al. 1983, Morris et al. 1997). The method has also been extended to simulate inviscid incompressible free surface flows (Monaghan 94). The implementation of the boundary conditions is the main problem of the SPH method.
Another approach for solving fluid dynamic equations in a grid free framework is the moving least squares or least squares method (Belytschko et al. 1996, Dilts 1996, Kuhnert 99, Kuhnert 2000, Tiwari et al. 2001 and 2000) which derived in the Finite Pointset Method (FPM). With this approach boundary conditions can be implemented in a natural way just by placing the particles on boundaries and prescribing boundary conditions on them (Kuhnert 99). The robustness of this method is shown by the simulation results in the field of airbag deployment in car industry. Here, the membrane (or boundary) of the airbag changes very rapidly in time and takes a quite complicated shape (Kuhnert et al. 2000).

FPM fluid code

FPM is a meshfree CFD finite difference code, mainly designed to overcome several drawbacks of classical CFD methods (Finite Element Method (FEM) , Finite Volume Method (FVM)). The main drawback of the classical methods (FEM,FVM) is the relatively expansive geometrical mesh-grid required to carry out all numerical computations. The computational cost to establish and maintain these grids becomes more dominant as the considered geometry becomes complex or moves in time. For several applications, the effort for grid maintenance is beyond acceptance, the computations take too long or fail completely. Thus, FPM opens up new fields of application in computational structural and fluid mechanics, or makes the handling of several problems much more easy.

General Equations

FPM is a mesh-free thermal CFD code for incompressible and compressible flows. FPM includes newtonian viscosity, natural convection, heat conduction, heat exchange at the boundaries.
FPM solves the general Navier Stokes equation as written below in a Lagrange form :

$$\begin{aligned} &\tfrac{d}{dt}\rho + \rho\cdot\nabla\mathbf{v} = 0 \\ &\tfrac{d}{dt}(\rho\mathbf{v}) + (\rho\mathbf{v})\cdot\nabla v + \nabla p - \nabla\mathbf{S} = \rho\cdot\mathbf{g} \\ &\tfrac{d}{dt}(\rho E) + (\rho E)\cdot\nabla\mathbf{v} + \nabla(p\cdot\mathbf{v}) - \nabla(\mathbf{S}\cdot\mathbf{v}) = (\rho\cdot\mathbf{g}\cdot\mathbf{v}) + \nabla\cdot(k\nabla^T T) \end{aligned} \qquad (1)$$

v : fluid velocity
ρ : density
p : pressure
S : deviatoric stresses
g : gravity
T : temperature
E : specific total energy per unit mass

For incompressible flows, these equations can be simplified as follows :

$$\begin{aligned} \tfrac{d}{dt}\rho = 0 \quad &\Rightarrow \quad \nabla \mathbf{v} = 0 \\ \tfrac{d}{dt}\mathbf{v} &= -\frac{1}{\rho}\nabla p + \frac{\eta}{\rho}\cdot\Delta\mathbf{v} + \mathbf{g} \\ \tfrac{d}{dt}T &= \frac{1}{\rho\cdot c}\cdot\nabla(k\cdot\nabla T) \end{aligned} \qquad (2)$$

Moving Least Square (MLS) approximation

FPM does not require the support of a mesh and therefore values are known at discrete "interpolation" points, which do not have a fixed connection like finite elements between them. The list of neighbor points is determined for each point at each time step in order to construct afterwards a proper interpolation function as described in Fig.1. For this purpose, a smooth interpolation of the discrete function values is constructed using polynomial functions, best fitted to the discrete values using a moving least square method (Fig.2).

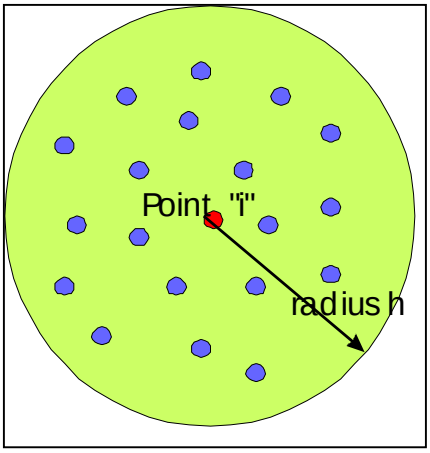

Fig. 1: Smoothing length

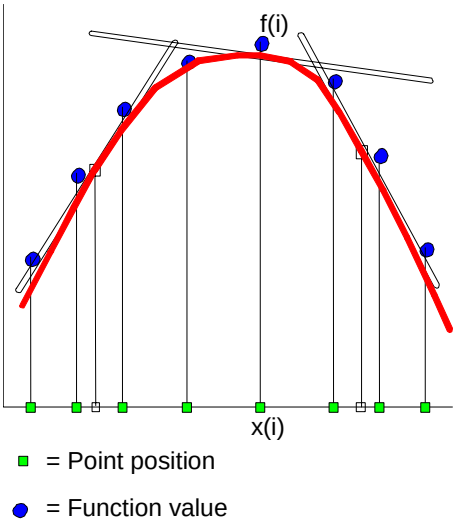

Fig. 2 : Moving least square method : f(i) stands for the value of point I of the function to be interpolated : pressure, density, velocities, temperature.

The interpolation function that is constructed is based upon the Moving Least Square (MLS) approximation. The idea is to find the local polynomial which minimizes the distance between the values at the discrete points and the approximated values on the function. This is done using a least square fit method as follows:

$$\sum_{i=1,N} W(x-x_i)(f_i - p_d(x,x_i))^2 \stackrel{!}{=} \min \tag{3}$$

where d is the degree of the polynom, d>=2 for Navier-Stokes as second order derivatives are required.

The weight function W(x-xi) decreases with respect to the distance between the location x of the central point and the neighbor points xi, so that points which are far away from the central point will have less influence than points which are closer. The domain of interpolation is limited by a sphere of radius h, called the smoothing length, so that points which have a distance greater than h will have no interaction.
The interpolation function can afterwards be derived. For Navier Stokes incompressible cases, second order derivatives have to be computed. In order to maintain an even distribution, points are generated or removed automatically during the simulation.

APPLICATION TO NUMERICAL PERMEABILITY PREDICTION

In order to perform accurate LCM filling simulations, physical parameters such as fabric permeability are needed. It is well known that the experimental measurement of that fabric property is very delicate.

Usually a fluid is injected at constant pressure (or constant flow rate) through several layers of fabric of cross section A and length L. Then pressure loss Δp and flow rate Q are measured, and the permeability K is calculated using Darcy's law:

$$K = \frac{QL\mu}{A\Delta p} \tag{4}$$

The simulation of flow through a periodic cell should provide a reliable solution and avoid that experimental procedure. Numerically, an injection at constant flow rate could be performed. Then the pressure loss can be computed by the FPM code and the permeability is also given by Eqn. 4. Fig.3 shows the fabric cell considered here for benchmark purpose (Belov et al, 2004). It is bounded by a box in contact with yarns that defines the computational domain. Shell elements surrounding the fiber tows prevent the particles from escaping the domain with proper contact. Also particles are not allowed to penetrate the tows. Finally the tows are considered to be rigid and fixed in space. The porosity of such a domain is 0.36.
Starting from an initially unfilled cavity, the domain is automatically filled by particles. The inflow velocity is constant and equal to 0.01 m/s. The fluid viscosity is constant and equal to 0.01 Pa.s. The computed pressure loss is ΔP= 417,6 Pa giving a saturated permeability of 2.28×10^{-10} m^2. Computations last around 20 minutes with a state of the art PC.

According to Belov et al., the saturated permeability of a single layer of such fiber reinforcement is in between 2.6 $\times 10^{-10}$ m^2 and 3.5 $\times 10^{-10}$ m^2 using the Lattice Boltzmann Method (LBM). Measurements provided values between 1.34 $\times 10^{-10}$ m^2 and 1.49 $\times 10^{-10}$ m^2.
The FPM code provides results in good agreement with experimental data.

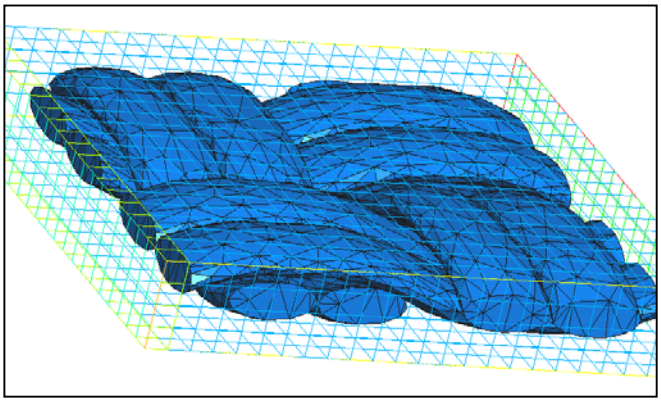

Fig. 4 : Fabric unit cell and domain used for the calculations

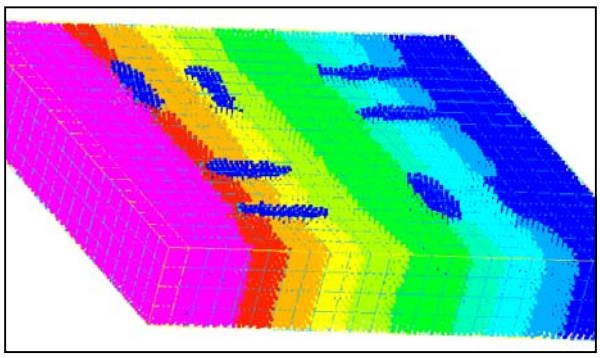

Fig.5 : Computed flow patterns and pressure field (blue spots are contact zones not wetted by the fluid)

CONCLUSION

FPM solves for compressible and incompressible flow problems and can be coupled to structural FE codes. An important feature regarding polymer composites manufacturing science is that chemical reactions, heat transfer, temperature dependent viscosity can be handled. To illustrate the potential of the code, the case of numerical permeability prediction of a fabric unit cell has been presented and compared with existing experimental data. The FPM code provides results in good agreement with experiments. Current work focuses on flow-induced fiber deformation.

REFERENCES

ASH N., POO J. Y., Coalescence and separation in binary collisions of liquid drops, *J. Fluid Mech*., vol. 221, 1990, p. 183 - 204.

Belov E. B., Lomov S. V., Verpoest I. , Peters T. , Roose D. , Parnas R. S., Hoes K. , and Sol H. . Modelling of permeability of textile reinforcements : lattice boltzmann method. *Comp. Sci. Tech.*, 64 :1069–1080, 2004.

BELYTSCHKO T., KRONGAUZ Y., FLEMMING M., ORGAN D., LIU W.K.S., Smoothing and accelerated computations in the element free Galerkin method, *J. Comp. Appl. Maths,*. vol. 74, 1996, p. 111-126.
CHORIN A., Numerical solution of the Navier-Stokes equations, *J. Math. Comput*,. vol. 22, 1968, p.745-762.

DILTS G. A., Moving least squares particle hydrodynamics. I: consistency and stability, *Hydrodynamics methods group report*, Los Alamos National Laboratory, 1996

GINGOLD R. A., MONAGHAN J. J., Smoothed particle hydrodynamics: theory and application to non-spherical stars, *Mon. Not. Roy. Astron. Soc.*, vol. 181, 1977, p. 375-389.

GINZBURG I., WITTUM G., Two-phase flows on interface refined grids modeled with VOF, staggered finite volumes, and spline interpolants, *J. Comp. Phys.,*. vol. 166, 2001, p. 302-335.

HANSBO P., The characteristic streamline diffusion method for the time dependent incompressible Navier-Stokes equations, *Comp. Meth. Appl. Mech. Eng*., vol. 99, 1992, p. 171-186.

HARLOW F. H., WELCH J. E., Numerical study of large amplitude free surface motions, *Phys. Fluids*, vol.8, 1965, p. 2182.

HIRT C. W., NICHOLS B. D., Volume of fluid (VOF) method for dynamic of free boundaries, *J. Comput. Phys.*, vol. 39, 1981, p. 201.

KELECY F. J., PLETCHER R. H., The development of free surface capturing approach for multi dimensional free surface flows in closed containers, *J. Comput. Phys*., vol. 138, 1997, p. 939.

KOTHE D. B., MJOLSNESS R. C., RIPPLE: A new model for incompressible flows with free surfaces, *AIAA Journal*, Vol. 30, No 11, 1992, p. 2694-2700.

KUHNERT J., *General smoothed particle hydrodynamics*, Ph.D. thesis, Kaiserslautern University, Germany, 1999.

KUHNERT J., An upwind finite pointset method for compressible Euler and Navier-Stokes equations, *preprint, ITWM, Kaiserslautern*, Germany, 2000.

KUHNERT J., TRAMECON A., ULLRICH P., Advanced Air Bag Fluid Structure Coupled Simulations applied to out-of Position Cases*, EUROPAM Conference Proceedings 2000*, ESI group, Paris, France

LANDAU L. D., LIFSHITZ E. M., *Fluid Mechanics*, Pergamon, New York, 1959.

LAFAURIE B., NARDONE C., SCARDOVELLI R., ZALESKI S., ZANETTI G., Modelling Merging and Fragmentation in Multiphase Flows with SURFER *, J. Comput. Phys.,* vol. 113, 1994, p. 134 - 147.

LUCY L. B., A numerical approach to the testing of the fission hypothesis, *Astron. J.,* vol. 82, 1977, p. 1013.

MARONNIER V., PICASSO M., RAPPAZ J., Numerical simulation of free surface flows, *J. Comput. Phys*. vol. 155, 1999, p. 439.

MARTIN J. C., MOYCE M. J., An experimental study of the collapse of liquid columns on a liquid horizontal plate, *Philos. Trans. Roy. Soc. London*, Ser. A 244, 1952, p. 312.
MONAGHAN J. J., Smoothed particle hydrodynamics, *Annu. Rev. Astron. Astrop*, vol. 30, 1992, p. 543-574.

MONAGHAN J. J., Simulating free surface flows with SPH, *J. Comput. Phys.*, vol. 110, 1994, p. 399.

MONAGHAN J. J., GINGOLD R. A., Shock Simulation by particle method SPH, *J. Comp. Phys*., vol. 52, 1983, p. 374-389.

MORRIS J. P., FOX P. J., ZHU Y., Modeling Low Reynolds Number Incompressible Flows Using SPH, *J. Comput. Phys*., vol. 136, 1997, p. 214-226.

TIWARI S., KUHNERT J., Grid free method for solving Poisson equation, *Berichte des Fraunhofer ITWM*, Kaiserslautern, Germany, Nr. 25, 2001.

TIWARI S., KUHNERT J., Finite pointset method based on the projection method for simulations of the incompressible Navier-Stokes equations, *to appear in M. Griebel, M. A. Schweitzer (Eds.), Springer LNCSE: Meshfree Methods for Partial Differential Equations,* Springer-Verlag, 2003.

TIWARI S., KUHNERT J., Particle method for simulations of free surface flows, *preprint Fraunhofer ITWM*, Kaiserslautern, Germany, 2000.

TIWARI S., A LSQ-SPH approach for compressible viscous flows, to appear in: *Proceedings of the 8th International Conference on Hyperbolic Problems Hyp2000*.

TIWARI S., MANSERVISI S., Modeling incompressible Navier-Stokes flows by LSQ-SPH, *Berichte des Fraunhofer ITWM*, Kaiserslautern, Germany, 2000.

PERMEABILITY OF THE WOVEN FABRICS

Bertrand Laine[1,2], Gilles Hivet[2], Philippe Boisse[3], Fabrice Boust[1], Stepan V. Lomov[4], Pierre Badel[3]

[1] *Département Matériaux et Systèmes Composites, Office National d'Etudes et de Recherches Aérospatiales, BP 72 – 29 avenue de la Division Leclerc, 92322 Châtillon Cedex, France :* *Bertrand.Laine@onera.fr* / *Fabrice.Boust@onera.fr*

[2] *Laboratoire de Mécanique de Systèmes et des Procédés, UMR CNRS 8106, ENSAM-Polytech'Orleans, 8 rue Léonard de Vinci 45072 Orléans Cedex, France :* *Gilles.Hivet@univ-orleans.fr*

[3] *Laboratoire de Mécanique des Contacts et des Solides UMR CNRS 5514, INSA de Lyon Bâtiment Jacquard, Rue Jean Capelle, 69621 Villeurbanne Cedex, France :* *Philippe.Boisse@insa-lyon.fr* / *Pierre.Badel@insa-lyon.fr*

[4] *Department MTM, Katholieke Universiteit Leuven, Kasteelpark Arenberg, 44 B-3001 Leuven Belgium :* *Stepan.Lomov@mtm.kuleuven.ac.be*

ABSTRACT: The ability to precisely predict the permeability of woven fabrics is compulsory to simulate the RTM processes without having to realize time consuming experiments for each new fabric. Channel network models are generally not working very well with laminates of woven fabrics because of the nesting between the plies that creates a highly complex network. Thus, 3D meshes of woven fabric unit cells are realized *via* a defined number of steps to resolve Stokes and Brinkman equations on a periodical elementary cell using a 3D FE code. Shearing and compression are the most important deformation modes and the determination of their respective influence on the permeability tensors is of prime importance. Therefore, a comparison between WiseTex and Hivet's models of sheared and copressed fabrics is presented. Finally, the representativeness of the elementary volume is discussed in the case of an idealised UD fabric.

KEYWORDS: permeability, woven fabrics, geometrical models, sheared fabric, 3D meshes, finite elements, elementary representative cell

INTRODUCTION

Out of the many processes that can be used to form composite parts, **R**esin **T**ransfer **M**oulding is one that allows producing high mechanical performances, high fibre volume fraction as well as complex shape parts. In the field of **L**iquid **C**omposite **M**oulding, the Darcy law is extensively used to describe the resin flux at the macroscopic scale through the preform by relating the local mean velocity to the pressure drop and the permeability Tensor, while tracking the free front versus time during the injection process [1]. The key concept here is the permeability [2], which links the microstructure of the reinforcement to the way the polymer resin flows through it. This parameter can be either measured experimentally

[3][4][5], predicted by numerical [6][7] or analytical [8][9][10] models. The first solution is certainly the best in term of quality of the results (when properly done) but suffers from time consuming affliction when the second is generally still not sufficiently accurate to avoid any experimental validation. Additionally, the numerical predictions need an extensive preliminary work on the geometry of the fabric [11] and possibly the construction of a 3D mesh [12] of the unit cell which can also be quite time consuming. The main goal of this study is to detail the specific problems related to the prediction of "wet" or "steady state" permeability of woven/braided fabrics. Indeed, the complex architecture and especially the crimp of the yarns create a particularly complex channel network at the interfaces between plies where nesting occurs. Furthermore, as these classes of fabrics can generally experience high geometrical deformations [13] (shearing especially but also compression), mesoscopic simulations of fabric deformation have to be realised in order to evaluate their respective influences on the permeability. Finally, a limited comparison between Hivet's [14] and WiseTex [15] modellers in the case of sheared, compressed and un-deformed fabric will be presented.

PERMEABILITY MODELS

Since 1856 and Darcy's founding article, a lot work has been done in the field of permeability. In particular, the Kozeny-Carman (K-C) formula gives a general relation for the permeability of porous media as function of the geometry (granular, cylindrical,… media) as well as the porosity. Later on, several researchers have proposed adaptation for the K-C equation to take into account the generally non-isotropic non-homogeneous nature of fibrous reinforcements. Recently, some authors have developed analytical or semi analytical models that allow the prediction of permeability in the case of woven and non-crimp fabrics.

Validity of the Channel Network Model for multi-plies laminates

However, excepted for non-crimp fabrics where the identification of the channel network is somehow "easier" (principally because there is no or little nesting between the plies), the models above-mentioned are generally limited to either mono-ply consideration or simplified geometries (the woven fabric is assumed to behave like a lay-up of several layers of UD for example). The figure bellows illustrates a simplified model of a plain weave fabric with rectangular yarns and its complementary volume which is used to determine the channel network ChN.

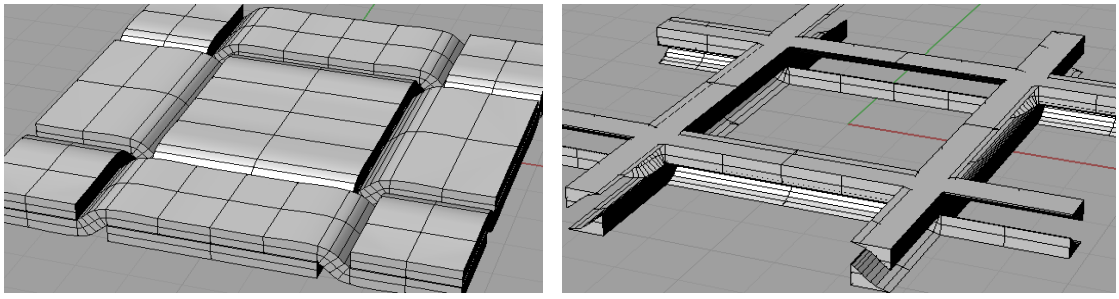

Fig. 1 Rectangular model of a plain weave fabric and its complementary volume

Then, to predict the permeability of this network within the periodic homogenization framework, the well known analogy between electricity and Poiseuil flow at low Reynolds

number in ducts is used together with the Kirchoff law ($\sum_{i=1}^{n} G_i = 0$ with Gi the hydraulic conductance of the ducts intersecting at the considered node) at the intersection nodes. The same procedure can be used in the case of multi-plies, as there is no nesting when using rectangular yarns and high fiber Vf (*cf* Fig. 2 bellows).

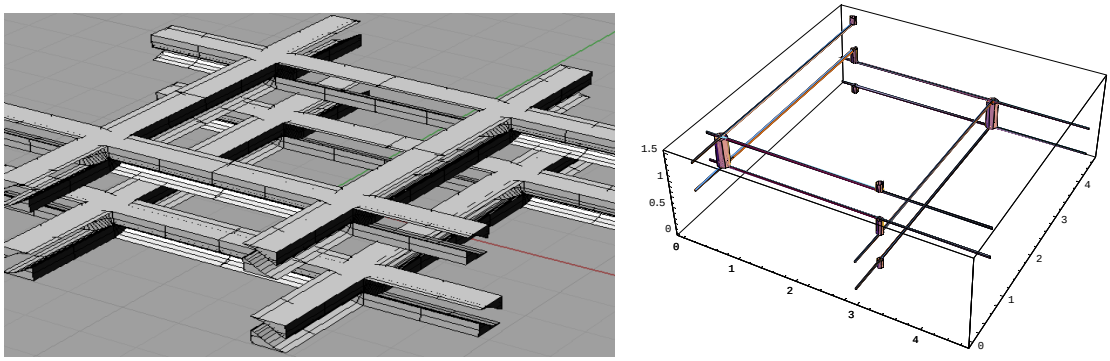

Fig. 2 Rectangular model for two plies and its associated ChN

Moreover, the permeability obtained with the ChN model is almost the same (<4% of difference) as the one obtained *via* 3D FE resolution of stokes equations in the geometry of the figure 2. In fact, the real difficulty comes when one tries to identify the ChN of a multi-plies of woven fabric modeled with non-rectangular yarns. The figures bellows represents the complementary volumes of a twill 2x2 for one and three plies.

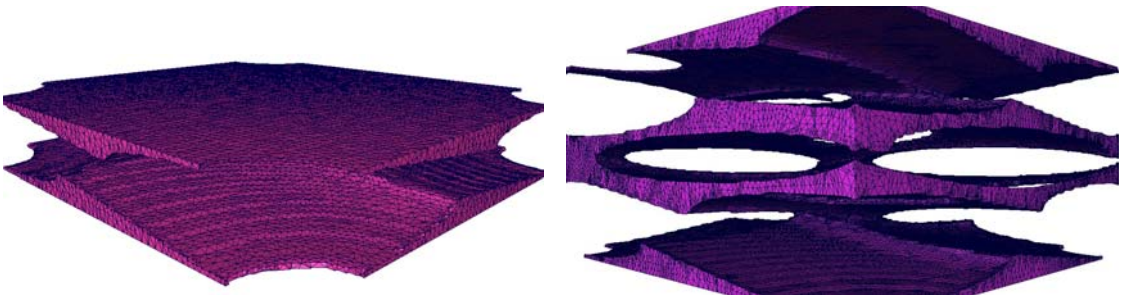

Fig. 3 Complementary volumes of a twill 2x2 (one quarter of the cell is represented)

In the case of a unique ply, the identification of the ChN is again quite straightforward, but the multi-plies case with random nesting (the unit cells of the stacked plies are randomly shifted from one to another) creates a highly complex ChN that can not (or only partially) be analytically defined as function of all the geometrical parameters. Finally, the table 1 bellow represents the permeability of a plain weave fabric as function of the yarns' geometrical section.

Table 1 Influence of the yarn's geometrical section on the permeability

	Number of plies	Lenticular Section	Elliptical Section	Rectangular Section
$K_{xx}(x10^{-11}m^2)$	1	11,84	11,71	1,16
$K_{xx}(x10^{-11}m^2)$	2	16,63	15,93	1,19

With an experimental result close to 10.10^{-11}, we clearly see that the rectangular geometry is too far away from the right result and thus a ChN description which would be based on it can not (at least not always) be used to predict the permeability of woven fabrics. Therefore, and especially when dealing with nested multi-plies, 3D accurate geometries have to be used together with an appropriate solver for Brinkman-Stokes equations.

ACCURATE 3D MODELS FOR PERMEABILITY PREDICTION

Using WiseTex modeler and Hivet's 3D model, accurate geometries can be constructed for permeability prediction. Once the geometrical parameters have been identified on the actual fabric, 3D models of the looming unit cell can be produced and eventually stacked to form the representative elementary volume (REV).

The Meshing

A meshing of the Stokes and eventually the Brinkman regions is realized using different commercial and dedicated software. Excepted for non-deformed Hivet's 3D models where meshing can be carried out directly from the 3D geometry, all the others geometries have to pass through a number of steps to finally obtain the 3D mesh. Firstly, the REVs are discretized into voxels (from hundred of thousands to about ten millions), then, this new geometry is filtered in order to remove some of the artifacts resulting from discretization and geometrical misfits (interpenetration as well as spurious voids between yarns). Afterward, the voxels' faces are divided into triangles and the surfaces dividing the different regions (Stokes; Brinkman and Exterior) are identified in terms of triangles. At this point, these surfaces define a set of closed volumes. After that, the number triangles forming the surfaces are lowered so that the final volumes do not represent millions of tetrahedrons and finally, a tetrahedral mesh is seeded from the existing triangular surface mesh. The above-described method can be applied to almost any kind of porous media. The figures bellows illustrate the 3D meshes that can be obtained *via* this technique as well as some results of 3D FE calculation.

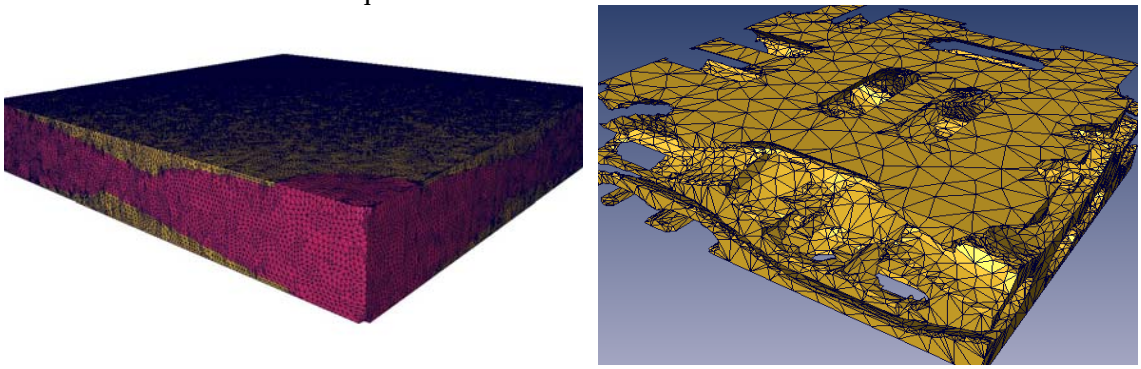

Fig. 4 Stokes and Brinkman mesh of a plain weave fabric (left) and complementary volume of two plies of a woven fabric.

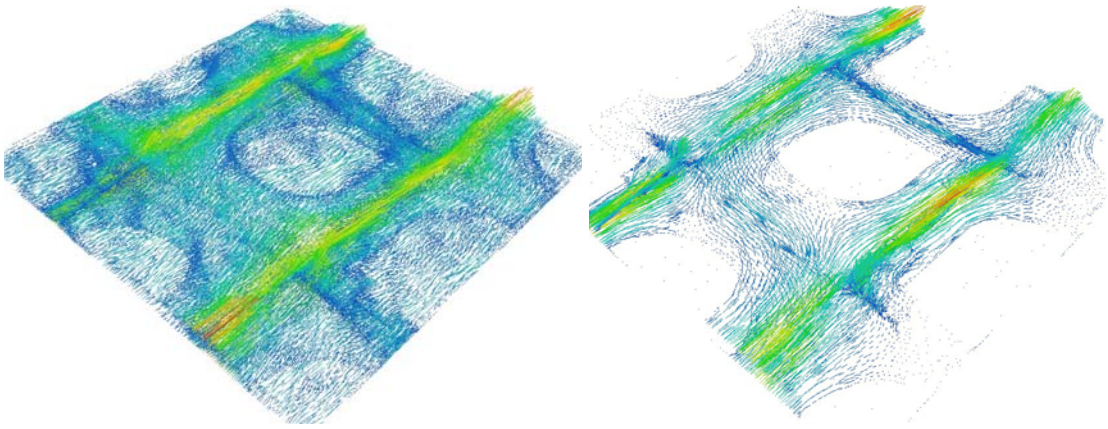

Fig. 5 Speed field from FE calculation with (left) and without Brinkman medium
Experimental result: 2.5 E-11 Left: Right:

Deformed geometries

In order to simulate accurately the injection of a complex shape part, one has to take into account the influence of both shearing and compression on the permeability of the REV. The WiseTex modeler allows us to obtain quite easily sheared and compressed 3D models (if it is fed with right mechanical properties). However, this is done the shearing is done in a mainly "geometrical way". On the other hand, the Hivet's model can be sheared and compressed using a mechanical FE code, which probably gives "more realistic" results but is also a "time consuming" process. The figure 6 shows an example of the influence of shearing on both in-plane principal direction of the permeability tensor.

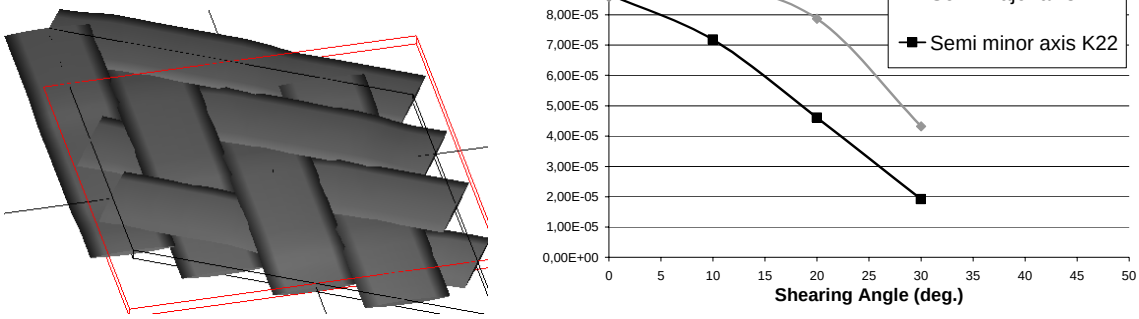

Fig. 6 Sheared geometry of a twill 2x2 and evolution of the permeability tensor

Comparison between the two models for both compression and shearing will be presented at the conference. The case of compression is of prime importance today with the increasing use of infusion in the industrial world. In general, the FE codes simulating the infusion process need both the thickness of the fabric versus pressure and the permeability of the fabric versus thickness. As this process mainly consists in a "through the thickness" impregnation of the fabric (from the upper conducting medium where the resin preferentially flows towards the fabric underneath because of the pressure gradient), the most relevant stationary/wet permeability value is the K_{zz}. The figure 7 represents a permeability prediction for ten plies of a balanced carbon twill 2x2. The blue surfaces are iso-speed and they clearly shows us two things: first of all, as we said in the first section, the channel network is highly complex and

would have been difficult to guess or determine analytically; and the second point is that our representative volume is maybe too small to be really representative of the percolation path(s) trough the thickness. Finally, the figure 8 illustrates the problematic of fabric compression using an FE code.

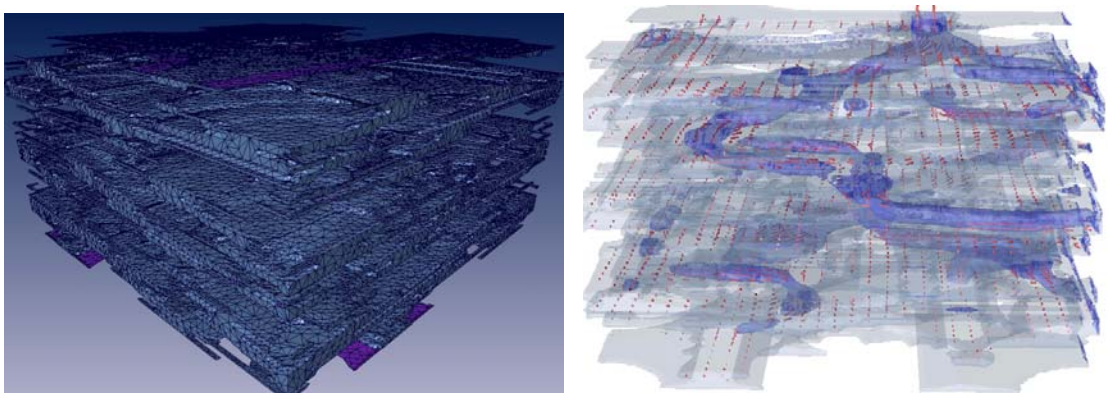

Fig. 7 Mesh and iso-speed surfaces for 10 plies of carbon fabric with a transversal pressure gradient

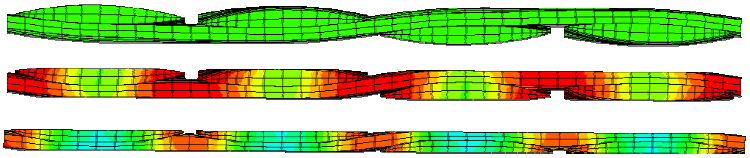

Fig. 8 E_{33} deformation during compression of a carbon twill 2x2 from relaxed state (up) to 46% (middle) and finally 94% of compression (bottom)

(RE)DEFINITION OF THE REV?

In order to predict the permeability of woven fabrics in the framework of periodical homogenisation, a REV has to be defined. The looming unit cell is generally used because of its geometrical periodical boundaries and convenient size. Nevertheless, the statistical geometrical variations that occur at the studied scale are only taken into account through the mean value of each geometrical parameter determined on the real fabric prior to geometrical modeling. In other words, we build up a “mean” unit cell with dimensions the mean dimensions observed on the actual reinforcement. The problem is that we have a non-linear equation for the permeability of a duct of radius R, and the hypothesis of the “mean cell” implies that the mean permeability (or the macroscopic permeability) of a fabric equals the permeability of the cell of mean dimensions, which is true is the permeability of a duct were linear with its radius. Therefore, how false is this hypothesis? Certainly not too false, because the cell of mean dimensions minimizes the permeability and an array of cells of distributed permeabilities (the reality) is not likely to maximize the overall permeability. The figure bellows illustrates the influence of the “erroneous” hypothesis in the simplest (and certainly not more realistic) case of one ply of an UD fabric with identical, impermeable, parallel square yarns and all the classical boundary conditions and simplification of Navier-Stokes equations.

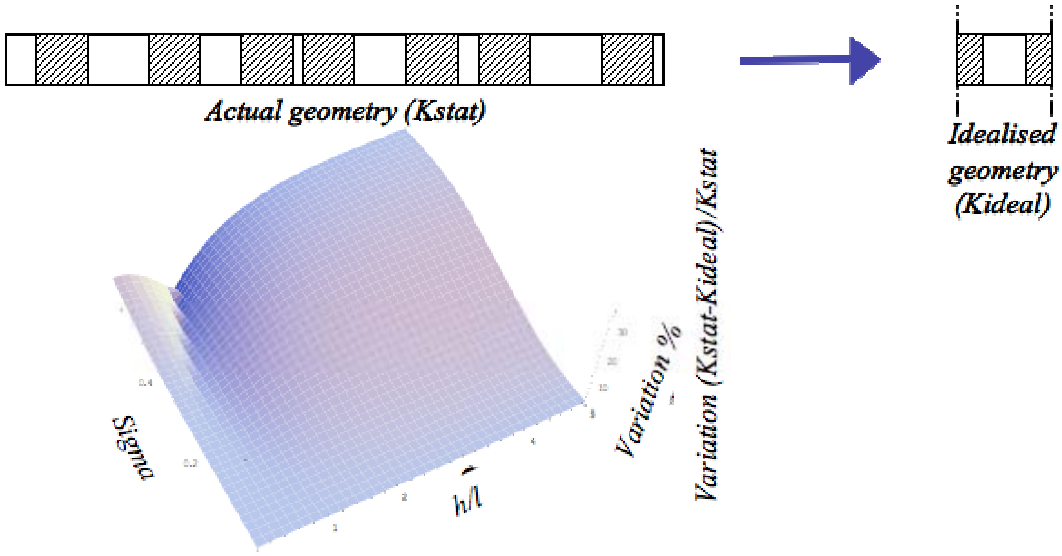

Fig. 9 Geometry of the model medium and influence of the statistical dispersion of the geometrical parameters on the permeability of the UD fabric

CONCLUSION

The particularities of woven fabrics in terms of permeability modelling have been exposed. Two three dimensional modellers exhibiting different advantages have been used to study the permeability of the woven fabrics along with a Finite Elements code to resolve the Stokes-Brinkman equations at the mesoscopic scale. The importance of the parameters describing the unit cell together with the influence of shearing and compression on its permeability have been studied. The influence of the shearing angle as well as compaction on the permeability principal values has also been studied and the importance of an accurate geometrical description discussed. Full set of results will be presented at the conference. Finally, the validity of the REV has been discussed and would need further developments.

REFERENCES

1. R. Gauvin and M. Chibani, “The modelling of Mold Filling in Resin Transfer Molding”, *Intern. Polymer Processing*, Vol.1, No.42, 1986.

2 H. Darcy, “Les fontaines publiques de la ville de Dijon”, *Dalmont*, Paris, 1856.

3. R. Gauvin, F. Trochu, Y. Lemenn, L. Diallo, “Permeability measurement and flow simulation through fiber reinforcement”, *Polymer Composites*, 2004. 17(1): p. 34-42.

4. Hoes K., Dinescu D., Sol H., Parnas R.S. and Lomov S.V., Study of nesting induced scatter of permeability values in layered reinforcement fabrics , *Composites Part A: Applied* Science *and Manufacturing*, 35, 2004, p. 1407-1418.

5. Laine B., Boust F., Boisse P., Hivet G., Lomov S., Fanget A., PermŽabilitŽ des renforts fibreux. Etude des Žcarts expŽrience-prŽdiction. *Revue des composites et matéraiux avancés*, 2006, 339-354

6. P.B. Nedanov and S.G. Advani, "Numerical Computation of the Fiber Preform Permeability Tensor by the Homogenization Method", *Polymer Composites*, 2002. 23(5): p. 758-770.

7. Fournier R., Coupez T. and Vincent M., (2005), 'Numerical determination of the permeability of fibre reinforcement for the RTM process', *European Finite Element Journal*, 14 (6-7), 803-818.

8. C. Binetruy, « Calcul et validation experimentale de la permeabilité et prévision de l'imprégnation de tissus en moulage RTM », *PhD*, 1996, Univ. Des Sciences et Technologies de Lille, 237p.

9. A. Endruweit, « Investigation of the influence of local inhomogeneities in the textile permeability on the resin flow in liquid composite moulding processes », *PhD*, 2003, Swiss Federal Institue of Technology, Zurich, 283p.

10. R. Loendersloot, « The structure-permeability relation of textile reinforcements », *PhD*, University of Twente, Netherlands, 2006, 228p.

11. J. Kuhn, and P. Charalambides, « Modeling of plain weave fabric composite geometry », *J. Composite Materials*, 1999. 33(3): p. 188-220.

12. B. Laine et al, « Permeability of the Woven Fabrics: A Parametric Study", *Proc. ESAFORM-6*, CD, 2005.

13. Lomov, S.V., Gusakov, A.V., Huysmans, G., Prodomou, A., Verpoest, I. « Textile geometry preprocessor for meso-mechanical models of woven composites », *Composites Science & Technology*, 60, 2000, p. 2083-2095.

14. G. Hivet, « Modélisation mésoscopique pour le comportement bi-axial et la mise en forme des renforts de composites tissés », *PhD*, 2003, ESEM Orléans / ENSAM Paris, 146p.

15. S.V. Lomov et al, *Comp A*, **32**, 1379, 2001.

MODELLING THE EFFECTS OF FABRIC STRUCTURE ON THE VARIABILITY OF PERMEABILITY

C.C. Wong, A.C. Long [1] and C.D. Rudd

School of Mechanical, Materials and Manufacturing Engineering,
University of Nottingham, University Park, Nottingham, NG7 2RD, U.K.

[1] Corresponding author's email: *andrew.long@nottingham.ac.uk*

ABSTRACT: Textile permeability in general shows a high variance. This work describes a method to model textile variability at the meso-scopic scale based on a generalised textile model. Inhomogeneities were introduced into the textile structure by randomly moving the tow paths at the crossovers according to a given Normal distribution. The effects of textile structure on the evaluated permeability variations were explored and demonstrated using non-crimp fabric and plain weave models. Fabric architecture was shown to be important in that it imposed a limit to the degree of variations of the tows. This study demonstrated that significant insights in flow behaviour for textile reinforcements can be provided by an efficient 2D model.

KEYWORDS: Liquid Composite Moulding (LCM), textile permeability, numerical simulation, variability.

INTRODUCTION

One of the crucial phases in Liquid Composite Moulding (LCM) processes is the injection of resin into the mould cavity. Impregnation of the textile reinforcement is determined by the textile permeability, which is a measure of the ease of fluid flow. In general, textile permeability shows a high variation [1, 2], consequently affecting the quality and cycle time of the product. This makes it difficult to predict the filling pattern and fill times accurately, thus reducing productivity.

Several researchers have studied the various factors which would affect fabric permeability values. Pan et al. [3] performed controlled uni-directional flow experiments for a plain weave and a 0°/90° non-crimp glass fibre fabric, and found that the permeability of the fabrics was primarily influenced by local changes in fibre deformation and superficial fabric density. Hoes et al. [4] measured the distributions of permeability for a plain weave, twill weave and a special PVC-coated layered fabric, using a radial flow method. They used the latter material to show that nesting is the major source of the variations in permeability values. The permeability scatter for all the fabrics tested in both studies was found to follow a Normal distribution.

In order to study the influence of fabric structure on permeability, Endruweit et al. [5] analysed five fabrics with different architecture and geometrical parameters and measured permeability using a radial flow set-up with automated data collection and analysis. They concluded that the more homogeneous the structure of a material, the lower is the permeability variation. In an attempt to model the variations observed experimentally, Endruweit et al. [6] assumed that the variation in local permeability is primarily caused by stochastic variations in fibre spacing, from which local permeability values can be calculated.

Injection simulations at the component level were then simulated for a bi-directional non-crimp fabric for a range of variations in fibre spacing to determine the global permeability variations. A trend was found between relative permeability variations and the maximum frequency of fibre tow waviness, which agreed with the experimental values. In general, the global permeability variation decreased with increasing mould dimensions.

The above attempted to describe the variations at the macro-scopic level. It is equally important to address variability at the meso-scopic level. Essentially, a fabric is defined by its structure and the interaction between the fibre bundles is the key to the variability of the fabric. Only by looking at the meso-scopic level can one analyse the effect of fabric architecture on variability and address issues such as localised inhomogeneities.

Using optical microscopy and X-ray micro-computed tomography, Desplentere et al. [7] measured geometrical parameters of the fibre bundles in 3D textiles. Considerable variations were found for these geometrical dimensions. Lundstrom et al. [8] determined the local permeability of non-crimp fabrics (NCF) from the dimensions of the flow channels with variable widths between the fibre tows. For a completely random distribution of the local permeability values, the global permeability was found to decrease with increasing maximum variation at the unit cell level, while for a correlated distribution, the permeability can either increase or decrease. To further study the effect of geometry variations on local permeability, Nordlund and Lundstrom [9] modelled the meso-scopic channels of a non-crimp fabric with variations in width, height and shape of the channels and the effect of the presence of stitches. The study identified the geometrical parameters that have the greatest affect on the local permeability. In order to realistically predict flow for a NCF, the effects of the stitching process and statistical variations of the channel dimensions have to be included in the model.

This study attempts to address permeability variation by modelling variability in the meso-scopic structure of the fabric itself. Specifically, the effect of fabric architecture on the variability of permeability is analysed. In contrast to the works of Lundstrom et al. [8] and Nordlund and Lunstrom [9], which are specific to NCFs, the methodology here is based on using a generalised textile modeller, TexGen [10]. Variability is modelled by randomly disturbing the paths of the fibre bundles according to a statistical distribution, and the effective permeability of the randomised flow domain is calculated based on a numerical method known as Grid Average [11].

MESO-SCALE PERMEABILITY MODELLING METHODS

TexGen

Textile models are generated using an in-house textile schema, TexGen [10]. It begins with vectors defining the textile interlacing pattern, which are smoothed and have volumes created around them to represent the tows. An analysis domain is defined in which the tows are repeated accordingly to fill up the domain. Some useful built-in functions include slice extraction, in-plane shearing to represent the effects of draping and statistical tow paths randomisation to emulate the variability seen in textiles (as described below). Output options include input files to mesh generators (for FE or CFD analyses) and data files for in-house permeability models, e.g. Grid Average [11] as used here.

Grid Average method

The Grid Average method [11] was developed to reduce the complexity of the flow problem. Firstly, the flow domain is discretised into a regular square grid in the x-y plane, as shown in Figure 1. For each grid element, the local permeability tensor is calculated as the thickness-weighted average of the individual permeabilities of the respective layers contained within the element. The permeability of a free channel with height h is approximated to $h^2/12$ (from

laminar flow between paallel plates) and the permeability of the porous tow is specified based on the fibre volume fraction using simple analytical models from Gebart [12], whereby the tows are modelled locally as either quadratic or hexagonal arrays of unidirectional fibres.

Periodic boundary conditions are imposed on the four sides of the computational domain. A pressure difference, ΔP, is imposed in a direction parallel to one of the global axes. Darcy's Law is coupled with the continuity equation to derive a partial differential equation for fluid pressure, which is then solved for saturated flow based on a finite difference scheme. The resulting flow rate is calculated from the evaluated pressure field, from which the effective permeability of the domain in the flow direction is back calculated using Darcy's Law.

Tow variations

In TexGen, variability in textile models is generated using the Monte-Carlo method, whereby the tow crossovers points within the fabric are randomly displaced along the global x- and y-axes independently. This movement will follow a Normal distribution with respect to the original coordinates of the points and a user-specified standard deviation of displacement. As the tow movement variation is increased, the tows will invariably begin to interfere with one another. In this study, cases with tow interference are discarded. The actual tow position distribution can be easily back calculated for a set of randomised cases.

The randomised model is dicretised using the Grid Average method. As periodic boundary conditions are imposed on the four sides of the flow domain in the solution, it is imperative that the model itself exhibits periodicity. For the analysis of a unit cell as shown in Figure 1, only two basic tows representing each layer are needed to ensure periodicity, with lengths equivalent to the diagonal dimension of the domain. A unit cell is defined here as the domain with the minimum dimensions which forms a repeatable representative cell of the fabric.

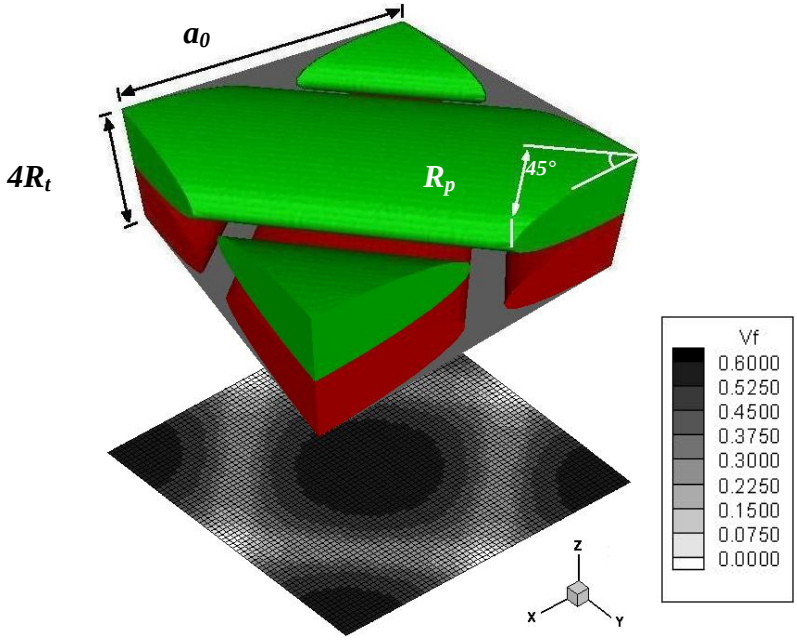

Figure 1 - Unit cell of a ± 45° non-crimp fabric model with dimensions as shown (top) and the discretised Grid Average mesh showing fibre volume fraction (bottom).

RESULTS

A plain weave and a non-crimp fabric (NCF) are modelled here (see Figure 2). Both the models have elliptical tow cross sections with semi major axis, R_p = 0.7mm and semi minor axis, R_t = 0.175mm, a_0 = 2.6mm and no stitches present in the NCF model (see Figure 1 for

definition of dimensions). The upper and lower layers of these models are not touching, so that tow variations can be introduced in the plain weave without resulting in interference. The tow local permeability is calculated for 60% V_f based on the Gebart model for a quadratic array of fibres. The computational domain size is 2.6 x 2.6 x 0.85mm, with nominal cell fibre volume fractions of 29.3% and 30.6% for the NCF and plain weave models respectively. The models are discretised using 50 divisions per unit, resulting in Grid Average meshes containing 17161 nodes. A pressure difference of 10^5 Pa is imposed in the direction of the global x-axis with a resin viscosity η of 0.308 Pa s (although permeability is independent of these values).

Randomised cases were generated for the two models by applying two standard deviations of nodal displacement at 14.83% and 29.65% with respect to the spacing between the tows. For each model and different tow variations, a total of 100 randomised cases were simulated and evaluated statistically. The achieved levels of tow variability and resultant mean and standard deviations of V_f, α and K_x are listed in Table 1. Generally, the standard deviation of K_x increases with increasing tow variations. Interestingly, the mean value of K_x for the NCF model decreased with increasing variability whilst the mean K_x value for the plain weave increased slightly.

The degree of permeability variation is somewhat limited for the plain weave cases. For the NCF model, when the tow position variation is doubled, there is an increase in permeability variations from 1.24% to 4.18%. The plain weave model exhibited an increase of only 11% in permeability variations from 1.73% to 1.93%. Similar observations can be made on the relative increase in the variations of the fibre volume fraction and fibre angle. The standard deviation of the fibre angles for the plain weave is almost the same for the two levels of tow path variability.

At applied tow movement variations of 14.83% and 29.65%, the NCF cases achieved variations of 10.50% and 20.83% respectively whilst the plain weave cases achieved 8.69% and 13.12% respectively. The plain weave model has reached its geometric limit of variation at an applied variation of 29.65%, as evident from the low level of resultant variability of 13.12%. In fact, 7 out of 10 randomised plain weave cases with 29.65% tow variation had to be discarded because of tow interference. The plain weave structure restricts the mobility of the tows more than the NCF does, and this is reflected in the permeability variation.

a) b)

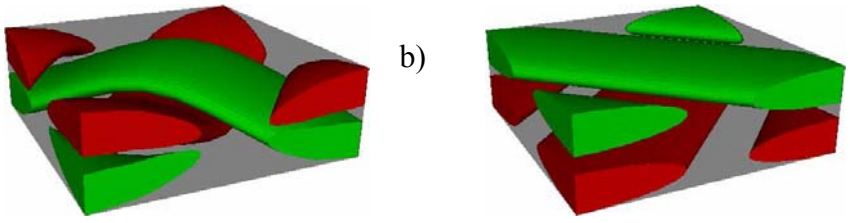

Figure 2 - (a) Plain weave model with a_0 = 2.6mm, R_p = 0.7mm and R_t = 0.175mm and (b) corresponding NCF model. Note the gap between the layers in both models.

Table 1 - Mean and standard deviation values for a NCF and a plain weave model with a_0 = 2.6mm, R_p = 0.7mm and R_t = 0.175mm.

Std. dev. of nodal position as % wrt space between tows		V_f	α (deg)	K_x (x 10^{-9} m^2)
Intended	**Achieved**			
Bi-directional NCF				
0.00	0.00	0.293	90	5.485
14.83	10.50	0.293 ± 0.000 (± 0.12%)	89.99 ± 3.90 (± 0.04%)	5.473 ± 0.068 (± 1.24%)
29.65	20.83	0.294 ± 0.001 (± 0.41%)	90.12 ± 6.93 (± 0.08%)	5.347 ± 0.224 (± 4.18%)
Plain weave				
0.00	0.00	0.306	90	1.629
14.83	8.69	0.304 ± 0.000 (± 0.09%)	89.98 ± 3.44 (± 0.04%)	1.665 ± 0.029 (± 1.73%)
29.65	13.12	0.305 ± 0.001 (± 0.21%)	89.98 ± 4.47 (± 0.05%)	1.674 ± 0.032 (± 1.93%)

The permeability distribution the plain weave correlates better with a Normal distribution than for the NCF (see Figure 3). The plain weave structure restricts the movement of the tows, particularly at the tow crossover points, where the point of overlap cannot differ too much between randomised cases. Hence most of the randomised cases exhibited a similar pattern of variation, and the predicted pressure distributions were very close to one another (see Figure 4). Calculated permeability values are hence equally likely to lie on either side of the mean. In contrast, tows in the NCF are less restricted compared to the plain weave, exhibiting a wider range of possible variation patterns. For the NCF model, in extreme cases a whole tow can move closer to an adjacent tow, which is not possible for a plain weave where crossovers impose periodic restrictions. As a result, NCF models exhibit distorted and non-uniform pressure distributions, as shown in Figure 5. The calculated permeability values of these extreme cases are much lower than the nominal value, and this is reflected in the predicted permeability distribution for NCFs.

The observation here on the effect of fabric structure on the shape of the permeability distribution is interesting, implying that fabric structure has an important influence on permeability variations at the meso-scale. However, published experimental observations [4, 5] suggest that the Normal distribution of permeability is seen for most types of fabrics. One can argue that as the NCF model used here does not include stitches as seen in a real NCF, then the tows are freer to move, creating more variable patterns. A previous study [13] has also indicated that it is perhaps more appropriate to model a larger domain when variability is involved.

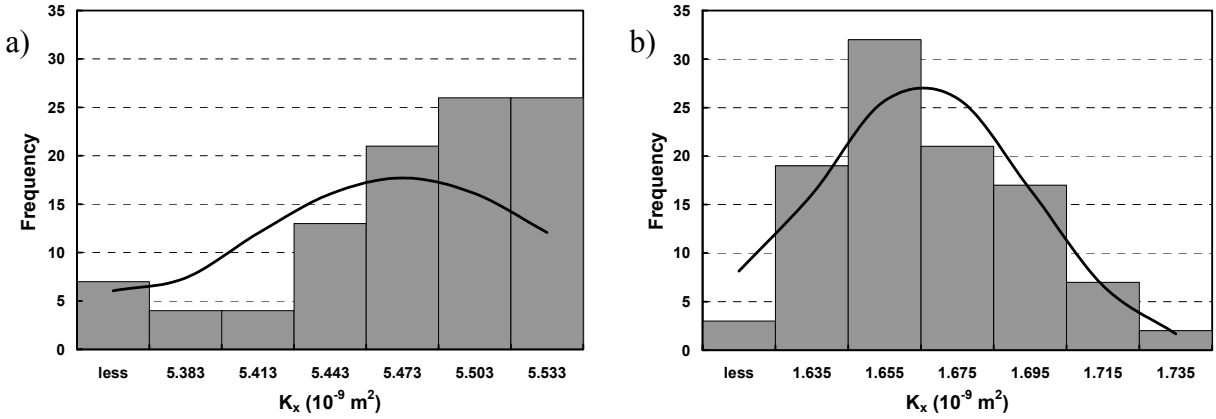

Figure 3 - Distributions of predicted K_x for (a) NCF and (b) plain weave models with applied nodal displacement standard deviation of 14.83% with respect to the spacing between the tows. Corresponding Normal distributions are shown with correlation coefficients of 0.648 and 0.934 respectively.

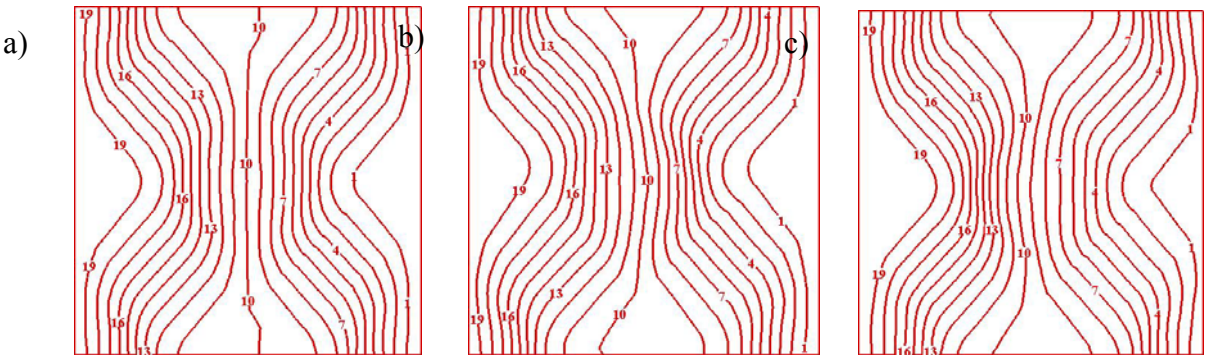

Figure 4 - Pressure distributions of (a) the nominal plain weave model with no tow variability and (b & c) typical cases with extreme tow variability. (a) The nominal case exhibits symmetrical pressure contours about the centre line 10. The pressure distributions in (b) and (c) are still quite similar to that of the nominal case (a).

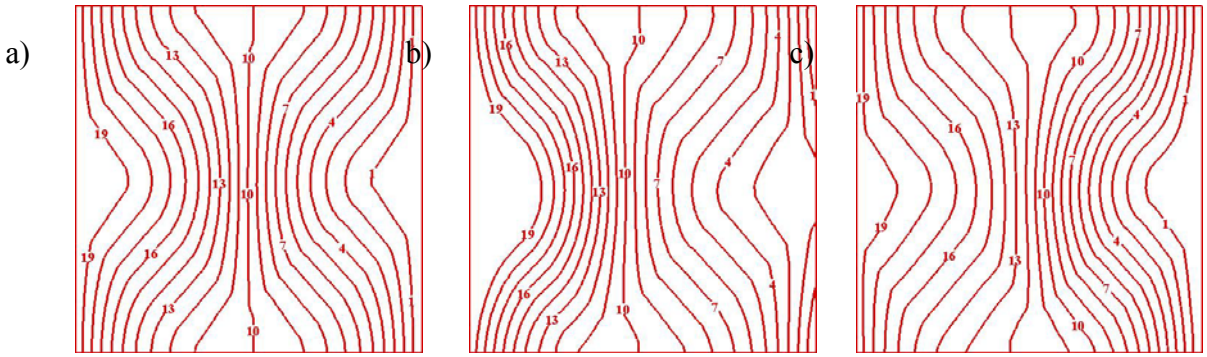

Figure 5 - Pressure distributions of (a) the nominal NCF model with no tow variability and (b & c) typical cases with extreme tow variability. (a) The nominal case exhibits symmetrical pressure contours about the centre line 10. In (b), the pressure distribution is distorted compared to (a) whereas in (c), the pressure contours are not symmetrical as line 10 has shifted to the right.

DISCUSSION

This study addresses variability in permeability at the meso-scopic scale. In this respect it is fundamentally different to previous studies which have addressed macro-scopic variability [3-6]. For example Endruweit's variability model [6] is applicable to a macro-scopic flow simulation where the effect of the structure is rather homogenised. The meso-scopic models presented here are based purely on the fabric architecture which is useful to address issues such as localised inhomogeneities. This may allow local phenomena such as a void formation to be studied in detail.

One limitation of the present study is that the fabric models have idealised geometries with a low fibre volume fraction, i.e. a lot of free space between the tows. The effective permeability of the domain will be dominated by the free space permeability, which is several orders of magnitude higher than the tow permeability, and thus variations of the tow paths will be less important. Furthermore, experimental measurements are based on several layers of fabric and nesting will affect the variability of permeability as shown in [4].

There are various ways to model variability in the textile models. In this study, the tows are assumed to move randomly at the crossover points according to a Normal distribution, which does not necessarily happen in real life. Non-crimp fabrics have stitches running through them, which would influence the tow alignment. Furthermore, the fibre tows, being long and tortuous, would be less likely to be randomly displaced at each crossover.

CONCLUSIONS

Textile permeability in general shows a high variation. Consequently, researchers have attempted to model such variability in order to better predict the filling times and flow pattern of LCM processes. This paper has described a method to model textile variability at the meso-scopic scale based on a generalised textile modeller. Inhomogeneities were introduced into the textile structure by randomly moving the tow paths at the crossovers according to a Normal distribution.

The variations of permeability for a plain weave fabric were compared to a NCF model with a similar cell fibre volume fraction. The architecture of the fabric is important in that it imposes a limit to the degree of variations of the tow paths. From the comparison between two types of fabric, the plain weave was seen to restrict the movement of the tows more than the NCF. This has two effects: the permeability variation is lower for the plain weave and the permeability distribution correlates better with a Normal distribution. This study demonstrated that significant insights in flow behaviour for textile reinforcements can be provided by an efficient 2D model.

ACKNOWLEDGEMENTS

The authors would like to acknowledge Martin Sherburn and Francois Robitaille for developing some of the theories and software that made the studies in this paper possible. The support of the following organisations is also acknowledged: UK Engineering and Physical Sciences Research Council (EPSRC), Dowty Propellers (Smiths Aerospace), ESI Software, Ford Motor Company and Formax UK Ltd.

REFERENCES

1. Lundstrom, T.S., R. Stenberg, R. Bergstrom, H. Partanen, and P.A. Birkeland, *In-plane permeability measurements: a nordic round-robin study.* Composites Part A, 2000. **31**(1): p. 29-43.
2. Luo, Y., I. Verpoest, K. Hoes, M. Vanheule, H. Sol, and A. Cardon, *Permeability measurement of textile reinforcements with several test fluids.* Composites Part A, 2001. **32**(11): p. 1497-1504.
3. Pan, R., Z. Liang, C. Zhang, and B. Wang, *Statistical characterizaton of fiber permeability for composite manufacturing.* Polymer Composites, 2000. **21**(6): p. 996-1006.
4. Hoes, K., D. Dinescu, H. Sol, R.S. Parnas, and S. Lomov, *Study of nesting induced scatter of permeability values in layered reinforcement fabrics.* Composites Part A, 2004. **35**: p. 1407-1418.
5. Endruweit, A., P. McGregor, A.C. Long, and M.S. Johnson, *Influence of the fabric architecture on the variations in experimentally determined in-plane permeability values.* Composites Science and Technology, 2005. Accepted for publication.
6. Endruweit, A. and A.C. Long, *Influence of stochastic variations in the fibre spacing on the permeability of bi-directional textile fabrics.* Composites Part A, 2005. **37**(5): p. 679-694.
7. Desplentere, F., S.V. Lomov, D.L. Woerdeman, I. Verpoest, M. Wevers, and A. Bogdanovich, *Micro-CT characterization of variability in 3D textile architecture.* Composites Science and Technology, 2005. **65**(13): p. 1920-1930.
8. Lundstrom, T.S., V. Frishfelds, and A. Jakovics, *A statistical approach to permeability of clustered fibre reinforcements.* Journal of Composite Materials, 2004. **38**(13): p. 1137-1149.
9. Nordlund, M. and T.S. Lundstrom, *Numerical Study of the Local Permeability of Noncrimp Fabrics.* Journal of Composite Materials, 2005. **39**(10): p. 929-947.
10. Sherburn, M., F. Robitaille, A. Long, and C. Rudd. *Geometric pre-processor for the calculation of physical properties of textiles*. in *Industrial Simulation Conference*. 7-9 June 2004. University of Malaga, Spain: EUROSIS-ETI.
11. Wong, C.C., A.C. Long, M. Sherburn, F. Robitaille, P. Harrison, and C.D. Rudd, *Comparisons of novel and efficient approaches for permeability prediction based on the fabric architecture.* Composites Part A, 2006. **37**(6): p. 847-857.
12. Gebart, B.R., *Permeability of unidirectional reinforcements for RTM.* Journal of Composite Materials, 1992. **26**(8): p. 1100-1133.
13. Wong, C.C. and Long, A.C, *Modelling variations of textile fabric permeability at the meso-scopic scale*. Accepted for publication in Plastics, Rubber and Composites.

Session 11

PERMEABILITY PREDICTION – II

WISETEX-BASED MODELS OF PERMEABILITY OF TEXTILES

Stepan V. Lomov[1], Ignaas Verpoest[1], Bart Verleye[2], Bertrand Laine[3], Fabrice Boust[3]

[1]*K.U. Leuven , Dept. MTM, Kasteelpark Arenberg, 44, B-3001, Leuven, Belgium*
Stepan.Lomov@mtm.kuleuven.be, fax +32-16-32-19-90, phone +32-16-32-12-10

[2]*K.U. Leuven, Dept. of Computer Science, Celestijnenlaan 200A B-3001 Leuven Belgium*

[3]*ONERA/DMSC 29 avenue de la Division Leclerc, F-92320 Chatillon France*

ABSTRACT: The software package *WiseTex* implements a generalised description of the internal structure of textile reinforcements on the unit cell level, integrated with mechanical models of the relaxed and deformed state of 2D and 3D woven, two- and three-axial braided, weft-knitted and non-crimp warp-knit stitched fabrics and laminates. The paper describes its integration with modelling of resin flow on meso-level.
Calculation of permeability is based on a voxel representation of the unit cell volume. A voxel is either empty (pore) or filled with fibres. The flow of the fluid in the pores is governed by Navier-Stokes equations (NS-voxels), inside the permeable tows – by Brinkman equation (B-voxels). In the latter case local permeability (micro-level) is calculated with the formulae of Gebart and Berdichevsky for a unidirectional array of fibres. These equations are solved by numerical schemes based on: (1) lattice Boltzmann, (2) finite difference or (3) finite element algorithms. The homogenised permeability of a unit cell is then determined using an average flux of the fluid through the unit cell under periodic boundary conditions for the given pressure difference on the unit cell facets.

KEYWORDS: Textile composites; internal geometry; permeability; modelling; software

INTRODUCTION

Textile composites are structured, hierarchical materials, having three structural levels:

1. The macro(M)-level defines the 3D geometry of the composite part and the distribution of local reinforcement properties.

2. The meso(m)-level defines the internal structure of the reinforcement and variations of the fibre direction and the fibre volume fraction inside the yarns and the fibrous plies. The internal structure is defined by the reinforcement textile architecture and deformations applied to the reinforcement during the part forming.

3. The micro(μ)-level defines the arrangement of the fibres in the RVE of the impregnated yarn or fibrous ply.

The calculation of the permeability of textile composites on the meso-level (a unit cell of the reinforcement) involves a two-way process: (1) homogenisation, which produces average

(effective) permeability of the material to be used in the macro-modelling of the composite part, and (2) calculation of the meso-flow field inside the unit cell under given macro conditions. The multi-level description of composites is a well-established approach to the calculation of the permeability [1-3]. The key step in the multi-level calculations is the meso-level.

The software package *WiseTex* implements a generalised description of internal structure of textile reinforcements on the unit cell level, integrated with mechanical models of the relaxed and deformed state of 2D and 3D woven, two- and three-axial braided, weft-knitted and non-crimp warp-knit stitched fabrics and laminates [2, 3, 9, 10]. The geometry provided by *WiseTex* could be transferred into finite element (FE) mesh of the yarns, which could be used for modelling of the flow through the textile. However, building a mesh for complex textile geometry is a problem in itself. The "short-cut" possibility for the representation of the internal geometry of a textile representative volume element (RVE) is mapping the geometric description of the textile meso-structure into a 3D grid of parallelepiped elements ("voxels"). The same mapping could produce a 3D mesh of the pores in the reinforcement, to be used in finite element, finite difference or other methods for calculations of the flow [4-8].

The paper discusses the "road map" for building voxel-based models for permeability of textile composites, starting from a generic model of internal geometry of the textile reinforcement. It can serve as an introduction to three other papers presented by the current authors in this conference (F. Desplentere, B. Laine and B. Verleye), which treat the individual models more in depth.

UNIFIED DESCRIPTION OF THE INTERNAL GEOMETRY OF TEXTILE REINFORCEMENT AND VOXEL REPRESENTATION OF THE UNIT CELL

Building a voxel discretisation of the RVE starts with the definition of the internal geometry of the reinforcement. If the model has to be sufficiently versatile, the unified description of the internal geometry is needed. Such a description has been developed by the present authors [2, 3, 9, 10] and implemented in a software *WiseTex*, which could be considered as a geometrical pre-processor for the calculation of mechanical properties and permeability of textile composites.

The unified format of data, covering a wide range of the reinforcement types (2D and 3D woven, braided, knitted, non-crimp fabrics - NCF) is described in [3] and shown in Figure 1. The yarns in the reinforcement are represented as "tubes", characterised by a succession of cross-sections (dimension and orientation of which could vary along the yarn path). The fibrous plies (in NCFs) are described as volumes ("slabs") containing fibres; the dimensions of the volumes and directions of the fibres in them depend on the disturbances ("channels" and "openings") given to the fibrous plies by the stitches.

Note that the geometry depicted in Figure 1 could be easily transferred to a finite element mesh for the yarn and "slab" volumes, as described in [3] and shown in Figure 2. The mesh, defining the surface of the yarns/"slabs", defines also the pore volume between the yarns/"slabs", and could be used for FE or other methods (e.g., FE-SPH).

The voxel representation of the yarns/"slabs" and pore volume is not based on the description of the surfaces, but rather on the continuous definition of pore/fibrous assembly in any point of the RVE of the textile.

For any point P inside the RVE the geometrical model describes the fibrous assembly near this point (Figure 1): physical and mechanical parameters of the fibres near the point (which are not necessarily the same in all points of the fabric), fibre volume fraction *Vf* and direction ***f*** of them. If the point does not lie inside a yarn, then *Vf=0* and ***f*** is not defined. For a point inside a yarn, the fibrous properties are easily calculated, providing that the fibrous structure of the yarns in the virgin state and its dependency of local compression, bending and twisting of the yarn are given.

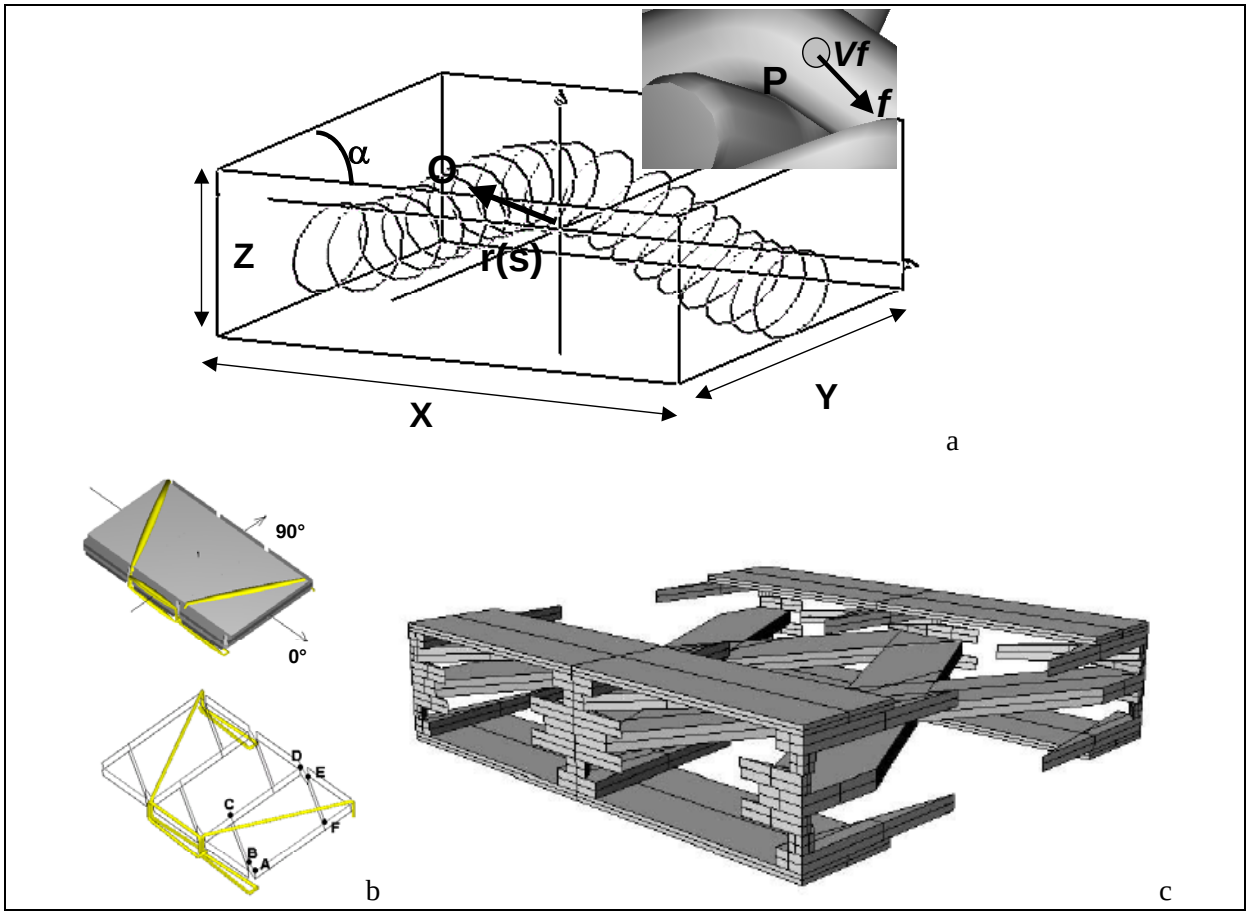

Figure 1 (a) Set of cross-sections defining a yarn in a unit cell, properties of fibres near point P; (b) Quadriaxial NCF, orientation of the fibres in the plies 0°/-45°/90°/45°:) Full geometrical model with stitching. Note a “channel” in the first 0° ply and slab representation of a ply with -45° "cracks". ABCDEF – vertices of the upper polygon of one of the slabs; (c) Example of the pore structure of biaxial NCF

The information of the local fibrous content is output in so-called Fibre Distribution (FD) mode. The fabric repeat is mapped into an orthorombic, regular grid of cells (= voxels), where each cell has homogenised properties according to the amount and respective orientations of the yarn sections it contains. The following data are stored in the FD Mode: (1) RVE (unit cell) size; (2) Data for all fibre types in the reinforcement: fibre diameter, density, mechanical properties; (3) For each cell/voxel: fibre type reference; average fibre orientation; average fibre volume fraction. The number of cells is chosen by the user.

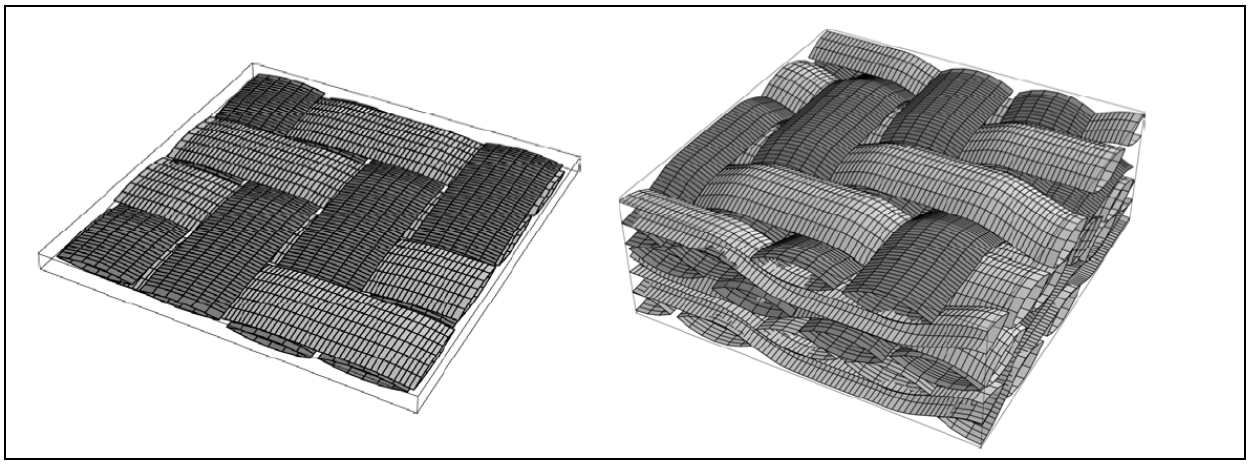

Figure 2 FE mesh for surfaces of yarns of one layer of woven fabric and a laminate

Averaging over a sub-cell is done as follows. The geometrical model gives an answer to the question "does a given point *P* in the RVE volume lie inside a yarn?" If answer is *yes*, then the fibre volume fraction (from the fibre count inside the yarn and the cross-section compressed dimensions) and the fibre orientation (from the yarn heart-line direction and the yarn twist) can be computed for the point *P*. Integrating over a sub-cell volume, the average parameters are computed for each of the fibre types present in the particular sub-cell

$$V_f = \frac{1}{V}\int_V v_f\,dv,\ \mathbf{A}_f = \frac{1}{V}\int_V \mathbf{a}_f\,dv,$$

where V is a subcell volume, v_f is the fibre volume fraction (of the fibres of the given type) near a given point P – centre of differential volume dv, $\boldsymbol{a_f}$ is fibre orientation vector at P, V_f is an average fibre volume fraction, $\boldsymbol{A_f}$ is an average fibre orientation (this vector is normalised after integration). The integrals are computed with a numerical formula:

$$\int_V f dv \approx \sum_{i=1}^{n} a_i f(P_i)$$

where n, coefficients a_i and reference points P_i inside a unit cell are pre-defined for a given polynomial order of accuracy (1,3,5 or 7, chosen by the user) [11].

PERMEABILITY OF THE REINFORCEMENT

The calculation of the permeability is based on a voxel representation of the unit cell volume (Figure 3a). A voxel is either empty (pore) or filled with fibres. The flow of the fluid in the pores is governed by the Navier-Stokes equations (NS-voxels), inside the permeable tows – by the Brinkman equation (B-voxels). In the latter case local permeability (micro-level) is calculated with the formulae of Berdichevsky [12] and Gebart [13] for longitudinal ("l") and transversal ("t") permeability of the unidirectional array of fibres:

$$K_l = \frac{d^2}{32V_f}\left(\ln\frac{1}{V_f^2} - \left(3 - V_f\right)\left(1 - V_f\right)\right) \qquad K_t = \frac{4d^2}{9\pi\sqrt{2}}\left(\sqrt{\frac{\pi}{4V_f}} - 1\right)^{5/2}$$

where K is the permeability, V_f is local fibre volume fraction, d is the fibre diameter.

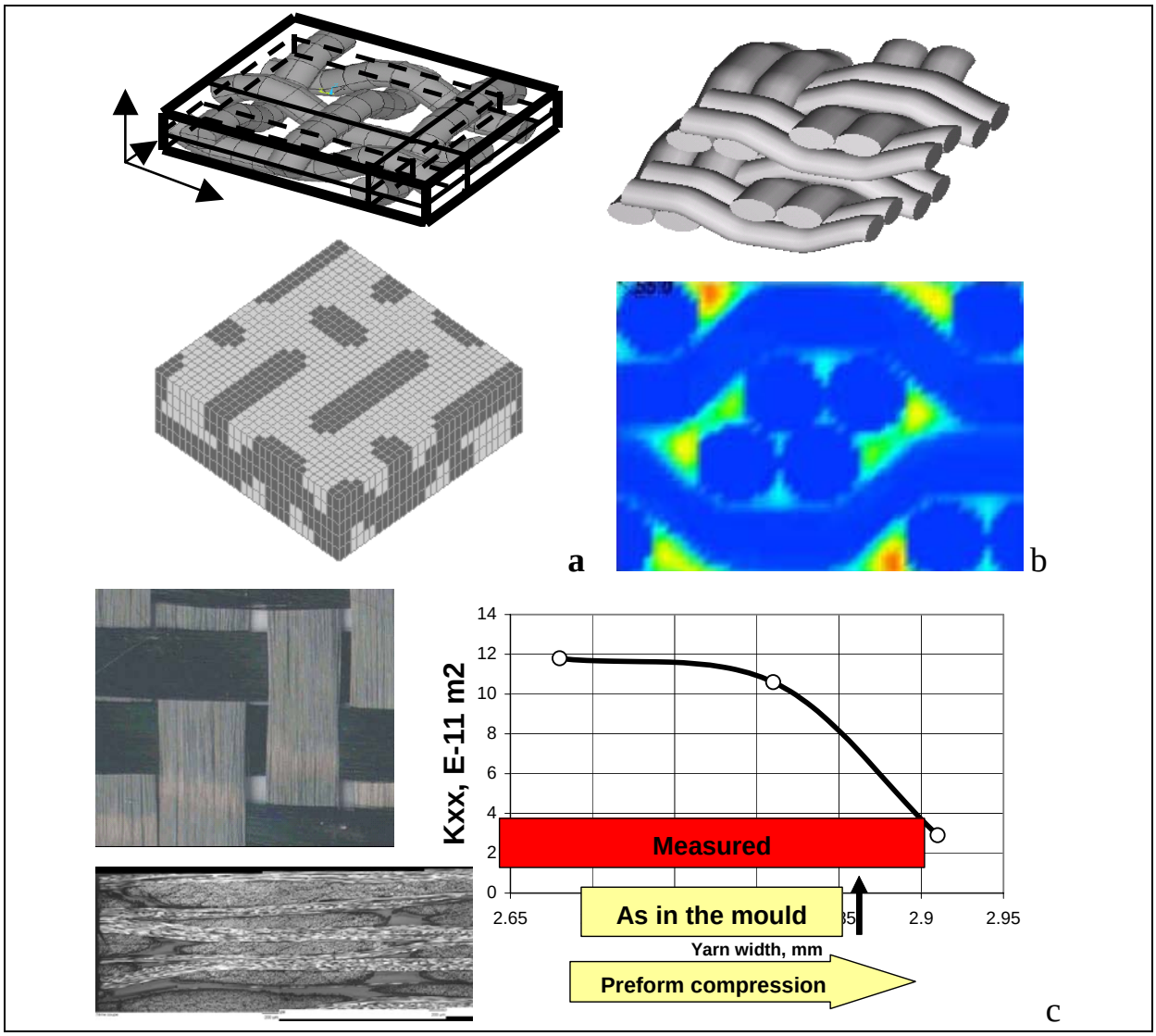

Figure 3 Calculation of permeability: (a) unit cell and voxel model; (b) Two layers of monofilament fabric: *WiseTex/LamTex* model and flow velocity field (finite difference method); (c) Carbon woven reinforcement: fabric, cross-section of the laminate (Vf=55%), finite element calculations with different compression of the fabric

The Navier-Stokes/Brinkman equations are solved by numerical schemes based on lattice Boltzmann [4], finite difference (based on a Navier-Stokes solver NaSt3DGP developed by the research group of Prof. M. Griebel in the institute of Numerical Simulation at the University of Bonn [14,16,17,18]) or finite element algorithms [5]. The homogenised permeability of a unit cell is then determined using an average flux of the fluid through the unit cell under periodic boundary conditions for the given pressure difference on the unit cell facets.

Figure 3b illustrates the calculation of the flow through a fabric made of monofilament fibres. The precise definition of the geometry, available for this type of fabric, results in a very good prediction of the permeability: measured [15] 270±20 μm^2, calculated 330 μm^2 by the lattice Boltzmann method and 270 μm^2 by the finite difference Navier-Stokes method. When a reinforcement with permeable tows is considered, the correct calculation of the preform compression is of major importance. Figure 3c illustrates how finite element calculations come close to the measurements, when the correct parameters of the reinforcement are chosen.

CONCLUSION

The textile internal geometry models of *WiseTex* provide a generic data format for the description of the distribution of the properties (micro-homogenised permeability of fibre bundles) in a RVE of a textile composite, discretised using voxel partitioning. The voxel models are effectively used for calculation of the permeability of the RVE (using finite difference, finite element or lattice Boltzmann methods for flow simulation). The versatility of the geometrical modelling makes the approach applicable to virtually any textile reinforcement structure using the same modelling and software implementation framework.

ACKNOWLEDGEMENTS

The work reported here was supported by EC (TECABS, ITOOL), government of Flanders (STWW and GBOU projects) and Research Council of K.U.Leuven (GOA and OT projects).

REFERENCES

1. Long, A.C., P.J. Blanchard, C.D. Rudd, and P. Smith The development of an integrated process model for liquid composite moulding. Composites part A, 1998; **29**: 847-854

2. Lomov, S.V., G. Huysmans, Y. Luo, R. Parnas, A. Prodromou, I. Verpoest, and F.R. Phelan Textile Composites: Modelling Strategies. Composites part A, 2001; **32**(10): 1379-1394

3. Verpoest, I. and S.V. Lomov Virtual textile composites software Wisetex: integration with micro-mechanical, permeability and structural analysis. Composites Science and Technology, 2005; **65**(15-16): 2563-2574

4. Belov, E.B., S.V. Lomov, I. Verpoest, T. Peeters, D. Roose, R.S. Parnas, K. Hoes, and V. Sol Modelling of permeability of textile reinforcements: Lattice Boltzmann method. Composites Science and Technology, 2004; **64**: 1069-1080

5. Laine, B., G. Hivet, P. Boisse, F. Boust, and S.V. Lomov, Permeability of the woven fabrics: a parametric study, in Procedings of the 8th ESAFORM Conference on Material Forming. 2005: Cluj-Napoca. 995-998

6. Verleye, B., M. Klitz, R. Croce, D. Roose, S.V. Lomov, and I. Verpoest, Computation of permeability of textile reinforcements, in 17th IMACS World Congress. 2005: Paris. CD edition

7. Schell, J.S.U., M. Renggli, G.H. van Lenthe, P. Ermanni, and R. Muller, On the use of micro-CT to determine the meso-structure of a glass fibre reinforced composite, in Proceedings ESAFORM-2004. 2004: Trondheim. 313-316

8. Delerue, J.-F., S.V. Lomov, R.S. Parnas, I. Verpoest, and M. Wevers Pore network modelling of permeability for textile reinforcements. Polymer Composites, 2003; **24**(3): 344-357

9. Lomov, S.V., A.V. Gusakov, G. Huysmans, A. Prodromou, and I. Verpoest Textile geometry preprocessor for meso-mechanical models of woven composites. Composites Science and Technology, 2000; **60**: 2083-2095

10. Lomov, S.V., E. Bernal, D.S. Ivanov, S.V. Kondratiev, and I. Verpoest Homogenisation of a sheared unit cell of textile composites: FEA and approximate inclusion model. Revue européenne des éléments finis, 2005; **14**(6-7): 709-728

11. Krylov, V.I. and L.T. Shulgina Reference book for numerical integration. 1966, Moscow: Nauka *(in Russian)*.

12. Berdichevski, A.L. and Z. Cai Preform permeability predictions by self-consistent method and finite element simulation. Polymer Composites, 1993; **14**(2): 132-143

13. Gebart, B.R. Permeability of Unidirectional Reinforcements for RTM. Journal of Composite Materials, 1992; **26**(8): 1100-1133

14. Griebel, M., T. Dornseifer, and T. Neunhoeffer Numerical Simulation in Fluid Dynamics, a Practical Introduction. 1998, Philadelphia: SIAM

15. Hoes, K., H. Sol, D. Dinescu, S.V. Lomov, and R. Parnas Study of nesting induced scatter of permeability values in layered reinforcement fabrics. Composites part A, 2004; **35**(12): 1407-1418

16. Verleye, B, M. Klitz, R. Croce, ea., Computation of the permeability of texiles, Report TW 455, Dept. Computer Science, K.U.Leuven, Leuven, Belgium, April 2006

17. Verleye, B, M. Klitz, R. Croce, M. Griebel, S.V. Lomov, D. Roose and I. Verpoest Predicting the permeability of textile reinforcements via a hybrid Navier-Stokes/Brinkman solver. Proc. of the 8th Int. Conf. on Flow Processes in Composite Materials

18. *http://wissrech.iam.uni-bonn.de/research/projects/nast3dgp*

PREDICTING THE PERMEABILITY OF TEXTILE REINFORCEMENTS VIA A HYBRID NAVIER-STOKES/BRINKMAN SOLVER

B. Verleye [1], M. Klitz [2], R. Croce [2], M. Griebel[3], S.V. Lomov[3], D. Roose[1], I. Verpoest [3]

[1] *K.U.Leuven Department of Computer Science*
Celestijnenlaan 200A B-3001, Leuven, Belgium, bart.verleye@cs.kuleuven.be

[2] *Universität Bonn, Institut. for Numerical Simulation*
Wegelerstr. 6, D-53115 Bonn, Germany, klitz@iam.uni-bonn.de

[3] *K.U.Leuven Department of Metallurgy and Materials Engineering*
Kasteelpark Arenberg 44, B-3001, Leuven, Belgium, stepan.lomov@mtm.kuleuven.be

ABSTRACT: Numerical computation of textile permeability is important for composite manufacturing. Using Darcy's law, permeability can be derived from a simulation of the fluid flow, i.e. after solving the Stokes, Navier-Stokes or Brinkman equations. The latter allow to model intra-yarn flow in case of permeable yarns. In this paper we present a numerical method for the calculation of the permeability of textile models based on a finite difference discretisation of the partial differential equations. Two different formulas for the calculation of the local permeability are discussed. Theoretical, numerical and in particular experimental validation is presented.

KEYWORDS: Textile composites, Permeability, CFD, Homogenisation

INTRODUCTION

For the manufacturing of composites with textile reinforcement, the permeability of the textile is a key characteristic and is of particular importance for the injection stage of Liquid Composite Moulding. The prediction of textile permeability is important due to the often encountered problems of non-uniform impregnation, which may even involve void and dry spot formation. Permeability is a geometric characteristic related to the structural features of the textile at several length scales. Textiles are porous media and the permeability tensor can be defined by Darcy's law

$$\left\langle \begin{pmatrix} u_x \\ u_y \\ u_z \end{pmatrix} \right\rangle = -Re \begin{pmatrix} K_{xx} & K_{xy} & K_{xz} \\ K_{yx} & K_{yy} & K_{yz} \\ K_{zx} & K_{zy} & K_{zz} \end{pmatrix} \left\langle \begin{pmatrix} \frac{\partial P}{\partial x} \\ \frac{\partial P}{\partial y} \\ \frac{\partial P}{\partial z} \end{pmatrix} \right\rangle . \quad (1)$$

Here, *Re* denotes the Reynolds number, $\vec{u} = \vec{u}(x, y, z)$ the fluid velocity, $P = P(x, y, z)$ the pressure, $\underline{\underline{K}}$ the permeability tensor of the porous medium and $\langle\ \rangle$ denotes volume averaging. Eqn. 1 is a homogenized equation, where information about the internal geometry of the reinforcement is taken into account in $\underline{\underline{K}}$. Finite element or finite difference Darcy solvers thus require $\underline{\underline{K}}$ as input. Since measurements of textile permeability are time- and resource-consuming, a reliable numerical prediction of $\underline{\underline{K}}$ is required.

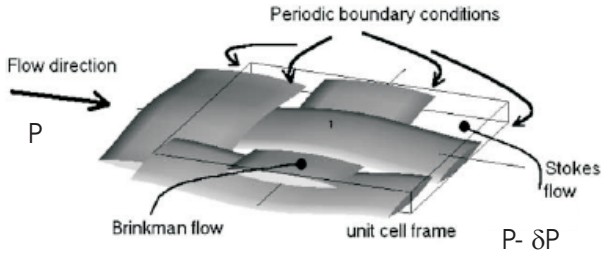

Fig. 1 A unit cell setup

For the calculation of $\underline{\underline{K}}$, we simulate the flow in a unit cell (Fig. 1) since textile has a periodic pattern. As textiles are also hierarchically structured materials, our model for fluid flow must also take into consideration the possible porosity of the yarns. Hence, in the following, if the yarns are porous, we will differentiate between inter-yarn flow and intra-yarn flow. The porosity is accounted for by the permeability tensor K_{tow}. In both cases we aim at the computation of the fluid velocity $\vec{u}$ and the pressure P in order to solve Darcy's law (1) for $\underline{\underline{K}}$.

In the case that the model is limited to creeping, single-phase, isothermal, unidirectional saturated flow of a Newtonian fluid, the inter-yarn flow is described by the incompressible Navier-Stokes equations (here in dimensionless form),

$$\begin{cases} \dfrac{\delta \vec{u}}{\delta t} + (\vec{u} \cdot \nabla)\vec{u} = -\nabla P + \dfrac{1}{Re}\Delta \vec{u} \\ \nabla \cdot \vec{u} = 0 \end{cases}. \tag{2}$$

Here, $\vec{u} = \vec{u}(x, y, z, t)$ and $P = P(x, y, z, t)$. If *Re* is small, the convective term can be neglected, and Eqn. 2 result in the Stokes equations. Later in this paper, we show numerically that for our applications both the Navier-Stokes and the Stokes equations can be used.

Intra-yarn flow depends on the local permeability tensor K_{tow} of the tow, and is described by the Brinkman equations [5] satisfying

$$\begin{cases} \dfrac{\delta \vec{u}}{\delta t} + (\vec{u} \cdot \nabla)\vec{u} + \dfrac{1}{Re}\underline{\underline{K_{tow}^{-1}}} \cdot \vec{u} = -\nabla P + \dfrac{1}{Re}\Delta \vec{u} \\ \nabla \cdot \vec{u} = 0 \end{cases}, \tag{3}$$

with the convection term included.

We develop numerical software for the calculation of the permeability of textiles, named *FlowTex*. The input of a single layer of the textile model is provided by the *WiseTex* software [11,13,19] which allows the characterisation of a single-layer of the reinforcement or a regularly or randomly nested laminate [12].

NUMERICAL SOLUTION OF THE NAVIER-STOKES EQUATIONS

For flow simulations in the irregular geometry of a textile, we have chosen to solve Eqn. (2) numerically on a regular staggered grid with a finite difference discretisation. An example of a textile geometry and its discretisation on a regular grid is shown in Fig. 2.

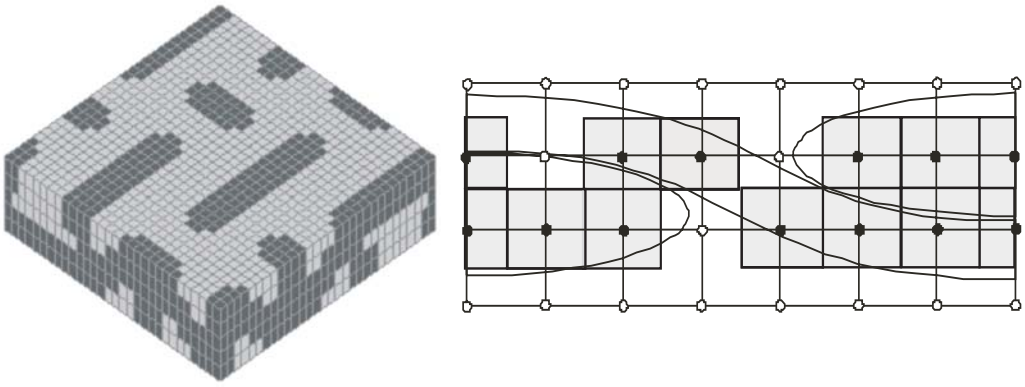

Fig 2 A 3D and 2D voxel representation of a textile geometry

In previous work the solution was performed using lattice Boltzmann algorithm [3]. The implementation described in this paper is based on the 3D finite difference Navier-Stokes solver *NaSt3DGP*, developed at the *Institute for Numerical Simulation* of the University of Bonn [1,7]. In order to apply the code for the computation of the permeability of textiles, several extensions to the code have been made. An interface between *FlowTex* and *NaSt3DGP* allows the input of the voxel description of the textile geometry [13,19] provided by WiseTex (Fig. 2). For the unit cell setup, we implemented periodic boundary conditions in three directions for the velocity, and periodic boundary conditions up to a constant gradient for the pressure (Fig. 1). To account for intra-yarn flow, the code has been extended to solve the Brinkman equations: we solve Eqn. 3 on the whole domain with variable $0 < K_{tow} \leq \infty$. It was shown by Angot [2] that this is a valid approach in which no extra interface conditions between the fluid and the porous part are required. This approach is a practical method to deal with the coupled problem of flow in a porous medium and flow in-between the yarns. An implicit treatment of the diffusive terms for the Navier-Stokes/Brinkman equations has substantially improved the speed of the permeability computations [17].

ANALYTICAL VALIDATION

In our previous papers [17,18] we presented numerical and experimental results that take the textile geometry at three different length scales into account: the macroscale of the textile part, the mesoscopic scale of the unit repeat cell, as well as the microscopic scale of the fibres within the yarns. In this section we give an analytical validation of the proposed Darcy's law for the calculation of the inter-yarn permeability with the help of homogenisation theory. Also, homogenisation theory provides us with a new possibility for the computation of the permeability tensor. Numerical validation of the latter approach will be given further in this paper.

The direct numerical treatment of fluid flow in porous media is difficult and time consuming due to the rapid variations of the pore scale. However, when the characteristic size of the obstacles in a repeat cell of the medium, e.g. of the yarns, is small compared to the whole

sample, homogenisation theory allows us to "average" or "upscale" the equations of fluid mechanics that hold on one scale of the porous medium to the next scales. Hence, we avoid the solution of the fluid equations in the complicated pore geometry by merely studying the geometry's homogenised influence on these equations [14].
Several authors have dealt with the homogenisation of the Stokes or Navier-Stokes equations in a periodic porous medium [9,14,15] and derive Darcy's law as the limiting equation in the homogenisation process. In Darcy's law information about the structure of the pore scale is only kept through the effective quantity of permeability. The permeability tensor $\underline{\underline{K}}$ in homogenisation theory is given as $K_{ij} = \frac{1}{|Y|}\int_Y \vec{w}_j^i \, \mathrm{d}\tau$, where j denotes the j-th component of the vectors w^i, which for $1 \le i \le n$ are the solutions of the so-called "cell problems":

$$\begin{aligned} &-\Delta_\tau \vec{w}^i + \nabla_\tau \pi^i = \vec{e}^i \text{ in } Y_F \\ &\mathrm{div}_\tau \, \vec{w}^i = 0 \text{ in } Y_F \\ &\vec{w}^i = 0 \text{ on } \partial Y_S \text{ and } \left\{\vec{w}^i, \pi^i\right\} \text{ is } Y-\text{periodic} \end{aligned} \tag{4}$$

Here, $\vec{e}^i$ denotes the unit vector, $\tau \in Y$, Y the unit repeat cell of the porous medium and Y_F and Y_S its corresponding fluid and solid part. Furthermore, $\vec{w}(\tau)$ and $\pi(\tau)$ are comparable to the fluid velocity and pressure of the Stokes equation.
From a numerical point of view, this offers a further possibility for the computation of the permeability tensor. The solution of the above cell problems in 3D amounts to three Stokes equations with external forces $(\vec{e}_i)_{1\le i\le 3}$, from which we obtain $(\vec{w}^i)_{1\le i\le 3}$ for the input of $\underline{\underline{K}}$. This leads to the same results as the computation of $\underline{\underline{K}}$ by Darcy's law since in the unit repeat cell these are equivalent problems [14]. Note that this method gives a straightforward definition for the computation of all components of $\underline{\underline{K}}$ whereas the calculation of $\underline{\underline{K}}$ via Darcy's law requires solving a 9x9 system of equations. However, for the calculation of e.g. K_{xx}, we neglect the influence of K_{xy} and K_{xz} in (1) which according to Table 1 is allowed and yields a direct calculation of K_{xx}.

LOCAL PERMEABILITY

If we want to include the intra-yarn flow into the flow simulations, we solve the Brinkman equations (3), which requires the local permeability in every grid point which lies inside the yarn. At micro-level, the fibres are considered as regularly packed cylinders. Gebart [6] presents analytical formulas for the permeability of a porous medium which consists of a quadratic packing of cylinders for both flow along and transversal to the cylinders

$$K_{Gebart,Along} = \frac{8}{57}\frac{\left(1-V_f\right)^3}{{V_f}^2} r^2, \tag{5}$$

$$K_{Gebart,Trans} = \frac{16}{9\pi\sqrt{2}}\left(\sqrt{\frac{V_{f\max}}{V_f}}-1\right)^{2.5} r^2, \tag{6}$$

with V_f the local volume fraction, r the radius of the cylinders and $V_{f\max} = \pi/4$. Berdichevsky et al. [4] on the other hand present formulas for the local permeability

$$K_{Berdi,Along} = \frac{r^2}{8V_f}\left(\ln\frac{1}{V_f^{\,2}} - (3-V_f)(1-V_f)\right) \tag{7}$$

$$K_{Berdi,Trans} = \frac{r^2}{8V_f}\left(\ln\frac{1}{V_f} - \frac{(1-V_f)^2}{(1+V_f)^2}\right). \tag{8}$$

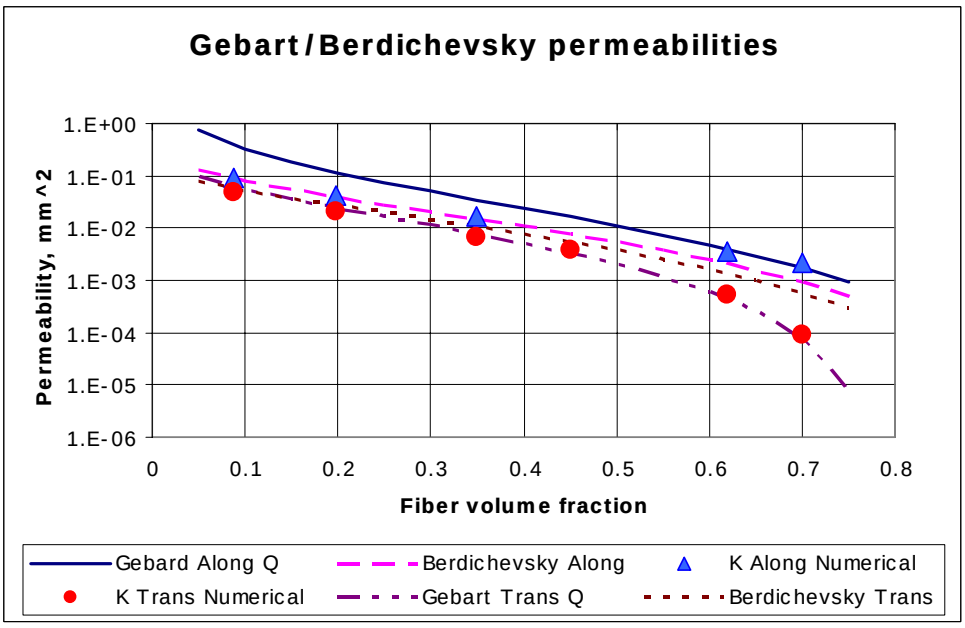

Fig. 2 Comparison of the Gebart/Berdichevsky formulas with numerical results

Fig. 2 shows a plot of the different formulas. We see that for the permeability along the fibres, the curves of Gebart and Berdichevsky show comparable results, although the formulas of Gebart give a higher permeability. For the permeability in the transversal direction, however, the formulas give different results for higher volume fractions.
Fig. 2 also shows the results of our computations with the software described above for a parallel square array of cylinders. The formula of Berdichevsky matches better with the numerical results for the flow along the fibres, although not for higher volume fractions. However, for the flow in the transversal direction, clearly the formula of Gebart gives better results. The *FlowTex* software calculates the local permeability in (and transversal to) the direction of the fibres according to (7) and (6). Once K_A and K_T are known, they are projected onto the main directions X, Y, Z which then yields the local permeability tensor K_{tow}.

VALIDATION

Analytical data

In this section we compare the numerical results of the permeability of a cubic array of spheres with analytical results. On the one hand we can compute the flow field with the Stokes equations and obtain $\underline{\underline{K}}$ from the applied pressure drop ∇P and the average velocity field $\langle \vec{u} \rangle$ in Darcy's law (1) and on the other hand the same permeability will be obtained by solving the cell problems (4). For a periodic array of spheres Sangani and Acrivos [16] found

general solutions of the Stokes equations in series formulation, whose coefficients are determined numerically. For several volume fractions Vf the authors computed the dimensionless drag force F to which the first entry of the permeability tensor is related by $K_{xx} = 1/6\pi rF$, with r the sphere radius.

Both the permeabilities from numerical simulations as well as the semi-analytical ones are listed in Table 1 for various values of $\chi = \left(Vf/Vf_{\max}\right)^{1/3}$, which is a scaled sphere volume fraction $Vf = 4\pi r^3/3L^3$, where $Vf_{\max} = \pi/6$ corresponds to the case where the spheres are in contact. First of all, we note that all the values are in good agreement with those obtained analytically by Sangani and Acrivos [16] and deviate no more than 0.5% from them. Furthermore, the results obtained from the cell problem and by Darcy's law are equal. This was to be expected as in homogenisation theory the cell problem is just an auxiliary problem for the definition of the permeability tensor and the derivation of Darcy's law. But also for actual text geometries, the permeability tensor obtained from the cell problem is accurate as shown in Table 2. Hence, homogenisation theory not only applies to our textiles but also offers an easier way to implement an efficient method for permeability computations.

Table 1: Computation of the permeability K_{xx} for a simple cubic array of spheres

χ	Resolution	K_{xx} : Darcy's Law	K_{xx} : Cell Problem	K_{xx} : Analytical
0.2	60^3	3.8135 E-01	3.8135 E-01	3.8129 E-01
0.4	60^3	1.2314E-01	1.2314E-01	1.2327E-01
0.8	80^3	1.3118E-02	1.3118E-02	1.3197E-02
1	100^3	2.5083E-03	2.5083E-03	2.5203E-03

Experimental validation

A comparison between the results of the Navier-Stokes/Brinkman solver with experimental data is given in Table 2. Information on the *Natte* textile and the *Carbon woven fabric* can be found in [8,10]. The Numerical and experimental results are in good agreement for the *Natte* textile (Fig. 3) and give reasonable results for the *Carbon woven fabric*. Table 2 also shows the results for a Parallel Square Array (PSA) of cylinders.

For a typical unit cell of textile, with a flow velocity typically used in Resin Transfer Moulding ($10^{-3} m/s$), the Reynolds number is about 0.05. As flows with a low Reynolds number can be described by the Stokes equations, we compare the solution of the Navier-Stokes equations with the solution of the Stokes equations (Table 2).

This shows that for our application, we do not have to solve the non-linear Navier-Stokes equations with pseudo time-stepping, but can solve the steady Stokes equations with a preconditioned iterative solver instead. This can lead to a considerable speedup of the permeability simulations in comparison with the time-stepping we use now to solve the Stokes equations. Such a sophisticated Stokes solver is presently under development.

Table 2 Comparison between Navier-Stokes and Stokes calculations

Method \ Setup	PSA V_f 62%	Natte	Carbon woven fabric
K_{xx} Navier-Stokes *(mm²)*	3.4e-03	3.3e-04	4.2e-04
K_{xx} Stokes *(mm²)*	3.4e-03	3.3e-04	4.2e-04
K_{xx} Cell Problem *(mm²)*	3.4e-03	3.3e-04	4.2e-04
K_{xx} Experimental *(mm²)*	-	2.7e-04 ±10%	1.0e-04 ±10%

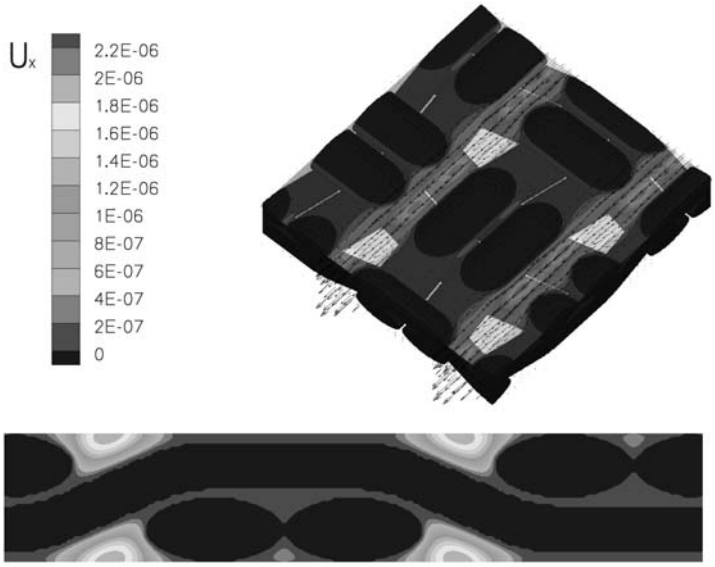

Fig. 3. 3D image and a 2D cut of the calculated flow field in the Natte model

CONCLUSIONS

Two methods for the calculation of the permeability of textiles have been presented. The solution of the Navier-Stokes/Brinkman equations with a finite difference solver yields the velocity and pressure field for Darcy's law. On the other hand, the permeability can be calculated via the definitions given by the theory of homogenisation. Both methods lead to the same numerical results, hence solving the Navier-Stokes/Brinkman equations on the unit-cell is a correct approach to obtain the textile permeability. Furthermore, the numerical results are in good agreement with experimental results.
Two formulas for the local permeability term of the Brinkman equation were discussed and compared with numerical results.

ACKNOWLEDGMENTS

This research is part of the IWT-GBOU-project (Flemish government) Predictive tools for permeability, mechanical and electro-magnetic properties of fibrous assemblies: modelling, simulations and experimental verification. R. Croce and M. Klitz were supported in part by the Sonderforschungsbereich 611 *Singuläre Phänomene und Skalierung in Mathematischen Modellen* sponsored by the *Deutsche Forschungsgemeinschaft*.

REFERENCES

1. *http://wissrech.iam.uni-bonn.de/research/projects/nast3dgp*
2. P. Angot, "Analysis of Singular Perturbations on the Brinkman Problem for Fictitious Domain Models of Viscous Flows", *Mathematical Methods in the Applied Sciences*, Vol. 22, 1999 pp. 1395.
3. E.B. Belov, S.V. Lomov, I. Verpoest, ea, "Modelling of permeability of textile reinforcements: Lattice Boltzmann method", *Composites Science and Technology*, Vol. 64, 2004, pp. 1069.
4. A. Berdichevsky and Z. Cai, "Preform Permeability Predictions by Self-Consistent Method and Finit Element Simulation", *Polymer Composites*, Vol. 14, 1993 pp. 132.
5. H.C. Brinkman, "On the permeability of media consisting of closely packed porous particles", *Applied Scientific Research*, Vol. 1, no. 1, 1947 pp.81.
6. B. Gebart, "Permeability of Unidirectional Reinforcements for RTM", *Journal of Composite Materials*, Vol. 26, no. 8, 1992 pp. 1100.
7. M. Griebel, T. Dornseifer and T. Neunhoeffer, "Numerical Simulation in Fluid Dynamics, a Practical Introduction", SIAM, Philadelphia, 1998.
8. K. Hoes, H. Sol, D. Dinescu, ea., "Study of nesting induced scatter of permeability values in layered reinforcement fabrics", *Composites part A*, Vol. 35, 2004, pp.1407.
9. U. Hornung (Ed.), "Homogenization and Porous Media", Springer Verlag, 1997.
10. B. Laine, G. Hivet, P. Boisse, ea, "Permeability of the woven fabrics: a parametric study", *Proc. of the 8th ESAFORM Conf. on Material Forming*, 2005. pp. 995
11. S.V. Lomov, G. Huysmans, Y. Luo, ea., "Textile composites models: Integrating strategies", *Composites Part A*, Vol. 32, no. 10, 2001 pp. 1379.
12. S.V. Lomov, I. Verpoest, T. Peeters, ea., "Nesting in textile laminates: Geometrical modelling of the laminate", *Composites Science and Technology*, Vol. 63, 2002 pp. 993.
13. S.V. Lomov, I. Verpoest, B. Verleye ea., "WiseTex based models of permeability of textiles", *Proc. of the 8th Int. Conf. on Flow Processes in Composite Materials.*
14. A. Mikelic, "Homogenization theory and applications to filtration through porous media", *Filtration in porous media and industrial application*, Lecture Notes in Mathematics, Vol. 1734, 2000, pp. 127.
15. E. Sanchez-Palencia, "Non-homogeneous media and vibration theory", *Lecture notes in Phys.*, Springer Verlag, 1980 pp. 127.
16. A. S. Sangani and A. Acrivos, "Slow flow through a periodic array of spheres", *Int. J. Multiphase Flow*, Vol. 8, no. 4, 1982 pp. 343.
17. B. Verleye, M. Klitz, R. Croce, ea., "Computation of the permeability of texiles", Report TW 455, Dept. Computer Science, K.U.Leuven, Leuven, Belgium, April 2006.
18. B. Verleye, M. Klitz, R. Croce, ea., "Computation of Permeability of Textile Reinforcements", *Proc. of IMACS 2005,* CD-edition, 2005.
19. I. Verpoest and S.V. Lomov "Virtual textile composites software Wisetex: integration with micro-mechanical, permeability and structural analysis." *Composites Science and Technology*, Vol. 65, 2005, pp. 2563.

A PERMEABILITY PREDICTION FOR NON–CRIMP FABRICS

Richard Loendersloot, R. Akkerman

University of Twente
Faculty of Engineering Technology, P.O. Box 217, 7500AE Enschede, The Netherlands: r.loendersloot@ctw.utwente.nl

ABSTRACT: A model is proposed to analyse the variation in the permeability of Non–Crimp Fabrics, originating from variations in the internal structure of the material. A geometrical description of the fabric based on the distortion induced by the stitch threads piercing through the fabric is employed. The distortions form channels which are mutually connected. It is assumed that these channels dominate the permeability of the fabric. A network of flow channels is subsequently defined, in which the variations, measured in the dimensions of the distortions, is explicitly accounted for. The variations in the internal structure of the fabric affect the averaged permeability significantly. Moreover, a network rather that a single unit cell is required to predict the averaged permeability and its variation properly. Finally, the spatial distribution of the randomly generated channel dimensions affects the permeability significantly.

KEYWORDS: composites, permeability, flow modelling, internal geometry, variability

INTRODUCTION

The closed mould production technology Resin Transfer Moulding (RTM) is a cost--effective method to manufacture near net–shaped composite products. The resin is injected into a cavity at a pressure of typically 2 – 10 bars, while a preform, consisting of dry semi–continuous fibres, fills the cavity. One of the key problems to obtain a reproducible product quality is the impregnation behaviour of the fibrous reinforcement. The permeability of a textile structure is difficult to predict and a significant amount of variation is present in measured permeability values.
This work focusses on the variability in the permeability originating from varitions in the internal geometry of a Non–Crimp Fabric (NCF). A network flow model is defined to predict the permeability and its variation based on the internal geometry of the fabric and its variations.
The geometrical model is based on the analysis of three different types of biaxial NCFs. The geometry of these fabrics was previously presented in [1].

GEOMETRICAL MODEL

Non–Crimp Fabrics (NCF) are frequently applied as reinforcement material for RTM based composites. NCFs consist of a stack of uni–directional, but mutually differently oriented fibre mats. The stacks are stitched together by a relatively thin thread to obtain sufficient structural integrity of the fabric.
Multiple layers of fibres are spread on the machine bed during the manufacturing of NCF. The fibre bed moves in the longitudinal direction of the machine ('machine direction'). A bar of needles spans the width of the fabric and the needles penetrates the fabric, leaving the stitch thread behind. The needle spacing *A* and the distance between subsequent needle penetrations, the stitch distance *B*, remain constant during the manufacturing process. Different stitch patterns are formed by applying a additional movement of the needle bar in cross direction [2]. Three different warp knitted stitch patterns are depicted in figure 1.

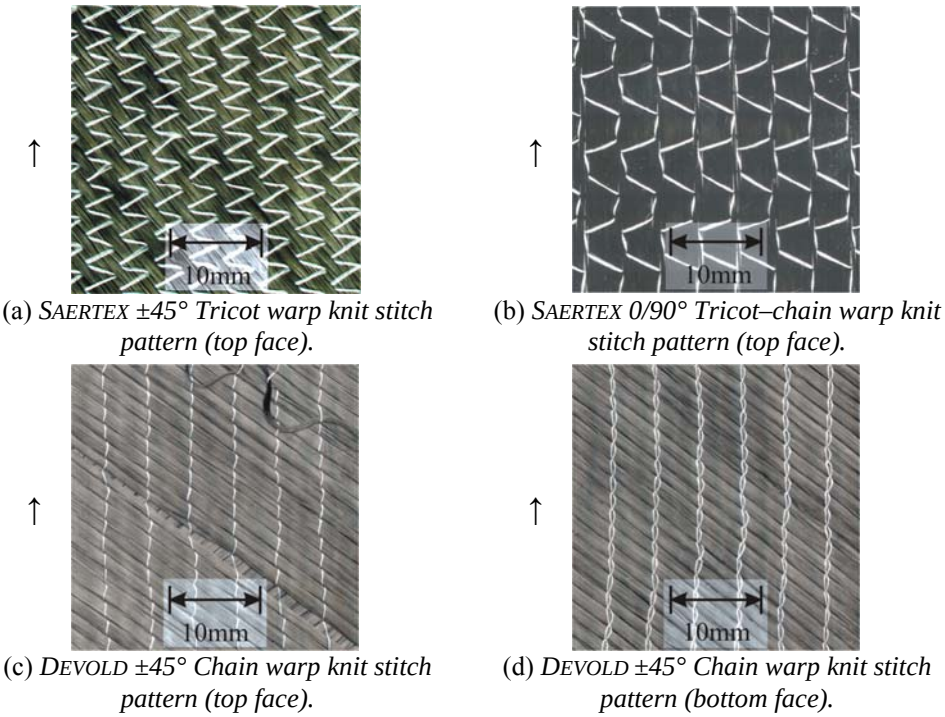

(a) *SAERTEX ±45° Tricot warp knit stitch pattern (top face).*

(b) *SAERTEX 0/90° Tricot–chain warp knit stitch pattern (top face).*

(c) *DEVOLD ±45° Chain warp knit stitch pattern (top face).*

(d) *DEVOLD ±45° Chain warp knit stitch pattern (bottom face).*

Fig 1: *Three stitch patterns (a-c). The bottom face is similar for all fabrics (d). The arrow indictaes the machine direction.*

Meso – Level Structure

The core of the geometrical model is the distortion of the fibre paths, induced by the stitch threads piercing through the fabric. A wedge shaped gap results, oriented in the direction of the fibres, as shown in the scanned image of a DEVOLD biaxial ±45° NCF depicted in figure 1. The width and length of the distortion are indicated (*b* and *l* respectively).

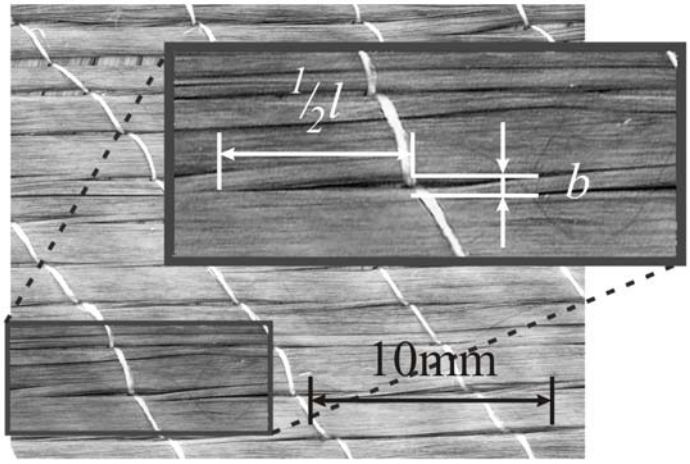

Fig.2: *Stitch Yarn induced fibre Distortions (SYD) of the top face of a DEVOLD biaxial ±45° NCF (chain knit pattern), with b the width and l the length of the distortion.*

The definition of the distortions was first presented by Lomov et al. [2], who referred to them as 'cracks' and 'channels'. Here the term 'Stitch Yarn induced fibre Distortion' (SYD) is used to comprise both these terms.

SYD Shape

It is assumed that the distortion is wedge shaped and symmetric along its longitudinal axis (aligned in fibre direction) and its transverse axis (perpendicular to the fibre direction). A set of four needle penetrations and the accompanying SYDs of a ±45° biaxial fabric is depicted in figure 3.

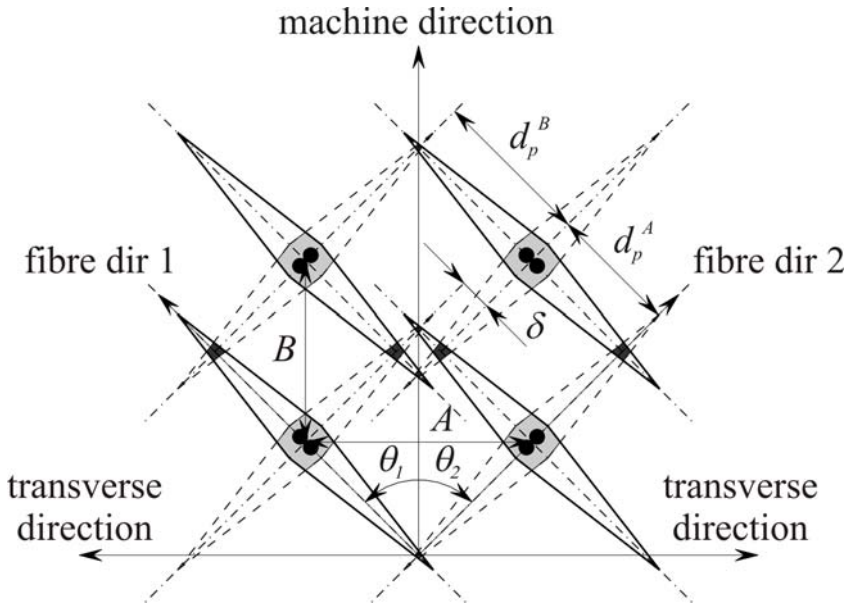

Fig. 3: *Schematic representation of the SYD configuration of a biaxial NCF. The light gray areas indicate the interaction regions between SYDs of top and bottom faces (solid and dashed lines respectively) in the centre of the SYD, the dark areas indicate the interaction regions in the tip. The dots indicate the stitch yarns piercing through the fabric.*

The stitch distances *A* and *B* are indicated, as are the fibre angles θi, the distance δ separating the tip of neighbouring SYDs and finally the projected stitch distances d_p^A and d_p^B.
Moreover, it is assumed that the shape of the SYD is constant in the through–thickness direction of the fabric. The height of the SYD directly follows from the height of the cavity (which is constant in case of RTM) and the total number of plies. Dimensionless parameters were introduced for the width (κ) and the length (λ) [1].

Statistical Distribution

The length and width of the SYDs were measured for the three different fabrics, shown in figure 1. The averaged width and length was measured for 100 SYDs on either side of the fabrics. The logarithmic values of the dimensions exhibit a normal distribution [1]. The length is assumed to be constant here. The fabric properties and measured widths *b* and standard deviations $\sigma_{\ln}$ of the ±45° chain knit fabric (figure 1c–d) are presented in table 1. This fabric is used in the flow model.

Table 1: *Material properties and measured averaged width and standard deviation (averaged over both faces) of the DEVOLD biaxial ±45° chain knit fabric.*

Parameter			value
Averaged width	$\bar{b}$	[mm]	0.28
Length	l	[mm]	3.89
Layer thickness	h	[mm]	0.5
Logarithmic standard deviation	σ_{ln}	[-]	0.33
Needle spacing	A	[mm]	5
Stitch distance	B	[mm]	2.5
Areal density	ρ_A	[kg·m^{-2}]	0.534
Fibre count		[-]	12K

FLOW MODEL

The flow model is based on the assumption that the flow in the SYDs dominates the overall flow, since the SYDs are an order of magnitude larger in size than the space between the filaments of the fibre bundle. The SYDs are treated as channels and the fluid flows from a SYD in one ply to the SYD in an adjacent ply through the interactions regions. These regions are indicated by the gray areas in figure 3.

Channel Flow Equations

The flow of resin through a fibrous reinforcement can be characterised as a laminar, viscous flow of an incompressible, Newtonian fluid. Hence the flow rate Φ in a channel with radius *r* is related to the pressure gradient in longitudinal direction d*p*/d*s* as:

$$\Phi = \frac{\pi r^4}{8\mu}\frac{\mathrm{d}p}{\mathrm{d}s} = \frac{K}{\mu}\frac{\mathrm{d}p}{\mathrm{d}s} \equiv \frac{1}{\Re\mu}\frac{\mathrm{d}p}{\mathrm{d}s}, \qquad (1)$$

with μ the dynamic viscosity, *K* the permeability and the flow resistance. However, the cross–sectional shape of the SYD is not circular and not constant over its length. Therefore

the hydraulic radius r_h is employed, defined as the twice the ratio of the cross–sectional area A_c over the perimeter P:

$$r_h = \frac{2A_c}{P}. \tag{2}$$

Subsequently the flow resistance R_i of the i^{th} channel is calculated by integration of the flow resistance $\Re$, given in equation (1), between the two points s_i and s_{i+1} (as indicated in figure 4):

$$R_i = \int_{s_i}^{s_{i+1}} \Re(s)\,\mathrm{d}s = \frac{8}{\pi}\int_{s_i}^{s_{i+1}} \left(r_h(s)\right)^{-4}\,\mathrm{d}s. \tag{3}$$

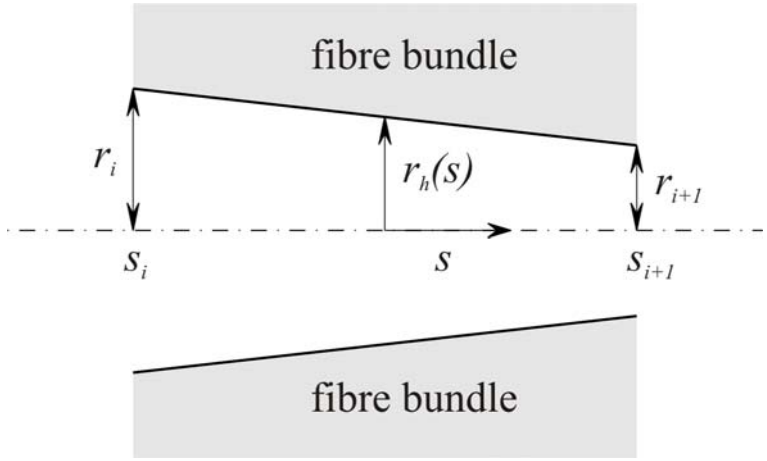

Fig. 4: *Linearly decreasing channel radius $r_h(s)$: r_i maximum, r_{i+1} minimum radius, s longitudinal coordinate.*

Single SYD Unit Cell

A single SYD is subdivided into six channel sections, see figure 5. The *a* and *b* variants of the channels section *I*, *II* and *III* are equal, based on the symmetrical shape of the SYD.

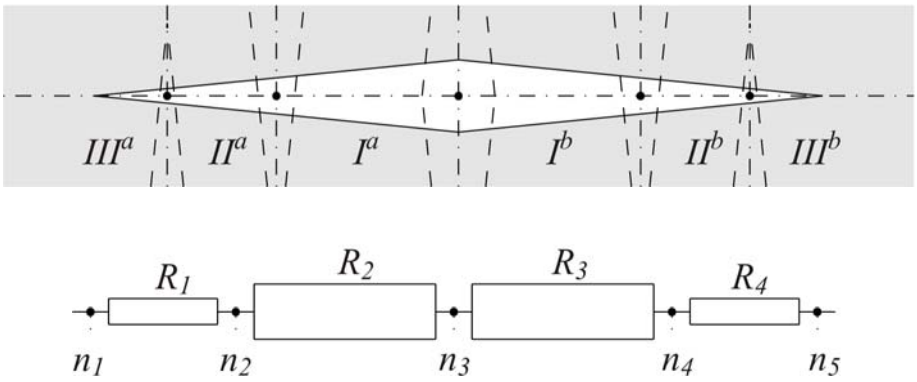

Fig. 5: *SYD subdivided into two times three sections. The dashed lines indicate SYDs of the adjacent ply, the dots are the centres of the interaction regions. The channel sections I and II are represented by a channel with an effective resistance.*

The dots ($n_{1,2,3,4,5}$) indicate the centres of the interaction regions between the SYDs of adjacent plies. The sections $III^{a,b}$ are dead ended sections and are discarded. The sections $I^{a,b}$ and $II^{a,b}$ are represented by channels with a flow resistances $R_{1,2,3,4}$.

Network Formulation

The effect of the variability in the dimensions of the SYDs on the averaged value of the permeability and its variation cannot be estimated based on a single SYD unit cell. Hence, a network of SYDs is formed, as depicted in figure 6. The light gray resistances correspond to section *I*, the dark gray to section *II*.

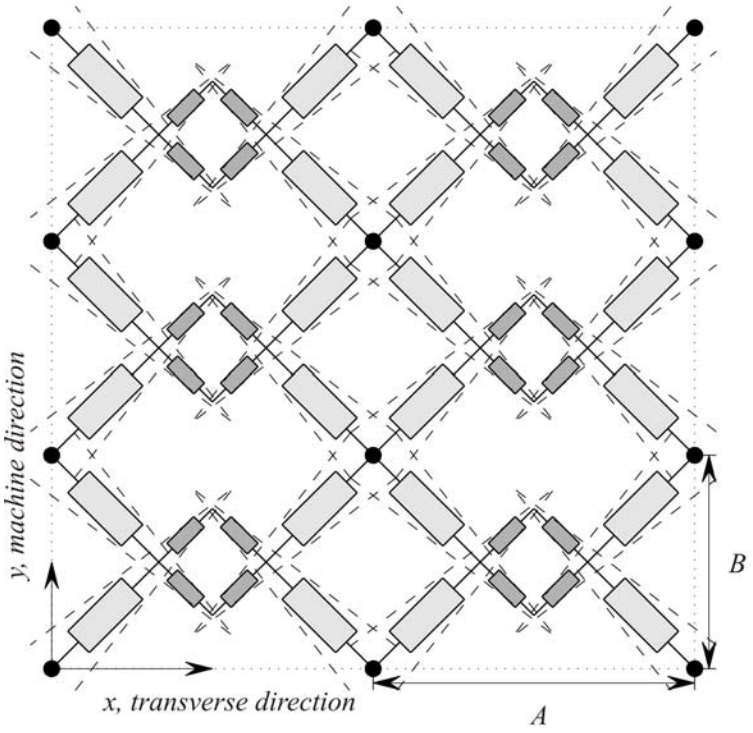

Fig. 6: *A network of flow resistances, representing a flow domain. The dots indicate the stitch penetration locations.*

The flow through a network is solved by employing a finite element discretisation. Pressure boundary conditions were used to apply a pressure gradient either in machine direction (*y* in figure 6) or in transverse direction (*x*).
A set of SYD widths was generated, based on the measured averaged width and its variation. The widths were assigned to the SYD of the network, either randomly or according to a predefined distribution. The permeability of the network was finally calculated by comparing the total volumetric flow rate with the pressure drop, see equation (1).

RESULT & DISCUSSION

A number of networks were analysed, based on fabric 3. The permeabilities in machine direction and transverse direction (figure 6) of the analysed networks are normalised on the permeability of a network with equally sized SYDs (referred to as the 'nominal permeability').

Amount of Variation

The amount of variation on the widths of the SYDs was varied between 0 and 150% of the measured standard deviation. The resulting normalised permeability K_N for a network of size $40A \times 60B$ drops to roughly 85% of the nominal permeability for $\sigma_{\ln} = \sigma_{meas}$ and to 70% for $\sigma_{\ln} = \sigma_{meas} \times 150\%$ (see figure 7). Note that the normalised permeability is expected to be higher than 1 if the averaged permeability of a series of single SYD unit cells is determined. This corresponds to a system of parallelly connected flow resistances. A network approach results in a different prediction of the permeability compared to a unit cell approach.

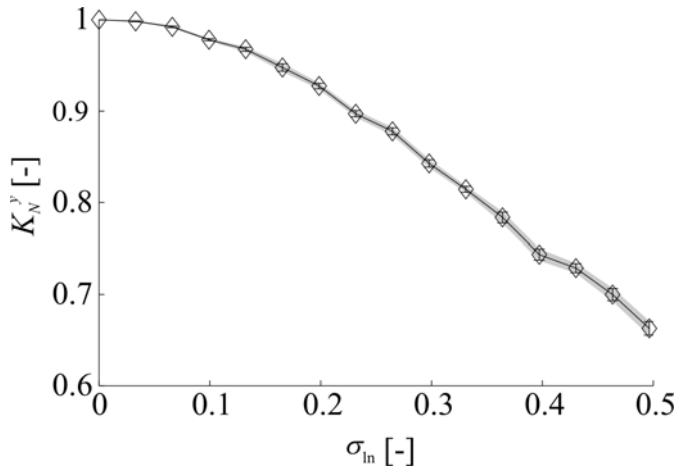

Fig. 7: *Normalised permeability as a function of the amount of variation based on a logarithmic standard deviation (measured standard deviation: $\sigma_{meas} = 0.33$, network size: $40A \times 60B$).*

Lower and Upper Bound

The lower and upper bounds of the permeability of the network are estimated by assuming that the widths either only vary in or perpendicular to the flow direction. The lower and upper bound (see figure 8) are found to be 40% below and 50% above the nominal permeability, irrespective of the flow direction.

This can result in a factor 3 difference between predicted – or measured – permeabilities for the given variation in the SYD dimensions.

Influence of Spatial Distribution

The set of randomly generated SYD widths can either be distributed randomly, or according to a certain predefined spatial distribution. The normalised permeabilities for a flow in the machine direction are shown in figure 8. The spatial distribution causes the clustering of channels with comparable size. The type of distribution determines where the clustering occurs (for example: clustering of large SYD widths in the centre). The normalised permeabilities approach the upper or lower bounds, in which the amount of order is maximal. A similar behaviour is observed for a flow perpendicular to the machine direction. The permeabilities approach the oppposite bound compared to a flow in the machine direction, in that case.

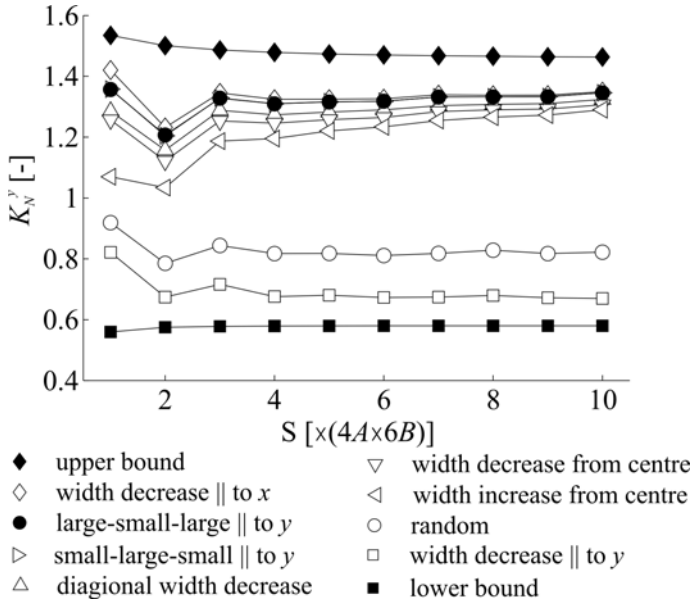

Fig. 8: *Normalised permeability in machine direction for various spatial distributions (K_N^y).*

The predicted permeability of the network is essentially different from the predicted permeability if only individual SYD unit cells are analysed. The level of order in the spatial distribution has a significant effect on the predicted permeability. Hence, both the variation and the spatial distribution have to be taken into account in a network formulation to predict the permeability and its variation properly.

CONCLUSIONS

The conclusions that can be drawn from the network approach, to predict the permeability of an NCF are:

- The variations in the internal structure of an Non–Crimp Fabrics have a significant effect on the macroscopic permeability of the fabric.
- It is not sufficient to average over a sufficiently large number of single SYD unit cells. A coupled network is required to obtain an accurate prediction of the permeability and its variation.
    - The spatial distribution of the dimensions of the SYDs in the network has a significant effect on the normalised permeability.

REFERENCES

1. R. Loendersloot, S.V. Lomov, R. Akkerman and I. Verpoest, "Carbon Composites based on Multiaxial Multiply Stitched Preforms. Part V: Geometry of Sheared Biaxial Fabrics", *Composites Part A*, 37 (2006) 103-113.

2 S.V. Lomov, E.B. Belov, T. Bischoff, S.B. Ghosh, T. Truong Chi and I. Verpoest, "Carbon Composites based on Multiaxial Multiply Stitched Preforms Part I: Geometry of the Preform". *Composites Part A*. 33 (2002) 1171-1183.

Session 2

EXPERIMENTAL ANALYSIS

VARIABILITY IN AEROSPACE VARTM PROCESSING

Pit Schulze[a], and Dirk Heider[a,b,*]

a) Center for Composite Materials, University of Delaware, Newark, DE 19716, USA*

b) Department of Electrical and Computer Engineering, University of Delaware, Newark, DE 19716, USA

Corresponding author: heider@ccm.udel.edu, (302) 831-8898

ABSTRACT: Vacuum-Assisted Resin Transfer Molding (VARTM) is widely used for large-scale composite manufacturing of civil and defense applications. Here, the infusion process reduces part costs due to a decrease in labor, material and equipment expenses compared to other composite manufacturing techniques. However, in order to replace conventional manufacturing methods for aerospace-quality parts such as autoclave processing, the VARTM process repeatability and part quality must be improved. This research is evaluating the influence of incoming material and processing condition on final part quality for three dominant VARTM process variations.

INTRODUCTION

Vacuum-assisted resin transfer molding (VARTM) has the potential advantages of relatively low cost with sufficiently high volume fractions of reinforcement and can be readily applied to large-scale structures. However, for many aircraft applications, VARTM does not currently provide sufficient repeatability or control of variability. In order to routinely produce VARTM parts of aircraft quality, the key factors of variability must be understood. This will enable the long-term objective of repeatable properties (property/weight) that are close to autoclave processed part levels at a lower cost.

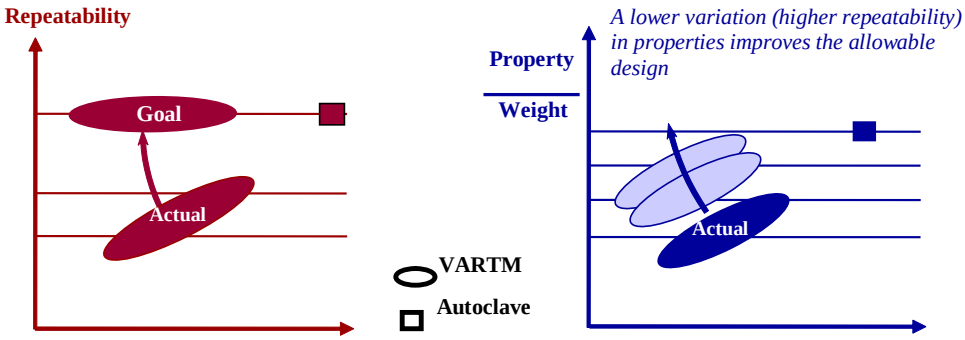

Figure 1: VARTM has the potential to reduce cost with equivalent repeatability compared to autoclave processing

There are many factors that influence the variability of the final part. The factors that play a major role in the cause of this variation need to be identified and the causes and effects of changes in these factors understood. Three main VARTM process variations have been considered: 1) The SCRIMP process [1], patented by TPI Composites is a vacuum infusion process using a high-permeability layer to rapidly distribute the resin on the part surface and then allow through-thickness penetration, 2) The CAPRI process [2], patented by Boeing Co. is a SCRIMP variation where a reduced pressure difference is used to minimize thickness gradients and resin bleeding, 3) The VAP process [3] is another SCRIMP variation, patented by EADS where a air-permeable membrane is used on top of the distribution media to allow continuous and areal venting reducing void content and creating a robust process variant.

VARTM PROCESS COMPARISON

UD-CCM's models [4,5] are used to investigate the effects of processing parameters and different processing scenarios on variation of resin flow, resin pressure and thickness variation of the composite laminate. The important material parameters include the permeability of the preform and distribution media for flow prediction as well as the compaction behavior to characterize dimensional tolerances. A new apparatus has been developed at UD-CCM [6] allowing measurement of the transverse permeability as a function of compaction and debulking cycles using both gaseous and liquid flow. The experimental cell provides insight into the variability of the incoming material and provides the needed understanding of the material changes during debulking to fully understand the CAPRI process. Figure 2 shows a typical compaction and permeability curve for a plain-weave preform subjected to debulking. An 80%-90% reduction in permeability is observed as well as a 4-5% decrease in thickness after 200 debulking cycles increasing significantly the fiber volume fraction in the part.

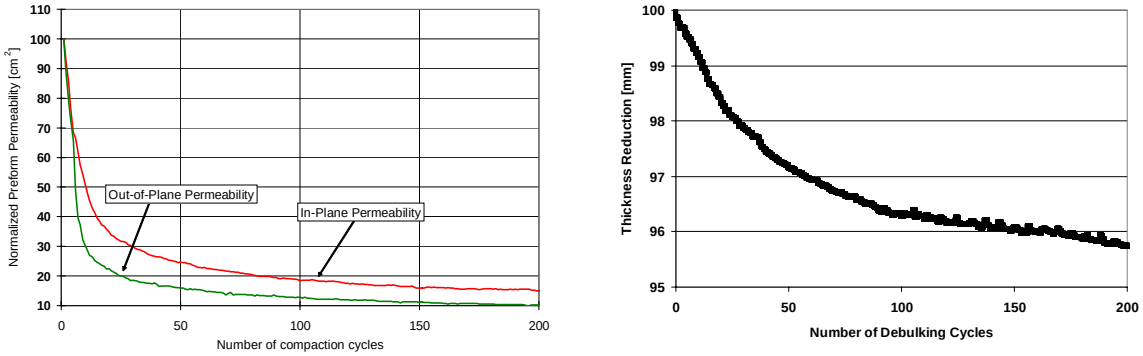

Figure 2: Debulking alters the thickness and permeability of the incoming reinforcement

All VARTM processes apply vacuum across the infusion and vent gates allowing resin flow into the reinforcement and compaction of the preform. The resulting pressure gradient during injection reduces the compaction pressure near the injection line and increases the thickness of the preform and reduces fiber volume fraction. After full infusion the pressure and thickness gradient can be reduced during a subsequent resin bleeding step. Models have been developed to predict the dimensional tolerances as a function of material parameters and process setup and can be used to optimize the CAPRI pressure during infusion and the required gel time and/or vacuum pressure during resin bleeding to minimize the final part thickness variation. Figure 3 shows the benefit and disadvantage of the CAPRI setup compared to conventional VARTM processing. The final cured part thickness is greatly reduced due to the vacuum debulking of the preform while the gradient is minimized with the application of partial vacuum in the infusion bucket. Nevertheless, a potential disadvantage is

the increase in infusion time due to the reduced pressure gradient and reduced permeability of the fabric.

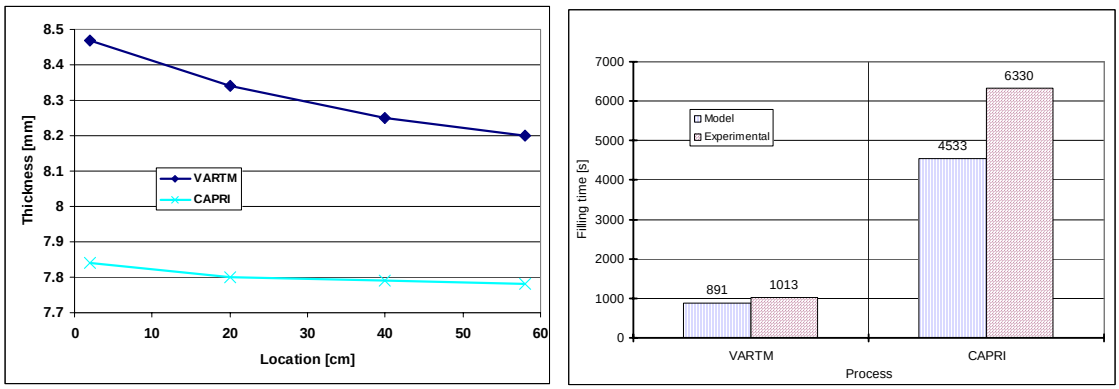

Figure 3: The CAPRI process improves fiber volume fraction and dimensional tolerances while increasing processing time

The VAP process provides an alternative approach to reduce variability. The air-permeable, resin-proof membrane allows application of continuous vacuum compaction on the complete surface even during infusion reducing the thickness gradient. The membrane also enables a more robust VARTM process that minimizes/eliminates the potential for dry spot formation and lowers void content due to continuous degassing of the resin during impregnation. Here, volatiles generated during processing can escape through the membrane layer and reduce the void content well below 1% for typical epoxy resin systems. Research has shown, however, that this innovative solution works only when the resin and membrane are compatible. For example, current membrane material supplied by W. L. Gore & Associates GmbH is effective with epoxy resin systems but inadequate for vinyl-ester systems, which have high styrene content. To fully control the membrane-based process and extend its use to a wider range of resins, a fundamental understanding of compatibility issues is currently developed.

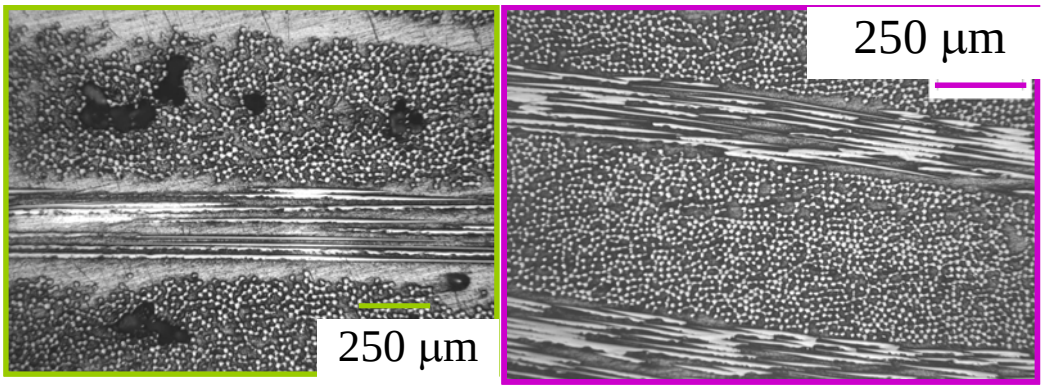

Figure 4: Vinyl ester part on the left shows high void content versus below 1% for the epoxy part

Automation is also key to improve repeatability of the VARTM process [7]. UD-CCM has developed the SMARTMolding Intelligent Process Control (IPC) system which has been implemented at various companies for production of VARTM components. This approach enables material, process, and part traceability along with semi-automated material lay-up, automated debulking and resin mixing, and resin infusion and control of dwell times and cure cycles. The automation capabilities enable monitoring of cycle times for all processing steps, sensing of the important process parameters through embedded sensors and QA/QC of the complete process.

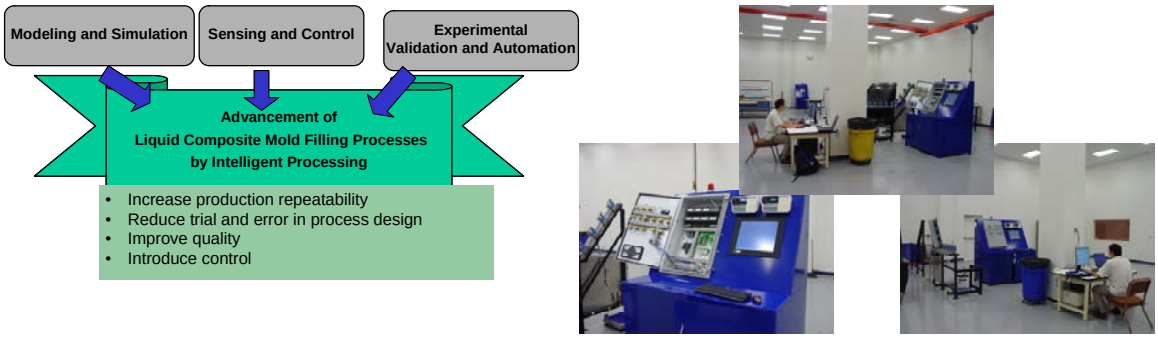

Figure 5: Industrial hardened automation is available
to provide QA/QC of the VARTM process

SUMMARY

The VARTM process is poised to penetrate the aerospace market. New process developments and a better fundamental understanding of the process allow part fabrication with improved dimensional tolerances and good mechanical properties at reduced total fabrication cost. Typical fiber volume fraction of above 55% with below 1% void content can be repeatable achieved bringing it close to autoclave properties. In addition, the material suppliers have commercialized new toughened resin systems and non-crimp fabric materials. Automation is also available to reduce the expert's input currently required to fabricate components. Still, continued research is on-going to allow for a better understanding of the infusion process in particular when the system is scaled up to large and complex geometry components.

REFERENCES

1. W. Seemann, "Plastic Transfer Molding Techniques For The Production Of Fiber Reinforced Plastic Structures", US Patent 4,902,215 (US), 02/20/90.
2. J. Woods, A. E. Modin, R. D. Hawkins, D. J. Hanks, "Controlled Atmospheric Pressure Infusion Process", International Patent WO 03/101708 A1.
3. Filsinger, J., Lorenz, T., Stadler and F., Utecht, S., (2001) Method and device for producing fiber-reinforced components using an injection method, *German Patent WO 01/68353 A1*.
4. K. T. Hsiao, R. Mathur, J. W. Gillespie Jr., B. K. Fink, S. G. Advani, "A Closed Form Solution for the Vacuum-Assisted Resin Transfer Molding Process", Journal of Manufacturing Science, 122, 2000, p. 463-472.
5. Advani, Suresh G, Sozer, E. Murat, "Process Modeling in Composites Manufacturing", Elsevier Marcel Dekker, Inc. 2003, p.151.
6. Y. Zhang, S. Scholz, S. Amouroux, J. W. Gillespie, Jr and D. Heider, "Measurement of Transverse Permeability Using Gaseous and Liquid Flow", Proceedings of the American Society for Composites. 20th Technical conference. Philadelphia, 2005.
7. D. Heider, J. W. Gillespie Jr., "Automated VARTM processing of large-scale composite structures", Journal of Advanced Materials, v 36, n 4, October, 2004, p. 11-17.

LIQUID COMPOSITE MOULDING: INFLUENCE OF FLOW FRONT CONFLUENCE ANGLE ON LAMINATE POROSITY

Gion A. Barandun, Paolo Ermanni

Centre of Structure Technologies, ETH Zurich, Leonhardstrasse 27, 8092 Zurich, Switzerland: gbarandun@ethz.ch

ABSTRACT: Advanced Liquid Composite Moulding processes using injection strategies with multiple gates often lead to unwanted filling patterns. Simulation and optimization can contribute to further enhance the filling process; nevertheless flow front confluences (weld lines) cannot be completely avoided. This paper presents the results of a study aiming at the investigation of the relationship between the confluence angle and the local laminate quality of the impregnated part. Part quality has been determined based on the porosity in the confluence zones and in the undisturbed part zones. A total of 108 specimens has been evaluated. Micrographic image processing has been done automatically by software to guarantee constant conditions for every image. Additionally, to globally visualize porosity, some parts have been processed using transmitted light and thermography. These inquiries allow a qualitative conclusion on the laminate structure and thus the porosity of the produced parts.

The micrographic image processing clearly shows that porosity is significantly higher in the confluence area, depending on the confluence angle. An angle of 20° (measured between the flow directions) leads to a porosity increase of approx. 1.5%, whereas an angle of 160° already increases the porosity more than 4%.

KEYWORDS: Liquid Composite Moulding, Part Quality, Porosity, Flow front confluence, Confluence Angle, Weld line, Micrographic image processing.

INTRODUCTION

A variety of commercially available process simulation tools are used to support the development of Liquid Composite Moulding parts [1, 2]. In this context, LCM process optimization using Evolutionary Algorithms is an actual research topic [3-5]. Objective functions include filling time, fill grade and criteria related to laminate quality, one of them being the angle between two colliding flow fronts. As a worst case scenario, two flow fronts joining with an angle of 180° (“head-on”) will form voids, as either the entrapped air cannot move towards a vent or, in case of vacuum assisted injection, areas with dry or not completely impregnated fibres might be generated. Those effects are occurring at angles below 180°, although in alleviated manner. This paper presents an experimental investigation targeting the quantification of the impact of the confluence angle on the porosity of the final part. Several samples are produced and then analysed by micrographic images.

EXPERIMENTAL PROGRAMME

The different confluence geometries are illustrated in Fig. 1. Samples have been manufactured in a glass tool, to be able to monitor flow front progression. Two symmetrically placed injection ports fill the form building a confluence zone between the two linear flow fronts. For this study, a biaxial (±45°) fabric from COTECH in conjunction with the SIKA Biresin L84T epoxy resin system were used. The resin was injected at 60°C (resin viscosity 60mPa s) with a constant pressure of 2 bar. 12 fibre layers were stacked into the cavity (height 5mm), resulting in a fibre volume content of 40.6%. As soon as complete cavity had been reached, the injection gates were closed.

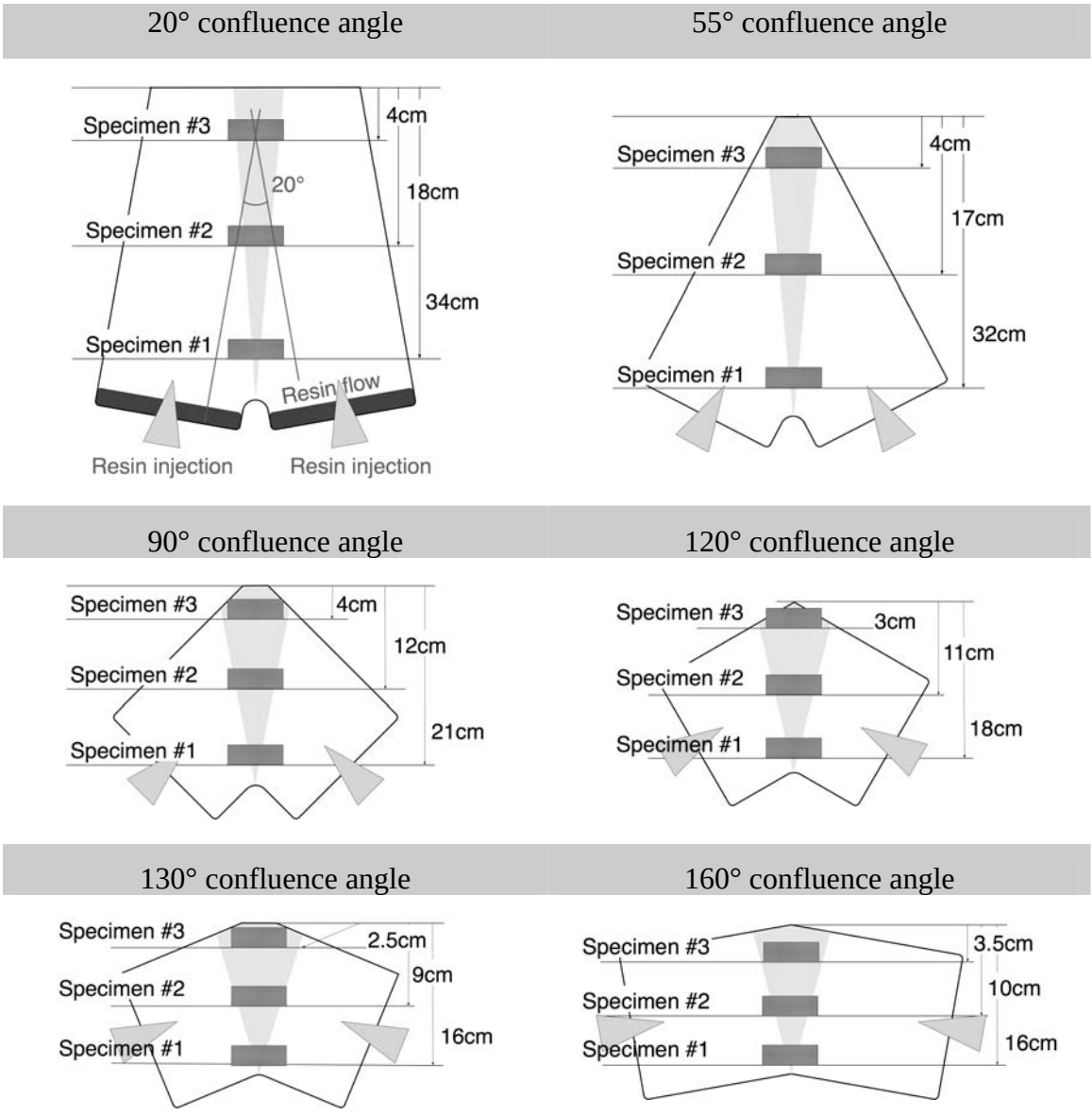

Fig. 1 Sample parts

The specimens for micrographic analysis were cut out from the sample parts as illustrated in Fig. 1. The image layer is always in flow direction, as shown in Fig. 2. The fibre orientation is the same in all images. As the fabric is isotropic, the flow direction has no influence on void formation.

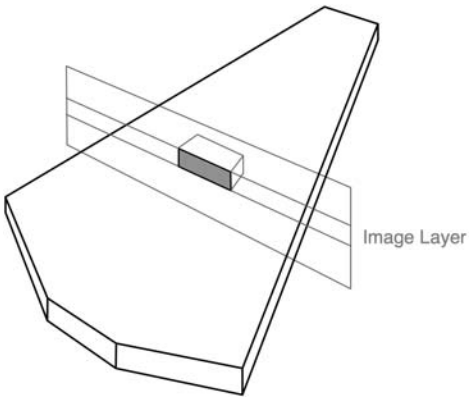

Fig. 2 Specimen orientation

RESULTS

Table 1 and Table 2 show the porosity values for the samples in the confluence and in the undisturbed zone respectively. Average values are summarized in Table 3. Three experiments were carried out for every confluence angle. Fig. 3 shows a micrograph of a laminate produced with confluence angle 55°. On the left hand side, the original picture can be seen. The right hand side shows the corresponding binary picture (entrapments marked in black) including the measurement frame and the scale. The frame is chosen in a way that takes into account the inevitable shading of the picture in the corners.

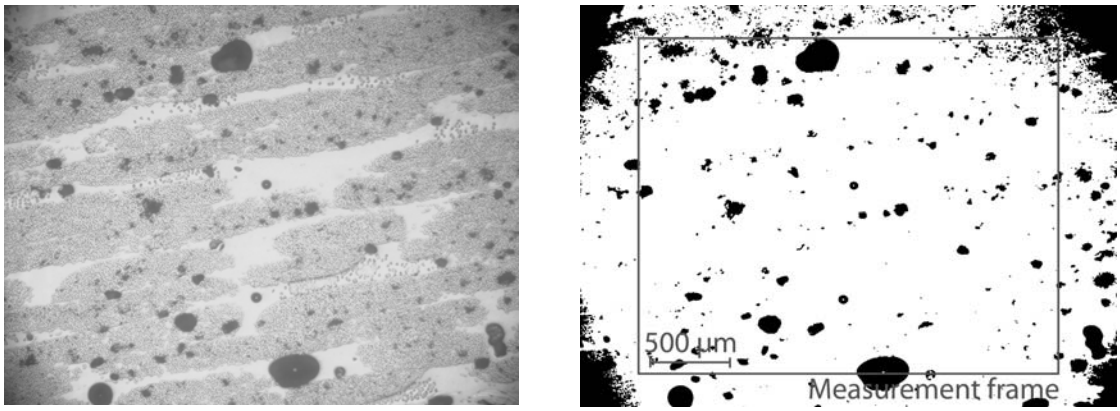

Fig. 3 Micrographic image of 55° sample. Right hand side picture shows binary representation for image data processing

Cutting samples were taken at three different positions in the confluence zone (Fig. 1). To be able to better quantify the effect of the flow front confluence, additional specimens have been cut out from undisturbed part zones. The values obtained were used as a reference to exclude

effects not directly related to flow confluence. As shown in Fig. 4 the porosity increases with increasing confluence angle.

Table 1 Porosity in confluence zone determined by micrographic image processing

		Angles	20°	55°	90°	120°	135°	160°
Porosity	Exp. #1	Spec. #1	1.46%	4.86%	n.a.	6.76%	5.70%	3.97%
		Spec. #2	3.03%	5.37%	n.a.	2.99%	4.81%	5.72%
		Spec. #3	3.58%	5.76%	n.a.	6.97%	4.86%	5.58%
	Exp. #2	Spec. #1	2.22%	3.28%	5.85%	4.12%	4.82%	8.87%
		Spec. #2	4.63%	3.35%	4.43%	4.09%	4.61%	7.56%
		Spec. #3	2.39%	4.22%	3.42%	5.28%	4.62%	5.99%
	Exp. #3	Spec. #1	1.69%	5.35%	6.6%	6.94%	8.70%	n.a.
		Spec. #2	4.90%	2.90%	6.34%	6.28%	5.15%	n.a.
		Spec. #3	2.87%	7.37%	6.25%	10.22%	5.82%	n.a.
		Mean value	2.97%	4.72%	5.48%	5.96%	5.45%	6.28%

Table 2 Porosity in undisturbed part zones

		Angles	20°	55°	90°	120°	135°	160°
Porosity	Exp. #1	Spec. #1	n.a.	1.43%	n.a.	2.98%	1.36%	1.04%
		Spec. #2	n.a.	2.11%	n.a.	2.69%	2.12%	1.19%
		Spec. #3	1.99%	3.20%	n.a.	2.28%	2.60%	3.05%
		Spec. #4	1.36%	3.52%	n.a.			
	Exp. #2	Spec. #1	1.15%	0.37%	n.a.	1.51%	0.54%	1.77%
		Spec. #2	0.97%	1.65%	n.a.	1.84%	1.29%	1.88%
		Spec. #3	1.79%	2.62%	n.a.	2.13%	2.10%	2.14%
		Spec. #4	1.50%	2.01%	n.a.			
	Exp. #3	Spec. #1	0.32%	2.40%	2.32%	3.41%	1.52%	3.20%
		Spec. #2	1.76%	2.93%	2.67%	2.55%	1.63%	2.75%
		Spec. #3	1.18%	1.52%	2.19%	2.33%	1.55%	2.78%
		Spec. #4	1.59%	2.72%	n.a.			
		Mean value	1.36%	2.21%	2.39%	2.41%	1.63%	2.20%

Table 3 Summary: Porosity due to flow front confluence

Angles	20°	55°	90°	120°	135°	160°
Total porosity	2.97%	4.72%	5.48%	5.96%	5.45%	6.28%
Basic porosity	1.36%	2.21%	2.39%	2.41%	1.63%	2.20%
Porosity due to confluence	1.61%	2.51%	3.09%	3.55%	3.82%	4.08%

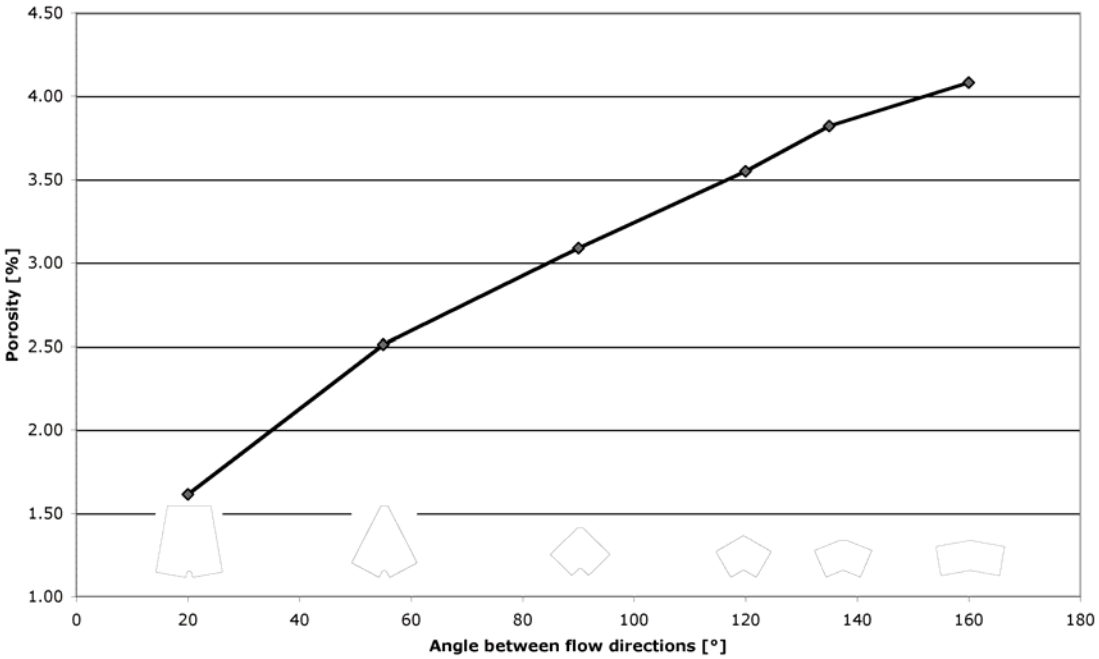

Fig. 4 Relative porosity vs. confluence angle

It seems that the effect of the confluence angle on porosity is reducing with angles above 60° (Fig. 5). As the basic porosity is about 2% for all measured samples, the porosity caused by the confluence rises from values below 2% for an angle of 20° up to 4% for an angle of 160°.

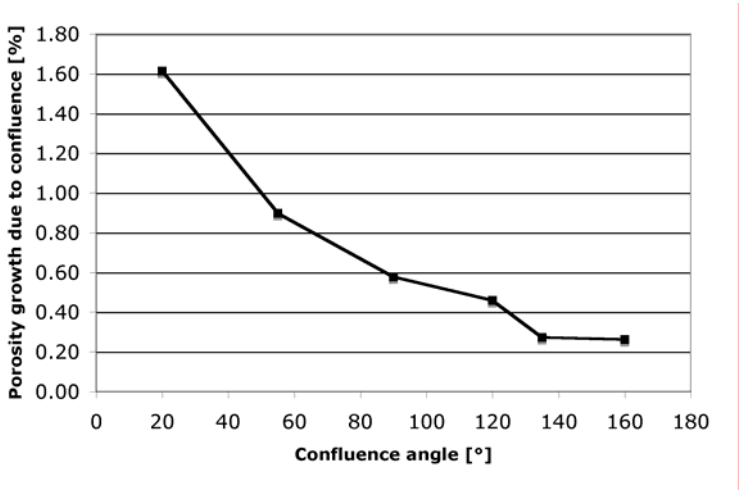

Fig. 5 Porosity growth rate vs. confluence angle. With increasing angle, the effect of the confluence diminishes

Evaluation of global porosity

Micrographics analysis only provides punctual information about laminate porosity. To obtain a global estimation of the porosity, images using transmitted light were produced for the parts with confluence angles of 55° and 160°. For this purpose, the laminates were placed into the manufacturing frame, as shown in Fig. 6, left hand side, laid on a light table and photographed with a digital camera. In undisturbed zones, the light is transmitted smoothly

through the part, whereas in the confluence zones, the light is scattered on the entrapped air, thus this zone appears darker than the rest. Fig. 6 shows the results for the 160° laminate. The confluence zone can be seen without magnification, as a darker area in the middle of the part, whereas for smaller angles it is more difficult to visualize the confluence zone.

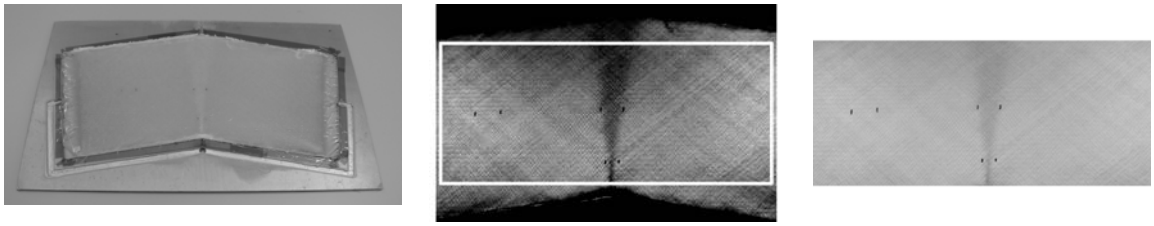

Fig. 6 Sample data processing using transmitted light: The area of interest is marked by the frame (middle image). The darker area resulting from the joining flow fronts is clearly visible

Data processing was performed using Matlab. The color image was first converted in a greyscale image (using Adobe Photoshop). The interesting zone was then cut out for data analysis (Fig. 6, right hand side). Matlab reads the image as matrix of grey values and thus allows analysis of intensity values over every row and column, as well as calculation of mean values for rows or columns. 0 stands for pure black and 255 for pure white. Fig. 7 shows the photograph and the horizontal mean intensity for the 160° and 55° sample, respectively.

The 55° sample is generally brighter; this is not only a result of better impregnation (due to the longer flow path and thus better wetting), but also due to white balance from camera software, because the 55° sample is bigger than the 160° sample. On both samples, the intensity increases toward the injection ports. This is in accordance to several sources [6, 7], stating worse part quality in the zone near the vents. However, to be able to correlate intensity values to porosity content, a wider range of images would be required, an the photographs would have to be taken in a dark room using RAW format, as this prevents any automatic image correction and white balance.

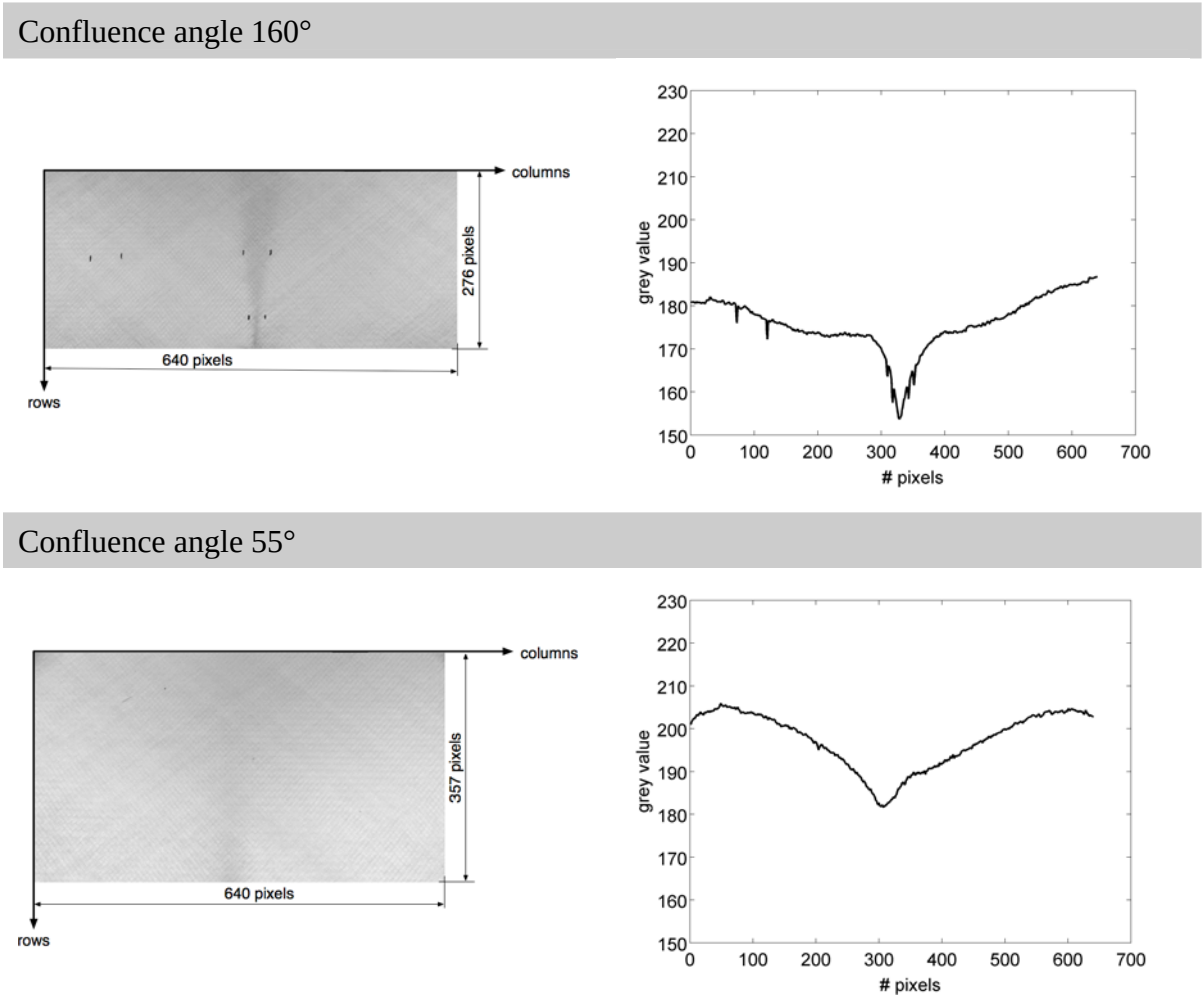

Fig. 7 Image processing using transmitted light: mean of grey value vs. image height

CONCLUSIONS

The results of this study have highlighted the influence of flow front confluences on the laminate porosity. This parameter needs to be taken into account during process development. In order to achieve optimum laminate quality, suitable filling patterns should have as few confluences as possible. In any case, the angle between the joining flow fronts should not exceed 60°. These results are particularly important for injection processes using multiple gates.

As a next step we plan to implement the results of this study in FELyX [8], our simulation and optimization software. Confluence length and angle will be included in the objective function of the Evolutionary Algorithm.

ACKNOWLEDGMENTS

The authors gratefully acknowledge the support by Alcan Technology & Management Ltd.

REFERENCES

1. P. J. C. Serrano, U. K. Vaidya, „Modeling and implementation of VARTM for civil engineering applications“, *SAMPE Journal*, Volume 41, no. 1, Pages 20–31, (2005).

2 M. Henne, C. Leppin, C. Gotschi, „Isothermal RTM simulation of GFRP parts for automotive applications“, *Proc. of International SAMPE Symposium and Exhibition*, Volume 46, Pages 35–347, (2001).

3. P. Simacek, S. G. Advani, „Desirable Features in Mold Filling Simulations for Liquid Composite Molding Processes“, *Polymer Composites*, Volume 25, no. 4, Pages 355-367 (2004).

4. G. A. Barandun, U. Fasel, J. S. U. Schell, P. Ermanni, „Development of an Optimization and Tool for LCM Processes using Evolutionary Algorithms“, *Advancing with Composites*, Milan, Pages 111–117 (2003).

5. B. Y. Kim, G. J. Nam, J. W. Lee, „Optimization of Filling Process in RTM using a Genetic Algorithm and Experimental Design Method“, *Polymer Composites*, Volume 23, no. 1, Pages 72-86 (2002).

6. J. Feuerlein, „Determination of the optimal flowfront-velocity“, *Semester Thesis 02-29, Centre of Structure Technologies, ETH Zurich* (2002).

7. T. S. Lundström, B. R. Gebart, C. Y. Lundemo, „Void formation in RTM“, *Journal of Reinforced Plastics and Composites*, Volume 12, Pages 1339–1349 (1993).

8. O. König, M. Wintermantel, N. Zender, „FELyX - The Finite Element Library eXperiment“, *Tech. rep., Centre of Structure Technologies, ETH Zurich* (2002).
URL http://felyx.sourceforge.net/downloads/FELyX-Paper.pdf

CHARACTERISATION OF WOOD FIBRE MATS AS REINFORCEMENT FOR THE RESIN TRANSFER MOULDING PROCESS

[1]R. Umer, [1]S. Bickerton, and [2]A. Fernyhough

[1]Centre for Advanced Composite Materials, Department of Mechanical Engineering The University of Auckland, Private Bag 92019, AUCKLAND, NEW ZEALAND
Corresponding Author's e-mail: s.bickerton@auckland.ac.nz
[2]Biopolymer Network, Scion, ROTORUA, NEW ZEALAND

ABSTRACT: Resin Transfer Moulding (RTM) process is a commonly used technique for the manufacture of advanced composite structures. This study explores the potential of wood fibres as reinforcement for RTM preforms, considering mats produced using dry and wet methods. The compaction response of these mats has been investigated with and without the presence of a test fluid, required compression loads being measured up to a fibre volume fraction of 0.4. A complex non-elastic compression response was observed which has significant influence on forces applied to moulds. In addition, permeability of these mats was measured as a function of fibre volume fraction. Reinforcement permeability and compaction response data were used to model a simple RTM process. Simulation results were compared with RTM experiments completed at two different fibre volume fractions.

KEYWORDS: Wood Fibre Mat, RTM, Compaction Response, Permeability.

INTRODUCTION

Resin Transfer Moulding is a closed mould composite manufacturing process in which a thermoset resin is injected into a mould cavity filled with reinforcing fibre. RTM process simulations are valuable for assessing production parameters, and for improving the quality of manufactured products. Important input parameters for RTM simulations include permeability characteristics and compaction response of the fibre reinforcement [1-3]. Conventionally, synthetic fibres such as glass, carbon and aramid are used as reinforcing materials. However, natural fibres such as wood, hemp, flax and sisal have attracted attention due to their low cost and environmental impact. Application of wood fibres is the focus of this paper, several mat styles being characterised and then utilised in RTM experiments. Modified paper manufacturing techniques were employed to prepare two types of wet formed mats, while the other two mats were dry formed. Only one type of wet and one type of dry formed mats are discussed in this paper.

The wood fibres used in this study are short in length (3 ~ 4mm), and require formation into easily handled "mats" before placement in an RTM mould. A detailed characterisation study has been performed on these reinforcements. For comparison to a typical synthetic fibre reinforcement, data was also collected for a glass fibre Continuous Filament Mat (CFM). A series of RTM experiments were performed, comparing fill times and clamping forces for the reinforcements studied. A simulation study is also presented, highlighting the implications.

MATERIALS PREPARATION

Radiata pine (*Pinus Radiata D. Don*) is classified as a soft wood. To use wood fibres as reinforcement for composite materials, these fibres can be separated and formed into mats. The process used to reduce wood into its component fibres is known as "pulping". High Temperature Thermo Mechanical Pulp (HTMP) prepared at Scion has been used in this project. The dry formed mats were prepared using a Dry Mat Former (DMF) developed at the University of Auckland. The wet formed mats were produced using a standard Papier Dynamic Former (PDF) at Scion. Fibres for this process were treated with latency removal (treatment under high temperature). CFM was used as a comparison to the wood fibre mats. CFM was chosen as it exhibits isotropic flow characteristic, and is commonly used as reinforcement in composites industry.

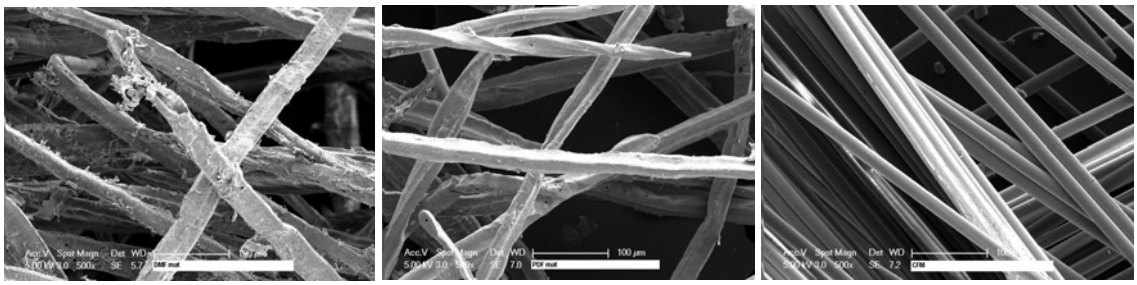

(a) (b) (c)

Fig.1 SEM images showing comparison between dry formed, wet formed and glass fibre mats: (a) Dry formed DMF mat, (b) Wet formed PDF mat and, (c) CFM.

Fig. 1 depicts SEM images demonstrating differences between the dry formed (Fig. 1a) and wet formed (Fig. 1b) mats, and the CFM (Fig. 1c). This shows that latency removal not only removed curls and extractives, but also removed flake like fines on fibre surfaces. These extractives and fines are likely to affect fibre to fibre friction, which will have an influence on compressibility and permeability. Lignin in the fibre cell wall is not removed, which is essential to maintain fibre stiffness. The fibre bundles in CFM are evident from Fig. 1c, whereas the wood fibres are individual fibres held together by frictional forces between fibres, and fibre/fibre interfacial bonding.

CHARACTERISATION AND RTM EXPERIMENTS

Experimental equipment

Fig. 2 presents a schematic of the reinforcement characterisation and RTM setup. A two piece aluminium mould was installed in an Instron 1186 testing machine. The upper platen was attached to a 200 kN load cell, and the lower platen was attached to the moving Instron crosshead. The mould has a central fluid inlet gate. A pressure transducer and shut off valve were positioned at this gate. The shut off valve prevents fluid flowing out of the mould during compaction experiments, allowing the central gate pressure to be recorded. A temperature sensor was placed inside the mould cavity to record any change in temperature, and hence fluid viscosity. Any deflection of the upper platen was monitored using a laser displacement gauge. Mineral oil (Mobil Vacuoline 1405) was used in this study as a test fluid to simulate a thermoset resin. The oil viscosity was found to be of 0.09 to 0.068 Pa.s, for a temperature range of 16 to 23^{o}C.

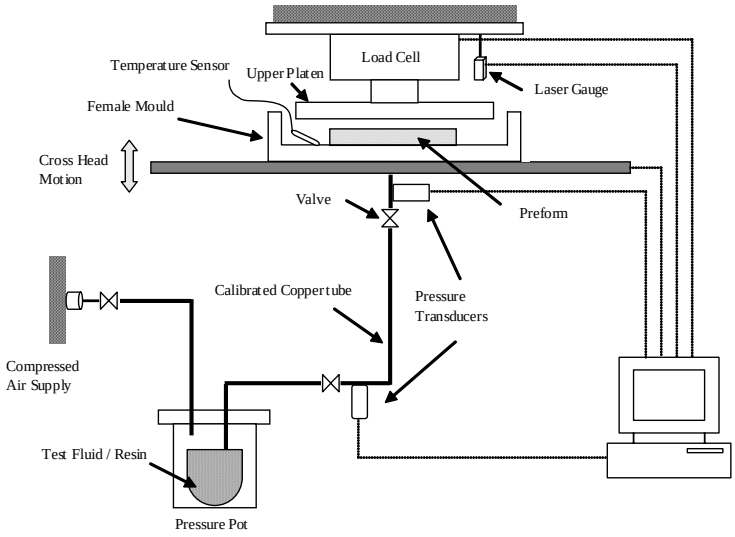

Fig. 2 Schematic diagram of the experimental characterisation and RTM setup.

Compaction Experiments

Table 1 provides the number of layers used in a sample of each type of reinforcement for all characterisation and RTM experiments. The mats were cut to a 20 cm diameter. A 1.5 cm diameter hole was punched in the center of all samples to establish 2D flow.

Table. 1 Description of samples for characterisation and RTM experiments.

Mat	*Fibre Material*	*Assumed fibre density (gm/cm^3)*	*Manufacturing method*	*Areal density (gm/m^2)*	*Thickness of a single mat (cm)*	*No. of Layers*	*Sample Diameter (cm)*	*Lay up*
DMF	Wood	1.5	Dry	350 ~ 400	0.45 ~ 0.5	5	20	$0^o/0^o$…
PDF	Wood	1.5	Wet	400	0.50	6	20	$0^o/90^o$…
CFM	Glass	2.58	-	450	0.15	8	20	$0^o/0^o$…

Two types of compaction experiment have been performed. The “Dynamic” experiments were completed to characterise response during periods of constant speed compaction. To account for stress relaxation in a simple manner, the long term behaviour of the material was characterised using a “Static” compaction test. Both types of experiment were completed with and without the presence of the test fluid.

Dynamic Compaction

During the dynamic tests the reinforcement was compacted at constant speed to a target fibre volume fraction (V_f) of 0.4, followed by a 10 minute period in which the sample was held at constant thickness. After this time, most of the stress relaxation was judged to have occurred. The CFM samples were compacted at a speed of 8 mm/min, while the wood fibre mats were compacted at 2 mm/min. The slower speed was used for the wood fibre mats due to their low permeability. For the saturated experiments, fluid was injected into the mould cavity prior to the experiment. Fluid was injected at low pressure (~ 150 kPa), to avoid any disturbance of fibres near the injection gate.

Static Compaction

The preform samples were compacted to a number of progressively increasing target V_f’s (0.2 to 0.4, at 0.05 steps) at a constant speed of 2 mm/min. The sample thickness was maintained constant for 10 minutes at each V_f, allowing the reinforcement to relax.

Permeability Experiments

A pressure driven radial flow permeability measurement was performed in the same setup as for compaction. A 2000 mm long and 2.8 mm internal diameter copper tube was calibrated for use as a flow meter. The sample was first compacted to an initial V_f of 0.15. Fluid was then injected at low pressure, allowing the sample to fully saturate without disturbing the reinforcement architecture. The sample was then compacted to decreasing cavity thicknesses until the final V_f of 0.4 was reached. At each target V_f, constant fluid flow rate (Q) was established, and the required injection pressure (P_{inj}) measured. Several flow rates were used at each V_f to check proportionality to the measured pressure drop. The permeability of the reinforcement was calculated by the following equation,

$$K = \frac{\mu Q}{2\pi h P_{inj}} \ln\left(r_o \Big/ r_i\right), \tag{1}$$

where K is the isotropic permeability, h is the cavity thickness, and r_o, r_i are the outer and inner radii of the sample respectively. See [4] for further details.

RTM Experiments

The RTM preforms were compacted at a constant speed of 25 mm/min until the target cavity thickness was reached. The test fluid was injected at a constant pressure of 300 kPa. Two experiments were carried out for each reinforcement at V_f*'s* of 0.3 and 0.4.

RTM PROCESS MODELING

Sample analyses of an RTM filling process are presented here. A flat circular part geometry has been considered, comparing predicted and experimental fill times and clamping forces required for application of the wood fibre mats and CFM.

Flow Modeling

Resin flow through the fibrous preform has been assumed to follow Darcy's law, resin velocities remaining in-plane. Simulations presented in this paper are based on empirical curve fitting of compaction and permeability data. The permeability data can be represented by:

$$K(V_f) = X.\exp.(Y.V_f), \tag{2}$$

where X and Y are constants defining the material.

Compaction Models

Deformation models to capture time dependent stress relaxation are under development [5]. A mixed elastic approach is applied here, which gives an approximation to the stress relaxation behaviour. Different elastic models are applied (dynamic dry, static dry and saturated) during an RTM cycle, depending on the local state of the reinforcement (i.e. cavity thickness reducing or constant, saturated or dry). For more details see [6]. Empirical curves have been fitted to each of the dynamic and static experiments. A five term polynomial provides an accurate fit over a wide range of fibre volume fractions.

$$\sigma(V_f) = AV_f^{\,4} + BV_f^{\,3} + CV_f^{\,2} + DV_f + E, \tag{3}$$

where *A, B, C, D* and *E* are model parameters.

Force analysis

Two force components act on an RTM mould, one due to the fluid pressure generated, F_{fluid}, and the other due to the compaction stress carried by the preform, F_{fibre}. The total clamping force is assumed to be the sum of these two components.

$$F_{clamp} = F_{fibre} + F_{fluid} \tag{4}$$

RESULTS AND DISCUSSIONS

Compaction

Fig. 3 presents both dry and saturated dynamic and static compaction response of DMF, PDF and CFM respectively. All mats exhibit stress relaxation. The PDF mats exhibit a peak stress of approximately 3400 kPa for dry dynamic compaction. DMF mats are less stiff with a peak stress of approximately 2500 kPa at the same V_f. This possibly is due to clumping of fibres into bundles, resulting in larger gaps being available for the structure to reorganise during compaction. The peak stress for the dry and saturated CFM is approximately 3 to 4 times less than that of wood fibre mats.

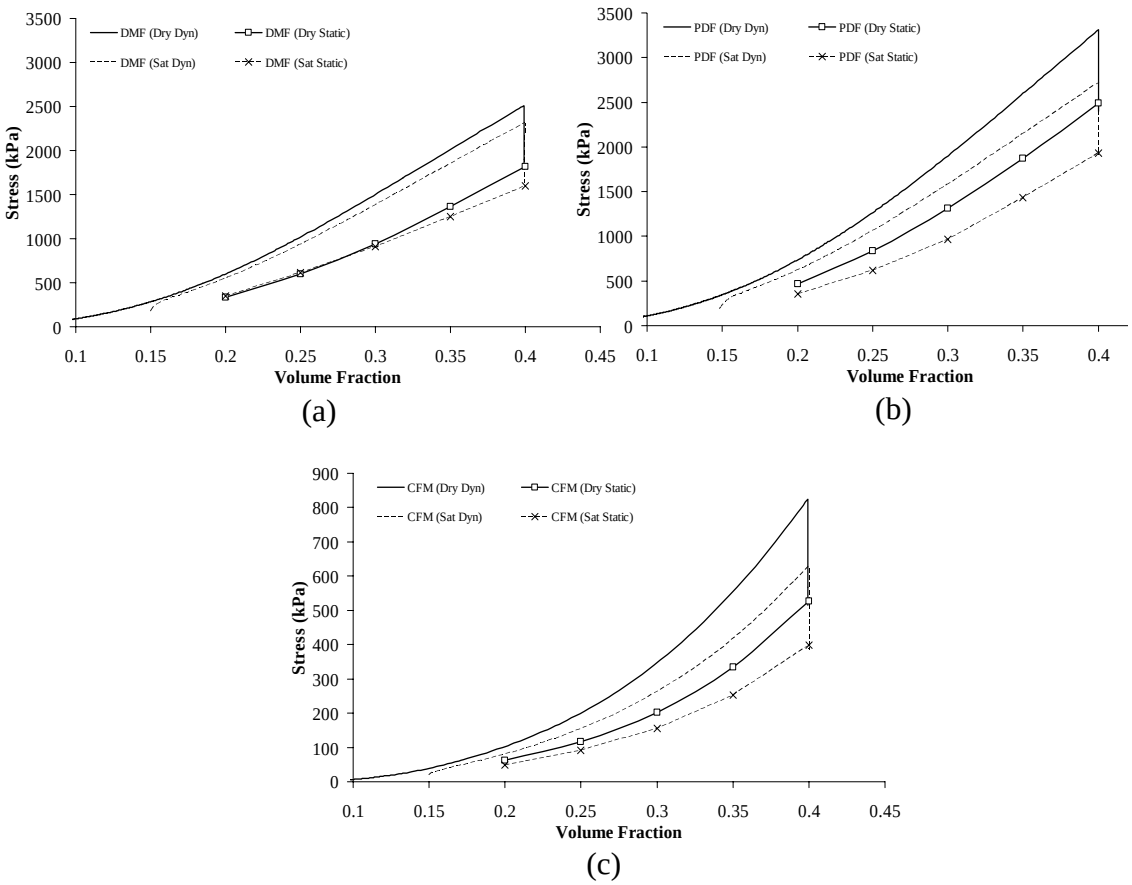

Fig. 3 Dry and saturated dynamic and dry and saturated static compaction response of (a) DMF, (b) PDF and, (c) CFM.

The dashed lines in Fig. 3 show compaction behaviour of reinforcing mats infiltrated with mineral oil. The DMF mat exhibit a peak stress of approximately 2300 kPa for dynamic compaction. Therefore, the presence of mineral oil has little influence on the compaction behaviour of the DMF, signifiying a small fibre lubrication effect. PDF showed greater potential for fibre lubrification under wet compaction, possibly due to the relatively smooth

surfaces formed by latency removal. CFM also displayed fibre lubrification, common for glass reinforcements [7]. Similar trends were found for the static compaction curves.

Permeability

Permeability data collected is presented in Fig. 4. The permeability of all three reinforcements decreases with increasing V_f as expected. Exponential trend lines are shown for each mat type, providing good fits over the range of V_f addressed. The DMF mats exhibit higher permeability as compared to PDF, possibly due to the formation of bundles, which then generate larger paths for flow. Across the range of V_f considered, permeability of the wood fibre mats is approximately two orders of magnitude lower than that of CFM. The wood fibre mats exhibit lower permeability as they are formed from individual fibres, as opposed to CFM which is formed from a continuous bundle of approximately 200 fibres. The compressed mats of individual wood fibres provide extremely torturous paths for resin flow, with very small effective diameter. CFM represents a more efficient packing of fibres, offering larger flow paths.

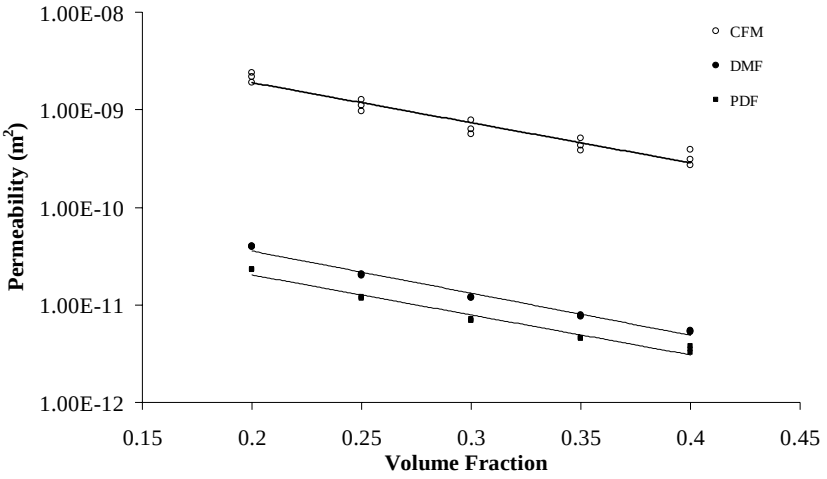

Fig. 4 Permeability comparison between the wood fibre mats and CFM.

RTM Experiments and Predictions

RTM clamping force traces for both wood fibre mats and the CFM are presented in Fig. 5. The RTM process predictions compare well with experiments completed at V_f = 0.3 and 0.4.In each experiment, the preform is compacted to the target V_f. This operation is completed at *t=0* second and fluid injection is initiated. A significantly larger peak force is generated during initial compaction of the wood fibre mats, due to higher resistance to compaction. All predicted traces show a sudden drop in clamping force at *t=0* seconds, as stress relaxation is assumed to occur instantaneously. It is clear that clamping forces after initial compression are strongly influenced by stress relaxation in the preform. These effects cannot be captured by a purely elastic preform compression model. At the completion of injection, the force drops due to the release of fluid pressure. The DMF mat fills in 187 and 380 seconds experimentally for V_f = 0.3 and 0.4 respectively. The predicted fill time were 163 and 332 seconds. The PDF mat fills in 258 and 468 seconds experimentally, and 252 and 527 seconds numerically. The peak clamping forces for both DMF and PDF at V_f = 0.4 are slightly over predicted. The CFM preforms take almost 70 to 80 times less time to fill, and require 3 to 4 times lower clamping forces. This is a consequence of their low permeability and greater resistance to compaction. The relatively large tooling forces and filling time for the wood fibre mat are expected based on the characterisation study.

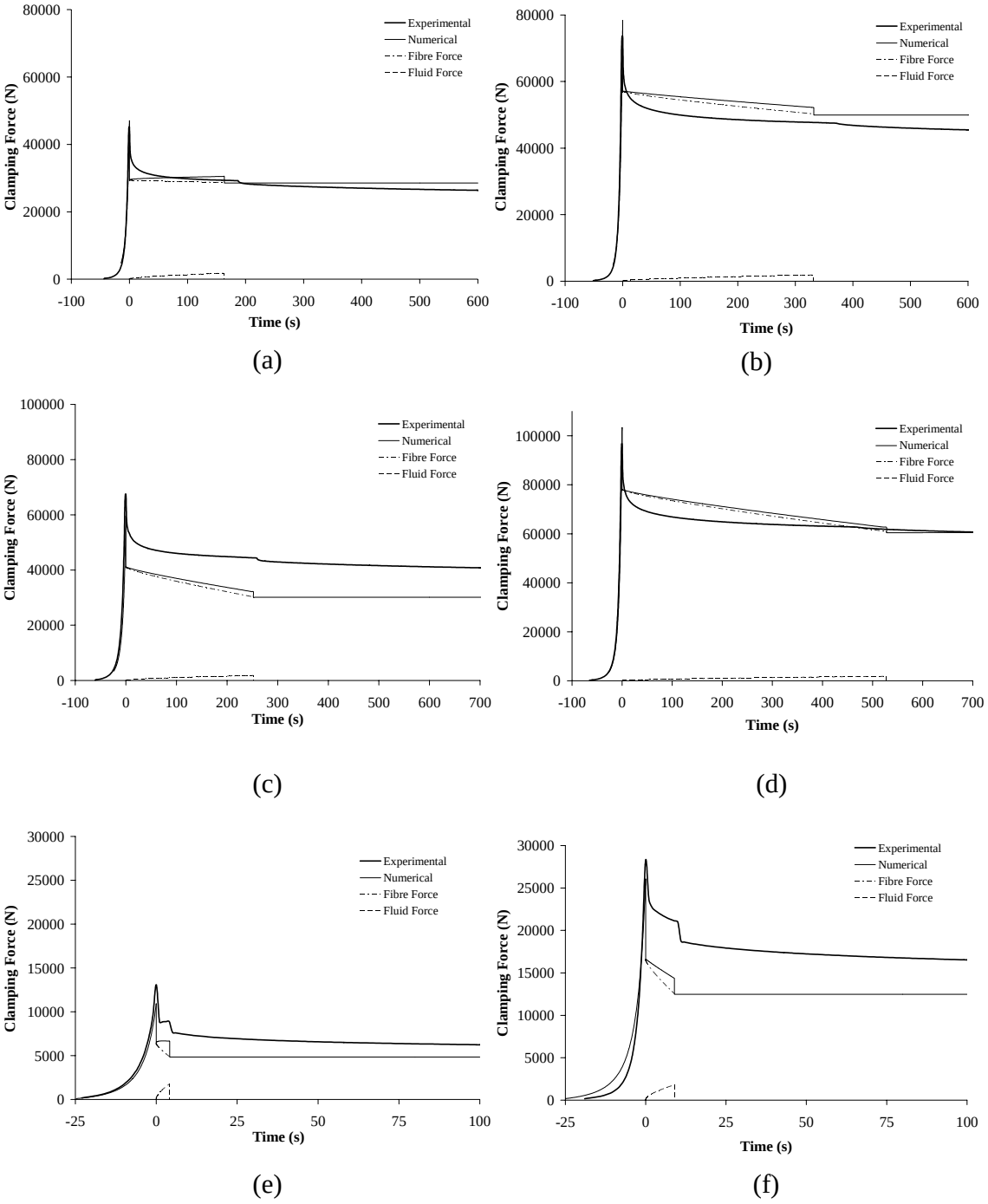

Fig. 5 Comparison of numerical and experimental RTM clamping forces. (a) DMF V_f = 0.30, (b) DMF V_f = 0.4, (c) PDF V_f = 0.30, (d) PDF V_f = 0.4, (e) CFM V_f = 0.30, (f) CFM V_f = 0.4

CONCLUSION

The main focus of this study has been to characterise wood fibre mats, assessing their potential for use in the RTM process. One type of dry formed mat and one type of wet formed mat were compared with CFM. The DMF mat is different in structure from the PDF mat due to greater amounts of fibre clumping and fibre interlocking. Fibres in the PDF mats are well separated and more evenly distributed. A range of compaction tests were carried out to compare dry and saturated preform samples. It was noted that the wood fibre mats required significantly larger force to compact to at similar fibre volume fractions as compared to the CFM. Of the wood fibre reinforcements, the DMF mats were the easiest to compress, attributable to the larger amount of fibre bundling. The DMF mats exhibited higher permeability than PDF mats due to larger channels open for fluid flow. It was found that the wood fibre mats have permeability two orders of magnitude lower than the CFM. An experimental study of the clamping force and fill time required during an RTM process was also presented, demonstrating the influence of non-elastic reinforcement deformation. RTM filling simulations were presented utilising a mixed elastic model approach. This approach has provided good predictions for clamping forces and mould filling time. While a time dependent deformation model is in development, this mixed model provides an attractive alternative for modelling RTM.

ACKNOWLEDGEMENTS

The authors would like to thank the Biopolymer Network, and The Foundation for Research Science and Technology, New Zealand for providing funding and materials for this study.

REFERENCES

1. S. Bickerton, M.J. Buntain, and A.A. Somashekar, “The viscoelastic compression behaviour of liquid composite molding performs”, *Composites Part A*, Vol. 34, 2003, pp. 431–44

2. P.B. Nedanov, and S.G. Advani, “A method to determine 3D permeability of fibrous reinforcements.” *Journal of Composite Materials,* Vol. 36, no.2, 2002 pp. 241-254.

3. E. Rodríguez, F. Giacomelli, and A. Vazquez, “Permeability–porosity relationship in RTM for different fiberglass and natural reinforcements”, *Journal of composite materials*, Vol. 38, no.3, 2004 pp. 259-268.

4. M.J. Buntain, and S. Bickerton, “Compression flow permeability measurement: a continuous technique”, *Composites Part A*, Vol. 34, no.5, 2003 pp. 445-457.

5. P. A. Kelly, R. Umer, and S. Bickerton. “Viscoelastic response of dry and wet fibrous materials during infusion processes”, *Composites Part A*, Vol. 37, no.6, 2006 pp. 868-873.

6. S. Bickerton, and M. Thiede, “An RTM tooling force analysis of complex planar geometries” *Proc. of the 36th Int. SAMPE Technical Conference, San Diego, U.S.A*, Vol. 36, November 15-18, 2004.

7. M.J. Buntain, and S. Bickerton, “Prediction of tooling forces in liquid composite moulding processes”, *SAMPE Journal*, Vol. 39, no.1, 2003 p. 8-15.

ALKALI TREATMENT OF JUTE FABRICS: INFLUENCE ON THE PROCESSING CONDITIONS AND THE MECHANICAL PROPERTIES OF THEIR COMPOSITES

Exequiel S. Rodríguez and Analía Vázquez

Research Institute of Materials Science and Technology, INTEMA – Materials Department, Engineering Faculty, National University of Mar del Plata. J. B. Justo 4302, B7608FDQ, Mar del Plata, Argentina.
Corresponding Author's e-mail: anvazque@fi.mdp.edu.ar

ABSTRACT: The aim of this work is to evaluate the effect of the fibers alkali treatment on the injection processing. Woven jute preforms were used to prepare the composites using the vacuum infusion technique. The fibers were treated with NaOH (5 wt%) for 24 h at room temperature. Single filament tests showed that the treatment was detrimental for the mechanical properties of the fibers. The injection times increased in the treated jute preforms as a consequence of the increase in the exposed area and the flow resistance. The preform permeability decreased, also, in the tubular structure collapse of the fibers, which could reduce the capillary pressure. Flexural and impact properties of the treated jute composites decreased mainly in the lower mechanical properties of the fibers.

KEYWORDS: Natural fiber composites, vacuum infusion, alkali treatment, processing conditions, preform permeability, mechanical properties.

INTRODUCTION

The idea of replacing glass fibers with natural fibers in composite materials is increasing. The success of natural fiber composites (NFCs) depends on their ability to overcome their main disadvantages (low fiber/matrix adhesion, fluctuations in fiber properties, low thermal and fire resistance) and the possibility of using well-studied glass fiber reinforced plastics (GFRP) processing techniques. Different approaches have been used to improve NFCs performance.
Chemical treatments of the fibers [1, 2], chemical modification of the resins [3, 4] and coupling agents [2, 5] have been employed to enhance fiber/matrix adhesion. Although many chemical treatments have proved to be suitable for enhancing NFCs mechanical properties, it is difficult to select the best treatment for a particular fiber. The intrinsic differences of natural systems coming from diverse geographical regions and different harvesting, production and processing condition make the available results difficult to compare, even for the same kind of fiber. A relatively simple chemical treatment is the alkali treatment (mercerization), which has been successfully used in fibers like jute, sisal, hemp, palm or flax [1-2,5]. In cotton there is more than a century of experience in the use of mercerization to improve fibers performance.

Regarding the processing technique, in vacuum infusion , a liquid resin is introduced into a closed mold with the dry reinforcement inside. The closed system eliminates most of the fumes that are liberated in hand lay-up. These methods allow better control over part dimensions and fiber volume fraction. Hence, resin infusion methods overcome many of the limitations of wet lay-up processes and have low cost. This is compatible with its use with low-cost fibers. Among all the natural reinforcements, jute appears to be a promising fiber suitable for vacuum infusion, because it is relatively inexpensive and commercially available in the required form.
In this work, natural fiber composites were obtained by vacuum infusion using untreated and alkali-treated jute fabrics. The effect of the treatment on the mechanical properties of the fibers, the processing conditions (injection times, flow pattern, perform impregnation) and the mechanical properties of the composites was studied. Although many studies about chemical treatments of natural fibers can be found in the scientific literature, there is very few research in which its influence on the whole obtaining process (fiber and matrix, processing and final product) is analyzed. The intention of the work was not to obtain the best treatment conditions, but rather to make evident the effects of the treatment on fibers, composite properties and on the processing conditions.

EXPERIMENTAL

Commercial jute bi-directional fabrics were used as reinforcement. The matrix was an epoxy vinylester resin: Derakane 411-350 Momentum from Dow Chemical. VE resin containing 45 wt% styrene was used as purchased without removal of inhibitors. The initiating system was comprised of methyl ethyl ketone peroxide (MEKP, 1.5 wt%) together with cobalt nafthenate (0.6 wt%).
The fibers were washed with detergent (2 vol% in aqueous solution, 15% active matter) and then immersed in beakers with a solution of 5 wt% NaOH for 24 h at room temperature. After that, the fibers were washed thoroughly with distilled water to remove the excess of NaOH and dried at 70ºC for 24 h under vacuum. The major fibres constituents (α-cellulose, hemicellulose and lignin) of the untreated and alkaline-treated jute fibre samples were determined by chemical analysis following standard procedures. The results are listed in Table 1.

Table 1. Jute chemical composition

Component (%)	Treated	Untreated
α-Cellulose	80.3	71.1
Hemi-cellulose	9.6	15.9
Lignin	7.6	11.8
Other components (ash, water, pectins)	2.5	1.2

Composites with 30 vol% of reinforcement were prepared using the vacuum infusion technique. Injections were conducted on an acrylic mold with a 4mm x 10mm x 450mm rectangular cavity. The resin enters through an injection point located on one side of the mold and the suction point was located in the opposite side. Two injections were performed for each kind of composite. Molded plaques were cured at 80ºC for 2 h, and post-cured at 110ºC for 3 h.

RESULTS AND DISCUSSION

- Effect of the alkali treatment on the fiber properties

After treatment, semicrystalline and amorphous portions in the fibers, such as hemicellulose, lignin and other alkali-soluble fraction, were preferentially removed. The following effects of the alkali treatment on natural fibers have also been reported in the literature:
- It cleans fiber surface removing impurities, waxy substances and natural oils. It also produces a rough surface topography, facilitating mechanical interlocking which leads to an improvement in fiber-matrix adhesion.
- Produces fiber fibrillation, i.e. axial splitting of the elementary fibers (or microfibers) that constitute the elementary fiber [3, 6]. This process leads to a decrease in fiber diameter, increasing the aspect ratio and the effective surface area available for wetting by a matrix in a composite. There is also an increase in fiber density as a consequence of the collapse of its cellular structure.
- Increases the number of free hydroxyl groups in the fiber surface, which improves the adhesion with resins like polyester or vinylester.
Also, there are more physical and chemical changes in the fibers affect the tensile modulus and the strength in an opposite manner. In favor: the decrease in spiral angle and the increase in crystallinity, the better rearrangement of the fibrils along the load axis and the increment in the fibers aspect ratio. Against: removal of lignin and hemicellulose, which play a cementing role, transferring the stress to the microfibrils. Therefore, the alkali treatment is an effective procedure to improve the mechanical properties of natural fibers, but its success depends on many variables, so it is very difficult to predict the effect over a particular natural system.
In order to evaluate the effect of the treatment on the mechanical properties of the fibers used in this work, single filament tests were performed. Table 2 shows the results for untreated and treated fibers. Both tensile strength and modulus showed an important drop after the alkali treatment. The treatment used in this work produced an excessive extraction of lignin and hemicellulose, probably with damage in the ultimate cells walls. The decrease in elastic modulus is an evidence of the loss of cementing material in the fibers. Mannan and Talukder [7] obtained similar results for dewaxed and delignificated jute. The fibers were treated with 17.5% NaOH for 1h at room temperature. On the other hand, Gassan and Bledky [8] reported an important increase in modulus and strength of jute yarns treated with a dense caustic soda solution (25 wt%) for 20 min under isometric conditions (the fibers are not allow to shrink). When the shrinkage is avoided, the tensile stresses developed in the fibers produce microfibrills orientation that is responsible for the increase in modulus. In slack conditions (free shrinkage) the authors reported a decrease in fibers modulus. Other authors [6, 9] have reported improvement in jute composites mechanical properties after fibers alkali treatment with solutions in the range of 5 to 10 % o NaOH for about 4h at room temperature.

Table 2. Single filament tests results

Fiber	Modulus (GPa)	Strength (MPa)
Untreated	30 ±14	505 ±165
Alkali-treated	12,2 ± 5,2	326 ±150

- Effect of the alkali treatment on the processing conditions

In reference to the processing conditions, the pressure difference needed to obtain an injection time (t_{inj}) of 60 seconds was calculated using Equation 1, derived from Darcy's law for constant pressure flow. The porosity (ϕ) and the resin viscosity (μ) at the temperature of each injection were used for the calculations. The permeability values for each porosity ($K_{preform}$) were calculated using the Carman-Kozeny model (Equation 2) and the constants for the model (n, C) were taken from previous work of untreated and non-washed jute [10]. The obtained injections times were 95 and 90 seconds for the untreated jute fabric and 135 and 128 seconds for the treated one. The processing conditions for two injections are summarized in Table 3.

$$\Delta P = \frac{L_{mold}^2 \mu\phi}{2 K_{preform} t_{inj}} \quad (1)$$

$$K_{preform} = \frac{\phi^{n+1}}{C(1-\phi)^n} \quad (2)$$

where, ΔP is the pressure difference driving the flow, L_{mold} is the flow front position.

In all of the injections conducted, the obtained injection time was higher than the estimated. This could be attributed to the decrease in the fabric permeability. The permeability values used in the calculations correspond to "as received" jute. When the fibers are washed, the coatings added to facilitate the woven/weaving procedure (potato starch and waxes) are eliminated and the fiber surface became rougher. Then, there is an increment in the exposed area and therefore in the flux resistance. Injection time was higher in the mercerized fabric because the treatment produced fiber fibrillation, i.e. axial splitting of the elementary fibers (or microfibers). This process led to a decrease in fiber diameter, increasing the exposed area even more than in the only washed fibers.

Table 3. Main processing variables

Variable	Injection with untreated jute	Injection with treated jute
Porosity	0.70	0.69
Kpreform (m^2)	4.25 x 10-9	4.63 x 10-9
ΔP (hPa)	625	570
μ (Pa.s)	0.310	0.263
t_{inj} estimated (s)	60	60
t_{inj} actual (s)	95	135

There is another factor that can increase injections times: the decrease in capillary pressure. During the injection, the resin can flow either among the bundles that constitute the preform (macroflow) or inside the bundles, i.e. among the fibers filaments (microflow) [11]. In natural fibers the possibility of resin flow inside the fibers lumen also exists. The driving force for the microflow is the capillary pressure developed in the intratow region that should be added to the static pressure in Darcy's law in order to have more accurate results. But if the collapse and compacting of the fibers structure occurs during mercerization, the microscopic flow is inhibited and the volumetric flow rate should decrease. There is no agreement in the literature on the real effect of the microflow on the injection times. Dungan and Sastry [12] claimed that the microflow decrease the overall permeability by increasing

penetration times due to the required wetting of the tows. The evidence for their proposal was the higher values of the saturated (or wet) permeability in comparison to the unsaturated (or dry) permeability. Pillai and Advani [13] explored the effect of delayed impregnation of fiber tows in porous media constituted of woven fiber mats. They modeled this phenomenon by the inclusion of a "sink" effect (or negative source term) in the equation of continuity for the flow in the intertow regions. On the other hand, other authors [14, 15] found that the capillary pressure can produce a wicking flow that is faster than the macroflow, obtaining unsaturated permeability values higher than the saturated ones. Chang and Morgan [16] explained that the wicking flow could be faster or slower than the macroflow depending on the relative values of capillary and viscous forces. The last ones dominate at high impregnation velocities, i.e., low porosities or high injection pressures. In the case of this work, the injection pressure is relatively low so a positive contribution of the capillary pressure to the permeability is expected, resulting higher in the untreated jute fabric than in the alkali treated one.

- Effect of the alkali treatment on the composites properties

The results of the mechanical properties of the composites are summarized in Table 4. In general, mechanical performance of a fiber composite basically depends on the strength and toughness of the matrix, and efficiency of interfacial stress transfer [5]. Specifically, the modulus does not depend on interface adhesion. The elastic stiffness is defined as the strain approaches to zero; thus the degree of adhesion has no bearing on the elastic stiffness of the system. The decrease in flexural modulus observed in the alkali treated jute composites compared to the untreated ones, is a consequence of the decrease in fibers modulus. The same trend was observed for the flexural strength.

Table 4: Mechanical properties of the composites

Property	untreated jute composite	treated jute composite
Flexural modulus (GPa)	6.6 ± 0.5	5.5 ± 0.2
Flexural strength (MPa)	103 ± 6	83 ± 6
Impact Energy (J/m)	56.5 ± 2.4	47.2 ± 4.2

The impact tests showed that the impact energy of the composites decreased when the jute fibers were treated. This result was predictable considering the factors that affect energy consumption during the impact:

- fiber/matrix adhesion: as explained before, an increase in the interfacial strength, which is expected after treatment, reduces energy consumption by avoiding fiber pull-out. In this case, the fracture of the material takes place with little change in the cracking plane, breaking the fibers instead of pulling them out.

- Fibers mechanical properties: their decrease after treatment is obviously unfavorable for the impact resistance.

- Fibers spiral angle: Pavithran et al. [17] found that fibers with high spiral angle formed composites with higher toughness than those with small spiral angles. Even though the comparison was done among different kind of fibers, the decrease in spiral angle that takes place during alkali treatment should be detrimental for the composites toughness.

- Analysis by scanning electron microscopy

In order to have a better understanding of the effects of alkali treatments on the jute composites, SEM micrographs were obtained form the fractured surface of the composites. Figures 1a-c-e and 1b-d-f shows the micrographs for the untreated and treated jute composites respectively. Fibrillation and diameter reduction is evident in the alkalized jute (Fig. 1b). Fig. 1d and 1f also show the damage in the cell walls and a rougher fiber surface. Also, the collapse of fibers lumen can be seen. This is responsible for the decrease in capillary pressure and therefore in preform permeability. On the contrary, the untreated jute (Fig. 1c and 1e) shows open lumens, which in many cases are full of resin (marked with arrows). Both composites showed good fiber-matrix adhesion and low pull-out, which is consistent with the results obtained in previous work [18].

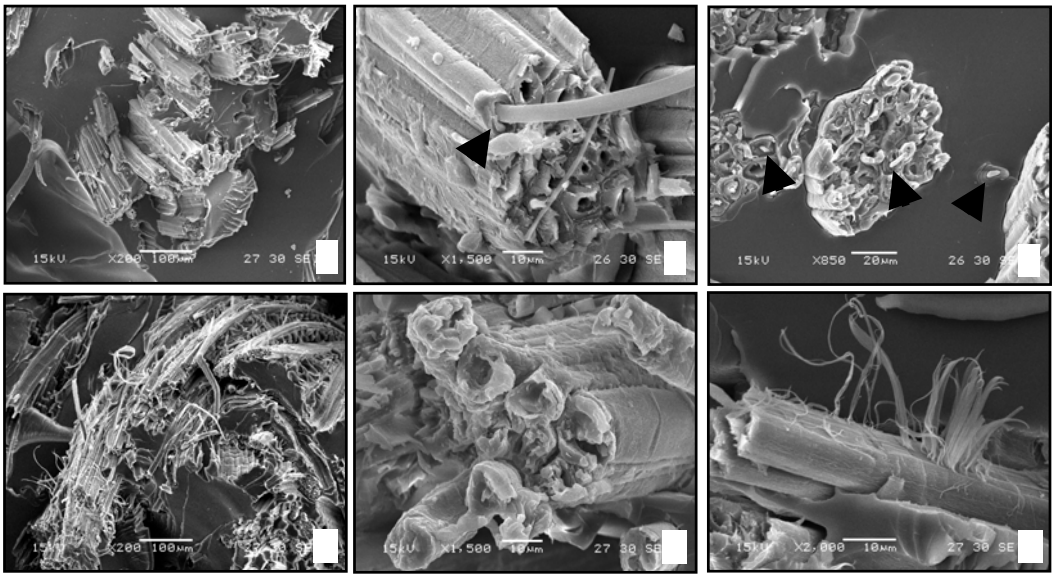

Fig. 1 SEM micrographies of the fracture surface of the composites

CONCLUSIONS

As a consequence of the severe alkaline treatment that was applied to jute fibers in this work, the following effects could be seen in fiber properties and processing conditions:
- The longer injections times obtained for the treated jute preforms were due the more compact and rougher fiber surface that produced the treatment. A lower capillary pressure that leads to lower preform permeability was expected as a consequence of the fiber lumen collapse that could be observed by SEM.
-The alkali treatment produced a drop in both tensile strength and Young's modulus of the fibers. This was attributed to the damage induced in the cell walls and the excessive extraction of lignin and hemicellulose, which play a cementing role in the structure of the fibers.
- The treatment also produced fibrillation, i.e. splitting of the microfibers that compound the technical fiber. This process leads to diameter lowering and higher dispersion in strength values. The high dispersion that presented the modulus values was in part due to deviations of

the cylindrical model for the fibers used in the diameter determination: optical micrographs showed that some of the fibers were split, had ramifications and presented a tape form rather than cylindrical.
- The composites processed presented a brittle behavior with lower flexural and impact properties in the case of the composites reinforced with treated jute. The drop in the mechanical properties of the fibers was the main cause of these results.

ACKNOWLEDGMENTS

The authors acknowledge to the National Research Council of Argentina (CONICET) for the financial support.

REFERENCES

1. I. Van de Weyenberg, J. Ivens, B. De Coster, B. Kino, E. Baetens and I. Verpoest, "Influence of processing and chemical treatment of flax fibres on their composites", *Comp Sci Technol*, Vol. 63, 2003 pp. 1241-1246.

2. P. Gañan, S. Garbizu, R. Llano-Ponte and I. Mondragón, "Surface modification of sisal fibers: effects on the mechanical and thermal properties of their epoxy composites", *Polymer Composites*, Vol. 26, no.2, 2005 pp. 121-127.

3. M.Z. Rong, M.Q. Zhang, Y. Liu, Z.W. Zhang, G.C. Yang and H.M. Zeng, "The effect of fiber treatment on the mechanical properties of unidireccional sisal-reinforced epoxy composites", *Comp Sci Technol*, Vol 61, 2001 pp. 1437-1447.

4. D. Ray, B.K. Sarkar and N.R. Bose, "Impact fatigue behaviour of vinylester resin matrix composites reinforced with alkali trated jute fibres", *Composites: Part A*, Vol. 33, 2002 pp. 233-241.

5. A.C. Albuquerque, K. Joseph, L. Hecker de Carvalho and J.R. Morais d'Almeida, "Effect of wettability and ageing conditions on the physical and mechanical properties of uniaxially oriented jute-roving-reinforced polyester composites", *Comp Sci Technol*, Vol. 60, 2000 pp. 833-844.

6. J. Gassan and A.K. Bledzki, "Posibilities for improving the mechanical properties of jute/epoxy composites by alcali tratment of fibres", *Comp Sci Technol*, Vol. 59, 1999 pp. 1303-1309.

7. H.A. Aziz, M.P. Ansell, S.J. Clarke and S.R. Panteny, "Modified plyester for natural fibre composites", *Comp Sci Technol*, Vol. 65, 2005 pp. 525-535.

8. A. O'Donell, M.A. Dweib and Wool RP, "Natural fiber composites with plant oil-based resin", *Comp Sci Technol*, Vol. 64, 2004 pp. 1135-1145.

9. Kh.M. Manan and M.A.I. Talukder, "Characterization of raw, delignified and bleanched jute fibres by study of absortion of moisture and some mechanical properties", *Polymer*, Vol. 38, no.10, 1997 pp. 2493-2500.

10. E. Rodríguez, F. Giacomelli and A. Vázquez, "Permeability-porosity relationship in RTM for different fiberglass and natural reinforcements", *Journal of Composite Materials*, Vol. 37, no.3, 2004 pp. 259-268.

11. R.S. Parnas, A.J. Salem, T.A.K. Sadiq, H-P. Wang and G. Advani. "The interaction between micro- and macroscopic flow in RTM preforms", *Composite Structures*, Vol. 27, 1994 pp. 93-107.

12. F.D. Dungan and A.M. Sastry, "Saturated and Unsaturated Polymer Flows: Microphenomena and Modeling", *Journal of Composite Materials*, Vol. 36, no.13, 2002 pp. 1581-1603.

13. K.M. Pillai and G. Advani, "A model for unsaturated flow in woven fiber preforms during mold filling in resin transfer molding" *Journal of Composite Materials*, Vol. 32, 1998 pp. 1753-1783.

14. Y. Luo, I. Verpoest, K. Hoes, M. Vanheule, H. Sol, A. Cardon, "Permeability Measurement of Textile Reinforcements with Several Test Fluids.Composites: Part A Vol. 32, 2001 pp.1497-1504.

15. G-W. Lee, N-J. Lee, J. Jang, K-J. Lee and J-D. Nam, "Effects of surface modification on the resin-transfer moulding (RTM) of glass-fibre/unsaturated-polyester composites", *Comp Sci Technol*, Vol. 62, 2002 pp. 9-16.

16. A.W. Chang and R.J. Morgan. Tow impregnation during Resin Transfer molding of bi-directional nonwoven fabrics, *Polymer Composites*, Vol. 14, no 4, 1993 pp. 335-340.

17. C. Pavithran, P.S. Mukherjee, M. Brahmakumar and A.D. Damodaran, "Impact properties of natural fibre composites", *Journal of Materials Science Letters*, Vol.6, no.8, 1987 pp. 882-884.

18. E. Rodríguez, R. Petrucci, D. Puglia, J.M. Kenny and A.Vázquez, "Characterization of composites based on natural and glass fibers obtained by vacuum infusion", *Journal of Composite Materials*, Vol. 39, no.3, 2005 pp. 265-282.

Session 3

MODELLING

A NEW FORMULATION FOR THE INFUSION OF A THERMO-REACTIVE RESIN INTO A COMPOSITE DEFORMABLE MEDIUM

P. Celle [1], S. Drapier [2], and J. M. Bergheau[3]

[1] *MeM/SMS*
Ecole Nationale Supérieur des Mines de Saint-Etienne
158, Cours Fauriel, F-42023 Saint-Etienne Cedex 2, FRANCE: celle@emse.fr

[2] *BioMM/CIS*
Ecole Nationale Supérieur des Mines de Saint-Etienne
158, Cours Fauriel, F-42023 Saint-Etienne Cedex 2, FRANCE: drapier@emse.fr

[3] *Laboratoire de Tribologie et Dynamique des Système, UMR 5513 CNRS/ECL/ENISE*
Ecole Nationale d'Ingénieurs de Saint-Etienne
58, rue Jean Parot, F-42023 Saint-Etienne Cedex 2, FRANCE: bergheau@enise.fr

ABSTRACT: Dry manufacturing composite processes consist in mixing reinforcements and resin during the final manufacturing stage, thus reducing storage and manufacturing cost. When furthermore, resin flow takes place in the through-thickness direction (infusion), it is possible to improve the quality of the final part and reduce tooling costs. However infusion processes are not fully predictable, mainly thickness and porosity are not straight to estimate. A numerical predictive model would be a proper candidate to help in developing and finalizing new composite solutions. In the present paper a complete model for the study of resin flow inside and outside a deformable porous medium is presented. This multi-physical model deals with mainly two types of problems. First, the interaction phenomena between the resin flow in a highly compressible preform, and second the coupling condition between this wet preform area and a purely fluid region.

KEYWORDS: infusion – Stokes – Darcy – FEM: Finite Element Method – composites materials – ALE Formulation – resin flow – LRI: Liquid Resin Infusion – RFI: Resin Film Infusion

INTRODUCTION

Resin Film Infusion (Figure 1-a) and Liquid Resin Infusion (Figure 1-b) consists in the infusion of a thermo-reactive resin in the preform transverse direction. Here, the RFI process is studied since its modeling leads to more exhaustive models than the LRI process. In this process, a dry fibrous preform is placed above a resin film. This assembly is enclosed in a vacuum bag, and a temperature cycle prescribed by an autoclave decreases the film resin viscosity until it becomes liquid. Then, vacuum induces a reaction pressure which leads to the impregnation of the preform by the resin in the transverse direction.

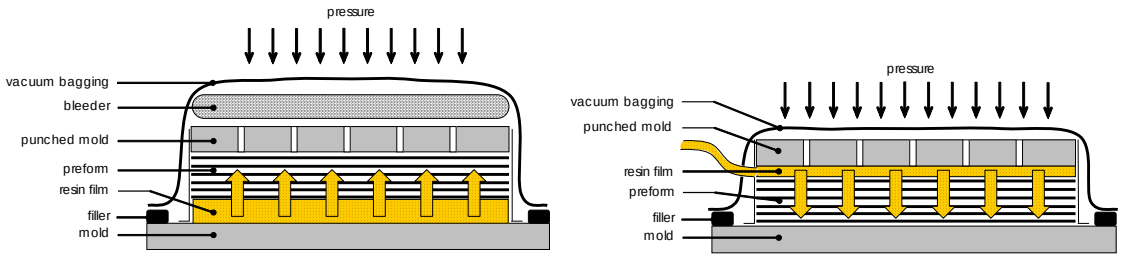

Fig. 1 Composite manufacturing processes by infusion – RFI (a) – LRI (b)

Infusion normal to the preform plane gives two advantages. First, time cycles are shorter due to the reduced distance resin has to travel. Second, the quality of impregnation is better when infusion of resin and its cure are dissociated. However, the thickness and the porosity of the finished part are not easily predictable. Currently in the literature there is no complete model able to describe the whole process due to complex mechanisms interacting. Here we propose a model able to describe the interaction phenomena between the porous medium and the fluid part, *i.e.* the flow in a deformable medium and conversely the modified mechanical response of the wet solid. This model is completed by a new boundary condition between the porous part and the purely fluid region.

THE PROPOSED MODEL

The following notation are used: a superscript is used to refer to the considered area (wet or dry preform f, resin r). An index is related to the component (fiber f, resin r or virtual domain d introduced to deal with ALE formulation). We write down x the material coordinates, X the initial coordinates, χ the reference coordinates used to tackle the ALE formulation.

The selected model

From industrial point of view, a macroscopical approach must be considered. This approach yields to reasonable computation times for such a heterogeneous structure. The proposed model relies on a homogenous representation of 3 regions connected with moving boundaries (see Figure 2): dry preform, wet preform and purely fluid region.

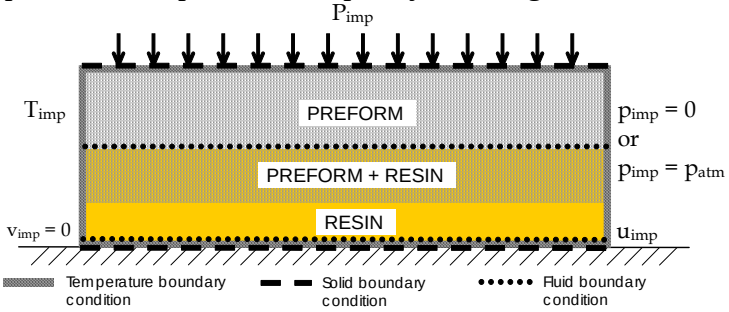

Fig. 2 Composite manufacturing processes by infusion – RFI (a) – LRI (b)

Macroscopical models for every component in each area are used to take into account the interactions between the components directly in mass balance and momentum conservation equations.

Modeling of the fluid flow

In this process, the resin flow is laminar (low Reynolds numbers). This resin behaves as a Newtonian incompressible fluid. Hence, inertial forces are negligible compared to viscous forces. The two areas concerned by the resin flow (wet preform and purely fluid region) undergo large rotations and deformations during the flow which prevent the model from using an Eulerian formulation to deal with the fluid flow.

ALE Formulation
The Aribitrary Lagrangian Eulerian formulation is an excellent way to study moving boundary problems for fluid flow. The formulation combines the best aspects of Lagrangian and Eulerian schemes, by introducing a reference domain where computations are performed. Hence, this formulation allows to study flows in a deformable area since this reference domain (coordinate χ) is attached to the mobile domain where fluid flow occurs. Moreover, this formulation permits to represent any change of properties (mechanical, compaction …) of the mobile domain and its consequence on the fluid flow. From a computational point of view, the quasi-Eulerian formulation is often used as the Cauchy stress tensor is employed instead of the First Piola Kirchhoff tensor. This formulation gives a new expression for the material derivative of any function f which has to be used in Eulerian conservations equations [2]:

$$\frac{Df\left(\vec{\chi},t\right)}{Dt}=\left.\frac{\partial f\left(\vec{\chi},t\right)}{\partial t}\right|_{\vec{\chi}}+\vec{c}\left(\vec{x},t\right)\cdot\vec{\nabla}_x f\left(\vec{x},t\right) \tag{1}$$

where $\vec{c}\left(\vec{x},t\right)$ is the convective velocity, *i.e.* the relative velocity between the resin particle $\vec{v}_r\left(\vec{x},t\right)$ and the velocity of the corresponding virtual domain $\vec{v}_d\left(\vec{x},t\right)$.

Flow in the wet preform
The capillary effects between fibers and resin can be neglected since it is reckoned that applied external pressure overrides surface tension effects. A macroscopical Darcy law is used to take into account the fluid flow in the compressible preform. In this law, inertial terms and volumic forces are neglected. This macroscopical model introduces the permeability tensor $\overline{\overline{K}}$ which has to be determined precisely in order to provide accurate results for the flow [4]. Recently, many studies have been conducted to accurately measure the permeability tensor [6]. The Darcy law is reliable as soon as the permeability remains low. The Darcy's equation [5] (mass balance and momentum conservation) expressed in terms of ALE formulation writes:

$$\begin{aligned}&\phi\, s\left(\vec{v}_r^{\,f}-\vec{v}_d^{\,f}\right)=-\frac{\overline{\overline{K}}}{\eta}\cdot\vec{\nabla}_x\, p_r^f\\&\frac{\partial\rho_r^f\left(\vec{\chi},t\right)}{\partial t}+\vec{c}_r^{\,f}\cdot\vec{\nabla}_x\,\rho_r^f+\rho_r^f\; div_x\,\vec{v}_r^{\,f}=0\end{aligned} \tag{2}$$

where ϕ is the porosity, s is the saturation ratio, η is the resin kinematics viscosity, $\vec{\nabla}_x$ is the gradient operator with respect to x, p_r^f is the resin pore pressure and ρ_r^f is the resin density in the wet preform area and $\vec{c}_r^{\,f}=\vec{c}_r^{\,f}-\vec{c}_f^{\,f}$.

Flow in the purely fluid area

As well as in the wet preform, inertial effects are neglected. In this purely fluid region, Stokes equations are used to predict fluid flow. Expressed in terms of ALE formulation the Stokes equations can be written as follows:

$$\begin{aligned} &\rho_r^r \, \vec{c}_r^r \cdot \overline{\overline{grad}}_x \, \vec{v}_r^r = -\overrightarrow{grad}_x \, p_r^r + \eta \, \vec{\Delta} \, \vec{v}_r^r \\ &\left. \frac{\partial \rho_r^r \left(\vec{\chi}, t \right)}{\partial t} \right|_{\vec{\chi}} + \vec{c}_r^r \cdot \overrightarrow{grad}_x \, \rho_r^r + \rho_r^r \, div_x \, \vec{v}_r^r = 0 \end{aligned} \tag{3}$$

Here the convective velocity $\vec{c}_r^r$ is the difference between the resin velocity $\vec{v}_r^r$ and the domain velocity $\vec{v}_d^r$, which has to be defined for instance with an elastic law.

Saturation

Two types of approaches are commonly used in the literature to deal with change in saturation. The transient approach gives a further relation between the resin pressure and the saturation. But the lack of information concerning this relation leads to the slug flow approach. This hypothesis yields a direct binary relationship between the resin pressure and the saturation:

$$s\left(\vec{x},t\right)=1 \quad for \quad p\left(\vec{x},t\right)\neq 0 \quad et \quad s\left(\vec{x},t\right)=0 \quad for \quad p\left(\vec{x},t\right)=0 \tag{4}$$

Modeling of the preform compressibility

The main feature of the provided model is related with the compressibility of the preform during the resin infusion [7]. These deformations result from the transient equilibrium between the loadings applied on the part by the vacuum bag and the pressure induced by the viscous liquid contained in the compressed saturated fabrics. A material formulation such as a Total or an Updated Lagrangian Formulation is suitable for this type of behavior.

Mass balance

Mass balance of the preform allows following the preform density evolution. This equation relates mass at times t and $t+\Delta t$ via the density and the Jacobian of transformation J [5]. Here the preforms are assumed to be deformable but composed of incompressible fibers.

$$J\left(\vec{x},t+\Delta t\right)\left(1-\phi\left(\vec{x},t+\Delta t\right)\right)=J\left(\vec{x},t\right)\left(1-\phi\left(\vec{x},t\right)\right) \tag{5}$$

Momentum equation

The preform compressibility experimental data for saturated and unsaturated flows has been studied for very particular boundary conditions and specific fiber networks [8]. In this approach, for a general use, we choose to formulate the behavior of the preform by a Terzaghy's constitutive law. In this constitutive law, the effective stiffness of the preform $\overline{\overline{\sigma}}_{ef}^{f}$ is completed by the action of the resin pressure inside the porous medium's pores ($s\ p_r^f$). This approach gives a continuous model for the wet and dry preform *i.e.* there is a direct continuity of stresses on the flow front:

$$\overrightarrow{div}_x \, \overline{\overline{\sigma}}_f^f \left(\vec{X}, t \right) = \vec{0} \quad \text{where} \quad \begin{cases} \overline{\overline{\sigma}}_f^f = \overline{\overline{\sigma}}_{ef}^{f} - s \, p_r^f \, \overline{\overline{I}} & \text{for wet preform} \\ \overline{\overline{\sigma}}_f^f = \overline{\overline{\sigma}}_{ef}^{f} & \text{for dry preform} \end{cases} \tag{6}$$

Boundary Conditions

Figure 3 summarizes both boundary conditions and interaction conditions between the two types of components (resin and preform) in the three area studied for the modeling of the RFI process. The interaction conditions are settled at the material scale between the wet preform and the resin in this wet preform. At the structural scale, the boundary conditions put together conditions imposed by the process itself and conditions prescribed on the interface to ensure the stress vector continuity.

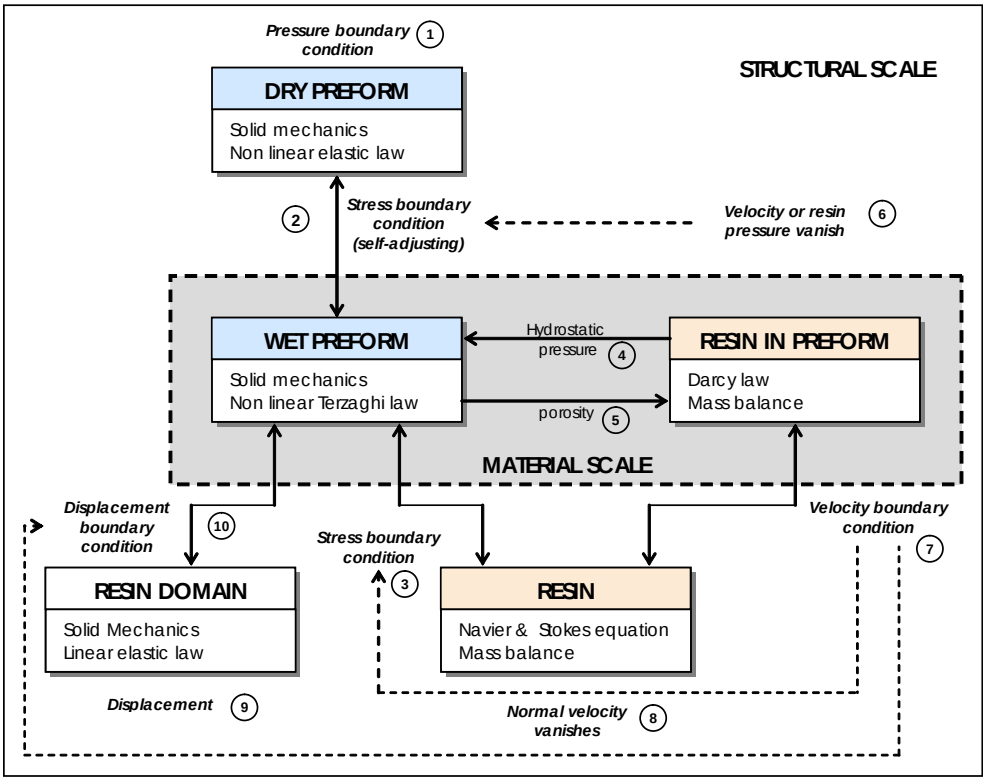

Fig. 3 Boundary conditions at structural scale and interaction at material scale

Thermo-chemical modeling

In this approach, unlike the mechanical modeling, three homogeneous domains are considered since resin flow is slow, *i.e.* fiber and resin temperature are very closed at a same spatial point. Two types of equations govern the thermo-physico-chemical phenomena. Heat transfer equation expresses the conservation of energy [3]:

$$\rho\, c\, \frac{DT}{Dt} = \overline{\overline{\sigma}} : \overline{\overline{D}} + div\left(\overline{\overline{\lambda}} \cdot \overrightarrow{grad\ T}\right) + \Delta H\, \frac{D\alpha}{Dt} \qquad (5)$$

where c is the specific capacity, $\overline{\overline{\lambda}}$ is the thermal conductivity tensor, ΔH is the heat of reaction and α the curing degree.
The curing equation expresses the transport of the curing resin mass α.

$$\frac{D\alpha}{Dt} = \frac{D\alpha}{Dt} + \vec{v} \cdot \vec{\nabla}\alpha \qquad (5)$$

There are many models in the literature for the material derivative $\frac{D\alpha}{Dt}$. These models are commonly constructed by coupling Arrhenius laws with power laws.

Review

Figure 4 summarizes the interactions between the behavior of the resin and preform in the wet preform. The bold boxes contain independent variables. Each variable is connected with conservation equations and physical laws.

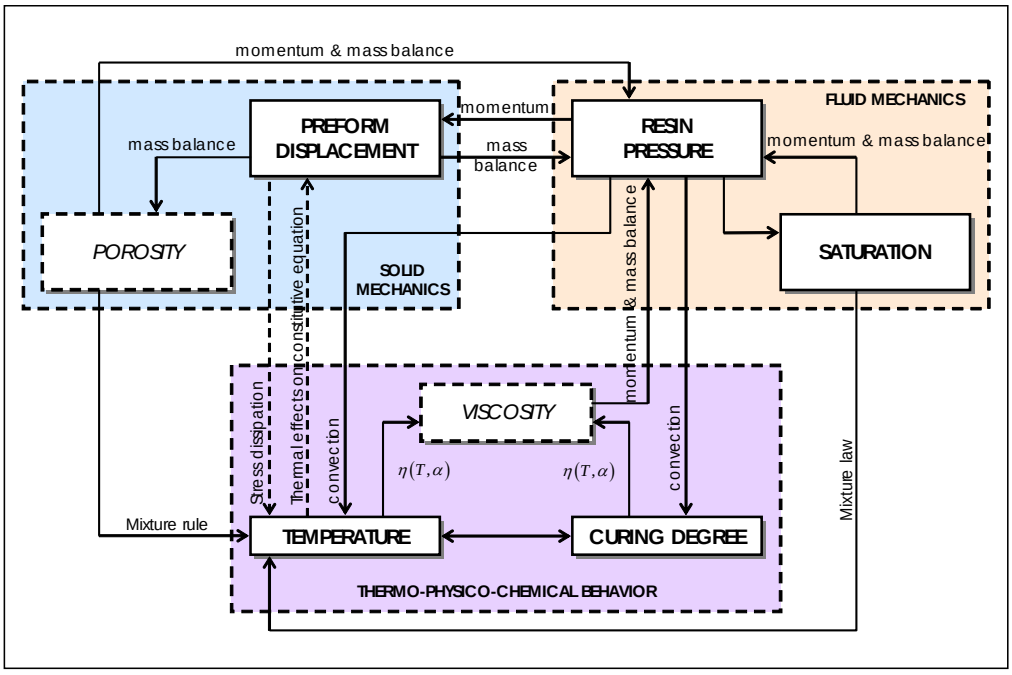

Fig. 4 Coupling between thermo-chemical, fluid and solid mechanical behavior

RESULTS

Mechanical interactions between the fluid and the solid part have been introduced in PAM RTM©. Here two types of numerical results are presented. The first one concerns the interactions phenomena in the wet preform. The purely fluid region is not taken into account, flow rate boundary conditions are used to feed in the preform. This modeling is suitable for a SCRIMP© like process. The second chosen example is a modeling of RFI process, the purely fluid region is introduced in the model.

Flow in a highly deformable media

This first result has been obtained with an exaggerated flow rate for a complex T-shape piece with permeability orientations. This exaggerated flow rate is prescribed in order to observe the porous medium deformations due to the internal pressure applied by the fluid inside the pores (Terzaghi hypothesis). The vacuum bag applies a mechanical pressure as presented in Figure 5-c. The proposed algorithm (Figure 5-a) uses an iterative scheme with a coupling between implicit Darcy and mechanical calculations until the filling of the part is complete (time explicit). Figure 5-c depicts the mesh of the T-shape piece with permeability orientations of the stacking. The core, *i.e.* the solid part without permeability orientations, is 10 times more permeable than the preform in the transverse direction. Figure 5-b shows the internal resin pressure obtained on the deformed configuration. The results obtained with this algorithm have been compared successfully on a simplest geometry with analytical results.

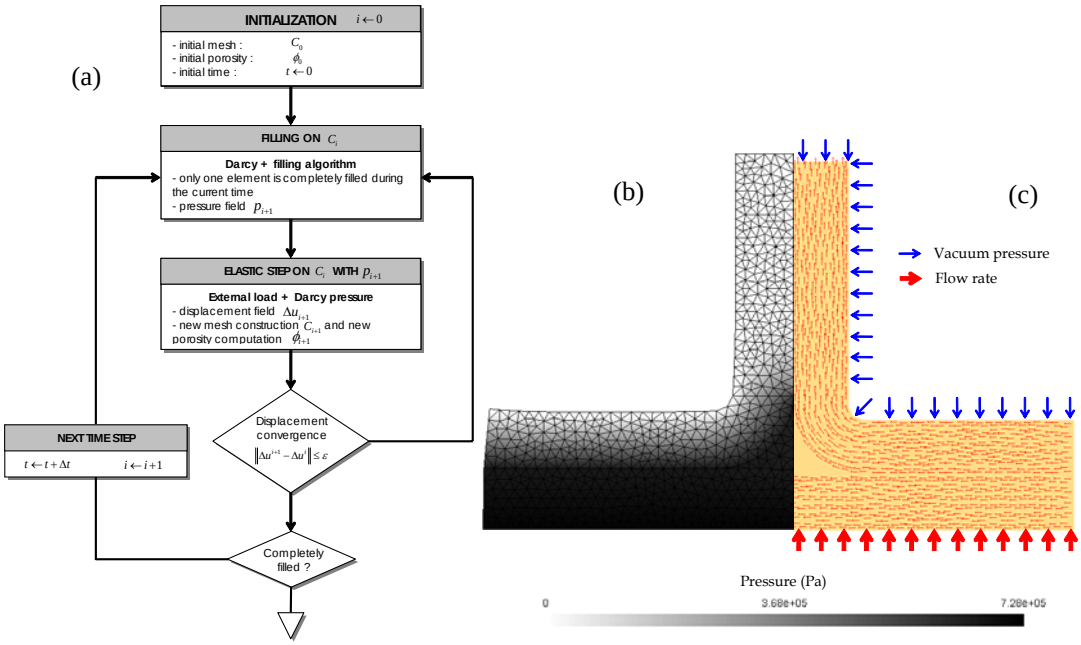

Fig. 5 Infusion of a T: (a) algorithm used - (b) pressure distribution (Pa) on the deformed configuration - (c) permeability orientation for the underformed configuration

Interaction between Darcy and Stokes Area

This second example adds the purely fluid domain in the previous algorithm.

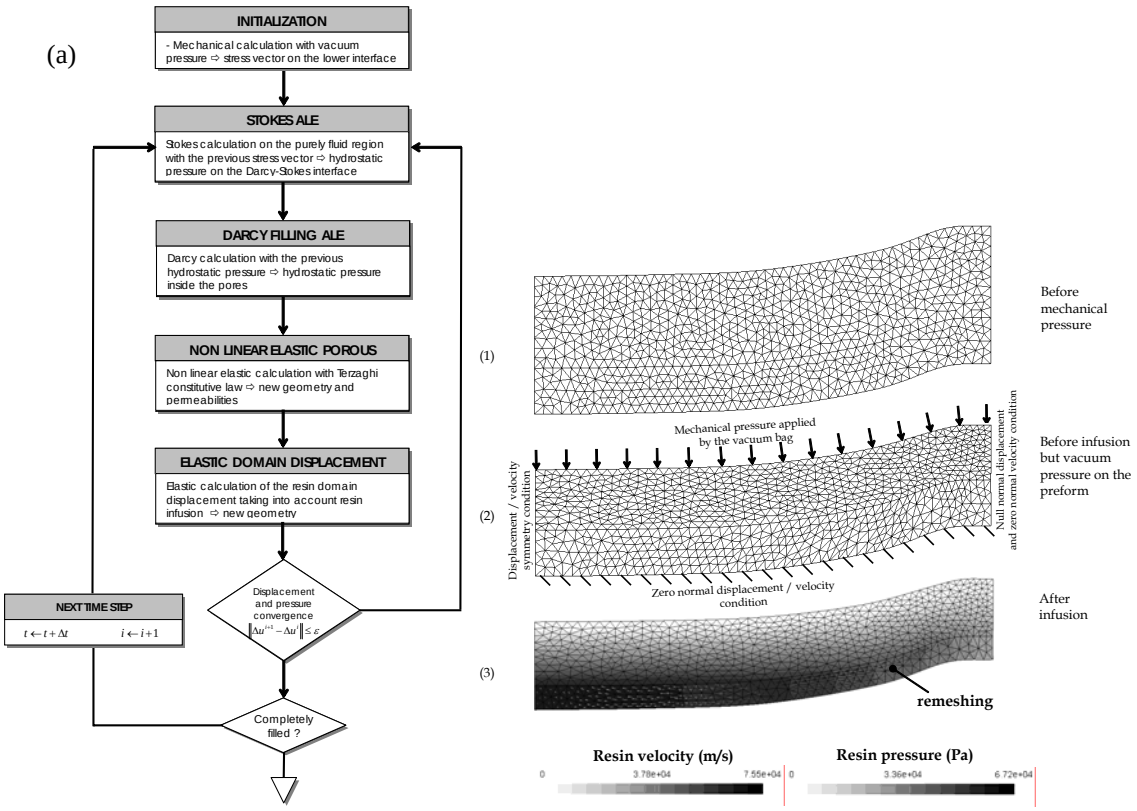

Fig. 6 Resin Film Infusion (RFI) of a curved panel – (a) proposed algorithm – (b) results at initial time (1), compression time (2), final stage (3)

A modified Beaver-Joseph-Saffman condition has been used to couple the Darcy and Stokes areas. This condition has been completed with a continuity of hydrostatic pressure on the interface. The proposed algorithm consists in a filling iterative scheme made of four implicit problems: fluid and solid mechanics in the porous area and fluid and domain displacement in the purely fluid region. This iteration loop is based upon a pressure, displacement and velocity criterion convergence. The Darcy and Stokes problems use an ALE formulation in order to observe an accurate mass balance. In the present results (see Figure 6-a,b,c) finite strains of the preform can be observed. Moreover, border and curvature effects give a non-constant pressure field that would be constant for a plane plate. The velocity pressure formulation for the Stokes problems and Darcy problems has been solved here by the Bubble Element formulation [1].

CONCLUSIONS

In this paper, a new model conceived to simulate non-isothermal resin infusion in a highly compressible preform was presented. This model can be applied in a large range of activities for all industrial processes involving infiltration in deformable porous media. Currently, experimental validations of the proposed RFI model have been carried out with Hexcel Reinforcement to provide a reliable tool. It is important to underline here that the lack of information and experimental data is the major drawback met for industrial use, mainly for the permeability measurement in the transverse direction in saturated and unsaturated regimes.

ACKNOWLEDGMENTS

The authors would like to thank ESI Group (http://www.esi-group.com) and Hexcel Reinforcement (http://www.hexcel.com) for their support to the present research.

REFERENCES

1. D. N. Arnold, F. Brezzi, and M. Fortin, "A stable finite element for the Stokes equations," *Estratto da Calcolo*, vol. 21, pp. 337--344, 1984.
2. T. Belytschko, W. K. Liu, and B. Moran, Nonlinear finite elements for continua and structures: *John Wiley & Sons*, Ltd, 2000.
3. J. M. Bergheau and R. Fortunier, Simulation numérique des transferts thermiques, *Hermès - Lavoisier ed*, 2004.
4. J. Bréard, Y. Henzel, and F. Trochu, "A standard characterization of saturated ans unsaturated flow behaviors in Porous media.," *presented at 12th International Conference on Composite Materials ICCM12*, Paris, 1999.
5. H. Darcy, Les fontaines publiques de la ville de Dijon: *Dalmont*, 1856.
6. S. Drapier, J. Monatte, O. Elbouazzaoui, and P. Henrat, "Characterization of transient through-thickness permeabilities of Non Crimp New Concept (NC2) multiaxial fabrics," *Composites Part A: Applied Science and Manufacturing*, vol. 36, pp. 877-892, 2005.
7. A. Farina and L. Preziosi, "Non-isothermal injection molding with resin cure and preform deformability," *Composites Part A: Applied Science and Manufacturing*, vol. 31, pp. 1355-1372, 2000.
8. M. Kaviany, Principles of heat Tranfer in Porous Media. New York: *Springer-Verlag New York*, 1995.

UNSATURATED MODELLING OF DUAL SCALE FLOW IN LIQUID COMPOSITE MOULDING PROCESSES

Y. Wang and S.M. Grove

Advanced Composites Manufacturing Centre
School of Engineering, University of Plymouth, Plymouth, UK, PL4 8AA

ABSTRACT: An unsaturated flow model is incorporated into a dual-scale model previously developed for resin flow through woven fibre mats. In this model, the two different scale flows are simulated at a same numerical scale. A sink and a source term are introduced for the two different scaled flows, respectively, based on mass conservation in the dual-scale domain. With this model, the micro flow inside fibre tows can be described in detail, including the axial flow in flow direction and the transverse flow in the cross section of fibre tows, while capillary effects have been included in the axial flow within the fibre tow. The transverse flow is simply regarded as being caused by the saturation difference between the inter-tow gaps and the intra-tow pore space. To close the equations in the model, a resin retention characteristic and microscopic diffusivity have been assumed (in the absence of experimental data). Finite element discretization of the governing equation is defined, and a simple implicit time integration method is suggested. A 1D example of RTM has been modelled, and results discussed.

KEYWORDS: RTM, Dual-scale model, Unsaturated flow, Capillary effect, FEA

INTRODUCTION

Liquid Composite Moulding (LCM), in its various industrial forms, is a widely used technology in the manufacture of advanced composite components. Because of its efficiency and cost saving, mathematical modelling of LCM processes has attracted more and more research interest in recent decades, and is playing an increasingly important role in technology applications. Considerable research effort has been devoted to process modelling, and several numerical simulation procedures have been developed [1,2]. In early studies, resin flow through dry fabric beds was modelled as a single flow at a single scale. The fibre preform is assumed to be fully saturated behind the resin front, and therefore Darcy's law is adopted to describe the superficial velocity of the resin flow, in which the pressure gradient in resin saturated region is regarded as the driving force. Incorporating the mass conservation condition, Darcy's law can be used to determine the progress of the resin font [3,4] where, normally, the permeability of porous fabrics is assumed to be a constant in a representative elementary volume (REV). However, the 'fully saturated' assumption is not a reality, especially for woven fibre mats, which consist of discrete fibre tows, and are microscopically heterogeneous. Investigation has shown that two different flow rates (a fast macro-flow in the gaps between fibre tows and a slow micro-flow in the passages inside tows) coexist in resin infusion process for this type of preform. Voids may be retained in tows after the resin has passed, due to incomplete impregnation.

An understanding of the formation of voids and/or dry spots is clearly important, as these features can have serious implications for composite quality and performance. This has been investigated through two-scale or two-layer models of flow through woven fibre mats. Lekakou and Bader [5] proposed a model of the macro- and micro-infiltration using Darcy's law, where separate permeabilities were used for different scale flows and capillary pressures were considered. Recently, Pillai [1] developed a rigorous dual-scale mathematical model which simulates the macro-flow using a volume average method. A sink term of the macro-flow is introduced which couples the two different scaled flows together based on a mass conservation. Darcy's law has been proven to be valid for the macro-flow, while an idealized cylindrical microscopic impregnation of fibre tows was assumed.

In this paper, based on the dual-scale model, we try to simultaneously model the macro- and micro-infiltration in LCM process in a same numerical scale. Similar to the sink term in the macro-flow case, a source term is introduced to the micro-domain which is caused by the resin sink from the identical local macro-domain. The resin macro-flow is assumed to have a distinct resin front, but in the micro-domain, no distinct resin front exists because of source term. The approach here is to adopt the variation of saturation to describe the resin impregnation inside fibre tow regions. A 1D numerical simulation example using this model will be presented.

THEORY

2.1 Governing equation

Based on the consideration of the dual-scale nature of woven fabrics, Pillai, employing the volume average methods, developed the following governing equations for the resin macroscopic flow in inter-tow gaps [1]:

$$\nabla \cdot \left\langle \mathbf{v}_g \right\rangle = -S \tag{1}$$

$$\left\langle \mathbf{v}_g \right\rangle = -\frac{K_g}{\mu} \nabla \left\langle P_g \right\rangle^g \tag{2}$$

where, $\left\langle \mathbf{v}_g \right\rangle$ is volume average resin flow velocity, S is a sink term accounting for the rate of resin absorption by the tows in per unit volume, $\left\langle P_g \right\rangle^g$ is gap average modified resin pressure, which is defined as $P_g = p_g + \rho_g g h$, μ is resin viscosity, K_g is resin permeability in inter-tow gaps. Theoretically, S is the mass loss in gaps due to resin infusion into fibre tows from the gaps, which can be expressed as:

$$S = \frac{1}{V} \int_{S_{gt}} \mathbf{v}_g \cdot \mathbf{n}_{gt} ds \tag{3}$$

where S_{gt} is total area of the tow-gap interface and $\mathbf{n}_{gt}$ is the normal vector of the surface.

Eqs. 1 and 2 assume that a distinct resin front exists in inter-tow gaps, which separates the space of the gaps into a fully impregnated region and a dry region, and they are only applicable for the part of resin flowing in the saturated region. However, the resin flowing

inside fibre tows normally has a slow velocity because of high resistance there. The resin movement inside fibre tows due to the local pressure gradient will lag behind that in inter-tow gaps, and resin will sink from inter-tow gaps into fibre tows at front region. As a result, an unsaturated region exists at the resin front in fibre tows, where the resin content is variable. In view of the fact that it is difficult to outline a distinct sharp resin front at numerical scale for the resin flow inside fibre tows, we believe that using saturation to describe the flow in fibre tow is a reasonably good solution [6,7]. By introducing the saturation, the resin flow inside the fibre tows can be expressed as:

$$\frac{\partial}{\partial t}\left(\varepsilon_f \rho \theta_f\right) = -\nabla\left(\rho \theta_f \left\langle \mathbf{v}_f \right\rangle\right) + R_f \tag{4}$$

$$\left\langle \mathbf{v}_f \right\rangle = -\frac{K_f}{\mu} \nabla \left\langle P_f \right\rangle^f \tag{5}$$

Eq. (4) is mass conservation equation, where θ_f is the saturation, which is the fraction of the void in fibre tows been occupied by resin, $\varepsilon_f = V_f / V$ is the fibre void fraction, V_f is the total volume of voids in fibre tows, ρ is resin density, R_f is a source term, a homogeneous mass production rate from other generating phase per unit volume. According to mass conservation, the source term in fibre tows is equal to the sink term in Eq. (1), i.e.

$$R_f = \rho S \tag{6}$$

Eq. (5) is the Darcy law applied on the flow inside fibre tows, where $\left\langle \mathbf{v}_f \right\rangle$ is the average superficial velocity of resin inside tow, K_f is permeability inside fibre tows. $\left\langle P_f \right\rangle^f$ is an average modified resin pressure inside fibre tow, which consists of the following components:

$$\left\langle P_f \right\rangle^f = \left\langle P_g \right\rangle^g + \left\langle P_f \right\rangle_f^f + \left\langle P_f \right\rangle_c^f \tag{7}$$

where $\left\langle P_g \right\rangle^g$ is the resin pressure in gaps as defined before, $\left\langle P_f \right\rangle_f^f$ is the resin pressure insider tows caused by the fibre deformation, which will not be considered in this paper. $\left\langle P_f \right\rangle_c^f$ is the resin pressure inside tows caused by the capillary effect.

Equations (1-7) fully describe the resin flow in a dual-scale fabric mat. But using Eq. 3 to calculate S is not easy and we need to know the detail of the woven structure of fabric reinforcement so that different cross sections of different architectures can be described in detail [8]. As a simpler alternative, we regard the saturation difference as the driving force for the sink/source term, assuming that once the fibre tow is fully saturated the local sink/source process will stop. Because the sink is a flow crossing the surface of fibre, similar to the treatment by Pillai [1], we also idealize that the cross section of fibre tows is a circle, and ignore the dynamic distribution of resin inside fibre tows. Finally the sink/source term can be approximated as:

$$R_f = \rho S = \rho D(\frac{\theta_g - \theta_f}{r_{tow}^2}) \tag{8}$$

where D is a parameter called as diffusivity (m^2/s) of the fibre tows, θ_g is the saturation at gap-tow interface, which is assumed to be 1 when the gap is occupied and 0 otherwise. θ_f is the saturation in fibre tow and r_{tow} is a normalized fibre radius which can be assumed as an average value for a deformed fibre tow.

2.2 The characteristics of dual-scale fibre reinforcement

To close the above equations, we need to know the permeability K_g and K_f, capillary component pressure $\left\langle P_f \right\rangle_c^f$ and diffusivity D. The Carman-Kozeny equation is normally employed to evaluate the permeability for axial flow along fibres and transverse flow across fibres when the fibres are considered as solid and of circular cross-section [5]:

$$K = \frac{r_f^2}{4k} \frac{\varepsilon^3}{(1-\varepsilon)^2} \tag{9}$$

where r_f is radius of fibre tow for macro-flow and is fibre radius for micro-flow. k is the Kozeny constant and ε is porosity as defined before (ε_g for macro-flow and ε_f for micro-flow).

It must be noticed that Eq. (9) is suggested for saturated flow but not strictly suitable for the unsaturated flow defined by Eqs. (4) and (5). In this paper, Eq. (9) was employed to estimate the macro-scale permeability K_g, but for the micro-scale permeability, which depends on the saturation of voids, we employed an empirical model by Gilham et al. [9] from water-soil research:

$$K_f = a\theta^n \tag{10}$$

where θ is saturation of fibre tows, a and n are two empirical parameters.

For the capillary component pressure, a model proposed for water retention characteristic [10] was adopted, which assumes that capillary pressure varies with saturation due to the change of the size of occupied pore space:

$$\left\langle P_f \right\rangle_c^f = \phi_0 + P_0\left(\exp(\alpha\theta) - \exp(\beta(1-\theta))\right) \tag{11}$$

where ϕ_0, P_0, α and β are four constants.

There is no reference data available for the value of diffusivity for fibre fabrics. According to its definition, diffusivity is related to permeability by [10]:

$$D(\theta) = \frac{K_f(\theta)}{\mu} \frac{\partial \left\langle P_f \right\rangle_c^f}{\partial \theta} \tag{12}$$

Using Eqs. (10) and (11), Eq. (12) can be rewritten as:

$$D = \frac{a\theta^n}{\mu} P_0 \left(\alpha \exp(\alpha\theta) + \beta \exp(\beta(1-\theta))\right) \tag{13}$$

In the next section, the proposed model will be applied to simulate a RTM process using finite element methods.

EXAMPLES

An example of 1D flow in a rectangular domain with resin being injected at one end (Fig.1) was employed to test the model. Due to lack of data for the capillary pressure inside fibre tows, an experimental result provided by Lin et al. [11] was adopted for illustration. Fig. 2 shows the fitting result of Eq. (11) to the experimental data. The corresponding fitting data are listed in Table 1. The other dual-scale parameters are listed in Table 2.

Table 1. Resin retention characteristic parameters

ϕ_0 (Pa)	P_0 (Pa)	α	β
–2009	2.823×10^{-3}	13.57	15.57

Table 2. Basic parameters used in simulation

ε_g	ε_f	μ_{resin} Pa.s	r_{tow} mm	K_g mm^2	a mm^2	n
0.1	0.3	0.4	0.3	5.6×10^{-5}	9.8×10^{-7}	2.0

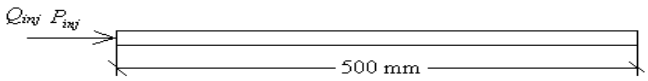

Fig. 1. 1D flow example

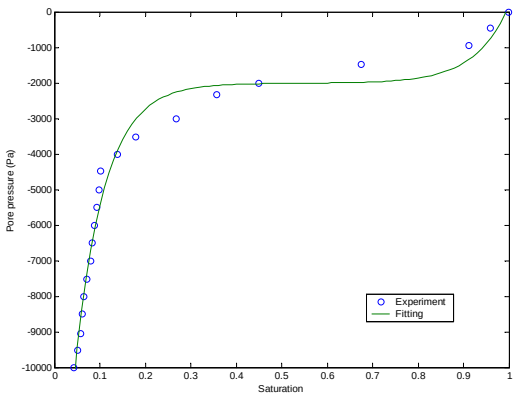

Fig. 2. Capillary pressure with saturation (data from Lin et al., 1998)

Figs. 3 to 6 show the modelling results at two different time steps under injection pressure P_{inj} = 150 kPa. We can see that a stable numerical result has been obtained. Fig. 3 shows the resin profile in the inter-tow gaps with an obvious sharp resin front. Two distinct regions in the gaps (fully resin impregnated or completely dry), separated by the sharp resin front, have been modelled successfully. Fig. 4 shows the corresponding resin pressure profiles in the gaps. It can be seen that the pressure distributions are concave curves rather than linear. This is consistent with the analysis, since, according to Equation (16), the pressure should have a concave shape when S > 0. Figs. 5 and 6 show the corresponding resin saturation and

pressure profiles in fibre tows. The resin saturation profiles do not have a significant sharp front but exhibit three distinct regions: (i) the resin front lags behind that in the gaps; (ii) a saturated region expands starting from the resin inlet port; (iii) an unsaturated region having a variation in resin content exists in the middle. The existence of three distinct regions is consistent with the experimental observation [12]. It has been noticed that the middle unsaturated part expands faster than the saturated part behind it. This implies that that the pressure-driven resin flow in the fibre tows is slower than the sink from the gaps because of the very low permeability in fibre tows. Thus it is concluded that resin infiltration from the macro-scale to the micro-scale plays an important role in the impregnation of fibre tows.

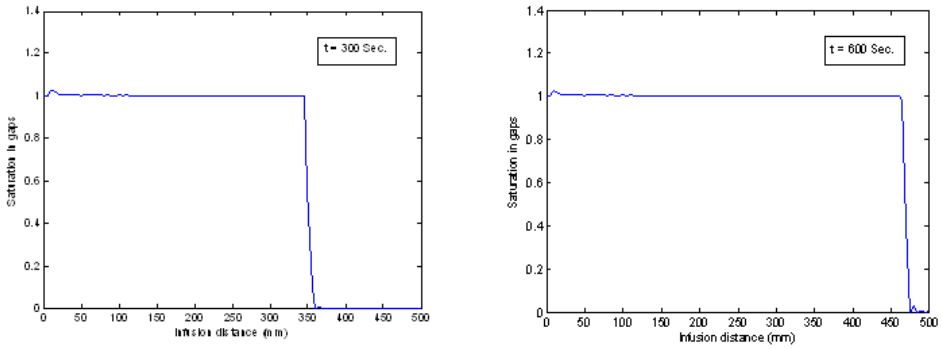

Fig. 3. Dual-scale simulation: saturation profiles in gaps

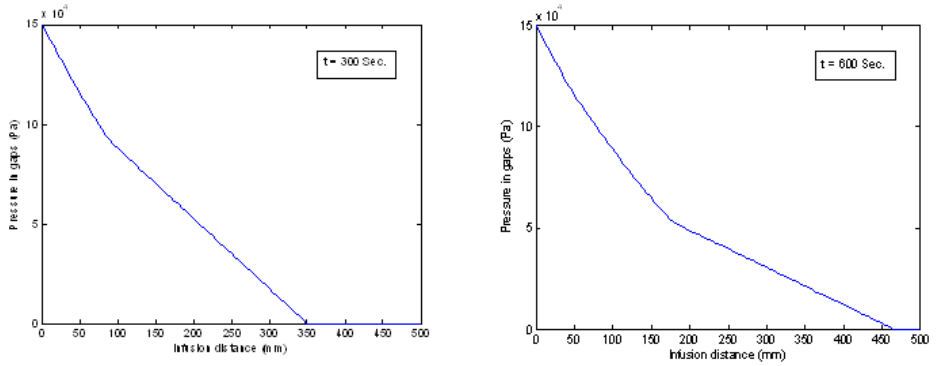

Fig. 4. Dual-scale simulation: pressure profiles in gaps

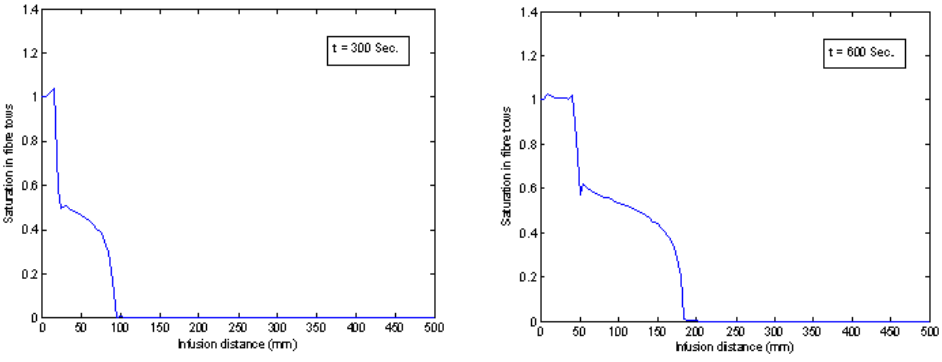

Fig. 5. Dual-scale simulation: saturation profiles in fibre tows

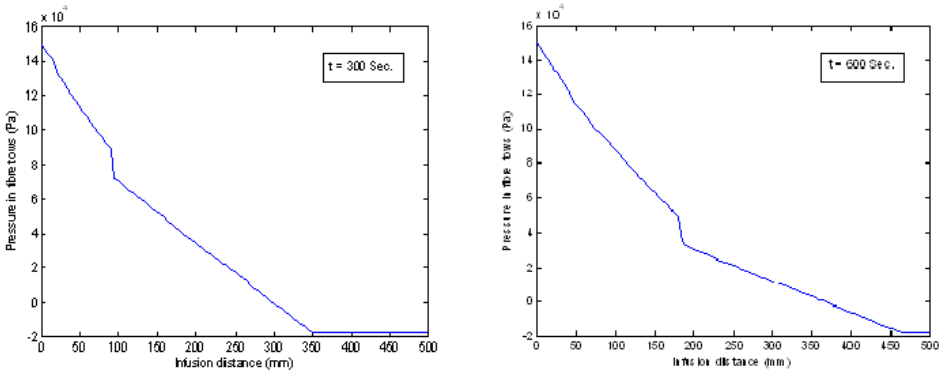

Fig. 6. Dual-scale simulation: pressure profiles in fibre tows

CONCLUSIONS

A dual-scale model for resin flow through woven fibre mats has been proposed by previous researchers. In this paper, this model has been successfully combined with an unsaturated flow model used in other disciplines. In the new model, the two different scale flows are simulated at a same numerical scale. A sink and a source term are introduced for the two different scaled flows, respectively, based on the mass conservation in the dual-scale domain. The results show that the model works very well. Stable numerical results have been obtained. Distinct resin sharp front has been simulated for the macro-scale flow in the inter-tow gaps, while smooth variation of the resin saturation in fibre tows has been modelled. The result of the smooth variation of the micro-scale resin saturation can be used to explain the bubble formation behind the sharp resin front. It is hoped that this theoretical approach will be applicable to future studies of void formation and transport.

REFERENCES

1. K. M. Pillai, "Governing Equations for Unsaturated Flow Through Woven Fibre Mats, Part 1. Isothermal Flows", Composites: Part A, Vol. 33, 2002, pp. 1007-1019.

2. C. D. Rudd, A. C. Long, and C. G. E. Mangin, "Liquid Moulding Technologies", Woodhead Publishing Limited, Abington Hall, Abington, Cambridge, UK, 1997.

3. F. Trochu, R. Gauvin, and D. M. Gao, "Numerical Analysis of the Resin Transfer Moulding Process by the Finite Element Method", Advances in Polymer Technology, Vol. 12, 1993, pp. 329-342.

4. X. L. Liu, "Isothermal Flow Simulation of Liquid Composite Molding" Composites: Part A, Vol. 31, 2000, pp. 1295-1302.

5. C. Lekakou and M. G. Bader, "Mathematical Modelling of Macro- and Micro-Infiltration in Resin Transfer Moulding (RTM)", Composites: Part A, Vol. 29, 1998, pp. 29-37.

6. D. Hillel, "Environmental Soil Physics", Academic Press, London, UK, 1998.

7. C. Hall and W. D. Hoff, "Water Transport in Brick, Stone and Concrete" Spon Press, New York, 2002.

8. K. M. Pillai and S. G. Advani "A Model for Unsaturated Flow in Woven Fiber Preforms during Mold Filling in Resin Transfer Molding", Journal of Composite Materials, Vol. 32, 1998, pp. 1753-1783.

9. R. W. Gilham, A. Klute, and D. F. Heermann, "Hydraulic Properties of a Porous Media: Measurement and Empirical Representation", Soil Science Society American Journal, Vol. 40, 1976, pp. 203-207.

10. Y. Wang, S. M. Grove, M. G. Anderson and J. –P. Renaud, "Modelling Water Retention in Porous Media", Journal of Hydrology, 2006, (Under review)

11. M. Lin, T. H. Hahn, and H. Huh, "A Finite Element Simulation of Resin Transfer Molding Based on Partial Nodal Saturation and Implicit Time Integration", Composites: Part A, Vol. 29:1998, pp. 541-550.

12. K. M. Pillai, "Modeling the Unsaturated Flow in Liquid Composite Molding Processes: A Review and Some Thoughts", Journal of Composite Materials, Vol. 38, 2004, pp. 2097-2117.

DEVIATION FROM DARCY'S LAW: AN IMPLICATION OF UNSATURATED FLOW IN DUAL-SCALE FIBER MATS IN LCM

Murthy S. Munagavalasa[1] and Krishna M. Pillai[2]

[1]S.C. Johnson & Son, Inc., 1525 Howe Street, Mail Station 153, Racine, WI 53403-2236, USA: MSMunaga@SCJ.COM

[2]Department of Mechanical Engineering, University of Wisconsin- Milwaukee, Milwaukee, WI 53201, USA: krishna@uwm.edu

ABSTRACT: Liquid Composite Molding (LCM) processes including RTM and VARTM are used for producing polymer matrix composite. In any typical LCM process a thermoset resin is injected/sucked into a mold cavity with a pre-placed preform of fiber mats. The dual-scale nature of those fiber preforms gives rise to the unsaturated flow during mold filling in LCM processes that is characterized by a modified continuity equation with a `sink' term due to the delayed absorption of resin by fiber tows behind the flow front. Application of the mathematically rigorous volume averaging method results in a momentum balance equation that has two additional terms apart from the pressure gradient terms associated with the Darcy's law. In this paper, we would explore the importance of these two terms (called the Brinkman term and the interfacial kinetic-effect tensor term) near the flow front in a dual-scale porous medium created by the dual-scale fiber mats. Through a numerical simulation of the unsaturated flow in an idealized dual-scale porous media, it is discovered that these two terms become significant in a small region behind the flow front where the sink term changes rapidly. So the results suggest that a modified form of Darcy's law needs to be used near the flow front during LCM mold-filling simulation in a dual-scale fiber mat.

KEYWORDS: RTM, resin transfer molding, LCM, liquid composite molding, unsaturated flow, Darcy's Law, polymer composites, dual-scale porous media

INTRODUCTION

Composite materials have become critically important in aerospace, automotive, and civil engineering areas along with the biomechanics and other fields because of their high stiffness to weight ratio, long fatigue life, increased corrosion resistance, and their ability to consolidate parts. Liquid composite molding (LCM) technologies such as the resin transfer molding (RTM), vacuum assisted RTM (VARTM), and Seeman Composite Resin Infusion Molding Process, are very important in the manufacture of polymer composites [1]. These composites consist of polymeric matrix which is interspersed with reinforcements such as carbon and glass fibers. In LCM, the composites are created by impregnating a fiber-packed mold cavity with resin by injecting it through the inlet gates of the mold. Numerical simulation of such mold-filling process in LCM is becoming indispensable for optimizing the mold design [2-5].

An LCM mold containing randomly oriented fibers of a random mat is an example of the single-scale porous medium. Here, all the pores are of the same length-scale. The fibers are impermeable and the spacing between fibers can be treated as homogeneous. However, if the

solid phase is porous with the pore size of a much smaller length-scale, the porous medium is then classified as a dual length-scale or dual porosity porous medium. Braided, woven or stitched fiber mats used in LCM processes, where fiber bundles are permeable to resin due to presence of pores between fibers within the bundles, fall under this category. The transport processes that occur inside this dual-scale porous medium are often significantly different from that of the single-scale porous medium. Babu and Pillai [6] discovered that the dual-scale porous media with continuous inter-tow gaps[1] (created by the stitched mats only) allow the lead-lag flow to manifest where the resin races along the gaps before fully impregnating the tows[2]. The delayed wetting of tows behind the resin front in the gap region leads to a region of partial saturation behind the front in such dual-scale fiber mats. The flow in such a region is called the *unsaturated* flow and is often characterized either by a visually observable region of a lighter hue as compared to the darker saturated region, or by a droop in the inlet-pressure history [6]. The onset of the unsaturated flow the dual-scale stitched mats can be predicted by certain dimensionless numbers such as the pore volume ratio and sink effect index [8]. A synopsis of some recent work on the unsaturated flow in dual-scale porous media was presented by Roy et al. [7].

Mathematically rigorous volume averaging method have been adopted to derive the averaged form of mass and momentum equations for the unsaturated flow in dual-scale porous media encountered during mold filling in LCM processes [9,17]. During the averaging process, averaging of the shear stress term of the Navier-Stokes equation in the gap region gives rise to a new quantity named the *interfacial kinetic-effects* tensor which includes the effects of liquid absorption by the tows, and the presence of slip velocity on their surface. Initial scaling analysis suggested that its effect on the momentum balance becomes negligible if the gradient of the rate of resin absorption by the tows is small [9]. However, beyond this qualitative insight, no estimate of the magnitude of this newly found term is available in the literature nor have we encountered any studies wherein the effect of spatial variation of the absorption rate on this term is discussed.

The objective of this work is to estimate the magnitude of two forces that results due to 1) the interfacial kinetic-effects at the tow-gap interface (the *interfacial kinetic-effects* force), as well as 2) the deceleration of the average velocity (the *Brinkman* force) in the unsaturated region of isothermal flow in a dual-scale porous medium. A finite element based numerical method is used to model 2-D isothermal unsaturated flow between two parallel porous plates. Parametric studies are conducted to evaluate the two forces in the unsaturated region just behind the flow front.

Summary of volume averaged transport equations

Pillai [9] rigorously derived the macroscopic transport equations for isothermal flow in the dual-scale porous media using the volume averaging method, the summary of which is presented in this section. Only the relevant gap-averaged balance laws will be listed; their derivation as well as the estimation of their various source and sink terms with the help of the single-scale model for the intra-tow flows is presented elsewhere [9].

Flow variables in LCM are invariably averaged in an averaging volume called REV or the representative elementary volume. For the fibrous dual-scale porous media, Pillai [9,17] has proposed an REV shown in Fig. 1 where the averaging volume consists of the gap and tow regions.

[1] Large-scale pores between tows will be referred to as the gap phase or gap region, or just gaps.
[2] Fiber bundles will be referred to as the tow phase or tow region, or just tows.

Mass balance equation for macroscopic flow in the gap region is given as

$$\nabla \cdot \left\langle \mathbf{v}_g \right\rangle = -S \tag{1}$$

Here $\left\langle \mathbf{v}_g \right\rangle$ is the volume-averaged liquid velocity in the inter-tow gaps, and is computed as $\left\langle \mathbf{v}_g \right\rangle = 1/\mathrm{V} \int_{\mathrm{V}_g} \mathbf{v}_g \mathrm{dV}$ where, as shown in Fig. 1, V and $\mathrm{V_g}$ are the total and the gap volumes for the REV. (Subscript g indicate quantities that are of the gap region.) *S* is the sink term and is equal to the volumetric rate of absorption of resin by the tows per unit volume as

$$\mathrm{S} = \frac{1}{\mathrm{V}} \int_{\mathrm{A_{gt}}} \mathbf{v}_\mathrm{g} \cdot \mathbf{n}_\mathrm{gt} \mathrm{dA} \tag{2}$$

where $\mathrm{A_{gt}}$ is the gap-tow interface area within the REV, and $\mathbf{n}_\mathrm{gt}$ is the unit normal at the gap-tow interface directed from gaps to tows.

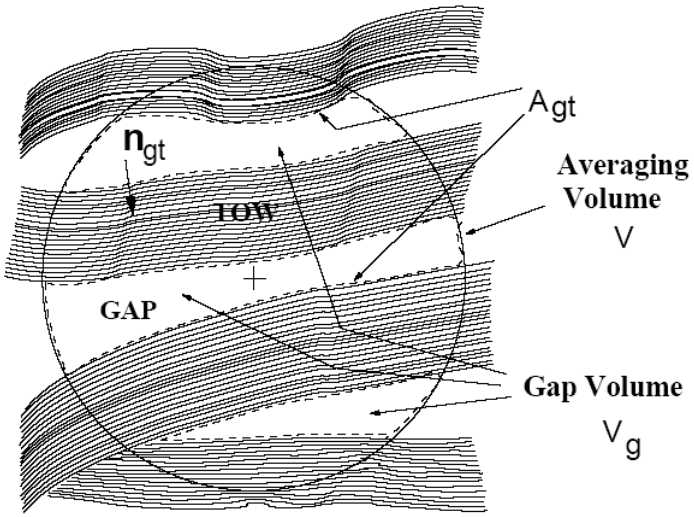

Fig.1. A typical Representative Elementary Volume (REV), or the averaging volume, for a fibrous dual-scale porous medium

The minus sign of the sink term in the continuity equation (1) suggests that the flow of the resin slows down in the unsaturated gap region because of the absorption of resin by fiber tows. An estimation of S requires the integration of resin flux into the tows, which in turn require solving the single-scale transport equations within the tow region [7,17].

Momentum balance equation for the gap region is derived to be

$$-\varepsilon_g \nabla \left\langle \mathrm{P}_g \right\rangle^g + \mu_g \left\{ \nabla^2 \left\langle \mathbf{v}_g \right\rangle + \nabla \cdot \mathbf{I} \right\} - \varepsilon_g \mu_g \mathbf{K}_\mathrm{g}^{-1} \cdot \left\langle \mathbf{v}_g \right\rangle = 0 \tag{3}$$

where $\varepsilon_\mathrm{g} = \mathrm{V_g} / \mathrm{V}$ is the gap volume fraction, $\left\langle \mathrm{P}_g \right\rangle^g$ is the gap-averaged resin pressure computed as $\left\langle \mathrm{P}_g \right\rangle^g = 1/\mathrm{V_g} \int_{\mathrm{V}_g} \mathrm{P}_g \mathrm{dV}$, μ_g is the viscosity of resin flowing in the gaps, and $\mathbf{K}_\mathrm{g}$ is the permeability tensor for flow in the gaps. **I**, the *interfacial kinetic-effects* tensor, is defined as

$$\mathbf{I} = -\mathrm{S}\delta + \frac{1}{\mathrm{V}} \int_{\mathrm{A_{gt}}} \left(\mathbf{v}_\mathrm{g} \mathbf{n}_\mathrm{gt} + \mathbf{n}_\mathrm{gt} \mathbf{v}_\mathrm{g} \right) \mathrm{dA} \tag{4}$$

with δ as the unit tensor. Note that $\mathbf{I}$ becomes identically equal to zero when the tows are impermeable. (Since $\mathbf{v}_g$ on gap tow interface becomes zero due to the no-slip condition on the solid tows.).

Eq. (3) is the dual-scale equivalent of the Brinkman's equation for single-scale porous medium [10]. This equation differs from that for single-scale porous medium in that the later equation does not contain the term $\mu_g \nabla \cdot \mathbf{I}$, which we would name as the *interfacial kinetic-effect force*[3], and which is likely to decelerate the gap flow in the regions of extreme gradients in the sink function S that take place very close to the flow front. The first term $-\varepsilon_g \nabla \langle P_g \rangle^g$ is the pressure force which drives the macroscopic gap flow. The second term $\mu_g \nabla^2 \langle \mathbf{v}_g \rangle$, which is to be called the *Brinkman force*, also tends to slow down the flow and becomes significant in areas of large changes in the gradients of the volume averaged velocities, such as at the interface of a dual-scale porous medium adjoining an open channel (section 2.11 in Ref. [14]). The last term $-\varepsilon_g \mu_g \mathbf{K}^{-1} \cdot \langle \mathbf{v}_g \rangle$ represents the net force at the solid-fluid interface.

ANALYZING FLOW IN A UNIDIRECTIONAL DUAL-SCALE MEDIUM

We study the unsaturated flow behind a resin front that is moving through an idealized unidirectional fiber mat, and which is represented as a set of parallel channels of width l_o (representing gaps in the dual-scale medium) separated by porous tows of thickness l_i each. (See Fig. 2A.) A target unit cell consisting of several thin REVs (Fig. 2B) is selected to conduct flow simulation in the gap region. The target unit cell is preceded by a hypothetical precursor unit cell, which is there merely to provide a realistic inlet velocity condition to the former. An exponentially increasing gap-to-tow `sink' velocity, along with a Beavers-Joseph slip velocity is imposed within the unit cell at the gap-tow interface [15]. The resultant flow field is used to estimate the non-Darcy terms in the gap-averaged momentum balance equation and evaluate their importance.

Reformulating the momentum balance equation

We now rearrange Eq. (3) to obtain an equation similar to Darcy's Law. Contracting both sides of Eq. (3) by taking a dot product with $\mathbf{K}_g$ and dividing both sides by $\varepsilon_g \mu_g$, we get

$$\langle \mathbf{v}_g \rangle = -\frac{\mathbf{K}_g}{\mu_g} \cdot \nabla \langle P_g \rangle^g + \frac{\mathbf{K}_g}{\varepsilon_g} \cdot \nabla^2 \langle \mathbf{v}_g \rangle + \frac{\mathbf{K}_g}{\varepsilon_g} \cdot (\nabla \cdot \mathbf{I}) \tag{5}$$

This equation can be regarded as a Darcy's Law with two correction terms: the first arising from the Brinkman force and the second from the interfacial kinetic-effect force. Retention of these two terms depends on how significant these terms are in the unsaturated region just behind the moving resin front.

Non-dimensionalizing Eqn. (5) and taking its x-component (see [15] for details) results in

[3] Note that all terms in Eqn. (3) has the dimensions of force per unit volume.

$$\left\langle v_g^{\,*}\right\rangle_x = -\frac{K_{g,xx}^{\,*}}{\mu_g^{\,*}}\frac{\partial\left\langle P_g^{\,*}\right\rangle^g}{\partial x^*} + \frac{K_{g,xx}^{\,*}}{\varepsilon_g}\frac{\partial^2\left\langle v_g^{\,*}\right\rangle_x}{\partial x^{*2}} - \frac{K_{g,xx}^{\,*}}{\varepsilon_g}\frac{\partial S^*}{\partial x^*} \tag{6}$$

Superscript * represents dimensionless quantities. The y-component of Eq. (5) is also satisfied as its both sides become identically equal to zero. After exploiting the inherent symmetries in the posed flow problem, Eq. (6) can be reorganized further [15] as

$$\left\langle v_g^{\,*}\right\rangle_x = -\frac{K_{g,xx}^{\,*}}{\mu_g^{\,*}}\frac{\partial\left\langle P_g^{\,*}\right\rangle^g}{\partial x^*}\left(1 - R_B - R_I\right) \tag{7}$$

where R_B, to be referred to as *Brinkman correction factor*, is the dimensionless ratio of Brinkman force to pressure force:

$$R_B = \frac{\mu_g^{\,*}}{\varepsilon_g}\left(\frac{\partial^2\left\langle v_g^{\,*}\right\rangle_x}{\partial x^{*2}}\right)\Bigg/\left(\frac{\partial\left\langle P_g^{\,*}\right\rangle^g}{\partial x^*}\right) = \mu_g^{\,*}\left(\frac{\partial^2\left\langle v_g^{\,*}\right\rangle^g{}_x}{\partial x^{*2}}\right)\Bigg/\left(\frac{\partial\left\langle P_g^{\,*}\right\rangle^g}{\partial x^*}\right) \tag{8}$$

In the above equation, $\left\langle v_g^{\,*}\right\rangle_x / \varepsilon_g$ is replaced by $\left\langle v_g^{\,*}\right\rangle_x$[4].

R_I, to be called the *interfacial kinetic- effect correction factor*, is the dimensionless ratio of interfacial kinetic-effect force to pressure force:

$$R_I = -\frac{\mu_g^{\,*}}{\varepsilon_g}\left(\frac{\partial S^*}{\partial x^*}\right)\Bigg/\left(\frac{\partial\left\langle P_g^{\,*}\right\rangle^g}{\partial x^*}\right) \tag{9}$$

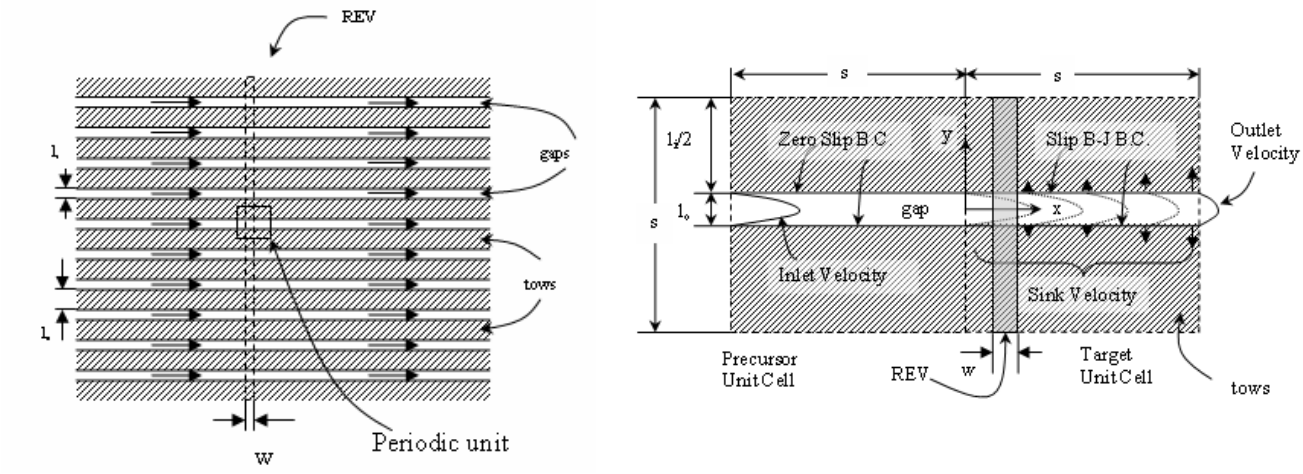

Part A Part B

Fig. 2. Part A: Schematic of a 2-D resin flow through gaps in a bank of porous and liquid absorbing 2-D tows (with infinite depth) stacked parallel to each other. The REV shown here is a thin disc of infinite width and a finite x-direction length 'w'. Part B: Exploded view of the periodic target unit cell of size 's' shown in Part A along with the hypothetical precursor unit cell. The sink velocity and slip boundary conditions exist only in target unit cell. Parabolic velocity profile is assumed at the entrance of the precursor unit cell.

[4] Note that ε_g being constant for our medium shown in Fig. 2 enables it to be moved inside the double derivative.

Flow simulation

A finite element based multiphysics software COMSOL Multiphysics 3.2 [16] is used to solve the point wise continuity and momentum balance equations in the gap region. Typical parameter values used in this simulation as well as other details are listed elsewhere [15]. The dimensionless velocity at the precursor cell inlet is assumed to be parabolic to resemble the fully developed flow through parallel plates and the dimensionless inlet velocity averaged over the inlet area is taken as unity. The interface between the two unit cells is treated as an internal boundary condition. Both the Beavers-Joseph slip boundary condition and variable sink velocity in the direction of flow is considered in the analysis.

Traditional volume averaging method, which requires that the representative elementary volume (REV) be of the same size as the unit cell, cannot be applied here as the effect of rapidly changing sink velocity on the correction terms will be lost. Instead, a specialized form of volume averaging method is adopted where the unit cell is subdivided into thin slices of REVs within which, the averaging of flow quantities is carried out. The width of these subdivided slices are one-tenth of that of the target unit cell throughout the unit cell except near the exit where the width is reduced to one-hundredth [15]. The much finer slicing of the unit cell closer to the flow front ensures that the volume averaged quantities (especially the absorption rate) are sufficiently accurate even in regions where the sink gradients are high.

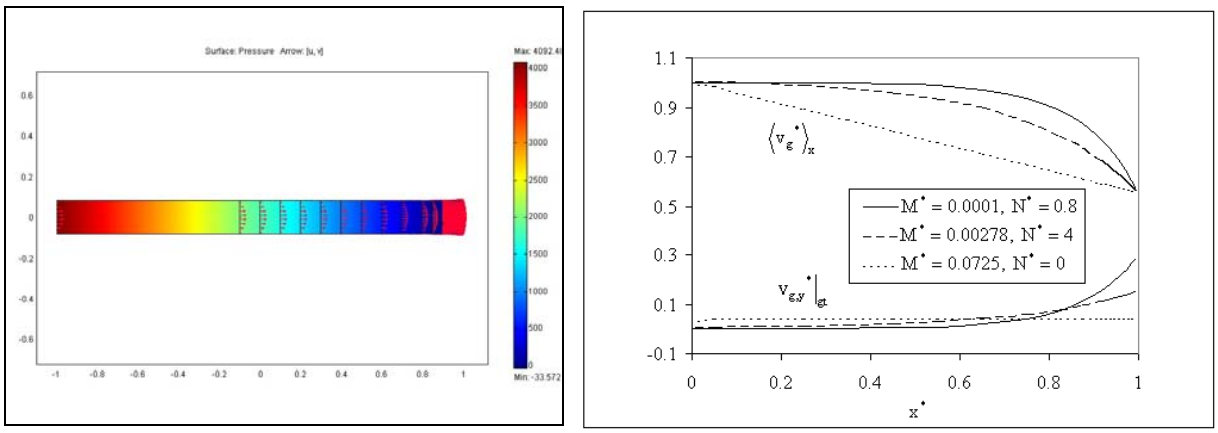

Part A Part B

Fig. 3 Part A: A COMSOL Multiphysics 3.2 schematic of pressure and velocity profiles in precursor and target unit cells. The smaller cells on the right hand side are within the target unit cell ($0 \le x^* \le 1$) and represent the sliced REVs. Part B: Various absorption rates at the gap-tow interface (the lower curves) within the target unit cell and the corresponding volume averaged velocity distributions (the upper curves).

Once the microscopic transport equations are solved (Fig. 3(A) describes a typical distribution of point wise velocity and pressure), macroscopic quantities such as $\left\langle v_g^* \right\rangle_x$ and $\left\langle P_g^* \right\rangle^g$ are computed for each REV slice by integrating the local velocity and pressure. Later the derivatives of these quantities are estimated through the backward differencing schemes such that each node value corresponds to the average at the REV slice.

RESULTS, DISCUSSION AND CONCLUSION

The gap-tow absorption velocity or the sink term as a function of x-coordinate is changed by varying parameters M^* and N^* of an exponential function $[v_{g,y}|_{gt} = M^* \exp(N^* x^*)]$ as shown in Part B of Fig. 3B such that the area under the curves remains the same in order to maintain constant outlet velocity. This figure also shows the variation of the volume-averaged x-velocity as a function of x^* confirming that the outlet velocity, and hence the total absorption rate within the unit cell, remains constant for all absorption rates considered.

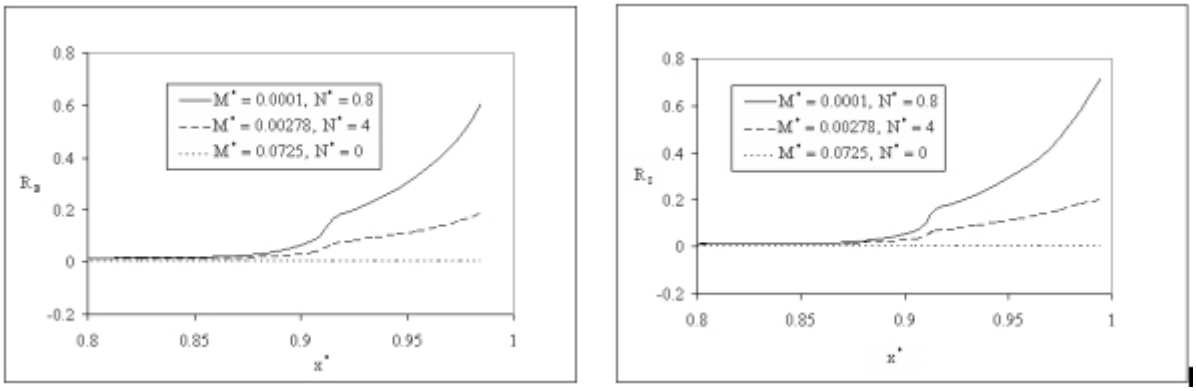

Part A Part B

Fig. 4 The Brinkman (RB) and interfacial kinetic-effect (RI) correction factors as a function of x^* are plotted in Parts A and B at various absorption rates.

Part A and B of Fig. 4 show R_B and R_I as functions of x^*. The plot indicates that both R_B and R_I are proportional to the gradient of the sink term. The *Brinkman correction factor* can reach a value as high as 0.6 and the *interfacial kinetic-effect correction factor* can reach values up to 0.7. For those tows that are directly behind the flow front where the absorption gradient is steep[5], the *Brinkman* and *interfacial kinetic-effect correction factors* become significant and hence cannot be discarded in the flow analysis unlike in fully saturated region. Although this means that unsaturated flow modeling is complicated near the flow front due to a large gradient in the sink term, this finding is of fundamental importance and suggests the retention of the correction factors R_B and R_I for accurate modeling of LCM processes.

See [15] for a description of dependence of R_B and R_I on the local Reynolds number, the slip velocity, and the slip coefficient.

After studying this interesting result, we can finally conclude that the hitherto neglected Brinkman and the interfacial kinetic-effect tensor terms in the momentum balance equation will become important in a small region just behind the resin front in a dual-scale fiber mat (especially the unidirectional one) due to a strong gradient in the sink term.

[5] The velocity of the flow front within the tow is inversely proportional to the extent of penetration of the flow front from the tow-gap interface. Since the tows directly behind the flow front in the gap region are just exposed to the resin, the extent of penetration is minimal and hence the gradient of absorption rate is very steep.

REFERENCES

[1] Rudd, C.D., Long, A.C., Kendall, K.N. and Mangin, C.G.E., *Liquid molding technologies*, Woodhead Publishing Ltd, 1997.

[2] Bruschke, M.V. and Advani, S.G., *RTM filling simulation of complex three dimensional shell-like structures*, SAMPE Q, Vol. 23(1), pp. 2-11, 1991.

[3] Fracchia, C.A., Castro, J. and Tucker III, C.L., A finite element/control volume simulation of resin transfer molding, *Proceedings of the American Society for Composites Fourth Tech. Conf.*, pp. 157-66, 1989.

[4] Fong, L.U., Varma, R.R., Liu, B., Bruschke, M.V. and Advani, S.G., *LIMS user's manual*, Centre for Composite Materials, University of Delaware, Newark, 1993.

[5] Moldflow Plastics Insight®, Moldflow Corporation (http://www. moldflow.com/), Lexington, MA.

[6] Babu, B.Z. and Pillai, K.M., Experimental investigation of the effect of fiber- mat architecture on the unsaturated flow in liquid composite molding, *J. of Compos. Mater.,* Vol. 38(1), pp. 57-79, 2003.

[7] Roy, T., Babu, B.Z., Jadhav, R.S., Munagavalasa, M.S. and Pillai, K.M., Some studies on modeling the unsaturated flow in woven, stitched or braided fiber mats in LCM, *Proceedings of the 7th Int. Conf. on Flow Processes in Comp. Mater. (FPCM7)*, Newark, 2004.

[8] Roy, T. and Pillai, K.M., Characterization of dual-scale fiber mats for unsaturated flow in liquid composite molding, *Polymer Composites*, Vol. 26(6), pp. 756-769, 2005.

[9] Pillai, K.M., Governing equations for unsaturated flow through woven fiber mats. Part 1. Isothermal flows, *Composites Part A*, Vol. 33, pp. 1007-1019, 2002.

[10] Tucker III, C.L. and Dessenberger, R.B., Governing equations for flow and heat transfer in stationary fiber beds, *Flow and rheology in polymer composites manufacturing*, Elsevier, Amsterdam, pp. 257-323, 1994.

[11] Bear, J. and Bachmat, Y., *Introduction to modeling of transport phenomena in porous media*, Kluwer Academic Publishers, Dordrecht, 1990.

[12] Whitaker, S., *The Method of Volume Averaging*, Kluwer Academic Publishers, Dordrecht, 1999.

[13] Slattery, J.C., *Single-phase flow through porous media*, AIChE J, Vol. 15(6), pp. 866-72, 1969.

[14] Kaviany, M., *Principles of heat transfer in porous media*, Springer, New York, 1995.

[15] Munagavalasa, M.S. and Pillai, K.M., Deviation from Darcy's Law: an implication of unsaturated flow in dual-scale porous media, manuscript to be submitted to *Journal of Porous Media* for publication.

[16] Comsol Multiphysics®, Comsol, Inc. (http://www.comsol.com), Los Angeles, CA.

[17] Pillai, K.M., and Munagavalasa, M.S., Governing equations for unsaturated flow through woven fiber mats. Part 1. Nonisothermal reactive flows, *Composites Part A*, Vol. 35, pp. 403-415, 2004.

FLOW MODELING OF THE COMPRESSION RESIN TRANSFER MOLDING PROCESS

Jeffrey M. Lawrence[1], Pavel Simacek[1], Susanna Laurenzi[2] and Suresh G. Advani[1]

[1]Center for Composite Materials and Department of Mechanical Engineering
University of Delaware, Newark, DE 19716
[2]School of Aerospace Engineering, University of Rome La Sapienza, via Eudossiana 18, 00184 Rome, Italy

ABSTRACT: The automotive industry has been reluctant in the use of advanced composite components due to long cycle times associated with their manufacturing processes. Recently, a promising Liquid Composite Molding (LCM) process coined as Compression Resin Transfer Molding has attracted interest. In this process, the fiber preform is placed in the mold in the same manner as in Resin Transfer Molding, but the mold is not closed entirely, creating a fiber-free channel on top of the preform. The measured amount of resin is injected into the mold which first fills this channel due to its high permeability. Then, the mold is closed, thus forcing the resin to infuse the preform. The final stage of the process compacts the preform to its final part thickness, hopefully saturating the entire perform with resin. Due to its similarity with compression molding process and injection through the thin thickness of the part, short processing times can be achieved. The goal in this process not unlike all LCM processes is to ensure resin does fill all the empty spaces between the fibers. However, this process introduces several new issues that must be addressed in the flow model. The first issue is to account for the compaction of fiber preform, both when it is dry and when it is saturated with resin. Literature has shown that fiber compaction is not only non-linear, but exhibits visco-elastic behavior as well. Furthermore, the through thickness flow behavior under compression with perform serving as one wall will require one to couple flow in reducing gap with impregnation inside a perform. Finally, with a complex mold, visualization of the flow progression can be difficult, so a new method of sensing is desired. This paper will describe how these issues can be addressed, and presents the results of an experimental study conducted on a small, lab-scale molding apparatus. The compaction behavior of the fabric is explored and will be incorporated in the modeling and simulation of the compression resin transfer molding.

KEYWORDS: Liquid Composite Molding, Compression Resin Transfer Molding, Mold Design

1. INTRODUCTION

Composite materials can be tailored to have better mechanical properties than metals, but their use can only increase by developing new cost- effective manufacturing technologies. One of the promising technologies available today is the Compression Resin Transfer Molding (CRTM). It can manufacture parts with high fiber volume fraction, high surface quality and excellent tolerance control of net shape and is suitable for high volume production. However, it requires initial investment in expensive equipment which the industry can recuperate with medium-high volume production. For this reasons, one of the potential main users of compression molding is the automotive industry with production runs of between 1000 and 10,000 parts per year requiring a good surface finish [1]. Therefore, developments are necessary to improve production times and part quality, including new

compression press systems. The aim of this research is to propose and validate a new cost effective press. Compaction behavior [2-4] of fabrics was investigated because compression modifies the processability by altering permeability to resin flow.

2. Modeling the Compression Resin Transfer Molding Process

To achieve fast, repeatable and reliable process one needs to acquire some predictive modeling capability to simulate the resin flow within the gap and preform during the injection. This capability is readily available for RTM process modeling, but to model the CRTM flow, it has to be somewhat extended. For modeling purposes, the injection can be divided into three phases. First, the resin is injected into the partially open mold cavity. This phase can be modeled directly by RTM simulations by treating the gap as a layer of high permeability distribution media, similar to DM in other RTM variations [1, 2]. In the second phase, the mold is being closed but there is still a gap between mold surfaces and preform. The squeezing of the gap part already filled with the resin will drive the resin into (i) the remaining unfilled gap regions and (ii) the preform. In the last phase, the mold is in full contact with the preform and the preform gets compacted to its target thickness. Some preform regions are already saturated with resin. The resin may be squeezed out from filled regions and be driven into regions that are still unsaturated. Practically, the individual phases may overlap. To model the second and third phase of the process with RTM simulation is nontrivial, but possible [5]. Essentially, the “squeezed” saturated regions – in gap or in preform – have to be replaced by a proper flow rate source and its magnitude must be modified with the time. Simultaneously, the material parameters must be continuously updated as the fiber volume fraction and permeability of the preform vary with the deformation. We were able to model these stages within our RTM simulation package, LIMS [6, 7], by taking advantage of its scripting and control capabilities [5]. It is, nonetheless, admitted that the resulting scheme is suitable for academic research but hardly for immediate industrial deployment and more robust approaches are in development.

3. Lab Scale Press Mechanism

One of the drawbacks of this process is the cost associated with the press / mold necessary to make composite components with this process. This cost will be recuperated by either high production yields typical of the automotive industry or the high cost of sophisticated parts in the aerospace industry. However, this benefit can not be realized in a laboratory setting. Therefore, it was desired to design and build a simple, inexpensive lab-scale press and mold in order to initiate research in this field. The first area to consider is the closing mechanism. Industrial presses and other clamping devices, such as Instron testing machines make injection and vent egress difficult [8]. It was desired to develop a closing mechanism independent of such a device that would allow for a lab-scale press with the ability to have tubing egress for resin injection and venting. The injection / compression molding process consists of a rapid traveling of the platens over a relatively short distance. Therefore it was decided to close the press using a heavy-duty hose. The hose is to be placed between two platens, and the inflation of the hose will raise the traveling plate, as seen in Figure 1.

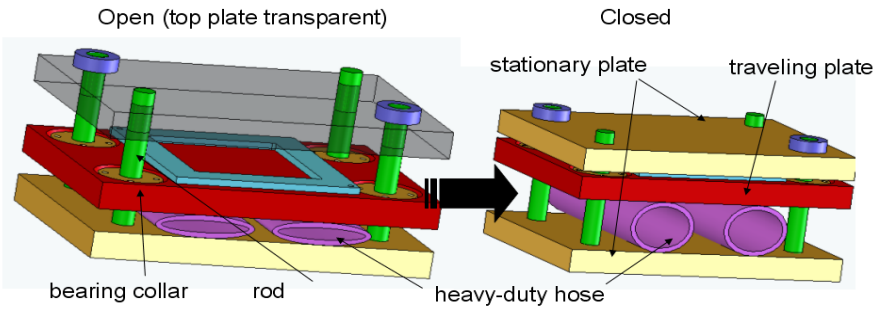

Figure 1: The inflation of a heavy-duty hose between two platens will generate the clamping of the press

3.1. Investigation of closing speeds /forces

The hose, of radius r_h, will have a circumference of $2\pi r_h$. This total perimeter will remain constant as the hose is inflated / deflated. At the state depicted in Figure 2, the hose is under an internal pressure of p_i, separates the lower (fixed) plate from the traveling plate by a distance d, and is in contact with the plates along a distance of l.
The hose, when placed in between the two plates and pressurized with fluid will contour to a rectangular geometry in the middle of the plate. At the ends, the unconstrained hose will assume the shape of a semi-circle. Therefore, the total perimeter in this configuration will be equal to the circumference of the original hose:

$$\text{cirm}=2l+\pi d = 2\pi r_h$$
$$\therefore l = \frac{\pi}{2}\left(2r_h - d\right) \quad (1)$$

Therefore there is a geometric constraint between the contact length (l) and the separation distance (d). There will be three forces counteracting the pressure in the hose: the weight of the traveling plate, the compaction pressure of the fabric, and the fluid pressure of the injecting resin.

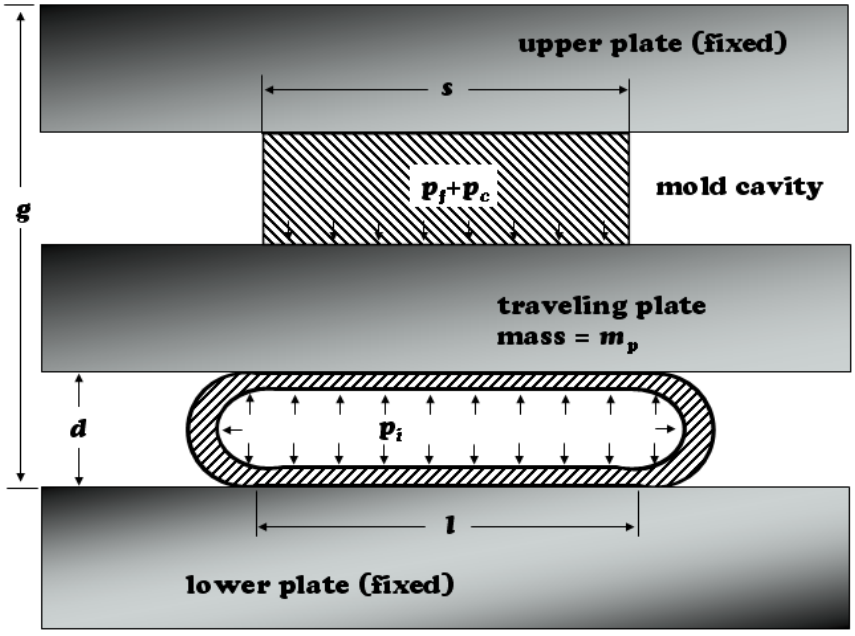

Figure 2: The internal pressure of the hose counteracts the weight of the traveling plate, the compaction pressure of the fabric, and the fluid pressure of the resin.

Force balance of the hose gives the following result:

$$p_i = \frac{2}{\pi}\frac{m_p + sh\left(p_f + p_c\right)}{h\left(2r_h - d\right)}, \quad d = 0..2r_h \tag{2}$$

Therefore, the internal pressure that is required to maintain the traveling plate with the fabric compaction and resin infusion can be found. Some analysis can be done to identify what type of water pump would be necessary to sustain typical manufacturing loads. One important factor to identify is the denominator term in equation (2). As the plate gets lifted to the point where the hose is fully inflated to a circle ($2r_h=d$), the required pressure would be infinite. Additionally, there is an exponential increase in the required internal pressure as the separation distance (d), approaches $2r_h$. This highlights the fact that this closing method is excellent for quick rising over a short distance, but is not adequate for lifting the plate over great distances. This formulation can be used to select an appropriate pressure source.

4. Compaction Testing

Different series of experiments were performed in order to highlight the viscoelastic behavior of preform during compression [9]. The first series of experiments consisted of evaluating the repeatability of the compaction process and the clamping force generated on dry preform. The second series of experiments investigated the material's hysteresis response under consecutive compression and the effects of the number of layers on the compression stress. The third series of experiments was performed to evaluate the effects of fluids on the preform response and compaction force.

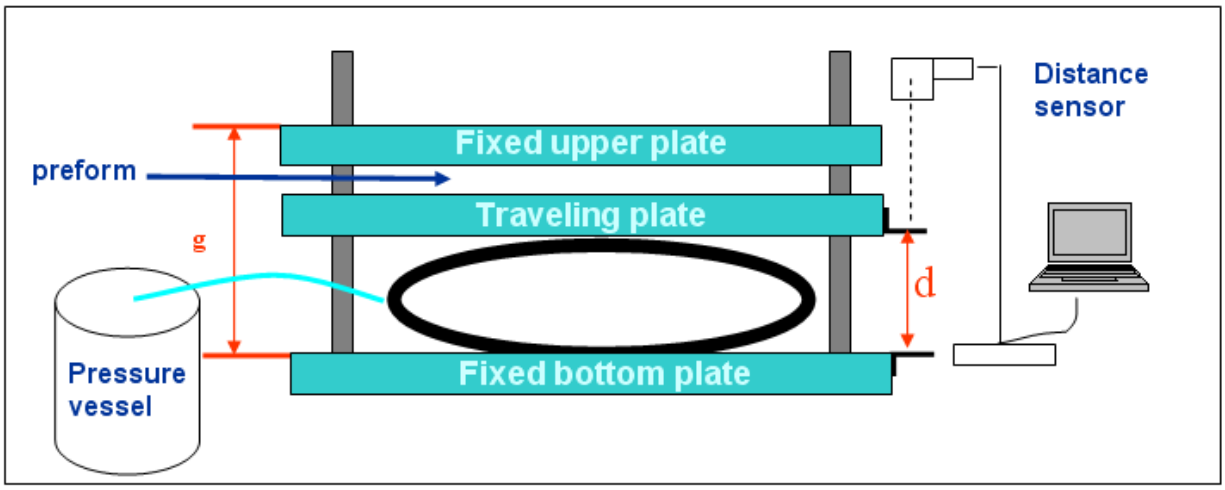

Figure 3: Schematic representation of set-up used for compaction tests

4.2. Experimental procedures

The set-up used for the compaction experiments is shown in Figure 3. The upper plate is fixed at determine height s, the layers are placed in the middle of traveling plate and the hose is inflated using a pressure vessel. The hose pushes the middle plate towards the upper fixed plate, compressing the material. When the distance d does not vary anymore, the maximum compression is reached. The measurement of both distances d and s is performed with a laser sensor having zero reference on the bottom plate. Knowing d and g, the clamping force is estimated from the calibration curve (equation (2) with correction) and the ultimate thickness

h of the preform is calculated using simple geometric relations. The clamping force is increased during the experiment by increasing the pressure inside the hose. In each experiment the pressure varied from 35kPa to 310kPa. The experiments were performed with both 5 and 10 layers of 12.7cm x 12.7 cm square pieces. In each experiment a new sample was used. In case of plain weave, during the lay-up step, particular attention was given to match warp to warp and weft to weft direction as best as possible. For experimental series of repeated compressions on the same sample, layers were separated and left without constriction between two consecutive compressions in order to allow recovery of any elastic deformation of fibers. For experimental series performed to evaluate the effects of fluids on compaction behavior, the stacking sequences were prepared by wetting and assembling layers as a classic hand lay-up process with no rolling.

4.3. Results and discussion

The repeatability of the compression process, verified during the calibration test, was confirmed with the first experimental series, obtaining similar value of fiber volume fraction for the same clamping force. The trend of fiber volume fraction of woven fabric and random mat was similar. Both material show a power law trend as reported in literature by other authors [4]. The curves obtained for woven show modest power exponent compared to the random, which means the volume fraction increases much more slowly with the increment of force as compared to the case of random. The results are reported in Figure 4: hysteresis due to permanent deformation is presented for both materials. The compression reduces the gaps among fibers and yarns and the fibers find new collocation. In case of random mat, the interlayer packing seems to be the most important factor causing the enhancement of fiber volume fraction. In fact, a bigger percentage increment of volume fraction has been carried out for 10 layers than 5 layers. In the case of woven, the hysteresis behavior is principally due to the nesting and intra-packing phenomena that globally increases the fiber volume fraction.

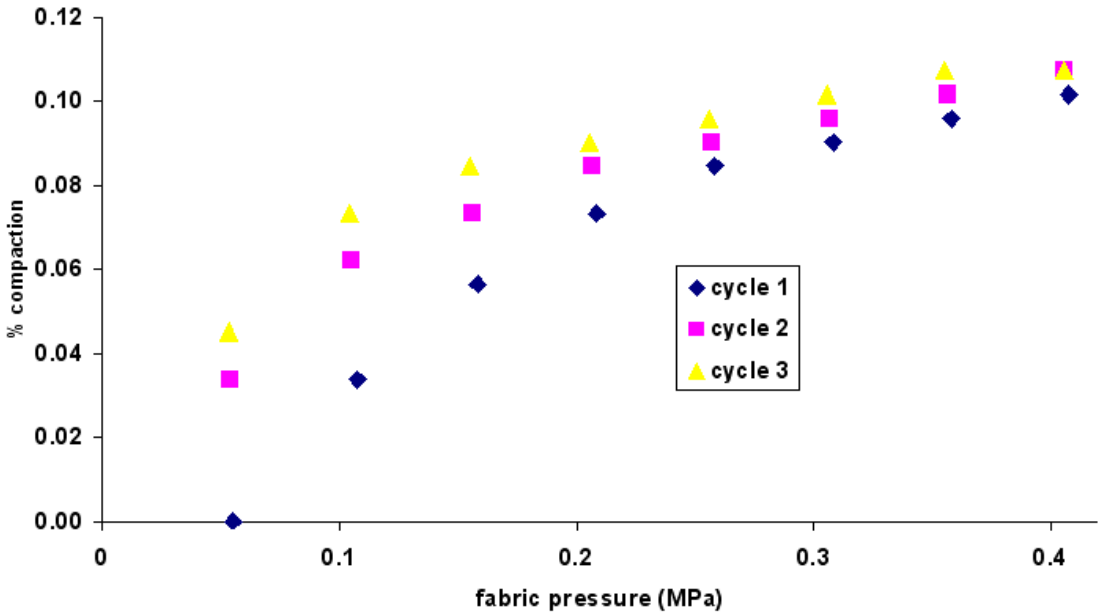

Figure 4: Percent compaction as a function of compaction pressure for three consecutive compressions performed on the same sample of random mat glass

In order to highlight the phenomenon of nesting, the thickness per layer as function of fabric pressure has been plotted. As shown in Figure 5, nesting exists at beginning of compression for woven but not for random.

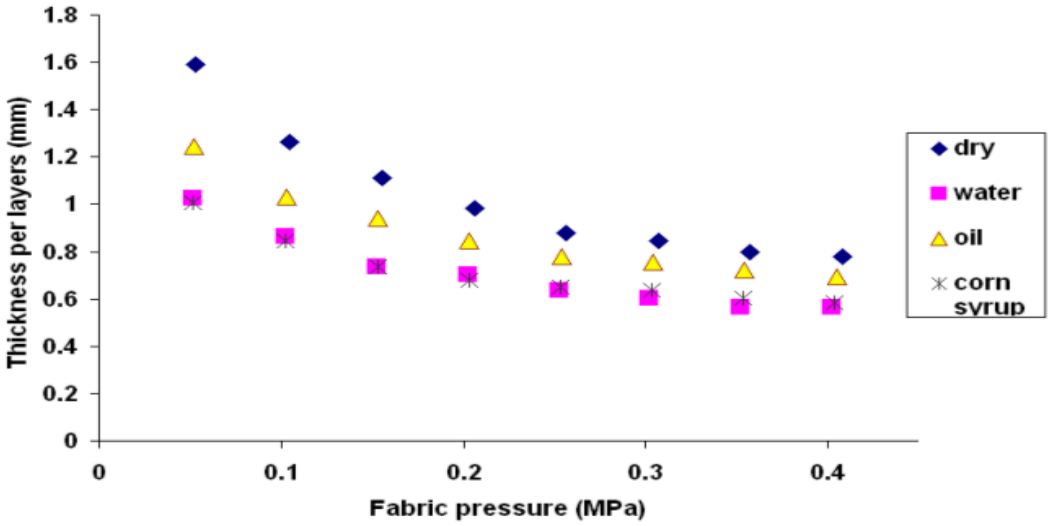

Figure 5: Thickness per layer versus fabric pressure for random mat glass. The viscosity of oil is 54 cps and the viscosity of corn syrup is 146 cps.

The dry preform shows the highest thickness per layer, comparing results obtained for dry assemblies and wetted assemblies. This phenomenon should be expected because of the friction between tows. The fluid serves to lubricate the fibers making the settling during the compression easier. Therefore, a lower compression force is required to obtain the same thickness (fiber volume fraction). Comparing the curves obtained using liquids, the curves with water show the lowest required compression force. This result could be due to both lubrication and wettability of water.

5. Injection of Parts

Now that the compaction tests have been conducted, and it is known that this apparatus can sufficiently compact the preform to appropriate levels, the next step is to use it to manufacture composite components. Previous sections of the paper described the design and construction of the press system. This was used to conduct the compaction tests. Next, a mold apparatus needs to be added in order to manufacture composite parts. For initial testing, it was decided to construct a mold to manufacture circular parts. The reason for this is the ease in which a circular mold can open / close and not bind up during operation. The mold was designed much like a piston system, with a ring and plunger.

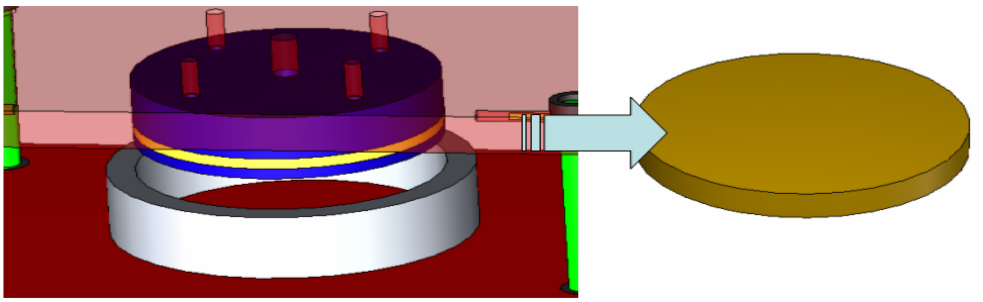

Figure 6: The mold was designed to manufacture circular disks to facilitate in the operation of the press

5.4. Manufacturing of parts

The procedure was as follows. First, the preform is placed inside the cavity. Then, the hose is inflated to raise the traveling plate such that the volume between the top of the preform stack and the top of the mold is equal to the volume of resin to be ultimately injected. Once the desired thickness is reached, the resin is poured into the mold. Next, the traveling plate is again raised, compacting the preform, until the laminate reaches the required fiber volume fraction. During this compaction process the thickness is monitoring by a distance sensor. When the final part thickness is achieved, the gate and vent are clamped, and the part is allowed to cure. The fiber volume fraction is determined by the following:

$$v_f = \frac{A_w n}{\rho_f h} \tag{3}$$

In equation (3), Aw is the weight per unit area of the fabric, n is the number of layers, ρ_f is the average fiber density, h is the thickness of the preform. The total volume of resin required in the cavity to impregnate the preform is:

$$V_{\text{resin}} = (1 - v_f)\pi R^2 h_{final} \tag{4}$$

In this, h_{final} is the thickness of the preform for a given number of layers to obtain the fiber volume fraction v_f; R is the radius of the cavity. Using the compaction curve as a rule of thumb establishes h_{final} for a given fiber volume fraction. The ultimate hose pressure can be determined in two ways. First, if there is no compaction curve available, the pressure inside the hose can be increased slowly until the ultimate preform thickness is achieved. The second way is to use the compaction curve for establishing the force required for compaction and therefore the pressure in the hose.

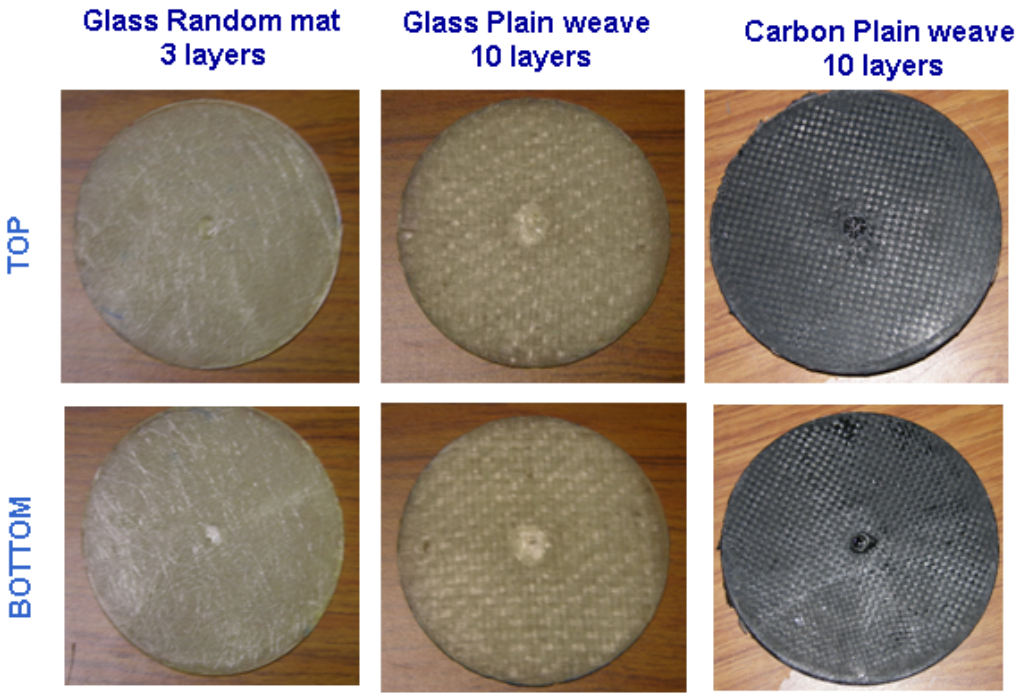

Figure 7: Examples of manufactured parts with the new low cost Compression RTM press

6. Conclusions

A simple mold was built to conduct exploratory experiments with the compression resin transfer molding process. The mold was designed to be very simple in operation, without the need of a press. Geometric and mathematical modeling was done to estimate the processing windows for the closing speeds and forces that could be realized. Once the press was built, compaction testing was done and compared to previous results. With this apparatus established as valid tool for investigation of compression RTM, a mold cavity was added, and compression RTM experiments were carried out. Circular disks of 4 inches in diameter were manufactured with E-glass random and plain weave fabric and also with carbon fabric. As predicted, the infusion time was very fast of the order of 5 seconds, and the resultant parts had fiber volume fraction in the range of 55-62 percent for woven fabric and 27-34% for continuous strand random mat.

7. Acknowledgments

The authors gratefully acknowledge the support provided by the Office of Naval Research (ONR) under Grant Number N00014-05-1-0832 for the "Advanced Materials Intelligent Processing Center" at the University of Delaware and by National Science Foundation and Department of Energy/National Energy Technology Laboratory under grant number DMI-0521789.

8. References

1. *Technology update: compression moulding.* Reinforced plastics. July-August 2003.
2. Chen, B., E.J. Lang, and T. Chou, *Experimental and theoretical studies of fabric compaction behavior*

in resin transfer molding. Materials Science and Engineering A, 2001. 317: p. 188–196.

3. Chen, B. and T. Chou, *Compaction of woven-fabric preforms: nesting and multi-layer deformation.* Composites Science and Technology, 200. 60: p. 2223-2231.
4. Saunders, R.A., C. Lekakou, and G. Bader, *Compression and microstructure of fibre plain woven cloths in the processing of polymers composites.* Composites, Part A, 1998. 29(a): p. 443-454.
5. Simacek, P. and S.G. Advani, *Simulating Three-Dimensional Flow in Compression Resin Transfer Molding Process.* Revue Europeenne des Elementes Finis, 2005. 14(6-7): p. 777-802.
6. Simacek, P. and S.G. Advani, *Desirable features in a Mold Filling Simulation for Liquid Molding Process.* Polymer Composites, 2004. 25(4): p. 355-367.
7. Simacek, P., S.G. Advani, and C. Binetruy. *Liquid Injection Molding Simulation (LIMS) A Comprehensive Tool to Design, Optimize and Control the Filling Process in Liquid Composite Molding*. in *JEC - Composites, n 8*. 2004. Paris, France.
8. Bickerton, S. and M.Z. Abdullah, *Modeling and evaluation of the filling stage of injection/compression moulding.* Composites Science and Technology, 2003. 63: p. 1359-1375.
9. Bickerton, S., M.J. Buntain, and A.A. Somashekar, *The viscoelastic compression behavior of liquid composite molding preforms.* Composites, Part A. 34: p. 431-444.

HEAT TRANSFER MODELLING DURING LIQUID COMPOSITE MOLDING MANUFACTURING PROCESSES: COMPARISON BETWEEN TWO MODELS

M. Deléglise[1], C. Binétruy[1], P. Castaing[2], and P. Krawczak[1]

[1] *Ecole des Mines de Douai, Polymers and Composites Technology and Mechanical Engineering Department*
941 rue Charles Bourseul, BP 10838, 59508 Douai Cedex, France
deleglise@ensm-douai.fr

[2] *CETIM,*
74, route de la Jonelière, BP 8261, 44326 NANTES Cedex 3, France

ABSTRACT: During composite molding processes, temperature is one of the most important parameter as an accurate temperature cycle is required to insure good wetting of fibres and good part properties such as final degree of cure, glass temperature and low residual stresses. For an accurate temperature prediction, proper characterization of the resin curing system is needed, as resin kinetics greatly affect temperature profiles. The other basic parameters to consider are the conduction of resin towards the mold walls and convective effects that depends on injection velocity. However local effects were shown to be of great importance as resin flows through a porous medium. Local convective effects that induce heat dispersion must be included in the general energy balance equation. A one-equation model based on the local thermal equilibrium assumption was thus developed using finite difference analysis. However, during fast injection processes the latter assumption does not hold anymore, heat exchange between resin and fibres has to be taken into account. A two-equation model was thus considered using finite element analysis. The comparison between both models shows that the one-equation model is sufficient for steady state analysis purposes, when long parts or slow injection schemes are involved for example. When transient temperature profiles have to be accurately defined, for highly reactive resins or for short part applications, the two-equation model is more appropriate.

KEYWORDS : Composites Manufacturing, Heat Transfer, Dispersion Coefficient

HEAT TRANSFER MODELS IN LCM PROCESSES

Heat transfer in composite manufacturing involves conduction of heat towards the mold walls, convection by the resin as it flows through the preform and heat generation as the resin cures. For LCM processes, two heat transfer models are reported in the literature.

The Non Local Thermal Equilibrium (NLTE) model or the two-equation model is derived by considering the energy balance in the two components (resin and fibers) separately [1-3]:

$$\phi\left(\rho C_p\right)_m \frac{\partial\left\langle T_m\right\rangle}{\partial t} + \left(\rho C_p\right)_m \nabla\left(\left\langle v_m\right\rangle\left\langle T_m\right\rangle\right) = \nabla\left(K_m \bullet \nabla\left\langle T_m\right\rangle\right) + H\left(T_m - T_f\right) + \phi\dot{s} \qquad (1)$$

$$\left(1-\phi\right)\left(\rho C_p\right)_f \frac{\partial\left\langle T_f\right\rangle}{\partial t} = \nabla\left(K_f \bullet \nabla\left\langle T_f\right\rangle - H\left(T_m - T_f\right)\right) \qquad (2)$$

where ρ , K and Cp are the density, the heat conductivity tensor and the heat capacity of the materials, ϕ is the porosity of the porous medium, $<v_f>$ is the injection average velocity, $\dot{s}$ is the heat generated by the curing reaction, and the subscripts f and m refer to the fiber (fabric) and to the resin (matrix) properties. H is the heat exchange parameter and is defined by [4] :

$$H = a_{fm} h_{fm} \qquad (3)$$

where h_{fm} is the heat exchange coefficient between resin and fibers, and a_{fm} is the specific area representing the fibrous architecture at tow scale, expressed for a woven fabric by [5]:

$$a_{fm} = \frac{4}{d_p} \qquad (4)$$

d_p being the length scale of the composite, set to be a fiber tow diameter as far as woven fabric is considered.
This model is precise but difficult to use as the heat exchange coefficient needs to be determined [6-10]. The alternative is to use the Local Thermal Equilibrium (LTE) model or the one-equation model based on the assumption that local resin and fiber temperatures are equal :

$$\left\langle T_m\right\rangle = \left\langle T_f\right\rangle = \left\langle T\right\rangle \qquad (5)$$

Applying the LTE assumption to equations 1 and 2 and using the volume averaging method [3], the one-equation model is obtained, assuming that no curing reaction is involved:

$$\left(\phi\left(\rho C_p\right)_m + \left(1-\phi\right)\left(\rho C_p\right)_f\right)\frac{\partial\left\langle T\right\rangle}{\partial t} + \left(\rho C_p\right)_m \left\langle v_m\right\rangle \cdot \nabla\left\langle T\right\rangle = \nabla \cdot \left(K_e \cdot \nabla\left\langle T\right\rangle\right) \qquad (6)$$

The effective conductivity tensor K_e is also called the stagnant conductivity and may be estimated as the average of the materials thermal conductivities, as described below :

$$K_e = \phi K_m + \left(1-\phi\right)K_f \qquad (7)$$

This assumption is valid under certain conditions. For instance, the temperature gradient between the two phases must be negligible, thus that the ratio of the thermal conductivities should be approximately unity. Numerical computations show that almost no temperature difference exists when non-metallic materials are considered, thus that the local thermal equilibrium assumption can be valid for LCM processes [11]. However, using one model or the other depends on the injection parameters. For instance, it was shown that the one-equation model breaks down when high injection velocities are used or when a significant heat generation occurs in one of the two phases [11-14].

HEAT DISPERSION DURING LIQUID FLOW IN POROUS MEDIA

Local variations of velocity are associated with the thermal conductivity tensor K by adding a thermal dispersion coefficient K_D to the effective thermal conductivity K_e in the one-equation model.

$$K = K_e + K_D \tag{8}$$

This coefficient is expected to depend on the velocity of the flow front, on the porosity and structure of the medium and on the thermal characteristics of the materials [1-3].
Characterization of the heat dispersion coefficient was performed for a given resin /fiber system [14] from an inverse method based on an analytical solution derived from the one-equation model at steady state [15] for a unidirectional non reactive flow through an isotropic preform. Steady state temperature profiles obtained numerically and experimentally are shown on Fig. 1.

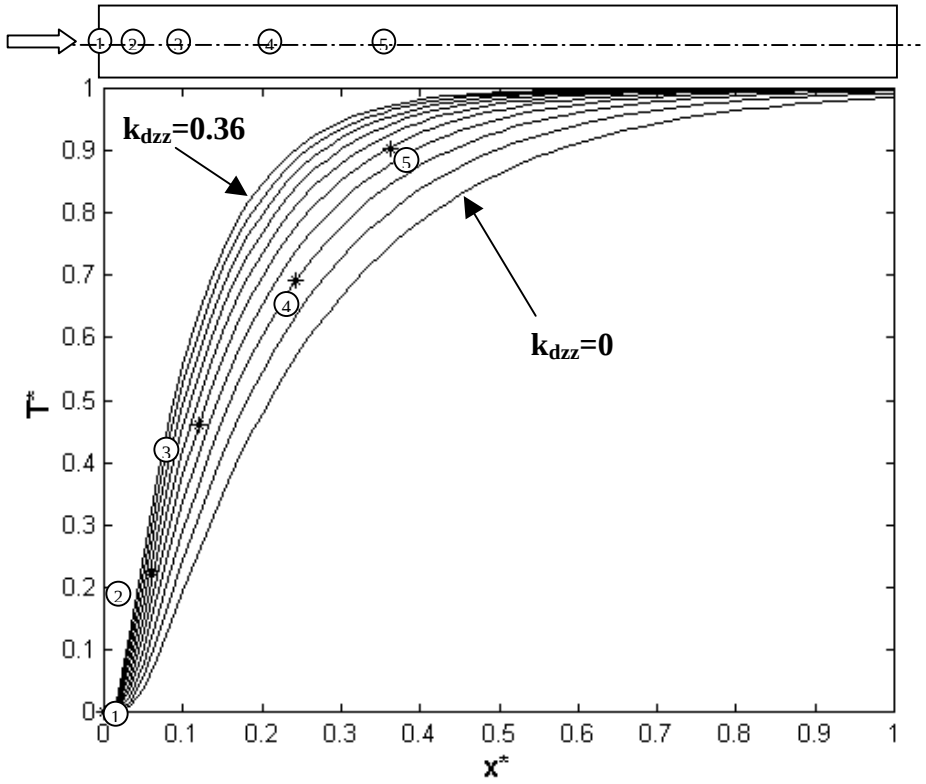

Figure 1 Numerical steady state temperate profiles (solid lines) obtained for different heat dispersion coefficient vs. experimental temperature profile (stars)

Good correlation at steady state is thus obtained between the experimental and the analytical temperature profile along the mold when heat dispersion is considered. However, at the transient stage, large discrepancies are observed, as shown in Fig. 2. The two-equation model is required, thus accurate characterization of the heat exchange coefficient h_{fm} would be needed.

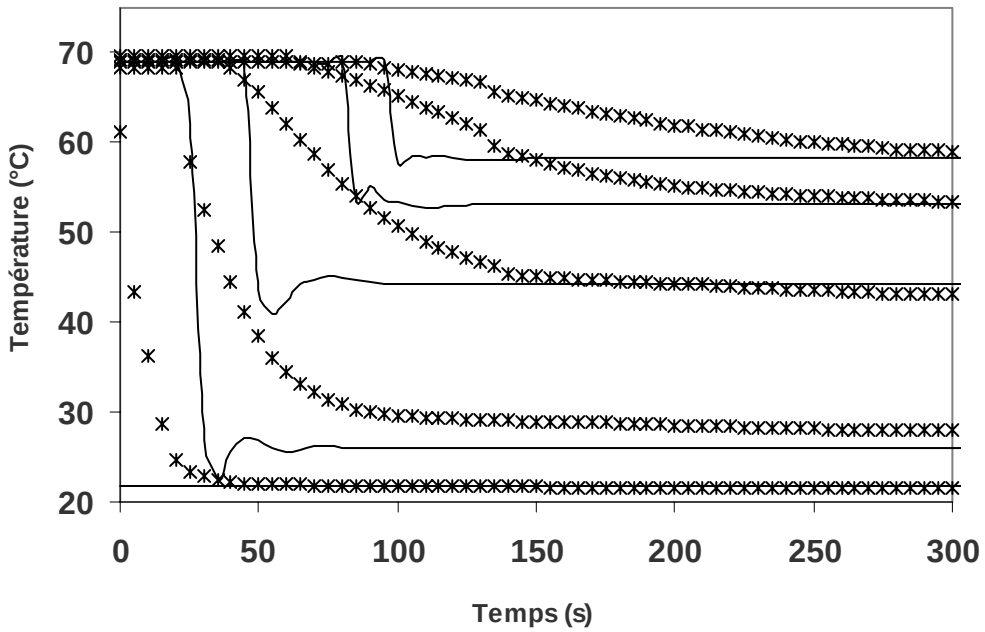

Figu r

ical (solid lines) and experimental (dotted lines) transient temperature profiles at different location along the flow front

HEAT EXCHANGE COEFFICIENT DETERMINATION

The method presented here for the heat exchange coefficient is based on an inverse method, the numerical solution being derived from the two-equation model :

$$\phi\left(\rho C_p\right)_m \frac{\partial T_m}{\partial t} + \left(\rho C_p\right)_m \langle v_m \rangle \frac{\partial T_m}{\partial x} = \left(k_m + k_d\right)\frac{\partial T_m}{\partial z^2} + H\left(T_f - T_m\right) \tag{9}$$

$$\left(1-\phi\right)\left(\rho C_p\right)_f \frac{\partial T_f}{\partial t} = k_f \frac{\partial T_f}{\partial z^2} - H\left(T_f - T_m\right) \tag{10}$$

where k_m and k_f are the conductivity of resin and fibers respectively and k_d is the dispersion coefficient. The equations are simultaneously solved using a multiphysics FE-based calculation tool (COMSOL Multiphysics 3.2). The program is inserted in an optimization program written with Matlab 6.5. The numerical temperature-histories for different locations along the flow direction are compared to experimental temperature profiles. The closest numerical solution to the experimental ones will determine the heat exchange coefficient corresponding to the injection considered.

EXPERIMENTAL SET-UP AND RESULTS

Glass fiber woven fabric (plainweave 5x4 woven fabric, Veterotex America) are placed into a closed mold with thermocouples located at the mid section of the preform as shown on Figure 3. A non catalysed vinylester resin (Derakane 411C50, Dow Chemichals) is employed. The recording of the temperature at the different locations is continued until the end of the experiment. When resin reaches the heated fibers, the temperature drops, as the average temperature of resin and fiber will be lower since the injected resin is cold.

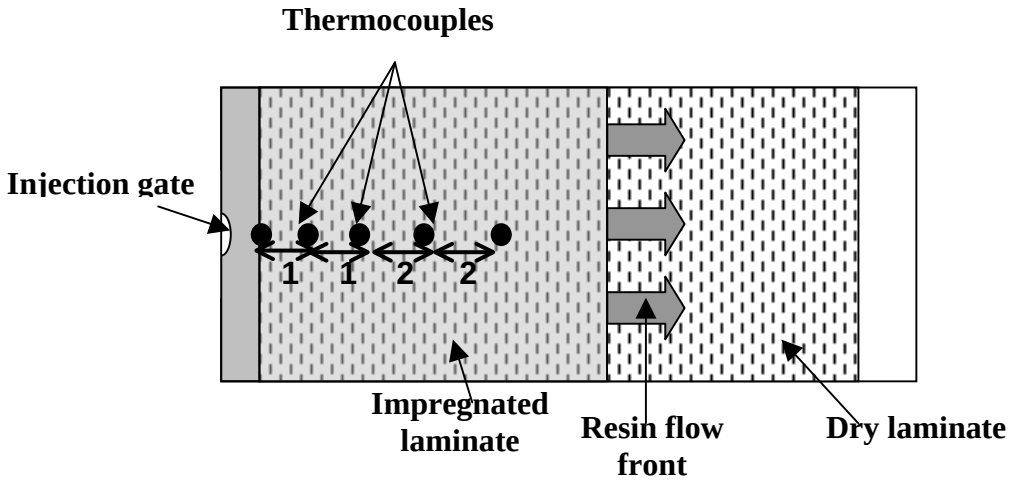

Figure 3 Experimental injection set-up and thermocouples location (unit : inch)

The heat transfer coefficient is determined by an optimization program that searches for the numerical solution parametered by the heat transfer parameter *H* closest to the experimental temperature profile.

Figure 4 represents the experimental temperature profiles along with the numerical solution derived from the one- and the two-equation models. Numerical curves fit better the experimental data when a two-equation model that includes the heat exchange effects between resin and fibers is used. Local thermal discrepancies of 15°C can be reached between the two numerical models.

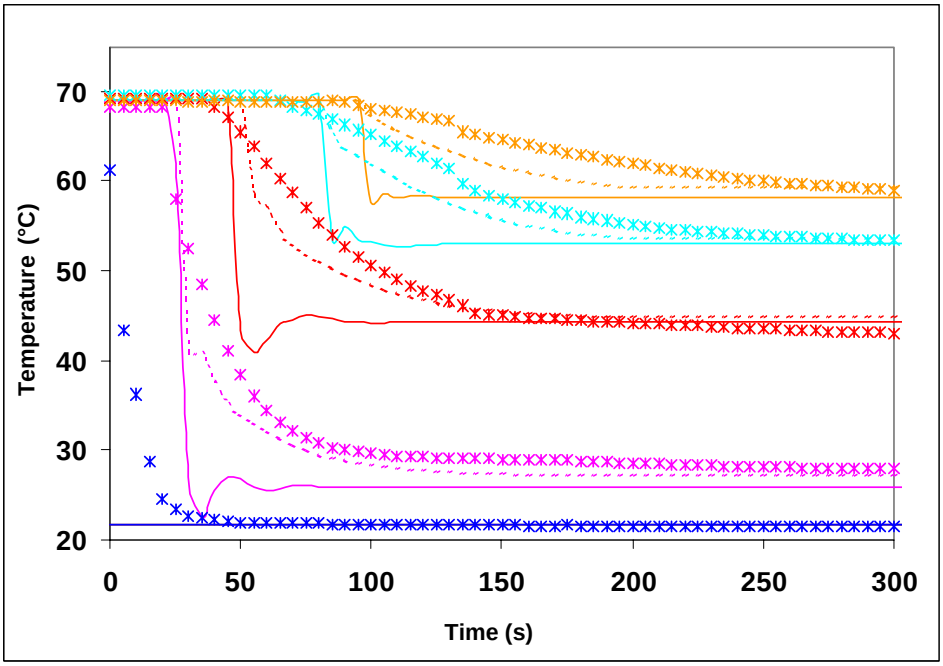

Figure 4 Comparison between one-equation model (solid lines), two-equation model (dotted lines), and experimental profiles (*) at different locations along the flow front direction

CONCLUSION

For accurate prediction of transient temperature profiles during the filling of a fibrous preform, it is necessary to consider the heat transfer coefficient between resin and fibers at the local scale. Numerical temperature profiles were obtained by implementing the two-equation model in a finite element code. The one-equation model without local heat exchange effects was also studied. It was shown that large temperature difference between the prediction of the two models can be obtained. The one-equation model would only give accurate temperature prediction at steady state. This model should only be used in slow processes, with slow temperature changes, whereas the two-equation model is needed for fast injection processes in order to correctly predict the curing kinetics of the resin system.

ACKNOWLEDGMENT

This work was partly supported by NSF under the grant number 971352.
The authors would like to thank CETIM de Nantes for funding and Pr. S. G. Advani from the Center of Composite Materials of the University of Delaware for advice.

REFERENCES

1. K.T Hsiao, S.G. Advani, "Modified Effective Thermal Conductivity Due To Heat Dispersion In Fibrous Porous Media", *International Journal of Heat and Mass Transfer*, Volume 42, Issue 7, 1 April 1999, pp. 1237-1254

2. S.G. Advani, M.V. Bruschke, R.S. Parnas, "Resin Transfer Molding Flow Phenomena in Polymeric Composites", *Flow and Rheology in Polymer Composites Manufacturing*, Elsevier 1994, pp 465-515

3. C.L. Tucker III and R.B. Dessenberger, "Governing Equations for Flow and Heat Transfer in Stationary Fiber Beds", *Flow and Rheology in Composites Manufacturin*g edited by Suresh G. Advani, Elsevier, 1994

4. K. Vafai, M. Sozen, Analysis of energy and momentum transport for fluid through a porous bed, *Journal of Heat Transfer*, Vol. 112, pp. 690-699, 1990

5. C. Brasquet, P. Le Cloirec, Pressure drop through textile fabrics – experimental data modelling using classical models and neural networks, *Chemical Engineering Science* Vol. 55, 2000, pp. 2767-2778

6. J.H. Yang, S.L. Lee, "Effect of Anisotropy on Transport Phenomena in Anisotropic Porous Media", *International Journal of Heat and Mass Transfer*, vol. 42, pp. 2673-2681, june 1998

7. S.L. Lee, J. H. Yang, "Modelling of effective thermal conductivity for a non-homogeneous anisotropic porous medium", *Int. J. Heat and Mass Transfer*, vol. 41, nos 6-7, pp. 931-937, 1998

8. R. Lin, L.J. Lee, M. Liou, "Non-isothermal mold filling and curing simulation in thin cavities with preplaced fiber mats", *International Polymer Processing*, vol VI, 1991, pp. 356-369.

9. M.L. Hunt, C.L. Tien, "Effects of thermal dispersion on forced convection in fibrous media", *Int. J. Heat and Mass Transfer* , Vol. 31, no. 2,pp. 301-309, 1988

10. M. Quintard, S. Whitaker, "Local Thermal Equilibrium for Transient Heat Conduction: Theory and Comparison with Numerical Experiments", *International Journal of Heat and Mass Transfer*, Vol. 38, No. 15, pp. 2779-2796

11. P-X. Jiang, Z-P. Ren, B-X. Wang, "Numerical Simulation of forced convection heat transfer in porous plate channels using thermal equilibrium and non-isothermal equilibrium models", *Numerical heat transfer part A*, vol. 35, 1999, pp. 99-113

12. F. Kuwahara, A. Nakayama, "Numerical Determination of Thermal Dispersion Coefficients Using a Periodic Porous Structure", *Journal of Heat Transfer*, vol. 121, February 1999, pp 160-167

13. C. T. Hsu, P.Cheng, "Thermal dispersion in a porous medium", *Int. J. Heat and Mass transfer*, vol. 33, No.8, pp. 1587-1597, 1990

14. M.L. Hunt, C.L. Tien, "Effects of thermal dispersion on forced convection in fibrous media", *Int. J. Heat and Mass Transfer*, Vol. 31, No. 2, pp. 301-309, 1988

15. M. Deleglise, P. Simacek, C. Binetruy, S.G. Advani, "Determination of the Thermal Dispersion Coefficient During Radial Filling of a Porous-Medium", *Journal of Heat Transfer*, Vol. 125, No. 5, pp. 875-880, 2003

Session 4

FORMING

PROCESSING OF LOW-VISCOSITY CBT THERMOPLASTIC COMPOSITES: HEAT TRANSFER ANALYSIS

Dr. Adrian Murtagh, Siora Coll and Dr. Conchúr Ó Brádaigh

Composites Research Unit
Dept. of Mechanical & Biomedical Engineering,
National University of Ireland, Galway, Ireland
Email: adrian.murtagh@nuigalway.ie

ABSTRACT: Cyclic butylene teraphthalate (CBT) thermoplastics offer significant advantages in terms of composite processing. Primarily, their inherent low viscosity means that fibre wet-out and impregnation can occur easily and rapidly, offering potential reductions in processing time and cost. CBT composites can offer the benefits of thermoplastics, including toughness and recyclability, without the high viscosities normally associated with these materials. These advantages are particularly significant for the manufacture of large-scale composite structures, for example, wind turbine blades. Existing technology using thermosets mean that it is getting more and more difficult to process large quantities of composite materials cost-effectively.

However, there are certain issues peculiar to CBT thermoplastics that must be overcome before large-scale processing can occur. High temperatures and rapid heating rates are unique to these materials when compared to traditional thermosets. The nature of the heat transfer mechanism for CBT materials heated this way is not very well understood. Previous experimental work in this area has provided some degree of understanding. The effect of different forms of material (pre-preg and power-impregnated dry glass fibres) has been investigated.

The heating mechanism of the various material forms is discussed and analysed. The temperature-dependent thermal conductivity of the various material forms is quantified using a guarded comparative longitudinal heat flow apparatus. A one-dimensional transient heat transfer model is obtained which will assist in determining if the necessary processing conditions are met before CBT processing is carried out.

KEYWORDS: Cyclic butylene teraphthalate (CBT) composites, resin film infusion, powder impregnation, composite tooling, heating mechanism, thermal conductivity.

INTRODUCTION

CBT™ (cyclic butylene teraphthalate) is a relatively new material that has been developed by Cyclics Corp. CBT is based upon using the cyclic oligomer form of PBT, a conventional engineering thermoplastic. PBT's natural properties mean that it has very good potential to be used in a range of thermoplastic composite applications [1]. Processing of CBT occurs when a catalyst is added to the material and when subsequently heated, the short-chain oligomer chains open and bond together to form the long-chain polymeric PBT-form of the material. The inherent low initial viscosity (circa. 150 mPa.s), resulting from the use of shorter chain oligomers, means that it is eminently suitable for rapid processing of thermoplastic composites. Previous applications for thermoplastic composites have been restricted by having to use much higher temperatures and pressures in order to 'wet-out' reinforcing fibres using the much higher viscosity polymer-form of the thermoplastic.

CBT-composites may be processed in a number of ways; however, two methods are most pertinent to the work that is discussed in this paper: resin film infusion / pre-preg and powder impregnation [2] (Figure 1). Resin film infusion (RFI) uses continuous carbon or glass fibre reinforcement that has been 'pre-impregnated' with the CBT-oligomer form of the material prior to being processed. A special catalyst is added to the CBT material that is not activated until a set temperature is reached. In essence, the CBT forms a resin 'film' mainly on one side of the reinforcement fabric that only fully 'wets-out' the fibres when secondary processing occurs at pressure. A more appropriate term to use would be 'semi-preg' rather than 'pre-preg' as only one side of the glass fabric is completely coated with CBT during the application stage. Plies may be stacked in a conventional manner and 'de-bulk' significantly when heat and pressure are applied during processing.

Powder-impregnated processing of CBT involves using dry continuous fibre reinforcements that are 'sandwiched' together, with an intervening layer of CBT dry powder between reinforcement layers. The powder is laid down during the lay-up process. Although more difficult to handle, powder impregnation does offer potential in terms of cost reduction (no need for additional pre-preg creation stage) and allows easier manipulation of the dry fabric layers as they are much more flexible compared to the 'boardy' and rigid RFI material. The higher bulk density of the powder also means that there is a more significant amount of de-bulking and thickness reduction that occurs for powder-impregnated CBT.

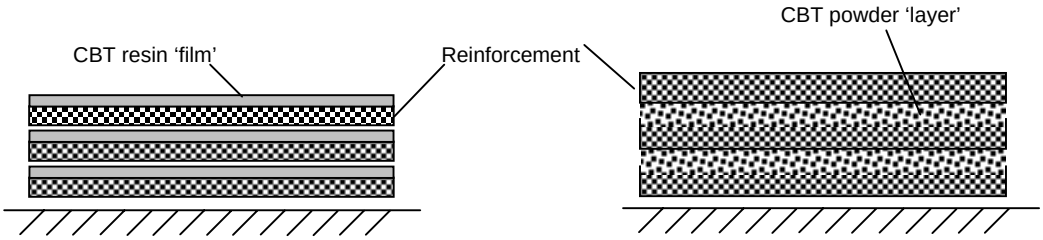

Figure 1 Simple schematic of RFI and powder-impregnated CBT/glass fibre forms

A heat transfer analysis will be especially important going forward for CBT processing in order to design appropriate heated tooling and to allow prediction of the temperature profiles, heat transfer rates, etc. throughout the thickness of CBT-composites. This will be essential for very large thermoplastic composites structures e.g. wind turbine blades, where thick root section thicknesses (greater than 100mm) and use of sandwich construction in the aerofoil sections greatly complicates the heat transfer issue [3].

HEAT-UP EXPERIMENTAL ANALYSIS

It is useful initially to carry out a direct comparison of 3 different material forms as regards heat-up characteristics during processing – dry glass fibres (reference), RFI and powder-impregnated glass fabric. To do this, a series of simple heat-up experiments was carried out. This involved placing a typical 6-layer lay-up on the surface of a heatable metal platen within a vacuum bag, attaching thermocouples at different points throughout the thickness and applying heat to a typical set-point of 195°C for CBT. The initial thickness of the dry glass fibre lay-up (using Saertex UD non-crimp glass fabric, 950 gsm) when vacuum is applied was 4.5 mm. Results for the dry glass only are shown in Figure 2. As expected, the temperatures within the glass fibres lag the platen temperature by up to 20°C. However, the application of vacuum pressure ensures that intimate contact is made between the glass fibre layers and heat transfer occurs quite efficiently by conduction.

Figure 3 shows the heat-up curve for a CBT-resin film infused glass fabric lay-up using the same type of glass reinforcement in terms of reinforcement type (unidirectional E-glass, 950 gsm). The initial stack thickness is significantly greater than with the dry glass, approximately 7.5 mm. This time, there is a much more significant temperature lag initially. The RFI layers are boardy and inflexible, even under vacuum pressure. Thermal contact resistance is much higher compared to dry glass due to the semi-rigid nature of the RFI form and non-intimate contact between the layers. Up to 120°C, the temperature of the top layer lags the bottom layer by up to 40°C. However, as the temperature of the stack approaches and passes 150°C, the heat transfer mechanism is significantly altered by a change in state of the CBT. It begins to melt prior to polymerisation taking place at higher temperatures. This phase change increases the heat transfer rate suddenly as the layers come into much more intimate contact as the liquid form of CBT removes any gaps between the layers and de-bulking occurs causing the thickness of the stack to reduce significantly. This sudden increase in heat transfer is seen as a ‘kink’ upwards on the time-temperature curve at around 130°C. The ‘kink’ is somewhat reversed between 140°C and 150°C (decrease in heat transfer rate) due to the latent heat of fusion effect as all of the CBT melts. Above 160°C, the through-thickness temperatures converge rapidly until the difference is only approximately 5-6°C at 190°C.

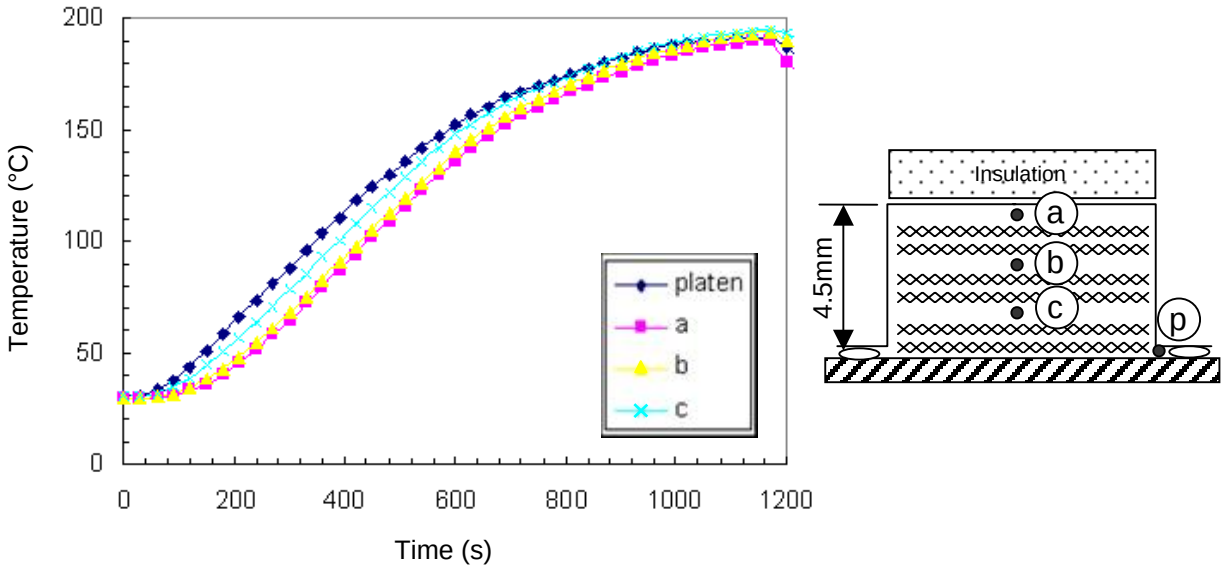

Figure 2 Heat-up of dry glass fibres

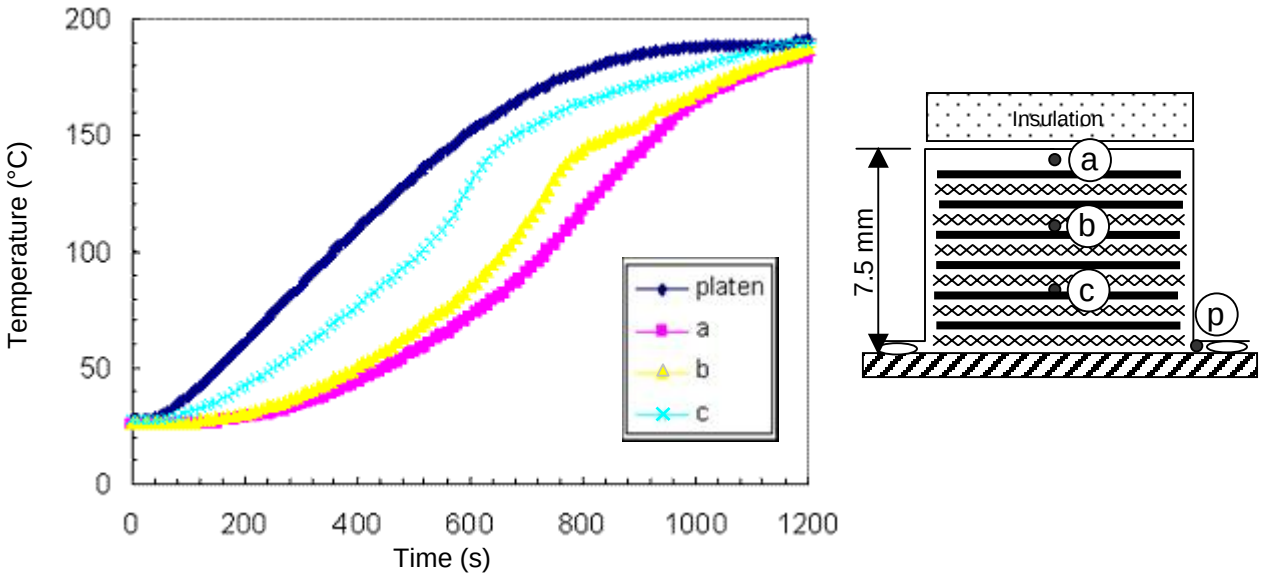

Figure 3 Heat-up of RFI/CBT-glass fibre layers

For the powder-impregnated form, the glass fibre layers (unidirectional E-glass, 950 gsm) were placed on the platen, with the CBT powder 'sandwiched' in between. The amount of CBT powder applied was the same amount as that used for the RFI-form in order to produce a final glass fibre volume fraction of 50%. Five identical powder layers were applied between the six glass fibre layers. When vacuum pressure was applied, the much greater bulk density of the CBT-powder meant the initial stack thickness was 10.4 mm, a 35% increase in thickness. It might therefore be expected that the powder impregnated form would exhibit the poorest heat transfer performance due to the greater thickness. The time–temperature heat-up curve is shown in Figure 4. Again, the through-thickness temperatures lag the platen temperature significantly. However, compared to Figure 3 (RFI-form), the heat transfer performance is significantly improved. 100°C is reached at Thermocouple A (top of the stack) after approximately 500s (8.3°C/min) compared to 720s for the RFI-form (5.8°C/min). This

may be attributed to a much greater intimate contact between the layers for the powder-impregnated form, allowing heat transfer by conduction to occur more readily, despite the increased thickness. Again, the latent heat of fusion effect as the CBT melts is seen as a kink 'downwards' in the slope of the graph at about 140-150°C. After this however, the temperatures converge rapidly as heat transfer occurs more readily through the fully 'wetted-out' glass fibre layers.

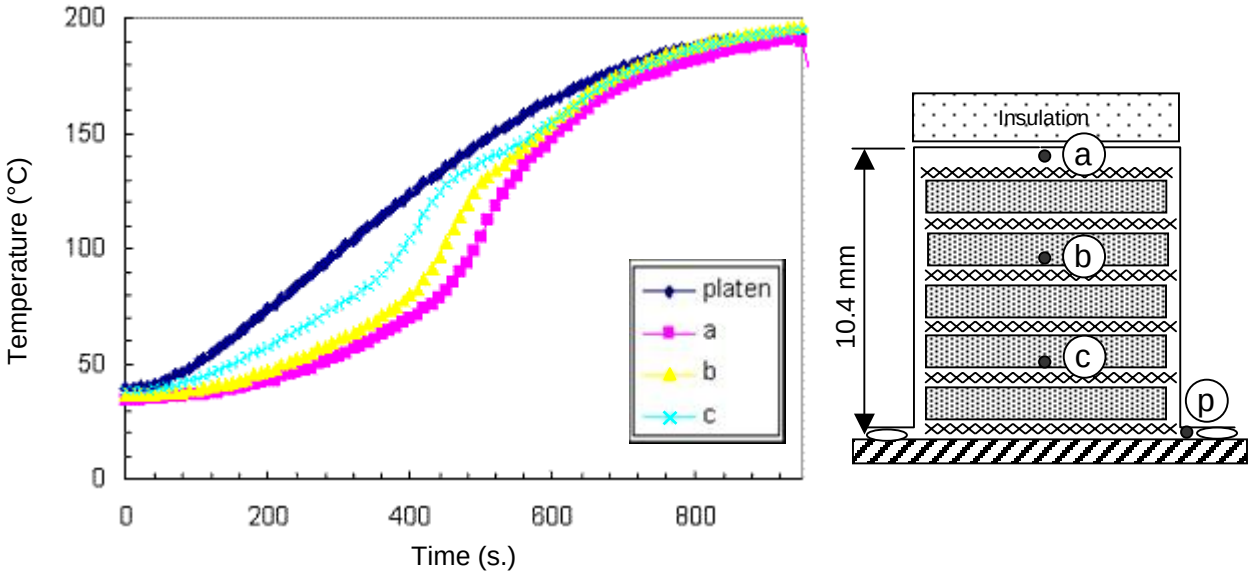

Figure 4 Heat-up of powdered CBT/glass fibre layers

THERMAL CONDUCTIVITY MEASUREMENT

The behaviour of CBT composites is quite complex as regards heating behaviour. It has been demonstrated how the presence of CBT (as either a resin film or powder) can initially insulate and prevent heat flow, then as the CBT begins to melt, heat flow is increased significantly. A detailed analytical study incorporating a non-linear model of phase change effects on the heat transfer is beyond the scope of this work. Instead, an alternative approach is taken in which an account is made of temperature-variant thermal conductivity with the lay-up during heating – this is a reasonable assumption to make if we assume that the lay-up stack including all of the glass fibre and CBT behaves as a solid continuum during heating.

In order to measure thermal conductivity, an apparatus designed and built by Lee [4] was used. This apparatus uses the guarded comparative longitudinal heat flow technique to measure 'k' values for different materials compared to a reference block of known conductivity. The design is based on a standard test method (ASTM E 1225-87). Although Lee only used his apparatus for measuring the thermal conductivity of dry fibre stacks, it was considered feasible to use it also for CBT RFI 'pre-preg' and CBT-powder impregnated glass fibre.

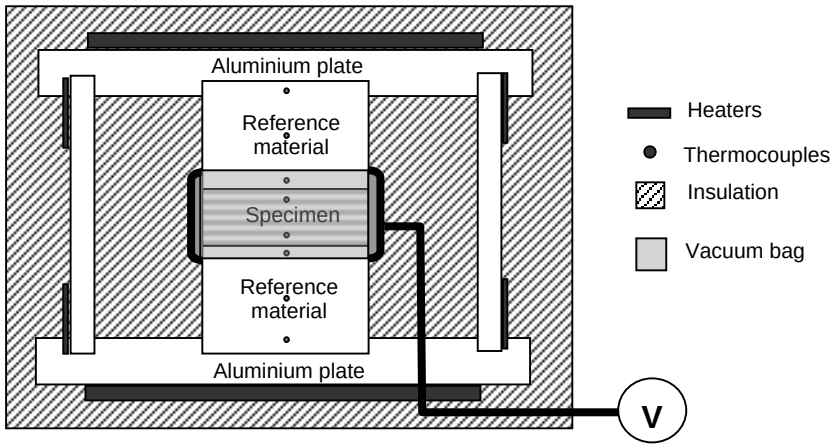

Figure 5 Schematic of thermal conductivity measurement apparatus

A schematic of the thermal conductivity test apparatus is shown in Figure 5. The test specimen (in our case the CBT/glass fibre combinations) was placed between the reference blocks. In order to minimise contact resistance between the top and bottom layers and the reference material surfaces, a layer of thermally conductive paste was applied. A vacuum bag was applied circumferentially around the stack. When vacuum was applied, this had the effect of compressing the stack, similar to that seen on the heated platen from the previous set of experiments. A set-point temperature was specified for both the top and bottom heaters and a steady-state temperature gradient was allowed to develop over a period of time. The 'k' value for the specimen material was calculated by comparing to a known conductivity for the Macor glass ceramic reference blocks at a particular temperature.

Results are shown in Figure 6. The 'k' values for the dry glass fibres (GF) were taken from [4]. The thermal conductivity for the RFI prepreg and the powder impregnated glass was measured at 90°C and 120°C. Due to wattage restraints on the equipment, it was not possible to measure thermal conductivity at higher temperatures. This is unfortunate as it is above 120°C that the thermal properties of CBT begin to vary significantly as it changes from a solid to a liquid.

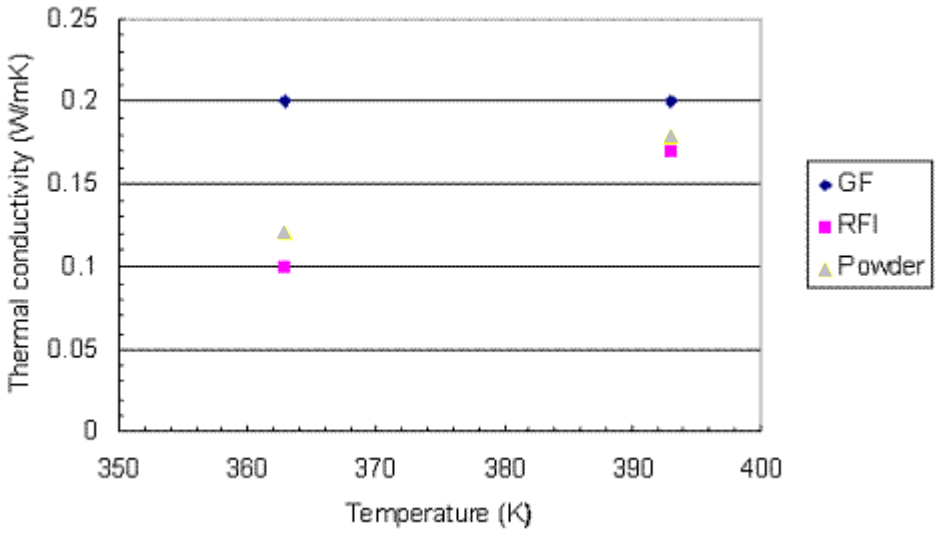

Figure 6 Thermal conductivity for material forms

1-D TRANSIENT HEAT TRANSFER MODEL

In general terms, the heating of a flat laminate with initial temperature T, thickness x, much smaller than its length and width, can be described as a simple 1-D heat conduction problem. Certain assumptions need to be made such as constant temperature boundary conditions, homogeneous make-up of the temperature slab, initially uniform slab temperature, etc. For our purposes, it will be useful to have a model which correlates experimental data with the predictive model using thermal conductivity data obtained in the previous section.

The standard law of thermal conservation of energy applies and the heat transfer equation may be written as [5]:

$$\frac{\partial}{\partial t}\left(\rho c_p T\right) = \frac{\partial}{\partial x}\left(k\frac{\partial T}{\partial x}\right) - Q \tag{1}$$

where ρ = material density, c_p is the specific heat, k is the thermal conductivity and Q represents the heat loss due to the latent heat of fusion upon melting.

It is assumed for the initial model that k is a function of temperature and that ρ and c_p are relatively constant with temperature. Also, we will only be modelling the heat transfer up to 120°C, prior to the phase change of the material, therefore Q can be considered to be zero. A more comprehensive model will be developed as part of future work to incorporate heating to higher temperatures.

Eqn. (1) is a partial differential equation and may be solved using the finite difference technique:

$$\frac{\partial T}{\Delta t} = \frac{k}{\rho c_p}\left(\frac{\Delta(\Delta T)}{\Delta x^2}\right) \tag{2}$$

Where $\Delta(\Delta T) = (T_{i+1} - T_i) - (T_i - T_{i-1}) = T_{i+1} - 2\,T_i + T_{i-1}$

$\delta T = T_{j+1} - T_j$, with i indexing across the node and j indexing over time.

A numerical algorithm developed by Pafko [6] was adapted for use here. Written in Visual C++, thermal conductivity, density, & heat capacity can all be functions of temperature, time, and position. Appropriate values were inserted into the algorithm for CBT using data obtained by experiment and modelled using a simple curve fit (thermal conductivity) and from material data sheets and the literature for density and specific heat [7].

A fixed temperature boundary condition experiment was carried out to help verify the model. A stack of six CBT-RFI / glass fibre layers was inserted between two platens pre-heated to 120°C. The temperature profile through the thickness was recorded.

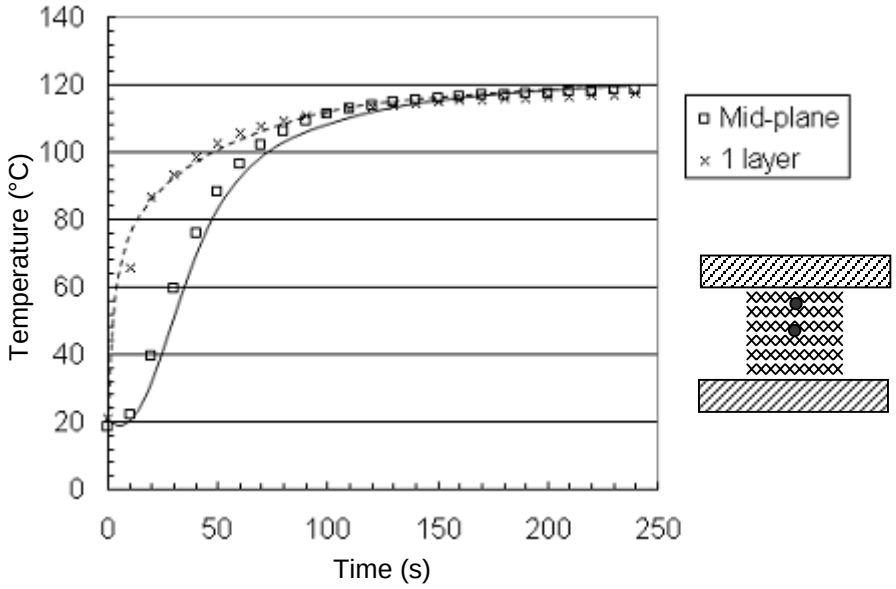

Figure 7 1-D experimental vs. model data

The experimental data is plotted against the model data in Figure 7. There appears to be good agreement for both the mid-point node and also at a node one layer in from the platen surface. As stated previously however, this model is only adequate for the initial heating stage up to 120°C and needs to be expanded to include phase change effects between 130-150°C, and subsequently, the heat transfer in the melt phase up to 195°C, the recommended polymerisation temperature for CBT.

REFERENCES

1. R. Eder. S. Winckler, "Processing of Advanced Thermoplastic Composites using Cyclic Thermoplastic Polyester", *Proceedings of the 22nd SAMPE Europe International Conference*, CNIT Conference Centre, Paris, 2001

2. S.M. Coll, A.M. Murtagh, C. O'Bradaigh, "Resin Film Infusion of Cyclic PBT Composites: A Fundamental Study", *Proc. 25th SAMPE Euro. Conf.,* Paris, 2004

3. D. A. Griffin, "Composite Technologies for Large Wind Turbine Blades", *Sandia National Laboratories Report*, Blade System Design Studies Volume 1, 2002

4. C. Lee, "An Investigation into the Transverse Thermal Conductivity of Fibre Beds", *Ph.D. Thesis*, University of Limerick, 2004

5. F.P. Incropera, D.P. De Witt, "Fundamentals of Heat and Mass Transfer", *John Wiley & Sons*, 1990

6. W. Pafko, "http://www.pafko.com/wayne/c/hx1Dvs.c.txt", online article, 2001

7. U. I. Thomann , M. Sauter, P. Ermanni, "A Combined Impregnation and Heat Transfer Model for Stamp Forming of Unconsolidated Commingled Yarn Preforms", *Composites Science and Technologies*, 64 (10-12, 2004

FILM STACKING IMPREGNATION MODEL FOR THERMOPLASTIC COMPOSITES APPLIED TO A NOVEL NET-SHAPE PREFORMING PROCESS

S.T.Jespersen [1], M.D.Wakeman [1], D.Cramer [2], V.Michaud [1], and J-A.E.Månson [1]

[1] *Ecole Polytechnique Fédérale de Lausanne (EPFL)*
Laboratoire de Technologie des Composites et Polymères (LTC),
CH-1015 Lausanne, Switzerland:
jan-anders.manson@epfl.ch

[2] *Fiberforge, 3768 Highway 82, suite 204, Glenwood Springs, CO 81621, USA.*

ABSTRACT: In order to assess candidate impregnation methods for a novel netshape preforming method that uses low cost feedstock materials and automation, the impregnation phenomena must be understood. The preforming method comprises automated deposition of UD carbon fibre yarns together with a thermoplastic matrix along a preprogrammed path creating preforms of stacked material which are preconsolidated before conventional stamp-forming. In order to evaluate different materials, improve stacking scenarios, and assess alternate preconsolidation routes, the infiltration kinetics must be considered in detail. The transverse infiltration of liquid thermoplastic polymer into a compressible unidirectional fibre bed has therefore been examined under isothermal conditions. An infiltration model, based on local fluid flow in compressible porous media has been extended to simulate infiltration of alternating matrix film and fibre layers, relating pressure, time, and temperature with the local fibre volume fraction, pressure and liquid and solid velocities in the stacked material. The model has been validated by comparison with experimental results. The fibre volume fraction distribution gives the optimum layer thickness values for a given set of conditions. In addition the results show that increased pressure leads to increased fibre bed compaction and hence decreases permeability and limits infiltration.

KEYWORDS: Thermoplastic composites, Impregnation, Net-shape preforming

INTRODUCTION

The high viscosity of most thermoplastics has been one of the main hindrances for introducing high fibre content composites in high volume applications [1]. In order to apply the most appropriate materials for a given process, the infiltration phenomena must be analysed. Methods to decrease impregnation time, such as commingling and powder impregnation, have been reported in the literature and are used in commercial products. In the net shape tailored preforming process examined here, where UD carbon fibres together with a Polyamide matrix are automatically laid along a preprogrammed path, [2,3], film stacking is a candidate route to reduce the infiltration length and lower impregnation time.

Impregnation of dry compressible preforms under constant pressure has been examined by Michaud *et al.* [4] for glass mat thermoplastics (GMT), extending an impregnation model by Sommer *et al.* [6,7], for the infiltration part of the process, previously used for soil theory and metal matrix composites. The preform relaxation and equilibration after infiltration was shown to dominate process time for pressures above 0.05MPa. This was also experimentally verified. Control of these steps is thus important in order to prevent or tailor an inhomogeneous reinforcement distribution [4,5].

To apply and experimentally verify the impregnation model for aligned fibre composites, a fibre bed consisting of aligned UD carbon fibres has been transversally infiltrated with a Polyamide (PA) resin. The impregnation front is anticipated to be well defined, and a slug-flow assumption can be applied [7]. The impregnation time is hence dominated by micro flow behaviour since no macro flow occurs.

In addition, with consideration of the conflicting demands of maximizing final part properties and minimizing production time and hence cost, the optimum stacking scenario must be defined. The uniformity of the final fibre distribution, the effect of resin rich core layers for improved processing [9], and the average fibre content are important parameters to study. To examine these parameters, the effect of processing variables on an industrial film stacking scenario must be understood in order to optimise the entire process. Since no current model was able to examine the film stacking scenario in its complete state, a new model was built to adapt the single interface infiltration model to the problem.

TRANSVERSE INFILTRATION

To mathematically describe the constant pressure driven isothermal saturated infiltration of a compressible porous medium by a Newtonian liquid, a one dimensional infiltration model has been written based on the work of Michaud *et al.* [4,5,8,10] and Sommer *et al.* [6,7]. The model is used as a base for a film stacking impregnation model, where the time and distance space is discretized to examine complex stacking sequences through time.

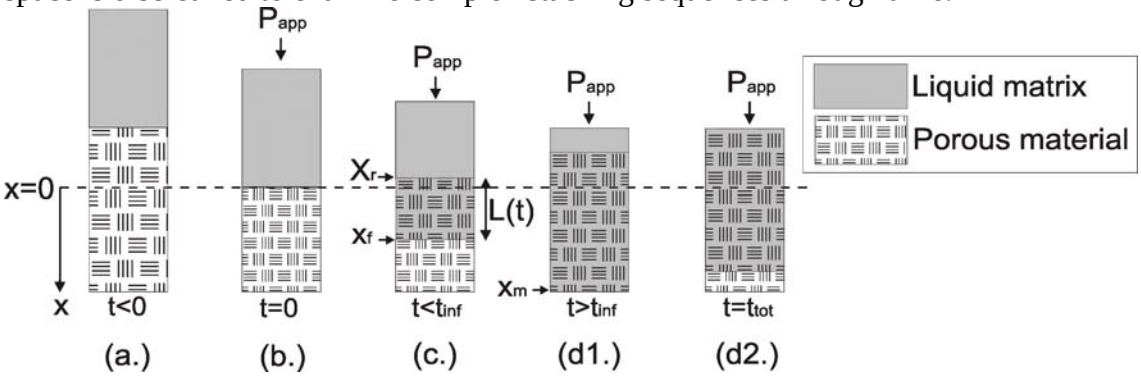

Fig. 1 Stages in the one dimensional infiltration model, after Michaud [4]

The initial condition before infiltration is a relaxed fibre bed adjacent to liquid polymer (Fig. 1a.). Pressure is then applied on the material, instantaneously compacting the fibre bed to the initial fibre volume fraction V_{fi} defined by the fibre network compliance, which has been measured for the UD fibre bed used (Fig. 1b). The impregnation front then progresses into the fibre bed with the velocity u_l (Fig. 1c.). At the same time, the fibre bed behind the impregnation front relaxes back into the matrix with the velocity u_s. At this main impregnation stage, momentum balance prescribes that the applied pressure P_{app} will be

balanced between the effective load on the fibre network σ and the liquid matrix pressure P_l. The infiltration model describes the volume fraction evolution between x_r and x_f over time. If the matrix layer has an adequate thickness, the impregnation front may advance to fully impregnate the fibre preform if the right processing parameters are used (Fig. 1 d1.). On the other hand, dry fibres will remain if the matrix layer is too thin (Fig. 1 d2.).

It is assumed that the gas in the dry fibre preform is at constant pressure and is driven out of the preform or absorbed in the matrix with negligible resistance. The liquid and solid phases are taken as incompressible and homogeneous versus time. Euler coordinates are used throughout with x=0 at the interface between liquid and solid after initial compression.

Isothermal steady impregnation of a porous medium with a Newtonian fluid is described by Darcy's law [8]. It is hence required that the flow is governed by viscous forces and has a Reynolds number, $R_e \leq 1$, which is the case here due to the high viscosity and small flow rates. Darcy's law, here without gravity effects states;

$$u_l - u_s = -\frac{K}{\nu(1-V_f)}\frac{dP}{dx} \tag{1}$$

dP/dx is the pressure gradient, $K(V_f)$ the permeability of the fibre bed calculated using the model from Gebart [11] using the measured fibre radius of 4μm and V_f the volume fraction fibre. The Newtonian matrix viscosity, ν, was measured and modelled with an Arrhenius relationship with ν=400Pa·s for 235°C and an activation energy of 70KJ/Mol.

Neglecting internal and body forces such as gravitational forces in the solid fibre bed and the liquid matrix, stress equilibrium in one dimension yields;

$$\frac{dP_l}{dx} + \frac{d\sigma}{dx} = 0 \tag{2}$$

Further relationships are found by applying mass conservation for liquid and solid phases respectively;

$$\frac{dV_f}{dt} + \frac{d(V_f u_s)}{dx} = -\frac{dV_f}{dt} + \frac{d((1-V_f)u_l)}{dx} = 0 \tag{3}$$

A "similarity solution" is used to simplify the problem as described by various authors [6,7]. This implies a Boltzmann transformation in Eulerian coordinates to find a reduced parameter X, which combines distance and time. The similarity solution will, following Mortensen et al [7], be valid for the case of constant applied pressure and a time independent viscosity.

$$X = \frac{x - x_r}{\psi\sqrt{t}} = \frac{x - x_r}{x_f - x_r} \tag{4}$$

where ψ is a time independent measure of the infiltration speed.

Factors for the velocities are then introduced. The infiltration front velocity u_l is governed by the factor $l(X)$.

$$u_l = \frac{\psi l(X)}{2\sqrt{t}} \tag{5}$$

The relaxation front velocity u_s is governed by the factor $s(X)$.

$$u_s = \frac{\psi s(X)}{2\sqrt{t}} \tag{6}$$

Boundary conditions
At the infiltration front: $x = x_l(t)$, $u_s = 0$, l=1+s(0), $V_f = V_{fc}$ and $P_l = P_g$, which remains constant as long as the gas is expelled or is absorbed in the matrix, and neglecting the capillary pressure drop at the infiltration front. At the preform relaxation front the conditions are as follows; $x = x_s(t)$, $P_l = P_{app} + P_g$ and $V_f = V_{fr}$.

Combining Eqn. 1 to 6 gives three non-linear first-order differential equations;

$$\frac{dV_f}{dX} = \frac{(l-s)(1-V_f)\nu\psi^2}{2KV_f \, d\sigma / dV_f} \tag{7}$$

$$\frac{ds}{dX} = [s - X - s(0)]\left(\frac{-V_{fi}'}{V_f}\right) \tag{8}$$

$$\frac{dl}{dX} = [l - X - s(0)]\left(\frac{-V_{fi}'}{1-V_f}\right) \tag{9}$$

From the development of Eqn. 8, follows that $d((1-V_f)l+V_f s)/dX=0$, showing the link between s and l, which simplifies the problem substantially since $l(X)$ can be found explicitly when $V_f(X)$ and $s(X)$ are known. Eqn. 7 and Eqn. 8 were solved for the two functions $V_f(X)$ and $s(X)$, as well as for the parameter ψ, in a commercial code Matlab™. A well converging optimum solution was found using sequential quadratic programming with initial values for ψ^2 and s(X=0) compared with known solutions for V_{fc} and $s(1)$.

The impregnation and relaxation length evolution with time is calculated by integrating the impregnation velocities over time. The corresponding real positions x to the values of X are then found to relate resin and fibre velocities, fibre volume fractions and pressures with x in the material as shown in Fig. 2a) and b).

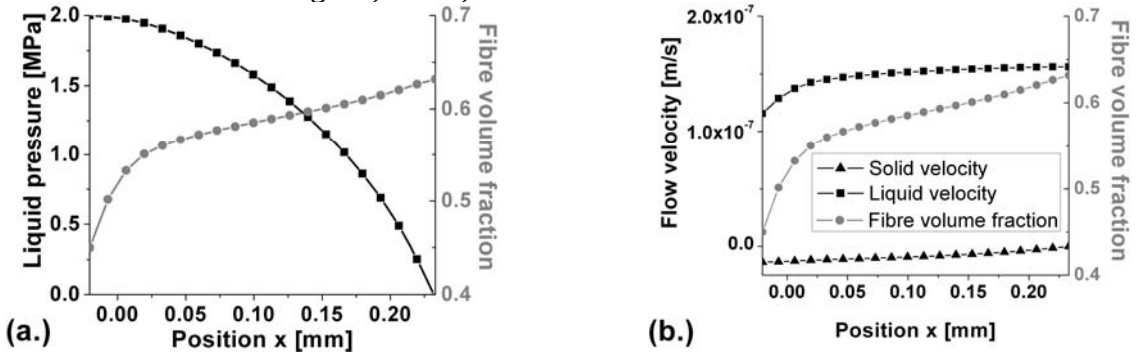

Fig. 2 The results for V_f together with a) polymer pressure and, b) flow velocities for 20bar applied pressure, 250°C and 75s impregnation time

FILM STACKING

The isothermal infiltration model described in the previous section has been extended in order to be able to model a film stacking scenario by discretizing time and position. The model is able to consider any number of layers and layer thicknesses giving freedom to examine, for example, the use of a polymer rich flow core. All data can be input via a graphical user interface (GUI) or be directly written into Excel.

To find the order of impregnation events all stacked layers are examined for each time step (typically 0.5s) from zero to a user specified impregnation time. When a fibre layer has been fully infiltrated or a matrix layer has been 'used up', the exact time for the event is recorded and excessive time is monitored. This ensures that intermediate fibre layers are impregnated from both sides and that impregnation can continue from one side if the other has "run dry" from polymer. The result is a vector called "*Interface*" containing the apparent infiltration time at all interfaces. Using the *Interface* values the amount of relaxation into the matrix for "upper-" xr_{up}(n) and "under-side" xr_{down}(n) for the dry fibre bed can be calculated, where n denotes the fibre layer. The infiltrated lengths xf_{up}(n) and xf_{down}(n) are determined correspondingly.

For each individual fibre/matrix interface, the fibre volume fraction is then found in discrete steps of a user defined step length of typically 1500 per mm. The step lengths are adapted to each individual layer thickness for improved accuracy. The pure matrix and fibre parts are subdivided in the same way. For each of the incremental steps, the fibre volume fraction is found using the previously predicted fibre volume fraction versus depth relation in the composite (x_r and x_f). An example of an arbitrary partially and fully impregnated composite can be seen in Fig. 3a) and b) respectively, from which an important variation in V_f is seen. The obtained simulation results can be used to improve the layer stacking sequence and, for example, the resin layer thickness and appropriate surface matrix layers if, for example, a matrix rich surface is desired.

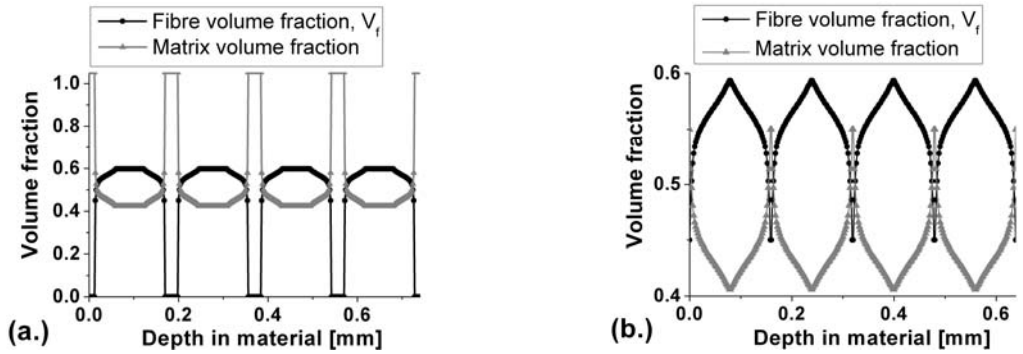

Fig. 3 The results with 4 fibre layers processed at 250°C and 10bar for: a) a partially infiltrated material after 30s and, b) a fully infiltrated material after 100s

The total time to complete impregnation of the composite is obtained by examining all individual layers and noting which has the longest infiltration time. If enough polymer thickness is specified, the optimum i'th layer thickness T_{film}(i) can be found that results in zero excess polymer. For the outer matrix layers the calculation is simpler, but for the i'th layer it takes the general form:

$$T_{film}(i) = xf_{down}(i-1) - xr_{down}(i-1) - xf_{down}(i-1)\cdot V_{fc} + xf_{up}(i) - xr_{up}(i) - xf_{up}(i)\cdot V_{fc} \quad (10)$$

The knowledge of the complete composite fibre volume fraction distribution gives the thickness at any time, the average fibre volume fraction, and the remaining porosity in the composite.

EXPERIMENTAL VERIFICATION

An experimental evaluation of the simulated results was performed by impregnating aligned unidirectional carbon fibres with a Polyamide 6/12 copolymer for varying pressure and time. The impregnation depth was evaluated by analyzing optical micrographs as seen in Fig. 4 illustrating the difference for a 15s and a 60s impregnation time at 250°C and nominally 6 bar. Due to scattering in the measured values, several measurements were taken and average values used for the impregnation length.

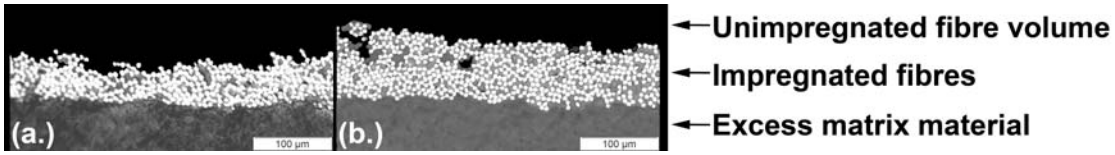

Fig. 4 Impregnation after: a) 15s, and b) 60s by nominally 6bar at 250°C

The first set of verification trials examined the effect of time on impregnation length, as shown in Fig. 5a using 6bar pressure and 250°C. The error bars for the simulation results correspond to the uncertainty in the pressure value for various experiments. The experimental results compare well with the simulation. It should be noted, that due to the machine response time, a non-negligible impregnation has already occurred at zero impregnation time, which is measured as the impregnation occurring when the applied pressure has just been reached and then removed. This will effectively move the experimentally based results towards a larger impregnation distance compared with the simulation results, especially for small impregnation times, which correlated well with the observed results. The second set of verification trials examined the effect of pressure on impregnation length for a fixed impregnation time of 60s. The pressure dependence of impregnation for a constant temperature of 250°C was measured and showed close correlation with simulation results, as seen in Fig. 5b.

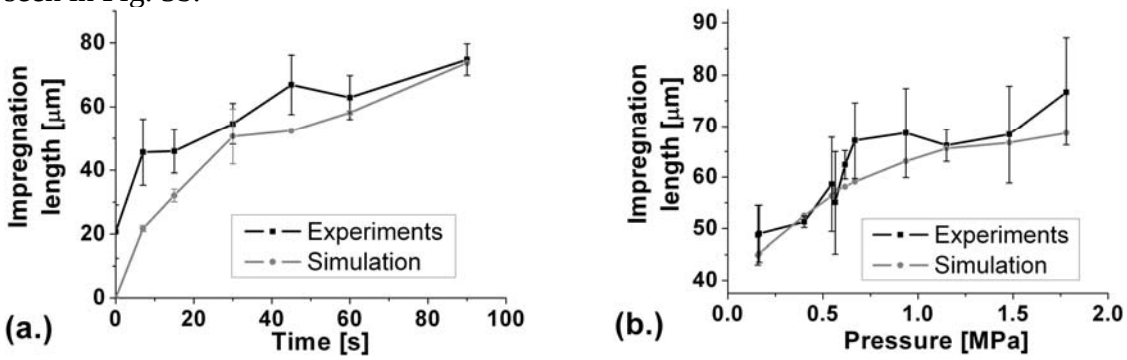

Fig. 5 Simulation results and standard deviation bars for experimental data

SIMULATION RESULTS AND DISCUSSION

Having verified the model against experimental impregnation values for changing time and pressure, the simulation model has been used to predict the effect of different stacking scenarios and processing parameters. Fibre layer thicknesses were measured in the relaxed state. The effect of temperature is shown in Fig. 6a.) for a stacking scenario with constant final thickness. Small variations (0.002mm) are due to discretization step size. When simulating the impregnation behaviour the necessary amount of matrix depends on the applied pressure as shown in Fig. 6b.) and hence fibre bed compression. The optimum

thickness, which is twice the size for the inner layers having two fibre interfaces, has been used in all following simulation runs to give the minimum final part thickness.

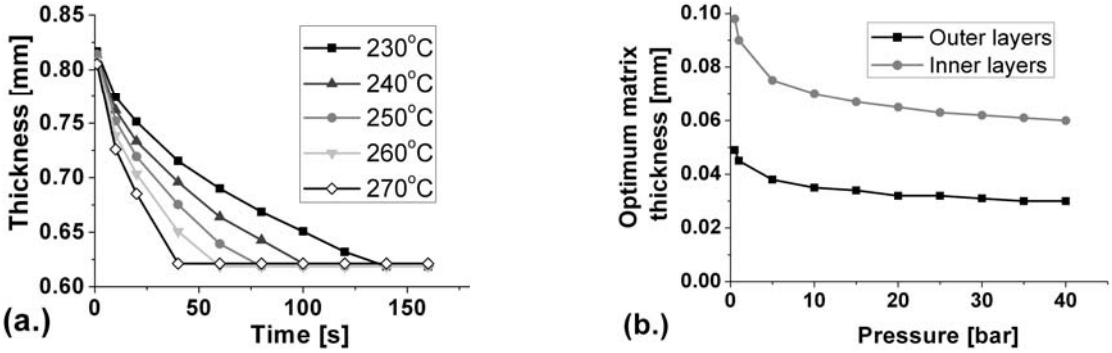

Fig. 6 a) Composite thickness evolution for four 0.2mm fibre layers and constant excess matrix, b) Necessary matrix thickness for outer and inner matrix layers depending on pressure for 0.2mm fibre layer thickness

One of the fundamental results from the simulation is the change in impregnation time with resin viscosity for different fibre layer thicknesses, here seen in Fig. 7 for constant fibre layer thickness scenarios. This can directly be used to find the impregnation cycle time for the given process and material combination.

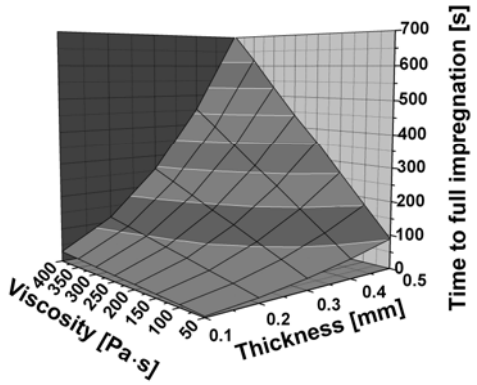

Fig. 7 Time to full impregnation as function of resin viscosity and fibre layer thickness

A pressure increase will increase the impregnation velocity up to a certain threshold value (here 20bar) even though the permeability decreases due to fibre bed compaction, as seen from Fig. 8a. By using this pressure, the impregnation time is optimized, but still depends on temperature, as shown in Fig. 8b, where the porosity content is monitored over time.

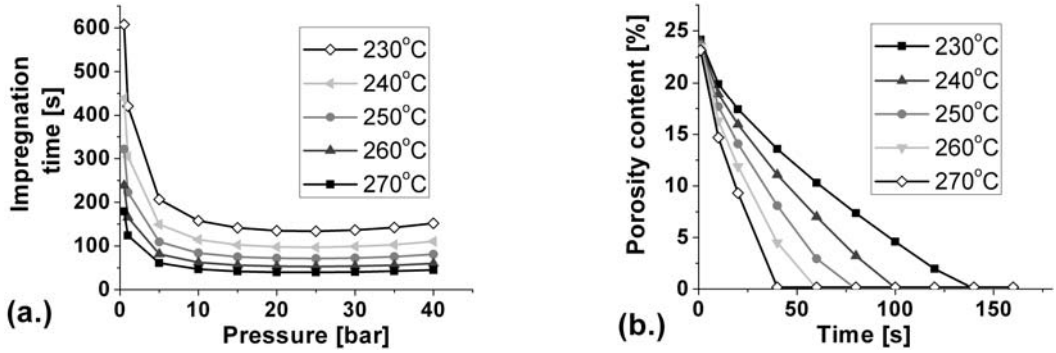

Fig. 8 For 0.2mm fibre layer thickness; a) Time for complete impregnation and b) The porosity content in the composite through process time at 20bar

CONCLUSIONS

An infiltration model has been developed and validated using the current process of film stacking of UD fibres and thermoplastic matrix layers. Experimental measurements show good agreement with simulation results without the need for fitting parameters. Using the model, it has been possible to find optimum layer thickness values for given processing conditions. Furthermore, an optimum pressure with respect to impregnation efficiency was found, which is smaller than the maximum applied pressure. This is explained by the fact that increased pressure compacts the fibre bed and hence decreases permeability and limits infiltration. The model can be used to optimize a given production scenario and the materials used, and thus help reduce the development cost for new fibre impregnation technologies.

Acknowledgements
This work was supported by Fiberforge. The authors wish to acknowledge from EPFL: G. Tornare and from Fiberforge: A. Burkhart and J. Fox-Rubin.

REFERENCES

1. J.-A. E. Månson, M. D. Wakeman, P. E. Bourban, and P. W. Sunderland, "Driving forces for cost-effective composites: new demands on materials and processes", *Proc. ICCM 12*, 1999.
2. M. D. Wakeman, D. Cramer and J.-A. E. Månson, "Technical cost modelling of an automated netshape preforming process for thermoplastic composites: a case study", *Proc. Sampe Paris*. 2005.
3. A. Ross, "Tailored carbon fiber blanks set to move into steel stamping area", *High-performance Composites*, January, 2006, pp. 24.
4. V. Michaud, and J.-A. E. Månson, "Impregnation of compressible fiber mats with a thermoplastic resin. Part I: Theory", *Journal of composite materials*, Vol. 35, no.13, 2001, pp. 1150.
5. V. Michaud, R.Törnqvist and J.-A. E. Månson, "Impregnation of compressible fiber mats with a thermoplastic resin. Part II: Experiments", *Journal of composite materials*, Vol. 35, no.13, 2001, pp. 1174
6. J. L. Sommer, and A. Mortensen, "Forced unidirectional infiltration of deformable porous media", *Journal of fluid mechanics*, Vol. 311, 1996, pp. 193.
7. A. Mortensen, C. San Marchi, and V. Michaud, "Capillarity in infiltration processing: A review of principles and their extension to reactive infiltration". *Proc. Int. Conf. High temperature capillarity*, 1997, pp. 249
8. V. Michaud, and A. Mortensen, "Infiltration processing of fibre reinforced composites: governing phenomena", *Composites part A-applied science and manufacturing*, Vol. 32, 2001, pp. 81.
9. M. D. Wakeman, P. Blanchard and J.-A. E. Månson, "Void evolution during stamp-forming of thermoplastic composites". *Proc. ICCM 15*, 2005
10. V. J. Michaud, J. L. Sommer, and A. Mortensen, "Infiltration of fibrous preforms by a pure metal: Part V. Influence of preform compressability", *Metallurgical and materials transactions A*, Vol. 30, 1999 pp. 471.
11. B. R. Gebart, "Permeability of unidirectional reinforcements for RTM", *Journal of Composite Materials*, Vol. 26 no. 8, 1992

SHEAR DEFORMATION BEHAVIOUR OF FIBRE-REINFORCED COMPOSITES USING A MODEL COMPOSITE SYSTEM

W.F. Stanley[1], P.J. Mallon[2]

[1]*Composites Research Centre, Dept. of Mechanical and Aeronautical Engineering, University of Limerick, Ireland: Email: Walter.Stanley@ul.ie (corresponding author)*
[2]*Irish Composites Ltd., Spiddal, Co. Galway, Ireland: Email: pat@irishcomposites.com*

ABSTRACT: Experimental methodologies have been employed in the past to determine both longitudinal and transverse steady intraply shear viscosities of molten unidirectional continuous fibre-reinforced composites past resulting in, however, conflicting results. Many physical difficulties are inherently associated with testing for these material properties of thermoplastic matrix based composites due to the elevated testing temperature and fibre entanglement due to manufacturing vagaries. A model composite system has been adopted to overcome these difficulties consisting of long, rigid and virtually inextensible fibres embedded in a room-temperature liquid, Newtonian matrix. Experiments have been carried out to investigate the important rheological parameters associated with the deformation of continuous fibre-reinforced composite materials in steady-shear flow, both along and transverse to the principal fibre direction. To provide a constant shearing motion a custom-built apparatus has been designed and constructed in which a thin, central plate can be drawn out at constant velocity from a test specimen while the shear force exerted by the plate on the specimen is measured. Experimental data has been collected for different pull-out velocities, fibre concentrations, and ply thicknesses and it has been found that the behaviour of the composite varies significantly with changes in these parameters. The observed deformation and results have been carefully interpreted and compared with other published data based on a similar model composite. The viscosities deduced from the experimental data were also compared with values predicted by various mathematical models put forward by several authors. It was concluded that the models grossly underestimate the viscosity values for all values of fibre volume fractions used. Discrepancies between the numerical and experimental results have subsequently been postulated.

KEYWORDS: model composite, unidirectional, intraply shear, viscosity.

INTRODUCTION

The experimental measurement of the intraply shearing viscosities of an advanced composite material, carbon fibre reinforced polyetheretherketone (PEEK), has already been published [1]. The paper describes the experimental difficulties associated with induced a state of steady shear throughout samples of the composite at the forming temperature of the material and highlighted the conflicting results between that study and other published data.
Experimental difficulties would arise by using the advanced thermoplastic composites by virtue of their physical properties i.e. the relatively high processing, hence testing, temperature, and quite significantly, fibre misalignment. The existence of relatively small

fibre misalignments had been noted in commercial composites; through a microscopic study of preimpregnated tapes of APC-2, it has been reported [2] that 83% of the fibres were within ±1° of being perfectly aligned, and measured maximum off-axis deviations of up to ±4° both in-plane of the tape and out-of-plane. The amount of fibres misaligned to 4° was 2-3% approximately, however upon moulding, due to adjacent fibres to reorient co-operatively, this value could typically increase to 10% of fibres. Another imperfection of the internal structure of the composite, namely fibre entanglement, is a direct consequence of this fibre misalignment. Thus, without these complicating factors characteristic of commercial composites, direct comparisons could be made between experimentally determined results and those proposed by numerical models.

Much in-road into establishing a database for the longitudinal and transverse intraply shear viscosities has recently been made using so-called 'model' composite systems, which are utilised to represent or imitate the properties of commercial composites. These model composites consist of a matrix that is a liquid at room temperature meaning that from an experimental point of view there is a significant advantage in that there is no need for a heat cycle. Several researchers [3-7] have made use of model composites consisting of larger diameter fibres than that found in commercial composites. This has the consequence that the fibres are straighter and more rigid which removes the complication of fibre misalignments and entanglements associated with commercial composite systems. There is also the advantage that with larger diameter fibres the model composite can be constructed by hand meaning that the fibre concentration can be controlled. This allows the effect of the concentration of fibres on properties to be investigated.

In this paper a custom-built experimental apparatus is described that was designed to provide experimental values for the longitudinal and transverse viscosities of model composite systems undergoing steady-shear deformation. The apparatus has originally been detailed for use in the elevated temperature tests on APC-2 [1]. The operation of the instrument is based on the principle of drawing a thin, flat plate from a composite specimen using a constant pull-out velocity and measuring the pull-out force as a function of the plate's displacement from its initial position. By aligning the fibres parallel to the pull-out direction or perpendicular to this direction the anisotropic behaviour of the test specimen can be characterised, and through appropriate mathematical analysis, the readings of pull-out force can be converted into corresponding values of longitudinal and transverse shear viscosity.

MODEL COMPOSITE SYSTEM

The material used in the experiments was a model composite that could be assembled by hand, thus avoiding the complications of fibre entanglement and misalignment that occur in the commercial composites. The desired features of the constituents of the model composite were as follows:

i) the matrix to be liquid at room temperature;
ii) the matrix viscous enough to construct a composite without a great deal of sample loss, but 'thin' enough to wet the fibres;
iii) the fibres to be straight, uniform, rigid and inextensible;
iv) both constituents, fibres and matrix, to have similar densities;
v) good adhesion between the matrix and the fibres.

Following previous work done on model composites [4-7], the composite selected consisted of long, rigid fibres of Nylon embedded in a liquid matrix of Golden Syrup. These constituents have density values of approximately 1.134gcm^{-3} and 1.45gcm^{-3} respectively. The Nylon fibres were manufactured using a standard extrusion process (Speciality Filaments Ltd), and supplied to order in a black colour with dimensions of 0.2mm diameter and 50mm length. The matrix was a Newtonian liquid with a viscosity of 70 Pa.s at 20°C. Comprehensive constituent examinations have been documented elsewhere [8].

APPARATUS

An illustration of the front-end of the experimental apparatus, with a sample to be tested *in situ*, is given in Figure 1.

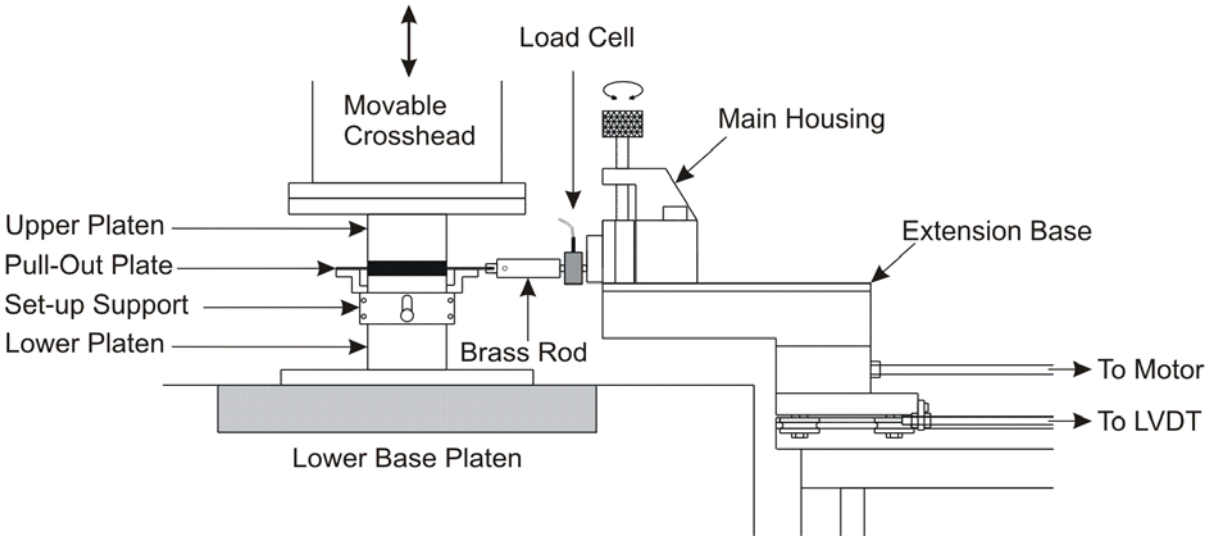

Figure 1: Illustration of the custom-built shear apparatus, indicating main parts of the rig.

The instrument consists of two principle units, one a commercially available Dartec rig to provide vertical motion for gap setting, and the other a side-mounted custom-built shear rig to provide the horizontal pull-out motion. The operating principles and technical details of the instrumentation and drive mechanism of the rig have been published [1, 2].

The temperature at which the test was conducted was of prime importance due to the high thermal sensitivity of the viscosity of the matrix. The surrounding ambient temperature was therefore controlled to within range of temperatures but was accurately recorded so that the resulting pull-out data could be standardised to 20°C. A Comark C9011 digital thermometer with a PP23L insertion probe, was used. The combination of the sensor and probe were calibrated by the manufacturer, according to NAMAS standards, to an accuracy of less than ±0.03% of the reading, or a maximum or ±0.1°C over the full temperature range.

SPECIMEN PREPARATION

Composite specimens were constructed in a delicate, indeed tedious, manner by hand. The fibre wetting procedure involved immersing bundles of the Nylon fibres, gripped by one hand, into a globule of the Golden Syrup. The matrix was worked into the fibre bundle by

careful manipulation of the compound by fingertip until a consistent composition was achieved with full fibre wetting. The procedure to construct the full composite sample and centralising the pull-out plate, attachment to the load cell etc. was a delicate procedure to ensure acceptable alignment, correct fibre volume fraction and so on.

EXPERIMENTAL PROCEDURE

With the composite fully laid-up and in position the test was started and the motor engaged. Figure 2 shows a typical experiment in progress for a composite specimen in which the fibres have been aligned with the pull-out direction. The gap between the pull-out plate and the fixed top and bottom plates, or equivalently the thickness of each composite layer, is 4 mm.

Figure 2: Photograph taken of a typical test in progress.

The photograph shows the classic sheared profile of the specimen through its thickness. The characteristic 'V' shape is evident within the composite showing the through thickness intraply shear.

RESULTS

It should be noted that because of the high temperature-dependence of the viscosity of the Golden Syrup matrix all results for the model composite tests have been standardised to a temperature of 20°C. This allows a direct comparison of graphs and results to be made. To investigate the effect of pull-out velocity a series of tests was carried out in which composite specimens were sheared using a range of different pull-out velocities, starting at the lowest velocity, $0.025 mms^{-1}$, and increasing in steps to the highest velocity, $1.25 mms^{-1}$. The fibre volume concentration in the tests was chosen to be 60% in order to coincide with the high volume concentration of fibres found in a typical commercial composite, while the thickness of each layer of composite was 4mm.

Figure 3 (a) contains a set of force versus displacement curves obtained for specimens in which the fibres were aligned with the pull-out direction. For the lower pull-out velocities, it is seen that the force immediately reaches a maximum point after which it gradually decreases over the remainder of the test. This suggests that at low shear rates an initial yield stress has to be exceeded at the start of a test in order for the material to deform. No such yielding behaviour was observed for the Golden Syrup alone, which implies that for the composite specimens some of the fibres might be coming into contact, thus leading to localised friction.

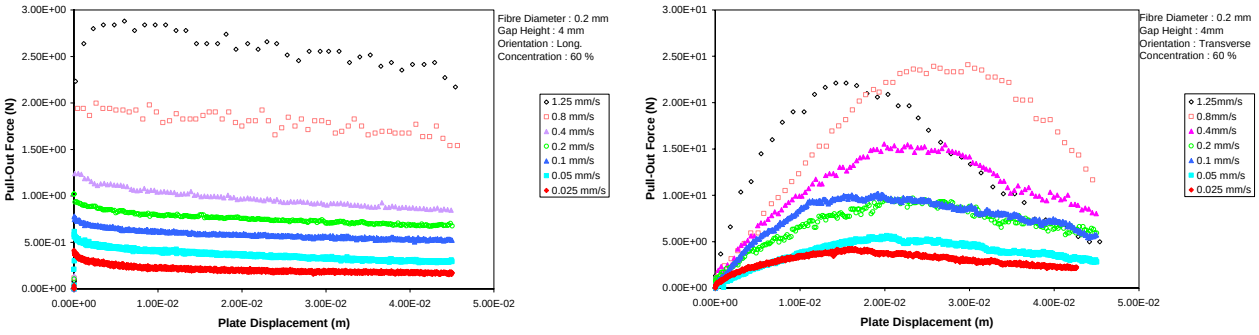

(a) (b)

Figure 3: Force versus displacement over 45 mm of shear for a range of pull-out velocities – (a) longitudinal direction, (b) transverse direction.

Force versus displacement curves for specimens in which the fibres were perpendicular to the pull-out direction are shown in Figure 3 (b). These graphs indicate a significantly different behaviour, with the pull-out force increasing steadily to a maximum value, before levelling off and starting to decrease.

During these tests it was observed that as the pull-out plate was withdrawn from the material, the fibres initially rolled over one another in what seemed to be a combination of rotational and translational flow, until after about 5-10mm of shear they bunched up as a result of the high fibre concentration. This led to a log-jamming effect (c.f. Figure 4) whereby each layer of composite appeared to become locked. A rapid build up in pull-out force was observed until a critical force was reached which was sufficient to draw the material at the front of the specimen from the enclosure of the fixed top and bottom plates, after which the force started to decrease. Examination of the internal structure of the sheared material showed a marked re-organisation and re-orientation of the fibres, with a distinct 'criss-cross' configuration.

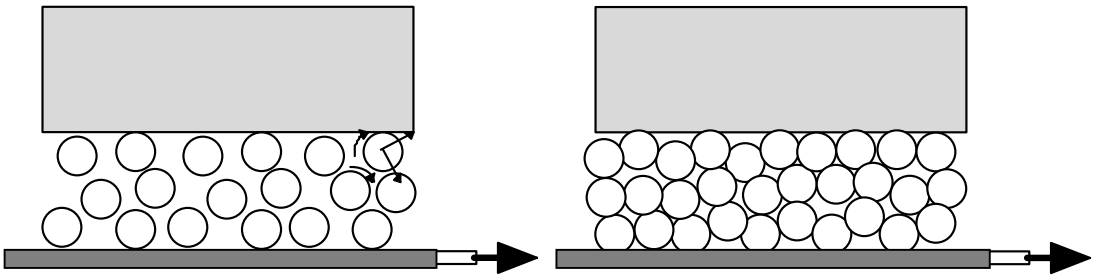

Figure 4: Simplified schematic of the effects on the fibres in a transverse shear test.

The experimental work was extended to determine the effect of fibre concentration on the composite's rheological properties. Tests were carried out on composite specimens of five different concentrations – 20%, 40%, 50%, 60% and 70%. The lowest value of concentration was set at 20% because, firstly, this would be the lower limit to any commercially available composite systems, and secondly, there was very much a practical reason for this value of 20% - below this concentration, it would have been extremely difficult to construct a composite with a somewhat even fibre distribution, although even 20% proved difficult to obtain successfully in practice. All specimens were sheared using a pull-out velocity of $0.1 mms^{-1}$, and the thickness of each layer of composite was 4mm. The longitudinal test results are shown in Figure 5.

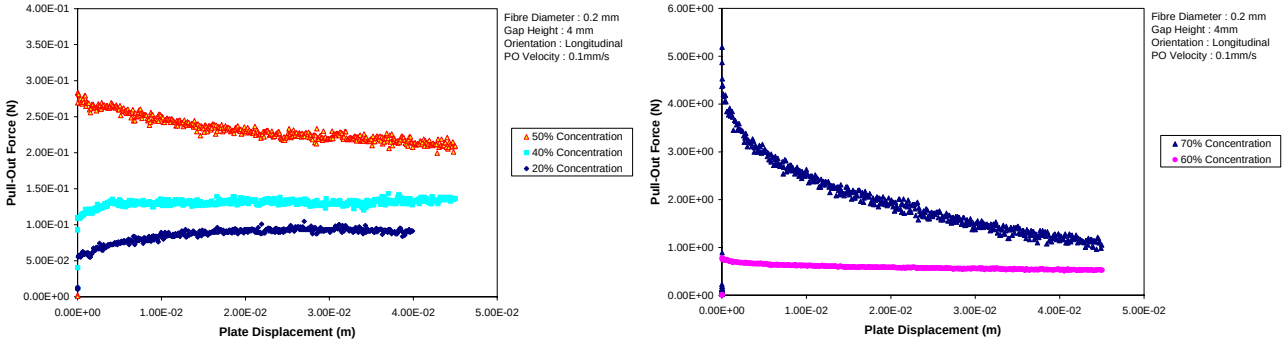

Figure 5: Force versus displacement curves obtained for specimens in which the fibres were aligned with the pull-out direction.

Force versus displacement curves for specimens in which the fibres were perpendicular to the pull-out direction are presented in Figure 6.

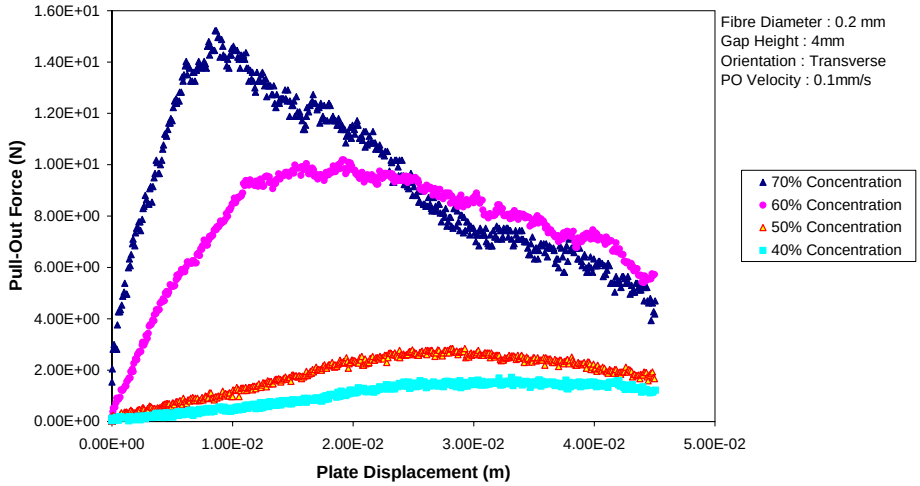

Figure 6: Force versus displacement curves obtained for specimens in which the fibres were aligned normal to the pull-out direction.

DISCUSSION

All of the results collected for 60% fibre volume concentration composites, tested in the longitudinal direction are presented in Figure 7. All shear rates are included in this plot.

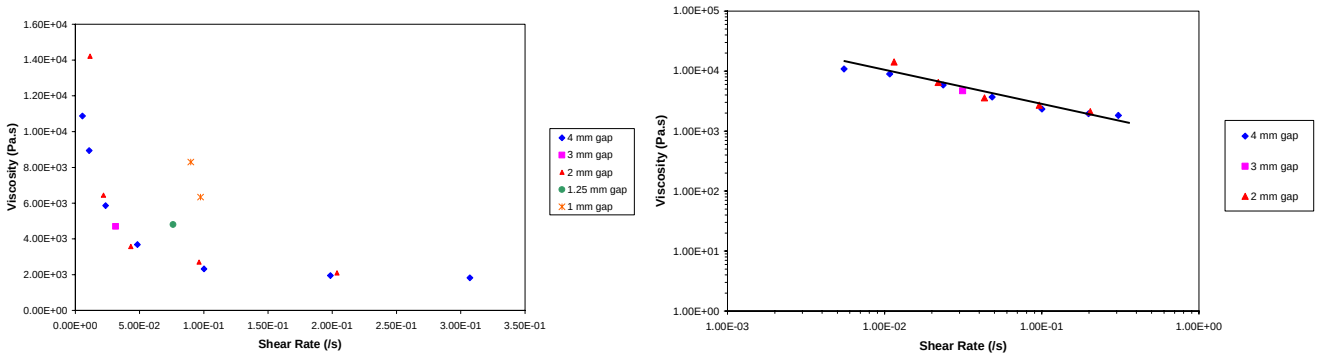

Figure 7: Calculated viscosity values versus shear rate, fibre volume fraction at 60 % - Longitudinal direction and the associated log-log plot.

From this plot it was observed that at the lowest shear rate, the longitudinal viscosity had relatively high values of 14,000 Pa.s for a 2 mm gap height, but, more importantly, ca. 11,000 Pa.s at a 4 mm gap height.[1] As the shear rate increased the viscosity values decrease rapidly before levelling off. This levelling off of viscosity may suggest that there was an identifiable region at the higher shear rates where the behaviour of the composite could be regarded as being approximately Newtonian. However, the shape of the curve is characteristic of pseudoplastic or shear-thinning polymer melts [9]. If one plots the viscosity values versus shear rate on a log-log scale, ignoring the outlying values recorded for the 1.25 and 1.0 mm gap heights, one can clearly see a 'power-law' region, typical of a polymer melt, over that shear rate range. In a similar manner, one may analyse the results derived from the experiments on the model composites, with the same preceding parameters, but with the fibres aligned in the transverse direction. Figure 8 is a plot of the viscosity values versus shear rates.

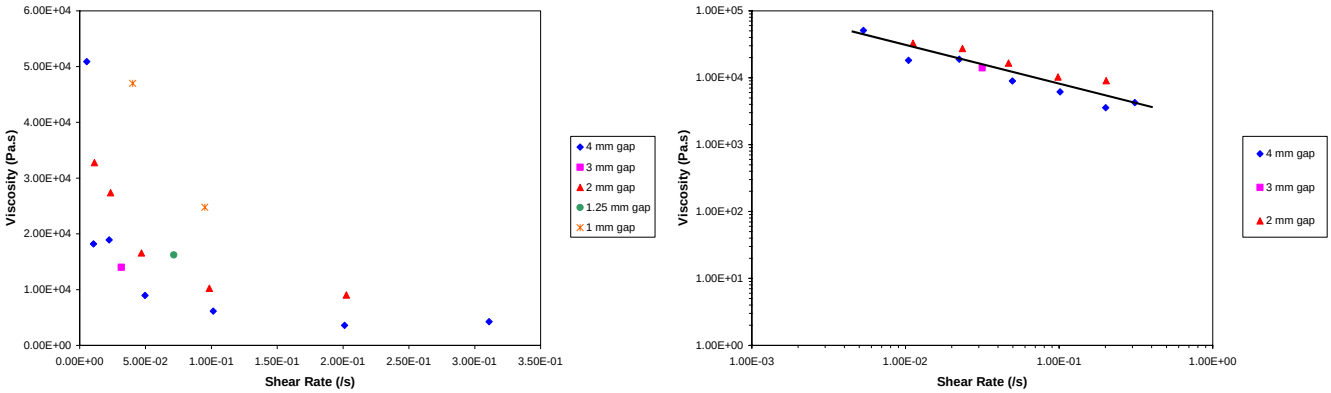

Figure 8:Calculated viscosity values versus shear rate, 60 % concentration - Transverse direction and the associated log-log plot.

Again, pseudoplastic behaviour is evident from this viscosity profile. In this principal direction, the viscosity drops off from in excess of 50,000 Pa.s at the lowest shear rate to approximately 4,000 Pa.s at the highest shear rate. Figure 9 shows the dependence of composite viscosity in both principle fibre directions against fibre concentration. For the lower values of concentration there appeared to be a relatively small dependence.

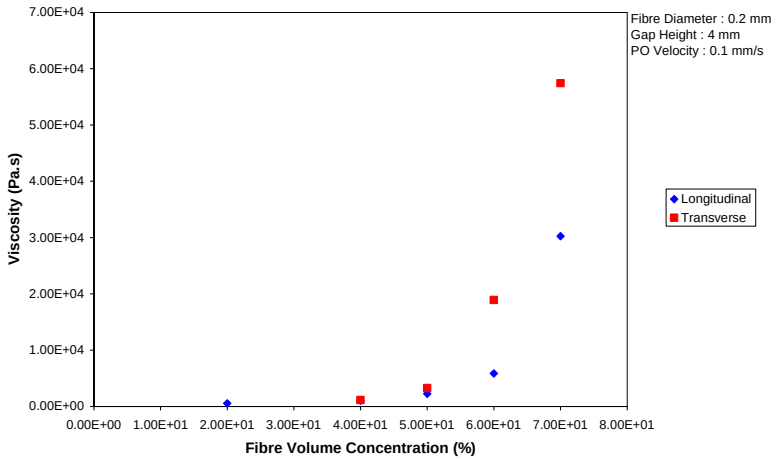

Figure 9: Viscosity versus fibre concentration at a single rate of shear – both longitudinal and transverse directions.

[1] 4 mm Gap Height was taken as the reference thickness when one compares the number of fibres through the thickness to a single ply of APC-2.

However, approaching 50% fibre volume concentration, this dependence was significantly more marked, in particular regarding the transverse behaviour. Throughout the range of fibre volume concentrations, the transverse viscosity values were greater than the corresponding longitudinal viscosity. This difference was again more apparent towards the higher values of concentration.

Roberts and Jones [5], who applied the method of dynamic testing to investigate the same composite system, also identified such a Newtonian region. They found the material to be frequency thinning with sharp decreases in longitudinal and transverse dynamic viscosities up to a given frequency, after which each viscosity levelled off. Roberts and Jones also found that for specimens of 60% fibre concentration, the transverse viscosity was significantly greater than the longitudinal viscosity, which agrees qualitatively with the data in Figure 9. Goshawk and Jones [6] carried out dead-weight loading tests to determine values for η_L and η_T. They also found the transverse viscosity to be much greater than the longitudinal viscosity for specimens of 60% concentration, but it is significant that in these tests η_L and η_T were found to be independent of shear rate, which clearly contradicts the above findings. Goshawk and Jones also reported that none of their specimens exhibited yield-like behaviour, whereas in the previous section clear indications of the existence of yielding behaviour was observed for specimens sheared along the direction of the fibres. The dynamic tests carried out by Roberts and Jones revealed an interesting variation of the ratio of the composite viscosities with fibre concentration. Surprisingly, it was found that the longitudinal dynamic viscosity η'_L was significantly higher than the transverse dynamic viscosity η'_T for fibre concentrations below 55%, while at a concentration of 55% η'_L was equal to η'_T, and for concentrations greater than 55% η'_T became much greater than η'_L. No such cross-over in viscosity values was observed by Goshawk and Jones in their dead-weight loading tests on the same model composite system. It was speculated that the disparity could be due to the relatively large strains imposed on the material in the dead-weight loading tests.

Table1: Comparison of viscosity ratios for model composites of increasing fibre concentrations.

	Current Study		**Roberts et al**		**Goshawk et al**	
Concentration %	$\frac{\eta_L}{\eta_M}$	$\frac{\eta_T}{\eta_M}$	$\frac{\eta'_L}{\eta'_M}$	$\frac{\eta'_T}{\eta'_M}$	$\frac{\eta_L}{\eta_M}$	$\frac{\eta_T}{\eta_M}$
20	7.99	*	2.73	1.93	2.85	3.71
40	14.89	16.25	5.83	4.10	7.43	26.57
50	32.14	46.38	7.76	6.71	*	*
60	83.38	268.97	11.04	12.61	134.29	262.86
70	430.23	816.63	21.37	38.44	*	*

In Table 1, the results of these previous investigations are shown along with viscosity values determined from the current study. For comparison purposes, the viscosities quoted are relative viscosities calculated by dividing the measured viscosity of the composite by the corresponding matrix viscosity η_M at the test temperature.

From the figure, it can be seen that the relative viscosities calculated in the current study and those derived by Goshawk and Jones are of the same order of magnitude, with the relative transverse viscosity greater than the relative longitudinal viscosity over the entire range of concentrations. It is significant that in the present study the ratio of the relative viscosities at 40% concentration is much closer to unity than the ratio for the data obtained by Goshawk and Jones, suggesting that at lower concentrations there might be a cross-over of viscosities.

Several authors [10-12] have put forward analyses that are concerned with determining formulae for the longitudinal and transverse shear viscosities of composites in terms of the fibre volume fraction and the shear viscosity of the matrix. The basic configuration considered in each analysis quoted is that of a composite/suspension comprising perfectly aligned, rigid fibres embedded in an incompressible Newtonian viscous liquid matrix. The fibres are understood to have a regular packing arrangement and have a large aspect ratio. Moreover, the composite system is undergoing steady shear in either along or transverse to the main axis of the cylinders. The experimental values for viscosity collected during the current study on the fibre concentration dependence are plotted together with the values predicted by the three analyses in Figure 10 and listed in Table 2. Throughout the range of fibre concentrations considered, the longitudinal viscosities are less than the transverse viscosities, which agrees qualitatively with the theories put forward by Christensen [11] and Pipes [12].

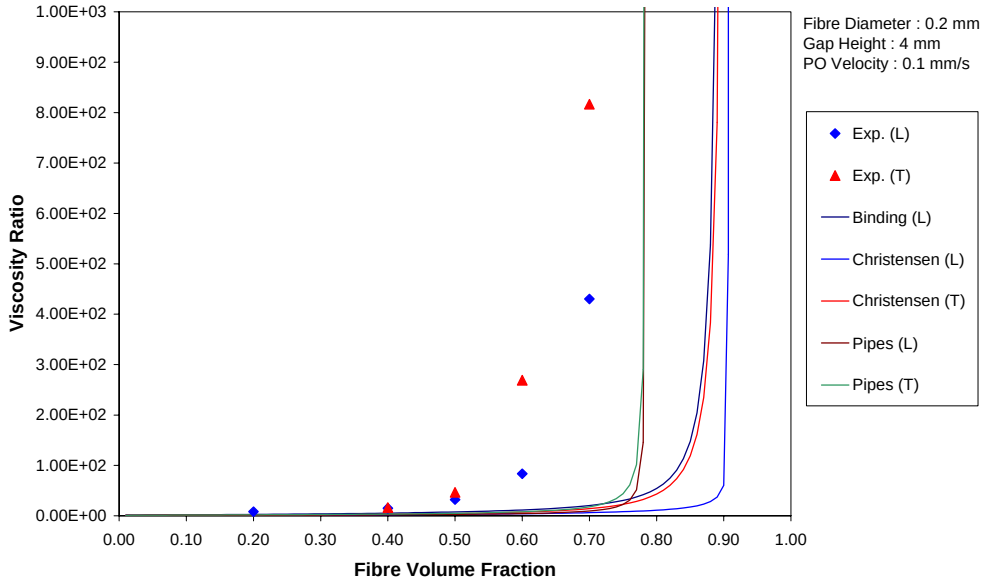

Figure 10: Comparison of the experimental and theoretical fibre concentration viscosity dependence.

Table 2: Comparison of experimental viscosity ratios with those arrived at by theoretical models, for the 0.2 mm fibre diameter model composites.

	Experiments		**Binding**	**Christensen**		**Pipes**	
Concentration %	$\frac{\eta_L}{\eta_M}$	$\frac{\eta_T}{\eta_M}$	$\frac{\eta_L}{\eta_M}$	$\frac{\eta_L}{\eta_M}$	$\frac{\eta_T}{\eta_M}$	$\frac{\eta_L}{\eta_M}$	$\frac{\eta_T}{\eta_M}$
20	7.99	*	2.84	1.50	1.58	1.51	2.02
40	14.89	16.25	5.32	2.37	2.89	2.25	3.49
50	32.14	46.38	7.54	3.08	4.31	2.97	4.95
60	83.38	268.97	11.49	4.20	7.14	4.47	7.94
70	430.23	816.63	20.34	6.20	14.23	9.44	17.88

Clearly, the values of η_L and η_T predicted by the models increasingly underestimate the measured values as the fibre concentration increases. The disparity between theory and experiment can be attributed to two factors. First, the models are based on geometrical arguments and do not take fibre-fibre interaction into consideration, which certainly does occur during the experiments and increases with fibre volume fraction. The fibre-fibre

interaction on a microscopic scale, i.e. two fibres moving with a relative velocity with an intervening Newtonian liquid, is the basic building block. This is representative of the macroscopic deformation behaviour of the whole composite. Secondly, in the models it is assumed that the fibres lie within the planes of shear and this will not necessarily be so during an experiment. If fibres become misaligned with the shear planes then a velocity gradient will exist along their length. Since the fibres are inextensible, there will be an increase in the drag on the fluid, which would translate into a higher measured viscosity. All of the theoretical models referred to base their assumptions on the idea of the continuum, which the experimental evidence certainly contradicts. Further, the viscosity ratios arrived at during a separate investigation on a real commercial composite [8], APC-2 indicate that the longitudinal value is approximately 1200 and the transverse value 500. These value are significantly greater than those predicted by the mathematical models for a fibre concentration of 60%.

CONCLUSIONS

A custom-built shear apparatus has been successfully developed and applied to investigate the steady-shear deformation of a model composite system consisting of straight, rigid fibres in a liquid, Newtonian matrix. The rheological behaviour of the composite has been investigated for different pull-out velocities and fibre concentrations with the following key results:

For high fibre concentrations, the longitudinal and transverse viscosities decrease rapidly with increasing pull-out velocity, before eventually levelling off to an approximately constant value. Calculations of the viscosities indicate that the transverse viscosity is much greater than the longitudinal viscosity over the entire range of velocities considered. The values of viscosity, for both the longitudinal and transverse directions, showed significant shear-thinning typical of a polymer melt.

Yield-like behaviour can occur when specimens are sheared along the direction of the fibres. This is most pronounced at high concentrations and low shear rates, and is believed to be caused by localised friction between neighbouring fibres. At high shear rates, these frictional contacts are easier to overcome and there is a transition to Newtonian behaviour.

Extensive re-organisation and re-orientation of fibres is observed for specimens sheared perpendicular to the fibre direction. With increasing concentration, there are indications that the properties of the composite become more solid-like.

The deformation of the composite at high shear rates and high concentration might be assisted by the formation of thin, resin-rich layers, resulting in a plug flow in which relatively little shearing occurs through the composite thickness.

The results from the model composite test series were also compared to those predicted by mathematical models. When the experimentally determined viscosity values for each fibre concentration were plotted against those predicted by the models, the models consistently underestimated the viscosities, in particular towards the higher levels of fibre concentration. It was speculated that the models describe purely idealised composite materials regarding their initial fibre distribution and the flow behaviour of perfectly aligned cylinders in a Newtonian matrix. As was evidenced during the experiments, a great deal of fibre-fibre interaction may take place during the shearing action of the composite, resulting in much larger shear forces being developed throughout the material, thus increasing the viscosity. Moreover, no model can predict the extremely complex nature of the fibre movement in the transverse direction, including the combined rotation and translation eventually leading to localised bunching and so on. Thus, the models derived to predict the viscosity of a composite, relative to the matrix viscosity, are quite limited in their characterisation of model composites, and hence, more significantly would be of limited benefit to predicting the shearing behaviour of a real commercial high fibre volume unidirectional composite system.

REFERENCES

[1] Stanley, W. F., and Mallon, P. J., "Intraply shear characterisation of a fibre reinforced thermoplastic composite", *Composites Part A: Applied Science and Manufacturing,* Volume 37, Issue 6 , June 2006, Pages 939-948

[2] Yurgatis, S. W., "Measurement of Fiber Misalignment in Aligned Fiber Composites and the Influence of Lamination on Misalignment Distribution", Proceedings American Society for Composites 3rd Technical Conference, 1998, pp. 587-596.

[3] Stanley, W.F., Roberts, R. and Mallon, P.J., "The Characterisation of the Shear Deformation Behaviour of Fibre-Reinforced Composites", Sixth International Conference on Automated Composites ICAC, Bristol, 23-24 September 1999, pp 31-44.

[4] Roberts, R.W. and Jones, R.S., ' Anisotropic Shear Flow in Continuous Fibre Composites', *Composites,* Volume 25, Issue 3, 1994, pp 171-176

[5] Roberts, R.W. and Jones, R.S., "Rheological Characterisation of Continuous Fibre Composites in Oscillatory Shear Flow", *Composites Manufacturing.* Volume 6, Number 3-4, 1995, pp 161-167

[6] Goshawk, J.A. and Jones, R.S., "Structure Reorganization during the Rheological Characterisation of Continuous Fibre-Reinforced Composites in Plane Shear", *Composites Part A: Applied Science and Manufacturing*, Volume 27, Issue 4, 1996, pp 279-286

[7] Roberts, R.W. and Jones, R.S., "Fibre Walk-Out During Small Amplitude Oscillatory Shear Flow

of Continuous Fibre Composites", *Composites Science and Technology,* Volume 58, Issue 6, 1998, pp 855-869

[8] Stanley, W. F., "Intraply Shear Characterisation of Fibre Reinforced Composites", Ph.D. Thesis , University of Limerick, October 2002

[9] Lenk, R. S., "Plastic Rheology", Maclaren, 1968.

[10] Binding, D. B., "Capillary and Contraction Flow of Long (Glass) Fibre Filled Polypropylene", *Composites Manufacturing*, Volume 2, Number 3/4, 1991, pp. 243-252

[11] Christensen, R. M., "Effective Viscous Flow Properties for Fiber Suspensions under Concentrated Conditions", Journal of Rheology, Volume 37, Number 1, 1993, pp. 103-121

[12] Pipes, R. B., "Anisotropic Viscosities of an Oriented Fiber Composite with a Power-Law Matrix", *Journal of Composite Materials*, Volume 26, Number 10, 1992, pp. 1536-1552

A CONSISTENT WOVEN FABRIC UNIT CELL AND PREPROCESSOR FOR MESO ANALYSES OF DEFORMATION AND PERMEABILITY

Gilles Hivet[1], Bertrand Laine[2], Philippe Boisse[3]

[1] *Laboratoire de Mécanique de Systèmes et des Procédés, UMR CNRS 8106, ENSAM-Polytech'Orleans, 8 rue Léonard de Vinci 45072 ORLEANS Cedex, France :* *Gilles.hivet@univ-orleans.fr*

[2] *Office National d'Etudes et de Recherches Aérospatiales*
29 avenue de la Division Leclerc, 92322 CHATILLON, France :
Bertrand.laine@onera.fr

[3] *Laboratoire de Mécanique des Contacts et des Solides*
UMR CNRS 5514, INSA de Lyon, Bâtiment Jacquard, Rue Jean Capelle, 69621 VILLEURBANNE Cedex, France : Philippe.boisse@insa-lyon.fr

ABSTRACT: Analyses of mechanical behaviour and resin flow at the mesoscopic scale, need accurate geometrical model and mesh of woven composite reinforcement unit cells. From experimental observations of yarn geometry for different cases of yarn structure and weave patterns a 3D model of the woven yarn shape is defined. From this yarn model, a consistent 3D geometrical model of fabrics is presented. This model ensures an accurate contact between yarns. It is called consistent because penetrations and spurious voids between warp and weft yarns are avoided. The yarn section shape varies along the trajectory, so that the influence of contact between yarns on their cross-section shape can be taken into account. A meshing preprocessor based on this geometrical model is then developed. Its consistency is important for analyses of the unit cell deformation and resin flow simulations within this strained woven cell.

KEYWORDS: Fabric, Unit cell, Geometrical model, Mesoscopical model, Meshing pre-processor, Geometrical consistency.

INTRODUCTION

In the LCM processes (RTM for example), the first step consists in forming the dry fabric before the resin is injected in a second step. Simulations of these processes (forming of the reinforcement and resin flow) are very interesting tools in order to predict the conditions for the feasibility of a composite part without expensive prototypes. Nevertheless, to perform these simulations, fabric mechanical properties and permeability properties have to be known. Experimental analyses may allow the obtaining of both mechanical properties and permeability [1][2][3][4][5]. These experiments are often expensive, time consuming and moreover don't enable to obtain results on non-existing fabrics. Thus, simulation is a possible alternative to obtain fabric properties. Since most of the fabrics are periodic material, it is possible to define an elementary cell from which the fabric can be constructed. The fabric behaviour (stiffness and permeability) is then deduced from the analysis of the elementary

cell. Finite element analysis is an efficient method to perform these computations, but it needs an accurate meshing of the unit cell [6][7]. The multi-scale nature of the fabric (macro-scale), composed of yarns (meso-scale), themselves composed of fibres (micro-scale) leads to a complicated geometry that is difficult to model. A simplified geometrical model has to be used to obtain the mesh of the elementary cell. Numerous models exist [8][9][10][11]. Nevertheless, meshes obtained with these models are not really well adapted to finite element analysis of the unit cell since contact surfaces between yarns are not described precisely enough. Interpenetration between yarns, likewise the existence of unreal voids (due to the modelling) significantly affects finite element results. The goal of this study is to present a tool for the definition of a consistent 3D geometrical model of fabric (i.e. that avoids interpenetration and spurious voids) and its application to a meshing pre-processor [12]. These meshes are applied to mesoscopic finite element simulations of fabric deformation [6] and injection simulation on the deformed reinforcement [13].

GEOMETRICAL MODELS OF THE WOVEN UNIT CELL

Experimental observations

Models have been developed to be able to give a description of fabric geometry at the initial state.

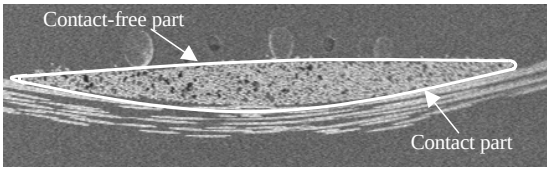

Fig.1 Transverse cut of a glass plain weave. Definition of yarn section

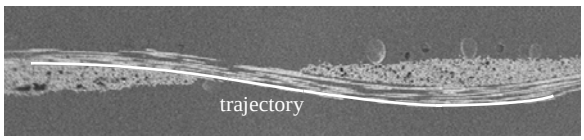

Fig 2 Transverse cut of a glass plain weave. Definition of the trajectory

There are two types of mesoscopic models. For the first type, yarns are assumed to be a composition of hinge rods. These rods can be deformable [8] or rigidities can be introduced by springs. The Kawabatta model is simple, but it is not 3D consistent. No 3D model can be made without interpenetration between the yarns of the two directions. Thus, coefficients identified concerning transverse crushing behavior are not physically consistent [6]. In the second type of model, the fabric is assumed to be the composition of 3D yarns that are supposed to be homogenous [14][15]. Their purpose is to give a better description of fabric geometry at the initial state. Most of them are based on the principle of a constant section with curvilinear trajectory. Curves used to represent elements can be sinusoids, splines, circles, or polynomials with elliptic section. Nevertheless, in general, consistency is not ensured. Some interpenetration can be noticed at the contact zone between warp and weft yarns. A main reason is that the constant section is not possible without interpenetration. The proposed geometrical model for fabrics will be consistent (no interpenetration and no spurious void). It is based on experimental observations. Then its application to a meshing preprocessor will be shown. Finally, we will apply the model to perform 3D finite element simulations on the elementary cell, in order to identify mechanical properties and permeabilities.

Different experimental methods can be used to observe the cross section and the trajectory. For many fabrics, the cohesion between fibers is not sufficient to ensure the conservation of

the cross section with contact. Thus, contact methods are not useable to identify dry fabrics geometry. Two other types of methods can be carried out. The first one is based on optical measures. These techniques enable to perform precise 3D geometrical measurements but only the visible parts can be obtained. The second one consists in coating a dry fabric sample with a resin to keep the original shape and then cut the sample. But the resin penetrates inside the yarn, between the fibers, and can modify its shape. None of these techniques is perfect but allowed us to obtain interesting information on the yarn section shape for a dry fabric at the initial state. Different materials and different weavings have been tested, some of them due to collaborations with University of Massachusetts Lowell (Fig. 1 to 5). It can be seen from these observations that the reorganization of the fibers in the yarn appears to be a very important phenomenon. The cross section is dissymmetric due to the contact, and it changes depending on boundary conditions on the fabric (Fig 1 to 5). Thus, the cross section has to change along the trajectory. It is clear that the assumption of a constant section is not correct.

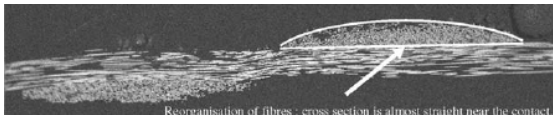

Fig. 3 Yarn cross section when the fabric is stretched in the opposite direction

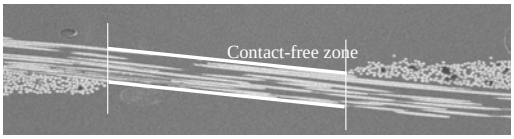

Fig 4 Transverse cut of a glass plain weave, contact free zone

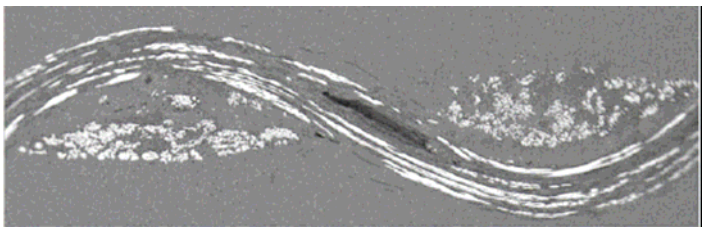

Fig 5 Transverse cut of a Twintex fabric

The second series of tests have been performed with optical measures. Some of the results are presented Fig. 6 for a carbon twill and a glass plain weave. The specificity of these two fabrics is that the carbon yarns are coated and the glass yarns are twisted. The consequence is higher cohesion between the fibers in the yarn. Here again, the cross section is dissymmetric. The contact zone between the yarns is large and the contact mainly influences the cross section shape. But the reorganization of fibers is not sufficient to get to the lenticular shape previously observed. There are lateral zones between the contact and contact-free sides.

Consistent 3D model of the geometry

The conclusion of all these experiments is that three different zones can be differentiated for the cross section: a contact zone, a contact-free zone, and a lateral zone that can be limited to only two points in case of a weak cohesion of fibers (Fig. 7). In the general case, these three zones can be approached through four conic curves for instance (parabolas, circles). Values chosen for the lateral conics parameters will make these vary from straight line to dot. Thus, all types of yarns observed can be represented using this model. For plain weave fabrics, the symmetry according to the vertical plane leads to a simplified form of the cross section.

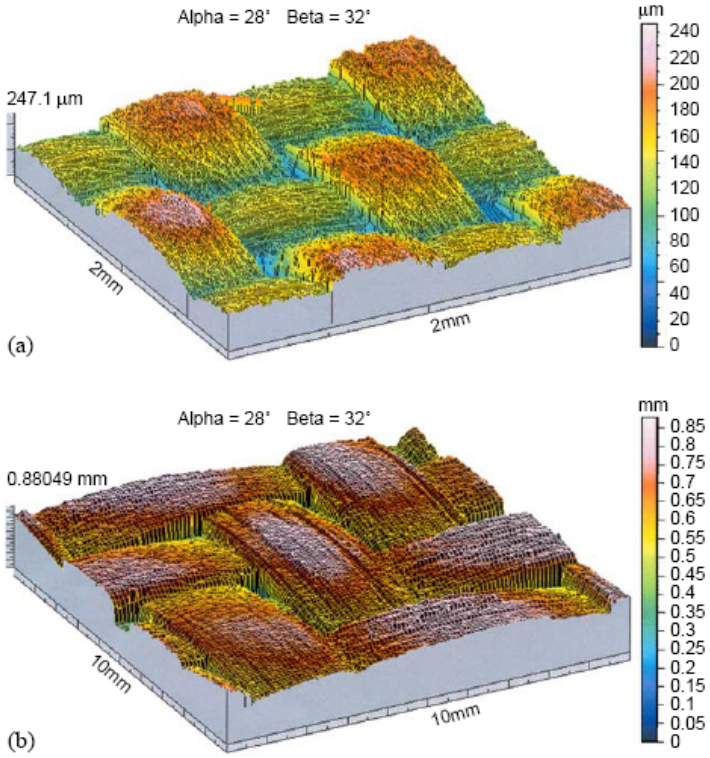

Fig 6. 3D optical measure of dry fabrics at the initial state
(a) unbalanced glass plain weave (b) carbon twill 2 ∗ 2..

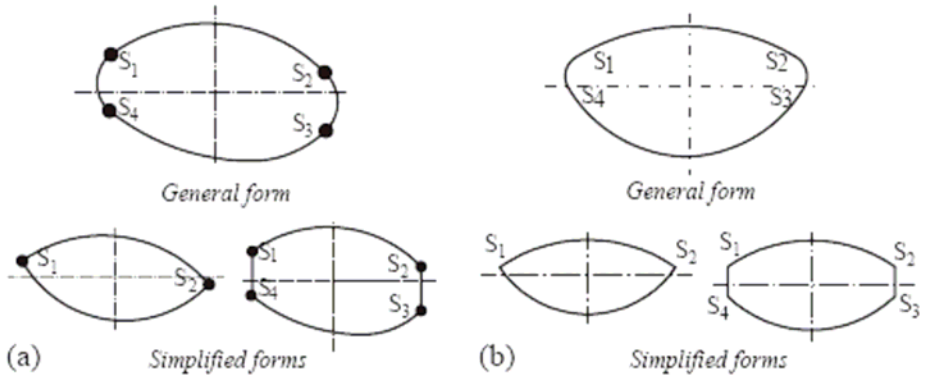

Fig 7. Models for the cross section of a 2D fabric: (a) generic (b) plain weave.

The trajectory is constrained by the necessary 3D consistency of the fabric model. For plain weaves, the contact zone will consist in the same conic as that of the cross section (Fig 1.). In the contact-free zone, no lateral load is applied to the yarn. Given that the bending rigidity of yarns is very weak, the contact-free part of the trajectory should be straight (Fig. 4). So, the trajectory is composed of conics and straight segments. Tangency conditions between conics and segments must be ensured.

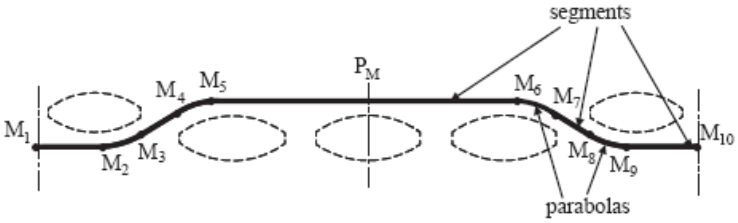

Fig. 8 Model of a trajectory for twill 3 ∗2.

For twills, the problem is a little bit more complex.A yarn passes over m and under n transverse yarns. When this yarn passes over the m transverse yarns, two cases may be considered:

• The yarn follows the original curvature of the transverse yarn cross sections. In this case, the yarn is curved when contact occurs.

• The transverse cross section flattens and the yarn keeps almost straight.

The second assumption is much more consistent with our previous observations. Moreover, when the fabric is deformed, tension in the fibers will make this second model more suitable. The trajectory obtained for any twill (or satin) is then very simple, which is a good point for model identification. This is presented in Fig. 8. Variations of section shape along the yarn are taken into account using control sections at control points (Fig. 9)[12].

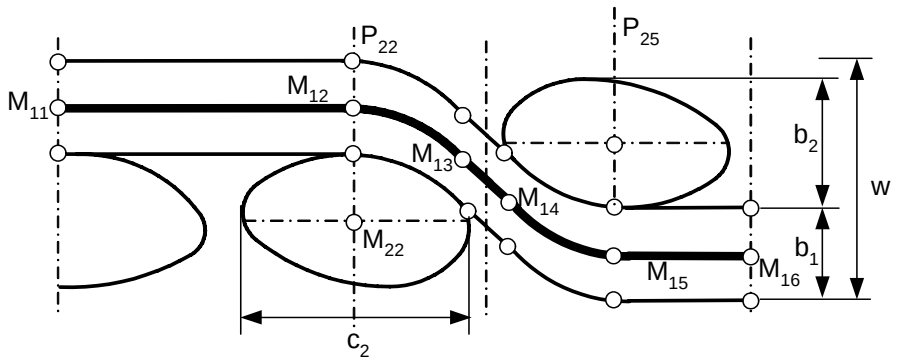

Fig. 9. Transverse cut in the direction 1 of the simplified model for a twill m*n.

The complete 3D model of the yarn is obtained through a smooth interpolation between the control sections, which respects the imposed trajectory. The interpolation is obtained using CAD software, such as PROEngineer®, which includes a “swept blend” feature that is able to build volumes using control sections and trajectories. The elementary cell of fabric is obtained by assembling m+n yarns. Figure 10 and 11 present the obtained geometry in the case of a 3*2 twill and of a 4*3 twill. Sections shapes at the beginning and the end of the contact are prescribed to ensure consistency. The model is said to be “consistent” because it guarantees there is no penetration between warp and weft yarns, and it imposes that contact happens where it should take place.

APPLICATIONS TO MECHANICAL AND PERMEABILITY PROPERTIES DETERMINATION

A meshing software such as Patran® can be used to obtain a finite element mesh from geometries obtained using the consistent 3D model. A PCL routine enables to generate automatically a hexahedral mesh of the elementary cell. In that way, a 3D geometrical

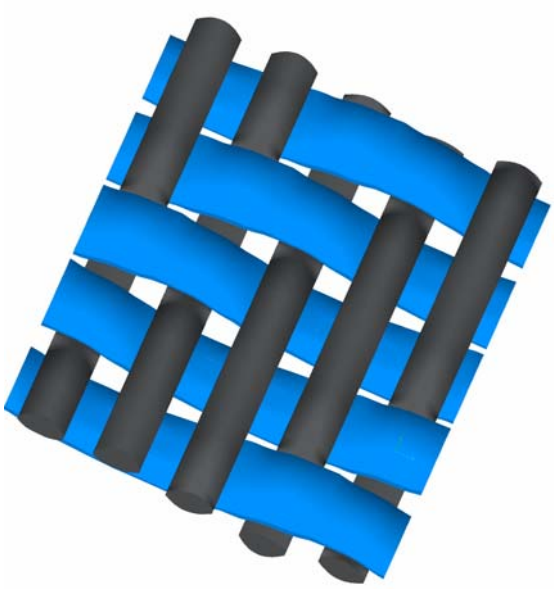

Fig. 10 3D model of a carbon twill 3*2

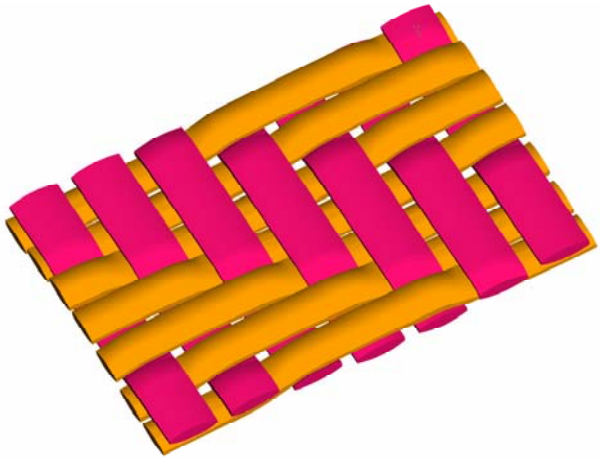

Fig 11 3D model of a carbon twill 4*3

meshing pre-processor of woven unit cells is defined. The mesh obtained in the case of a plain weave is presented figure 12. These meshes permit to perform virtual tests in order to obtain the mechanical behaviour of the fabric from finite element simulations [6]. These analyses permit to investigate the influence of different parameters. They also allow analysing fabrics before their manufacturing. An example of the shear deformation of twill 2*2 is presented figure 13.

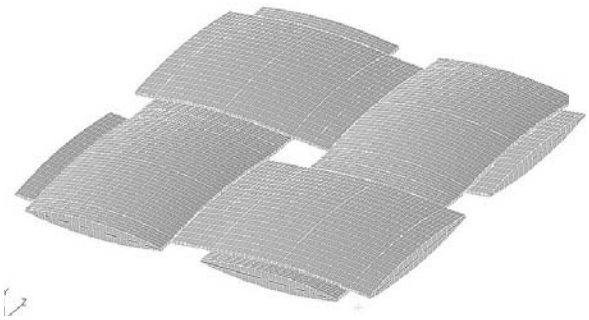

Fig. 12 3D mesh for a plain weave fabric

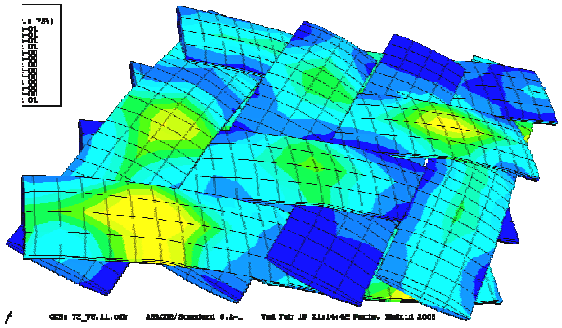

Fig 13 Finite element simulation of the shear deformation of a twill 2*2

The 3D preprocessor is also used for the generation of the channel network geometry that is the complementary volume of the reinforcement. The obtained mesh (Fig. 12) permits to simulate the resin flow (Fig. 13) and to deduce the permeability matrix [13].

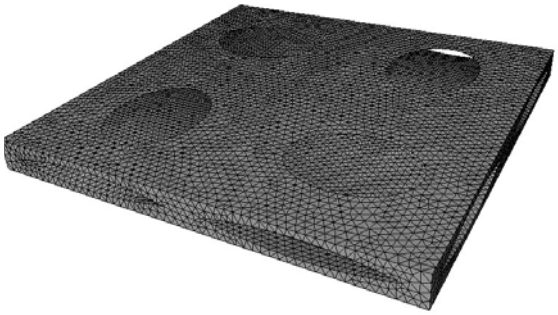

Fig. 14 Mesh of the complementary part of a plain weave

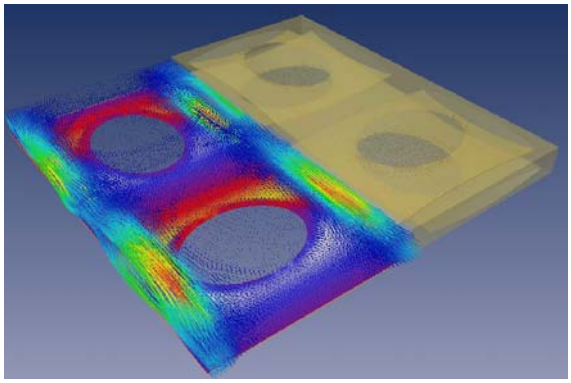

Fig. 15 Resin flow in a glass plain weave

CONCLUSION

A consistent 3D geometrical model for woven fabrics has been defined. It is adapted to most weavings. It insures no penetrations and no spurious voids in the contact zone between warp and weft yarns. It is the first stage of a 3D geometrical meshing preprocessor of the unit woven cells. Using PROEngineer® and Patran®, hexahedral meshing of the fabric geometrical model can be obtained. This permits 3D finite element analyses of elementary cells in order to determine the mechanical behaviour properties by virtuel tests. It can also be used to simulate resin flow in the complementary volume of the yarns and in that way calculate the permeability parameters. Future developments will concern more complex types of fabrics, such as 2.5D or 3D fabric.

ACKNOWLEDGMENTS

This work has been partly made within the European specific targeted research project ITOOL ‘Integrated Tool for Simulation of Textile Composites’,

REFERENCES

1. Prodromou, A.G. and J. Chen, On the relationship between shear angle and wrinkling of textile composite preforms. *Composites Part A: Applied Science and Manufacturing*, 1997, 28, 5, p. 491-503

2. Buet-Gautier K, Boisse P. Experimental analysis and modeling of biaxial mechanical behavior of woven composite reinforcements, *Experimental Mechanics*, 41-3, 2001, p. 260-269.

3. Cao, H. S. Cheng, T. X. Yu, B. Zhu, X. M. Tao, S.V. Lomov, T. Stoilova, I. Verpoest, P. Boisse, J. Launay, G. Hivet, L. Liu, J. Chen, E.F.d. Graaf, R. Akkerman, A cooperative benchmark effort on testing of woven composites, *Proc. of ESAFORM7 Conference*, Norway, 2004, p. 305-308.

4. Gauvin, R., Trochu, F., Lemenn, Y., Diallo, L. Permeability measurement and flow simulation through fibre reinforcement. *Polymer Composites*, 1996, 17, 34-42.

5. Hoes K., Dinescu D., Sol H., Parnas R.S. and Lomov S.V., Study of nesting induced scatter of permeability values in layered reinforcement fabrics , *Composites Part A: Applied Science and Manufacturing*, 35, 2004, p. 1407-1418

6. Boisse, P., Gasser, A., and Hivet, G., Analyses of fabric behaviour : determination of the biaxial tension-strain surfaces and their use in forming simulations. *Composites Part A: Applied Science and Manufacturing*, 32, 2001. p. 1395-1414.

7. Fournier R., Coupez T. and Vincent M., (2005), 'Numerical determination of the permeability of fibre reinforcement for the RTM process', *European Finite Element Journal*, 14 (6-7), 803-818

8. Kawabata, S., M. Niwa, and H. Kawai, The finite-deformation theory of plain-weave fabrics. Part I : The biaxial deformation theory. *J. Textile Institute*, 64, 1973, p. 21-46.

9. Kuhn, J. and P. Charalambides, Modeling of plain weave fabric composite geometry. *J. Comp. Mat*., 33, 1999, p. 188-220.

10. Lomov, S.V., Gusakov, A.V., Huysmans, G., Prodomou, A., Verpoest, I. Textile geometry preprocessor for meso-mechanical models of woven composites. *Composites Science & Technology*, 60, 2000, p. 2083-2095.

11. Robitaille, F., Long, A.C., Jones I.A., Rudd, C.D. Automatically generated geometric descriptions of textile and composite unit cells, *Composites Part A: Applied Science and Manufacturing*, 34, 2003, p. 303-312.

12. Hivet G., Boisse P., Consistent 3D geometrical model of fabric elementary cell. Application to a meshing preprocessor for 3D finite element analysis., *Finite Elements in Analysis and Design*, 42, 2005, 25-49

13. Laine B., Boust F., Boisse P., Hivet G., Lomov S., Fanget A., Perméabilité des renforts fibreux. Etude des écarts expérience-prédiction. *Revue des composites et matéraiux avancés*, 2006, 339-354

14. Kuhn, J. and P. Charalambides, Modeling of plain weave fabric composite geometry. *J. Composite Materials*, 1999. 33(3): p. 188-220.

15. S.V. Lomov, A.V. Gusakov, G. Huysmans, A. Prodomou, I. Verpoest, Textile geometry preprocessor for meso-mechanical models of woven composites, *Composites Science & Technology*. 60 (11) (2000) 2083–2095

Session 5

MATERIALS CHARACTERISATION - I

STATISTICAL CORRELATIONS IN THE PERMEABILITY TENSOR

Laura M. McGrath, Qiang Liu and Richard S. Parnas

Institute of Materials Science: Polymer Program, University of Connecticut, Storrs, CT, 06269, USA: rparnas@ims.uconn.edu

ABSTRACT: The determination of accurate permeability values is critical to process simulations for Resin Transfer Molding (RTM). New instrumentation was developed for high throughput permeability measurements. The design extends the work of Hoes [1] with new sensor design, much larger sensor pattern, and new analysis software. The new set-up was used to measure the permeability of a basalt woven 3/1 twill fabric. A comparison with previous work on 2/2 twill and plain woven fabrics reveals a relationship between the breadth of the anisotropy distribution, the principal components of the permeability tensor and fabric structure. This relationship has implications for manufacturing reliability, and may help explain why certain fabrics process much more consistently than others do.

KEYWORDS: Permeability, Reliability

INTRODUCTION

Accurate permeability values are extremely important for resin flow simulation and mold design in resin transfer molding (RTM). RTM has gained rapid acceptance [2] among composite processing techniques for its ability to mold large, complex shaped parts with a good surface finish. Yet, problems often occur due to non-uniform impregnation, void and dry spot formation [3], and lengthy impregnation cycles. If the permeability is known, the flow behavior can be properly computed as well as the mold clamping pressure, strength of the mold for shape retention [4] and pressure distributions in the mold.

Permeability is dependent on the pore geometry of the porous filler media of the composite [5]. Analytical models [6] have been developed to calculate the permeability of fabric materials yet they often do not take into account the actual complexity of the pore geometry. Numerical models are either very computationally intensive [7] or need time-consuming acquisition of the 3-D pore structure [8].

Permeability values are primarily obtained by experimentation via unidirectional flow (UD) methods (saturated or unsaturated) [9] or radial flow methods [9a, 9c, 9d]. In the UD flow experiments, permeability values in a specified direction are measured. In a saturated UD experiment, the fabric is compressed in a mold and the test fluid is forced through the mold. The flow rate and the pressure drop are recorded versus the length of the mold at steady-state [9a]. Whereas, in an unsaturated UD experiment, the fluid flows through the dry fiber bed, replacing the air present in the material. UD experiments are susceptible to edge effect errors (*i.e.* the fluid prefers the path of least resistance: flowing through the space devoid of fabric at the mold wall). Another drawback is that at least three measurements must be done to fully characterize the in-plane permeability tensor.

The radial test (or 2D test) can only be used with unsaturated flow methods. Fluid is injected into the center of the mold under either constant injection flow rate or constant injection pressure. The fluid superficial velocity can be determined with a transparent top plate and a video camera. The main advantage of the 2D test is that it allows the determination of both the in-plane permeability components and their angle in one single experiment [1].

The work presented here builds on the work of Hoes et al. [10], in which we have constructed a 2D unsaturated experimental set-up with two stiff metal plates and electrical sensors which record the flow front progression as a function of time. The apparatus presented supports a highly automated system that can be replicated with high frequency (5-10 per hr). As permeability is a statistically distributed parameter it can only be characterized by multiple experiments. With improved test frequency, we are now able to address the large standard deviation that prevails in permeability reporting. The rapid measurement methods also allow statistical corroborations to be made of the effects of fabric structure and anisotropy on permeability.

EXPERIMENTAL

Materials

The permeability measurements, replicated 64 times, were obtained for 6 layers of preformed basalt fabric, twill 3/1, from Albarrie Co., Canada. The properties are shown in Table 1. The 6 layers compressed to 4.661 mm in thickness resulting in a fiber vol. % of 35.8%. Data from the bottom and top plates are analyzed individually, in order to discern any non-uniformities in the vertical distribution of fluid. The angle, θ, between the warp direction of the fabric and the permeability principle axis is reported.

Three glass fabrics (Syncoglas R420, Syncoglas RE144/255, and CNF crowfoot) (Table 1) were also tested to verify the operation of our apparatus and to compare with previous work [1, 8, 9a].

Table 1. Properties of fabrics used in permeability measurements

Properties	*Basalt Fabric*	*Syncoglas R420*	*Syncoglas RE144/255*	*CNF crowfoot*
Areal Density, g/m^2	750	420	380	2900
Fiber Density, g/cm^3	2.7	2.52	2.52	2.52
Warp Yarn Linear Density, tex (g/km)	660	600	310	66.14
Weft Yarn Linear Density, tex (g/km)	330	600	580	33.07
Weave pattern	Twill 3/1	Plain weave 1/1	Twill 2/2	Twill 3/1
Yarn #/10 cm in warp	59.5	36.0	45	220
Yarn #/10 cm in weft	78	34.0	40.8	213

The permeability measurements were conducted with diluted corn syrup (DCS), (DI H_2O:'Nugget' brand light corn syrup, 11:3). The DCS has a viscosity near 0.1 Pa·s at room

temperature and is Newtonian in the shear rate ranges used in experimentation. The average viscosity of the DCS before and after experimentation was used.

Sensor Design

Electrical sensors made from a piece of copper wire with nylon insulation were fixed into the mold plate through a small screw. An O-ring is compressed when the sensor is screwed into the plate, sealing the mold and locking the sensor wire into place. The design permits the sensor to be slightly recessed below the plate level if desired which allows the permeability measurement of electrically conductive fabric. The sensor plate is placed at a low electrical potential (e.g. 5V). Thus, when an electrically non-conductive fabric is used in combination with a conductive test fluid, the fluid will generate a conductive bridge between the plate and the sensor core. This allows the flow front progression to be recorded as a function of time.

The back end of the copper wire is soldered to a ribbon cable leading to data acquisition cards in the computer. Two cards (National Instruments PCI-DIO 96), one for each plate, are used. There are 96 digital channels on each card, permitting 96 sensors in each plate. In the center of the top plate, a sensor is positioned to detect the incoming fluid and to begin the experiment clock.

Mold Design

Stainless steel mold plates, 40 cm long, 40 cm wide, and 3.2 cm thick (Figure 1) were designed with channels 1.9 cm wide (in the rear of each plate) at angle increments of 22.5°. Either 6 or 7 sensors are evenly spaced and inserted into the channels through the mold wall to detect fluid flow.

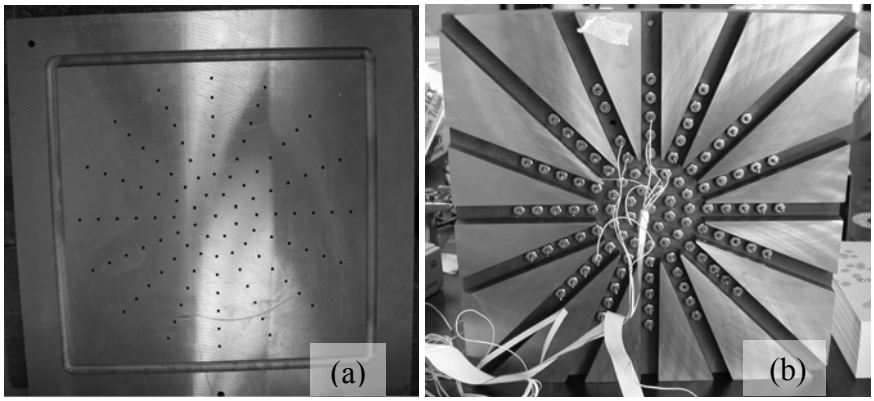

Figure 1. Top mold plate with mounted sensors (a) front view and (b) rear view

The bottom plate is the same as the top plate with the exception of a fluid injection port in the center. A hole of the same size as the injection port is punched in the middle of the fabric to allow uniform fluid penetration throughout the perform thickness.

Fluid Injection and Data Acquisition

The unsaturated 2D permeability experiment is conducted at a constant flow rate. The fluid is pumped into the mold by a Masterflex I/P pump (model no. 77601-10) through a flow meter and a control valve. A pressure transducer is positioned in the injection tube just below the surface of the sensor plate to measure the injection pressure and is connected to the PC. The experiment is monitored and controlled through Labview software which provides the permeability in a few seconds after the experiment concludes. The sensor trigger times from the top plate and from the bottom plate can be collected and analyzed separately to check for flow non-uniformity across the preform thickness.

Data Analysis

Data acquired from permeability experiments was derived in order to determine the flow pattern and the in-plane permeability tensor. The flow pattern, obtained from sensor trigger times, provides the shape of the advancing elliptical flow front, i.e., the angle of the permeability principle axes or the anisotropic ratio of the elliptical flow front. As the flow front is represented by an ellipse (Figure 2), the data acquired is used to determine the angle θ and the ratio a/b.

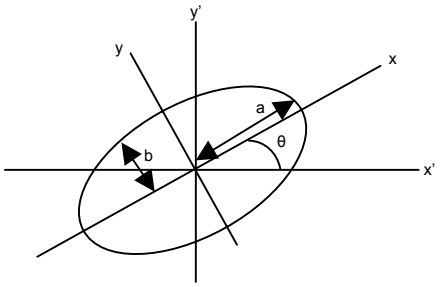

Figure 2. Ellipse representing the fluid flow front, with x' and y' as the lab coordinates

Labview data acquisition program establishes the sensor trigger time as the elapsed time from when the fluid hits the center sensor on the top plate (time = t_o) until the fluid triggers each sensor (time = t). When the flow front hits any sensor at time t, the distance between that sensor and the plate center, d, can be expressed as:

$$d = \sqrt{\frac{(m_1 t + r_o^2 + c)(1 + \tan^2(\alpha - \theta))}{\frac{1}{a/b} + \frac{a}{b}\tan^2(\alpha - \theta)}} \qquad (1)$$

Where:
α = angle between sensor line and lab coordinate axis x'
r_o = radius of injection hole, 3.188 mm
c = constant, accounts for uncertainty in the initial conditions at $t = 0$.
t = time at which a sensor is triggered

And m_1 is a function of flow rate and fabric properties:

$$m_1 = \frac{Q}{\pi h \phi} \tag{2}$$

Where:
Q = injection flow rate, h = preform thickness, ϕ = porosity

Rearranging eq. 1 provides the sensor time as a function of the fluid flow front shape and the experimental parameters:

$$t = \frac{d^2\left[1+(a/b)^2\tan^2(\alpha-\theta)\right]}{m_1(a/b)\left[1+\tan^2(\alpha-\theta)\right]} - \frac{r_o^2+c}{m_1} \tag{3}$$

In eq. 3, parameters d and α are known for each sensor. Parameter m_1 is known once the injection flow is set, and the preform thickness and porosity are chosen. Each sensor trigger time t is measured and recorded by the data acquisition system. Thus eq. 3 can be written for each sensor, providing an over specified set of equations for the unknowns: a/b, θ, and c. The best fit values of (a/b), θ and c are found through iteration.

After the flow front shape is found, the inlet pressure information is used to find the principal components of the permeability tensor. For constant injection rate, the increase of the mold inlet pressure over time is closely approximated by [7]:

$$P_{in} = \frac{\mu Q}{4\pi h K_{rr}} \ln\left(1 + \frac{Qt}{\phi \pi h r_0^{\,2}} + \frac{c}{r_0^{\,2}}\right) \tag{4}$$

Where:
P_{in} = inlet pressure , K_{rr}= geometric mean of K_{xx} *and* K_{yy}, $\sqrt{K_{xx}K_{yy}}$

Eq. 4 differs from previous derivations [7] because the parameter c is included to account for non-ideal entrance effects.

Plotting P_{in} vs. $\ln(1+\frac{Qt}{\phi\pi h r_0^{\,2}}+\frac{c}{r_0^{\,2}})$ results in a line of slope, $\frac{\mu Q}{4\pi h K_{rr}}$, from which K_{rr} is obtained. As K_{rr} is equal to the geometric mean of K_{xx} and K_{yy} and to (a/b), $(a/b)=\sqrt{K_{xx}/K_{yy}}$, the individual values of K_{xx} *and* K_{yy} are easily found.

RESULTS AND DISCUSSION

Basalt Permeability

The basalt in plane permeability data is shown in Table 2. The data in each cell is given as average ± standard deviation. The unit for permeability is length^2, and 1 m^2 = 1.01325 × 10^{12} Darcy [11]. The angle θ, between the warp direction of the fabric and the permeability principle axis (the one with larger permeability values), is defined as clockwise from the former to the latter, seen from above.

The results derived from the sensors in the bottom and top plates correspond well together corresponding to good fluid flow in all basalt layers uniformly. The square root of the permeability anisotropic ratio is just slightly larger than 1, which also corresponds well with visual observations of the anisotropic ratio of the elliptical flow front. At 35.8% fiber vol. %, the alignment of the principle axis for the basalt fabric, K_{xx}, is quite close to the warp direction, as indicated by the small angle θ in Table 2.

Table 2. In-plane permeability results for basalt fabric

	Anisotropic ratio of permeability (l^2)	*Angle θ, Deg*	*K_{xx}, Darcy*	*K_{yy}, Darcy*
Bottom Plate Data	1.374 ± 0.097	-3.47 ± 5.60	857.85 ± 218.88	625.71 ± 174.19
Top Plate Data	1.389 ± 0.091	-6.34 ± 6.35	858.43 ± 227.46	617.98 ± 166.71

The statistical distribution of the basalt permeability data is shown in Figure 3.The anisotropic ratio ('a' in Figure 3c) of the basalt fabric has a much smaller standard deviation than observed in previous measurements where sufficient data was collected to generate reliable statistics. This smaller standard deviation may be related to a high correlation between K_{xx} and K_{yy}. To determine the correlation between K_{xx} and K_{yy}, plots as shown in Figure 5 were constructed. Because the permeability principal axis is very close to the warp direction, we use K_{warp} to represent K_{xx} and K_{weft} to represent K_{yy}.

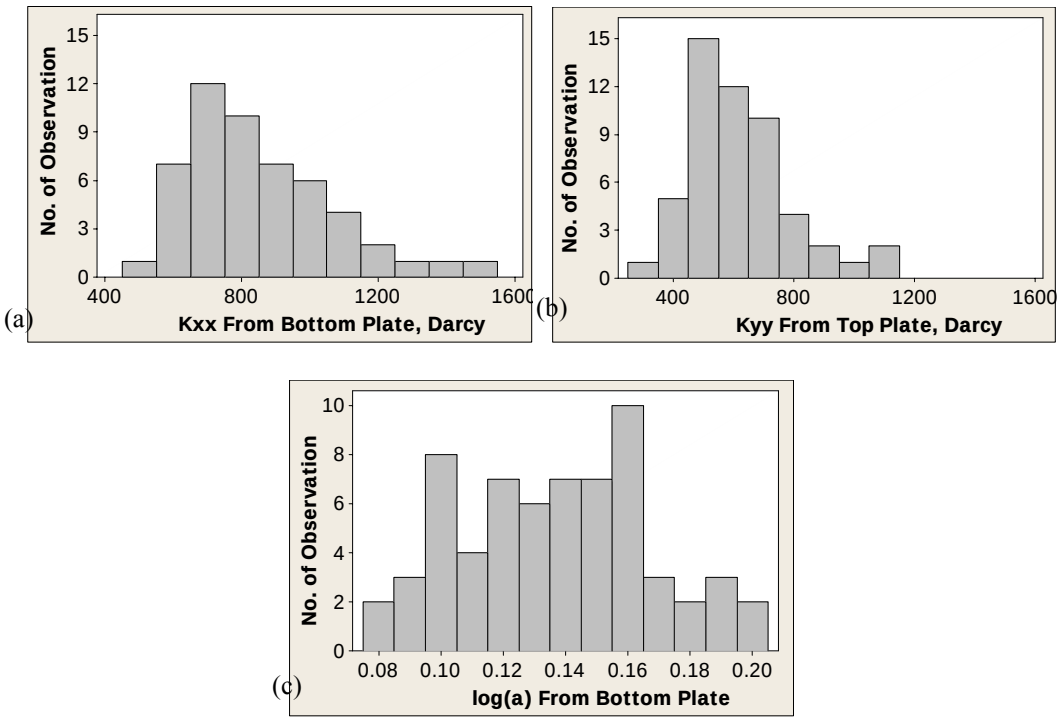

Figure 3. Permeability Distribution

For basalt, a large correlation coefficient, R^2, between K_{xx} and K_{yy} is shown in Figure 4a and compared to Figures 4b and 4c of R420 and RE 144/255 glass fabrics [1]. Glass fabric, RE 144/255 (Figure 4c), has a much smaller correlation between K_{warp} and K_{weft}, compared to the

basalt fabric where as R420 glass fabric (Figure 4b) has negligible correlation. The t-test is used for all three fabrics to determine if the correlation between K_{warp} and K_{weft} is significant. After the t statistic was calculated, the P-value associated with that t statistic was found from the t probability distribution. The P-value provides the confidence level in the (significance) correlation coefficient. For example, the P-value of the correlation coefficient of basalt fabric is less than 0.001, which means that this correlation coefficient is significant at a greater than 99.9% confidence level. (More precisely, there is less than 0.1% chance of being wrong by rejecting the hypothesis that the correlation coefficient is insignificant). With similar reasoning, we find that the correlation coefficient for RE144/255, a 2/2 twill glass fabric, is also significant with a greater than 99.9% confidence level. However, the P value for the R420 plain weave glass fabric is 0.327. This means that the correlation coefficient between K_{warp} and K_{weft} is not significant for the R420 fabric.

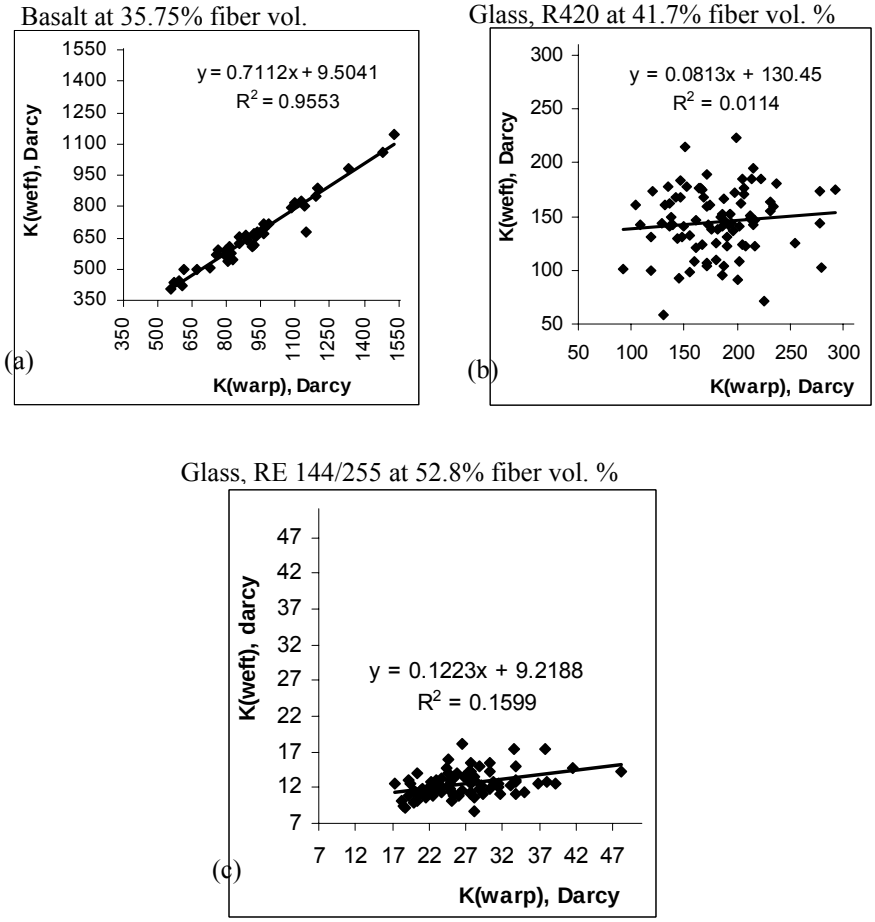

Figure 4. Permeability correlations in warp and weft directions for different fabrics.

Such large differences in the correlation coefficients between these fabrics may be caused by the difference in the fabric structures. It is known [1] that broad permeability distributions can result from the nesting of yarns in the neighboring layers (or the relative shifts between neighboring layers). For the fabrics discussed above, nesting probably causes the broad distribution of the components of the permeability tensor. However, nesting appears to have different effects on the distribution of the permeability anisotropy, depending upon the fabric structure. Plain weave R420 has the broadest distribution of anisotropy and basalt twill fabric the narrowest.

The high correlation between K_{warp} and K_{weft} for basalt fabric is desirable for RTM processing because a consistent flow pattern will be obtained. In the cases where a broad distribution of anisotropy is obtained and there is little correlation between K_{warp} and K_{weft}, variable flow patterns may occur for different injections, rendering control and part-to-part consistency difficult to achieve.

CONCLUSIONS

A new sensor system and data analysis procedure to derive flow pattern was developed for the in-plane permeability measurement with expected use for electrically conductive reinforcement. This apparatus can be used to calculate the flow front orientation angle in addition to the anisotropy and principal components of the permeability tensor. Measurements of the permeability of basalt woven twill showed that our experiments are reproducible and consistent with previous work. These measurements reveal that different fabric structures may have very different anisotropy distributions even when the distributions of the components of the permeability tensor are similar. Fabrics with a high degree of correlation between permeability components and a small variability in anisotropy are expected to be easier to process.

ACKNOWLEDGEMENTS

The authors recognize the financial support (grant no. 4000020035) of Oak Ridge National Laboratory, a multi-program science and technology laboratory managed for the U.S. Department of Energy. Thanks to Kevin Horner (Albarrie Co., Canada) for their generous donation of the basalt fabric.

REFERENCES

1. Kris Hoes, PhD Thesis, Vrije Universiteit Brussel, Brussels, (2003).
2. (a) K. L. Adams, W. B. Russel and L. Rebenfeld, International Journal of Multiphase Flow, 14 (2), 203-215 (1988). (b) Jingyi Xu and Yulu Ma, China Plastics, 6 (1), 9-16 (1992).
3. L. Baichen, S. Bickerton and S. G. Advani, Composites, 27A (2), 135-141 (1996).
4. R. S. Parnas, Liquid Composite Molding, Carl Hanser Verlag, Munchen, 2000, 5
5. F. A. L. Dullien, Porous Media: Fluid Transport and Pore Structure, 2nd Ed., Academic Press, Inc. San Diego, California, 1992, pp. 6
6. T. A. K. Sadio, S. G. Advani, R. S. Parnas, International Journal of Multiphase Flow, 21 (5), 755-774, (1995).
7. T. Kruckenberg and R. Paton, Resin Transfer Molding for Aerospace Structures, Kluwer Academic Publishers, Dordrecht, The Netherlands, 1998, pp. 196
8. J.-F. Delerue, S. V. Lomov, R. S. Parnas, I. Verpoest, M. Wevers Polymer Composites, 24 (3), 344-357, (2003).
9. (a) R. S. Parnas and A. J. Salem, Polymer Composites, 14 (5), 383-394 (1993). (b) P. Ferland, D. Guittard and F. Trochu, Polymer Composites, 17 (1), 149-158, (1996). (c) R. Gauvin, et. al., Polymer Composites, 17 (1), 34-42, (1996). (d) R. B. Gebart and P. Linström, Polymer Composites, 17 (1), 43-51, (1996). (e) T. S. Lundström, et. al., Composites, 31A (1), 29-43, (2000).
10. Kris Hoes, et. al., Composites, 33A, 959-969, (2002).
11. R. Pan et al., Polymer Composites, 21 (6), 996-1006, (2000).

MEASUREMENT OF PERMEABILITY OF CONTINUOUS FILAMENT MAT GLASS-FIBRE REINFORCEMENTS BY SATURATED RADIAL AIRFLOW

R. Pomeroy [1], S. Grove [1], J. Summerscales [1], Y. Wang [1], A. Harper[2]

[1] *School of Engineering, Faculty of Technology, University of Plymouth, Drakes Circus, Plymouth PL4 8AA, UK :* ross.pomeroy@plymouth.ac.uk, s.grove@plymouth.ac.uk, j.summerscales@plymouth.ac.uk , yu.wang@plymouth.ac.uk

[2] *Plastech Thermoset Tectonics Ltd., Manufacturing Technology Centre, Chilsworthy Beam, Gunnislake, Cornwall, PL18 9AT, UK:* rtmharper@aol.com

ABSTRACT: The measurement of fibre reinforcement permeability is important for the understanding, optimisation and modelling of RTM and resin infusion processes. This work investigates the use of a saturated radial air flow experiment for measuring the permeability of continuous filament mat (CFM), which is a common reinforcement type used for industrial RTM parts. The use of air, rather than liquid resin, is cleaner, quicker and potentially easier to control. The paper considers the problems inherent in using a compressible fluid, and the requirements for maintaining laminar flow. It describes the instrumentation used for flow and pressure measurement, and the effect of varying flow rate. Results compare favourably with published permeability values based on liquid flow experiments, and are independent of flow rate within the range of values investigated.

KEYWORDS: Continuous filament mat, air permeability, saturated radial flow, resin transfer moulding.

INTRODUCTION

Resin Transfer Moulding (RTM) and Light-RTM (L-RTM) are closed mould processes used for the manufacture of fibre-reinforced polymer composite components, ranging from industrial to aerospace applications. Continuous filament mat (CFM) glass-fibre reinforcement materials are suitable for many industrial RTM parts, due to their lofty, in-plane isotropic nature and low cost compared to more organised fabrics. They are relatively preformable, and produce composites with moderate fibre content (typically less than about 40% by volume).

There is both industrial and academic interest in the characterisation and understanding of the factors affecting CFM permeability (K). This is conventionally defined by Darcy's law [1-3], where the volumetric flow rate (Q) of resin through cross-section A depends on the pressure gradient (∇P) and the resin viscosity (μ):

$$Q = \frac{KA}{\mu}.\nabla P \tag{1}$$

The measurement of permeability is usually carried out by observing either one-dimensional linear or radial flow [2, 4]. Either a transient/wetting flow or a steady/saturated flow may be used, and either the flow rate or the pressure gradient must be held constant. There is a large body of literature on this subject [1, 4-13], including some novel approaches to permeability measurement [14-16].

The traditional approach is to use either thermosetting resin or some substitute liquid of comparable viscosity. This is messy, involves high in-mould pressures and is 'destructive', meaning that the technique is not suitable for on-line, in-situ measurement in an industrial context. To combat these problems, investigations involving the flow of air and other gases instead of resin have been made [17-23], which range from macro-scale permeability testing through to localised measurements using arrays of sensors. These have been used for localised preform defect detection and investigation of inertia effects.

The use of air flow is therefore an attractive proposition for permeability measurement, and prompted this work to investigate the saturated radial flow of air for the permeability characterisation of CFM at various fibre fractions.

THEORY

Air Flow Considerations

Various concerns are associated with the use of air as a fluid for permeability measurements. These including matching the creeping or laminar flow seen in RTM processing [24] and the density and viscosity effects of using a compressible fluid. In the literature, both flow characteristics and compressibility are discussed in terms of the Reynolds number (Re):

$$\mathrm{Re} = \frac{\rho l u}{\mu} \tag{2}$$

where ρ is density, u is flow velocity and l is a reference length.

The Darcy model is considered to be satisfied at Re < 1 [25], therefore suggesting that numbers at these levels reflect laminar flow. In addition, it is considered that the compressibility of gases and inertia effects may be ignored at Re < 0.1 [24, 26]. Here, though, care must be taken; due to the impracticalities of measuring localised flow velocities and pore diameters the reference length (l) and flow velocity (u) are taken as fibre diameter and superficial flow velocity respectively. Therefore, as flow path diameters and localised flow differ considerably between CFM and ordered fibres, inconsistencies may exist between the flow regimes. However, the literature does document appropriate Reynolds numbers and the use of specific flow rates of gases in order to ensure laminar flow [17, 18, 22-24].

As long as compressibility effects are avoided, the viscosity of air depends only on the absolute temperature [27]:

$$\mu_2 = \mu_1 \left(\frac{T_1 + C}{T_2 + C} \right) \left(\frac{T_2}{T_1} \right)^{3/2} \tag{3}$$

where μ_2 is the viscosity of air at temperature T_2, and μ_1 and T_1 are reference values (e.g. μ_1 = 1.81 x 10^{-5} Pa.s at T_1 = 293 K) . C (= 117 K) is Sutherland's constant. This applies to dry air; reference [27] also provides a correction factor for relative humidity (RH), which causes only a 0.25% variation in density over a 60% range in RH, therefore indicating that humidity is an negligible factor in viscosity calculations.

Experimental Design

The experimental design is shown schematically in Fig. 1. Here a volumetric flow controller (Omega Engineering) with a zero to 8.33 x 10^{-5} $m^3.s^{-1}$ range and a certified calibrated accuracy of 1% of full scale, controls the volumetric flow of air which then passes through the base mould platen and permeates out radially through the 300 mm diameter samples. In order to measure the resultant pressure gradient across the sample a Setra differential pressure transducer (Kempston Controls Ltd) was used. This had a zero to 623 Pa range and a certified calibrated accuracy of 0.25% of full scale. Data were captured on a Datataker DT500 data logger with Delogger software, which also measured air flow temperature via a K-series thermocouple mounted in the base mould platen.

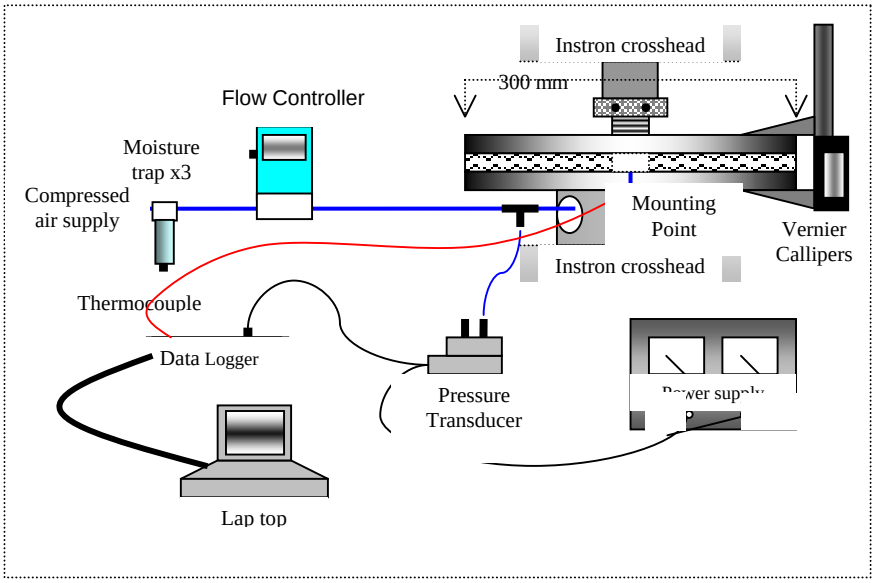

Fig.1: Schematic illustration of the experimental design

Permeability Calculation

Calculation of permeability from the experimental parameters is shown as Eq. 4, which is obtained by integrating Eq. 1. Note that measured permeability K depends on the radius of the central injection hole (r_0):

$$K = \frac{\mu Q}{\Delta P 2\pi d} \ln\left(\frac{r}{r_0}\right) \tag{4}$$

ΔP is the pressure difference between r_0 and radial position r, and d is the cavity depth.

METHODOLOGY

Unifilo U813-300 was kindly donated by Saint-Gobain Vetrotex for these experiments. The nominal reinforcement areal weight is 300 gm^{-2}, with a tolerance of between 225 and 345 gm^{-2} [28]. Each 300 mm-diameter sample comprised 6 layers, with 13.6 mm diameter injection holes, cut using a hydraulic press and cutting tools. These were then accurately weighed, and a fibre volume fraction (V_f) calculated from measured cavity thickness.

The samples were placed between the aluminium mould platens and compressed using an Instron Universal testing machine to the approximate depth required for a fibre volume fraction of 10%. The cavity depth was then measured accurately using Vernier callipers.

Air flow rate through the samples was controlled initially at 1.67 x 10^{-5} m^3s^{-1} (1 $Lmin^{-1}$) and differential pressure and airflow temperature recorded every second over a 20 s period. This was then repeated at flow rates of 3.33 x 10^{-5}, 5 x 10^{-5}, 6.67 x 10^{-5} and 8.33 x 10^{-5} m^3s^{-1} (1, 2, 3, 4 and 5 $Lmin^{-1}$ respectively, as shown on the flow controller).

The whole process was then repeated at progressively smaller cavity depths to a V_f of approximately 35%, over 10 samples in total.

This experimental method was then repeated, (over a limited range of flow rates) on 10 and 14-layer samples. This was to investigate whether inter-ply pore spaces had any influence on measured permeability.

RESULTS AND DISCUSSION

Experimental Errors

The effects of random measurement errors on calculated V_f and permeability were considered in terms of the combination of worst case inaccuracies. These included E-glass density of between 2550 and 2620 kgm^{-3} [28], flow controller accuracy to 1% of full scale, pressure transducer accuracy to 0.25% of full scale, vernier calliper's in-house calibrated accuracy to 5 x 10^{-6} m, sample outer radius (r) to 5 x 10^{-4} m, and viscosity to 5 x 10^{-7} Pa.s.

Permeability Results Analysis

Fig. 2 illustrates the experimental results obtained, including an experimental uncertainty of 2 standard deviations, for the various flow rates within the flow controller's working range. This shows that at all but the lowest V_f, where pressure differences were very small and therefore least precise, that the variation of results between test samples was significantly larger than the results obtained at different flow rates. A 'significant' variation is here taken to mean that a value falls outside the ± 2 standard deviation range.

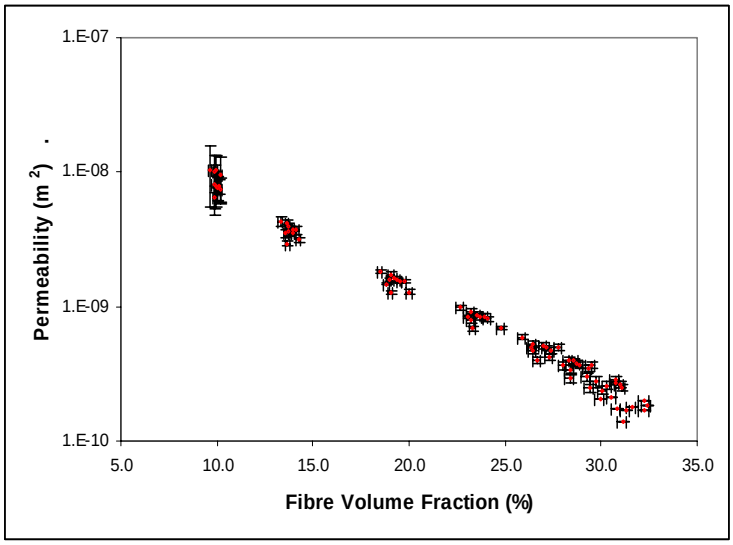

Fig. 2: Permeability vs. fibre volume fraction including 2-standard deviation error bars for permeability across flow rates used and random error bars for V_f.

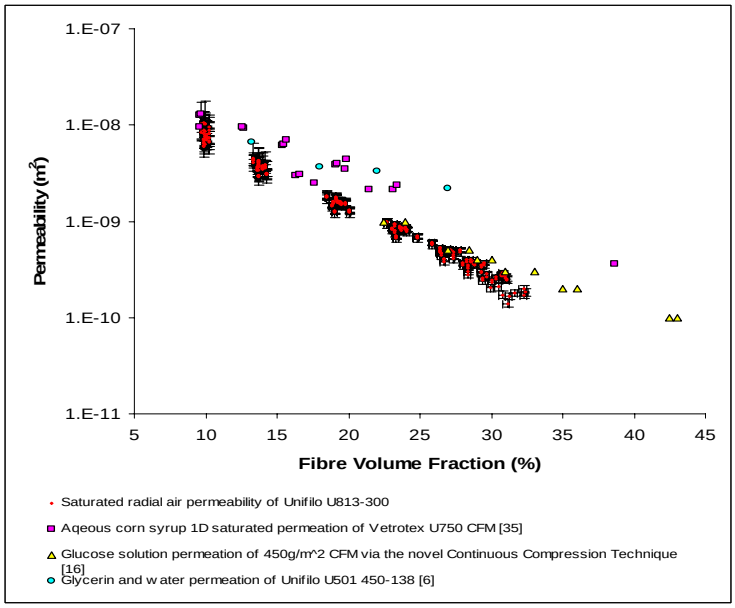

Fig. 3: Measured permeability vs. V_f, including random error bars, compared with published liquid permeability data.

Fig. 3 includes the random error bars for both permeability and V_f and compares these with published data for measurement of permeability using liquids [8, 15, 29]. In

general this plot shows that the results achieved using radial flow of air have a lower level of scatter than published data for the liquid techniques. It should also be noted that the published data are for a CFM of higher areal weight (450 gm^{-2}) than used in these experiments, which might be expected to return a difference in permeability due to variations in fibre architecture. Therefore close agreement with published liquid permeability data for CFM has been shown.

CONCLUSION

By comparison with published liquid permeability results for similar reinforcements, confidence in permeability measurement using the steady-state radial flow of air has been achieved. Statistical analysis of the results has verified the precision of the equipment used to measure experimental parameters. Varying the flow rate (within the range of the flow controller used) did not have a significant effect on measured permeability.

Thus the cleaner and more versatile technique using air as a permeating fluid may be considered suitable for the permeability measurement of CFM reinforcement. The practical implementation of these results could permit the benchmarking of a given reinforcement type against reference material, by direct comparison of pressure difference and/or air flow. The equipment could be easily adapted to measure fibre loft (resistance to compression), while simultaneously measuring permeability, thus providing important characterisation information to the moulder. Work is in progress to extend the technique to other fibre architectures, and to develop models for permeability optimisation.

ACKNOWLEDGMENTS

RP would like to acknowledge the receipt of an EPSRC CASE studentship, jointly sponsored by Plastech Thermoset Tectonics. We are grateful to St-Gobain Vetrotex for the supply of Unifilo CFM.

REFERENCES

1. J. Summerscales, F. J. Guild, N. R. L. Pearce and P. M. Russell, “Voronoi Cells, Fractal Dimensions and Fibre Composites”, *Journal of Microscopy*, 201 (2), 153-162 (2001).

2. S. G. Advani and M. V. Bruschke, “Resin Transfer Molding Flow Phenomena in Polymeric Composites”, in *Flow and Rheology in Polymer Composites Manufacturing*, S.G. Advani (Ed), 1994, Elsevier Science: Amsterdam, p 608.

3. W. G. Gray and C. T. Miller, “Examination of Darcy’s Law for Flow in Porous Media with Variable Porosity”, *Environmental Science & Technology*, 38, 5895-5901 (2004).

4. P. Mitschang, A. Ogale, J. Schlimbach, F. Weyrauch and C. Weimer, “Preform Technology: A Necessary Requirement for Quality Controlled LCM-Processes”, *Polymer & Polymer Composites*, 11 (8), 605-622 (2003).

5. E. Rodríguez, F. Giacomelli and A. Vázquez, "Permeability-Porosity Relationship in RTM for Different Fibreglass and Natural Reinforcements", *Journal of Composite Materials*, 38 (3), 259-267 (2004).

6. T. S. Lundström, R. Stenberg, R. Bergström, H. Partanen and P. A. Birkeland, "In-Plane Permeability Measurements: A Nordic Round-Robin Study", *Composites: Part A*, 31, 29-43 (2000).

7. Y. S. Song, K. Chung, T. J. Kang and J. R. Youn, "Prediction of Permeability Tensor for Plain Woven Fabric by Using Control Volume Finite Element Method", *Polymers and Polymer Composites*, 11 (6), 465-476 (2003).

8. M. Devillard, K. Hsiao, A. Gokce and S. Advani, "On-Line Characterization of Bulk Permeability and Race-Tracking during the Filling Stage in Resin Transfer Molding Process", *Journal of Composite Materials*, 37 (17), 1525-1541 (2003).

9. R. S. Parnas, J. G. Howard, T. L. Luce and S. G. Advani, "Permeability Characterization Part 1: A Proposed Standard Reference Fabric for Permeability", *Polymer Composites*, 16 (6), 429-445 (1995).

10. E. Carter, A. Fell, P. Griffin and J. Summerscales, "Data Validation Procedures for the Automated Determination of the Two-Dimensional Permeability Tensor of a Fabric Reinforcement", *Composites: Part A*, 27A, 255-261 (1996).

11. N. Pearce, F. Guild and J. Summerscales, "The Use of Automated Image Analysis for the Investigation of Fabric Architecture on the Processing and Properties of Fibre-Reinforced Composites Produced by RTM", *Composites: Part A*, 29A, 829-837 (1998).

12. N. R. L. Pearce, J. Summerscales and F. J. Guild, "Improving the Resin Transfer Moulding Process for Fabric-Reinforced Composites by Modification of the Fabric Architecture", *Composites: Part A*, 31, 1433-1441 (2000).

13. K. A. Olivero, Y. K. Hamidi, L. Aktas and M. C. Altan, "Effect of Preform Thickness and Volume Fraction on Injection Pressure and Mechanical Properties of Resin Transfer Molded Composites", *Journal of Composite Materials*, 38 (11), 937-957 (2004).

14. B. Gebart and P. Lidström, "Measurement of In-Plane Permeability of Anisotropic Fiber Reinforcements", *Polymer Composites*, 17 (1), 43-51 (1996).

15. M. J. Buntain and S. Bickerton, "Compression Flow Permeability Measurement: A Continuous Technique", *Composites: Part A*, 34, 445-457 (2003).

16. M. Deléglise, C. Binétruy and P. Krawczak, "Solution to Filling Time Prediction Issues for Constant Pressure Driven Injection in RTM", *Composites: Part A*, 36 (3), 339-344 (2005).

17. S. Kim, J. Opperer and I. Daniel, "Determination of Permeability of Fibrous Medium Considering Inertial Effects", *Int. Comm. Heat Mass Transfer,* 29 (7), 879-885 (2002).

18. S. K. Kim, J. G. Opperer and I. M. Daniel, "Gas Flow Method for Detecting Local Preform Defects by Inverse Estimation of Space-Varying Permeability", *Journal of Composite Materials,* 37 (15), 1367-1383 (2003).

19. S. Kim and I. Daniel, "Transient Gas Flow Technique for Inspection of Fibre Preforms in Resin Transfer Molding", *Composites Part A,* 36 (12), 1694-1699 (2005).

20. B. Hwang, M. Um and I. Daniel, "A New Technique to Determine In-Plane Permeability of Fiber Preforms: Gas Flow Method", *Proceedings of the Second Asian-Australasian Conference on Composite Materials (ACCM-2000),* 179-184 (2000).

21. Z. Liang, C. Zhang, B. Wang and C. Shih, "In-Situ Measurement and Monitoring of Fiber Preform Permeability for Liquid Composite Molding", *45th International SAMPE Symposium and Exhibition*, 2053-2062 (2000).

22. M. Um, I. Daniel and B. Childs, "A Gas Flow Method for Determination of In-Plane Permeability of Fiber Preforms", *Polymer Composites,* 22 (1), 47-56 (2001).

23. J. Opperer, S. Kim and I. Daniel, "Characterization of Local Preform Defects in Resin Transfer Molding by the Gas Flow Method and Statistical Analysis", *Composites Science and Technology*, 64, 1921-1935 (2004).

24. L. Ding, C. Shih, Z. Liang, C. Zhang and B. Wang, "In Situ Measurement and Monitoring of Whole-Field Permeability Profile of Fiber Preform for Liquid Composite Molding Processes", *Composites: Part A,* 34, 779-789 (2003).

25. V. Michaud and A. Mortensen, "infiltration Processing of Fibre Reinforced Composites: Governing Phenomena", *Composites: Part A,* 32, 981-996 (2001).

26. L. Nilsson and S. Stenström, "A Study of the Permeability of Pulp and Paper", *International Journal of Multi-Phase Flow,* 23 (1), 131-153 (1997).

27. G. Kaye and T. Laby, *Tables of Physical and Chemical Constants*, Longmans, London, p 249 (1966).

28. P. Thornburrow, Market Development Manager, Saint-Gobain Vetrotex, Nottingham, UK. Personal communication via email (2005).

29. R. Parnas and K. Flynn, "NIST Standard Reference Database 63, Web Version 1.0 1998", http://srdata.nist.gov/permeability/ , (accessed 2005).

MECHANICAL PROPERTIES AND PERMEABILITY MEASUREMENTS OF FIBRE REINFORCEMENTS: A CONTINUOUS METHOD

S. Comas-Cardona, C. Binetruy and P. Krawczak

Polymers and Composites Technology & Mechanical Engineering Department
Ecole des Mines de Douai, 941 Rue Charles Bourseul, F-59508 DOUAI, FRANCE
Corresponding Author's e-mail: comas-cardona@ensm-douai.fr

ABSTRACT: Composites manufacturing using LCM (Liquid Composite Molding) involves resin flow and sometimes further compression or unloading of the fiber reinforcements. Therefore a proper modeling of such processes requires a model for fiber reinforcement in compression. Several mechanical models are available, but none of them includes permanent deformation. Moreover saturated permeabilities of fiber reinforcements are essential parameters for LCM simulations. A common way of measuring such permeabilities relies on liquid injection techniques that induce uncertainties and a wide scattering of the results. This paper proposes an experimental methodology to measure permanent deformations involved with unidirectional compression of fiber reinforcements. Compression tests are further exploited to propose a reliable and generic measurement method that provides the in-plane and through-thickness permeabilities. Characterization results are given for a glass twill-weave fabric and a non-crimp fabric.

KEYWORDS: compression, fiber reinforcements, permanent deformation, permeability

INTRODUCTION

Structural composite materials are increasingly produced using one of the Liquid Composite Molding (LCM) processing techniques. The common feature of such processes is that a liquid resin is forced through fiber reinforcements. During infusion processes, the fiber reinforcement may unload and eventually, when the injection is completed, it may not fully recover [1]. A proper modeling of LCM processes, especially estimating the final thicknesses of the manufactured parts requires to have models for compression of fiber reinforcements that include permanent deformation. Numerous previous studies focused on fiber reinforcement compression modeling [2,3], but none of them seemed to include permanent deformations. Modeling LCM manufacturing processes also requires to input accurate fiber reinforcement permeabilities. Most techniques rely on fluid injection experiments that require an injection equipment, a mold and any device able to sense the flow. Other limitations are common errors associated with the measurement such as the deflection of the mold or edge effects [4]. Another in-plane permeability measurement method is based on the compression of saturated fiber reinforcements [5,6]. It limits the equipment required to

a material testing machine to continuously measure in-plane permeability with respect to fiber volume fraction.

This article deals with an experimental methodology to measure permanent deformations during unidirectional compression of dry and impregnated fiber reinforcements. That compression setup is further exploited in this paper to propose a reliable and generic measurement method that provides the in-plane and through-thickness permeabilities for a wide range of fiber volume fractions and materials. Characterization results are given for a glass twill-weave fabric and a carbon non-crimp fabric (NCF).

EXPERIMENTAL SETUP

Unidirectional compression tests on fiber reinforcement samples are carried out on a material testing machine with force cells of 10 kN and 100kN. For the compression of dry fabrics, the sample is simply inserted between two platens (Fig. 1). Force and crosshead position (sample height) are recorded during the compression test.

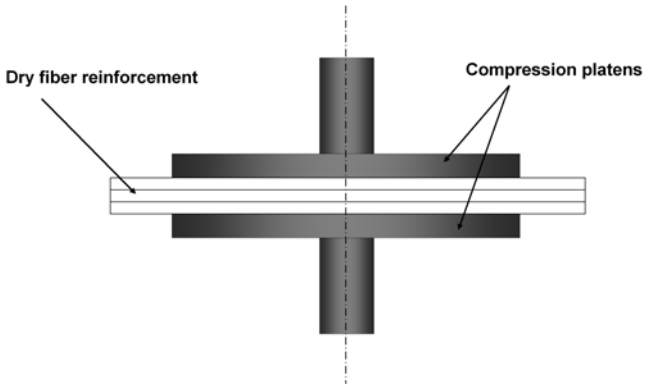

Fig. 1 Experimental setup for dry fiber reinforcement compression tests.

In the case of the compression of impregnated fabrics, the setup is modified as shown in Fig. 2. The fabric, impregnated with silicone oil, is inserted between the platens. The combination of a low viscosity fluid, a low crosshead speed and a perforated compression platen allows to limit pressures due to the expelled fluid flow and therefore to measure the mechanical response of the impregnated fabric in drained conditions.

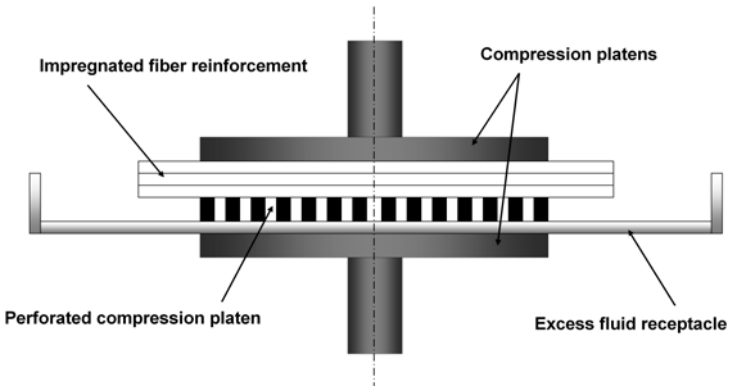

Fig. 2 Experimental setup for impregnated fiber reinforcement compression tests under drained conditions.

To measure permanent deformations (plasticity), the sample is loaded up to a maximum strain ε^{max}, and subsequently unloaded to provide the amount of permanent deformation retained in the sample ε^{p} (Fig. 3). Each cycle gives a point of the plastic strain vs. total strain curve. Engineering strain is calculated as $\varepsilon = (h_o - h)/h_o$ and stress as $\sigma = F/A$ where h is the height of the sample, h_o the initial height of the sample, F the force applied to the sample and A the area of the sample in contact with the compression platens.

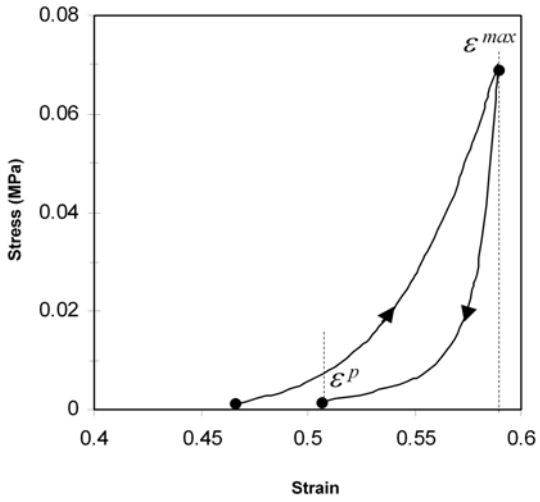

Fig 3 Example of loading-unloading compression test response that allows to extract plasticity.

Material	Glass twill-weave fabric	Carbon NCF
Areal weight	1500 g/m^2	230 g/m^2
Number of plies	4	10
Stacking sequence	[0°,90°,90°,0°]	[+45°,0°,0°,-45°,90°,90°, -45°,0°,0°,+45°]
Initial sample height	6.8 mm	4.5 mm
Crosshead speed	0.5 mm/min	0.5 mm/min
Silicone oil viscosity (21°C)	0.1 Pa.s	0.1 Pa.s

Table 1 Experimental conditions and material properties.

PERMANENT DEFORMATIONS

For the glass twill-weave fabric considered in this study (Tab. 1), the plastic strain develops linearly and represents 60% of the total strain (Fig. 4). Plasticity is influenced by the impregnation: lubrication facilitates yarn and fiber imbrications. However, for the carbon NCF (Fig. 5), the presence of fluid does seem to influence permanent deformations developing in the fabric. That difference of behavior may be due to the difference of textile architecture between the two materials. For twill-weave fabric

permanent deformations are governed by nesting (yarn/yarn interactions) and fiber/fiber interactions whereas for NCF only fiber/fiber interactions are present.

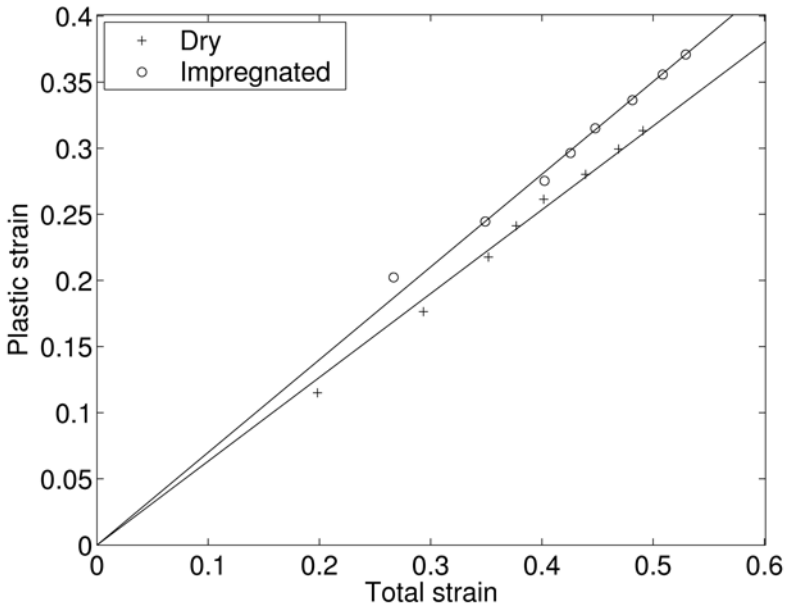

Fig. 4 Permanent deformations of the glass twill-weave in dry and impregnated states.

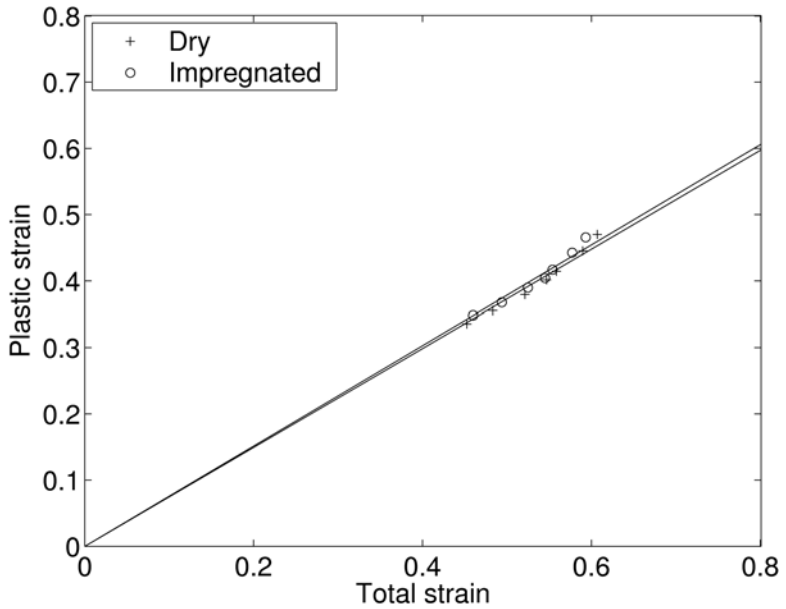

Fig. 5 Permanent deformations of the carbon NCF in dry and impregnated states.

PERMEABILITY MEASUREMENTS

So far, for permanent deformation measurement, the aim of the compression tests has been to limit the fluid pressure. From now on, in order to measure permeabilities, the purpose of the measurement method [8] is to generate fluid flow and fluid pressure within the sample using proper compression speeds and fluid viscosities. For in-plane permeability measurement, in-plane flow is generated using the setup depicted in Fig. 1

with an impregnated sample and a receptacle. For through-thickness permeability measurement, the generation of a purely transverse flow using a compression test is difficult to achieve. However, using the setup shown in Fig. 2, fabric compression forces the fluid out, in the three directions of the sample. Those two types of compression tests induce fluid pressure and fiber effective stress response. In order to extract the fluid pressure out of those experiments, the fiber effective stress has to be measured and subtracted to the previous experiments.

The effective stress response is measured combining a test with the setup in Fig. 2, a low compression speed, and a low fluid viscosity in order to zero the fluid pressure. That experiment called the reference compression is performed with a fluid viscosity of 0.1 Pa.s and a compression speed of 0.5 mm/min.

In-plane permeabilities

Once the experimental fluid pressure is measured, one can solve for the conservation of mass and Darcy's law in the sample. If the fiber reinforcement is transversely isotropic (K_x=K_y), an analytical solution exists (Tab. 2). But in most cases when the fiber reinforcement is anisotropic, an inverse method algorithm adjusts the permeability of the simulation results to match the simulated liquid pressure to the experimental liquid pressure. The anisotropy ratio is needed to calculate the two in-plane principal permeabilities. Results for the in-plane permeability, calculated for the glass and carbon fabrics, are in excellent agreement with the ones measured with the unidirectional or central injection methods (Figs. 8 and 9).

	Transverse isotropic fiber reinforcement		Anisotropic fiber reinforcement	
	In-plane permeability ($K_x = K_y$)	Through-thickness permeability K_z	In-plane permeabilities ($K_x \neq K_y$)	Through-thickness permeability K_z
Analytic	✓			
FDM (2D cylindrical)	✓	✓		
FEM	✓	✓	✓	✓

Table 2 Methods to extract permeabilities depending on the material anisotropy.

Through-thickness permeability

Once the in-plane permeabilities are known, the compression tests inducing through-thickness flow (Fig. 2) can be analyzed using an inverse method as detailed above. Results for glass twill-weave and carbon NCF are given in Figs. 6 and 7. No comparison with experimental data using injection techniques is given since such measurements are very difficult to realize. However, the orders of magnitude obtained are in a proper range for through-thickness permeability.

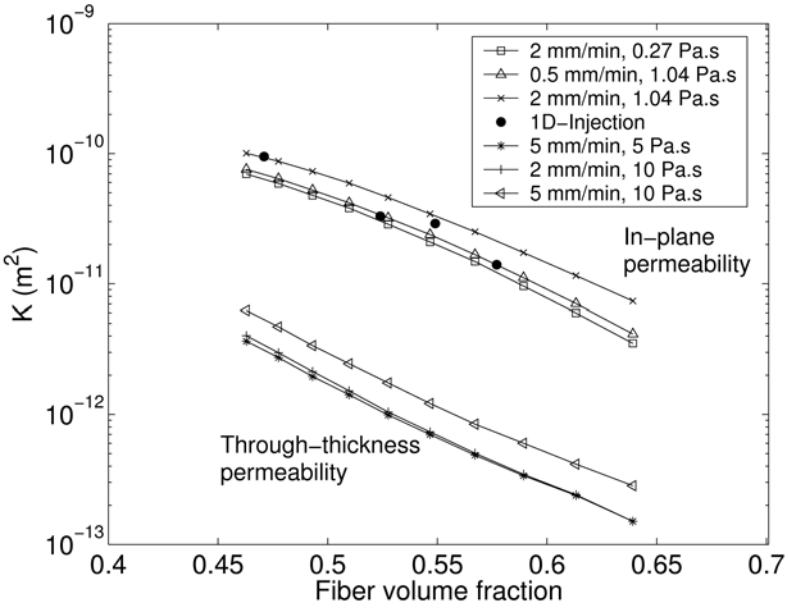

Fig. 6 In-plane and through-thickness permeabilities of the glass twill-weave fabric extracted from the compression tests. The black circles (●) are in-plane permeabilities obtained using the unidirectional injection method.

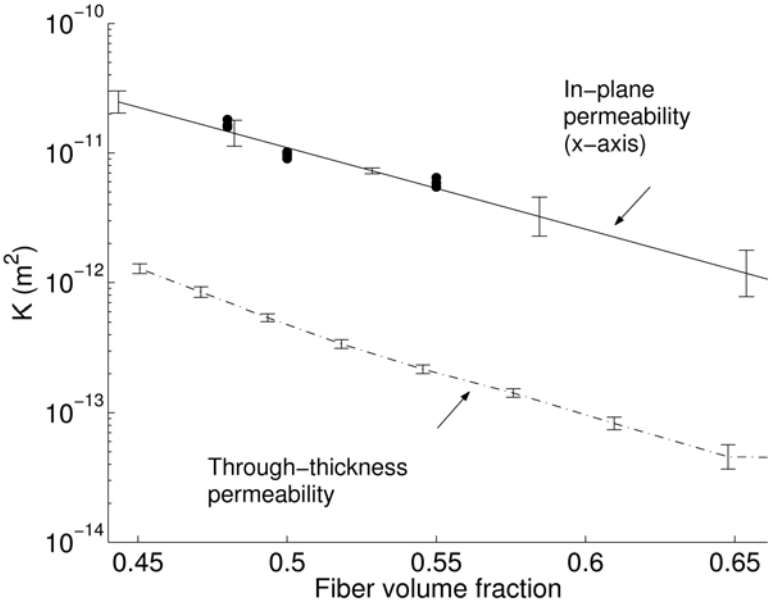

Fig. 7 In-plane and through-thickness permeabilities of the carbon NCF extracted from the compression tests. The black circles (●) are in-plane permeabilities obtained using the central injection method.

CONCLUSION

The results obtained for plasticity characterization show the importance of permanent deformations during unidirectional compression of the glass twill-weave fabric and carbon NCF studied. Also a methodology for fiber reinforcement permeability measurement using a compression test setup has been described. That method offers the

main advantage of being continuous over a wide range of fiber volume fractions. Moreover, once the anisotropy ratio is known, the method allows the determination of the in-plane and through-thickness permeabilities. That method also eliminates lots of drawbacks present in the injection methods such as edge effects or mold deflection. This methodology can also be applied to fabrics that have been sheared prior to compression.

ACKNOWLEDGEMENTS

The authors would like to thank the Advanced Technologies Development Center, Dassault Aviations (France) for providing the carbon fiber reinforcements and funding part of the study.

REFERENCES

[1] Tackitt KD, Walsh SM, *Mat. Manufact. Processes*, 20 (2005), p. 607-27.

[2] Rudd CD, Bulmer LJ, Morris DJ, *Mat. Sci. Technol*, 12 (1996), p. 436-44

[3] Toll S, Manson JAE, In: Proc. of the FRC Conf. 1994, Newcastle upon Tyne, UK, p. 25/1-25/10.

[4] Lundstrom TS, Stenberg R, Bergstrom R, Partanen H, Birkeland PA, *Compos. Part A*, 31 (2000), p. 29-43.

[5] Ait si Ahmad M, Fasi-Ferhi O, Poitou A, Bojji C, *Mécaniques & Industries*, 3 (2002); p. 27-34.

[6] Buntain MJ, Bickerton S, *Compos. Part A*, 34 (2003), p. 445-57.

[7] Comas-Cardona S, Binetruy C, Krawczak P, Unidirectional compression of fibre reinforcements Part 1: A non-linear poro-elasto-plastic behaviour. Submitted to *Compos. Sci. Technol*. (2005)

[8] Comas-Cardona S, Binetruy C, Krawczak P, Unidirectional compression of fibre reinforcements Part 2: A continuous permeability tensor measurement. Submitted to *Compos. Sci. Technol*. (2005)

Session 9

MATERIALS CHARACTERISATION - II

MODELING OF RESIN CURE KINETICS FOR MOLDING CYCLE OPTIMIZATION

Edu Ruiz [1], F. Waffo [1], J. Owens [2], C. Billotte [1], F. Trochu [1]

[1] *Chaire sur les Composites à Haute Performance (CCHP), Centre de Recherches En Plasturgie Et Composites (CREPEC), Département de génie mécanique,*
École Polytechnique, Montréal (Québec) HC 3A7 http://cchp.meca.polymtl.ca
edu.ruiz@polymtl.ca

[2] *GM Research and Development Center, Materials and Process Lab*
john.n.owens@gm.comT

ABSTRACT

During the last years, the numerical simulation of Liquid Composites Molding (LCM) turned out to be a useful tool to assist in process design and optimization. To appropriately simulate LCM manufacturing, accurate material characterizations must be carried out. In a more competitive industrial environment, fast and reliable characterization techniques are required to implement effective numerical simulations. Resin cure kinetics modeling software called ***PolyKinetic*** has been developed to assist in material characterization and process simulation. In this work, recent advances on resin cure kinetics modeling are presented and compared. Different kinetic models for an epoxy resin are discussed. Modeling of the percentage of catalyst is also included, together with rheological analyses and a model of gel time to estimate the allowable injection time from calorimetric data. ***PolyKinetic*** software turns out to be a very useful tool to characterize the cure kinetics of thermosetting resins in a fast and reliable way. ***PolyKinetic*** is a freeware package available to all the scientific and industrial community through the *Chaire sur les Composites à Haute Performance* (***CCHP***) of École Polytechnique de Montréal.

INTRODUCTION

Polymer composite materials have been increasingly used in several industrial applications for the last few years. As the composite industry grows, thick parts and pieces of complex shape have become more common. Thermoset composites have also gained much interest in the automotive industry and many applications have successfully demonstrated their effectiveness. High specific mechanical properties, corrosion resistance and low fatigue effects are main factors for the selection of such materials over traditional metallic solutions. Liquid Composite Molding (LCM) and other manufacturing techniques such as Sheet Molding Compound (SMC), Resin Transfer Molding (RTM) or Compression RTM have gained attention due to their capability to produce composite parts in medium to large production volumes. Resin cure kinetics and the evolution of viscosity play a key role to ensure proper fiber impregnation and reduce cycle time. From the thermal point of view, the molding cycle is closely related to the chemical and

rheological behavior of the resin. Therefore, to optimize the molding cycle in LCM manufacturing, the chemical and rheological behaviors of thermosetting polymers must be well known. Based on the material behavior during resin cure, a computational analysis of the process cycle can be carried out. Process simulation allows a proper selection of processing parameters such as the injection pressure and the mold and resin temperatures [1, 2]. In a more competitive industrial environment, fast and reliable characterization techniques are required to implement numerical simulations for engineering design and process planning.

In this work, recent advances on resin cure kinetics modeling are presented and compared. Different kinetic models for an epoxy resin are discussed. Modeling of the percentage of catalyst is also included, together with rheological analyses and a model of resin gel time to estimate the allowable injection time from calorimetric data. Resin cure kinetics modeling software called ***PolyKinetic*** has been developed to assist in material characterization for process simulation and optimization.

MODELING OF RESIN CURE KINETICS

Modulated Differential Scanning Calorimetry (M-DSC) is a well known technique to measure the curing reaction of thermosetting resins. Assuming that the non-reversible heat flow measured is entirely related to the exothermic reaction of the polymer, M-DSC data can be used to determine the reaction rate $d\alpha/dt$ and the degree of conversion α in the following form:

$$\dot{H} = \frac{dH}{dt} = \frac{d\alpha}{dt} \cdot H_T \tag{1}$$

$$\alpha = \int_o^t \frac{d\alpha}{dt} \cdot dt \tag{2}$$

where $\dot{H}$ is the instantaneous heat generated by the cross-linking polymerization of the resin, and H_T is the total heat of reaction during cure. A large number of studies have been conducted on the cure kinetics of thermosetting polymers, and various kinetic models have been proposed in the literature [3-6]. Generally, researchers have studied the connection of the chemical reaction with the other independent variables, such as time and temperature. In general, kinetic models can be of phenomenological or mechanistic origin. A phenomenological model captures the main features of reaction kinetics, but ignores the details of how individual species react with one another. On the other hand, mechanistic models are obtained from the balance of chemical species involved in the reaction. Hence, they provide better prediction and interpretation. However, because thermosetting reactions are rather complex, mechanistic models usually require more kinetic parameters than phenomenological models. Therefore phenomenological models are more popular for thermosetting polymers. Although several simultaneous reactions occur during the curing process, simple models have been developed based on the assumption that only one chemical reaction can represent the whole cure process. Kamal and Sourour [3] have shown that the following model describes adequately the cure kinetics of epoxy resins:

$$\frac{d\alpha}{dt} = \left(K_1 + K_2 \cdot \alpha^m\right) \cdot (1-\alpha)^n \tag{3}$$

$$K_{1,2} = k_{1,2} \exp\left(-E_{1,2} / T\right)$$

where K_1 and K_2 are rate constants with an Arrhenius type of dependence with temperature, and m and n are catalytic constants. Ruiz and Trochu [4] have also proposed a kinetic model based on Bailleul's model [5] considering the effects of glass transition temperature on the reaction rate. In this approach, the rate of conversion $d\alpha/dt$ is defined by the following set of equations:

$$\frac{d\alpha}{dt} = K_1(T)\cdot K_2(\alpha)\cdot K_3(T,\alpha)\cdot K_4(I_d) \tag{4a}$$

$$K_1(T) = k_{ref}.\exp\left[-A\cdot\left(T_{ref}/T-1\right)\right] \tag{4b}$$

$$K_2(\alpha) = \sum_{i=0}^{s} a_i\cdot\alpha^i \tag{4c}$$

$$K_3(T,\alpha) = (\alpha_{\max}-\alpha)^n; \qquad n = f(T) \tag{4d}$$

Recently, Riccardi et al. [6] have proposed a novel kinetic model to describe the cure of epoxy resins following a chemical mechanism. The following kinetic equations result from the proposed model:

$$\begin{aligned}\frac{d\beta}{dt} &= k_1 - (k_1+k_2)\beta \\ \frac{d\alpha}{dt} &= k_3(1-\alpha)\ i_0\beta\end{aligned} \tag{5}$$

where i_o is the initial concentration of initiator, and β the ratio between the initiator concentration in the active and inactive forms. Parameters k_1 and k_2 are Arrhenius functions of temperature. When the curing temperature reaches the glass transition temperature of the resin, a strong increase of the resin viscosity is observed. The reaction rate is not controlled anymore by the speed of the chemical reaction, but more by the speed of the diffusion of the reactants [7]. The mobility of the reactants is then restricted and limited by the reduction of the free volume. To consider the diffusion effect, Poehlein and al. [7] introduced a diffusion factor $f(\alpha)$ to correct the kinetic model predictions:

$$\left(\frac{da}{dt}\right)^{corrected} = \frac{da}{dt}\cdot f(\alpha); \qquad f(\alpha) = \frac{1}{1+\exp\left[C(\alpha-\alpha_c)\right]} \tag{6}$$

where C is a constant, and α_c the critical conversion. For $\alpha << \alpha_c$, $f(\alpha)$ is equal to unity and the effect of diffusion is negligible. The selection of a proper catalyst percentage is a key factor here, because it allows reducing cycle time and thus increases productivity. Han and al. [8] proposed a standard kinetic model to consider the effect of the concentration of catalyst on the cure reaction. According to this model, the rate of conversion of the resin is directly proportional to the concentration of catalyst. Consequently, the Kamal-Sourour model of equation 3 can be expressed in the following way:

$$\frac{d\alpha}{dt} = [B]\left(k_1' + k_2'\alpha^m\right).(1-\alpha)^n \tag{7}$$

$$\text{with } \frac{k_1}{[B]} = k_1' \text{ and } \frac{k_2}{[B]} = k_2'$$

where $[B]$ is the concentration of catalyst, and k_1' and k_2' are normalized Arrhenius functions.

PolyKinetic is a freeware initially developed at the *Chaire sur les Composites à Hautes Performance* (CCHP) of *École Polytechnique de Montréal*. This software allows the modeling of resin cure kinetics from experimental results of differential scanning calorimetry. As illustrated in Fig. 1, the software is composed of three main modules: (1) processing of DSC data; (2) modeling of cure kinetics; and (3) prediction of resin cure under various experimental conditions. All the above kinetic models were included in ***PolyKinetic*** to provide an easy and robust solution and compare their respective performance to predict resin cure. ***PolyKinetic*** uses a least-square Levenberg-Marquardt non linear regression algorithm to calculate the unknown parameters of the kinetic models.

EXPERIMENTAL CURE ANALYSES

M-DSC data of an epoxy anhydride-based resin were collected for various heating rates (from 1 to 5°C/min) and different percentages of catalyst (from 1 to 2,5 parts per weight). These experimental data were entered into ***PolyKinetic*** and used to construct various kinetic models. Initially, a Kamal-Sourour model was created to fit DSC data. As can be seen in Fig. 2, reaction rates and degrees of conversions are well described by this phenomenological model with a minimum error at the end of the chemical reaction. Similar results were also obtained with Ruiz model with a slight improvement at the end of cure. The mechanistic model of Riccardi was then calculated to fit experimental data. As shown in Fig. 3 (a), an appropriate prediction of the degree of conversion is obtained with this approach, although an important error is observed at the end of the chemical reaction. To improve the predictions at the end of cure, the model of Riccardi was combined with the diffusion control equation (6) as depicted in Fig. 3 (b). Even if the use of a diffusion control equation improves the model predictions at the end of cure, it seems that the mechanistic model is not as well suited as Kamal-Sourour one to fit these experimental data.

The interest of having an accurate kinetic model lies in its capability to predict higher degrees of conversion for a given temperature cycle. To compare the predictions of different kinetics model, a new technique called *IsoConversion Map* [9] was proposed. This technique is based on the isoconversion methodology [10] that permits to compare dynamic and isothermal DSC data. As shown in Fig. 4, the *IsoConversion Map* consists of two sets of curves, one for constant heating rates and one for constant temperatures. To estimate the degree of conversion for a given temperature cycle consisting of heating rates and isothermal cures, the two set of curves are sequentially used (see example in Fig. 4). In this way, the resulting evolution of the degree of conversion is extracted directly from DSC data (i.e., without kinetic modeling). In this work, the *IsoConversion Map* methodology was applied to evaluate the experimental DSC data for a temperature cycle consisting of two heating rates followed by two isothermal cures at 80°C and 150°C respectively. Fig. 5 depicts a comparison of experimental cures obtained through the *IsoConversion Map* with Kamal-Sourour and Riccardi mechanistic models. It can be clearly observed that the prediction of Kamal-Sourour model is far from the experimental data, while the mechanistic model gives an accurate prediction. This shows that Riccardi's mechanistic model is

more appropriate to calculate the degree of conversion than other more standard phenomenological models.

RHEOLOGICAL STUDIES

To optimize the molding cycle in LCM manufacturing, the evolution of resin viscosity during the injection stage must be known with accuracy. Characterization and modeling of the viscosity of a non-reactive resin as a function of temperature follows a well known and relatively simple experimental procedure. In the case of reactive resins, rheological analyses are complex and less accurate. In this work, isothermal rheological analyses were carried out to characterize the complex viscosity evolution of an epoxy resin for various percentages of catalysts. The determination of the gelation point for thermoset resins is critical to evaluate the rate of polymerization and it is a key factor in process cycle optimization. The gel point is usually defined as the time at which the storage modulus exceeds the loss modulus (i.e., tan $\delta = 1$), but this point corresponds to a high resin viscosity. In LCM process analysis, a processing gel time may be defined as the point at which the resin viscosity curve has a slope of 10% (see Fig. 6 (a)). This criterion results in a viscosity increment between 2 to 5 times from the initial value. At this point the resin will not flow under normal injection pressures. Fig. 6 (b) shows the extracted gel times from rheological data while applying the 10% slope criterion. The gel time can also be estimated from DSC data if a given degree of conversion is related to the resin gelation point. In this work, for the epoxy resin tested, a degree of conversion of 20% was considered at the gel point. For each dynamic DSC curve, the time at which the resin reaches 20% of conversion has been extracted and plotted in Fig. 7. As observed in the kinetic models presented before, at the beginning of the reaction the resin cure kinetics follows an Arrhenius type of temperature dependence. Therefore, the gel time can be evaluated by a time integral Arrhenius function as follows:

$$Gel\ \ time(T,t) = t_{ref} - \int_0^t \exp\left(-B \cdot \left(T_{ref} / T - 1\right)\right) \cdot dt \tag{8}$$

$$t_{ref} = C \cdot \exp\left(-D \cdot \mathrm{CatPhr}\right) \tag{9}$$

where T_{ref} is a reference temperature, B, C and D are constants and t_{ref} a reference time function of the percentage of catalyst *CatPhr* in the resin formulation. The parameters of the proposed gel time model were obtained from the experimental values extracted from dynamic DSC data (see Fig. 7). The gel time model fitted to dynamic DSC data was then used to predict the gel times during isothermal cures. The predictions of the proposed model were then compared to the experimental gel times extracted from rheological tests. As shown in Fig. 8, a good agreement is observed between the experimental rheological data and the model predictions. Therefore one may conclude that the proposed model is appropriate to predict processing gel times.

CONCLUDING REMARKS

In order to understand the impact of epoxy cure kinetics modeled by a mechanistic approach, a comparative study was conducted between the phenomenological and mechanistic models. Through the use of the *IsoConversion Map* technique, it has been observed that a mechanistic model is more accurate than phenomenological ones. A gel time model is also proposed to

calculate the allowable injection time directly from dynamic DSC data. The results of this model were compared to rheological data, and a good agreement could be observed between the two. All the above kinetic models were included in ***PolyKinetic*** freeware for easy and robust identification of resin kinetic parameters.

REFERENCES

1. F. Trochu, Edu Ruiz, V. Achim, S. Soukane, "Advanced Numerical Simulation of Liquid Composite Molding for Process Analysis and Optimization", *Composites Part A*, Vol. 37, no. 6, 2006, pp 890.
2. Edu Ruiz, V. Achim, S. Soukane, F. Trochu, J. Breard, "Optimization of injection flow rate to minimize micro/macro voids Formation in Resin transfer molded composites", *J. of Composite Sci. and Tech.*, Vol. 66, no. 3, 2006, pp 475.
3. M. R. Kamal, "Thermoset characterization for moldability analysis", *Polymer Engineering and Science*, Vol. 4, no. 3, 1974, pp. 239.
4. Edu Ruiz, F. Trochu, "Thermo-mechanical properties during cure of glass-polyester RTM composites: elastic and viscoelastic modeling", *J. of Composite Materials*, Vol. 39, no. 10, 2005, pp 881.
5. J.-L. Bailleul, V.Sobotka, D. Delaunay, Y. Jarny, "Inverse Algorithm for Optimal Processing of Composite Materials", *Composites Part A*, Vol. 34, no. 8, 2003, pp. 695.
6. C. C. Riccardi, J. Dupuy, R. J. J. Williams, "A Simple Model to Explain the Complex Kinetic Behavior of Epoxy/Anhydride Systems", *J. of Polymer Science: Part B: Polymer Physics*, Vol. 37, 1999, pp 2799.
7. C.-S Chern, G.W Poehlein, "A kinetic model for curing reactions of epoxides with amines", *Polym. Eng. Sci.*, Vol. 27, no. 11, 1987, pp 788.
8. S. Han, W. G. Kim, H. G. Yoon, T. J. Moon, "Kinetic Study of the Effect of Catalysts on the Curing of Biphenyl Epoxy Resin", *J. of Applied Polymer Science*, Vol. 68, 1998, pp. 1125.
9. Edu Ruiz, Internal report, *Ecole Polytechnique de Montreal*, 2002.
10. A. Atarsia and R. Boukhili, "Relationship Between Isothermal and Dynamic Cure of Thermosets Via the lsoconversion Representation", *Polymer Eng. and Sci.*, Vol. 40, No. 3, 2000, pp 607.

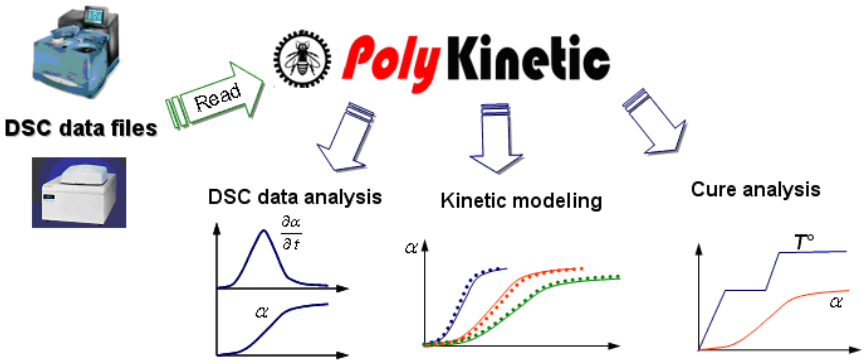

Figure 1. Schematic representation of *PolyKinetic* software modules

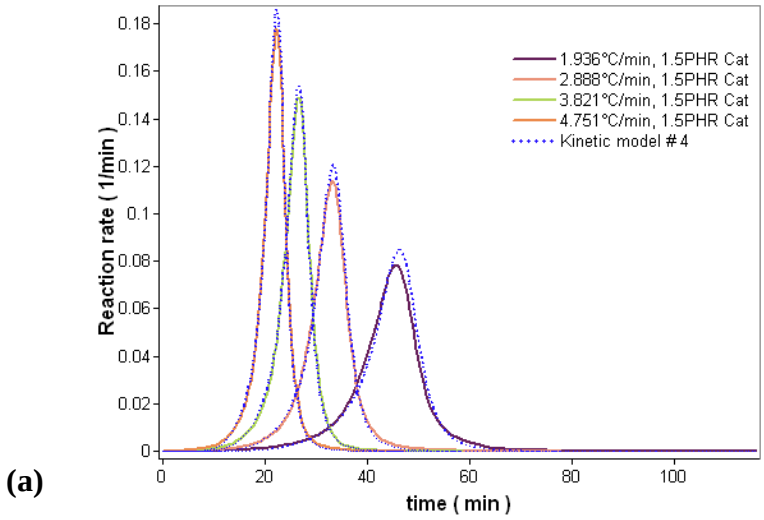

Figure 2. Evolution of reaction rates (a) and degrees of cure (b) and predictions of the fitted Kamal-Sourour model (kinetic model 4) for various heating rates

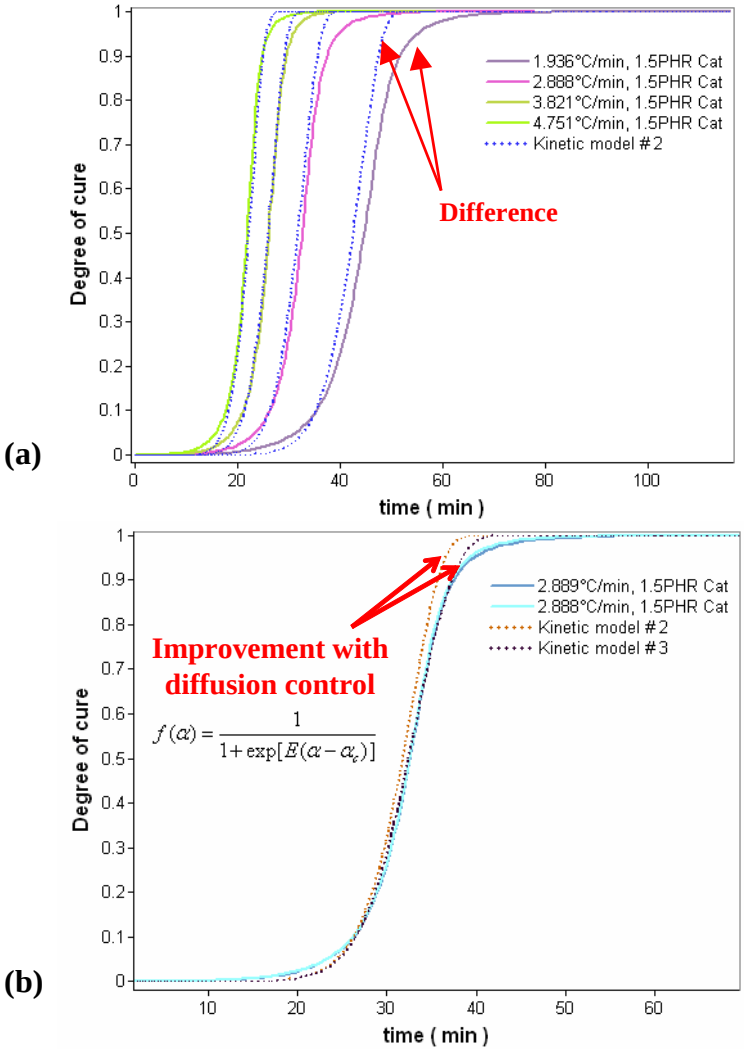

Figure 3. Degrees of cure versus time for different heating rates: a) comparison of experimental data with Riccardi's model predictions (kinetic model 2); b) improvement of Riccardi's model with diffusion control.

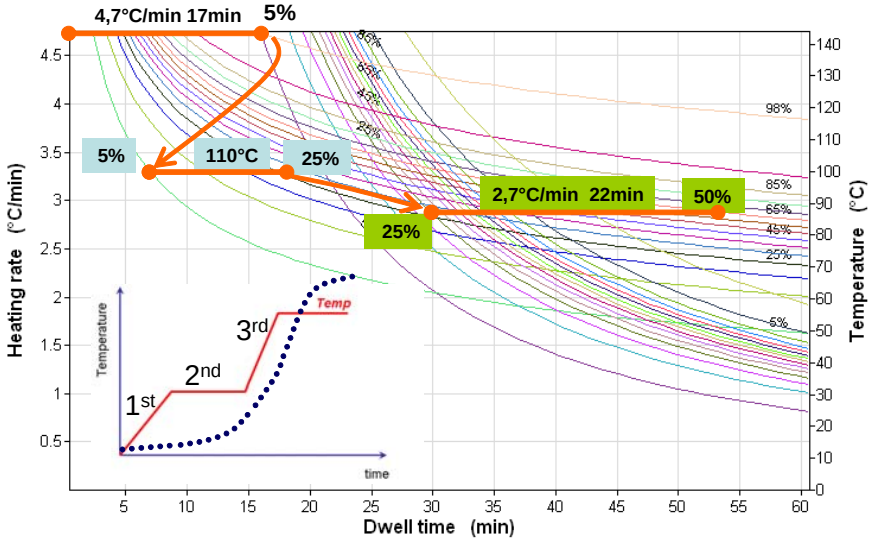

Figure 4. *IsoConversion Map* used to predict the degree of conversion.

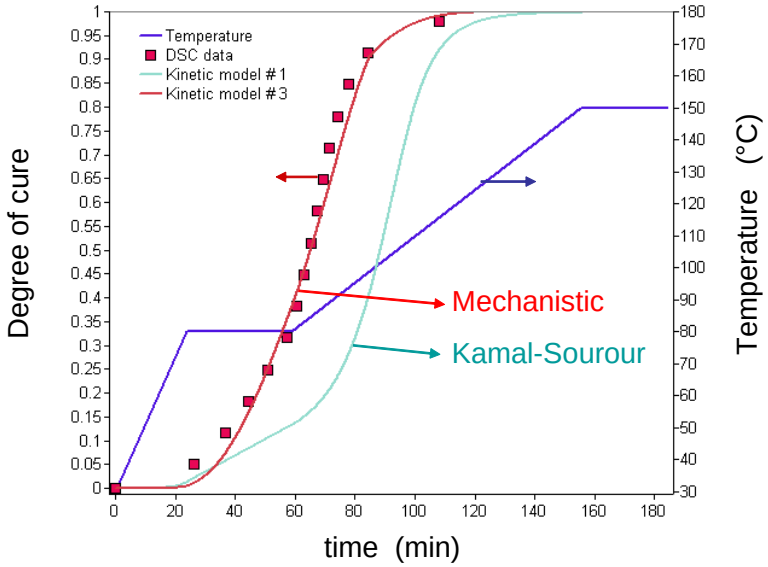

Figure 5. Comparison of experimental data obtained by isoconversion with Kamal-Sourour and Riccardi mechanistic models.

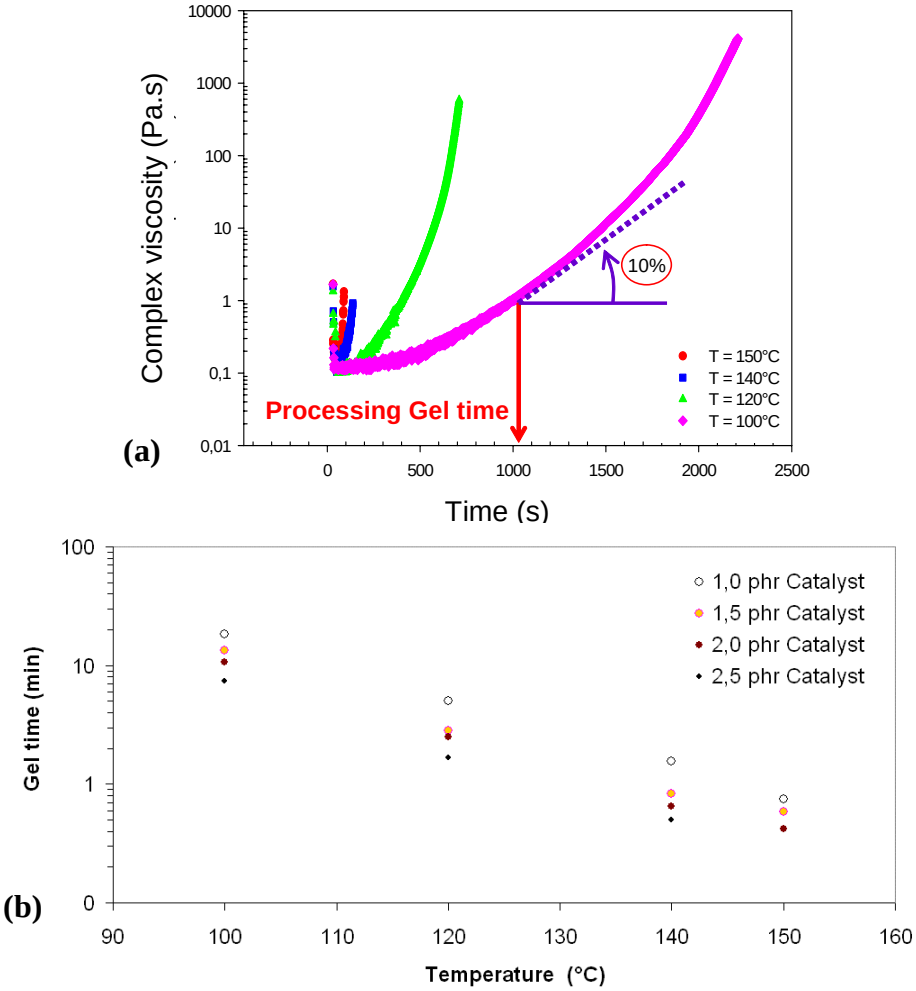

Figure 6. Rheological data for isothermal cures: a) viscosity evolution during cure; b) gel times for various isothermal temperatures and different percentages of catalyst.

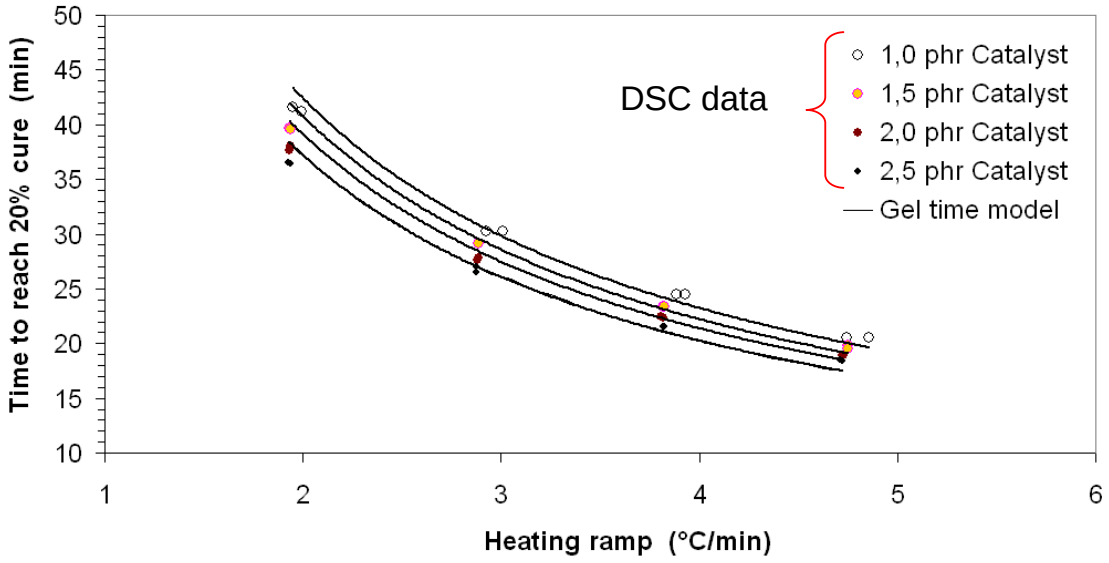

Figure 7. Gel times calculated for 20% of conversion from dynamic DSC data and predictions of the proposed gel time model.

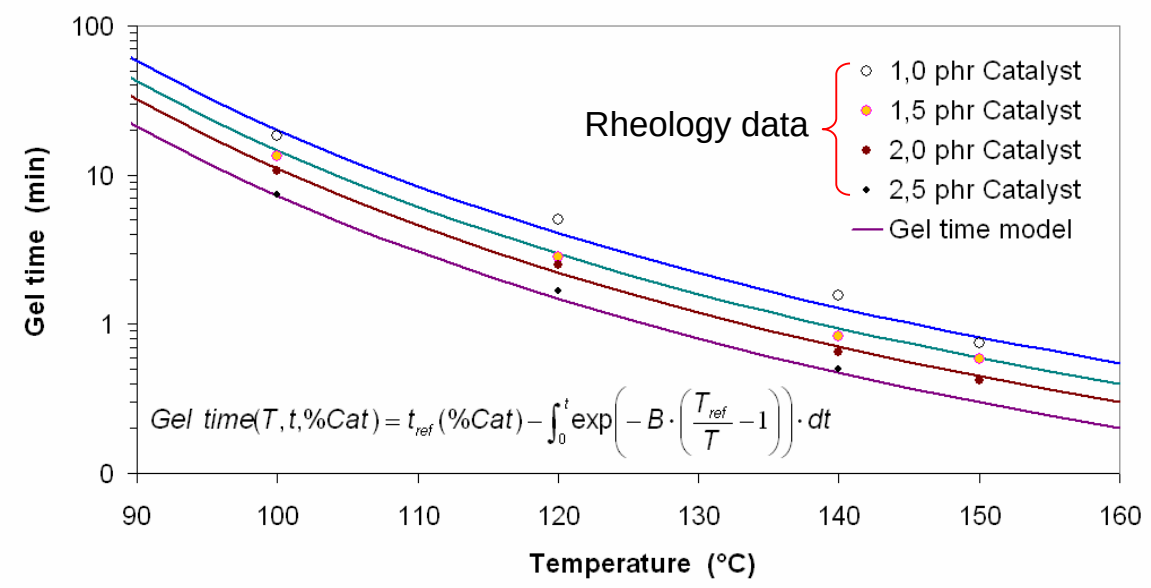

Figure 8. Comparison of experimental gel times from rheological data with predictions of the proposed gel time model for various percentages of catalyst.

A STEREO PHOTOGRAPHY SYSTEM FOR MONITORING FULL FIELD THICKNESS VARIATION DURING RESIN INFUSION

Q. Govignon [1], S. Bickerton [1], J. Morris [2], and J. Lin [2]

[1]*Centre for Advanced Composite Materials, Department of Mechanical Engineering*
[2]*Communication & Information Technology Research, Dept. of Computer Science*
The University of Auckland, Private Bag 92019, AUCKLAND, NEW ZEALAND
Corresponding Author's e-mail: s.bickerton@auckland.ac.nz

ABSTRACT: This paper focuses on laminate thickness measurement during the Resin Infusion process. It is part of a larger project to establish a comprehensive data acquisition system for characterisation of this complex process. The acquisition of detailed thickness data is motivated by the need to develop an accurate simulation tool for Resin Infusion. After presenting several compaction studies on a typical glass fibre fabric, the paper will quickly review the current techniques used to monitor laminate thickness evolution, highlighting the disadvantages of single point measurement methods. Stereophotography offers the possibility of full field measurement of laminate thickness, a brief introduction to the theory being presented here. Initial results show the potential of the technique, though an improvement is required in the image reconstruction algorithm to obtain the thickness resolution required.

KEYWORDS: VARI, Thickness measurement, Stereophotography, Compaction.

INTRODUCTION

The Resin Infusion process (a.k.a. VARI, VARTM, SCRIMP, RIFT) has developed as a low cost method for manufacturing large composite parts. It has been used mainly to produce structural parts for the marine, civil, and military sectors [1, 2]. It has also been shown that aircraft quality composite structures can be produced [3, 4]. However, the process still presents some challenges to industry with regards reliability and repeatibility. Due to the complex nature of the Resin Infusion process, trial and error development is expensive and inefficient. Therefore a comprehensive simulation model of the VARTM process is required.

Resin Infusion is a closed mould Liquid Composite Moulding (LCM) process that presents some similarities to Resin Transfer Moulding (RTM). The current analysis schemes adopted for RTM flow simulations assume resin flow through the preform behaves as flow through a porous medium. The modelling of porous flow is governed by Darcy's law:

$$\langle v \rangle = -\frac{1}{\mu}[K]\nabla P \qquad (1)$$

where $\langle v \rangle$ is the fluid averaged velocity vector, μ is the fluid viscosity, K the permeability tensor for the preform, and ∇P is the local pressure gradient in the resin.
For Resin Infusion, two-part rigid moulds are replaced by single side rigid moulds sealed with a vacuum bag. Bag flexibility induces a new aspect absent in RTM: the thickness of the laminate being dependent on local resin pressure. During processing both the transfer of the

matrix and the compaction of the reinforcement are achieved using one atmosphere of pressure. Compaction stress supported by the reinforcement is therefore a balance between atmospheric pressure and the resin pressure:

$$\sigma_f = P_{ATM} - P \tag{2}$$

Due to the variation of resin pressure in the laminate during mould filling and post-filling, laminate thickness varies during both the mould filling and post filling stages. It is therefore important to be able to accurately monitor these thickness changes, which may significantly affect reinforcement permeability and thus resin flow.

Previous studies by the authors have employed laser gauges to provide point measurements of laminate thickness [5]. Inconsistent results have prompted the development of a system capable of simultaneously capturing the thickness field of an entire laminate. Previous work by Anderson et al. concerned the development of a stereophotographic system to measure thickness using specialised CCD cameras [6]. This paper introduces the development of a stereophotographic system using general use cameras and alternative algorithms to reduce setup costs. Efforts will also be made to improve thickness resolution and increase the field of measurement.

REINFORCEMENT COMPACTION

Consider evolution of reinforcement fibre volume fraction (V_f) during different phases of a typical Resin Infusion process. Vacuum is applied initially to the reinforcement before resin injection. The reinforcement supports all of the externally applied pressure ($\sigma_f = P_{ATM}$) and a dry maximum V_f is reached. During resin infiltration, two deformation mechanisms occur in the wetted portion of the laminate. As the flow front passes a particular point a local increase in V_f occurs, due to the lubricating effect of the fluid causing a rearrangement of fibres in the reinforcement. The resin pressure locally is low ($P \approx 0$) and the compaction pressure high ($\sigma_f \approx P_{ATM}$), thus V_f increases. As the flow front progresses past this point resin pressure increases, the compaction stress applied to the reinforcement decreases, and a decreases in V_f occurs. Finally, once the mould is filled and resin flow to the inlet is stopped, resin pressure throughout the laminate slowly decreases, and a higher V_f is recovered.

The compaction response of a laminate depends on a number of material parameters including fibre material, reinforcement architecture, and number of fabric layers. Process parameters such as compaction speed also play a role. Compaction speed, number of layers, and resin presence are explored experimentally below.

Experimental Setup

The reinforcement used in this study is an 821g/m² biaxial stitched glass fabric (balanced 0-90°). Circular samples were cut to a diameter of 200 mm. The compaction experiments were performed using a two piece aluminium mould mounted in an Instron 1186 testing machine. The Instron was used in load control mode, allowing specific compaction stresses to be applied to the samples. The major advantage of the testing machine is high accuracy in the measurement of the displacement and load. However, care must be taken in the setup of the mould, as small errors in cavity thickness lead to significant V_f discrepancies. Significant care was taken to ensure that the mould platens were well aligned, and that zero cavity thickness was well established.

Influence of Loading Rate

The first set of compaction experiments were performed to determine the influence of the applied load rate. For simplicity, a test fluid was not introduced to simulate the presence of resin. Samples composed of 6 fabric layers were progressively loaded to a compaction stress of 1.0 bar at a constant loading rate. Load was held constant at this level for 5 minutes allowing creep to take place. The load was then removed at the same rate until an equivalent stress of 0.2 bar was achieved, and another period of constant force was applied. A set of five tests were performed at each of the load rates 0.2, 0.4 and 0.6 kN/min. These speeds were chosen as they roughly approximate the loading rates applied during initial application of vacuum to a dry laminate.

Table 1: Influence of the loading rate on the resulting V_f.

Compaction speed	0.2kN/min	0.4kN/min	0.6kN/min
Mean maximum V_f	53,20%	52,99%	52,83%
Mean V_f after unloading	51,67%	50,56%	50,04%

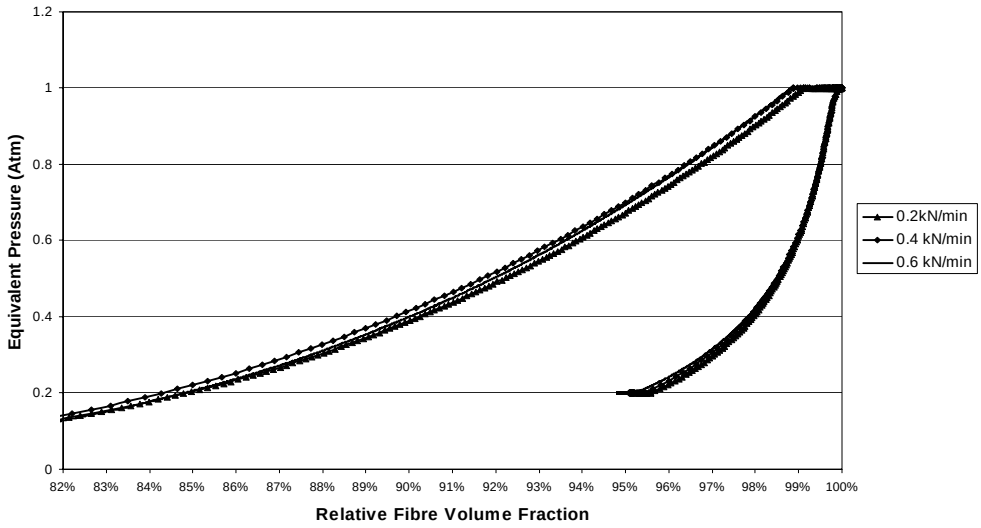

Figure 1: Comparison of the compaction behaviour at various loading rate.

The fibre volume fractions achieved after initial application of vacuum and after unloading to 0.2 bar are presented in Table 1 (averaged across five tests). V_f is seen to decrease slightly with increasing loading rate, the samples showed increasing rigidity. Figure 1 presents V_f versus compaction stress traces for three typical experiments. These traces have been normalised against the maximum V_f achieved, to highlight any significant differences between the shapes of the curves. Considering the similarities between these curves, and the V_f data presented in Table 1, loading rate is assumed to have negligible effect for the remainder of this study. Therefore, the remainder of the tests were performed at a loading rate of 0.6 kN/min.

Influence of the Number of Layers

It has been widely documented that the number of layers of reinforcing fabric significantly influences the compaction behaviour of a laminate [7, 8]. The strength of this effect depends on the architecture of the reinforcement. To study the strength of this effect for the biaxial fabric, compaction samples composed of 3, 6, 9, 12 and 15 layers have been tested. The same compaction strategy was applied as above. Table 2 presents the V_f values achieved at various stages, in each case being an average of five tests. The V_f values diminish with increasing

numbers of layers, but do not approach a limit. Figure 2 presents V_f versus compaction stress traces for five typical experiments, with the data being normalised against the maximum V_f. This figure demonstrates a high degree of similarity between four of the curves, the overall behaviour being very similar for samples composed of at least 6 layers. Samples of 6 layers were used for the remaining compaction studies.

Table 2: Influence of the number of layers on the V_f.

Number of layers	3	6	9	12	15
Mean V_f after first compaction	52,5%	50,2%	49.7%	49.4%	49,3%
Mean V_f after unloading	50,2%	48,0%	47.6%	47.3%	47,1%
V_f after second compaction	52,9%	50,8%	50.3%	50.1%	49,9%

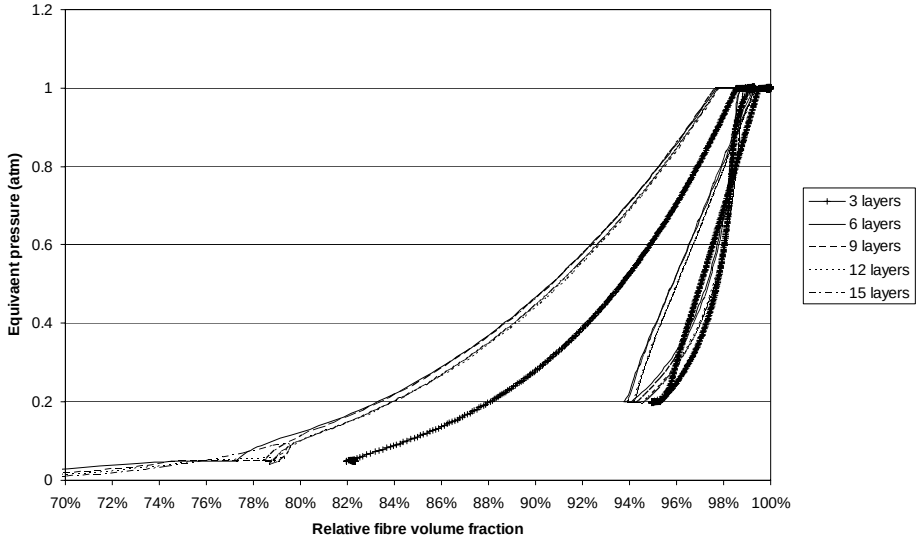

Figure 2: Compaction curves related to the maximum volume fraction for different number of layer.

Wet Compaction Response

Compaction experiments were completed to demonstrate the influence of the presence of a viscous fluid. Another focus of this study was the application of different pressures at vents during filling and post-filling, following on from previous studies exploring the possibility for V_f control [5]. Samples of 6 layers were subject to a similar compaction strategy as described above, using a loading rate of 0.6 kN/min. For these experiments, fluid was injected slowly into the reinforcement following the initial period of holding at 1.0 bar. This pressure was maintained constant, allowing any further relaxation to occur due to the presence of the fluid. The reminder of the test was carried out as described above. This compaction cycle was modified to simulate the use of different pressures during processing. Pressure at the vents during filling and post-filling were set at values of 0.01, 0.3, and 0.5 bar. The various strategies applied are detailed in Table 3.

Table 3 presents V_f's achieved at three instances in the compaction cycle. The final column in this table presents the V_f achieved at completion of the process, essentially the V_f of the finished product. This data presents a small potential for controlling the V_f of the resulting composite (48.2 to 51.8%), which appears to depend only on the pressure applied during post-filling. These results do not reflect the larger degree of V_f control demonstrated in a previous study of the actual resin infusion process [5], in which a V_f range between 47.1 and 59.1% were achieved for the same biaxial fabric. In that study it was shown that pressure levels set during both filling and post-filling significantly influenced the final V_f of the laminate. Method A (according to Table 3) gave the largest V_f of 59.1%, and method E the lowest value

of 47.1%. It should be noted that V_f data for this Resin Infusion study was determined by measuring mass fraction of the resulting laminates. This method does not account for any residual void content. However, visual inspection of the laminates leads the authors to believe that void content is not the sole reason for discrepancies between the compaction studies described here, and the previous Resin Infusion tests. Such discrepancies can be best explored by full field cavity thickness measurements. This issue has provided motivation for the stereophotography equipment described below.

Table 3: Result of the wet compaction tests.

Vacuum pressure during mould filling / postfilling (mbar)	Method	V_f after first compaction	V_f after unloading	V_f after second compaction
500/10	A	47,68%	46,60%	51,50%
300/10	B	49,10%	47,42%	51,66%
10/10	C	50,54%	48,05%	51,82%
500/300	D	47,29%	46,27%	49,32%
300/500	E	48,83%	47,16%	48,83%
300/300	F	48,70%	47,17%	49,65%
500/500	G	47,66%	45,95%	48,20%
10/300	H	50,93%	48,44%	50,83%
10/500	M	51,14%	48,61%	50,11%

THICKNESS VARIATION MEASUREMENT DURING RESIN INFUSION

Laser Gauges

Variations of laminate thickness during Resin Infusion are very influential, mould filling times being affected by the variations in V_f, and hence reinforcement permeability. Thickness variations have been measured in the past using LVDTs. These sensors rely on contact, and for that reason apply a limited but measurable stress to the laminate [9]. Laser gauges have also been used as a non-contact option [5], but along with LVDTs, they provide measurements only at a single point. Another drawback of laser gauges is the very small sampling area; the thickness data may have significant variation depending on the place of the measurement, whether made at the centre of a fibre tow, or between two tows. Figure 3 presents sample laminate thickness data from four Resin Infusion tests, performed without distribution media. In each case 12 layers of the biaxial fabric were employed, being infused with mineral oil, under identical conditions. In all four tests an initial drop in laminate thickness is observed as the resin front passes the measurement position. Beyond this time the four traces exhibit quite different, and puzzling behaviour. Our ability to interpret this data is severely limited as measurement is completed at a single point, providing further motivation for development of full field measurements.

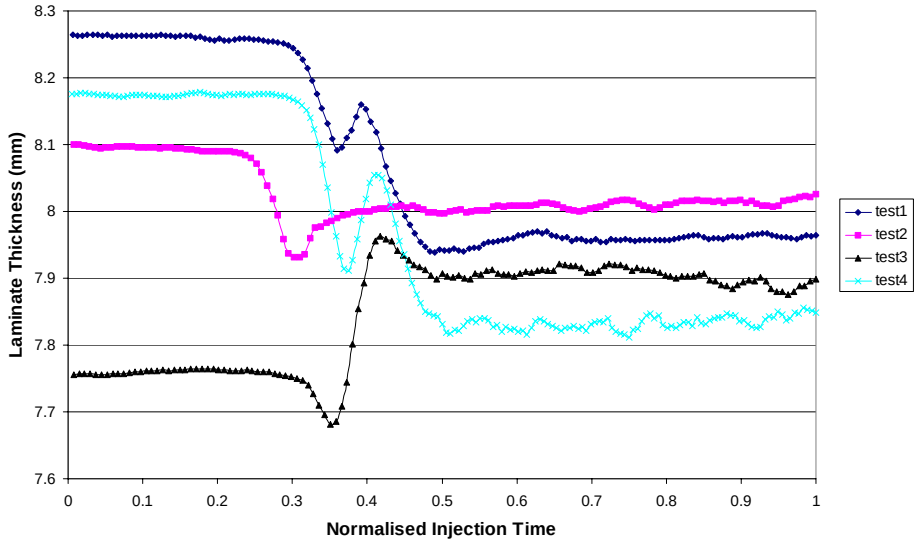

Figure 3: Comparison of the laser transducer reading on four similar experiments.

Stereophotography

Theory

Direct distance measurement techniques, *e.g.* laser range-finders and SONAR, scan a single probe beam through a scene and measure time-of-flight or phase differences from which distances are trivially derived. These techniques are relatively slow, being dependent on mechanical scanning systems, and thus not well suited to the acquisition of dense 3D maps of fast processes.

Stereophotography is based on triangulation - two cameras at different positions establish two lines to each binocularly visible point in the scene. This results in dense 3D environment maps at speeds determined by the rate at which images can be transferred from the cameras to a computer and processed. Figure 4 shows the arrangement used in our system. Note that we use a *verging* axis system to obtain better accuracy from our cameras - by maximising the number of binocularly visible points and using most of the image planes of each camera[10].

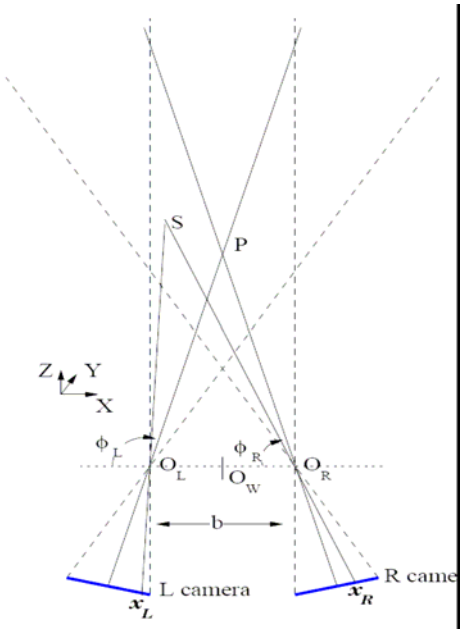

Figure 4: Stereo camera arrangement:
$O_{L|R}$ - optical centres of left—right cameras;
P - fixation point (intersection of camera optical axes);
S(X,Y) - scene point;
$x_{L|R}$ -x-coordinate of projection of *S* onto camera image planes;
$\phi_{L|R}$ - angles between optical axes and baseline;
b - camera separation

In Figure 4, two cameras are positioned with their optical centres separated by a distance, *b*, along the baseline and aligned at angles, ϕ_L and ϕ_R to the baseline. The optical axes intersect at the *fixation point*, *P*. A typical scene point, *S(X,Y,Z),* appears at x_L in the left camera image and x_R in the right camera image. The difference, $d=x_L - x_R$ is known as the disparity. If world coordinates are referenced to an origin, O_W (mid-point of the baseline joining the camera optical centres) and axes *X, Y* and *Z*, as shown in Figure 4, then the coordinates of a scene point are:

$$X = \frac{b}{2}\frac{(f\tan\phi_R + x_R)(f - \tan\phi_L x_L) + (f\tan\phi_L + x_L)(f - \tan\phi_R x_R)}{(f\tan\phi_R + x_R)(f - \tan\phi_L x_L) - (f\tan\phi_L + x_L)(f - \tan\phi_R x_R)} \tag{3}$$

$$Z = -(\frac{b}{2} + X)\frac{f\tan\phi_L + x_L}{f - \tan\phi_L x_L} \tag{4}$$

(5)

$$Y = \frac{Z}{f\sin\phi_L} y_L \tag{5}$$

where *f* is the focal length. Thus, given a correct match between the points on the image planes (*xL, yL)* and (*xR, yR)* corresponding to a scene point (*X, Y, Z)*, the coordinates of the scene point can be discovered. In practice, determining a correct match automatically is a non-trivial problem. Fortunately, in this particular application, one major source of matching difficulties – occlusions or points visible in one camera only - will be absent: the smooth, continuous single surface of the mould enables smoothness and continuity constraints to be added to the matching algorithm. We have painted the surface of the mould with a fine, random pattern of coloured spots to provide sufficient texture to reduce the probability of false matches due to sensor noise, variations in reflectance with angle, *etc*. Furthermore, a small window of pixels (typically 9*9) was used as the basis for matching to reduce the effects of noise (We use the term 'noise' here to include all sources of intensity mismatch[10]).

Setup

Two Canon EOS 20D digital SLR Camera with resolution of 8.2 Mega-pixels are used for image acquisition. These cameras are mounted on a series of precision rotation stages, and a goniometer to allow for very precise alignment. The cameras are connected to two synchronized computers that control the cameras and store the images. The cameras must be aligned to converge exactly on the same point, ensuring they capture same plan area. Calibration is carried out using a precise grid, allowing for any inherent distortion of the camera lenses, and allowing the determination of the orientation and baseline between the cameras. Determination of the orientation and baseline are necessary for the triangulation process used to determine 3D shape of the subject.

To facilitate stereo-matching of the two images during the Resin Infusion processing, a random pattern is painted on the vacuum bag. This pattern must present very fine random features at a high frequency as the matching window is a square of 13*13 pixels. After several trials, the selected pattern is painted with spray-cans of cyan, magenta, and yellow, applying a random arrangement of very small paint droplets. It is also very important to provide good lightning to the subject, and to prevent any reflections on the surface. Reflections are usually affect each camera differently, causing major problems during image matching.

The stereophotography rig is mounted over a temperature controlled Resin Infusion table. Fluid pressures inside the laminate are measured at three locations using pressure transducers mounted on the underside of the table. Fluid flow rate into the laminate is monitored by continuously weighing the resin pot using a mass balance attached to the data acquisition computer.

Figure 5: Details of the stereophotography rig.

Results

Several reconstructed 3D images are presented in Figure 6. A snail model has been used previously to prove the technique, however, the depth variations in this object are much greater than those expected in a laminate during Resin Infusion. This model is 22 cm long and 12 cm wide, and includes small variations in texture having depth of 0.5 mm. A 3D reconstruction from a Resin Infusion experiment is also presented in Figure 6. The laminate was constructed of 10 layers of a 450 g/m² Continuous Filament Mat (CFM) fabric, 50 cm long and 27 cm wide. CFM was chosen for it's large thickness, and large thickness changes during processing. The 3D reproduction of the laminate thickness is covered with the actual texture captured by the cameras, providing a visually pleasing result. However, while the image appears to show a reasonable thickness variation behind the flow front, it has become clear during processing of the data that the current stereo-matching algorithm is incapable of resolving laminate thickness to the required accuracy. A resolution on the order of 0.03 mm is the goal of this work, but currently we are only able to achieve approximately 0.5 mm. Alternative matching algorithms have been sourced, and will be implemented in the near future.

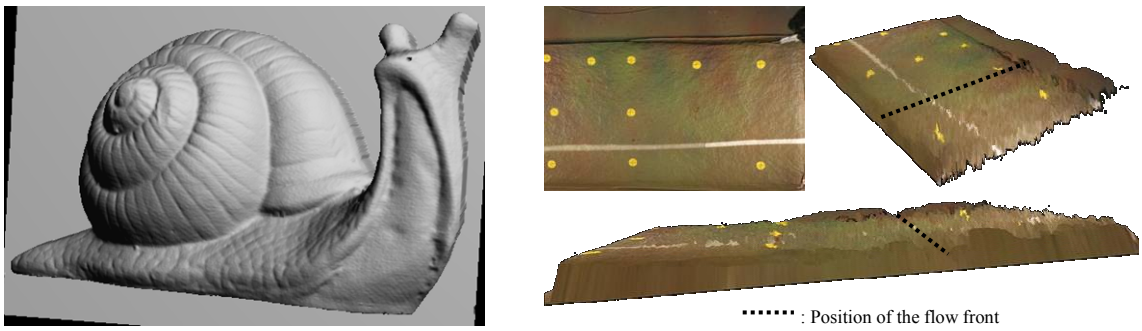

Figure 6: 3D images reconstructed using the Stereophotography technique.

CONCLUSION

The main focus of this study was to demonstrate the potential of full field laminate thickness measurement during the Resin Infusion process. Several compaction studies have been presented demonstrating the complex nature of fibre reinforcements, and the influence of several process parameters. The complexity of reinforcement compaction response motivates

the detailed measurement of laminate thickness evolution, vital if accurate process simulations are to be developed. The disadvantages of single point measurement techniques has motivated the authors to develop a stereophotographic system for monitoring full field thickness variation. A full field measurement will help to explain spatial variations in laminate thickness, which appear to produce erratic results from experiment to experiment using single point techniques. An experimental facility has been established, and the technique validated against test 3D shapes. An initial Resin Infusion experiment has been subjected to the stereo technique, and while the results are visually pleasing, it is clear that the current image matching algorithm does not provide the accuracy of thickness resolution required. Efforts now focus on the implementation of an appropriate matching algorithm.

ACKNOWLEDGEMENTS

The authors thankfully acknowledge the funds received from the Foundation for Research, Science and Technology New Zealand to carry out this research. They also would like to acknowledge High Modulus (NZ) Ltd. for the donation of reinforcements.

REFERENCES

[1] G. Marsh, "Putting SCRIMP in context," *Reinforced Plastics*, vol. 41, pp. 22-26, 1997.

[2] C. Williams, J. Summerscales, and S. Grove, "Resin Infusion under Flexible Tooling (RIFT): a review," *Composites Part A: Applied Science and Manufacturing*, vol. 27, pp. 517-524, 1996.

[3] B. Berenberg, "Liquid composite molding achieves aerospace quality," *High-Performance Composites*, vol. 11, pp. 18-22, 2003.

[4] R. W. Koon, S. C. Parsons, L. K. Flansburg, and R. Loeslien, "VARTM of integrated secondary aircraft structure," presented at 34th International SAMPE Technical Conference, Baltimore, MD; USA, 2002.

[5] B. Daval and S. Bickerton, "Exploring the potential for laminate quality control using VARTM," in *36th Int. SAMPE Technical Conference*. San Diego, CA: SAMPE, 2004.

[6] H. M. Andersson, T. S. Lundstrom, B. R. Gebart, and P. Synnergren, "Application of Digital Speckle Photography to Measure Thickness Variations in the Vacuum Infusion Process," *Polymer Composites*, vol. 24, pp. 448-455, 2003.

[7] F. Robitaille and R. Gauvin, "Compaction of textile reinforcements for composites manufacturing. I: Review of experimental results," in *Polymer Composites*, vol. 19, 1998, pp. 198-216.

[8] P.A. Kelly, R. Umer, and S. Bickerton, "Viscoelastic response of dry and wet fibrous materials during infusion processes," *Composites Part A: Applied Science and Manufacturing*, vol. In Press, Corrected Proof.

[9] L. Joubaud, V. Achim, and F. Trochu, "Numerical simulation of resin infusion and reinforcement consolidation under flexible cover," *Polymer Composites*, vol. 26, pp. 417-427, 2005.

[10] J. Liu, P.J. Delmas, G. Gimel'farb, and J. Morris, "Stereo reconstruction using an image noise model," presented at Digital Image Computing: Techniques and Application (DICTA2005), Cairns, Australia, 2005.

EXPERIMENTAL INVESTIGATION OF THE COMPRESSIBILITY AND PERMEABILITY OF FABRIC REINFORCEMENTS

E.C. van de Ven, R. Loendersloot, R. Akkerman

UNIVERSITY OF TWENTE
Faculty of Engineering Technology, P.O. Box 217 NL-7500AE Enschede, The Netherlands:
e.c.vandeven@utwente.nl

ABSTRACT: A measurement method for the out-of-plane permeability is presented in this paper. The developed permeameter is capable to measure both compression as well as the out-of-plane permeability. First results show an out-of-plane permeability that is in accordance with values found elsewhere. The compression test needs some more refinement and is not discussed here. The design of the instrument is such that it is relatively easy to change a preform between subsequent tests. A first attempt has been made to measure the viscosity of the test fluid in-line.

KEYWORDS: composites, transverse permeability, determination, design, experiment

INTRODUCTION

In Resin Transfer Moulding (RTM) a porous pre-placed preform is impregnated by a resin in a closed mould. The flow in thickness direction of a preform is often regarded as negligible. This simplification is allowed for products with a small thickness compared to the in-plane dimensions. The flow in the mould will be approximately two-dimensional. However, the increasing application of RTM for structural components has led to thicker components in which the flow through the thickness can not be neglected. Consequently, knowledge of the permeability in transverse direction, K_z, is receiving an increasing amount of attention.
Another field in which the permeability in transverse direction is needed is the field of the infusion technologies. The resin is generally injected through a transport medium on top of the preform, after which the resin impregnates the fibres in transverse direction. A second aspect of the infusion technologies is the compression behaviour of the fabric. The compressibility and the permeability are interrelated [1] and therefore it is desirable to gain knowledge on both simultaneously.
The presented work comprises the design of a permeameter and results of measurements of the transverse permeability during impregnation of the fabric. Measurements at a fixed cavity height are possible. The design of the instrument is largely based on standard tools [2]. This work was a part of a project in which the National Aerospace Laboratory and the Centre of lightweight constructions participated together with the University of Twente and was financed by the Netherlands Agency for Aerospace Programmes.

EQUIPMENT AND DESIGN

The functions that have to be fulfilled are translated into design constrains resulting in the following list:

- The cavity size has to be adjustable.
- Race tracking must be avoided at all times.
- The diameter of the cavity must be such that a steady-state flow through the preform is established during the measurement.
- It has to be possible to measure both unsaturated and saturated permeability.
- The pressure before and after the preform has to be measured.
- The wetting time of the preform should be measured.
- The permeameter does not need to handle thermosets, only test fluids will be used during measurements.
- The permeameter does not require vacuum to be applied.
- The permeameter must be capable to measure the compression force before as well as during injection.

The design constrains led to the permeameter presented in this paper. It consists of five parts: the lower section, upper section, internal section, top lid and the compressing section. See Fig. 1.

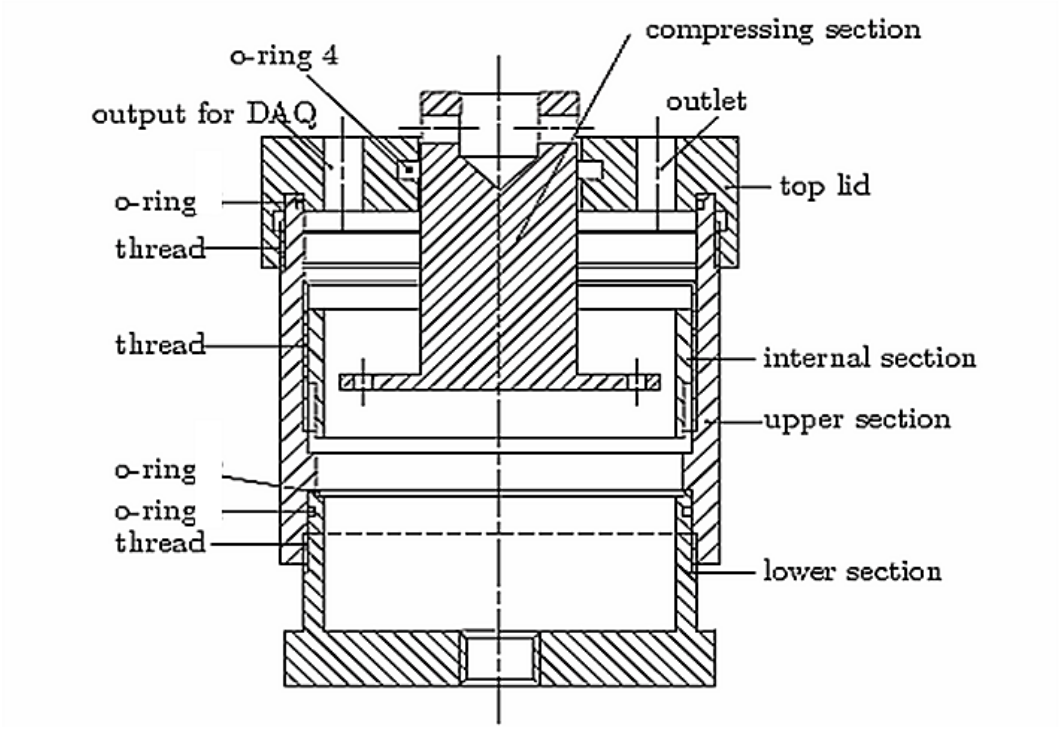

Fig 1 Composition drawing of the design of the permeability instrument.

The liquid enters the permeameter through an inlet in the bottom. The fluid flows in upward direction. The lower section reaches up to the bottom of the preform. The preform edge rests on a sealing ring inside this part. The upper section is connected to the lower section with a thread on the outside of the lower section. This simplifies preform change between experiments.

The internal section is placed inside the upper section. The function of this part is to compress the preform on its edge. A thread is present on the internal section. The preform is tightly sealed by screwing it downwards onto the preform. It ensures that no race tracking occurs.
The edge of the preform is covered with Poly Ethylene (PE). It serves as adhesive between the different layers that form the preform and tight sealing of the preform is ensured in combination with sealing rings. The top lid closes the cavity. A piston is present through the top lid. The piston can be translated vertically to control the cavity height inside the body. With this feature the fibre volume fraction (V_f) can be preset prior to the measurement.
The preform is placed in the tubular cavity. Each side of the tube is closed with a lid, such that a completely closed system is formed. Fixation and compression of the preform is achieved by a set of soldered copper pipes. The fluid obstruction of the copper pipes is small compared to the obstruction by the preform itself. Fig. 2 illustrates the position of the copper pipes in relation to the preform.

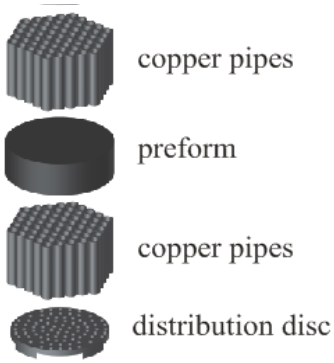

Fig 2 The position of the copper pipes in relation to the preform.

The permeameter is placed in a press, which controls the required vertical position of the piston to be set at the desired height. A load cell connected to the piston measures the applied closing force. A linear variable displacement transducer (LVDT) is placed outside the cavity to measure vertical motion and the resulting cavity height. A perforated aluminium disk is placed underneath the lower set. This disk ensures the liquid to be distributed evenly prior to entrance into the lower copper pipes set. Visual inspection of the preform showed that the liquid level is even when the preform is reached. The cavity height and compression are better controlled, if the vertical motion of the copper pipes is restricted to the motion of the compression section.
The viscosity is measured in-line in a section of the inlet tube. This section has a reduced diameter. This viscosity can be calculated using the Hagen-Poiseulle equation, which relates the pressure drop ΔP to the viscosity μ:

$$\Delta P = \frac{128 Q_v L}{\pi d^4} \mu \tag{1}$$

Here μ is the viscosity, Q_v the volume flow, L the tube length and d the tube diameter.
The permeameter placed in the press is shown in Fig. 3.

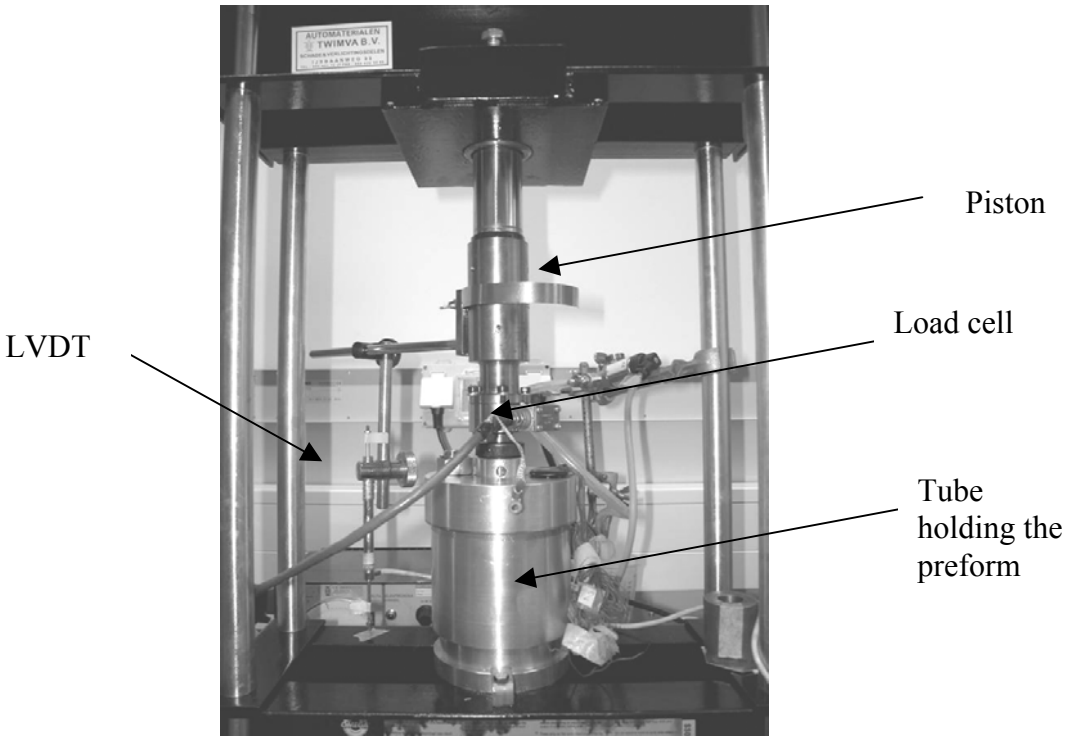

Fig 3 Overview of the instrument placed in the press

DATA ACQUISITION

The load on the preform is measured with a 10 kN load cell. The output is between 0 and 10 volts and fed into a data shuttle.
The pressure is measured by pressure transducers KOBOLT type 3272.072.192 at three locations: two underneath and one above the preform. See figure 4.

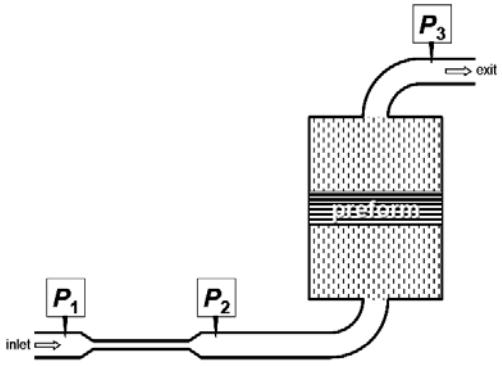

Fig 4 Location of the pressure transducers

A reference pressure transducer is connected directly to the pressurised air system to monitor the injection pressure. The range of the transducers is 0 to 2.5 bars absolute pressure. The output of the transducers is a 0 to 10 Volt signal.
The mass flow has to be measured to determine the saturated permeability. The mass of the pressure vessel holding the test liquid is measured as a function of time, obtaining the mass flow Q_m. The decrease of mass is constant in time if a steady-state flow is obtained,

$$\frac{dm}{dt} = Q_m = \text{constant} \qquad (2)$$

The weight of the pressure vessel itself is large compared to the decrease of its weight. An accurate measurement is therefore difficult. It is necessary to compensate a large part of the total weight of the vessel. A spring was connected to the top of the pressure vessel to this end. This spring compensates for the net weight of the vessel. A small load cell is used to measure the change of weight of the vessel. Evidently, the flow going into the instrument should be equal to the flow through the preform. The pressure and flow measurement are synchronized.

PREFORM PREPARATION

The preform consists of a stack of circular shaped fibre mats. The stack has to be high enough to provide sufficient flow length through the preform.
The preforms were prepared at the National Aerospace Laboratory (NLR) using a computer controlled cutting machine type (Zund M1600). The stack cannot be cut at once. The layers were cut individually.
The cutting procedure, developed at the NLR, enables to produce automatically cut, circular preforms with smooth, non ravelling edges. Ravelling of the edges occurs when the blade of the knife is oriented parallel to the fibre bundle. The fibres are then pushed aside rather than cut, due to the relative loose structure of the fibre mat. The structure is stabilized by applying a Poly Ethylene (PE) film to the fibre mat. See Fig 5.

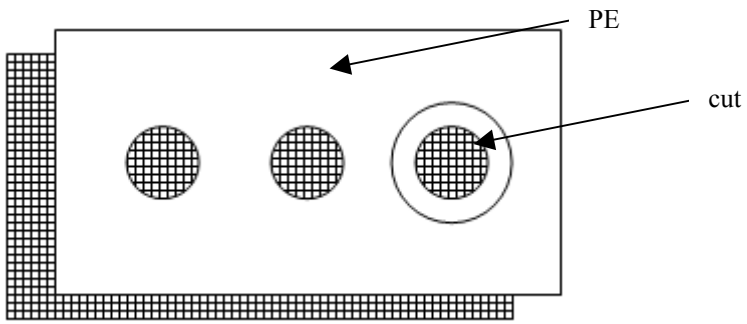

Fig 5 PE film on the fibre mat

The cut is made through the PE stiffened part, leaving a circular region free of PE.

The preform, consisting of 30 layers (depending on the fabric about 10-12 mm thickness), is made by stacking the single layer preforms onto each other. A weight is placed on top to provide some compressive force. The PE is melted during 15 min at 150°C causing the individual single layer preforms adhere together. The result is shown in figure 6.

Fig 6 A stacked 30 layer preform

The fluid is injected with a constant pressure. A pressure vessel is used to this end. The injection pressure is 0.2-0.3 bars. No vacuum is being applied to the instrument. Only saturated flow is measured.

RESULTS & DISCUSSION

A number of experiments were performed using a 2/2 twill carbon fibre fabric (Ten Cate CD 202). First the flow front shape was checked visually. To this end the preform was placed without the upper lid and piston to make the arrival of liquid visible. Thus no compression was exerted on the preform. This causes a lower fibre volume fraction and therefore a less favourable situation to obtain a flat flow front. Even in this situation the liquid arrived in the middle as well as in the edges on the same time. Therefore a flat flow front was assumed in further measurements. The flow front advances in the order of 0.02 mm/sec through the tube and through the preform.
The pressures at the entrance of the viscosity meter (P_1), at the entrance of the cavity (P_2) and above the cavity (P_3) were measured (see figure 4). ΔP_{visc} is the difference between P_1 and P_2, subscript "visc" denotes the viscosity. ΔP is the pressure drop between P_2 and P_3 that is used for the permeability calculation. Note that only the saturated permeability is measured. The permeability is calculated according to Darcy:

$$K_z = \frac{Q_v \mu h}{\Delta P A} \qquad (3)$$

Here K_z is the out-of-plane permeability, Q_v the volumetric flow rate, μ the viscosity of the test fluid, ΔP the pressure difference over the preform and A the area of the preform.
The pressure and the mass flow are recorded as a function of time during the measurement. Fig. 7 shows a typical output. The preform has been compressed to 55 % fibre volume fraction (V_f). The injection pressure is 0.2 bar.

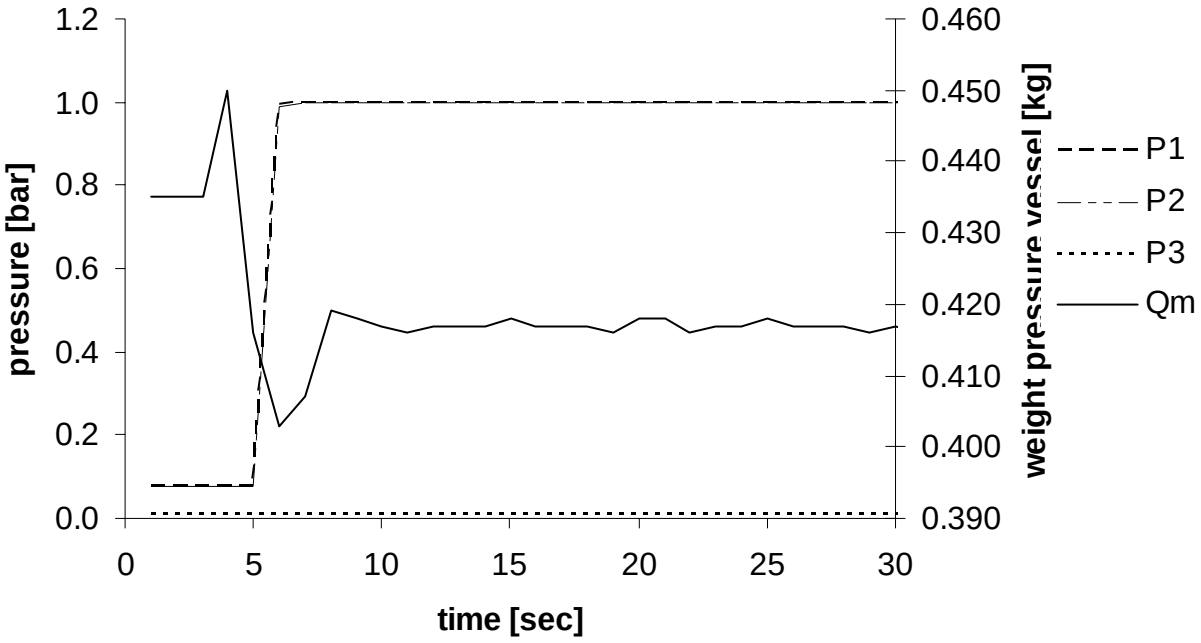

Fig 7 Pressure and flow rate versus time preform under compression to 55% V_f

The pressure transducer response at the start of the measurement is presented in Fig. 7.
The pressure difference between P_1 and P_2 is very small and hardly distinguishable. A fast increase of pressure at the moment the flow front reaches the preform is observed. The preform used has been impregnated already in previous experiments, the wetting process does not occur anymore. Table 1 shows measurement results of repeated experiments on a single preform.

Table 1 Results of a permeability measurement

Exp #	Q_m [kg/sec]	Q_v [m^3/sec]	μ [Pa.s]	h [m]	A [m^2]	ΔP [x10^5 Pa]	ΔP_{visc} [x10^5 Pa]	K_z [m^2]
1	$8.78x10^{-5}$	$8.25x10^{-5}$	0.03	0.0106	$4.3x10^{-3}$	0.990	0.002	$6.17x10^{-11}$
2	$6{,}74x10^{-5}$	$6{,}34x10^{-5}$	0.03	0.0106	$4.3x10^{-3}$	0.986	0.002	$4.75x10^{-11}$
3	$5{,}71x10^{-5}$	$5{,}37x10^{-5}$	0.03	0.0106	$4.3x10^{-3}$	0.978	0.002	$4.06x10^{-11}$
4	$4{,}87x10^{-5}$	$4{,}58x10^{-5}$	0.03	0.0106	$4.3x10^{-3}$	0.971	0.002	$3.49x10^{-11}$

From these results it can be seen that the viscosity cannot be calculated according to Eqn 1 as ΔP_{visc} shows to be too small to give a reliable result. This is due to the accuracy of the

pressure sensors and the low volumetric flow in combination with the diameter of the tube applied. Its diameter has to be modified, see Eqn 1.
When performing a measurement the volume flow rate reads an equilibrium value after a short settling time. This value is subsequently used for the calculation of the out-of-plane permeability.
The results depicted in table 1 show that the out-of-plane permeability changes to lower values when the measurement is repeated with the same preform kept in place. This is directly related to Q_v through the preform. The pressure over the preform (ΔP) changes slightly (-2%) during the measurements whereas Q_v decreases with 45%. The pressure change is due to the air supply system. Considering μ, and A constant, the change of Q_v is attributed to a change of out-of-plane permeability. Fibre bundles can slip to a more dense packing during loading and unloading due to lubrication by the test liquid. This results in a significant difference between dry and wet preform compaction [3]. So V_f is not constant and h is not constant as recorded by the LVDT. This means that only a first measurement is useful for actual process simulations.

CONCLUSIONS

The conclusions that can be drawn from the experiments to measure the permeability are:

- The several layers of a preform are molten together by use of an empirical process; the seal quality has to be controlled better.
- Out-of-plane permeability data are in accordance with the literature, reliable permeability data can be obtained from the permeameter.
- Slip between fibre bundles can occur in saturated permeability measurements due to lubrication. For actual process situations only the first measurement on a new preform is useful.

ACKNOWLEDGEMENTS

The support of the Netherlands Agency for Aerospace Programmes (NIVR) is gratefully acknowledged.

REFERENCES

1. S. Bickerton, M.J. Butain and A.A. Somashekar “The viscoelastic compression behavior of liquid composite molding preforms”, C*omposites Part A*, Vol. 34, pp 431-444 (2003).

2. S. Drapier, A. Pagot and A. Vautrin and P. Henrat “Influence of the stitching density in the transverse permeability of non-crimped new concept”, (NC@) Multiaxial Reinforcements: Measurements and Predictions), *Composites Science and Technology*, Vol. 62, pp 1979-1991 (2002).

3. J.F.A. Kessels, A.S. Jonker and R.Akkerman “Fully 2½ D flow modeling of resin infusion under flexible tooling using unstructured meshes and wet and dry compaction properties», *Composites Part A: Applied Science and Manufacturing, In Press, Corrected Proof*

Session 6

SIMULATION - I

A FAST NUMERICAL APPROACH TO REDUCE VOID FORMATION IN LIQUID COMPOSITE MOLDING

Edu Ruiz[(a)(*)], V. Achim[(a)], J. Bréard[(b)] S. Chatel[(c)] and F. Trochu[(a)]

(a) Chaire sur les Composites à Haute Performance (CCHP), Centre de Recherches En Plasturgie Et Composites (CREPEC), Département de génie mécanique,
École Polytechnique, Montréal (Québec) HC 3A7 http://cchp.meca.polymtl.ca
(b) Laboratoire de Mécanique, Physique et Géosciences, Université du Havre,
Quai Frissard, BP 540, 76058 Le Havre Cedex, France
(c) European Aeronautic Defense and Space Company, Corporate Research Centre (EADS CCR),
12 rue Pasteur BP 7692152 Suresnes Cedex, France

(*)e-mail: edu.ruiz@polymtl.ca

ABSTRACT: Liquid Composite Molding (LCM) regroups a number of well known manufacturing techniques of fiber-reinforced polymer composites based on resin injection through fibrous reinforcements. LCM processes such as RTM (Resin Transfer Molding) have been increasingly used to manufacture parts for a wide range of industrial applications and were shown to be cost-effective in the low to medium range of volume production. To improve the performance of these processes, more scientific knowledge of the impregnation phenomena is required. It has been recently observed that the resin velocity during impregnation of the fibrous preform is a key factor that governs the formation of macro/micro voids trapped between or inside the fiber tows. An inverse relationship of the volume of macro/micro voids with the fluid velocity indicates the existence of an optimum velocity that minimizes the void formation during mold filling. In this work, a new numerical simulation and process optimization procedure is proposed to minimize void formation during the filling stage in LCM. The approach consists of calculating the flow rate to be injected at each time step in order to guarantee an optimum impregnation velocity at the flow front that minimizes the formation of macro/micro voids. Experimental injections were conducted to validate the proposed approach. A test case was carried out on a composite part to highlight the advantages of the proposed optimization. This numerical tool brings an added value to standard LCM simulations and opens up the scope of a whole range of new applications of process optimization.

INTRODUCTION

During the past years, polymer composite applications have gained ground for technological, economical and environmental reasons. The aerospace, marine and automotive industries have pioneered the use of high performance composites in numerous structural and semi-structural applications. Nowadays, a wide number of applications have appeared in different fields such as biomedicine, petroleum plants, bridges, etc. Liquid Composite Molding (LCM) regroups a number of techniques to manufacture fiber-reinforced polymer composites. LCM processes such as Resin Transfer Molding (RTM) have been increasingly used to manufacture parts for a wide range of industrial applications demonstrating the cost effectiveness of this technology in the low to medium range of volume production. In RTM manufacturing, during the injection stage, a liquid resin impregnates the fibers before it cures and solidifies. If the fibrous reinforcement is not fully impregnated, voids are created resulting in a decrease of

mechanical properties and surface quality of the part. To improve process performance, void formation during resin impregnation must be reduced. The fibers typically used in LCM are described as a dual-scale porous medium [1]. As shown in Fig. 1 for a unidirectional glass fabric, porosities can be observed at two identifiable scales. Porosities at the macroscopic scale are defined as the free spaces between fabric tows (see Fig. 1(a)), while the microscopic scale represents the free spaces between tows (see Fig. 1(b)). This double scale porous medium leads to a two-level impregnation mechanism (i.e., filling of the micro and macro-pores). Researchers have experimentally studied the infiltration phenomena and concluded that the resin velocity influences the formation and location of the voids in the part [1, 2]. During impregnation of a double-scale porous medium, the forces that induce the motion of the fluid are of two different nature: the viscous and the capillary forces. Bréard et al. [1] carried out a microscopic study of the porosity and void content of RTM composite specimens manufactured at different injection flow rates. It was found that for low resin velocities, the capillary forces become dominant inducing the fluid flow to travel through the fabric tows, where the porosity is smaller and the total surface tension higher. As shown in Fig. 2(a), in the case of capillary dominant flows, macro-voids can be trapped in the open spaces between fiber tows. In the opposite case, for high resin velocities, the viscous forces are predominant forcing the fluid flow to travel trough the open spaces between tows (see Fig. 2(b)). As depicted in the microscopic image on Fig. 2(b), in case of viscous dominant flow, microscopic voids appear inside the fiber tows due to the difference between the viscous resistance in the tows and in the open channels. In the past, researchers have published several experimental investigations on the formation of micro and macro-voids [1-4]. Some analyses were also performed to identify and describe the mechanisms of void formation [5-6]. In practice, the injection flow rate should be optimized and controlled to minimize void formation. Numerical simulation is a useful tool of virtual prototyping in composite manufacturing. Computer analyses are addressed to model, predict and control the events that occur during the fabrication of LCM parts, although no much information is given about the impregnation of the fibers. In this work, a practical numerical methodology is presented to calculate the optimum injection flow rate that minimizes void formation and improves RTM processing. The proposed numerical approach results in a fast calculation of the optimal transient injection rate to open/close the injection gates and vents even in the non-isothermal case.

OPTIMAL IMPREGNATION VELOCITY

Various researches [7-9] have demonstrated that the percentage of macro/micro-voids formation is a near logarithmic function of the fluid flow velocity (v). As shown in Fig. 3, the volume of macro and micro void formation can be estimated as an inverse logarithmic function of the impregnation velocity. In this work, void formation was measured for three kinds of reinforcements: a monofilament mat Unifilo 101 from Vetrotex, a bi-directional glass fabric NCS 82620 and a woven fabric consisting of single end glass rovings Rovcloth 2454 from Fiber Glass Industries. For each reinforcement rectangular composite plates of 35 x 25 cm and 3 mm thick were impregnated with an epoxy resin. For each composite plate manufactured, the resin injection flow rate was varied between 6 and 18 ml/sec and the void content measured by comparison with the composite density (following the norms ASTM D792-00 and ASTM D3171-99). As depicted in Fig. 4 for the Unifilo 101, a nearly constant void formation was observed along the length of the composite plates. The figure also highlights the influence of the injection flow rate (or injection velocity) on the formation of voids. This experimental analysis demonstrates the existence of an optimal injection velocity that minimizes the void formation in the fibrous reinforcement [2, 7]. Instead of relating the

fluid velocity to the percentage of voids trapped, researchers [2-4, 7-9] have used an dimensionless parameter called the *capillary number* (*Ca*). This dimensionless number represents the relative effect of viscous forces and surface tension acting across an interface between a liquid and a gas. It takes the following form:

$$Ca = \frac{\mu \ v}{\gamma} \tag{1}$$

where μ the viscosity of the fluid, γ the surface tension at the interface air/resin and v is the fluid velocity. Patel et al. [2] measured the voids trapped for a large number of fluids and flow velocities. When void fractions are plotted against *Ca*, the experimental curves merged into a master characteristic curve. Void formation measured as a function of fluid velocity (as shown in Fig. 4) can then be transformed into a function of *Ca*. Using the surface tension characterized by Patel et al. [2] for an epoxy resin γ = 35 mN/m and a resin viscosity of μ = 0,1 Pa.s, the measured void contents were compared for the three reinforcements as a function of *Ca* (see Fig. 5). It can be observed that minimum void formation is obtained for a *Ca* of 3,8 e-2 for the Unifilo 101, while the FGI and NCS fabrics appear to have a minimum number of voids at lower *Ca* (not allowed by the injection system used in this work).

OPTIMIZATION OF THE INJECTION FLOW RATE

As detailed in [10], once an optimal capillary number is identified for a combination of resin and fibers, the optimal impregnation velocity (v_{imp}^{opt}) can be calculated as follows:

$$v_{imp}^{opt} = \frac{Ca_{opt} \ \gamma}{\mu} \tag{2}$$

Darcy's law is widely used to model the fluid flow through porous media. It establishes the relationship between the fluid velocity and pressure gradient ∇P:

$$\vec{v}_{front} = -\frac{[K]}{\mu\phi}\nabla P \tag{3}$$

where $\vec{v}_{front}$ is the fluid macroscopic velocity at the flow front, $[K]$ is the permeability tensor of the porous medium, μ is the resin viscosity and ϕ is the total porosity of the dual-scale porous medium. Assuming that the micro/macro voids appear in the partially saturated regions near the flow front, the injection flow rate can be optimized by setting the front velocity equal to the optimal impregnation velocity:

$$\left\| \vec{v}_{front}^{opt} \right\| = v_{imp}^{opt} \tag{4}$$

Neglecting the mold deformation, the global mass balance of the fluid indicates that the flow rate across the fluid flow front Q_{front} is equal to the flow rate Q_{inj} injected at the inlet gate:

$$Q_{front} = Q_{inj} \tag{5}$$

In a finite element control volume simulation (FE-CV), for a given time step (i.e., a step during part filling) the flow rate at the flow front Q_{front} is calculated by the flow front velocity $\left\|\vec{v}_{front}\right\|$ passing trough the flow front area A_{front}:

$$Q_{front} = A_{front} \left\|\vec{v}_{front}\right\| \tag{6}$$

The optimal flow rate at the flow front Q_{front}^{opt} (i.e., the flow rate that minimizes void formation), can be calculated by considering the flow front area and the optimal impregnation velocity as follows:

$$Q_{front}^{opt} = A_{front} \cdot \left\|\vec{v}_{front}^{opt}\right\| = A_{front} \cdot v_{imp}^{opt} \tag{7}$$

If an optimal impregnation velocity is desired at the flow front, the flow rate Q_{front} may be corrected in the following way:

$$\frac{Q_{front}}{Q_{front}^{opt}} = \frac{\left\|\vec{v}_{front}\right\|}{v_{imp}^{opt}} \tag{8}$$

To correct Q_{front}, the injection flow rate must be modified. To do so, an initial injection flow rate is corrected with the ratio between the calculated flow front velocity and the optimal impregnation velocity as expressed in equation (8). Regrouping equations (5) and (7), for closed loop iteration in *k*, the corrected injection flow rate that minimizes the formation of macro/micro voids is:

$$Q_{inj}\Big|_{k+1} = \left(\frac{v_{imp}^{opt}\ Q_{inj}}{\left\langle \left\|\vec{v}_{front}\right\| \right\rangle} \right)_k \tag{9}$$

where $\left\langle \left\|\vec{v}_{front}\right\| \right\rangle$ is the averaged flow front velocity for all the elements located on the flow front calculated in the following way:

$$\left\langle \left\|\vec{v}_{front}\right\| \right\rangle = \sum_{i=1}^{n} \left\|\vec{v}_i / \phi_i\right\| / n \tag{10}$$

Combining equations (1), (2) and (4), equation (10) can now be expressed as a function of the optimal capillary number as follows:

$$Q_{inj}\Big|_{k+1} = \left(\frac{Ca_{opt}\ Q_{inj}}{\left\langle \left\| Ca_i \right\|_{i=1,n} \right\rangle} \right)_k \tag{11}$$

The proposed optimization is limited to flows where velocity variations at the flow front are not too high. This is the case for preforms with very different permeabilities or parts of complex geometries where the flow is separated to travel around inserts. Note that even on these cases, the proposed methodology will reduce the formation of macro/micro voids compared to a non-controlled injection. Open channels (such as edge effects) should not be considered in this calculation because macro/micro voids are not trapped in these free spaces.

NUMERICAL IMPLEMENTATION

The numerical implementation of the optimization algorithm is based on a finite element approximation [11] of Darcy equation combined with an iterative procedure to correct the injection flow rate as proposed by equation (11). The algorithm starts with a standard filling simulation with the optimal impregnation velocity v_{imp}^{opt} imposed at the injection gate. The averaged capillary number $\left\langle \left\| Ca_{opt} \right\|_{i=1,n} \right\rangle$ is then extracted from the finite elements at the flow front. This capillary number is then used in equation (11) to rescale the injection flow rate. For each time step, a closed loop iteration is performed until the averaged capillary number in the vicinity of the flow front approaches the optimal value Ca_{opt}. The resulting injection flow rate is then used as a new boundary condition to advance the flow front to a new transient position defined by the filling algorithm. Finally, a new time step is computed, and the iterative process repeated until the mold is totally filled.

APPLICATION EXAMPLE

To illustrate the capabilities of the proposed optimization procedure, an application example was performed for an automotive part. The isothermal filling of a car hood (see Fig. 6) was simulated at constant injection pressure, constant injection flow rate and with the optimized injection flow rate from equation (11). Fig. 7 shows a comparison of the void formation calculated for the three injection strategies simulated.

The injection performed at constant pressure shows a high formation of voids (around 4%) at the middle of the radial geometry resulted from the central injection (see Fig. 7(a)). Similar results were obtained for an injection at constant flow rate because of the variations of the flow front velocity during filling of the car hood (see Fig. 7(b)). To optimize filling, the injection flow rate was adjusted in order to keep the capillary number at the optimum value. The final void distribution of Fig. 7(c) shows that the void formation decreased to nearly zero when the optimized injection is applied. Therefore the optimization strategy allowed reducing the total void content to a minimum, which will result in better mechanical properties for the final part.

CONCLUSIONS

This study concerns the optimization of the injection flow rate to minimize the void formation in composite parts manufactured by Resin Transfer Molding. The quality and mechanical performance of composite parts is strongly dependent on the percent of macro/micro voids. In this work, an optimization methodology was presented to reduce the percent of macro/micro voids formed during RTM manufacturing. The optimization is based on the optimal capillary

number at the fluid flow front position. To demonstrate the capabilities of the proposed algorithm, a test case on an automotive part was presented. The optimized injection (calculated with the proposed algorithm) was compared with an injection at controlled resin pot pressure. The optimization showed a minimization of the void formation for similar filling times. Finally, the injection optimization proposed in this work is shown to be a useful tool to minimize the percentage of voids formed within the fibrous reinforcement and increase the performance of composite parts by injection molding.

ACKNOWLEDGEMENTS

The authors are grateful to the National Science and Engineering Research Council of Canada (NSERC) and Fonds Québécois de Recherche sur la Nature et la Technologie (FQRNT) for their financial support. The authors would also like to thank CREPEC (Centre de recherche en plasturgie et composites) and ESI-Group for supporting this work.

REFERENCES

1. J. Breard, Y. Henzel, F. Trochu, R. Gauvin, “Analysis of dynamic flows through porous media. Part I: Comparison between saturated and unsaturated flows in fibrous reinforcements”, *Polymer Composites*, Vol. 24, no. 3, 2003, pp. 391.
2. N. Patel, L.J. Lee, “Effects of fiber mat architecture on void formation and removal in liquid composite molding”, *Polymer Composites*, Vol. 16, no. 5, 1995, pp. 386.
3. G.W. Lee, K.J. Lee, “Mechanism of void formation in composite processing with woven fabrics, *Polymer & Polymer Composites*, Vol. 11, no. 7, 2003, pp. 563.
4. A.D. Mahale, R.K. Prud’Homme, L. Rebenfield, “Characterization of voids formed during liquid impregnation of non-woven multifilament glass networks as related to composite processing”, *Composites Manufacturing*, Vol. 4, no 4, 1993, pp. 199.
5. M. Spaid, F. Phelan, “Modeling void formation dynamics in fibrous porous media with the lattice Boltzmann method”, *Composites Part A*, Vol. 29A, 1998, pp. 749.
6. C. Binétruy, B. Hilaire, J. Pabiot, “Tow impregnation model and void formation mechanism during RTM”, *Journal of Composite Materials*, Vol. 32, no. 3, 1998, pp. 223.
7. L. Labat, J. Breard, S. Pillut-Lesavre, G. Bouquet, “Void formation prevision in LCM parts”, *The European Physical Journal, Applied Physics*, Vol. 16, 2001, pp. 157.
8. N. Patel, L.J. Lee, “Modeling of void formation in liquid composite molding. Part II: Model development and impregnation”, *Polymer Composites*, Vol. 17, no. 1, 1996, pp. 104.
9. N. Patel, L.J. Lee, “Modeling of void formation in liquid composite molding. Part I: Wettability analysis”, *Polymer Composite*s, Vol. 17, no. 1, 1996, pp. 96.
10. E. Ruiz, V. Achim, S. Soukane, F. Trochu, J. Bréard, “Optimization of injection flow rate to minimize micro/macro-voids formation in resin transfer molded composites”, *Composites Science and Technology*, Vol. 66, 2006, pp. 475.
11. F. Trochu, R. Gauvin, D-M. Gao, “Numerical analysis of the resin transfer molding process by the finite element method”, *Advanced Polymer Technology*, Vol. 12, no. 4, 1993, pp. 329.

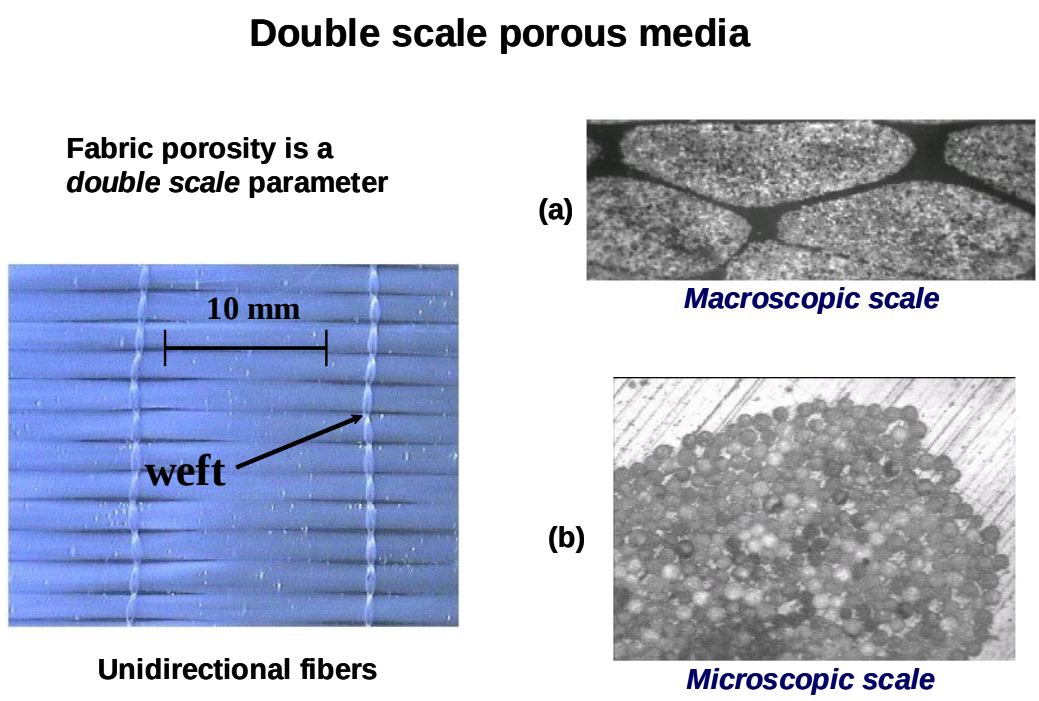

Figure 1. Fibrous reinforcements possess the structure of a dual scale porous medium: a) macroscopic voids can be observed between fiber tows; and b) microscopic voids exist between filaments.

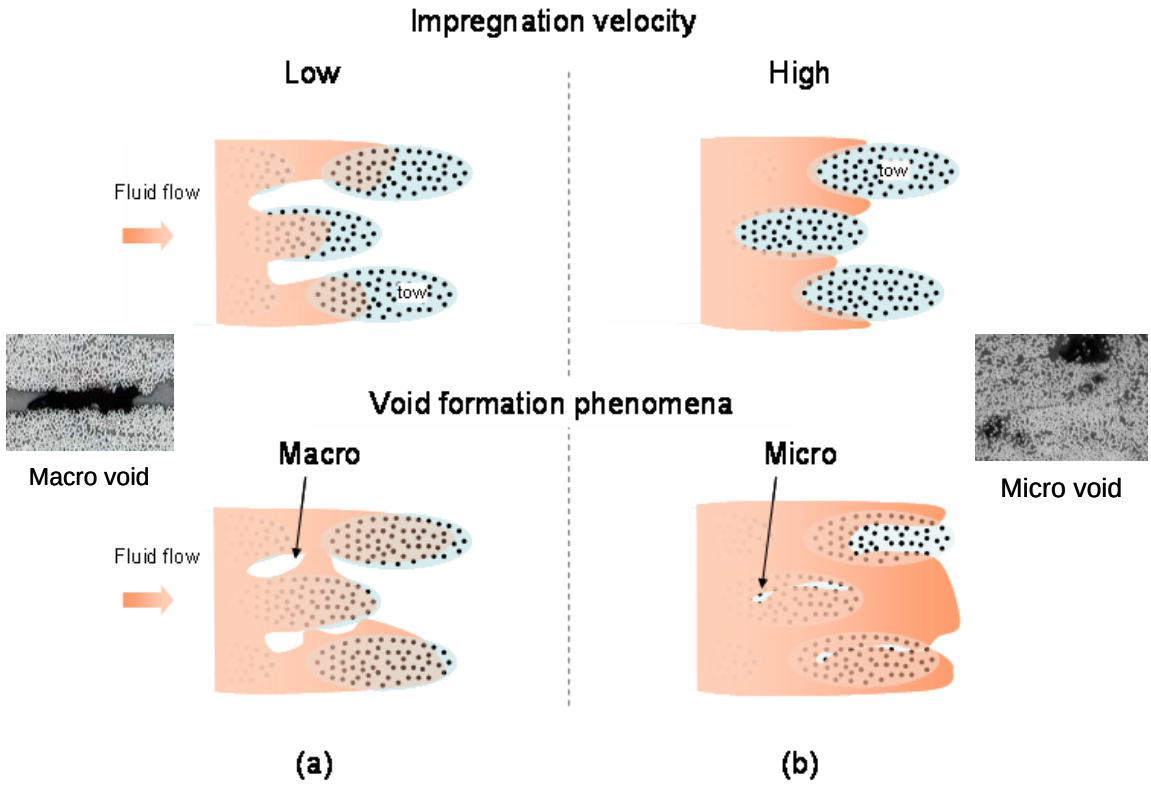

Figure 2. Impregnation mechanisms in a dual scale porous medium: (a) formation of macroscopic voids due to capillary forces (low resin velocity); and (b) formation of microscopic voids due to viscous forces (high resin velocity).

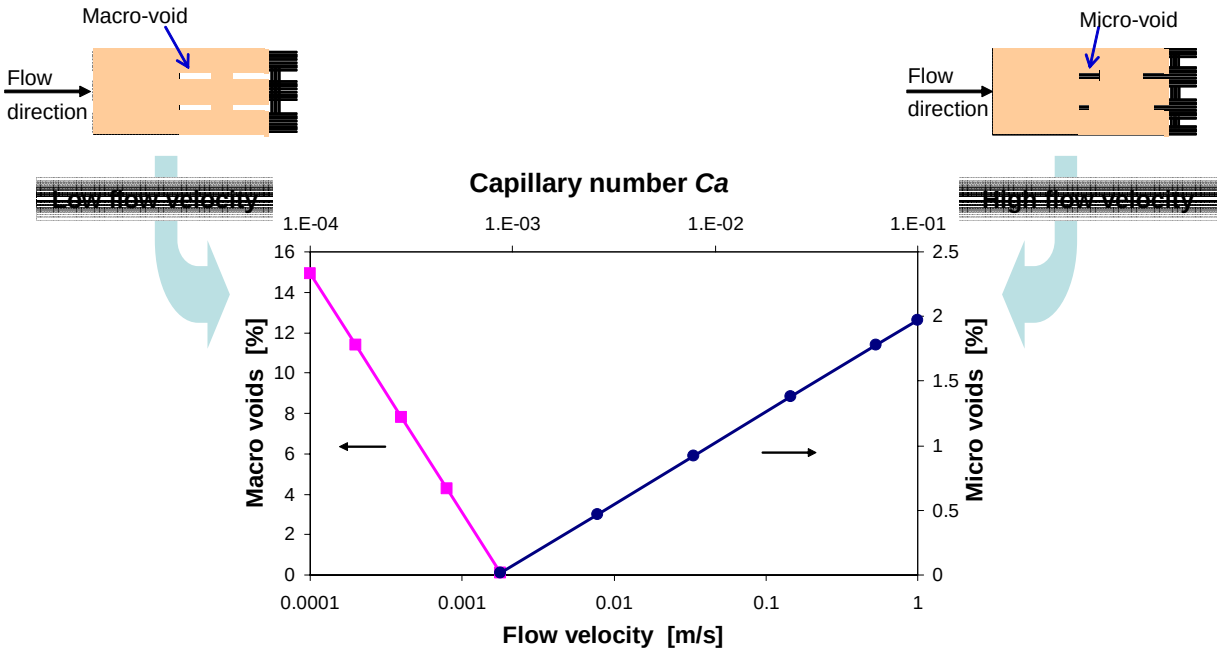

Figure 3. Macroscopic and microscopic void formation during fiber impregnation.

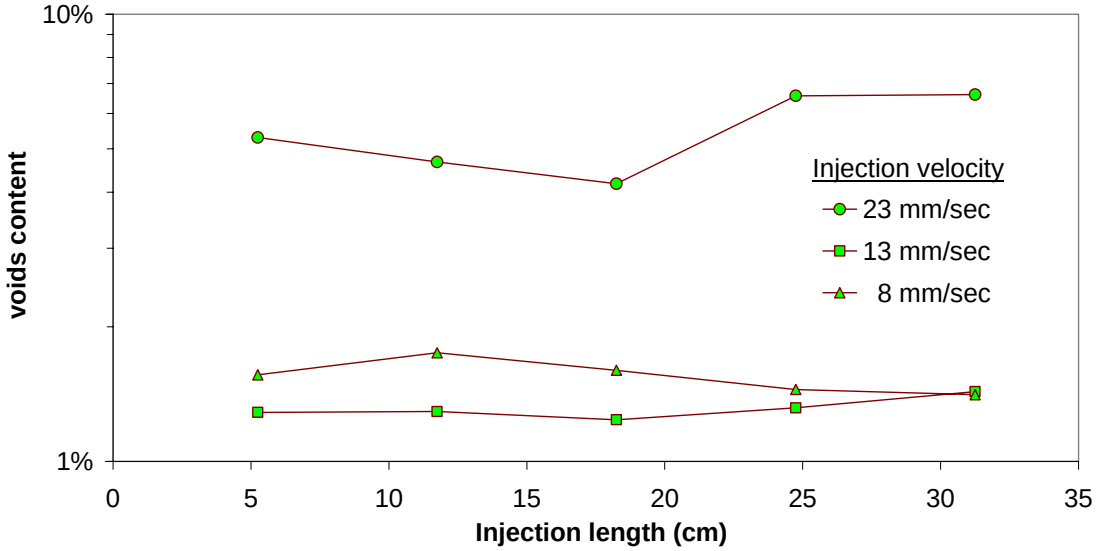

Figure 4. Measured void contents as a function of the injection length for the Unifilo 101 glass mat. Results for three injection flow rates are reported.

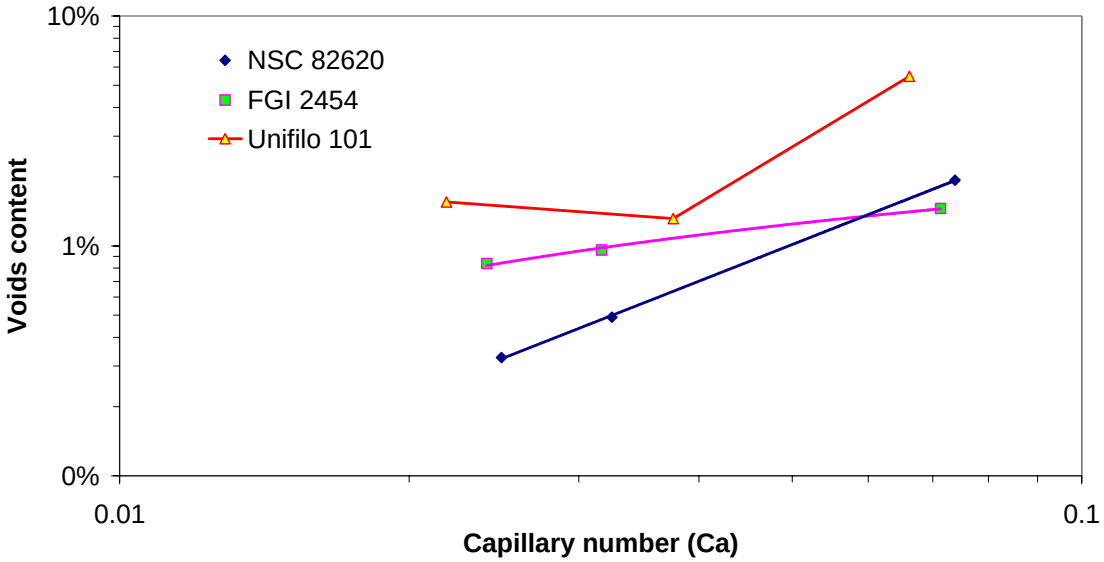

Figure 5. Measured void contents as a function of the capillary number for the 3 reinforcements tested. An optimal *Ca* exists for the Unifilo 101.

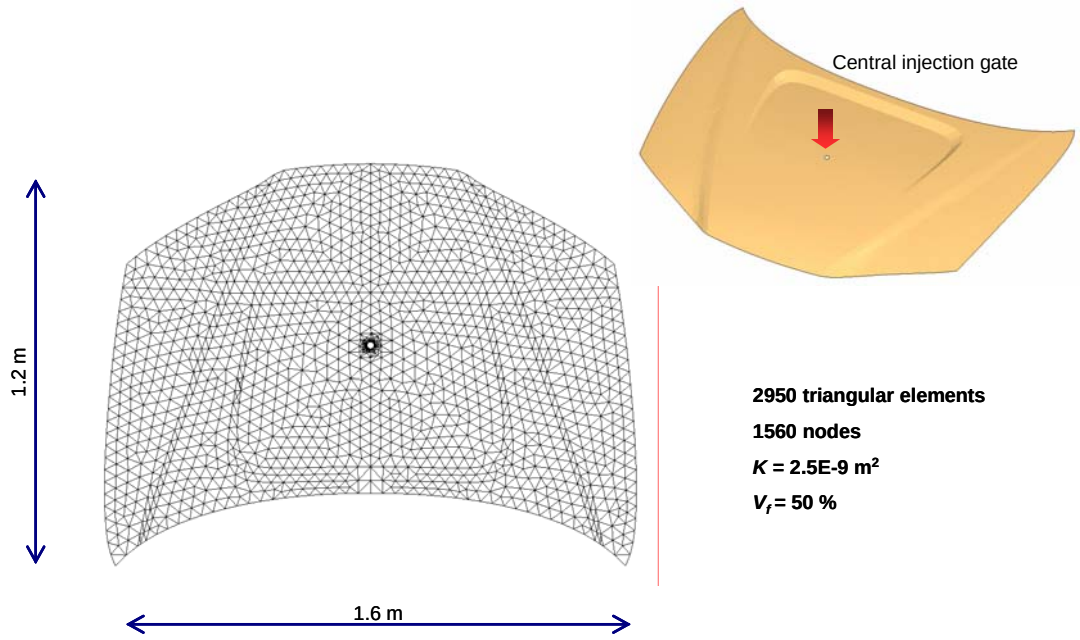

Figure 6. Geometry and 2D finite element mesh of the car hood used as application example.

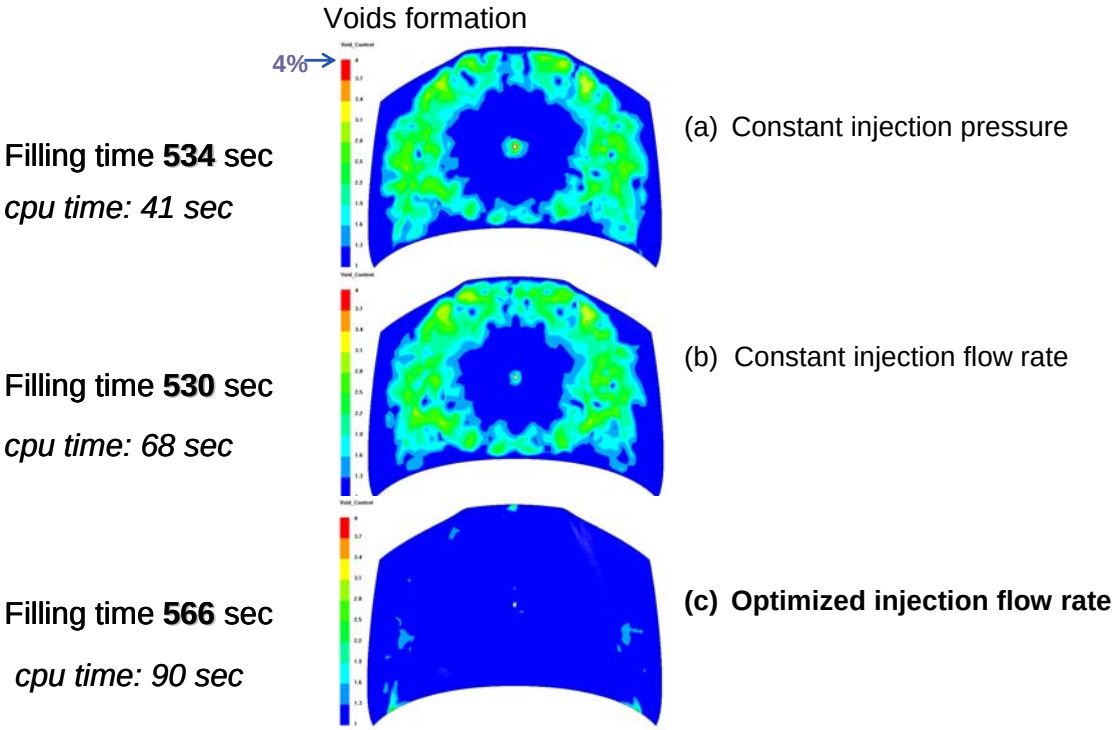

Figure 7.Comparison of calculated void formation on the car hood for three injection strategies.

SIMULATION OF PROCESS INDUCED DEFECTS IN RESIN TRANSFER MOULDED WOVEN CARBON FIBRE LAMINATES AND THEIR EFFECT ON MECHANICAL BEHAVIOUR

Bijoysri Khan, Kevin D Potter, and Michael R. Wisnom

Department of Aerospace Engineering
University of Bristol, University Walk, Bristol, BS8 1TR, UK

ABSTRACT: With increasing usage of composites in primary structural applications and the drive towards efficient manufacturing routes like RTM there is a need to review the defect acceptance criteria. Amongst other manufacturing induced defects, distortion in the fibres in the form of waviness, become significant when loaded in compression. Also associated with any disorientation in the fibre tow path is the accumulation of resin rich pockets. In this work both in-plane and out-of-plane fibre waviness, and resin rich layers on the surface were simulated in flat panels. It was found that the presence of fibre waviness caused a significant reduction of up to 35.2 % in the compression strength. The failure initiated where the fibre misalignment was the greatest. In the case of resin rich regions the failure did not initiate from the resin rich layer itself. Instead the initiation of delamination was found to occur at a region demarking the deformed and the undeformed layers. The reduction in tensile strength was 32%.

KEYWORDS: Resin transfer moulding; fibre wrinkling; fibre folding; resin rich layer; compression; delamination;

INTRODUCTION

Resin transfer moulding offers a means of producing a high volume of parts at low cost. With the increasing shift of focus towards efficient manufacturing methods there is a growing emphasis on using RTM in the aerospace industry for manufacture of primary structure components. For such specialised applications many manufacturing deviations come under scrutiny and an understanding of the defects and their effect becomes essential. Issues like void generation, fibre wrinkling, folding, resin richness, complexities around 3-D geometrical features and their effect on mechanical performance are now of relevance in the industry [1-4]. Waviness in fibres is a manufacturing defect that can be induced in the manufacturing step depending on the process used. For example waviness could occur in filament wound tubes [5], or in the inner radii of L sections cured in a female mould due to corner consolidation. In the RTM process also there is a possibility of waviness induced in the preforming operation. Generally waviness can be either in-plane or out-of planes and can be defined by the ratio of the amplitude of the wave to its wavelength. The wavelength can vary from short to large distances and when deviations in fibre paths occur the space between the distorted fibre path is taken up by the matrix leading to resin rich regions. Thus defects of waviness and resin rich regions could co-exist. Waviness in either form becomes an important issue when parts are subjected to compression [4]. Composites are known to be inherently weaker in compression than in tension, Rosen [6] derived a relationship, between the compressive strength and the shear modulus of the matrix of a composite with initially straight fibres which buckle in phase but this gives values that are far too high. When fibre waviness is taken into account the predicted strength values are reduced considerably [7, 8]. When unidirectional composites

containing wavy fibres are compressed the misaligned fibres (with respect to the loading axis) are subjected to shear loading. The load when the shear stress exceeds the interlaminar shear strength of the composite is an upper bound on failure and it has been found by many that the failure occurs where the fibre misalignment is greatest [9,10]. Thus in the present work an attempt is made to simulate some of these defects in simple flat laminates and look at the initiation of failure in these samples. The effects on mechanical performance are reported. Also tensile tests were carried out on specimen with resin rich regions to study the effect on damage initiation.

MATERIALS AND SPECIMEN PREPARATION

All the test laminates were made using dry carbon fibre, 5-harness satin woven fabric and RTM 6 epoxy resin both supplied by Hexcel UK. In our work the 0 degree direction of the woven cloth is considered to be the warp direction and the weft fibres therefore are the 90 direction. A resin transfer moulding facility developed at the University of Bristol was used to make the Carbon-epoxy flat laminates. The tool is comprised of a fixed cavity formed between the top and bottom plate with a spacing of 4.2 mm. A stacking sequence of $((\pm 45),(0/90))_{3s}$ was used to make specimens with and without defects. 12 layers of dry fabric were cut to the required size and stacked together to form the preform. After loading the mould, the top and bottom plates were closed and the assembly of platens was then heated to 120 deg C and the cavity with the preform was evacuated to 1000 mbar. Resin was injected into the mould at 3.5 bars pressure and after completion of the filling process the mould was then heated to its cure temperature of 180 deg C and held at this temperature for two hours. From the cured laminate test specimens were cut to the required size using a diamond disc cutter. The edges of the specimen were then polished to get a smooth surface.

Simulation of defects:

Localised kinking of fibres can occur during manufacture when the process step induces axial compression on the fibres. This buckling of the fibres can either be in-plane or out of plane depending on the local constraining conditions. Thus the difference between folding and wrinkling is very fine and often difficult to distinguish.

Wrinkling in this test programme is defined as that in which in-plane deviations of the fibre tows occur. The wrinkled plies were the sub surface plies (layer number 2, 4 and 6 from the top) and were the primary load carrying (0/90) plies.This was done on only one side to simulate a real life situation where not necessarily all plies will be wrinkled at a particular location. They were simulated in the middle of the gauge section and constituted 25% of the total ply count. The extent of wrinkles was limited to a length of 16 mm and they were distorted in-plane by three tow widths, or approximately 7 mm. This resulted in a localised fibre disorientation of about 30 deg as can be seen in Figure 1. To get wrinkles in the fabric the areas outside the desired 16 mm length were shear deformed against one another in the in-plane direction, by a specified amount of three tow widths. While doing the lay up it was ensured that all the wrinkled plies are wrinkled in the same direction and made to fall at a coincident location with respect to the centre of the gauge length.

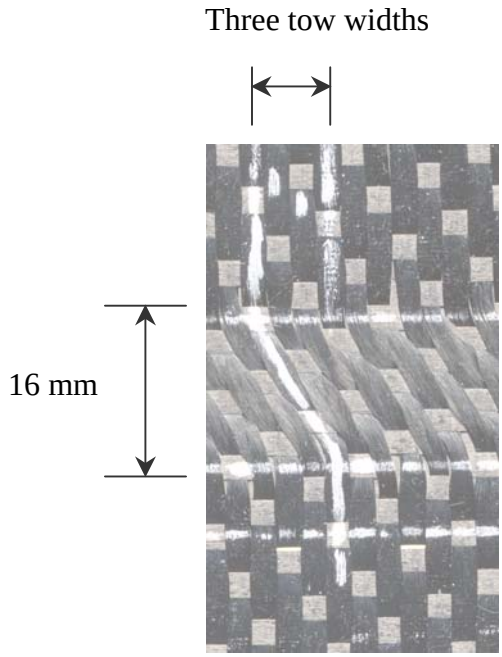

Figure 1. Picture showing in-plane fibre tow distortion in simulating wrinkling of fabric.

Folding of the fibres in the test samples is defined as out-of-plane fibre distortion, and was simulated on 100% of the plies in the through thickness direction (i.e. the entire stack of plies $[(\pm 45),(0/90))_{3s}]$) by crimping the preform in the through thickness direction. For doing this, a preforming tool was made. This consisted of arranging precured carbon fibre rods spaced 8 mm apart on one side of the preforming tool while two rods were placed on the opposite side so as to fall in the centre of the span between the rods on the opposite side. The entire assembly was then heated to the preforming temperature of 150 deg C. After a specified time of 20 minutes the pressure was released and the preform taken out and allowed to cool. Due to the manufacturing difficulties some variation in the fold parameters was seen. Thus fibre folding was simulated in the gauge section with a wavelength between 7 and 8.5 mm and amplitude of about 0.6 mm, as shown in Figure 2. The distortion of the surface fibres was observed to be more than the fibres at the mid plane. The measured angular deviation observed at the centre of the laminate was found to be in the range 18 to 29 degrees.

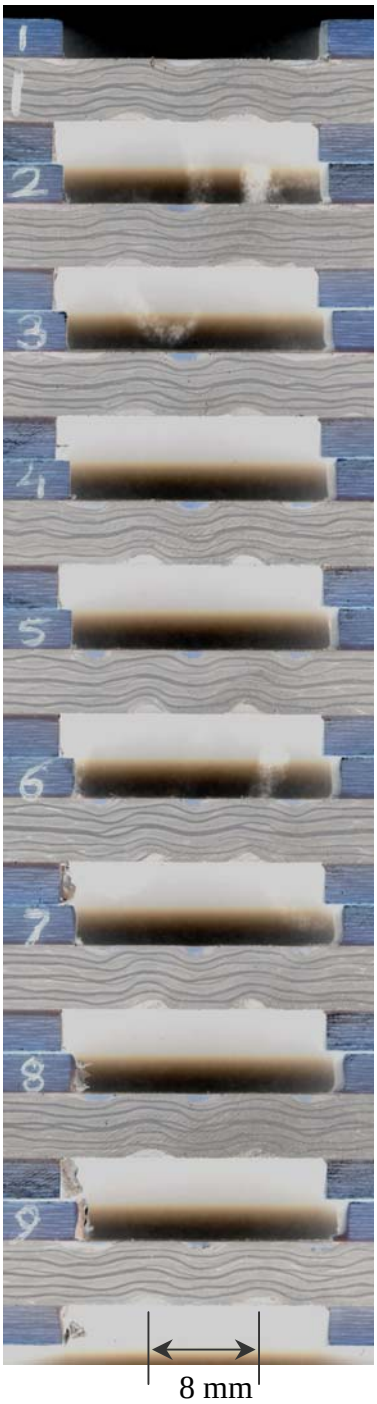

Figure 2. Out of plane fibre distortion simulating fabric folding .
(Picture in negative to show clarity in fibre distortion).

Resin richness: These are regions especially around corner radii, where a layer of resin is often found to be accumulated. These regions of resin richness form locally when the fibres get compacted to one side more than they would normally at other places. To simulate the resin rich layer within the flat specimen a forming tool of the desired resin rich geometry was fabricated. The preform stack with the forming tool was then placed in a vacuum bag. The entire assembly was then subjected to the preforming operation as described above. Using this method and after a few trials a successful resin rich zone of up to 12 mm long and 0.6 -0.7 mm depth was achieved as shown in Figure 3.

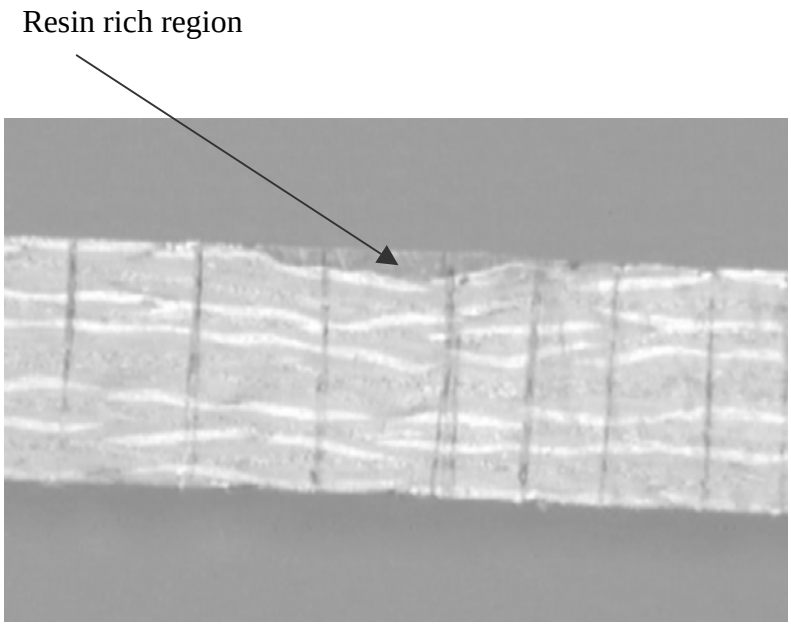

Figure 3. Resin richness simulated on the top surface of the specimen

Specimen preparation:
From the resin rich test panel, tensile test specimens were cut to dimensions 25 mm wide and 250 mm long (with a grip length of 60 mm), and emery paper of grit size 100 was used between the specimen and the jaws of the test machine to grip the samples at either ends. For the ply waviness studies, compression tests were carried out using the Imperial College Standard Test (ICST) rig. Compression specimens of 100 mm length and 10 mm width were cut from the laminates and end tabs of length 40 mm were bonded on both sides at both ends giving a gauge section of 20 mm. All specimens were tested in an Instron machine under displacement control at a crosshead speed of 0.5 mm/minute. The failure stresses are calculated based on the nominal ply thickness of 0.36 mm to compare with other data. For a 12 plied laminate the total thickness was 4.32 mm, compared with actual thicknesses ranging between 4.20 and 4.28 mm.

RESULTS AND DISCUSSION

When the specimens with no defects were loaded in tension they showed an increasing stress-strain response till failure and there was some evidence of delamination close to the failure stress. The delamination was observed to occur at the interface between the weft fibres and the resin rich pockets formed at the spaces corresponding to the crimps in the fabric weave. When these samples were loaded in compression the failure was sudden with fracture running through the entire thickness of the sample. The compressive failure stress was 492 MPa, 21% lower than the tensile failure stress of 625 MPa.

Fibre wrinkling:
During the compression test, the edge was observed carefully and delamination cracks were observed to appear within the wrinkled layer region. Closer examination revealed that the cracks relate to the interface between the outer most angle plies and the adjacent wrinkled layers (0/90), Figure 4. Possibly the location of the cracks corresponds to a place where the fibre tows of the wrinkled layer are cut where they meet the edge of the sample. The initiation stress was found from observation of the specimen edge during the test to be about 319 MPa and

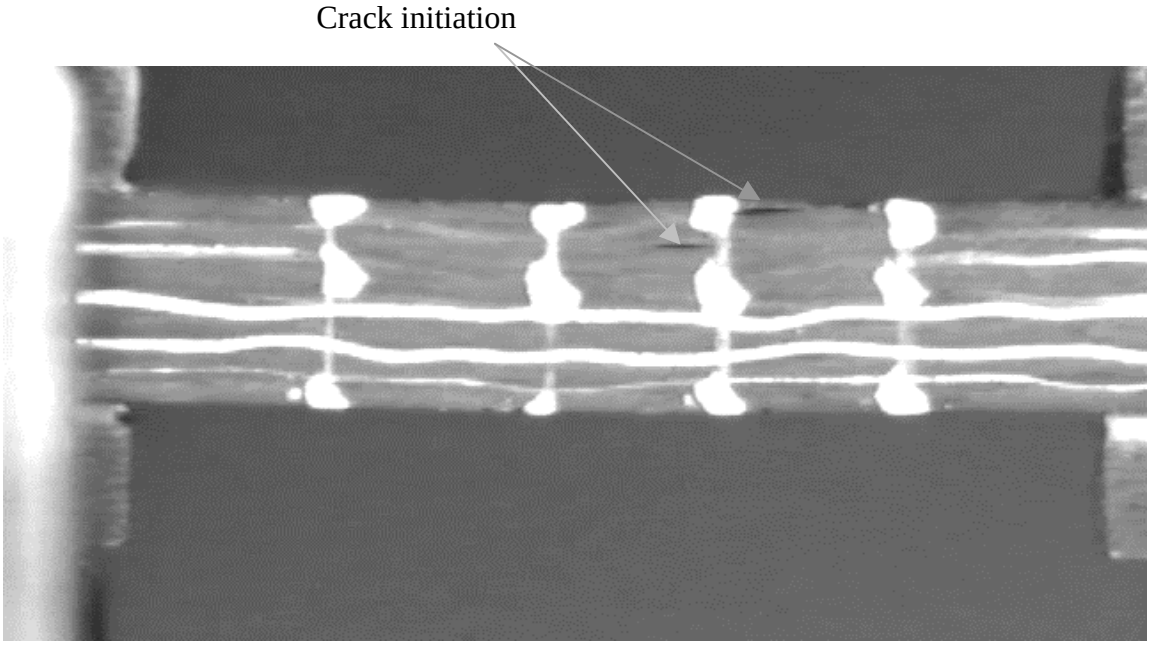

Figure 4. Picture showing the initiation of delamination at the interface of the wrinkled and angle plies in the specimen. (Note the white dots are marked on the specimen edge to monitor strains during the test)

the failure stress 370 MPa, which is 35.2 % lower than the failure stress of 492 MPa obtained from pristine laminates. The localised angular distortion of the wrinkled fibres (in-plane) is about 30 deg from the nominal fibre axis, which will significantly affect the stiffness properties locally and together with its asymmetric location will lead to bending of the specimen. Therefore delamination occurs early between the interface of the angle and axial plies within the wrinkled region. The wrinkling is uniform in all the specimens and initiation is from a specific feature i.e. the interaction of the local fibre tow path and the specimen edge, which probably explains the small scatter, with a c.v. of about 5 %.

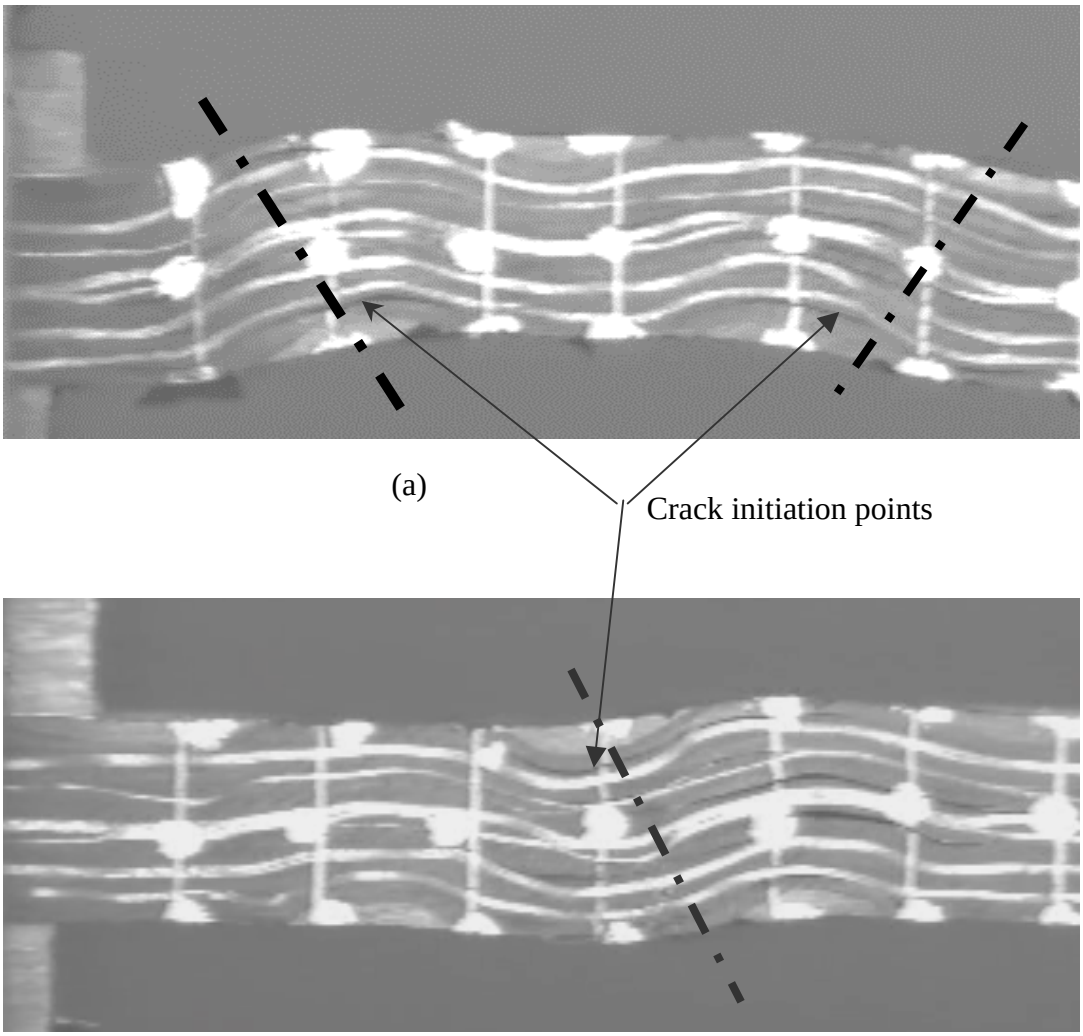

Figure 5. Different types of failure pattern observed in the samples (a) with delamination initiation at two locations and (b) with one initiation location. The dashed line denotes the general plane of failure corresponding to maximum fibre misalignment.

Fibre folding:

When the specimens were tested in compression, prior to reaching the peak load there was a discernable slope change in the load-deflection plot and at this point the specimen showed substantial cracks /delamination initiation between the surface and the subsurface plies, as shown in Figure 5 (a) & (b) resulting in sudden out of plane buckling of the specimen. At this juncture there was a significant drop in load and with increasing displacements, more delamination cracks began to appear and grow. The specimen edge was carefully monitored during the test and from the visual observations the stress corresponding to the damage initiation was found out to be about 138 MPa and was closely followed by the specimen failure at about 140 MPa. Thus the damage initiation stress is about 72% lower than the base line data of 492 MPa for the pristine laminate. It was also seen that there was not much time interval between the appearance of the first crack and the final failure. The fibre folding from the manufacturing process showed a slight variation in the degree of folds, Figure 2. In specimens where the fold was uniform throughout the gauge section the failure initiated simultaneously from the transition between the straight fibres and the fibres with folds located

at both ends of the gauge section. Also since there were three folds in the gauge section the two outer folds were in phase with each other and this facilitated the out of plane displacement of the entire central section in unison, Figure 5(a). This kind of failure occurred at an early stage and the central gauge section was found to displace laterally thereby registering a lower failure initiation stress of about 111 MPa. In specimens with non uniformly distributed folds or varying fold geometry, Figure 5 (b) the failure occurred at the place where the severity of the fold was greatest. Usually it was observed that the most severely folded fibres lay closer to one of the supported ends and a higher initiation stress of about 163 MPa was recorded. The difference in the two failure types observed explains the large scatter (c.v. of 21%) in the data. In all these cases the failure could be attributed to shear induced delamination initiation at the sub surface ply as indicated in the Figures 5 (a) and (b).

Resin richness:

As a result of manufacturing variabilities the resin rich layer thickness varied between 0.6 mm and 0.7 mm. It may be recalled that the resin rich layer was created using a preforming tool on one side. As a result, there was deformation of the plies that was greatest at the surface and negligible beyond the mid plane, Figure 6 (a). These samples were tested in tension with six samples in this category. No failures were observed in the resin rich regions. The initiation of the 1st set of cracks appeared at the interface between the deformed and undeformed fibres which roughly corresponds to the mid plane, Figure 6 (a) & (b), with no failure in the resin region. The initiation stress for the delamination of about 300 MPa is 46.9% lower than the baseline samples. Soon after, a 2nd set of cracks appeared at 305 MPa within the deformed region, at the interface between one of the sub-surface angle plies and the adjacent axial plies, Figure 6 (b). The volume fraction is estimated to be about 68% in the region below the resin–rich layer, provoking early delamination. Many such delamination cracks appear in the vicinity of the resin rich region, causing the deformed plies to separate and straighten up at about 389 MPa. The specimens fail completely at about 428 MPa, and the reduction in strength is 32 %.

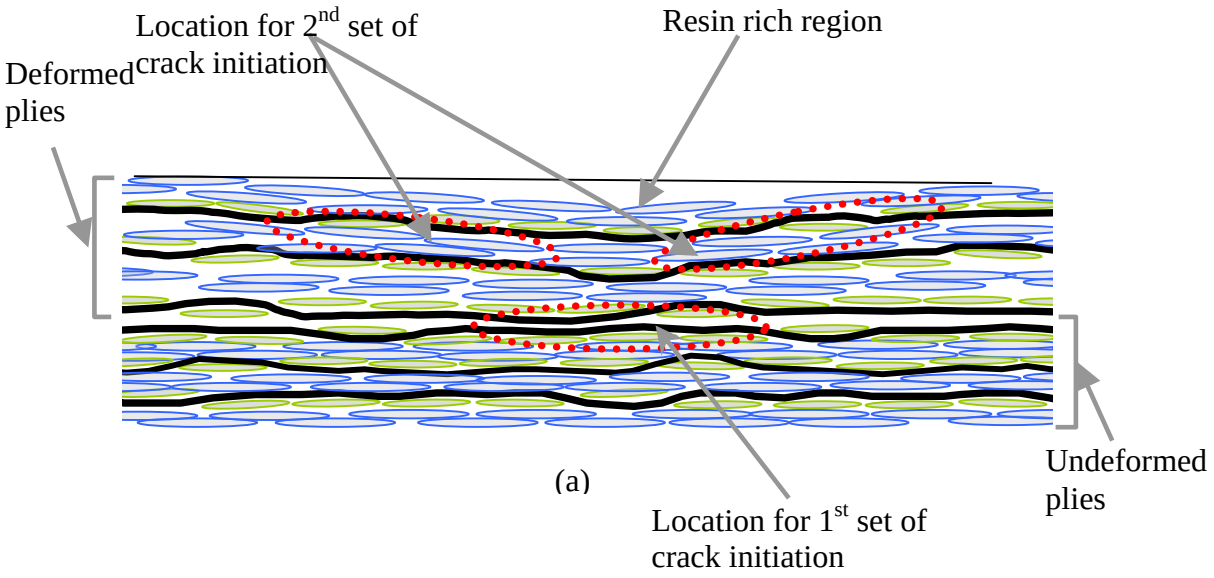

Figure 6. Schematic diagram (a) with picture showing initiation of delamination in (b) at the interface between the straight and deformed layers and subsequent propagation

CONCLUSION

- Wrinkling of the 0 degree fibres by approx 30 degrees in-plane in one half of a quasi-isotropic laminate reduced the compressive strength by about 35 %. Damage initiated at a stress 35.2% below that of the pristine specimens, with small cracks where the wrinkled plies were cut at the edge.

- When all the fibres are folded by approximately 29 degrees out-of-plane, the compressive strength is reduced by 71.5 %, with damage initiating just before failure.
- Failure in this case occurs at the place where the deviation in the fibre angle is greatest, believed to be controlled by the local interlaminar shear strength of the misaligned layers.
- For specimens with a resin rich layer on one surface loaded in tension no failure was observed in the resin rich region. Failure initiated primarily as delamination cracks in the region demarcating the straight fibres and the sub surface layers which were deformed as a result of the way the resin rich regions were formed.
- Damage in this case initiated at 46.9% below the pristine samples. Due to the asymmetric location of the resin rich region across the mid plane, bending was induced, with a reduction in ultimate tensile strength of about 32 %.

ACKNOWLEDGEMENT

This work was carried out as part of the ELRIPS DARP project funded by the UK Engineering and Science Physical Research Council, Department of Trade and Industry and Ministry of Defence in collaboration with Airbus UK, Shorts, Dowty Propellers, Hexcel, MSC and QinetiQ.

REFERENCES

1. Piggott, M.R. The effect of fibre waviness on the mechanical properties of unidirectional fibre composites: A review, Compos Sci & Technol (1995) 53: 201-205
2. Mrse, A.M. and Piggot, M.R. Compressive properties of unidirectional carbon-fibre laminates: I A compact flexure beam for compression testing, Compos Sci & Technol (1993) 46: 213-217
3. Mrse, A.M. and Piggot, M.R. Compressive properties of unidirectional carbon-fibre laminates: I, The effect of unintentional and intentional fibre misalignment, Compos Sci & Technol (1993) 46: 219-227
4. Hale, R.D. and Villa, M. Influence of opposing wave nesting in compression-loaded composites, J Comp Mater. (2003) 37(13): 1149-1166.
5. Hsiao, H.M. and Daniel, I.M. Elastic properties of composites with fibre waviness, Compos Part A, (1996) 27A: 931-941
6. Rosen, B.W. Mechanisms of composite strengthening Chapter 3, Fibre Composite Materials. ASM (1965).
7. Davis, J.G. jr Compressive strength of fibre reinforced composites materials, Composite Reliability, (1975) ASTM STP 580, 364-377.
8. Hahn, H.T. and Williams J.G. Compression failure mechanisms in unidirectional composites, Composite Materials: Testing and Design (1986) Seventh Conference, ASTM STP 893, 115-139
9. Adams, D.OH and Bell, S. J. Compression strength reductions in composite laminates due to multiple-layer waviness, Compos Sci & Technol (1995) 53: 207-212.
10. Wisnom, M.R. Analysis of shear instability in compression due to fibre waviness, J Rein. Plast. and Compos. (1993) 12: 1171-1189.

SIMULATION OF ENTRAPMENTS IN LCM PROCESSES

René Arbter, Paolo Ermanni

Centre of Structure Technologies
ETH Zurich, Leonhardstr. 27, 8092 Zurich, Switzerland: rarbter@ethz.ch

ABSTRACT: Entrapments in liquid composite moulding (LCM) can be simulated based on elementary physical assumptions. In this contribution, mainly the conservation of the entrapped gas mass and the ideal gas law have been taken into account. In addition an algorithm tracking the evolution of the gas entrapments during the injection has been implemented. Simulation results considering non-moving and moving gas entrapments are presented and discussed. Furthermore injection experiments in a glass-tool have been performed to validate simulation results. The detection and tracking methods implemented could be verified and turned out to be reliable. Limitations of the simulation were found for small bubbles.

KEYWORDS: Liquid Composite Moulding, gas entrapment, process simulation, gas transport.

INTRODUCTION

Dry spots resulting from gas (air) entrapments are a serious problem in LCM processes Voids on mirco and meso scale have been extensively investigated in the past in order to better understand their formation and transport mechanisms and their influence on the laminate quality.
The formation of micro voids has been studied in Ref. 1. It was found that the distribution and size of voids could be explained by mechanical gas entrapment at the flow front and by the ideal gas law. In Ref. 2 the deformation of the shape and the break up of drops moving through an array of solid cylinders was investigated.
In addition to mirco voids, macroscopic gas entrapments can occur in unstable processes. These dry spots have a dramatic influence on the mechanical properties of the concerned component.

PROCESS SIMULATION

LCM-simulations including macroscopic gas entrapments have been performed using FELyX. This is an open source finite element software for solving structural problems as well as for LCM filling problems. To consider the formation of entrapments and their evolution methods for their detection and tracking were implemented.

Modeling and simulation of gas entrapments is based on following assumptions:

- Conservation of the entrapped gas mass. Absorption and/or vaporization effects between the resin and the entrapped gas are not considered.
- The entrapped air is behaving like an ideal gas. Ideal gas law is assumed to be valid
- Injection takes place at constant temperature.
- The viscosity of the entrapped gas is negligible compared to the viscosity of the resin. Thus the pressure within the gas entrapment is constant.

DETECTION OF ENTRAPMENTS

In each time step the current entrapments have to be localized. For this purpose a recursive detection algorithm for unfilled areas has been implemented in FELyX. The detection function starts at an unfilled node, marks it and marks all neighbour nodes which are not filled either. All marked nodes belong then to this unfilled area.

Unfilled areas which are directly connected to a vent are detected at first, as they can obviously not be considered as entrapments. Therefore the detection starts at each vent node. After the detection of the vent areas, all remaining unfilled areas can be identified as entrapments.

TRACKING OF ENTRAPMENTS

To calculate the current pressure within the entrapment the mass of the entrapped gas needs to be known. Mass estimation is cumbersome because the nodes belonging to a specific entrapment may change for every time step, due to the fact that new entrapments can occur between two time steps and existing entrapments can move, join, split or even dissolve. Thus the correlation between entrapment nodes during two consecutive time steps needs to be investigated. Since the location of the nodes is difficult to evaluate with respect to the membership to a certain entrapment, particularly if entrapments are close to each other, only the membership of nodes to entrapments is evaluated.

In the following we consider five scenarios, which can occur to entrapments:

- Splitting entrapment: two (or more) entrapments of the current time step consist of a high fraction (> 75%) of nodes that already belonged to an entrapment of the previous time step.
- Joining entrapments: two (or more) entrapments of the previous time step have a high fraction of nodes that belong to an entrapment of the current time step.
- New occurring entrapment: none of the previous entrapments has a high fraction of common nodes with the new entrapment.
- Dissolving entrapment: none of the entrapments of the current time step has a high fraction of common nodes with this entrapment of the previous time step.
- Moving entrapment: this is the most frequently occuring scenario. An entrapment of the current time step has a high fraction of member nodes which have belonged to an entrapment of the previous time step. Unlike for the case of a splitting entrapment only one predecessor exists.

This tracing strategy is illustrated by the following example. Five entrapments with a specified number of nodes are shown on the left side of Figure 1. On the right side a set of five entrapments is shown for the next time step.

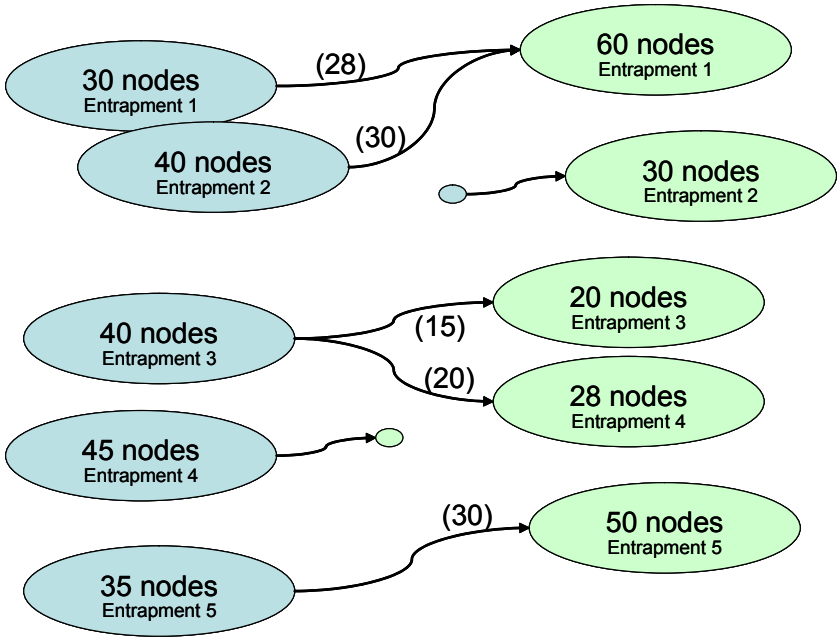

Fig 1: Entrapments and their member nodes for two successive time steps

In order to track the evolution of the entrapments, the information is bundled in two matrices as shown in Figure 2. The matrix RIN on the left side ("reappear in new") describes how many nodes of the old entrapments reappear in the new entrapments, while the matrix AIO on the right side ("appeared in old") describes how many nodes of the new entrapments already belonged to an old entrapment.

Old Entrapments \ New Entrapments	1	2	3	4	5	
1	45%	0	0	0	0	
2	50%	0	0	0	0	
3	0	0	75%	71%	0	split
4	0	0	0	0	0	
5	0	0	0	0	60%	
		new				

$$\frac{\#\text{same nodes as in previous}}{\#\text{nodes in new entrapment}}$$

RIN („Reappear in new entrapment")

Old Entrapments \ New Entrapments	1	2	3	4	5	
1	93%	0	0	0	0	
2	75%	0	0	0	0	
3	0	0	38%	50%	0	
4	0	0	0	0	0	dissolve
5	0	0	0	0	86%	
	merge					

$$\frac{\#\text{same nodes as in previous}}{\#\text{nodes in old entrapment}}$$

AIO („appeared in old entrapment")

Fig. 2: correlation matrices for entrapment tracing

Merging entrapments are characterized by columns with two or more high correlation values in the AIO-matrix, splitting entrapments by rows with two or more high correlation values in the RIN-matrix. Dissolving entrapments are characterized by rows without high correlation values in the AIO-matrix, new entrapments can be found by columns without high correlation values in the RIN- matrix. Finally, moving entrapments belong to none of the previous cases and have a high correlation either in the RIN- or in the AIO-matrix.

MOVING ENTRAPMENTS

Generally speaking, entrapments can expand or compress according to surrounding pressure changes and/or can move if they undergo a pressure gradient.

The mobility of entrapments is implemented based on elementary rules. In this context the edge of an entrapment is considered as a flow front and is simulated applying the volume of fluid algorithm [3]. Furthermore, an additional feature taking into account the the fact that no liquid can spill out of an empty control volume has been implemented.
This problem is exemplified in Figure 3. We consider an entrapment in a mesh of triangular elements (blue). The control volumes are highlighted in red. The green marked element is at the edge of the entrapment in flow direction. On the nodes 1 and 2 a pressure boundary condition is applied since both nodes belong to the entrapment. Obviously the pressure at node 3 will be lower than the pressure at nodes 1 and 2 . The resulting pressure gradient would produce a flow from node 1 and 2 to node 3, even though nodes 1 and 2 are actually empty, thus resulting in simulation errors, namely in the determination of the filling time and in the flow pattern. With respect to the simulation of the entrapment mobility, this undesired flow would also prevent node 3 from being depleted. Therefore the front edge of the entrapment would not move and entrapments would not expand when the surrounding pressure decreases.

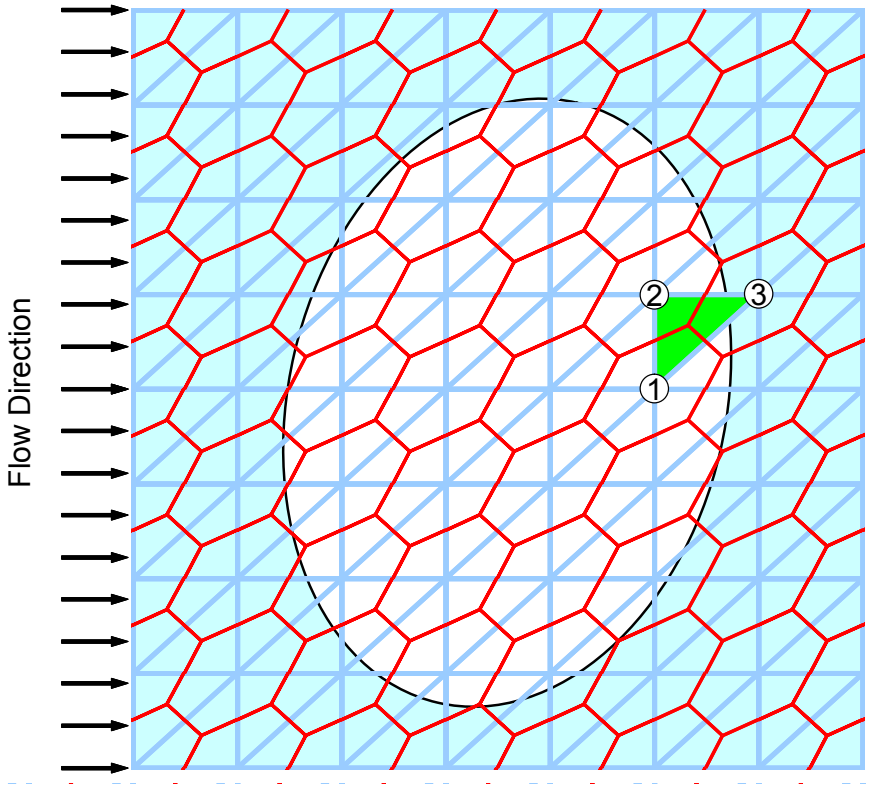

Fig 3: Control volumes and element at the front of an entrapment.

Figure 4 shows a sequence simulating the movement of a gas entrapment. The entrapment dissolves when it reaches the flow front.

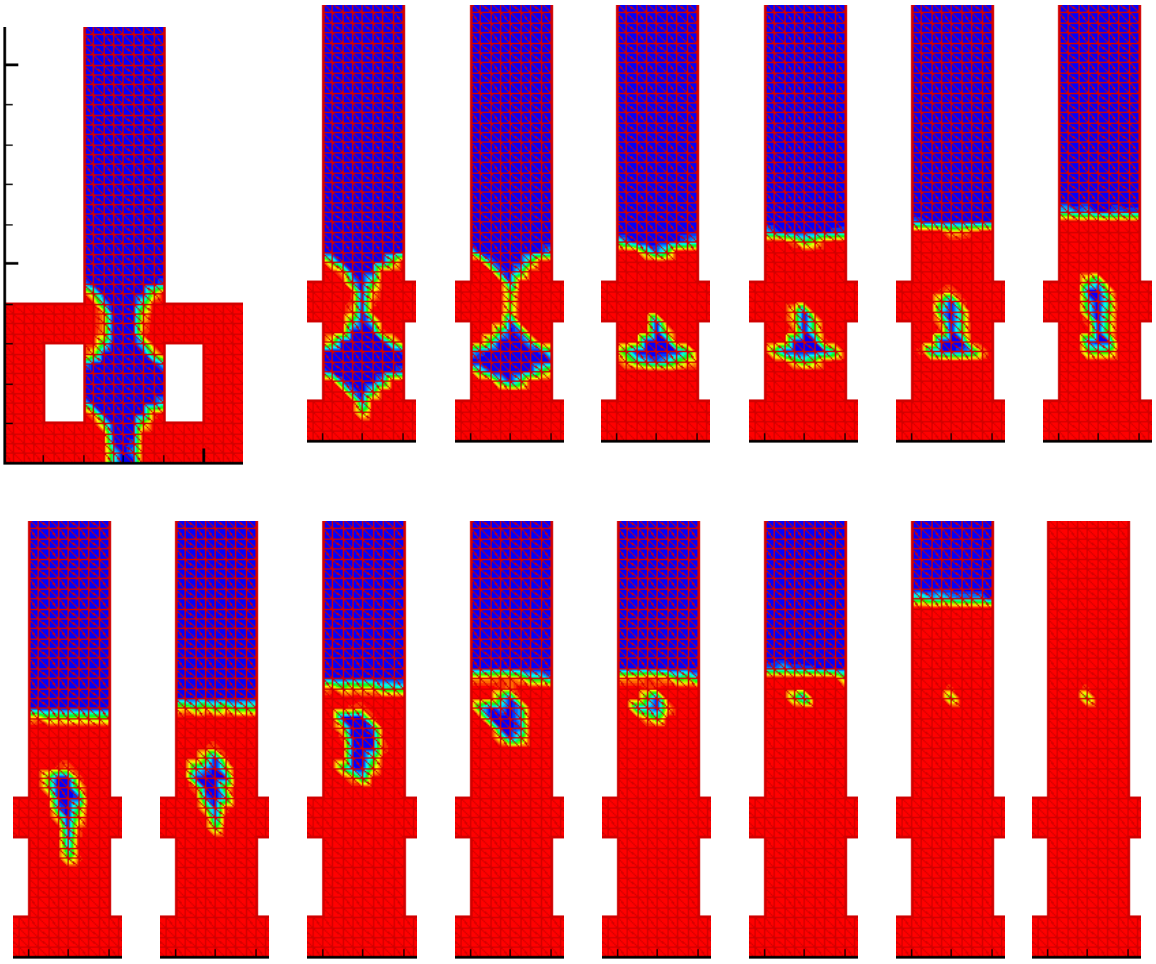

Fig. 4: Fill simulation of a moving entrapment (red regions are filled).

It can be seen that the entrapment is moving faster than the fluid. To understand this behavior a 1D flow channel is considered. Without disturbances and without entrapments there is a uniform, linear pressure distribution. This is illustrated by the resulting isobars in Figure 5 (left). If an entrapment occurs as shown on the right side of Figure 5, the pressure distribution is disturbed. High pressure gradients result on the left and on the right edge of the entrapment. (red marked areas). According to Darcy's law these high pressure gradients lead to high flow velocities on the left and on the right of the entrapment. The fast flowing resin in front of the entrapment clears the way for the entrapment and the resin behind the entrapment fills the area behind it.

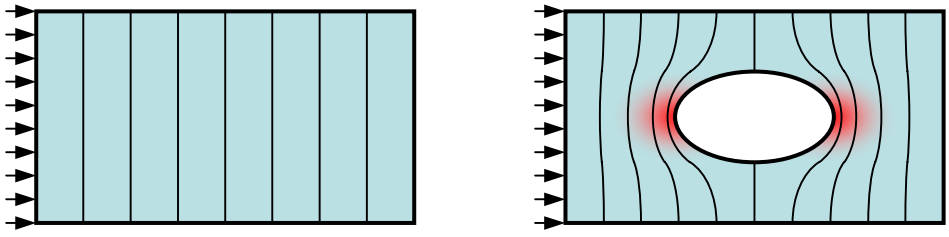

Fig. 5: pressure distribution in flow channel
without entrapment (left) and with entrapment (right)

NON-MOVING ENTRAPMENTS

Entrapments that occur in corners or that cannot move due to other reasons are compressed or expand until pressure equilibrium is reached. This mechanism is simulated using a closed flow channel without vents as shown in Figure 6). The dashed lines show the state of equilibrium for the two injection pressure values used for the simulation (50, 100….). After the pressure equilibrium between injection pressure and entrapment pressure is reached the pressure at the injection gate is reduced to $p_2 = p_1/2$. After a while, the entrapment expands again until the new pressure equilibrium is reached again. However, as highlighted in Figure 6, the straight flow front is destroyed and the resin takes the way of the least resistance. The size of the fingers depends on the mesh density, since the minimal width of a finger is determined by the width of the control volumes. In the simulation shown in Figure 6 16 elements in width were used.

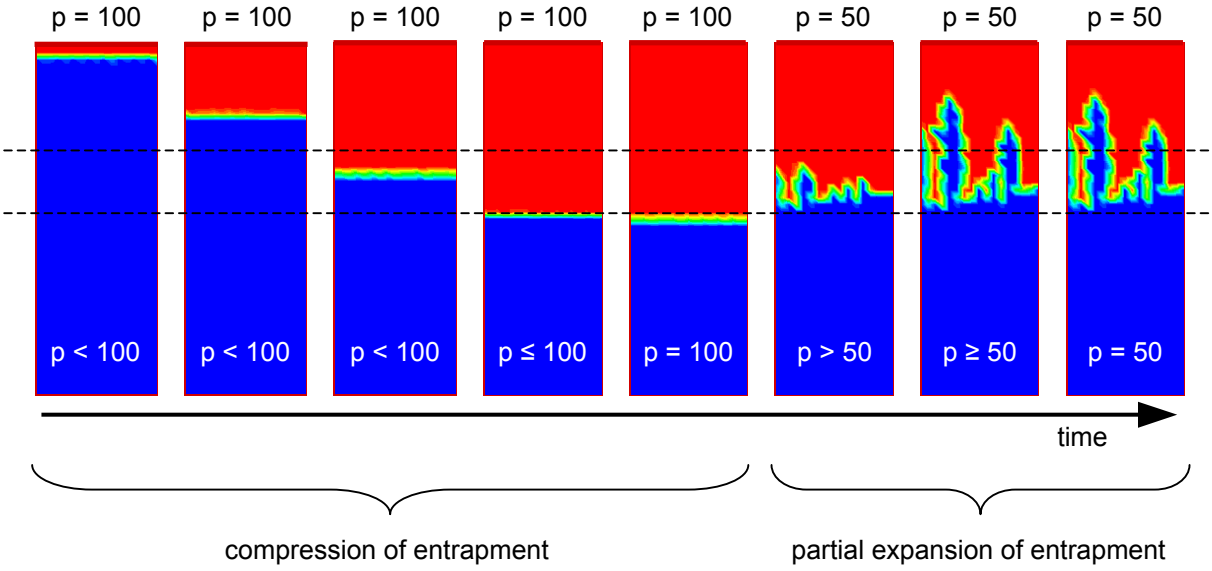

Fig 6: compressed and re-expanding entrapment

EXPERIMENTAL INVESTIGATION OF MOVING ENTRAPMENTS

The arrangement used for the simulation has been reproduced in a glass-tool in order to validate the simulation results. The sequence of pictures shown in figure 7 shows the flow pattern observed through a glass lid. A 0/90° woven fabric with 40 % fiber volume content was used.

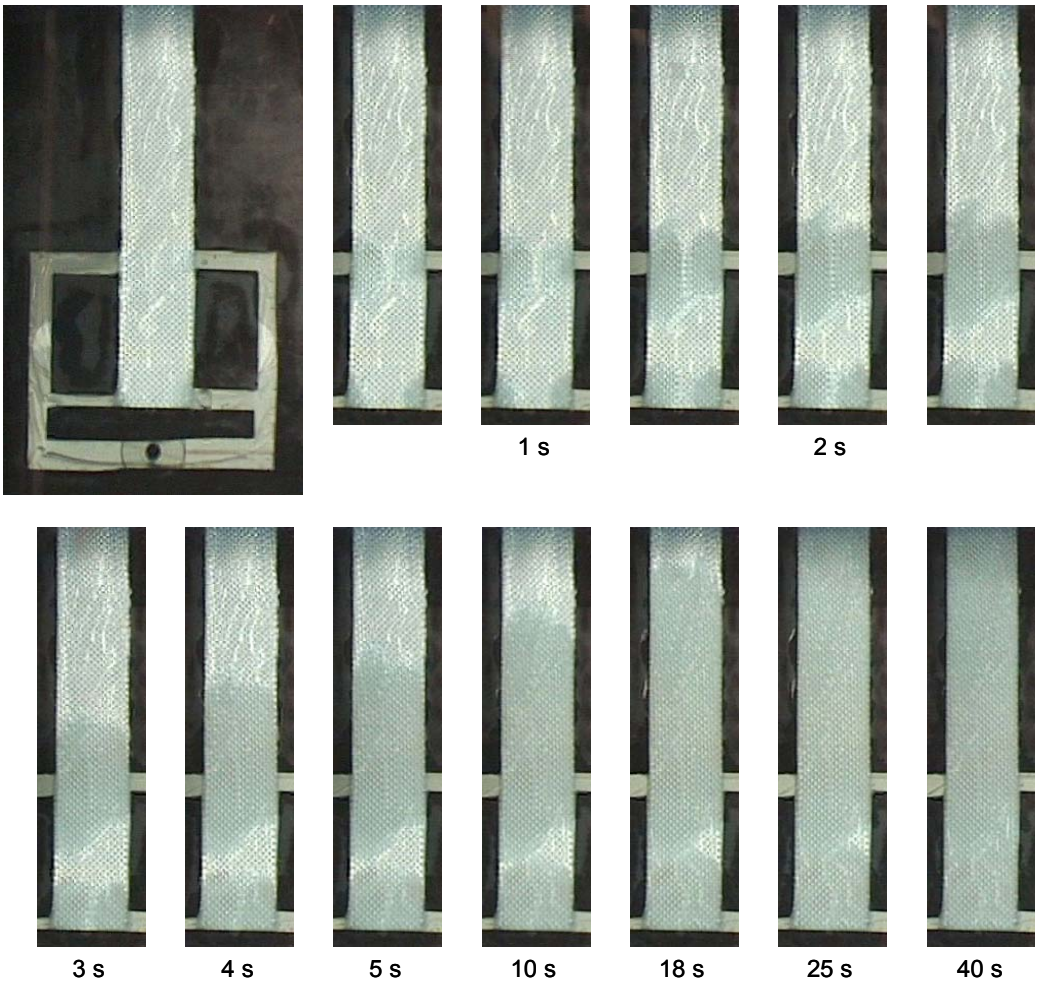

Fig. 7: entrapment evolution in a 0/90° fabric

Figure 7 shows that the entrapped air is spilled out not as a whole bubble but separated into many small bubbles. This effect could be easily seen during the injection experiments. The image in Figure 8 shows typical air bubbles traveling through the saturated areas of the laminate. These bubbles have a diameter up to 1 mm. The size might depend on the roving diameter of the used fabric.

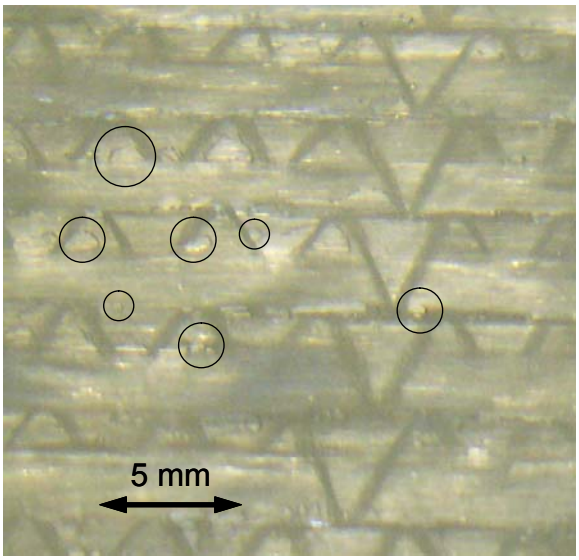

Fig. 8: small bubbles travelling through filled areas.

CONCLUSIONS

An algorithm to simulate gas entrapment mechanisms based on elementary laws has been developed and implemented in the LCM-simulation tool FELyX. The algorithm is able to detect and track gas entrapments. Results achieved so far are encouraging, showing that the algorithm is correctly simulating gas-entrapment mechanism with respect to their size and pressure..
Nevertheless the experimental program has shown, that the simplification to blur the fabric as an homogeneous porous material leads to wrong simulations of gas entrapments. As shown in Figure 7, entrapments do not vanish as one whole bubble, but as many small bubbles. Provided that entrapments appear in areas with pressure gradients toward the flow front, the resulting small gas bubbles that travel through the resin are likely to create zones with high matrix porosity. For this reason, entrapments will probably degrade the matrix quality, even if they seems to dissolve during the injection. However, in most cases entrapments don't move at all since they stay at one location, e.g. they may be trapped in a corner.

This behavior of the entrapments cannot be simulated on a macro scale using the elementary physical laws implemented in the code. The restriction of the minimal bubble size to at least one control volume makes it impossible to simulate moving entrapments realistically. Beside this, other effects like surface tension forces that are neglected in these macroscopic simulations may become important. For realistic simulations of the progression of entrapments more sophisticated entrapment models taking into account the different nature of the flow progression in and between the fibre bundles will be required.

REFERENCES

1. T. S. Lundström, B. R. Gebart, C. Z. Lundemo, "Void formation in RTM", *Journal of Reinforced Plastics and Composites,* Vol. 12 (1993).

2 K. Kang and K. Koelling, "Void transport in resin transfer molding ", *Polymer Composites,* Vol. 25(4), pp. 417-432 (2004).

3. C. W. Hirt and B. D. Nichols "Volume of Fluid (VOF) Method for the Dynamics of Free Boundries", *Journal of Computational Physics*, Vol. 39, pp. 201-225 (1981).

ISOTHERMAL FLOW ANALYSIS IN LIQUID COMPOSITE MOLDING PROCESSES

M. Hattabi[1], J. Echaabi[1] and A. Saouab[2]

[1] *Equipe de Recherche Appliquée sur les Polymères, Département de Génie Mécanique, ENSEM, Université Hassan II Aïn Chok, BP 8118, Oasis, Casablanca, Maroc.*
m.hattabi@ensem-uh2c.ac.ma, j.echaabi@ensem-uh2c.ac.ma

[2] *Laboratoire de Mécanique Physique et Géosciences du Havre, Université du Havre, 25, rue Philippe Lebon, BP 540,76058 Le Havre Cedex, France,*
abdelghani.saouab@univ-lehavre.fr

ABSTRACT: In this study, we present a simple technique for revealing of the key parameters of the RTM (resin transfer moulding) process, as permeability and the kinetics of the front. The variations of permeability during the treatment shows the capillary effect which is modelled for two configurations. The analysis of the front kinetics allowed making the identification of the tensor of permeability and the examination of the capillary number put in evidence a non saturated zone which can be characterized by a critical length.

KEYWORDS: Resin Transfer Moulding, Flow front, Relative permeability, Void, Capillary Pressure, Critical Length.

INTRODUCTION

Composite molding is a technique more and more used in the industry. The family of processes LCM "liquid composite molding" and it's by products (RTM, LRI, RFI) is commonly used at present in aeronautics, automobile industry, water sport, civil engineering and aeolian industry. In the case of the resin transfer molding (RTM), the process consists of the injection of a thermoset resin in a closed mold containing a fibrous glass reinforcement arranged in advance. This process allows the manufacture of high quality composite parts with complex geometries within limited dimensions. Numerical simulation tools of these procedures were finalized and are the subject of numerous programs of validation. The optimization of the parts material health remains a crucial point to go into.

With the use of Darcy's law, relation between the flow debit through a porous medium and the fall of pressure in the mold cavity, the process corresponding to the filling of the mold can be predicted. Several works were realized in the case of the RTM on this phase of filling [1-3]. Faced with the complexity of the identification of the tensor of permeability, several researchers concentrated their efforts on the experimental techniques. The influential factors in the estimation of permeability are the technique of measurement, the mold edge effect, the direction of the flow and the interaction between the resin and the reinforcement. Several authors tried to measure the loss of pressure according to the debit to verify the linear behavior described by Darcy's law. The anisotropy of reinforcements was also studied, among other things by [4-5]. These works have for common point the use of a central injection mould one of whose patches is transparent thus allowing to follow the flow front.

The knowledge of the permeability of fibrous reinforcements is essential to the simulation of the RTM process. In this article, we model permeability according to the parameters of control and we present the expression of the capillary number and of the critical length for 1D and 2D. We have measured permeability for a radial injection using a simple measurement technique. A mould has been designed and fitted out with a transparent patch displaying the front flow. The analysis of the front kinetics has allowed the identification of the permeability tensor. The measurement results and the consideration of the capillary number have revealed a non-saturated zone which is characterized by a critical length.

EXPERIMENTAL SETUP

The realized apparatus consists in a parallelepiped cavity with the dimensions 270x270x3.4 mm used for a radial injection. The mould consists of a steel bottom and of a glass or Plexi-glass top. Injection is done by means of a buzzard placed at the centre of the mould and connected to a hydraulic jack by a flexible hose equipped with a distributor to evacuate air bubbles. The hydraulic jack containing glycerine is activated by a drive machine (figure 1). The fluid impregnated the reinforcement inside the mould cavity according to a bidirectional flow (2D) before being evacuated to the other end of the mould by means of hole placed at the bottom of the mould. The technique of radial injection (2D) has some benefits on the measurement of the unidirectional permeability (1D). It allows to make a single measurement of the permeability tensor and to eliminate the edge effects usually met in the techniques of measurement of unidirectional permeability. Experimental setup allows following the evolution of the front flow according to time and to measure the fall of pressure of injection between two successive placements of the front. From this information, the permeability of the reinforcement can he easily inferred. The realized assembly allows only the resin injection with a constant debit.

Concerning the measurement of the pressure injection, a pressure sensor is placed exactly at the point of injection. A transparent upper patch containing several circles of various diameters and lines with various angles allows to display the forms and to measure the beams of the front flow (fig. 2) during the filling [6].

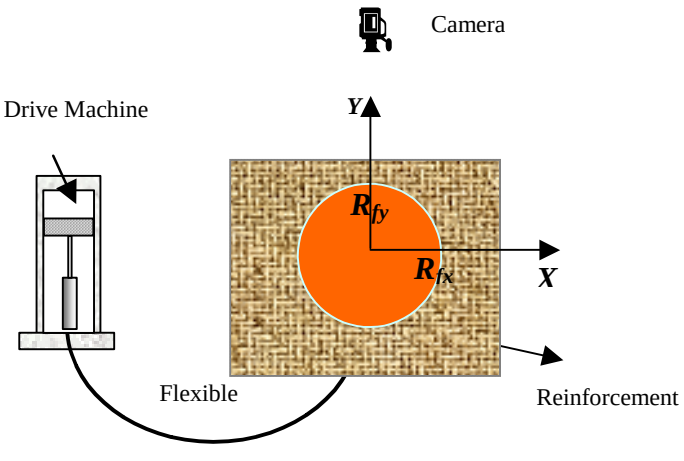

Fig. 1 Principle of experimental assemblies

Fig. 2 System of measurement

ANALYTICAL MODELLING

The pressure equation

The satisfaction of the reinforcement by the resin is likened to the flow of an incompressible and thermally insulated Newtonian fluid through a homogeneous porous medium. It is governed by the equation of continuance and Darcy's law. Within the framework of the radial injection, an analytical solution can be easily deduced. It leads to a ruling equation of the dynamics frontally according to the field of pressure.

$$P(r) = A \ln r + B \tag{1}$$

Table 1 Permeability, Capillary Number and Critical Length in injection 1D and 2D

	At constant debit (Qinj. = constant)	
Injection mode	1 D	2 D
K	$K = \frac{\mu Q_{inj}}{A\phi}\frac{x_f}{\Delta P}$	$K = \frac{\phi\mu}{2}\frac{\left(r_f^2 - r_0^2\right)\ln(r_f/r_0)}{t\ \Delta P}$
C_a	$C_a = \frac{K\Delta P}{\phi\ L\ \gamma\ \cos(\theta)}$	
C_a	$C_a = \frac{\mu Q_{inj}}{LA\phi^2\ \gamma\cos(\theta)}x_f$	$C_a = \frac{\mu Q_{inj}}{2}\frac{\left(r_f^2 - r_0^2\right)}{t}Ln\left(\frac{r_f}{r_0}\right)$
L_{cv}	$L_{cv} = D_f\left[\frac{\mu Q_{inj}}{LA\phi^2\ \gamma\cos(\theta)}x_f\right]^{-1}$	$L_{cv} = D_f\left[\frac{\mu Q_{inj}}{2}\frac{\left(r_f^2 - r_0^2\right)}{t}Ln\left(\frac{r_f}{r_0}\right)\right]^{-1}$

The pressure field depends only on the radial distance to the injection gate because the porous medium is ensured to be isotropic (i.e., $K_x = K_y = K_z = K$).

The conditions are as follows:
$r = r_0$ is the beam of the threshold of injection and the $r = r_f$ is the beam of the flow front;
With $P_i(t)$ is the pressure of injection and $P(t) = P_f$ is the pressure at the flow front.
By successive integrations, the pressure distribution in the mould is obtained:

$$P(r) = \left(P_i - P_f\right)\frac{\ln\left(r/r_0\right)}{\ln\left(r_f/r_0\right)} + P_i \tag{2}$$

Let us call back that from a numerical point of view within of the simulation of LCM processes, different approaches were used to resolve the continuity equation and Darcy's law [1-3]. The prediction of the permeability of reinforcements was also the subject of numerical approaches by resolving the equation of Stokes on an elementary volume. However, the use of this method remains still limited. For that reason, in practice, the measurement of the permeability is still essentially made from the study of some flow types which lead to some analytical solutions allowing the estimation of the permeability value.

Two methods can then be used. The first one is linked to a unidirectional flow (1D) and the second one for the radial flow (2D). In our study, we use an isotropic reinforcement. The general solution formulating the expression of permeability is presented in table 1. It is obtained by resolving the equation of pressure with a condition of injection with constant debit within the frameworks of unidirectional and radial flows.

Capillary effect

By observing the kinetics of the follow-up of the flow front, the evolution of the capillary number is examined. Several researchers concentrated on the one-dimensional shape of Darcy's law with the capillary pressure in the flow front [7-8]. As a result, the rigorous and precise description of the flow in the neighbourhood of the front cannot be treated on Darcy's [9] law basis alone. Indeed, this takes into account only driving forces due to pressure or to the compulsory debit. At the level of the front and because of the non saturation of the reinforcement, it becomes imperative to take into account the contribution of the capillary pressure. Wong [10] suggests defining a critical length of the flow L_{cv} (Cross-over length) to quantify the effect of the capillary pressure. This approach was resumed by Weitzenböck [11] who redefines this length by:

$$L_{cv} = \left(\frac{D_f}{C_a} \right) \tag{3}$$

Where: C_a is the capillary number and D_f (m) the diameter of the fibre where the pore is placed at the level of the supposed material front that one suppose subjected to the fall of pressure $\Delta P = P_{inj.} - P_{fr.}$ (with $P_{inj.}$ pressure of injection and $P_{fr.}$ pressure of the front).
On the basis of Ahn's works [7], Weitzenböck estimates capillary pressure P_c (Pa), on a function of the porosity and a parameter F called "Factor of Shape". This factor, often measured experimentally, depends on the alignment of fibres and on the direction of the flow. This capillary pressure for a fibrous reinforcement is defined by:

$$P_c = \left(\frac{F}{D_e} \right) \gamma \cos(\theta) \tag{4}$$

Where: γ is the superficial tension of the fluid (N/m), θ is the contact angle of solid liquid, D_e is the equivalent diameter of the pore and F is the factor of shape (F = 4 for a flow along the fibres and $F=2$ for a transverse flow in fibres). The advantage of relation 4 is that it makes it possible to consider a possible affinity between the fibres and the fluid used for the measurement of permeability through the contact angle.

Table 1 gives the expressions of the critical length that we have calculated for unidirectional and bidimensional flows. Critical length allows appreciating the importance of the effect of the capillary pressure for a given attempt. To estimate the importance of this capillary effect in our radial injection experiences, we calculated the capillary modified number according to the fall of pressure, to the physical properties of the fluid and the characteristics of the reinforcement.

$$C_a = \frac{\mu u}{\gamma \cos(\theta)} \tag{5}$$

Where, u is the relative velocity of flow when fluid soaks dry fibres.
By using Darcy's law, this capillary number becomes:

$$C_a = \frac{K}{\phi\ \gamma\ \cos(\theta)} \frac{\Delta P}{L} \tag{6}$$

$\frac{\Delta P}{L}$ is the pressure drop through the reinforcement of permeability K. Equation (6) was also used by Foley and al. [12] who found a transition where permeability decreases with a capillary number of the order of 0.01.

The analysis of the flow through a fibrous medium (particularly within the framework of the measurement of the permeability) can be examined by using critical length, which measures the importance of the capillary effect during the soaking of the reinforcement. This effect depends on the capillary number and on the type of reinforcement.

Afterward, values used in this study are: velocity of injection $U_{inj.}=0.35$ *cm/s* or $U_{inj.}=1.5$ *cm/s*, a factor of shape $F=2$,$\mu= 0.12$ *Pa.s* (glycerine), superficial tension of the fluid $\gamma=60\ 10^{-3}$ *N/m* and the contact angle of solid liquid $\theta=0°$ [13].

We present the evolution of the critical length of the flow according to the capillary number for two flow configurations of 1D and 2D (figure 3). Results show that when the capillary number increases, the critical length of the flow decreases considerably. Also one note that from a capillary number of the order of 10^{-4} the critical length of the flow becomes very short which means a transition toward saturation. Figure 4 represents the ratio between the critical lengths of the flow and the position of the front according to the kinetics of the front for two configurations (1D and 2D). At the beginning of the experiences an important decrease in the ratio is observed, which is more important for 1D than for 2D.

The importance of the capillary effect depends on the parameters of the moulding. Thus effect decreases if the time of filling decreases; that is, if the pressure where the debit of injection increases. It also decreases if the porosity decreases. The curves also show that this effect is important at the beginning of injection and decreases with the length the front (figure 3).
Figure 5 shows also that the critical length and therefore the capillary effect decreases when the speed of injection increases [14] and decreases when the porosity decreases (figure 6) in agreement with the literature.

Figure 7 represents the rate of void according to the capillary number for two different velocities of injections. This percentage is calculated by means of the model formulation in (7) with couple reinforcement / fluid equivalent for a flow through an isotropic medium. We observe that the rate of void decreases also when the capillary number increases as noticed by [13].

$$V = -57.849 - 17.16 Log(C_a) \tag{7}$$

Where: V is the percentage of void and C_a the capillary number.

DISCUSSION

The results that we present here are obtained for a central injection whose beam of injection is $R_0=2$ *mm*. The flow of the injected fluid is realized through an isotropic medium with velocities of injections of 0.35 cm/s, 1.5 cm/s and a viscosity of 0.121 Pa.s. Permeability is measured by means of a radial injection mould with reinforcements of 8 and 9 plies corresponding respectively to porosities 0.69 and 0.65.

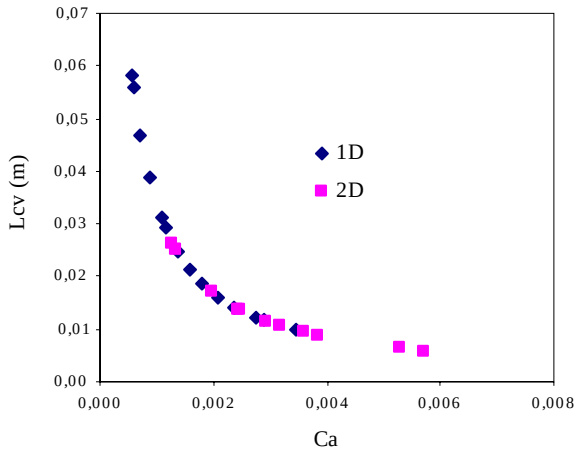

Fig. 3 Evolution of the critical length vs the capillary number for Unidirectional and Radial injections

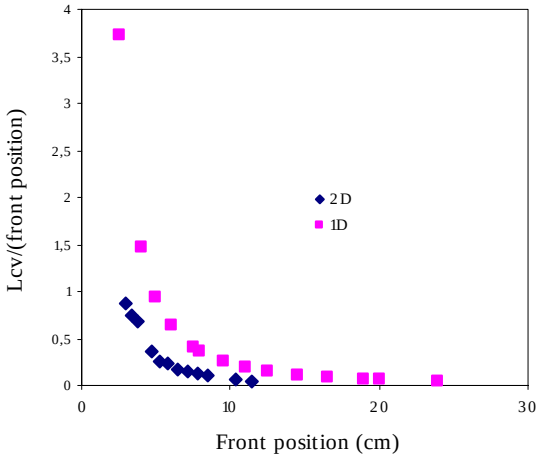

Fig. 4 Evolution of the ratio of the critical length and the position of the front for 1D and 2D injections

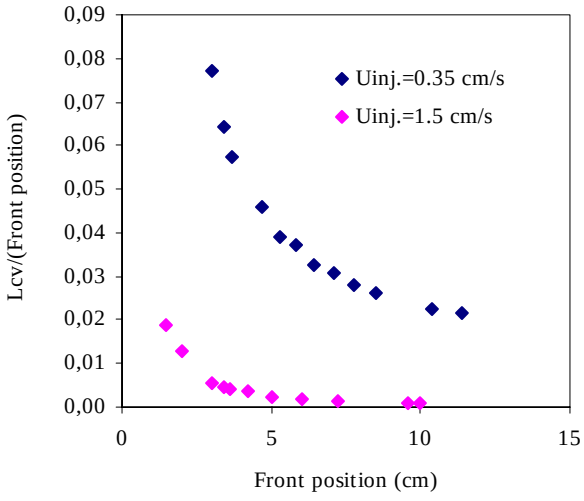

Fig. 5 Evolution of the report of the critical length and the position of the front for two debits of injection

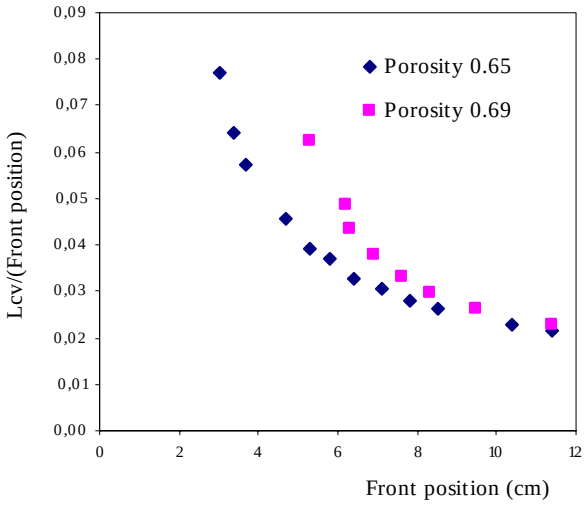

Fig. 6 Evolution of the critical length for two different porosities

During the experiments, the fall of pressure varies between 0 and 1 Bar. For a velocity of constant injection or constant debit), we measure the fall of pressure (ΔP), the position of the

flow front (r_f) and corresponding time (t). Permeability K is then calculated (table 2) knowing the beam of injection r_0, the porosity of the reinforcement ϕ and the viscosity of the fluid μ.

In figure 8, we present calculated permeability (table 1) according to the pressure of injection measured for two different porosities. Results show that when the fall of pressure increases, permeability decreases. This last one becomes constant from a fall of pressure of 0.25 Bar and this independently from the pressure. This variation of permeability can be explained by a non linear behaviour of Darcy's law, and can also be accounted for by a non-saturation of the environment. The result represented in figure 8 is in agreement with the evolution of the critical length according to the position of the front (figure 6).

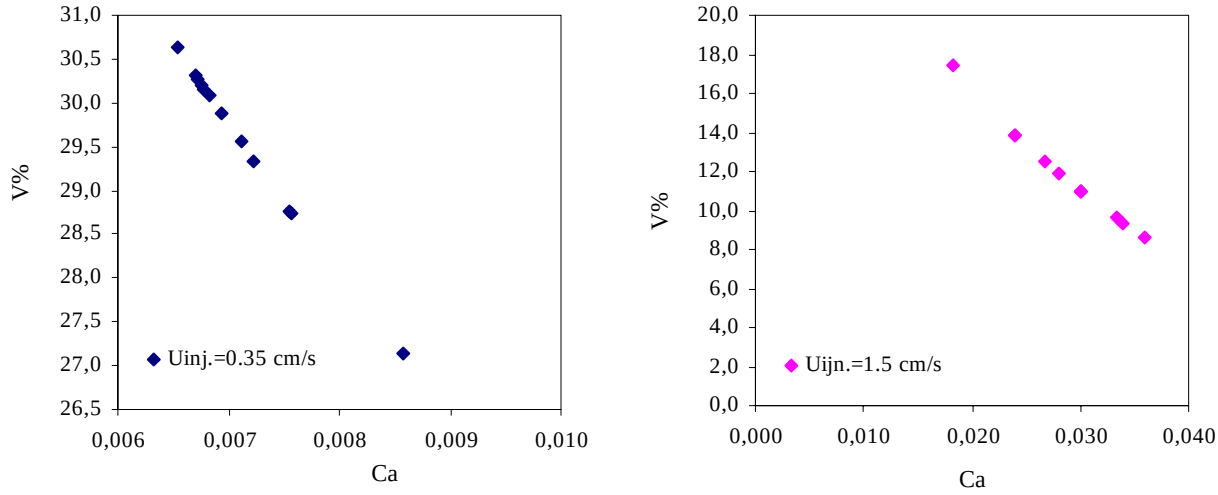

Fig. 7 Percentage of the void for two velocities of injection.

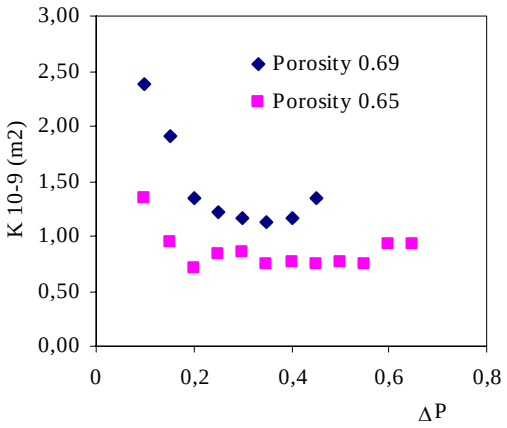

Fig. 8: Evolution of permeability vs the fall injection of pressure (2D)

Number of plies	8	9
Porosity	0.69	0.65
Permeability (Averaged value) (10^{-9} m^2)	1.45	0.85
Permeability (Averaged value) (10^{-9} m^2) [15]	0.462	

Table. 2 Values of permeability for a 2D radial injection (isotropic reinforcement)

The values of permeability obtained spread out between 1.12 10^{-9} and 2.38 10^{-9} m^2 for a porosity of 0.69 whereas those for a porosity of 0.65 are contained between 0.74 10^{-9} and 1.35 10^{-9} m^2. Average values are respectively of 1.45 10^{-9} and 0.85 10^{-9} m^2.
To estimate the accuracy of measurement, we took into account the uncertainties of all the values. The relative error of permeability is of the order of 16 %.

CONCLUSION

A simple experimental assembly was finalized and allows making measures of pressure and flow front to calculate permeability for different porosities.
The objective of the work is to estimate the importance of the capillary effect for the made tests. This capillary effect is modelled by the critical length whose expression was calculated in 1D and 2D. The obtained results show that this effect is important at the beginning of the injection and becomes unimportant for a fall of pressure of the order of 0.25 Bar. The used assembly and the chosen parameters of moulding allow to make reliable measurement of permeability.

REFERENCES

1. A. Saouab, J. Breard and G. Bouquet, “Modélisation numérique de l’injection d’une résine à travers un renfort de composite à matrice polymère ” 4ème Congrès de mécanique, Faculté de Mohammadia, Avril 1999, Maroc.

2. A. Shojaei S. R. Ghaffarian and S.M.H. Karimian, “Numerical simulation of three-dimensional mold filling process in resin transfer molding using quasi-steady state and partial saturation formulations”, Composites Science and Technology , 62, 2002, pp. 861-879.

3. M. Hattabi, I. Snake, J. Echaabi and M.O. Bensalah, “Flow front simulation in the liquid composite molding processes” Compte Rendus de Mécanique, pp. 585-591, Juillet 2005.

4. R. Gauvin, F. Trochu, Y. Lemenn and L. Diallo, “Permeability measurement and flow simulation through fiber reinforcement” *Polymer Composites,* Vol.17, pp.34-42, 1996.

5. J. Bréard J., A. Saouab & G. Bouquet, “Mesure de la perméabilité spatiale d’un renfort tridimensionnel pour matériaux composites à matrice polymère”; *Eur Phys JAP* 1, pp. 269-278, 1998.

6. M. Hattabi, J. Echaabi, M.O. Bensalah, J. Bréard and A. Saouab, “Analyzes flow during on-line Injections and Radial Application in the Measure of Permeability”, Journal of Reinforced Plastics and Composites, 24, pp. 1909-1920, 2005.

7. K. J. Ahn, J.C. Seferis, and J.C. Berg. “Simultaneous measurement of permeability and capillary pressure of thermosetting”, Polymer *Composites*, 12 (3), pp. 146-152, 1991.

8. Z. Dimitrovova, G. Suresh and G. Advani, “Mesolevel analysis of the transition region formation and evolution during the liquid composite moulding process”, Computers and Structures 82, 1333–1347, 2004.

9. K.L. Pillai, and S.G. Advani, “Numerical Simulation of Unsaturated Flow in Woven Fiber Preforms During the Resin Transfer Molding Process”, *Polymer Composites,* Vol. 19, N° 1, February 1998.

10. P.Z Wong, Flow in porous media: permeability and displacement patterns, MRS Bull., pp. 32-38, 1994.

11. J.R. Weitzenböck, R.A. Shenoi, and P.A.Wilson, “Measurement of 3D permeability”, Composites-Part A: Applied Science and Manufacturing; 29A (1-2): pp.159-169, 1998.

12. M.F. Foley, and T. Gutowski, *23rd International SAMPE Technical Conference*, 23, 326-340, 1991

13. N. Patel and L. J. Lee, “Effects of fiber mat architecture on void formation and removal in liquid composite molding”, Polymer Composites; 16(5): pp. 386–399, 1995.

14. Dave R. *Journal of Composite Materials*24, pp. 22-41, 1990

15. Ferland P., D. Guittar & F. Trochu, “Concurrent for Permeability Measurement in Resin Transfer Molding”, Polymer Composites, Vol. 17, N° 1, Februery 1996.

SIMPLE MODELS FOR MOLD FILLING STAGE IN LIQUID COMPOSITE MOLDING AND THEIR APPLICATIONS TO STRUCTURE-PROCESS COUPLED OPTIMIZATION

Chung Hae Park [1], Abdelghani Saouab [1], Joel Bréard [1], and Rodolphe Le Riche [2]

[1] *Laboratory of Mechanics, Physics and Geosciences, University of Le Havre*
25 rue Philippe Lebon, BP540, F-76058, LE HAVRE, FRANCE: chung-hae.park@univ-lehavre.fr , abdelghani.saouab@univ-lehavre.fr , joel.breard@univ-lehavre.fr

[2] *CNRS UMR 5146 and 3MI, Ecole des Mines de Saint-Etienne,*
158 cours Fauriel, F-42100, SAINT-ETIENNE, FRANCE: leriche@emse.fr

ABSTRACT: The current paper is composed of two parts. In the first part, we present the analytical and semi-analytical models to estimate mold filling time in Liquid Composite Molding processes. Their accuracy and efficiency are examined through a comparison with Control Volume / Finite Element simulations.
In the second part, we propose an integrated optimization of structural performance and manufacturing cost. The simple models are incorporated into the optimization procedure to investigate the couplings between structural performance and manufacturing costs. By considering manufacturing at the early stage of product design, excessive manufacturing costs which sometimes arise for the best structural performance can be avoided. In order to be cost effective, different manufacturing routes need to be selected depending on part dimensions, loading conditions and design criteria.

KEYWORDS: LCM (Liquid Composite Molding), Analytical model, Mold filling, Integrated optimization, Cost effective manufacturing

INTRODUCTION

LCM (Liquid Composite Molding) processes refers to composites manufacturing processes which employ liquid resin infiltration into a preform i.e. a dry fabric reinforcement put in the closed mold. LCM processes have been widely used in aeronautic industries, because of their advantages in terms of cost reduction, part integration and control of volatile problem.
From the manufacturing point of view, the main issues are reducing cost (part of which is process cycle time) and eliminating defects such as dry spots and micro/macro voids in the finished article. Thus, predicting resin flow kinetics and pressure distribution in the mold is essential to optimize the process. There have been numerous studies on numerical simulation of mold filling [1]. On the one hand, numerical simulations accurately predict the resin flow kinetics at the expense of a heavy computational cost,

and even more so when the simulations are repeated to optimize the process. For example, computational cost is a burden when simulating resin infusion with high permeability layer because the resin flows through the thickness as well as in planar directions which require three dimensional meshes. On the other hand, closed form models, which typically make more assumptions but are computationally more efficient than numerical simulations, may be preferred for design if their inaccuracy does not invalidate the final solutions. This is the case for the optimization of injection gates and vents.

From the viewpoint of design procedure, it has been a common practice to optimize process parameters only after the structural design is decided. In LCM processes, however, there exist strong couplings between mechanical performance and manufacturing. Fiber volume fraction and orientation are key parameters to structural performance such as stiffness and strength. On the other hand, they are also major factors influencing the preform permeability, a key parameter to productivity and manufacturability in LCM processes. Hence, this procedure, where the manufacturing is considered after the structural design is finalized, may require excessively high manufacturing cost or labor even if it may lead to the best structural performance. For example, it is acknowledged that up to 80% of the manufacturing cost of the structure is fixed once the preliminary structural configuration has been decided [2]. This dilemma calls for an optimization method that simultaneously considers structural performance and manufacturing cost. To investigate the couplings between mechanical performance and manufacturing and to consider many design solutions in the preliminary design stage, it is more efficient to use closed form models rather than numerical simulations.

Besides, this optimization approach can provide a good guideline for optimal selection of manufacturing route. In fact, the criteria for process selection are numerous: the complexity of part geometry, the environmental regulation, industrial strategies, level of part quality (quantity of residual void) etc. Arguably, cost effectiveness and manufacturability are the primary criteria among them. The cost of composite structures is composed of material cost, labor cost and tooling cost. Generally, it is not an easy task to accurately predict the total manufacturing cost, since it is affected by many factors such as labor rate, machine rate, factory lay-out, batch size, etc. However, it is evident that the mold filling time plays a major role in process cycle time since the polymer curing time is usually fixed for a specific resin. Hence, mold filing time can be a metric for the cost-effectiveness of manufacturing process. In addition, it can be a guide to estimate the manufacturability to prevent premature gelation of resin.

In the first part of this article, we present analytical and semi-analytical models for RTM, CRTM and LRI process. In the second part, using these models, a preliminary conceptual design is performed through simultaneous optimization of the structure and the process.

SIMPLE MODELS FOR LCM PROCESSES

Resin Transfer Molding

In RTM processes, analytical solutions are easily derived for the specific mold geometries such as linear channel-like injection and radial injection. To deal with general shaped mold, a simple model was developed for resin transfer molds containing thin flat preforms with isotropic permeabilities [3]. The time required to fill the mold can be calculated by treating the resin flow inside the mold as partly radial and partly channel-like flow. This simple model for mold fill time of two dimensional resin

transfer molds with isotropic permeability can be applied to the preform with anisotropic permeability through the coordinate transformation [4].

We consider complex mold geometry (0.23m × 0.14m) with a circular insert in Fig. 1. Using the simple model, we estimate the mold filling times for 4 different injection gates: single gate at A, B, C and simultaneous injection at three gates. The injection pressure is 0.1MPa, and the injection gate radius is 1.5mm. The preform permeability is 10^{-10}m^2 and the resin viscosity is 0.1Pa s. The results are compared with those by numerical simulation by CV/FEM (Control Volume / Finite Element Method) [5]. Good agreements are observed even for the complex mold geometry with inserts (Fig.5).

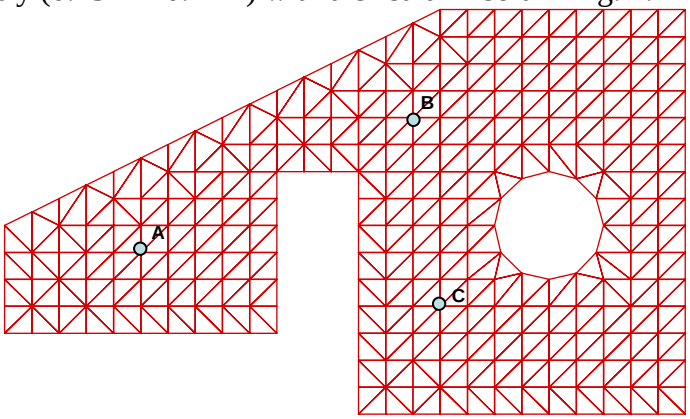

Fig. 1 Mold geometry for the validation of simple model for RTM

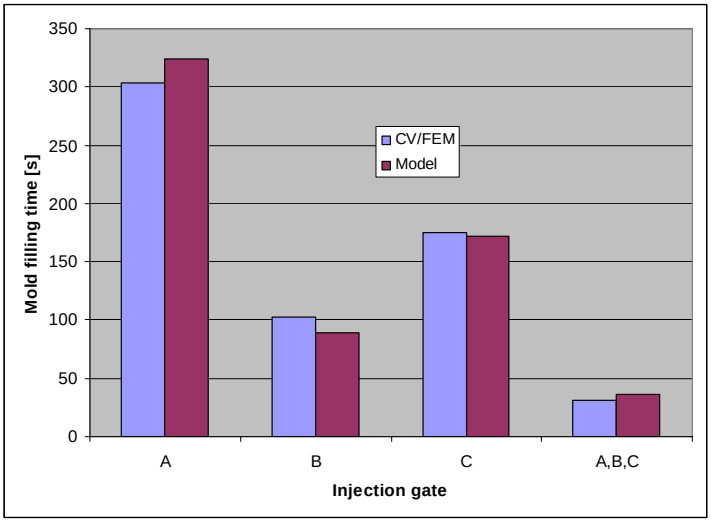

Fig. 2 Comparison of mold filling time in RTM

Compression Resin Transfer Molding

Saouab et al. proposed closed form solutions for CRTM processes [6]. In the present study, we consider separate injection and compression process: injection at constant pressure and compression at constant mold closing speed. For a linear flow condition (Fig. 3), we can derive the closed form solutions for total mold filling time as a sum of injection time (t_{inj}) and compression time (t_{comp}).

$$t_{inj} = \frac{\mu(1-V_f)L^2}{2KP_{inj}}\left(\frac{1-V_f}{V_f}\right)^4\left(\frac{V_{fo}}{1-V_{fo}}\right)^4, \quad t_{comp} = \frac{H}{U_c}\left(\frac{V_f}{V_{fo}}-1\right) \tag{1}$$

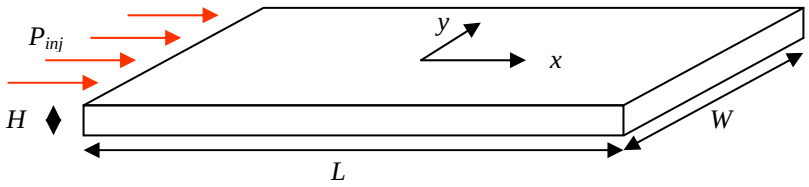

Fig. 3 Mold geometry and dimensions

We can see that the total mold filling time can be decided from U_c, mold closing speed, and the V_{fo}, fiber volume fraction at the moment when the injection ends and the compression begins. Mold closing speed is decided by the constraints of maximum

pressure in the mold and the total mold clamping force which is the sum of resin pressure and compaction pressure by preform deformation. Then, we can obtain the V_{fo} to minimize the mold filling time.

$$F_{mold} = F_{resin} + F_{fiber} = \frac{U_c \mu L^3 W}{3KH} + A_s \frac{\sqrt{V_f / V_o} - 1}{\left(\sqrt{V_{\max} / V_f} - 1\right)^4} LW \qquad (2)$$

Liquid Resin Infusion

A striking difference of LRI from conventional RTM process is the adoption of High Permeability Layer (HPL or High Permeability Medium, HPM) to facilities the resin flow and to reduce the infusion time. The resin flow in HPM leads much faster than in reinforcement, due to the big difference in permeability. This preferential flow in HPM induces the through thickness resin flow. Hence, a new approach is required considering cross flow. The mold filling process in LRI can be divided into 3 steps (Fig. 4).

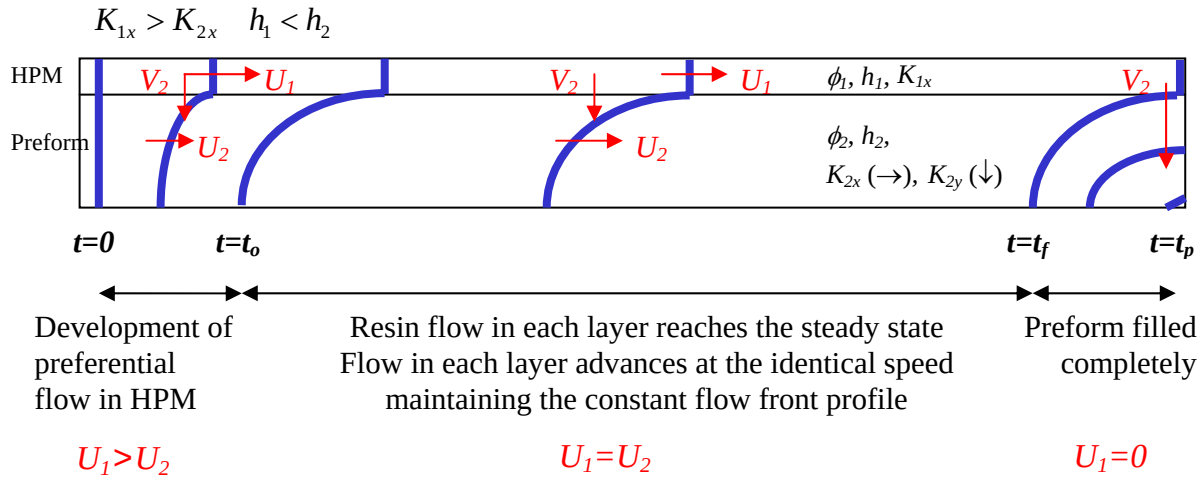

Fig. 4 Mold filling process in LRI

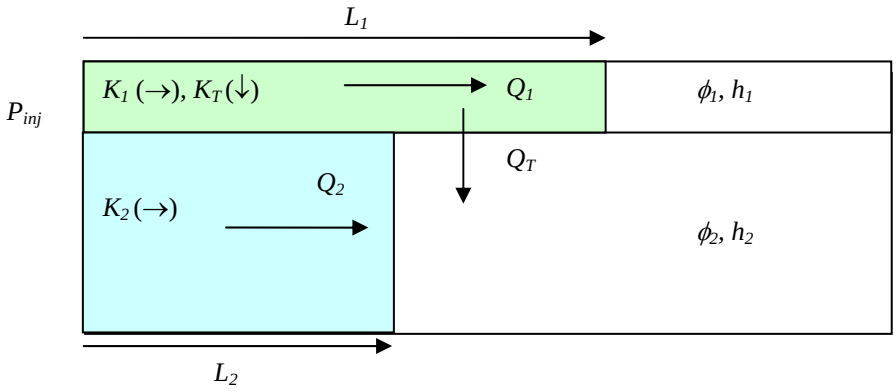

Fig. 5 Flow kinetics in LRI ($0<t<t_f$)

Until the flow reaches the end of HPM ($t=t_f$), it is assumed that the pressure distribution is linear at each layer (Fig. 5). From these pressure distributions, we can obtain average pressure of transverse flow from HPM to fiber preform $P_m = \frac{P_{inj}}{L_1}\frac{L_1 - L_2}{2}$.

From Darcy's law we can relate the resin pressure with flow rate. Considering mass conservation of each layer, we can describe the next governing equations.

$$\begin{cases} \dfrac{K_1}{\mu}\dfrac{P_{inj}}{L_1}h_1 - \dfrac{K_T}{\mu}\dfrac{P_{inj}}{h_1}\dfrac{(L_1-L_2)^2}{2L_1} = \phi_1 h_1 \dfrac{dL_1}{dt} \\ \dfrac{K_2}{\mu}\dfrac{P_{inj}}{L_2}h_2 + \dfrac{K_T}{\mu}\dfrac{P_{inj}}{h_1}\dfrac{(L_1-L_2)^2}{2L_1} = \phi_2 h_2 \dfrac{dL_2}{dt} \end{cases} \quad (3)$$

Once the flow reaches the tip of HPM, the transverse flow from HPM to preform and the longitudinal flow in preform fill the remaining dry preform (Fig. 6).

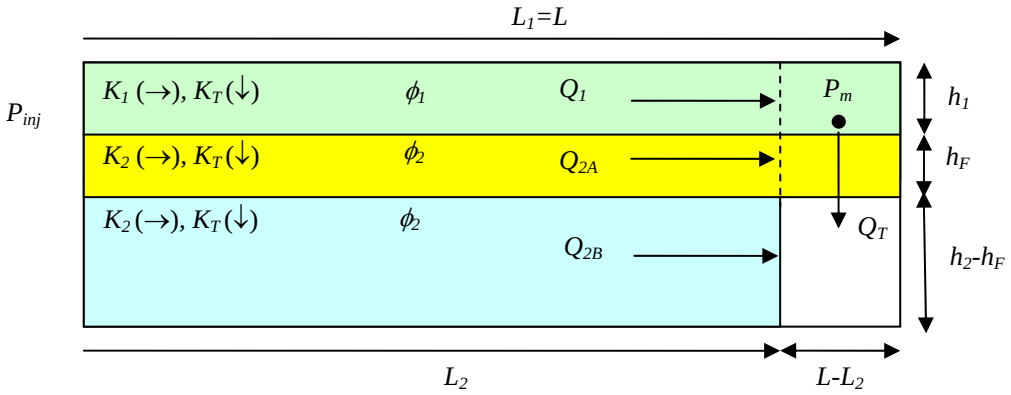

Fig. 6 Flow kinetics in LRI ($t_f < t < t_p$)

We adopt the assumption of linear pressure distribution again. P_m is the average pressure in the zone of (L-L_2) and (h_1+h_F). From Darcy's law, we can describe the relations of each flow rate. Taking into consideration the mass conservation of each zone, we can derive the governing equations.

$$\begin{cases} Q_1 + Q_{2A} = Q_T \\ Q_{2B} + Q_T = -\phi_2 \dfrac{d\left((h_2 - h_F)(L - L_2)\right)}{dt} \end{cases} \quad (4)$$

We introduce an assumption that the unfilled zone (L-L_2 and h_2-h_F) of preform maintains the constant aspect ratio. These set of coupled PDEs can be solved by simple numerical integration scheme such as Runge-Kutta method. We present the comparison of the results by models and CV/FEM simulations in Tables 1~2 and Fig. 7.

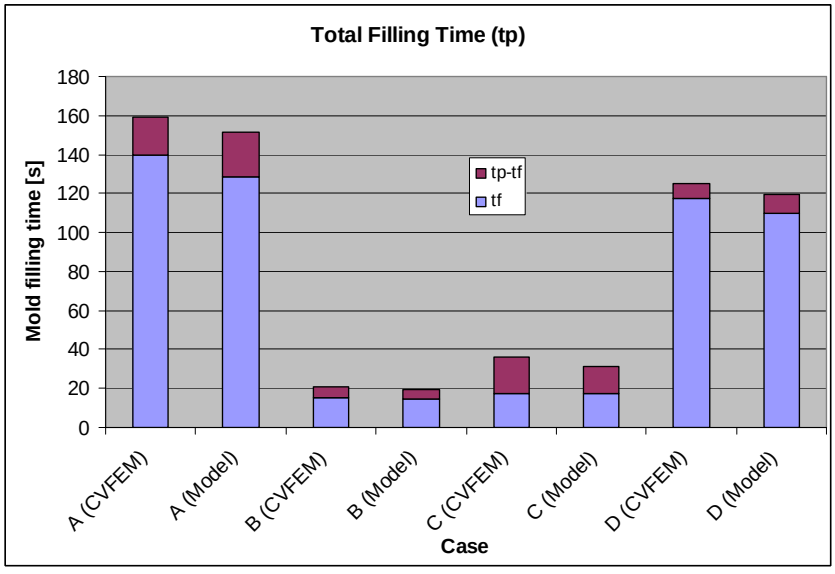

Fig. 7 Comparison of mold filling time in LRI

Even though it is not a closed form solution, the proposed model shows a much better numerical efficiency than numerical simulation. A CV/FEM simulation with 3507 nodes and 6000 triangular elements takes 1897 seconds of CPU time with Pentium 4 processor of 2.6GHz. With the same CPU, on the contrary, the simple model needs only

1.2 second for one calculation (120 seconds for 100 calculations) using the time increasing step of 10^{-4} second in Runge-Kutta method.

Table 1 Material properties for simple LRI model

ϕ_1	ϕ_2	K_T [m^2]	K_2 [m^2]	μ [Pa s]	h_1 [m]	L [m]	P_{inj} [Pa]
0.99	0.5	1.47×10^{-11}	8.80×10^{-11}	0.1	0.002	0.3	1.00×10^{5}

Table 2 Sample cases for preform permeability and thickness

Case	K_1/K_2	h_2/h_1
A	10	10
B	100	5
C	100	10
D	10	5

STRUCTURE-PROCESS COUPLED OPTIMIZATION IN LCM

Integrated Optimization of Structural Performance and Manufacturing Process

We suggest an integrated optimization method simultaneously considering structural performance and manufacturing process. The design objective is the minimization of structural weight. We assign structural and process constraints at the same time. As a structural constraint, the stiffness is considered to constrain the strain under the load. As process constraints, the mold filling time, the mold clamping force and the maximal pressure are treated.

To achieve these purposes, four parameters are optimized: layer number, layer stacking sequence, final fiber volume fraction and final part thickness. Fiber orientation is selected from the pre-assigned angle set. In this work, we employ the 4 angle set composed of 0°, 45°, 90°, -45°. The layup of laminated plate is assumed to be symmetric. As the optimization scheme, we apply the genetic algorithm. To deal with the layer number variation, crossover and mutation operators are modified as in Park et al. [6]. Elastic moduli of composites can be obtained from the moduli of the constituents by the Halpin-Tsai equations. As a metric of the structural stiffness, we define the strain norm using classical lamination theory.

$$\varepsilon = Max_{top,\,bottom}\left[\sqrt{0.5\times(\varepsilon_1+\varepsilon_2)^2+0.5\times(\varepsilon_1-\varepsilon_2)^2}\right] \tag{5}$$

The permeability according to the fiber volume fraction variation is obtained using Kozeny-Carman equation. The anisotropic permeability tensor in each layer can be related to the principal permeabilities by tensor transformation equation. The gapwise averaged permeability model is applied to obtain the perform permeability composed of layers with different orientations, assuming that the in-plane permeabilities in principal directions are of the same order.

Sample Problem

As a design object, the rectangular plate under the flexural bending is regarded. The mold geometry and injection port location are illustrated in Fig. 3. We consider RTM, CRTM and LRI as a candidate for manufacturing route. The unidirectional carbon stitched mat (fiber density: 1.79g/cm^3, areal weight: 152g/m^2) is used as reinforcement. The in-plane permeabilities of mat are 10^{-9} m^2 in fiber direction and 1.33×10^{-10} m^2 in

transverse direction at the fiber volume fraction of 0.4, while the permeability in the thickness direction is 1.33×10^{-13} m^2. For the sake of easy layup, four plies stacked in the same orientation make up one layer. The resin viscosity is 0.15Pa s. In RTM process, the injection pressure is maintained at 0.15MPa. In CRTM process, injection is performed under the constant pressure of 0.12MPa. Maximum allowable mold clamping force is 300kN and maximum allowable pressure is 0.15MPa. Mold closing speed should not exceed 1 mm/s. In LRI process, injection pressure is assumed to be 99.5kPa, the difference between atmospheric pressure (0.1MPa) and vacuum pressure (500Pa). HPM permeability is 10^{-8} m^2 and its thickness is 1 mm.

Results and Discussion

For the various loading conditions and plate dimensions, optimal material configurations are obtained for each manufacturing process (Tables 3~4).

Table 3 Results of structure-process coupled optimization
(L=0.5m, W=0.5m, ε_c=0.001, t_c=240s)

Loading		Process	Weight [g]	Optimal configuration			
M_x [N]	M_y [N]			V_f	H [mm]	Stacking sequence (symmetric layup, |s)	Layer number
0	10^3	RTM	2962.38	0.4145	8.20	$90^3\ 0^2$ |s	10
		CRTM	2898.55	0.4255	7.99	$90^4\ 0$ |s	10
		LRI	2898.55	0.4255	7.99	$90^4\ 0$ |s	10
10^3	10^3	RTM	4340.88	0.4612	11.79	$90\ 0^2\ 90\ 0\ 90^2\ 0$ |s	16
		CRTM	4197.28	0.5573	10.89	$90\ 45\ -45\ 0^6$ |s	18
		LRI	4432.10	0.4496	12.10	$0\ 90\ 45\ –45\ 90\ 0^3$ |s	16

M_x and M_y denote the moment per unit length

Table 4 Results of structure-process coupled optimization
(L=1.0m, W=0.5m, ε_c=0.001, t_c=600s)

Loading		Process	Weight [g]	Optimal configuration			
M_x [N]	M_y [N]			V_f	H [mm]	Stacking sequence (symmetric layup, |s)	Layer number
0	10^3	RTM	6166.75	0.3951	8.61	$90^3\ 0^2$ |s	10
		CRTM	5924.75	0.4145	8.20	$90^3\ 0^2$ |s	10
		LRI	5797.11	0.4255	7.79	$90^4\ 0$ |s	10
10^3	10^3	RTM	8780.60	0.4549	11.96	$90\ 0^2\ 90\ 0^4$ |s	16
		CRTM	8681.87	0.4612	11.80	$0\ 90^2\ 0\ 90\ 0^3$ |s	16
		LRI	8684.37	0.4611	11.80	90 0 45 -45 0 -45 45 0 |s	16

We can see that optimal material configuration changes according to the manufacturing route as well as the loading conditions, the design constraints and the plate dimensions. Cost-effectiveness of each process can be investigated with the optimization results referring to the material cost and the batch size. For example, CRTM process results in lighter structure than LRI process does under the same design constraints, in some case (e.g. M_x=1000N, M_y=1000N, L=0.5m, W=0.5m). However, CRTM process needs more fiber mats (18) than LRI does (16) for each product. Furthermore, the total manufacturing cost also depends on the batch size. Since the equipment and tooling cost per product is critical, LRI may be better in terms of manufacturing cost, for the low

production number. On the other hand, the equipment and tooling cost goes marginal, as the production number increases. Otherwise, we can assign different mold filling time constraints with the aid of more exact model for the total manufacturing cost evaluation.

CONCLUSIONS

Analytical and semi-analytical models have been proposed for Liquid Composite Moldings: Resin Transfer Molding, Compression Resin Transfer Molding and Liquid Resin Infusion. They are not only numerically efficient but also accurate enough to be applied in a global optimization procedure. The semi-analytical LCM models have been applied to the integrated optimization of structural performance and manufacturing process. In the preliminary design stage, this approach provides a good guideline to predict the cost-effectiveness of each process for given design criteria, structural size and loading conditions.

ACKNOWLEDGEMENTS

The authors would like to acknowledge the Prof. Woo Il Lee and Dr. Moon Koo Kang at Seoul National University in Korea for the use of RTM simulation code.

REFERENCES

1. J. Mackerle, “Finite Element Analyses and Simulations of Manufacturing Processes of Composites and Their Mechanical Properties, A Bibliography (1985-2003),” *Computational Materials Science*, Vol. 31**,** 2004, pp. 187-219.

2. K. Wang, D. Kelly, and S. Dutton, “Multi-Objective Optimisation of Composite Aerospace Structures,” *Composite Structures*, Vol. 57, 2002, pp. 141-148.

3. A. Boccard, W. I. Lee, and G. S. Springer, “Model for Determining the Vent Locations and the Fill Time of Resin Transfer Molds,” *Journal of Composite Materials*, Vol. 29, No. 3, 1995, pp. 306-333

4. C. H. Park, W. I. Lee, W. S. Han and A. Vautrin, "Multi-Constraint Optimization of Composite Structures Manufactured by Resin Transfer Molding Process," *Journal of Composite Materials*, Vol. 39, No. 4, 2005, pp. 347-374.

5. M. K. Kang and W. I. Lee, “A Flow Front Refinement Technique for the Numerical Simulation of the Resin Transfer Molding Process,” *Composites Science and Technology*, Vol. 59, 1999, pp. 1663-1674.

6. A. Saouab and J. Bréard, “Analytical Modeling of CRTM and RTM Processes: Part A. General Mathematical Development,” *International Journal of Forming Processes*, Vol. 9, No. 3, 2006, in press

Session 10

SIMULATION - II

NUMERICAL SIMULATION OF THE INFUSION PROCESSES VALIDATION & PARAMETRIC STUDY

Tariq Ouahbi [1], Abdelghani Saouab [1], Joel Bréard [1], Pierre Ouagne [1], Sylvain Chatel [2]

[1] *Laboratoire de Mécanique, Physique et Géosciences , Université du Havre*
25 rue Philippe Lebon, BP 540, 76058, Le Havre, France
tariq.ouahbi@univ-lehavre.fr , abdelghani.saouab@univ-lehavre.fr

[2] *European Aeronautic Defence and Space – Corporate Research Center*
12 rue Pasteur, BP 76, 92150 SURESNES Cedex
sylvain.chatel@eads.net

ABSTRACT: The infusion process has been developed to be a cost-effective technique for the fabrication of large and complex composite structures [1]. Thus, this process has been identified as an alternative to the RTM (Resin Transfer Moulding) as well as the conventional autoclave prepreg technique [2].
In the infusion process, it is important to predict resin infusion time and final thickness of the part according to the process condition such as compaction pressure and resin temperature. Hence, in the present study, we propose a numerical model to simulate the resin infusion through the fibre preform and to predict the resin infusion time. A validation of the numerical resin infusion model is made through the comparison between experimental and numerical results, and a good agreement is observed. Based on this model, a numerical code has been developed to calculate resin infused height for various values of compaction pressure and resin temperature.
In the parametric study, the influence of compaction pressure on the final height of the part is investigated. The infusion time is also studied for the various process conditions.

KEYWORDS: Infusion Process, Hydro-Mechanical Coupling, Infusion Height Percentage, Resin Infusion Time.

INTRODUCTION

The large composite parts are increasingly used particularly in aeronautic industry. The LCM (Liquid Composites Molding) processes are being employed to manufacture high quality and complex-shaped fibre reinforced polymeric composite parts. We can classify them into two groups: the injection by resin transfer (RTM & derivatives) and the infusion by resin infiltration (Infusion & derivatives). In infusion processes, dry textile preforms are infiltrated by semi-cured resin (Fig. 1) and the resin is consolidated and cured in a single step, eliminating the labour to lay-up of prepreg tapes.

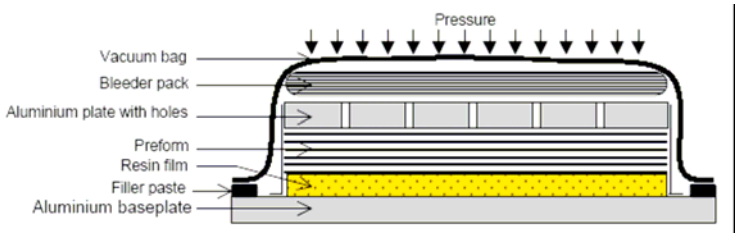

Fig. 1 Resin infusion process setup.

Several investigators have studied and proposed models for the RFI (Resin Film Infusion) process used in composites manufacturing. Resin flow through the dry fibres is conventionally modelled as an unsaturated flow through porous media, where Darcy's law is employed. The determination of the exact location of the flow front is an important issue in the analysis. When high pressure gradients are applied, it is necessary to treat the fibre layers as deformable. A study on this fluid-structure interaction problem has been performed by Ambrosi and Preziosi [3]. Another important issue is the elimination of entrapped air since the presence of voids can significantly degenerate the quality of the composites. A mathematical model of void formation during the RFI process has been developed by Sevostianov et al [4]. In a paper of Blest et al. [5], the modelling and simulation of resin flow, heat transfer and the curing of multilayer thermoset composites by the resin film infusion process has been treated. Loos and MacRae [6] have developed an analytical model for two-dimensional resin film infusion process, which can be used to simulate non-isothermal infiltration of a hot-melt resin into a textile preform of complex shape. A non-isothermal RFI process for stitched stiffened panels was numerically modelled by Han et al [7]. The performance of the stitched stiffened panels under compressive loading has been compared with that of the unstitched stiffened panels. Recently, an analytical formulation of governing equations for flow of incompressible fluid through compacting porous media and their application to vacuum infusion of composite materials was made by Correia et al [8].
The objective of this work is to develop and to verify a comprehensive numerical model for the simulation of the infusion processes, and for the prediction of the final thickness and the resin infusion time. Particularly, the fibre reinforcement is considered as deformable and the resin infiltration is held through the thickness of the preform.

ANALYSIS OF INFUSION PROCESSES

We propose a set of governing equations modified to consider the preform deformation and the resin infiltration at the same time. Then a numerical formulation is employed with the models for the material properties (such as preform and resin).

Governing equations

Hydrological flow in consolidating soil was initially discussed by Biot in 1941 [9]. These theories have been adapted to composites manufacturing by Gebart [10], Gutowski [11, 12]. The basis of all models is the continuity equation (eq. 1), where q is the relative velocity, V_f the fibre volume fraction and u_{si} the solid velocity. The resin flow through the fibre system is a typical example of flow through a porous media, which, on the macroscopic scale, is well described by the Darcy's law (eq. 2) [13] relating linearly the fluid velocity q to the pressure gradient ∇p by the resin viscosity μ and the permeability K_z of porous medium.
As presented in table 1, we represent the whole formulations corresponding to the modelling of Hydro-Mechanical (HM) coupling applied to the infusion process.

Table 1 Equations for the HM coupling analysis

Equations		Dependent variables
Mass balance (eq. 1)	$\nabla \cdot q = \frac{1}{V_f}\left(\frac{\partial V_f}{\partial t} + u_{si}\nabla V_f\right)$	q, V_f
Darcy's law (eq. 2)	$\nabla p = -\frac{\mu}{K_z(V_f)} q$	p
Force balance (eq. 3)	$\nabla \cdot \sigma_z^{'} - \nabla p = 0$	$\sigma_z^{'}$
Constraint-Fibre volume fraction relation (eq. 4)	$\sigma_z^{'} = C_z(V_f)$	None
total :	4 equations	4 variables (scalars)

Experimental device for Hydro-Mechanical coupling

In infusion processes, the fibre volume fraction can change dynamically as the applied pressure is re-distributed between the resin and the preform. Hence, it is important to model the compaction of the fabric and its relation with the fibre volume fraction as a function of the applied pressure. In addition, the permeability of fabric depends on the fibre volume fraction. Thus, it is also of significance to model the relationship between the permeability and fibre volume fraction.
An experimental device with hydro-mechanical coupling HMz was developed [14] and used to obtain and the permeability ($K_z = 2.10^{-13}.V_f^{-3,06}$) and the compressibility of perform ($V_f = 0{,}483 + 0{,}123.\sigma_z^{'} - 0{,}045.\sigma_z^{'2} + 0{,}009.\sigma_z^{'3} - 9{,}3.10^{-4}.\sigma_z^{'4} + 3{,}71.10^{-5}.\sigma_z^{'5}$).

Numerical formulation

The numerical algorithm used in this study is based on a one dimensional discretization of the governing equation by the finite difference method with a moving boundary flow front. The pressure and the saturation values are calculated at the nodes. The fibre volume fraction and the permeability are computed and assigned to each element. The combination of equations (1) and (2), gives the following governing equation, expressed in the 1D form:

$$\frac{\partial}{\partial z}\left(-\frac{K_z}{\mu}\frac{\partial P}{\partial z}\right) = \frac{1}{V_f}\frac{\partial V_f}{\partial t} + \frac{1}{V_f}\frac{\partial V_f}{\partial z} v_k{}^f \qquad (5)$$

where $v_k{}^f$ is solid velocity (fibre velocity) in transverse direction.
The term $(\frac{1}{V_f}\frac{\partial V_f}{\partial z} v_k{}^f)$ in RHS of the equation (5) represents the relaxation or the compression of the wet fibres. To deal with it, the initial grid of the field is deformed in such a manner to take into account the relieving or the compression of the porous environment [15, 16] during the calculation. This assumption simplifies the governing equation (5) to:

$$\frac{\partial}{\partial z}\left(-\frac{K_z}{\mu}\frac{\partial P}{\partial z}\right) = \frac{1}{V_f}\frac{\partial V_f}{\partial t} \qquad (6)$$

NUMERICAL SIMULATION (Validation & Parametric study)

Firstly, a validation of the numerical resin infusion model is made through the comparison between experimental and numerical results. Then, we perform a parametric study to investigate the influence of processing conditions on the final part thickness and the resin infusion time.

Experimental validation of the numerical infusion model

A numerical validation of the infusion model has been made by an inverse method in Ouahbi et al [17]. The experimental device with the hydro-mechanical coupling HMz is used to validate the resin infusion model. The analyses are performed for two cases of boundary conditions:
- imposed displacement (according to the pre-assigned compaction velocity)
- imposed compaction pressure (σ_z)

The flow can be controlled in injection, with imposed resin pressure (P_i) or with imposed resin flow-rate (Q_i). In this work, the fibrous reinforcement is placed between the two grids of the experimental device (HMz) and the flow is controlled with imposed flow-rate ($Q_0 = 1{,}7.10^{-6} m^3/s$). Once the steady state is reached, the displacement or the compaction pressure of the experimental device is imposed.

Imposed displacement

The results for compaction pressures by numerical calculation and experimental measurement are compared with each other in the case of imposed displacement, and a good agreement is shown in fig. 2.

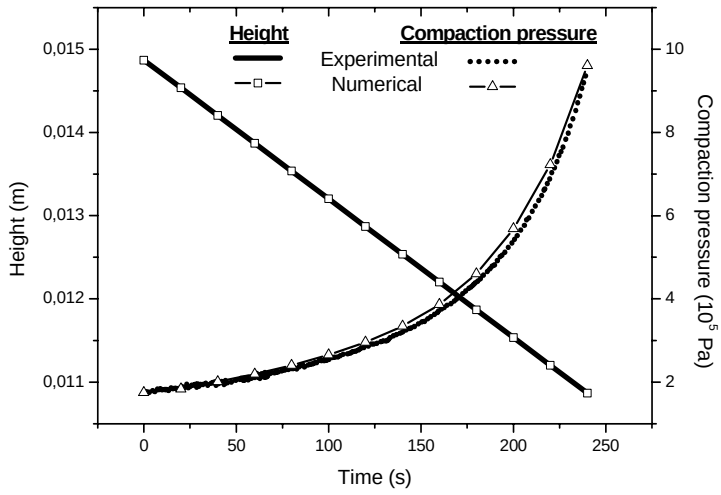

Fig. 2 Comparison of the compaction pressures by numerical calculation and experimental measurement along the time evolution.

Imposed compaction pressure

In this case, we impose a ramp rate of compaction pressure (1kN/min) up to 6 bars and then this compaction pressure is maintained. The comparison between experimental and numerical results for the part height evolution according to time is shown in Fig. 3.

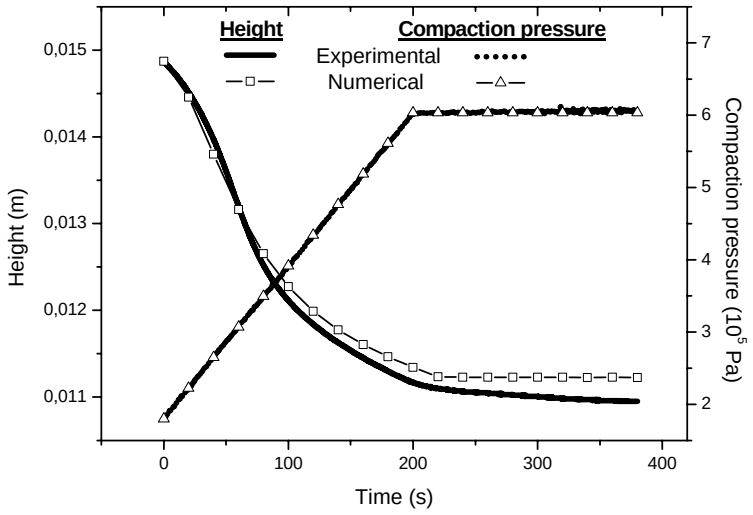

Fig. 3 Comparison of the part heights by numerical calculation and experimental measurement along the time evolution.

Numerical results and parametric study

The numerical prediction for resin infusion process is performed for an initial fibre volume fraction of 40%. The resin temperature is 90°C, the viscosity variation in function of temperature is treated as same way as in [1]. Five different compaction pressures of 1, 2, 3, 4 and 5 (10^5 Pa) are considered. As can be seen in Fig. 4, the infusion height, as expressed in percentage, increases in the course of time.

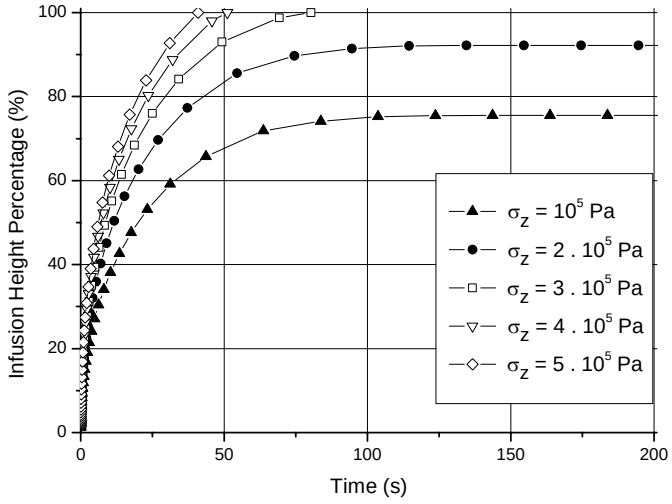

Fig. 4 The time-dependent evolution of the infusion height percentage for different pressure compactions.

Given an initial fibre volume fraction of 40% and a fixed compaction pressure of 200 kPa, four different resin temperatures of 80, 90, 100 and 110 °C are considered (Fig. 5). As can be expected, higher temperature leads to a faster infusion at the beginning of mould filling. However, it also results in a faster curing of resin and the total infusion height was not reached. Lower resin temperature resulted in longer infusion time, but the resin cure reaction is also delayed. As a result, the total infusion height is attained.

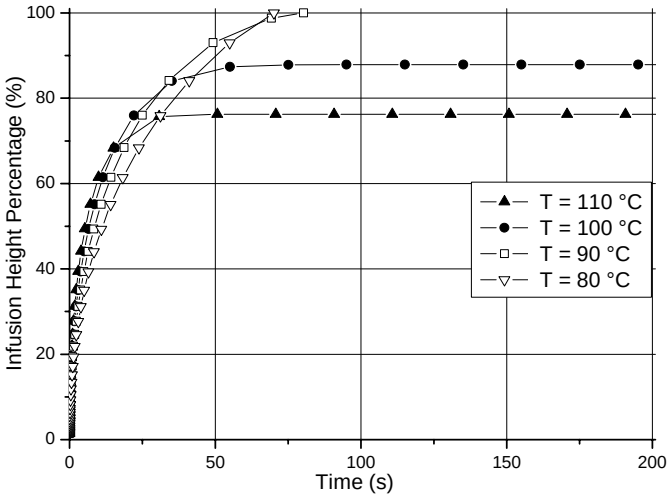

Fig. 5 The time-dependent evolution of the infusion height percentage for different resin temperatures.

The ratio between the initial and the final height of the part in function of compaction pressure was presented in Fig. 6. We also illustrate the relation of the final fibre volume fraction versus compaction pressure.
The final volume fraction of the part increases with the increase in compaction pressure.

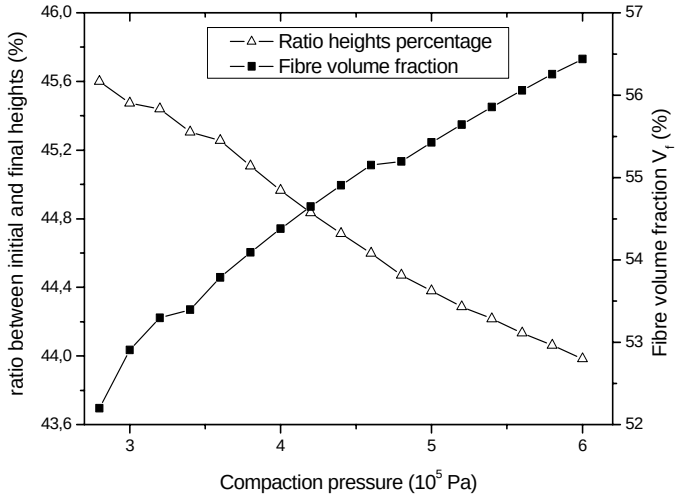

Fig. 6 Representation of the final fibre volume fraction in function of the compaction pressure.

In Fig. 7, a representation of the infusion time in function of the compaction pressure is provided. The infusion time is the time necessary for the resin to completely infuse the part, and it does not include the cure time.

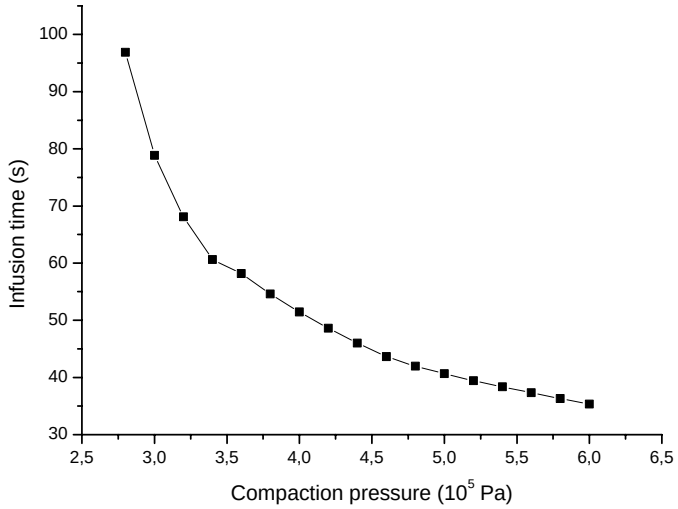

Fig. 7 Representation of the time infusion in function of the compaction pressure.

As seen in Fig.7, the infusion time decreases according to the increase in compaction pressure. Hence, this information can be used to determine the compaction pressure necessary for a total process cycle time to be achieved.

CONCLUSIONS

A numerical modelling of infusion process considering hydro-mechanical coupling and perform deformation was made. An experimental validation of the numerical resin infusion model was made by an experimental device with hydro-mechanical coupling HMz. A comparison between experimental and numerical results was made, and we obtained a good agreement. The infusion height was investigated for different compaction pressures and resin temperatures. The simulation can also be used to predict the resin infusion time and the final fibre volume fraction.

ACKNOWLEDGEMENTS

The authors would like to acknowledge the financial supports by the 'Haute Normandie' Region and by the European Aeronautic Defence and Space Company (Corporate Research Center France) 'EADS-CCR'.

REFERENCES

1. J. Park, MK. Kang. "A numerical simulation of the resin film infusion process", *Composite Structures*, Vol. 60, 2003, pp. 431-437.

2. V Antonucci, M. Giordano, L. Nicolais, A. Calabrò, A. Cusano, A. Culoto, S. Inserra. "Resin flow monitoring in the resin film infusion process", Materials Processing Technology, 143-144, 2003, pp. 687-692.

3. D. Ambrosi and L. Preziosi. "Modelling matrix injection through elastic porous performs", *Composites Part A: Applied Science and Manufacturing*, Vol. 29, 1998, pp 5-18.

4. I. Sevotianov, VE. Verijenko, CJ. Klemperer. "Mathematical model of cavitation during

resin film infusion process", *Composite Structure*, Vol. 48, 2000, pp. 197-203.

5. DC. Blest, S. McKee, AK. Zulkifle, P. Marshall. "Curing simulation by autoclave resin infusion," *Composite Science and Technology*, Vol. 59, 1999, pp. 2297-2313.

6. AC. Loos, JD. MacRae. "A process simulation model for the manufacture of a blade-stiffened panel by the resin infusion process", *Composite Science and Technology*, Vol. 56, 1996, pp. 273-288.

7. NL. Han, SS. Suh, JM. Yang, HT. Hahn. "Resin film infusion of stitched stiffened composite panels", *Composites Part A: Applied Science and Manufacturing*, Vol. 34, 2003, pp. 227-236.

8. N.C. Correia, F. Robitaille, A.C. Long, C.D. Rudd, S.G. Simacek, S.G. Advani. "Analysis of the vacuum infusion moulding process: I. Analytical formulation", *Composites Part A: Applied Science and Manufacturing*, Vol. 36, 2005, pp. 1645–1656.

9. MA. Biot. "General theory of three dimensional consolidation", *Journal Applied Physics*, Vol. 12, 1946, pp. 155–164.

10. BR. Gebart. "Permeability of unidirectional reinforcements for RTM", *Journal of Composite Materials*, Vol. 26, no.8, 1992, pp. 1101–1133.

11. TG. Gutowski, T. Morigaki, Z. Cai. "The consolidation of laminate composites", *Journal of Composite Materials*, Vol. 21, 1987 pp. 172–88.

12. TG. Gutowski TG, G. Dillon. "The elastic deformation of fiber bundles", In: Gutowski TG, editor. *Advanced composites manufacturing*. Willey; 1997. pp. 138–9.

13. H. Darcy. "Les fontaines publiques de la ville de Dijon" *Dalmont*, Paris, 1856.

14. P. Ouagne et J. Bréard, "Sollicitation HydroMécanique de milieux fibreux en vue de l'optimisation des procédés d'infusion", *14èmes Journées Nationales sur les composites JNC 14*, Compiègne 2005.

.

15. M. Danis, C. Del Borrello, E. Lacoste, O. Mantaux, "Infiltration of fibrous preform by a liquid metal: modelization of the preform deformation", (*ICCM12*), 1999, paper n° 877.

16. E. Lacoste, O. Mantaux, M. Danis. "Numerical simulation of metal matrix composites and polymer matrix composites processing by infiltration : a review", *Composites Part A: Applied Science and Manufacturing*, Vol. 33, 2002, pp. 1605-1614.

17. T. Ouahbi, A. Saouab, P. Ouagne, J. Breard, S. Chatel. "A Simulation Model for the Infusion Process", *The 9th International ESAFORM Conference on Material Forming*, 2006, Paper n° 61.

A FAST SOLUTION METHOD FOR MODELING THE RTM-PROCESS USING SIMPLIFIED GEOMETRIES

F. Klunker[1], G. Ziegmann[1]

[1]*Institute for Polymer Materials and Plastics Processing*
Clausthal University of Technology, Agricolastrasse 6, 38678 Clausthal-Zellerfeld, Germany
and Corresponding Author's e-mail: florian.klunker@tu-clausthal.de

ABSTRACT: The Resin Transfer Moulding (RTM) process is a technology to produce fibre reinforced parts: fibres are placed in a mould and resin is injected into the closed mould, impregnating the fibres. After curing the resin the part will have more or less its final shape. In order to reduce the costs and time of engineering, a lot of work has been done to simulate this process. The equation most often used for simulating this process is Darcy's Law.
The simulation programs based on Darcy's Law are often using a finite element / control volume approach. This technique can be applied to nearly every kind of geometry with accurate results in a convenient time, but it requires the user to have experience in the RTM-process in order not to do too many simulation experiments by trial and error while trying to optimise the process parameters. In this publication a fast solution method is presented for modelling the RTM-process using simplified geometries, which is often applicable in manufacturing of RTM-parts. The resulting numerical technique is based on the theory for ordinary differential equations. It can be used for predicting the best injection zones due to time and dry spots caused by entrapped air as a result of flow fronts which are getting into contact without control.

KEYWORDS: RTM, analytical modelling, numerical analysis

INTRODUCTION

Fibre composites offer the opportunity to do light weight construction. Due to their anisotropic mechanical behavior it is possible to save up to 30% of the weight compared to metallic parts with the same properties. Some fields of applications are the automotive, nautive, aircraft and sports industry.
Another advantage is that complex shaped parts can be created with only a small amount of waste material. Several techniques to produce fibre reinforced parts [4] exist.
The Resin Transfer Molding (RTM) is one technique to produce fibre reinforced parts [4,6,9]. Dry fibres are inserted into a mould, resin is injected and after curing the final part can be demolded. The challenge of this technique is to

- inject the resin without remaining dry spots, meaning unimpregnated fibres,
- predict the appearing mold pressure to do a cost effective mold construction,
- reduce residual stresses due to shrinkage of the curing resin.

Those difficulties are caused by the design concept of the parts: the anisotropic property of the fibres causes a complex flow behavior. Simulation tools for simplifying the design

process were developed [1,15]. In many cases a discrepancy between reality and experiment has been observed. In order to improve accuracy of the flow simulation there are several proposals to refine the modelling of the process [2,7,11,13].
The design process consists of several stages. First, the main idea has to be developed, after that the design is getting more and more detailed. While simulation is getting present in all construction stages, it would be helpful to see possible difficulties concerning the flow behavior in the early stage of the design. The usual way to do RTM simulation is to create a mesh from a given CAD-File, import it into the RTM software and apply process and material parameters. But during the design process often there are no valid geometries or some detailing ideas are missing, so that creating pre-final parts would increase the time of engineering.
In this paper a solution is presented to do RTM simulation mesh free. It can be applied in an early stage of the construction process by selecting "important" points. The formulation can be done with ordinary differential equations. The accuracy is of course lower than within the usual RTM-simulation, but due to the high performance, several possibilities for application are opened:

- automatic injection port and vent location proposals,
- cost and process analysis for feasability studies,
- automisation and real time control of the process,
- rough estimation of the rheological behavior taking into account the influence on void content.

THEORY OF THE FAST SOLUTION ALGORITHM

Governing Equations

The stationary flow through porous media is often modelled by Darcy's Law [1-15]:

$$v = -\frac{K}{\mu} grad(p) \tag{1}$$

where v is the volume averaged velocity, K the permeability tensor, μ the resin viscosity and p the fluid pressure. If ρ describes the density of the resin, the continuity equation can be written as [11]

$$\frac{\partial \rho}{\partial t} + div(\rho v) = 0 \tag{2}$$

It is often assumed that the flow is at steady state [15], meaning that the time derivative is neglected, and the fluid is incompressible so that Eqn. 2 can be simplified. Using Darcy's Law in Eqn. 2, the resulting equation is

$$div(\frac{K}{\mu} grad(p)) = 0 \tag{3}$$

This is an elliptic partial differential equation describing the pressure field of the impregnated region of the RTM process at one time step.

Fast Solution Algorithm

For a one dimensional problem, the solution for Eqn. 3 can be written as

$$P(x) = \frac{P_2 - P_1}{L} x + P_1 \tag{4}$$

where P_1 is the pressure at the injection port, P_2 the pressure at the vent and because of the low viscosity of the air it can be assumed that it is also the pressure of the flow front. L is the infiltrated length and $x \in [0, L]$ the position within the wet fibres.

For higher dimensional problems the solution is depending on the shape of the part. One possibility to solve this problem is by using the Finite Element Method (FEM). The advance of the flow front from timestep to timestep is often done by a so called Control Volume Method (CV). This technique is used by several authors [1,15] to simulate the process. With the combination of heat equation and curing those programs lead to a powerful tool for designing the processes. With special tools it can even be used for optimizing the process parameters [3,5,14].

When new parts are designed it is also required to fulfill the conditions of the production. With simulation it is possible to influence the design process before the first experiments are made. The fast solution algorithm offers the opportunity to investigate the flow behavior even without a final shape. It deals with one dimensional domains describing the flow and the geometry approximately. This is done by a set of nodes connected by one dimensional domains.

The node N_i of s nodes is given. From this nodes flow Q_{ij} of fluid to the nodes $N_j, j = 1,..,s$ are given. Because of the incompressibility of the resin, the remaining fluid Q_{ii} in node N_i is zero, meaning:

$$\sum_{j=1}^{s} \dot{Q}_{ij} = 0. \tag{5}$$

Because of the 1D-geometry of the domains, it can be assumed

$$\dot{Q}_{ij} = v_{ij} A_{ij} = A_{ij} \frac{K_{ij}}{\mu} \frac{P_i - P_j}{L_{ij}} := D_{ij}(P_i - P_j). \tag{6}$$

with v_{ij} the velocity of the flow front in the domain leading from node i to node j, $\dot{Q}_{ij}$ is the volume flux through cross section A_{ij}, K_{ij} the permeability and L_{ij} the length. With these definitions the pressure inside the domains can be calculated with

$$\sum_{j=1}^{s} \dot{Q}_{ij} = \sum_{j=1}^{s} D_{ij}(P_i - P_j) = 0. \tag{7}$$

Taking into account that L_{ij} is varying with domains which are partially filled, this can be used for calculating the progress of the flow front in the second step with Eqn.1. The theory needed for solving these equations is the theory about ordinary differential equations. For this kind of equations several numerical solvers are available [16].

APPLICATIONS

Prediction of Filling Time

With the fast solution algorithm it is possible to do rough simulations in fractions of a second. As an example a steering wheel is presented showing the quality of the algorithm.

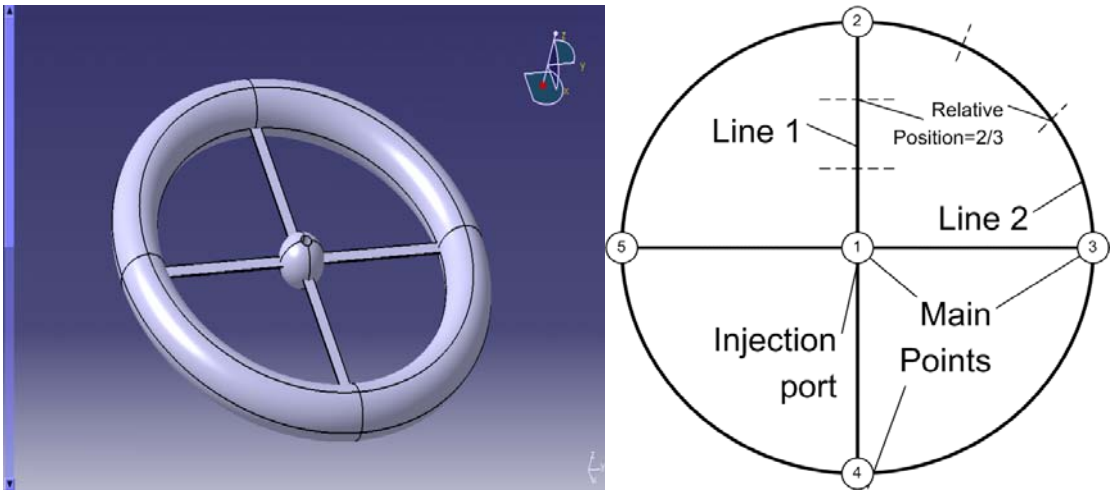

Figure 1: The complex model on the left can be simplified to a model which can be handled by the fast solution method.

A torus with 20mm radius and a diameter of 150mm is connected with a cross shaped structure having a cross section area of $0.01 \times 0.001 m^2$. In the center there is a sphere with a diameter of 40mm. This geometry is transferred to a one dimensional geometry as sketched in fig. 1. In the simulation an information about the area of their cross section of the lines is saved, so that the volume based formulation can be applied. The permeability is set to 10^{-11} m^2 for all lines and the viscosity is set to 0.1 mPas. The errors of calculation are expected to be at the sphere in the center and the connections at the outer ends of the crosses.
A simulation with PAM-RTM has been done leading to a simulated filling time of 356.000s. Using the fast solution algorithm, it leads to a simulated filling time of 335.100s which is an error of 5.8%. Using a simple step control technique to reduce the calculation time, the result was 357.472s which is an error of 0.4%.
This improvement is not caused by errors during the stepping process; it is just caused by the rough stop criterion which is cancelling the iteration process of reaching a filling factor of exactly one for every line after a few iterations.
In a second step, a similar geometry is used again: The cross in the middle has a bigger cross section: $0.02 \times 0.02 m^2$. The objective of this modification was to see a better result compared to the simulation in PAM-RTM because the relative part of a non 1D flow should be reduced.
The filling time simulated with PAM-RTM is 11.364s. With the original shape and the fast solution algorithm it is 10155s, so resulting in an error of 11.9%. Using stepping techniques it is 10760s, so the error is reduced to 5.6%. This error is higher than in the first experiment. The reason for that behaviour has to be investigated in detail.

Proposals of Injection Points and Vent Locations

With the fast solution algorithm it is possible to predict the flow behaviour in the part as function of the injection position. Using the part in fig. 1 the injection positions are varied on the different connections between the main points. Due to the symmetric nature of the part, it has been done on line 1 and line 2. The results of the part with the thin cross are presented in the upper row of fig 2. The position of the injection port is simulated at 100 positions between the prior injection port having the relative position of zero and the connection of the torus and the cross with a relative position of one. The lines should be smooth but the filling time is dependent on the stop criterion.

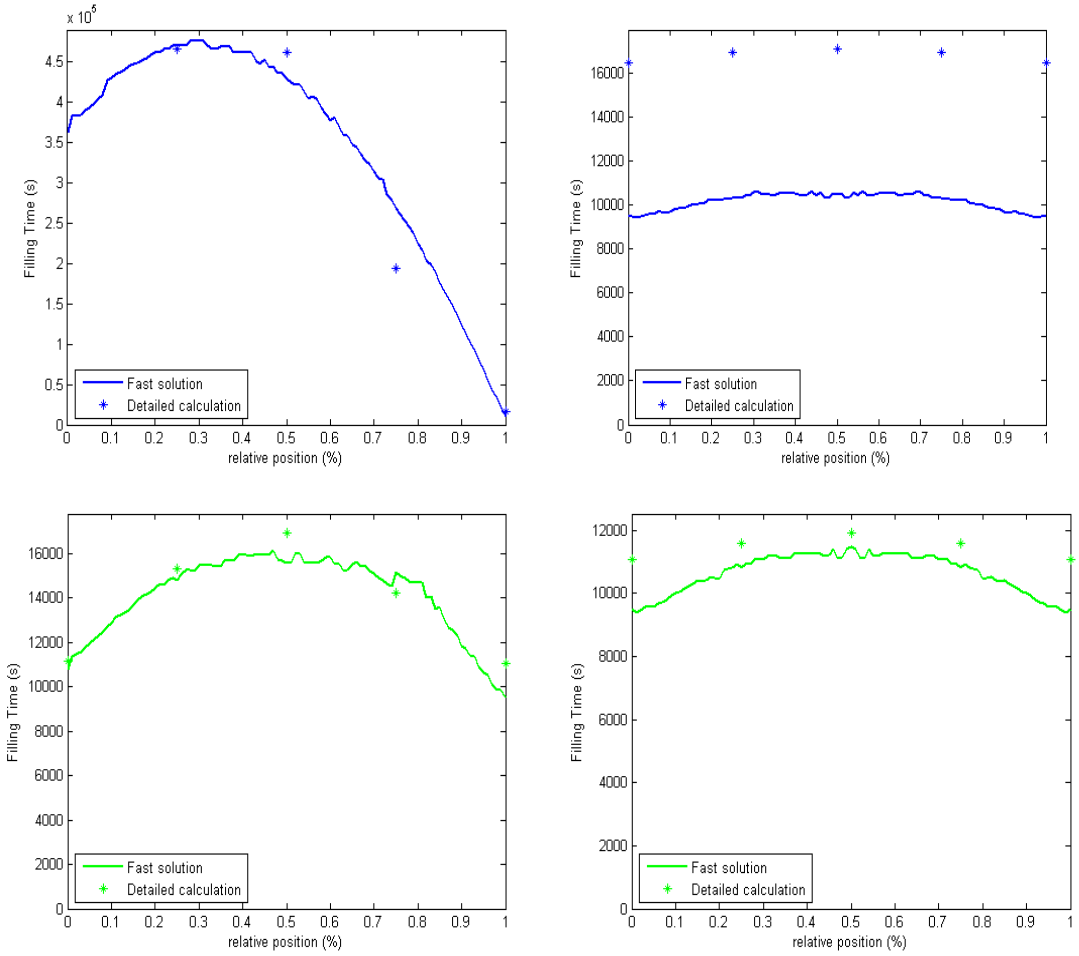

Figure 2: Results of the Filling Times when the injection port location is moving on Line 1 (left) and Line 2(right). The upper row represents the results for the thin cross.

It can be seen that the best injection port position on line 1 is at the relative position one which is equal to the main point 2 and the worst is close to the relative position of 1/3. The times differ with factor of about 35. Varying the position on line 2, the results are symmetric to the middle of the line. Here also 100 simulations have been done with the result that again the connection points of torus and cross is the best position.
Comparing these results with those of PAM-RTM it is shown again that the times are underestimated. The basic shape of the injection times can be seen. The accuracy of the filling times especially in the case of varying the injection port location on line two is low (relative error: about 80%). This is due to the missing model of the sphere in the middle. The time required to fill this sphere is approximately 4000 seconds. Subtracting that time the error is about 20%.
The results of the five 3D simulations with about 35000 elements were achieved after 4 hours. The results of the 200 one dimensional simulations were achieved after 2 minutes.
The simulation of the steering wheel with the thick cross was showing more accuracy while varying the injection point position: as it can be seen in the lower row of fig. 2 the relative error does not exceed 15% and the basic shape of the simulations run in PAM-RTM could also be reproduced.

LIMITATIONS

Due to the modelling with 1D-geometries the applicability of the fast solution method is limited. Some topics which cannot be represented should be explained.

VARI

One of the further developments of RTM is the Vacuum Assisted Resin Infusion (VARI). In this process, one part of the mould if substituted by a foil. Instead of using pressure to inject the resin into the mould, the resin is infused by applying vacuum at the outlet.
When this process is modelled, the deflection of the preform due to the lower compaction pressure because of the pressurized resin has to be taken into account. The pressure is a local variable influencing the permeability and so the solution on the whole domain. It seems possible to model such a behaviour with the volume based formulation, but the authors assume that the number of nodes have to be increased and in this case the advantage compared to FE/CV-techniques is decreased a lot.

2D and 3D flows of a general Shape

Describing multidimensional flows with the fast solution algorithm requires implementing handling rules. For general flow fronts this would decrease the computational performance.
For the case of radial or elliptical flow fronts which are for example present in cone shaped parts, the volume flux equation can also be written in the shape like Eqn. (7). As an example the solution for Eqn. (3) in case of a point injection into an isotropic media is

$$P(r) = P_1 + (P_2 - P_1)\frac{\ln(r/r_0)}{\ln(r_f/r_0)}, r_0, r_f > 0, r \in [r_0, r_f]. \tag{8}$$

In Eqn. (8) r_0, r_f are the radiuses of the injection point and the flow front. When this expression is deviated and used it in Eqn. (7), the standard form can be received:

$$\dot{Q}_{ij} = v_{ij} A_{ij} = A_{ij} \frac{K_{ij}}{\mu} \frac{P_2 - P_1}{\ln\left(\frac{r_f}{r_0}\right)} \frac{1}{r} := \tilde{D}(P_2 - P_1). \tag{9}$$

Heat Conduction and Resin Cure

The temperature is a local variable often depending on position and time. A one dimensional formulation is often not accurate. The resulting temperature depends on the material properties, having an influence on the curing of the resin. This leads to the same problem as it is described in section for VARI. The fast solution algorithm can be used for isothermal processes or for checking the possible limits of the parameters used in a detailed model. So it can support a decision if a simulation with heat conductivity is necessary.

POSSIBLE FUTURE APPLICATIONS

It has been shown that the described procedure can reproduce the behavior of the filling times. In general it cannot produce results with the accuracy of the standard FE/CV codes, but it support the user finding strategies for a given process.

Cost analysis for feasability Studies

In a cost analysis process the filling time is an important parameter for the feasibility of a process. The filling time has an influence on the number of parts which can be produced, so also for the number of tools which have to be ordered. It also has an influence on the curing behavior which can be estimated in advance for selecting special resins.

Automation and Real Time Control of the Process

Uncontrolled flow can decrease the sucess rates of RTM-parts [3]. The control of processes often requires transient formulations and reference functions. In general, an exact model of the process is not required because the actuator should be changed in every time step. Due to the fast solution got, it is possible to calculate flow front information quickly. This can be used for opening vents and injection ports to influence the flow.

Rough estimation of the rheologic Behavior

Void contents decrease the mechanical performance of fibre reinforced parts. Several authors indicated that the balance of capillary number and permeability has an influence on the void content [10,12]. In conclusion to that some authors found out that the void content is dependant on the direction of impregnation [11].
There are already models existing handling formation of void contents. At our institute similar models were also developed, showing that the amount of macro and micro void content is dependent on the velocity of the flow front. The detection of regions containing voids is dependent on the size of the elements. With the fast solution algorithm and parameter studies at simple parts it is possible to propose a mesh sizing so that a proper mesh can be built.

CONCLUSION

A fast solution algorithm has been developed. It is a volume based formulation and it can be used for one dimensional flows. The applicability has been shown at a complex part. A general applicability is not yet given. The future work is to generalize the model without a loss of performance. The limits of applicability have to be formulated, so that standard applications have decision rules of applicability.

REFERENCES

[1] M. Bruschke and S. G. Advani, "A finite element/control volume approach to mold filling in anisotropic porous media", *Polymer Composites*, Volume 11, Pages 398–405 (1990).
[2] M. Deleglise, C. Binetruy, and P. Krawczak, "Solution to filling time prediction issues for constant pressure driven injection in RTM". *Composites Part A: Applied Science and Manufacturing*, Volume 36, Pages 339– 344 (2005).
[3] M. Devillard, K. T. Hsiao, and S. G, Advani, "Flow sensing and control strategies to address race-tracking disturbances in resin transfer molding - Part II: automation and validation", *Composites Part A: Applied Science and Manufacturing*, Volume 36, pages 1581–1589 (2005).
[4] M. Flemming, G. Ziegmann, and S. Roth, "Faserverbundbauweisen", Springer, Berlin (1999).
[5] J. Gou, C. Zhang, Z. Liang, W. Ben, and J. Simpson, „Resin transfer molding process optimization using numerical simulation and design of experiments approach" *Polymer Composites,* Volume 24, Pages 1–12 (2003).
[6] U. Huber, "Zur methodischen Anwendung der Simulation der Harzinjektionsverfahren", Dissertation, Kaiserslautern (2002).
[7] B. Joel, Y. Henzel, F. Trochu, and R. Gauvin. Analysis of dynamic flows through porous media. Part I: Comparison between saturated and unsaturated flows in fibrous reinforcements. *Polymer Composites*, Volume 24, Pages 391–408 (2003).
[8] P. Knaber and L. Angermann, „Numerik partieller Differentialgleichungen - eine anwendungsorientierte Einführung", Springer, Berlin, Heidelberg, New York (2000).
[9] M. Louis, „Zur Simulation der Prozesskette von Harzinjektionsverfahren", Dissertation, Kaiserslautern (2004).
[10] T. Lundström, "Bubble transport through constricted capillary tubes with application to resin transfer moulding", *Polymer Composites*, Volume 17, Pages 770–779 (1996).
[11] B. Markicevic, D. Heider, S.G. Advani, and S. Walsh, "Stochastic modeling of preform heterogeneity to address dry spots formation in the vartm process", *Composites Part A: Applied Science and Manufacturing*, Volume 36, Pages 851–858 (2005).
[12] N. Patel and L. James Lee, "Modeling of void formation and removal in liquid composite molding. Part II: Model development and implementation". *Polymer Composites*, Volume 17, Pages 104–114 (1996).
[13] K. Pillai and S.G. Advani "Numerical simulation of unsaturated flow in woven fiber preforms during the resin transfer molding process", *Polymer Composites*, Volume 19 Pages 71–80 (1998).
[14] E. Ruiz and F. Trochu, "Comprehensive thermal optimization of liquid composite molding to reduce cycle time and processing stresses", *Polymer Composites*, Volume 26, Pages 209–230 (2005)
[15] X. Song, "Vacuum Assisted Resin Transfer Molding (VARTM): Model Development and Verification", PhD thesis, Virginia, 2003.
[16] E. Hairer and G. Wanner, "Solving Ordinary Differential Equations 1. Nonstiff Problems", Springer, Berlin, Heidelberg, New York, 2000.

NONCONFORMING ELEMENTS FOR LIQUID COMPOSITE MOLDING PROCESS SIMULATIONS

Piaras A. Kelly and Sam Jennings

Department of Engineering Science, School of Engineering, University of Auckland, Private Bag 92019, Auckland, New Zealand : pa.kelly@auckland.ac.nz

ABSTRACT: Liquid Composite Molding (LCM) processes are now a prevalent group of manufacturing methods for advanced composite materials. They offer many advantages over more traditional manufacturing methods, such as the ability to deal with large and complex shapes. Numerical simulations can lead to better predictions of process parameters. The standard procedure for the simulation of these processes is to use a Control Volume (CV) method. One problem with the CV method is that resin mass is not conserved on an element level, and this has consequences for accuracy. An attractive alternative to the CV method is to use a *single* grid of non-conforming finite elements. Such non-conforming elements encompass essential mass conservation properties. In this study it is shown how the standard non-conforming triangular element can be adjusted to ensure mass conservation on the element level and to ensure continuity of the fluid flux across inter-element boundaries. Numerical experiments are carried out which show that single grids of such elements, and nonconforming quadrilateral elements, produce accurate results in the case of the Injection Compression Molding process.

KEYWORDS: Simulation, Finite Element Method, Control Volumes, Injection/Compression Molding, Conservation of mass, Nonconforming elements

INTRODUCTION

Liquid Composite Molding (LCM) is a family of advanced composite materials manufacturing processes, including Resin Transfer Molding (RTM), Injection Compression Molding (I/CM) and Vacuum Assisted Resin Transfer Molding (VARTM). In these processes, a fibrous material is laid out in a mould, compacted under pressure, impregnated with a polymer resin and finally allowed to cure. In RTM, rigid molds are used to compact the fibrous material to its final thickness before resin injection. In I/CM, the upper mold is brought down with velocity- or force-control but not to the part's final thickness; this allows for ease of resin flow during injection and the final compaction to the final thickness helps drive the injected fluid through the part. In VARTM, a flexible bag covers one side of the part and vacuum pressure drives the fluid through the fibrous material. The LCM processes offer many advantages over more traditional manufacturing methods, such as the ability to deal with large and complex shapes and the reduction in exposure to harmful emissions.

Mathematical models and numerical simulations of the LCM manufacturing processes can lead to better predictions of flow paths, mould filling times, required mould forces, preform final thicknesses and of the optimal positioning of injection ports and vents.

The governing equation for the injection phase of these processes is derived from the conservation of mass of both the fluid and solid phase:

$$\nabla \cdot \left(h \frac{\mathbf{K}}{\mu} \nabla p \right) = \frac{\partial h}{\partial t} \tag{1}$$

where h is the thickness of the component, p is the fluid pressure, $\mathbf{K}$ is the permeability tensor and μ is the fluid viscosity. If thickness gradients are small enough to be neglected, then Eqn. 1 reduces to

$$\nabla \cdot \left(\frac{\mathbf{K}}{\mu} \nabla p \right) = \frac{\dot{h}}{h} \tag{2}$$

where $\dot{h} = dh/dt$. In RTM applications, $\dot{h} = 0$. In I/CM applications with rigid moulds, $\dot{h}$ will be constant throughout the part – it will be a known of the problem in velocity controlled compression, an unknown in the case of a force/pressure driven compression. In flexible mould / vacuum-bag processes, $\dot{h}$ will in general vary and be an unknown of the problem.

Inherent in Eqn. 2 is the conservation of (fluid) mass relation

$$\nabla \cdot \mathbf{q} = -\frac{\dot{h}}{h}, \tag{3}$$

where $\mathbf{q}$ is the Darcy velocity, with $\mathbf{q} = \phi \mathbf{v}$, and ϕ is the porosity, $\mathbf{v}$ being the fluid velocity, and Darcy's law for fluid flow,

$$\mathbf{q} = -\frac{\mathbf{K}}{\mu} \nabla p \tag{4}$$

The standard procedure for the numerical solution of Eqn. 1 (or 2) is to use a Control Volume method, whereby one grid of elements is used to evaluate fluid pressures, for example using the Galerkin Finite Element Method. A second grid (of control volumes) is then used to advance the fluid over some time interval. This ensures that fluid fluxes (pressure gradients) are evaluated *within* elements, and possible discontinuous pressure gradients at element boundaries are avoided. A large number of simulations have been carried out using this method, for RTM, I/CM, and flexible-bag processes, e.g. [1,2].

One problem with the Control Volume method, when used to simulate processes for which the Darcy velocity field is not divergence-free, for example I/CM and VARTM, is that resin mass is often not conserved on an element level, and this has consequences for the accuracy of the method. For example, for a linearly (P1) interpolated pressure p_{FE}, the FEM solution for $\mathbf{q}$ within any given element, $\mathbf{q}_{FE}$, is, from Eqn. 4,

$$\mathbf{q}_{FE} = -\frac{K}{\mu} \nabla p_{FE}, \tag{5}$$

a constant. Thus $\nabla \cdot \mathbf{q}_{FE} = 0$, and, from Eqn. 3, mass is not conserved within the element. Note that, in an RTM simulation (with constant permeability/thickness), where $\dot{h} = 0$, mass is conserved and this is not an issue.

Another approach is to use the so-called mixed methods, which yield a more accurate velocity and a locally conservative fluid mass. Here, both Eqns. 3 and 4 are discretised and a solution for both *p* and **q** is sought simultaneously, on either a single grid or on overlapping grids. The commonest scheme is to take *p* constant and **q** to vary linearly over an element/volume. The velocity obtained is more accurate than that using the standard Galerkin FEM with the CV scheme, but the mixed methods are computationally much more expensive.

An attractive alternative to these approaches is to use a *single* grid of finite elements. When non-conforming elements are used, essential mass conservation properties are encompassed. These elements are discussed in the next section.

ELEMENTS WITH CONSERVED MASS

Nonconforming (and conforming) P1 elements have been used to simulates I/CM processes (e.g. [3]) and have been shown to perform well. The performance of conforming and nonconforming P1 elements in IC/M and VARTM processes can be improved using a device introduced by Chou and Tang [4]. Here, the flux **q** is first approximated over an element *E* by the linear function $\mathbf{q}_a$, using a Taylor series expansion about the barycentre $\mathbf{x}_B$ of the element,

$$\mathbf{q}_a(\mathbf{x}) = \mathbf{q}_a(\mathbf{x}_B) + \left.\frac{\partial \mathbf{q}}{\partial \mathbf{x}}\right|_{\mathbf{x}=\mathbf{x}_B} (\mathbf{x} - \mathbf{x}_B), \qquad \mathbf{x} \in E\,. \tag{6}$$

Assuming that $\mathbf{q}_a$ varies over the element according to

$$\mathbf{q}_a(\mathbf{x}) = \begin{bmatrix} r + sx \\ t + sy \end{bmatrix}, \tag{7}$$

then

$$\left.\frac{\partial \mathbf{q}}{\partial \mathbf{x}}\right|_{\mathbf{x}=\mathbf{x}_B} (\mathbf{x} - \mathbf{x}_B) = s(\mathbf{x} - \mathbf{x}_B) = \frac{1}{2}(\nabla \cdot \mathbf{q}_a)(\mathbf{x} - \mathbf{x}_B) \tag{8}$$

The conservation of mass requirement is then

$$\int_E \nabla \cdot \mathbf{q}_a \, dS = \int_E f \, dS = \Delta f_E \tag{9}$$

where Δ is the area of the element and

$$f = -\frac{\dot{h}}{h}, \tag{10}$$

so that f_E is the average of f over the element, or, equivalently, $\nabla \cdot \mathbf{q}_a = f_E$. Thus

$$\mathbf{q}_a(\mathbf{x}) = \mathbf{q}_a(\mathbf{x}_B) + \frac{f_E}{2}(\mathbf{x} - \mathbf{x}_B), \quad \mathbf{x} \in E. \tag{11}$$

Assuming one has first computed the flux $\mathbf{q}_{FE}$ using the standard Galerkin FEM, as in (5), one has

$$\mathbf{q}_a(\mathbf{x}) = -\frac{K}{\mu}\nabla p_{FE} + \frac{f_E}{2}(\mathbf{x} - \mathbf{x}_B), \quad \mathbf{x} \in E \tag{12}$$

The second term on the right here is the correction to the FEM solution which ensures conservation of mass. It depends only on the instantaneous value of $\dot{h}/h$ and the element geometry, and so is the same for both conforming and non-conforming elements of the same geometry.

Continuity of Flux across Nonconforming Element Boundaries

Although the formulation described above ensures that mass is conserved over an element, there is no guarantee that the flux obtained is continuous across element boundaries. For the case of nonconforming linear triangular elements, the continuity of flux across element boundaries can be guaranteed by writing

$$\mathbf{q}_a(\mathbf{x}) = -\frac{K}{\mu}\nabla p_{FE} + \frac{f_E}{2}(\mathbf{x} - \mathbf{x}_B) + \mathbf{C}_E, \quad \mathbf{x} \in E \tag{13}$$

where $\mathbf{C}_E$ is a small constant correction term [4]. It can be shown that

$$\mathbf{C}_E = \frac{1}{2}\begin{bmatrix} x_B f_E - \frac{1}{\Delta}\sum_{i=1}^{3} \bar{x}_i \int_E f N_i dS \\ y_B f_E - \frac{1}{\Delta}\sum_{i=1}^{3} \bar{y}_i \int_E f N_i dS \end{bmatrix} \tag{14}$$

where (x_B, y_B) are the barycentre coordinates, Δ is the area of the element, $(\bar{x}_i, \bar{y}_i)$ are the coordinates of the *vertices* of the element, and N_i are the three non-conforming element shape functions. Since $\int_E N_i dS = \Delta/3$, this implies that so long as f is *constant* along the mould, which is often the case in practice, $\mathbf{C}_E$ is zero and the flux is continuous, otherwise the correction term needs to be included. It was shown in some recent work [5] that a *regular* grid of right-sided elements, $\mathbf{C}_E$ is zero also for the case of *linearly* varying $\dot{h}$.

NONCONFORMING QUADRILATERAL ELEMENTS

Much research has been carried out recently into finite element analysis with non-conforming elements, in particular with quadrilateral elements, e.g. [6] (see [7]). This allows for a more powerful general meshing of moulds, using arbitrary arrangements of triangular and/or quadrilateral non-conforming elements.

As an illustrative example, consider the following simple problem: a square-shaped mould of length l and width w contains a uniform fibrous material initially filled with resin to $w \times l_1$. The upper mould is brought down at a constant velocity. The following data is used (the subscript "1" denotes values at the start of the simulation):

$$\dot{h} = -10^{-4}\,\text{m/s}\,(6\text{mm/min})$$
$$h_1 = 4\text{mm},\ \phi_1 = 0.5,\ \mu = 0.1$$
$$l_1 = 0.2\text{m},\ l = 0.4\text{m},\ w = 0.2\text{m}$$

The Carman-Kozeny relation was used to relate permeability to volume fraction (thickness):

$$K = \frac{d^2}{16k}\frac{(1-V_f)^3}{V_f^2}, \tag{15}$$

with $d = 10 \times 10^{-6}$, $k = 3.125 \times 10^{-3}$.

The problem was solved in six different ways, using piecewise linear triangular elements and quadrilateral elements:

T1:	triangle, single grid, conforming elements (with mass conservation)
T2:	triangle, single grid, non-conforming elements (with mass conservation)
T3:	triangle, control volumes
Q1:	quadrilateral, single grid, conforming elements
Q2:	quadrilateral, single grid, non-conforming elements
Q3:	quadrilateral, control volumes

The interpolation functions used for the case Q2 are given in the Appendix. Results for the fill-time were compared with the exact solution

$$T = -\frac{h_1\phi_1}{\dot{h}}\frac{l-l_1}{l} \tag{16}$$

and are shown in Fig. 1. The plot of percentage error against number of degrees of freedom (nodes) shows that the nonconforming triangular element with the mass conservation correction term performs well. Also, the non-conforming quadrilateral element performs satisfactorily when compared with the control volume method.

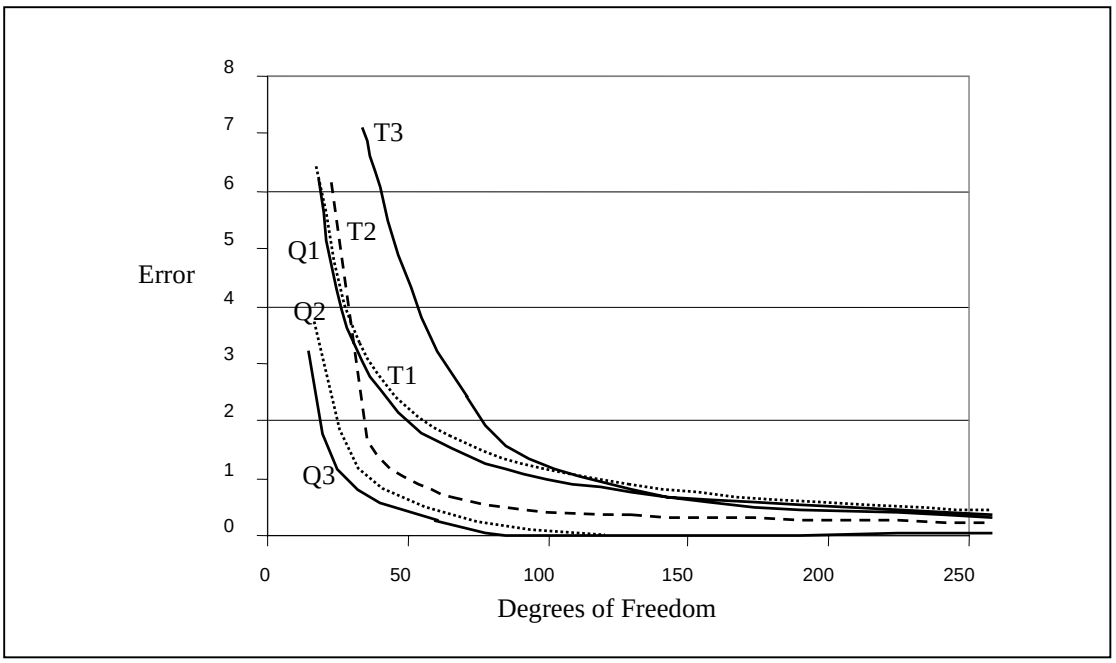

Fig. 1 % Error of IC/M flat-plate filling using different elements

CONCLUSIONS

In this study, the governing equations of LCM were solved using a number of different variants of the Finite Element Method. In particular, solutions were obtained using single-grid schemes with and without mass conservation, and with the standard CV method, involving triangular and quadrilateral elements. Numerical experiments were conducted to gauge the accuracy of the various schemes against standard solutions. It was demonstrated that triangular non-conforming elements with a mass-conservation correction term perform well in I/CM simulations, as do nonconforming quadrilateral elements, showing that simple single-grid meshes can be used productively for LCM simulations.

APPENDIX

The standard bilinear (conforming) Q4 element has as span $\{1, x, y, xy\}$. This span cannot be used for a nonconforming element since it cannot generate interpolation functions which are zero or 1 at the element mid-sides. Rotating a rectangle by 45 degrees, or equivalently, using the span $\{1, x, y, x^2 - y^2\}$ allows one to generate the interpolation functions. This can be amended to $\{1, x, y, x^2 - \frac{5}{3}x^4, y^2 - \frac{5}{3}y^4\}$ for greater accuracy [8]. This leads to the shape functions, in terms of natural coordinates (ξ, η), such that the four nodes of each element are located at $(\xi, \eta) = (\pm 1, \pm 1)$,

$$N_1(\xi,\eta) = \frac{1}{4} + \frac{1}{2}\xi - \frac{3}{8}\left[\left(\xi^2 - \frac{5}{3}\xi^4\right) - \left(\eta^2 - \frac{5}{3}\eta^4\right)\right]$$
$$N_2(\xi,\eta) = \frac{1}{4} + \frac{1}{2}\eta + \frac{3}{8}\left[\left(\xi^2 - \frac{5}{3}\xi^4\right) - \left(\eta^2 - \frac{5}{3}\eta^4\right)\right]$$
$$N_3(\xi,\eta) = \frac{1}{4} - \frac{1}{2}\xi - \frac{3}{8}\left[\left(\xi^2 - \frac{5}{3}\xi^4\right) - \left(\eta^2 - \frac{5}{3}\eta^4\right)\right]$$
$$N_4(\xi,\eta) = \frac{1}{4} - \frac{1}{2}\eta + \frac{3}{8}\left[\left(\xi^2 - \frac{5}{3}\xi^4\right) - \left(\eta^2 - \frac{5}{3}\eta^4\right)\right]$$

REFERENCES

1 A. Saouab, J. Breard, P. Lory, B. Gardarein and G. Bouquet “Injection simulations of thick composite parts manufactured by the RTM process”, *PComp. Sci. Tech.*, Vol.61, 2001, pp.445-451.

2 X. Song, “Vacuum Assisted Resin Transfer Molding (VARTM)”Model development and verification”, *PhD Thesis*, Virginia Polytechnic Institute and State University, 2003.

3 X-T. Pham and F. Trochu, “Simulation of Compression Resin Transfer Molding to Manufacture Thin Composite Shells”, *Polymer Comp.*, Vol.20, 1999, pp.436-459.

4 S-H. Chou and S. Tang, “Conservative P1 conforming and nonconforming Galerkin FEMS: effective flux evaluation via a nonmixed approach, SIAM J. Numer. Anal, Vol.38, 2000, pp. 660-680.

5 P.A. Kelly and S. Bickerton “Numerical simulation of liquid composite molding processes”, *Proc. Of the fifth Canadian International Composites Conference (CANCOM),* 2005, pp.16-19.

6 C. Park and D. Sheen, “P1-nonconforming quadrilateral finite element methods for second-order elliptic problems’, *SIAM J. Numer Anal*, Vol.41, 2003, pp. 624-640.

7 Z. Chen, “Finite Element Methods and their applications’, pub. *Springer*, 2005.

8 Z. Cai, J. Douglas and X. Ye, “A stable nonconforming quadrilateral finite element method for the stationary stokes and Navier-Stokes equations, *Calcolo*, Vol.36, 1999, pp.215-232.

SIMULATION OF ARTICULATED COMPRESSION RESIN TRANSFER MOLDING

V. Achim, S. Soukane*, R. Gauvin, and F. Trochu

CREPEC
Centre de Recherches en Plasturgie et Composites, Département de Génie Mécanique, École Polytechnique de l'Université de Montréal
** Corresponding author's e-mail: sofiane.soukane@polymtl.ca*

ABSTRACT

Liquid Composite Molding (LCM) is increasingly used in industry to manufacture high performance composites. This technology encompasses a family of composite manufacturing processes that consist of injecting a resin through a fibrous reinforcement. The latter can be placed in a rigid closed mold (*Resin Transfer Molding* – RTM) or covered by a flexible membrane (*Vacuum Assisted Resin Infusion* - VARI). In order to accelerate the resin flow, the mold cover can also be moved to compress the reinforcement (*Compression Resin Transfer Molding* – CRTM and *Articulated Compression Resin Transfer Molding* – ACRTM). The present effort focuses on ACRTM and emphasizes the main advantages of the technique. Unlike CRTM where the mold cover is usually made of a single part, ACRTM can be considered as a generalized version, in which the mold cover contains several pieces that can be articulated separately. Once enough resin is injected, each segment of the mold cover is compressed to complete the impregnation of the reinforcement. Numerical modeling and simulation is used to show how only the impregnated zones of the reinforcement need be compressed, therefore minimizing the total load on the mold cover while ensuring a complete impregnation of the reinforcement in a timely manner.

KEYWORDS: Modeling, Articulated Compression Resin Transfer Molding

INTRODUCTION

Composite materials are used in a large number of industrial applications ranging from high performance automotive and aerospace structures to common consumer products. Because composites combine high mechanical performance, low weight and good resistance to corrosion, further increase can be expected in their industrial usage. Five major ways to manufacture composites are presently in use: hand lay-up, autoclave, pultrusion, filament winding and liquid composite molding (LCM). A tradeoff between manufacturing cost, performance and geometric complexity governs the choice between the above processes. When the part geometry becomes complex as often encountered in the automotive and aerospace sectors, LCM remains the only reasonable alternative. LCM actually represents a family of composite manufacturing processes that consist of injecting a reactive liquid resin through a fibrous reinforcement. Among the several existing LCM techniques, Resin Transfer Molding (RTM) uses closed and rigid molds. The RTM process is well suited to manufacture complex small to mid-size parts. However, a problem arises with RTM for composite parts

with a high fiber content. Indeed, the permeability of the fibrous reinforcement drops drastically with an increase of the fiber content. Consequently mold filling is completed after a much longer period of time, resulting not only in a low overall throughput of the process, but sometimes in a non uniform impregnation of the reinforcement. One way to overcome this limitation is to design a mold with a thicker cavity to let the injected resin flow above the fibrous reinforcement (Fig. 1a). Once enough resin has filled up the cavity, the injection is stopped (Fig. 1b) and the upper part of the mold is pushed towards the fibrous reinforcement to compress the fibers, hence achieving a complete impregnation and reaching the desired fiber volume content (Fig. 1c). This technique is commonly called *Compression Resin Transfer Molding* (CRTM). It was studied extensively by Pham et al. [1], who modeled the process and developed a numerical algorithm to simulate injection and compression of the fibrous reinforcement in the case of displacement control of the mold cover. This work was further extended by Pham and Trochu [2, 3] for thin shells, then to include the case of pressure control in bladder assisted injection. More recently Achim et al. [4] have generalized this work to the case of an articulated mold cover.

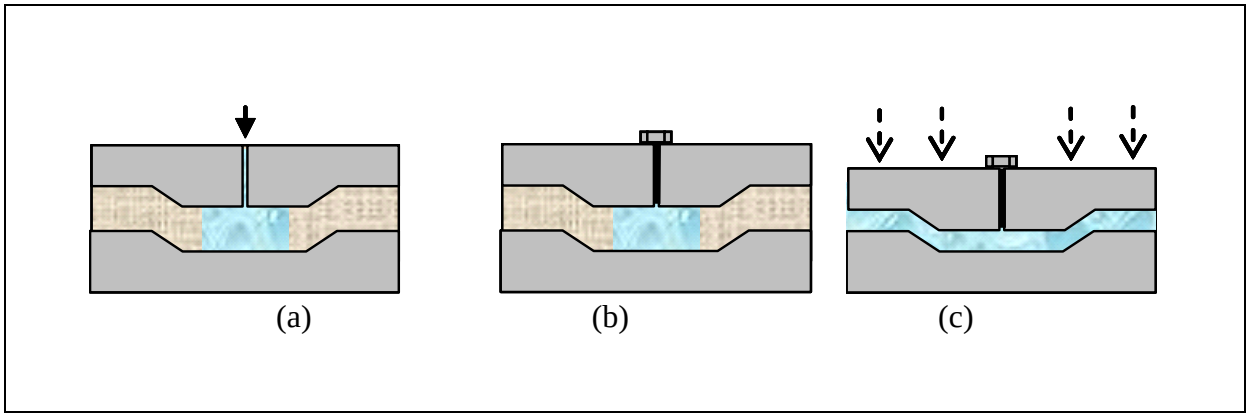

Fig. 1 Main steps of Compression Resin Transfer Molding (CRTM)

In this paper a generalized version of CRTM commonly called ACRTM is presented. Unlike CRTM where the mold is made of a single piece, ACRTM compresses the reinforcement with a mold cover made of several pieces that can be articulated separately. Using modeling and simulation, it will be shown how the wet zones of the reinforcement are compressed to complete the impregnation process in a timely manner.

ARTICULATED COMPRESSION RESIN TRANSFER MOLDING (ACRTM)

In CRTM the mold cover is usually made of a single rigid part, so the pressure applied during compression is uniformly distributed over the mold cover. Consequently, the mechanical press used in the process needs to provide an increasing force to overcome the resistance of the resin flow caused by the decrease in permeability of the reinforcement during compression. However, it is possible to minimize this effort if the mold cover is made of several pieces that can be articulated separately. This alternative is called ACRTM and consists of compressing only the newly impregnated part of the reinforcement. To illustrate the concept, Fig. 2 shows a mold made of four different pieces where the resin is injected from the left side. In the first step (Fig. 2a) the resin is injected underneath the first segment of the mold cover. Segment 1 is then pushed toward the base plate of the mold until the desired thickness is reached. In the meantime segment 2 is moved upward to let the resin

accumulate underneath it (Fig. 2b). The same operation is repeated with the remaining segments (Fig. 2c, d, e).

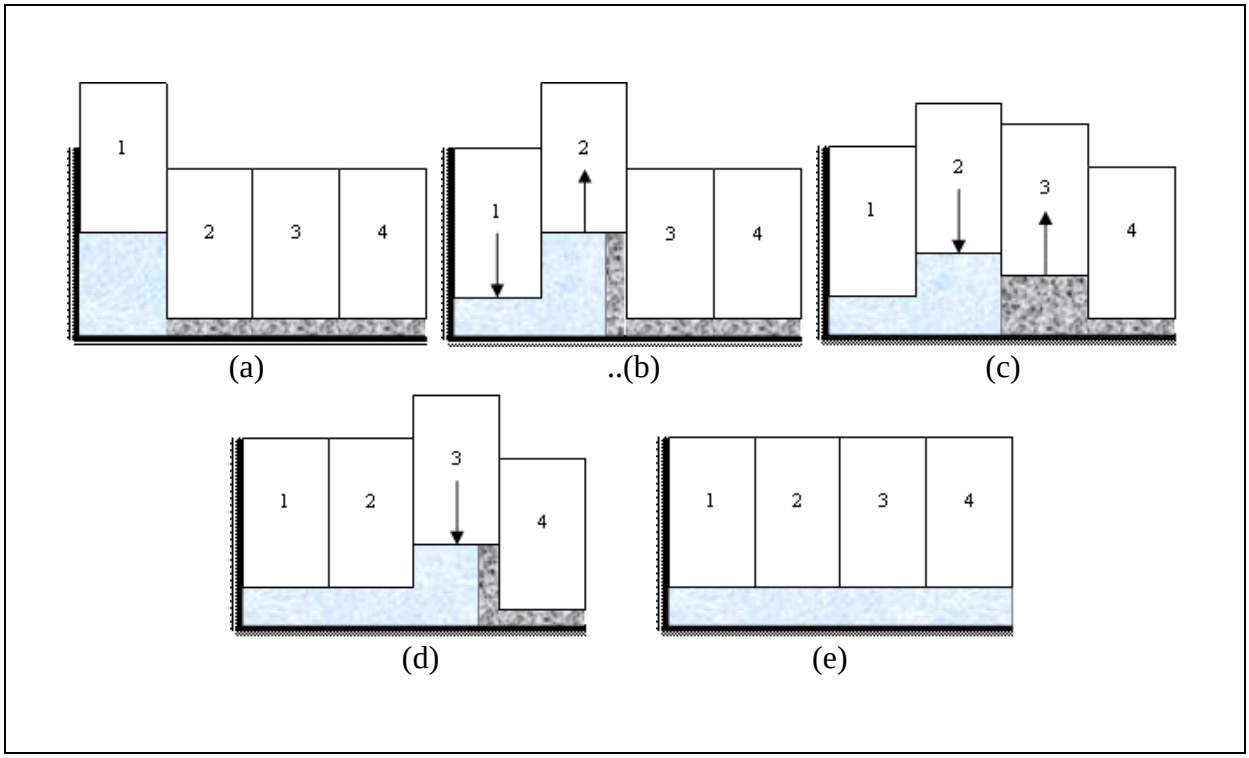

Fig. 2 Main steps of Articulated Compression Resin Transfer Molding (ACRTM)

GOVERNING EQUATIONS

The injection of a liquid resin through a fibrous reinforcement is generally considered as a flow through a porous medium and consequently governed by Darcy's law. The latter relates the average fluid velocity $\mathbf{v}$ (Darcy's velocity) to the pressure gradient ∇P as follows:

$$\mathbf{v} = -\frac{[\mathbf{K}]}{\mu}\nabla P \tag{1}$$

where $[\mathbf{K}]$ is the permeability tensor of the porous medium and μ is the resin viscosity. Darcy's velocity is related to the resin velocity via the porosity ϕ of the porous medium by:

$$\mathbf{v} = \phi\ \mathbf{v}_r \tag{2}$$

and Darcy's law may be reformulated as:

$$\mathbf{v}_r = -\frac{[\mathbf{K}]}{\phi\ \mu}\nabla P \tag{3}$$

The continuity equation for the liquid phase in a deformable porous medium leads to the following global mass balance [3, 4]:

$$div\left(h\phi \mathbf{v}_r\right) = -\frac{\partial h}{\partial t} \tag{4}$$

Using Eqn. 3, Darcy's law for compressible porous media is finally obtained:

$$div\left(h\frac{[\mathbf{K}]}{\mu}\nabla P\right) = \frac{\partial h}{\partial t} \tag{5}$$

In the case of CRTM or ACRTM processes the term of the right hand side of Eqn. 5 is set by the imposed displacement of the mold cover during the compression stage. The equation may therefore be rewritten as:

$$div\left(h\frac{[\mathbf{K}]}{\mu}\nabla P\right) = \mathbf{v}_{\mathbf{Cover}} \tag{5}$$

where $\mathbf{v}_{\mathbf{cover}}$ is the velocity of the mold cover during compression. The governing equations are solved by the finite element method [5].

FILLING OF AN AUTOMOTIVE HOOD

In order to fill the automotive hood of Fig. 3a by ACRTM, the mold mesh is divided into several segments (see Fig. 3b). The injection port is located in the center of the part while vents are set at the bottom and top right corners.

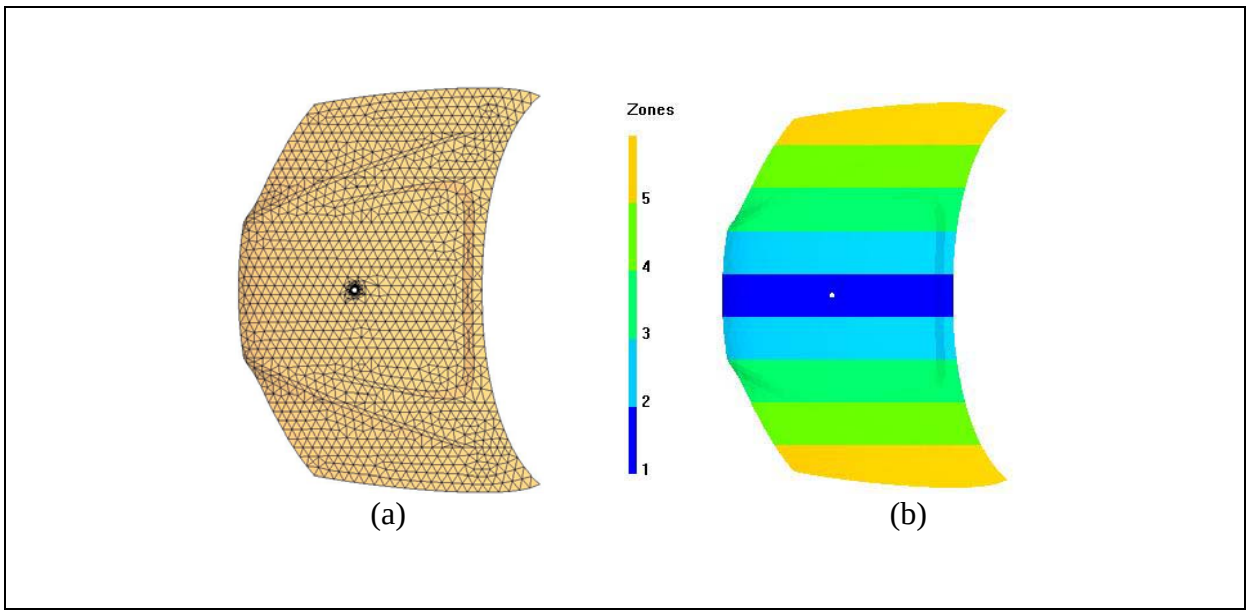

Fig. 3 The mold cover is split into segments in order to carry out ACRTM

The inlet pressure is set to 10^5 Pa to inject a resin of viscosity 0.1 Pa.s and the vents are kept at 0.28 10^5 Pa. The initial height of the mold cavity is 12 mm and the initial fiber content is low (16%). Since the fiber content will vary during compression, the variation of permeability as a function of the fiber volume content is provided in Fig. 4.

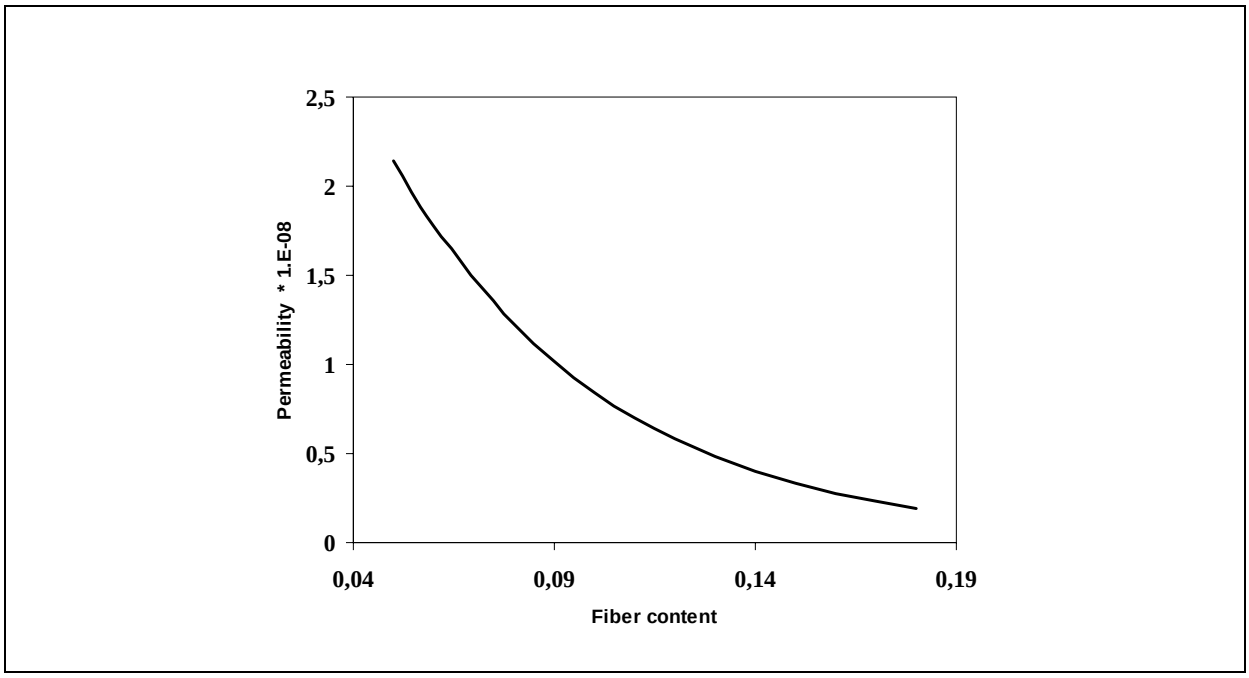

Fig. 4 Permeability vs. fiber content for the reinforcement used in the simulations

After 7 sec, the resin is already transferred underneath the 3 central segments of the mold cover as depicted in Fig. 5a and enough resin has been injected to fill up the entire cavity. The compression of the central segments starts as seen in Fig. 5b and a decrease in thickness of the corresponding zone is observed. The thickness keeps on decreasing with compression of the segment until it reaches a value of 4 mm, then the adjacent segments of the mold cover are moved down to continue the compression (see Fig. 6).

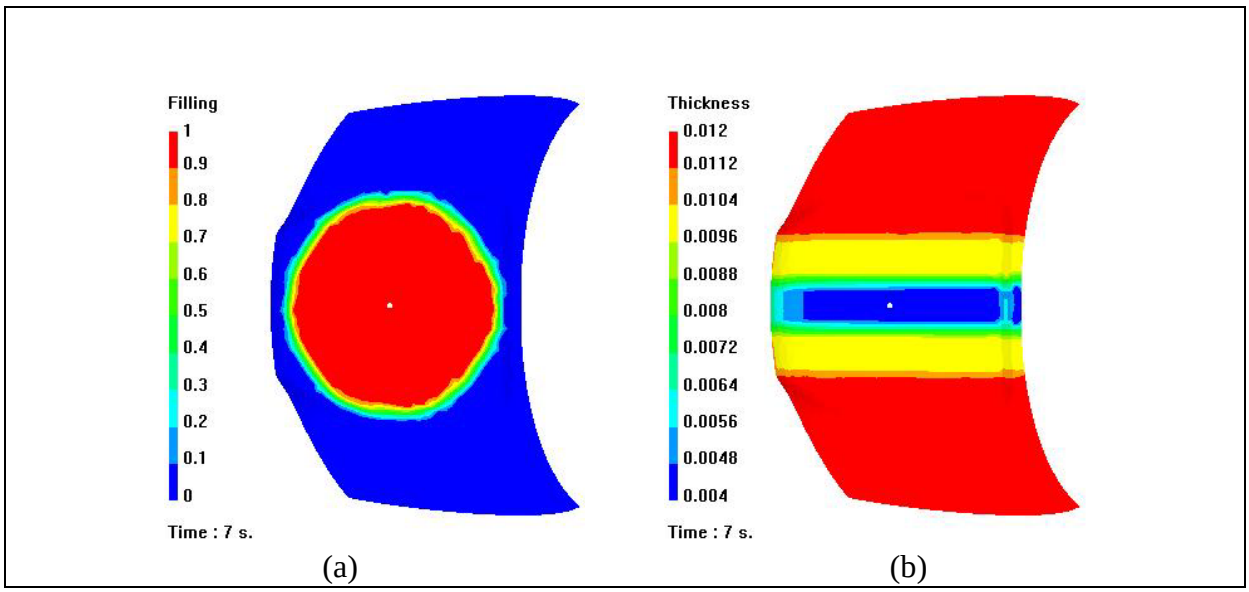

Fig. 5 Beginning of the compression process after 7 sec of filling: (a) flow front at 7 sec; (b) thickness distribution at 7 sec

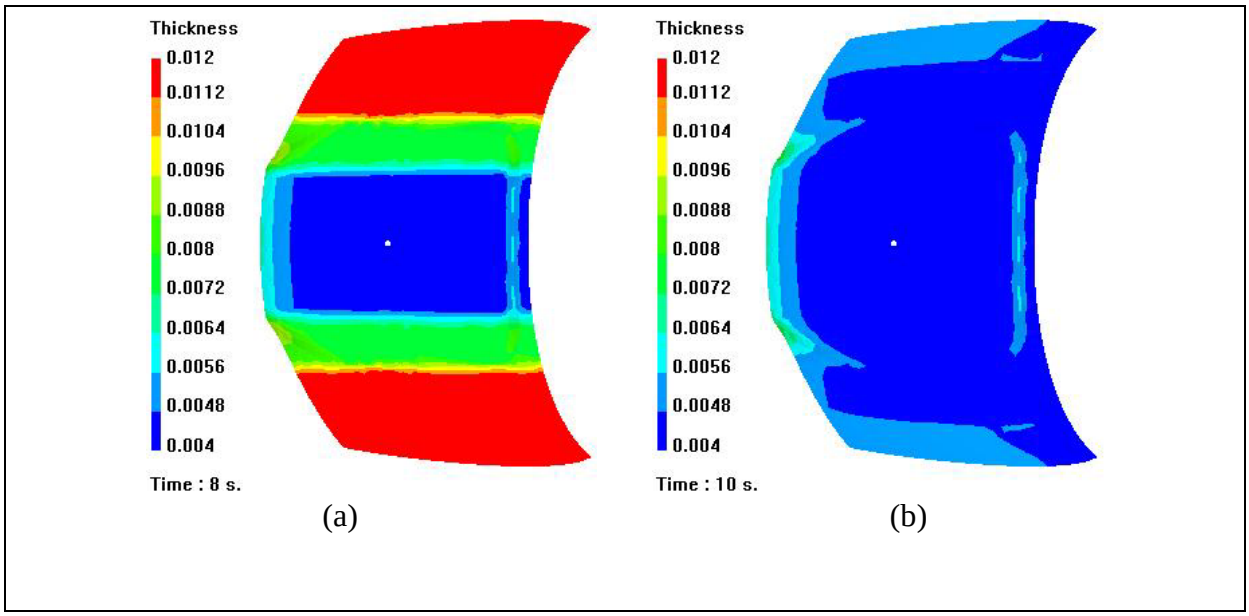

Fig. 6 Thickness variation during compression (ACRTM): (a) at 8 sec; (b) 10 sec

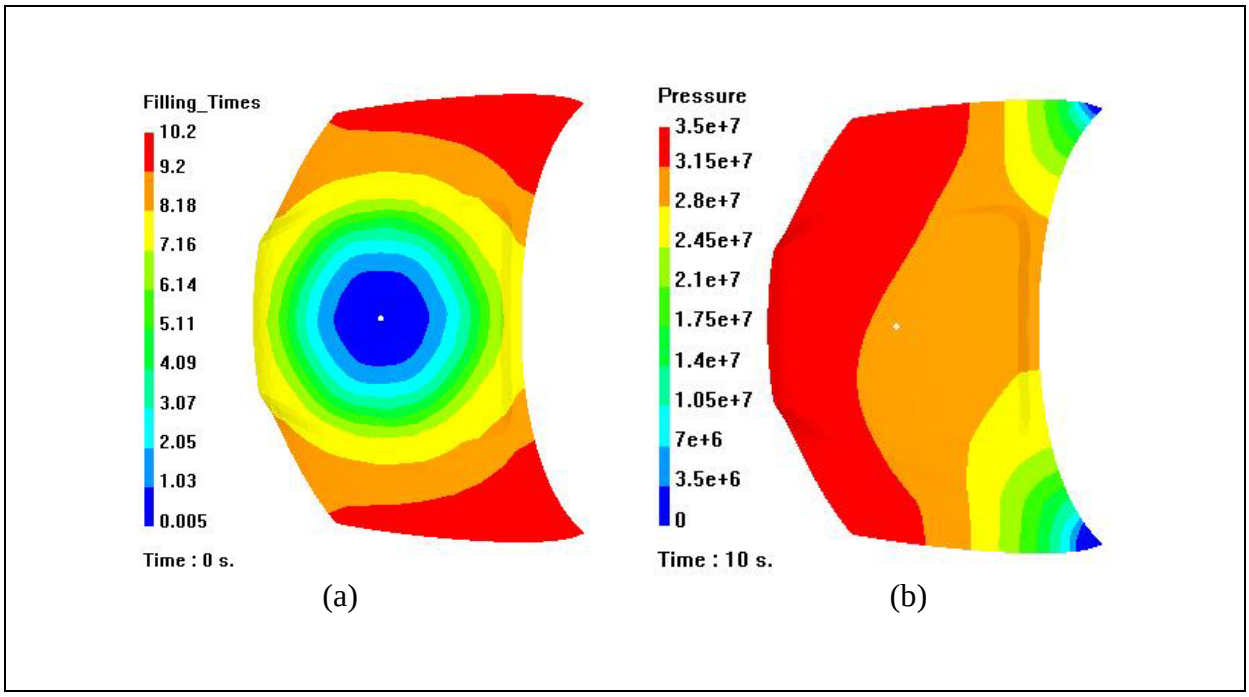

Fig. 7 Filling of the hood by the ACRTM process: (a) filling time distribution; (b) pressure distribution

The total filling time obtained is nearly 10 sec (see Fig. 7a) and the maximum pressure reached in the mold cavity is 3.5 10^7 Pa.

In order to illustrate more clearly the advantages of ACRTM, it is interesting to compare the previous results to those of a CRTM simulation. The same properties of the resin and the reinforcement are therefore considered. The variation of permeability as a function of the fiber volume content is given by the same curve as in Fig. 4. The initial height of the mold cavity is 12 mm. No compression is carried out until enough resin to fill up the entire mold cavity has been injected. The compression starts 7 sec after the injection began. Fig. 8 shows the thickness variations during compression. Note that the thickness is not uniform since the mold cover is moved vertically while the automotive hood is not perfectly planar. Figures 9a

and 9b depict respectively the progression of mold filling in time and the final pressure distribution attained in the mold cavity. It is important to note that the final pressure of 6.4 10^7 Pa reached in CRTM is twice as much as the one of ACRTM. For the same compression pressure, ACRTM would give a smaller filling time.

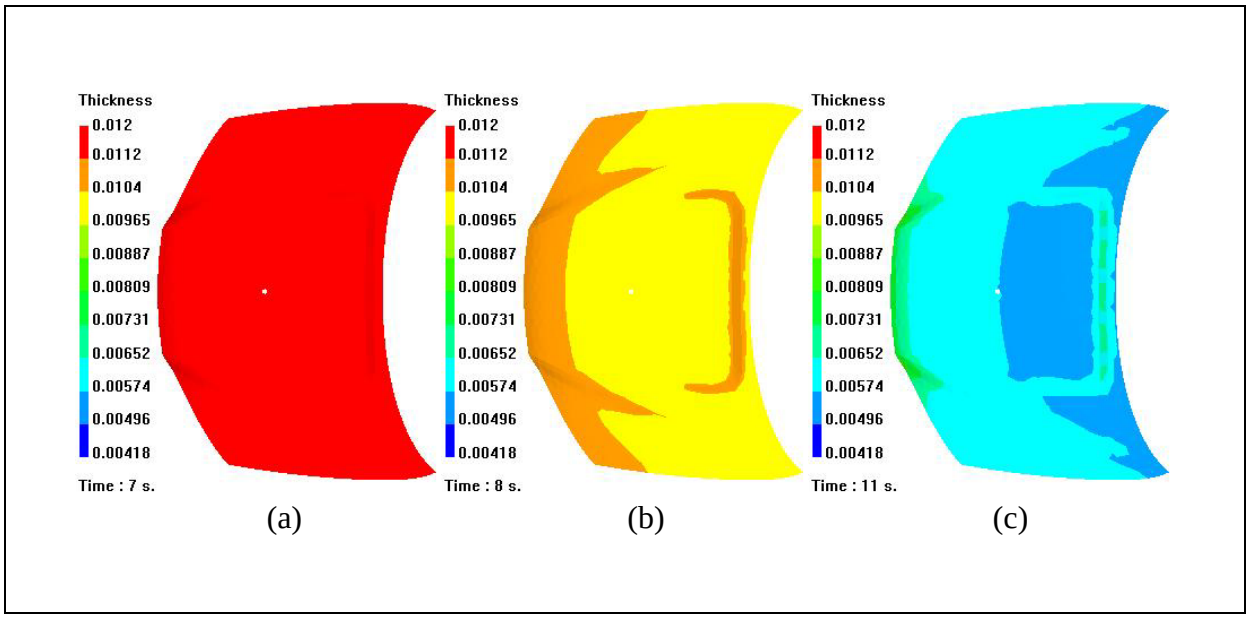

Fig. 8 Thickness variation during filling: (a) at 7 sec; (b) 8 sec; and (c) 11 sec

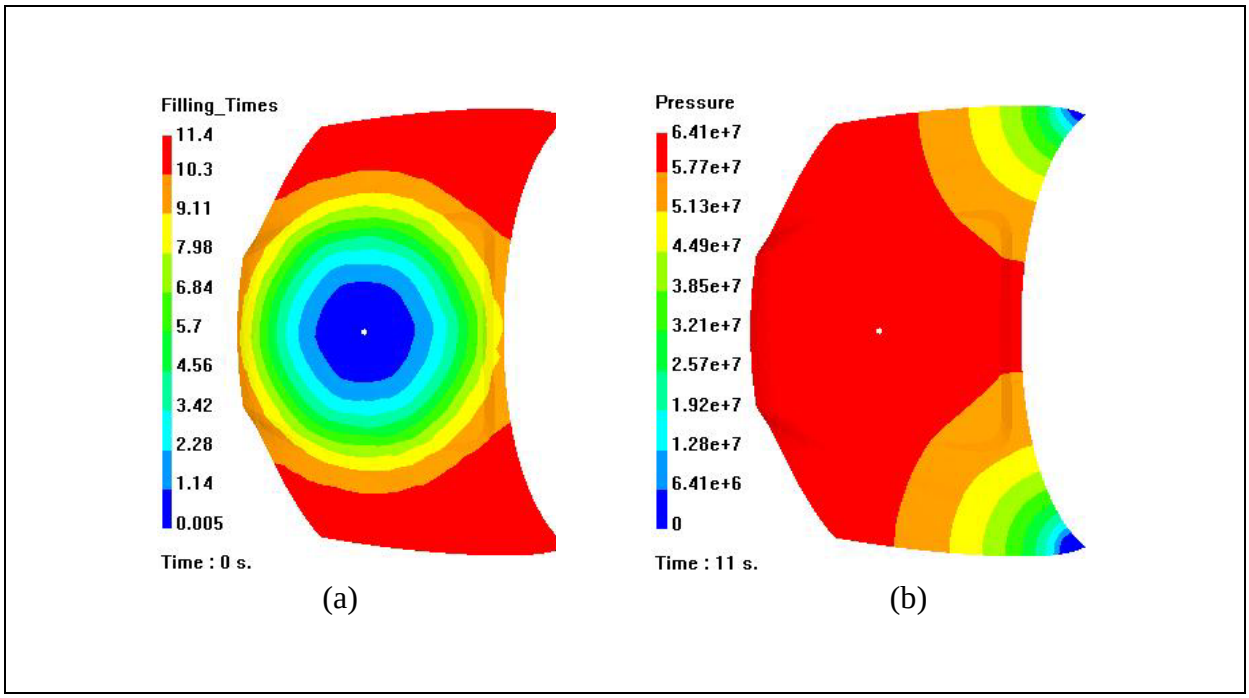

Fig. 9 Filling of the hood by the CRTM process: (a) filling time distribution; (b) pressure distribution

CONCLUSION

A model of Articulated Compression Resin Transfer Molding (ACRTM) was developed based on the general Darcy equation for compressible porous media and the resin continuity equation. The final form of the governing equation was solved for complex parts using the finite element method. The filling of an automotive hood was considered to illustrate this approach. It was shown how the mold cover can be divided into several segments intended to carry out the compression process. Simulation results were compared to those of CRTM. ACRTM used less energy to transfer the resin for the same range of filling times. For the same compression pressure, this process would allow filling parts more quickly than RTM or CRTM. However, like in CRTM one difficulty remains for parts with nearly vertical walls: it is not possible in that case to impose a uniform compression to the reinforcement. In addition, an articulated mold will necessarily be more complex, and hence more expensive than a rigid one.

ACKNOWLEDGEMENTS

The authors are grateful to the National Science and Engineering Research Council of Canada (NSERC) and Fonds Québécois de Recherche sur la Nature et la Technologie (FQRNT) for their financial support. CREPEC (Centre de recherche en plasturgie et composites) and ESI-Group are also gratefully acknowledged for their contributions.

REFERENCES

1. X.-T. Pham, F. Trochu, “Analysis of Consolidation in the Flexible Bladder Process for Thin Composite Parts by Finite Element Method”, *Journal of Reinforced Plastics & Composites*, Vol. 19, no. 03, 2000 pp 182-218.

2. X.-T. Pham, F. Trochu, “Simulation of Compression Resin Transfer Molding to Manufacture Thin Composite Shells”, *Polymer Composites*, Vol. 20, no. 3, 1999, pp 436.

3. X.-T. Pham, F. Trochu, R. Gauvin, “Simulation of Compression Resin Transfer Molding with Displacement Control”, *Journal of Reinforced Plastics & Composites*, Vol. 17, no. 17, 1998, pp 1525-1556.

4. F. Trochu, E. Ruiz, V. Achim and S. Soukane, “Advanced Numerical Simulation of Liquid Composite Molding for Process Analysis and Optimization”, *Composites Part A*, doi: 10.1016/j.compositesa.2005.06.003.

5. F. Trochu, R. Gauvin and D. M. Gao, "Numerical Analysis of the Resin Transfer Molding Process by The Finite Element Method", *Advances in Polymer Technology*, Vol. 12, no. 4, 1993 pp. 329-42.

A SIMPLIFIED NUMERICAL APPROACH TO SIMULATE RESIN TRANSFER MOLDING WITH A DISPERSION MEDIUM

Edu Ruiz [1], S. Chatel [2] and F. Trochu [1]

[1] *Chaire sur les Composites à Haute Performance (CCHP), Centre de Recherches En Plasturgie Et Composites (CREPEC), Département de génie mécanique, École Polytechnique, Montréal (Québec) HC 3A7* http://cchp.meca.polymtl.ca
edu.ruiz@polymtl.ca

[2] *European Aeronautic Defense and Space Company, Corporate Research Centre (EADS CCR), 12 rue Pasteur BP 7692152 Suresnes Cedex, France*
sylvain.chatel@eads.net

ABSTRACT: Resin Transfer Molding with a Dispersion Medium (DM-RTM) is a liquid composite molding manufacturing technique well suited for high fiber volume aeronautical parts. DM-RTM, also known sometimes as Liquid Resin Injection (LRI), consists of incorporating a highly permeable dispersion medium into the laminated preform to accelerate fiber impregnation. This cost-effective molding technology is contemplated for use in the manufacturing of large size aeronautical parts of complex shape because of its ability to quickly fill-up the mold, and hence reduce total cycle time. The high difference in planar permeability between the dispersion medium and the fibrous preform (of almost three orders of magnitude) induces a through-thickness flow that cannot be neglected event for thin parts. The resulting three-dimensional filling of the mold cavity can no longer be assumed to take place following a two-dimensional uniform flow front through the thickness of the part. To improve the performance of such a process, more scientific knowledge of three-dimensional impregnation phenomena is required. This work concerns the analysis of through-thickness flows coupled with standard planar filling simulations. Numerical simulation is a useful design tool in the virtual prototyping of the molds required to produce complex composite parts by resin injection. Computer analyses aim to model, predict and control the events that occur during the fabrication of composite parts by liquid composite molding. In this work, a pseudo three-dimensional numerical analysis is presented to simulate mold filling in presence of a dispersion medium. The numerical approach is validated with experimental results that demonstrate the capability of the proposed "*simplified*" solution. A test case was carried out on a composite part to highlight the advantages of the numerical simulation. Finally, DM-RTM filling is applied to a complex aeronautical part.

KEYWORDS: DM-RTM, integrated approach, aeronautics, composite

INTRODUCTION

Over the last few years, thermoset composites have played a key role in the development of new commercial aircrafts because of their high specific properties, corrosion resistance and low fatigue. Recently, a wide variety of new manufacturing processes has appeared as an alternative to high cost pre-impregnated fabrics and autoclave cured composites. Liquid Composite Molding (LCM) techniques such as Resin Transfer Molding (RTM) and Vacuum Assisted Resin Infusion (VARI) have become increasingly popular for structural parts. These techniques based on resin injection through fibrous reinforcements allow a significant reduction of manufacturing costs through usage of complex 3D braided fabrics and multifunctional integration. Resin Transfer Molding with a Dispersion Medium (DM-RTM) is a liquid composite molding manufacturing technique well suited for high fiber volume aeronautical parts. DM-RTM, also known as Liquid Resin Injection (LRI), consists of incorporating a highly permeable dispersion medium into the laminated preform to accelerate fiber impregnation. This cost-effective molding technique begins to be used for the manufacturing of aeronautical parts of complex shape, because of its ability to quickly fill up the mold and reduce total cycle time. The ability to numerically predict the different manufacturing stages is well recognized as playing a key role in the industrialization of such processes. Numerical simulation tools able to predict the isothermal and non-isothermal injection stages of RTM [1-3], compression RTM [4], VARI [5], articulated RTM [6] and various similar processes have been developed over the last 10 years. Efforts have also been made to simulate SCRIMP-like processes [7-8] were a high permeable media is used to assist in resin infusion under vacuum conditions. In this work, unidirectional flow experiments have been conducted to study the DM-RTM process. A one dimensional model has been developed to characterize the coupled permeability of the fabric and the dispersion medium. Finally, a finite element model has been coded to solve the complex 3D impregnation phenomena and apply it to a real aeronautical part.

GOVERNING EQUATIONS

The impregnation of a porous preform by a liquid resin can be modeled as a transient Darcy's flow [1]. Darcy's law enables estimating the average superficial fluid velocity **v** from the pressure gradient ∇P via the following relationship:

$$\mathbf{v}_r = -\frac{[\mathbf{K}]}{\phi\ \mu}\nabla P \tag{1}$$

where $[\mathbf{K}]$ is the permeability tensor of the porous medium, μ the resin viscosity and ϕ denotes the porosity of the porous medium. In the case of the DM-RTM process, a highly permeable dispersion medium is added above the fibrous preform to facilitate resin impregnation of the laminate (see Fig. 1). Important differences between the permeability of the dispersion media and the laminate (more than 1,000 times) induce a complex 3-dimensional resin flow. Due to the higher permeability of the dispersion medium (DM), resin initially flows through it forcing a though-thickness impregnation of the low permeability laminate. As depicted in Fig. 2 for a representative unit cell, the in-plane and through-thickness flows can be divided into three main flows: (A) the in-plane flow in the DM, (B) the in-plane flow through the laminate and (C) the through-thickness flow from the DM into the laminate. These resin flows can be estimated by applying Darcy's law with a pressure

gradient ΔP_X^{DM} in the DM, ΔP_X^{fibers} through the laminate and ΔP_Z between them. Dividing the unit cell in the upper layer for the DM and in the lower layer for the laminate, equation (1) can be rewritten for each section in the following form:

$$Q^{DM} = -\frac{[\mathbf{K}_{DM}]}{\phi_{DM}\ \mu\ A}\nabla P_{DM} - Q_t \tag{2}$$

$$Q^{fibers} = -\frac{[\mathbf{K}_{fibers}]}{\phi_{fibers}\ \mu\ A}\nabla P_{fibers} + Q_t \tag{3}$$

where Q^{DM} is the flow rate through the dispersion medium, Q^{fibers} the flow rate in the laminate, A the in-plane area of the unit cell and Q_t the flow rate between the dispersion medium and the laminate. Two finite elements (FE) approaches are proposed to iteratively evaluate the complex resin flow in the DM-RTM process. In both cases, the DM is considered independent of the laminate. As shown in Fig. 3, a two-dimensional FE mesh is used to describe the DM and calculate the in-plane resin flow through equation (2). The in-plane flow in the laminate can be evaluated with equation (3) on a 2D FE mesh in the case of thin laminates (i.e., for shell-like composites) and on a 3D FE mesh for thick composites. In the first case, for thin laminates, the through-thickness flow Q_t can be estimated by applying Darcy's law between the DM and the laminate. As depicted in Fig 4 (a) for two face-to-face finite elements representing respectively the DM and the laminate, averaged node pressures can be used to evaluate the through-thickness flow in the following way:

$$Q_t = \frac{\mathbf{K}^T_{fibers}}{\phi_{fibers}\ \mu\ A}(P_{cg}^{DM} - P_{cg}^{fibers}) \tag{4}$$

where $\mathbf{K}^T_{fibers}$ is the transverse through-thickness permeability of the thin laminate, P_{cg}^{DM} the averaged pressure at the center of the finite element representing the dispersion medium, and P_{cg}^{fibers} the averaged pressure in the finite element representing the laminate. In the case of thick laminates modeled by a 3D FE mesh (see Fig 4 (b)), the pressure at the interface between the DM and the laminate is set for the nodes on top of the 3D mesh. Darcy's law (equation (1)) is then solved for the thick laminate, and the tree-dimensional flow calculated. The transverse flow Q_t can then be evaluated as the normal flow through the face of the upper element. Fig. 5 shows the proposed flow chart to solve the filling problem in DM-RTM for thin and thick laminates respectively.

NUMERICAL AND EXPERIMENTAL VALIDATION

To validate the accuracy of the proposed numerical solution, a 2D through-thickness finite element geometry was created. The accurate 2D FE solution was used as reference to evaluate the degree of prediction of the proposed simplified solution. Fig. 6 shows a comparison between the 2D FE solution and the simplified approach for a rectangular plate of 40 cm length, a fibrous preform of 2 mm thick (50% fiber volume content) and a dispersion medium of 0,5 mm thick (80% porous media). A Newtonian fluid with a viscosity of 0,1 Pa.s was injected under a constant injection pressure of 1e6 Pa. A good agreement between both

solutions can be observed. The proposed simplified approach models the 2D Darcy's flow through the thickness of the laminate.

An experimental validation for materials used for aeronautical composite parts was also conducted in CRC to validate the proposed model. Experimental injections were carried out for different injection conditions. Carbon fabric rectangular plates of 70 x 9 cm and 4 mm thick (70% fiber volume content) were layered above a dispersion medium of 0,5 mm thick (90% porous). A liquid resin with a viscosity of 0,02 Pa.s was then injected at constant injection flow rate. The resin flow front evolution in the dispersion medium and the fibers was recorded using fiber optic sensors. As depicted in Fig. 7, the experimental flow front positions in the DM and through the laminate were compared to the numerical predictions using the simplified approach. It was observed that when in-plane flow in the laminate region is not considered (i.e., zero in-plane permeability of the fibers $\mathbf{K}_{fibers}^{X}$), then the numerical solution diverges from experiments as can be seen at the beginning and at the end of resin injection (see arrows in Fig. 7). Hence it can be inferred that the in-plane flow through the laminate plays a key role at the beginning of the impregnation as well as at the end of mold filling. From this experimental validation one may conclude that the proposed simplified approach accurately predicts the resin flow in the dispersion medium and through the laminate for thin composite parts manufactured by DM-RTM.

CASE STUDY

A test case was carried out for a real aeronautical part to demonstrate the capabilities of this new numerical approach. The composite part consists of a fuselage panel, auto-stiffened panel of 3,5 x 3 meters, with a ratio between length and thickness higher than 1000. A preliminary study showed the difficulties to reproduce the different resin flows for this kind of process with standard numerical solutions (i.e., using shell elements with averaged permeabilities or 3D elements). Fig. 8 displays a preliminary result for a shell mesh with an average permeability (i.e., thickness weighted permeability). It was experimentally observed that the filling prediction with averaged permeability did not represent the DM-RTM process. As illustrated in Fig. 9, important differences were obtained between the averaged permeability solution and the proposed simplified approach (i.e., differences in filling times and different shapes of the flow front). As depicted in Fig. 10, the proposed solution allows a fast analysis of the evolution of the resin front in the DM and through the laminate.

CONCLUDING REMARKS

In this work, a methodology is proposed to compute three-dimensional flows in the Resin Transfer Molding with a Dispersion Medium (DM-RTM). Two numerical solutions were proposed based on finite element analysis. The first one considers the case of thin laminates (i.e., shell-like composites), while the second one is focused on thick laminates. The complex 3-dimensional resin flow evolution is solved by a simplified approach consisting of calculating the in-plane flow in the DM followed by the transverse through-thickness flow, so that finally the in-plane flow through the laminate can be numerically estimated. Numerical and experimental validations demonstrate that the in-plane flow through the laminate plays a key role at the beginning and at the end of resin injection. A good agreement between measured and predicted flow fronts in the DM as well as through the laminate was observed for the experimental validation presented. Finally, a test case was studied for an aeronautical

composite part to highlight the advantages of the proposed numerical formulation. This simplified approach can accurately predict the evolution of the resin flow in the dispersion media and through the laminate for thin composite parts manufactured by DM-RTM.

ACKNOWLEDGEMENTS

The authors thank the National Science and Engineering Research Council of Canada (NSERC) and Fonds Québécois pour la Recherche sur la Nature et la Technologie (FQRNT) for their financial support. CREPEC (Centre de recherche en plasturgie et composites) and ESI-Group are also gratefully acknowledged for their contributions, as well as Arnaud Alix from Dassault Aviation.

REFERENCES

1. F. Trochu, R. Gauvin, D-M. Gao, “Numerical Analysis of the Resin Transfer Molding Process by the Finite Element Method”, *Advances in Polymer Technology*, Vol. 12, no. 4, 1993, pp. 329.
2. A. Saouab, J. Breard, P. Lory, B. Gardarein, G. Bouquet, “Injection simulations of thick composite parts manufactured by the RTM process”, *Composites Sci. and Technology*, Vol. 61, no. 3, 2001, pp. 445.
3. W. Chang, N. Kikuchi1, “Analysis of non-isothermal mold filling process in resin transfer molding (RTM) and structural reaction injection molding (SRIM)”, *Computational Mechanics*, Vol. 16, no. 1, 1995, pp. 22.
4. X-T. Pham, F. Trochu, “Simulation of Compression Resin Transfer Molding to Manufacture Thin Composite Shells”, *Polymer Composites*, Vol. 20, no. 3, 1999, pp. 436.
5. P. Hubert, B.W. Grimsley, R.J. Cano, R.B. Pipes, “Dimensional Stability of Complex Shapes Manufactured by the VARTM Process”, *Annual Technical Conference of the Society of Plastics Engineers*, San Francisco, May 5-9, 2002.
6. V. Achim, “Simulation numérique du procédé VARI et ses dérivés”, MsC.A. thesis, École Polytechnique de Montréal, 2004, 94 p.
7. V.M.A. Calado, S.G. Advani, “Effective average permeability of multi-layer preforms in resin transfer molding”, *Composites Science and Technology*., Vol. 56, no. 5, 1996, pp. 519.
8. X. Sun, S Li, L.J. Lee, “Mold Filling Analysis in Vacuum-Assisted Resin Transfer Molding. Part I: SCRIMP Based on a High-Permeable Medium”, *Polymer Composites*, Vol. 19, no. 6, 1998, pp. 807.

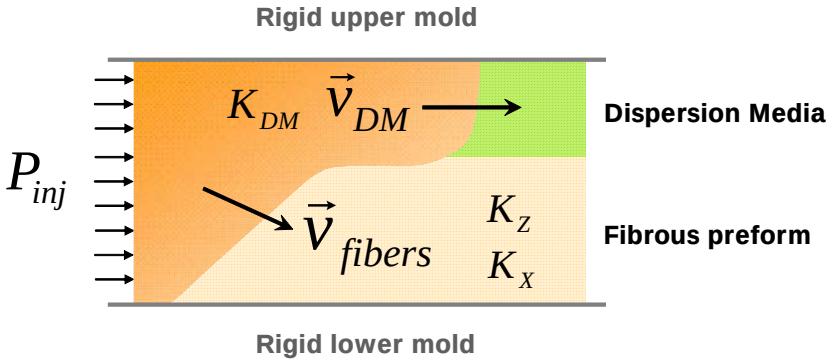

Figure 1. DM-RTM manufacturing process: a highly permeable dispersion medium is added above the fibrous preform to facilitate resin impregnation.

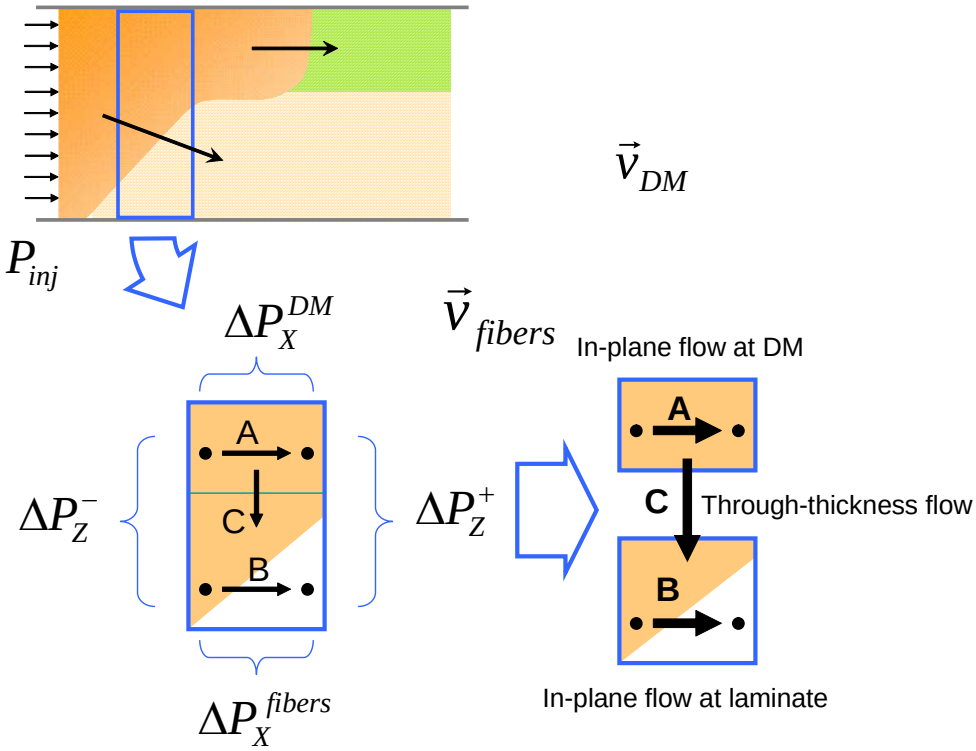

Figure 2. Pressure and resin flow distribution during DM-RTM mold filling.

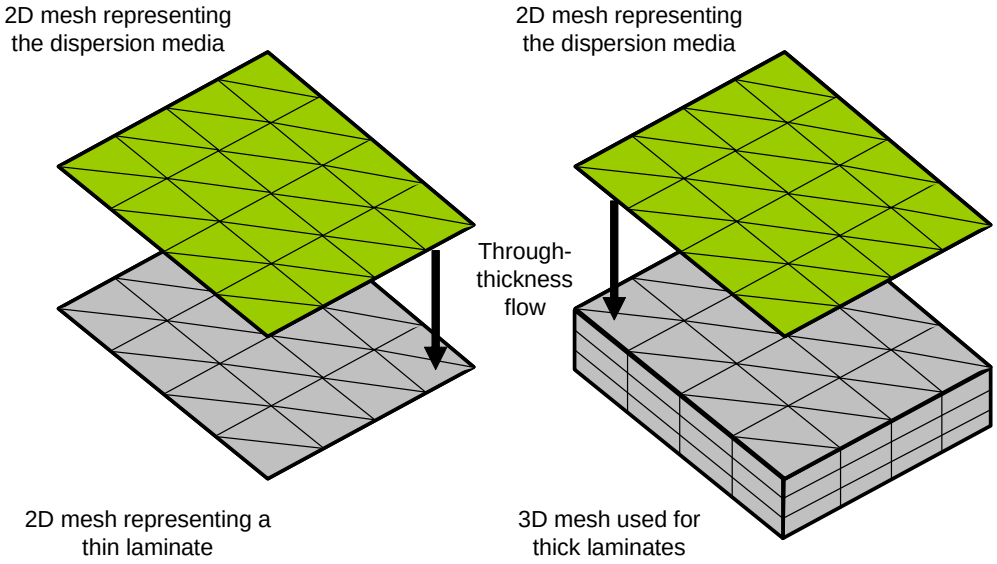

Figure 3. Two proposed geometrical representations: a 2D FE mesh is used to describe thin laminates (i.e., for shell-like composites) and a 3D FE mesh is used in the case of thick composites. In both cases a 2-dimensional FE mesh is used to describe the DM.

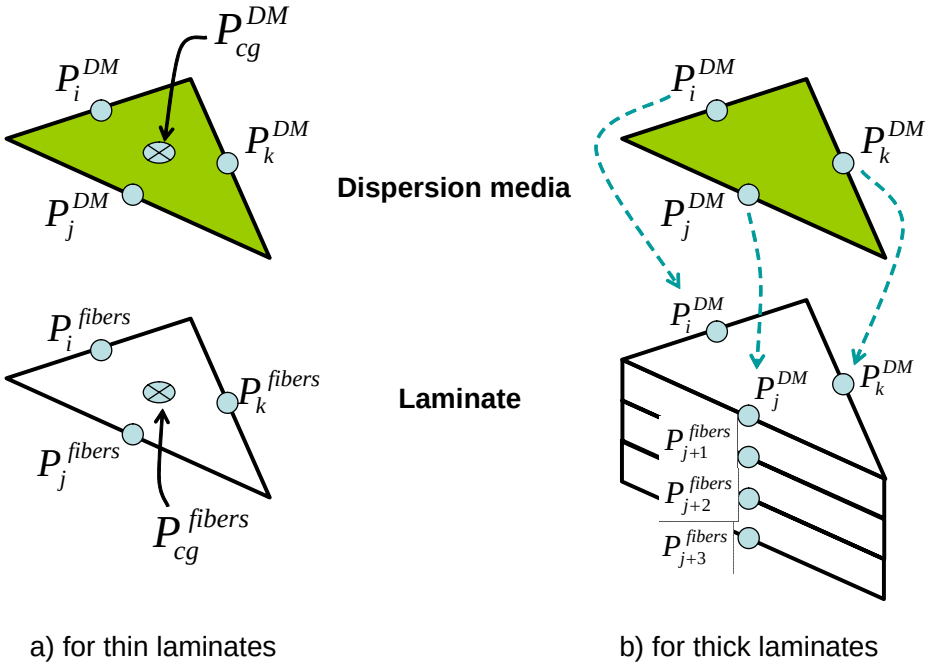

a) for thin laminates b) for thick laminates

Figure 4. Pressure distributions for the two proposed numerical solutions.

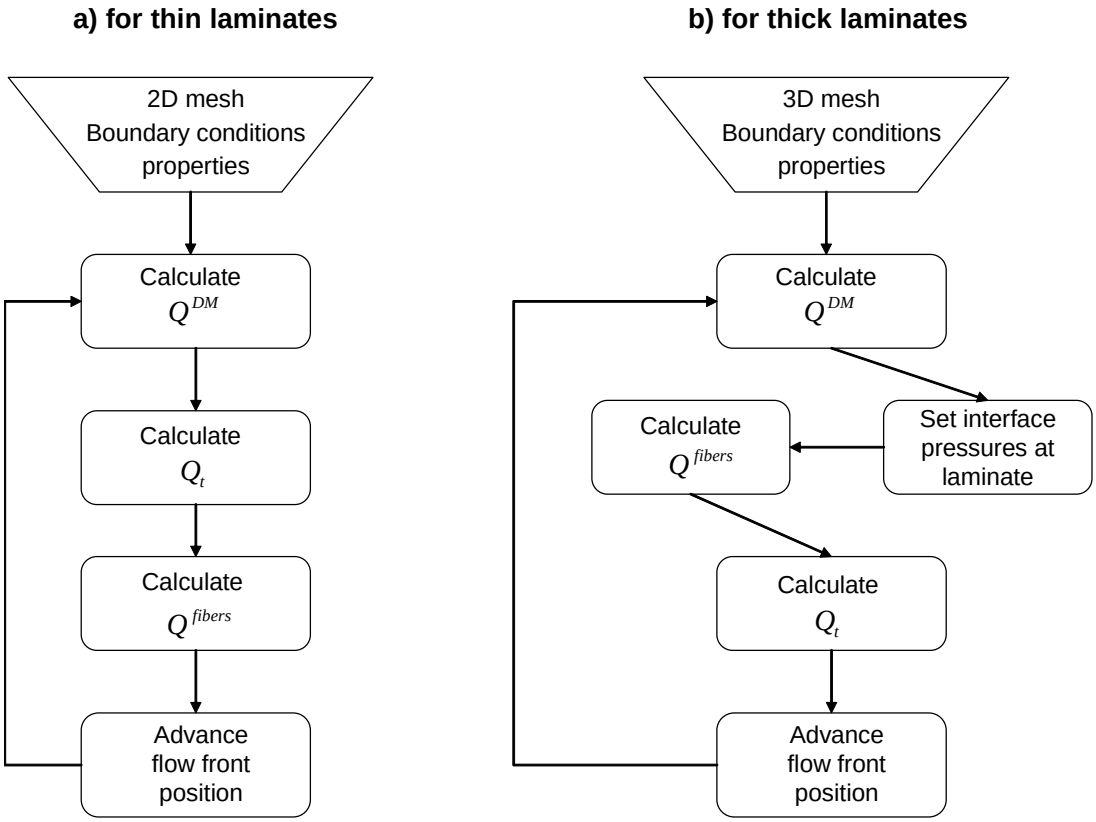

Figure 5. Flow chart of the finite element solver used to simulate DM-RTM mold filling for thin and thick laminates respectively.

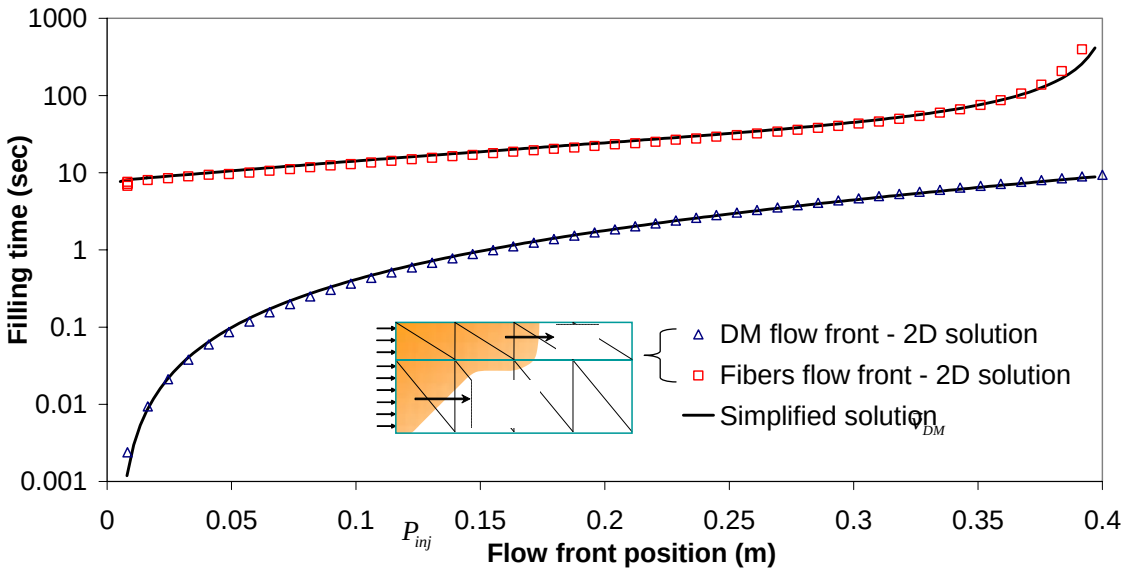

Figure 6. Comparison of the proposed simplified DM-RTM solution with a 2D through-thickness FE solution.

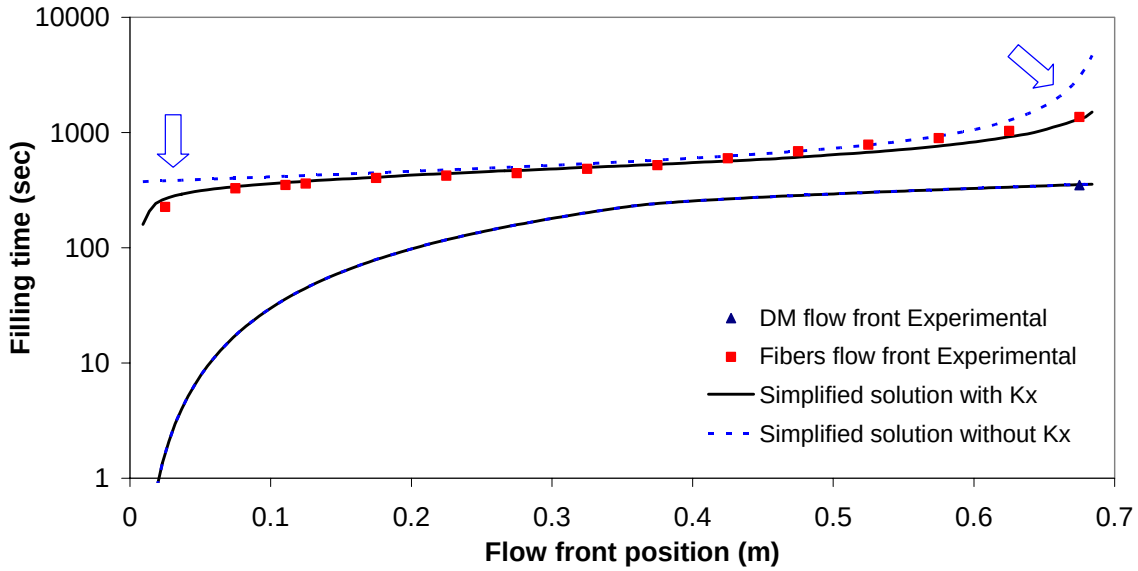

Figure 7. Experimental validation of the proposed simplified approach to simulate DM-RTM mold filling.

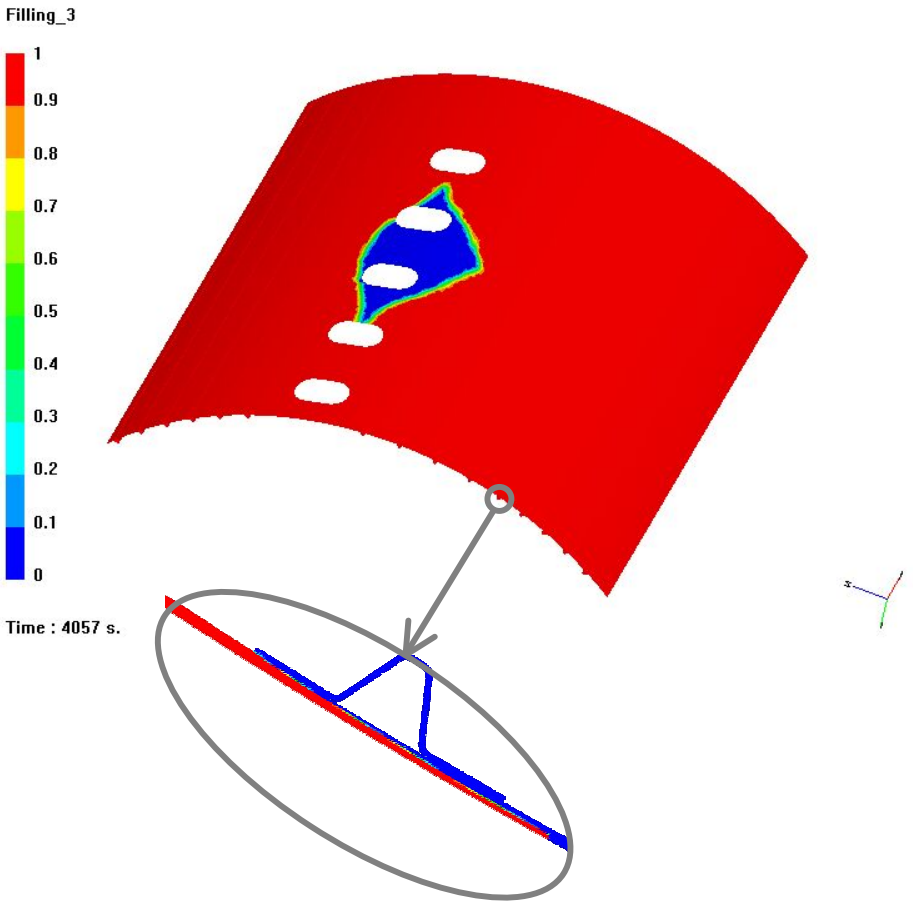

Figure 8. Filling results of the aeronautical composite part with the average permeability solution for a mesh of shell elements.

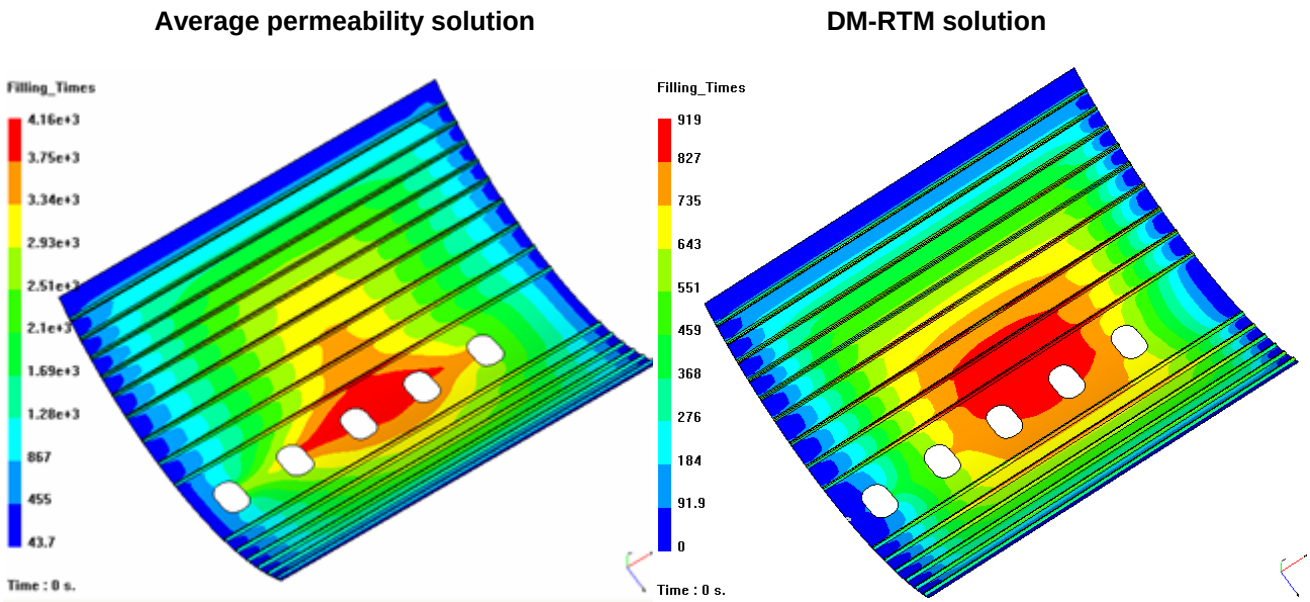

Figure 9. Comparison between the average solution and the proposed DM-RTM solution.

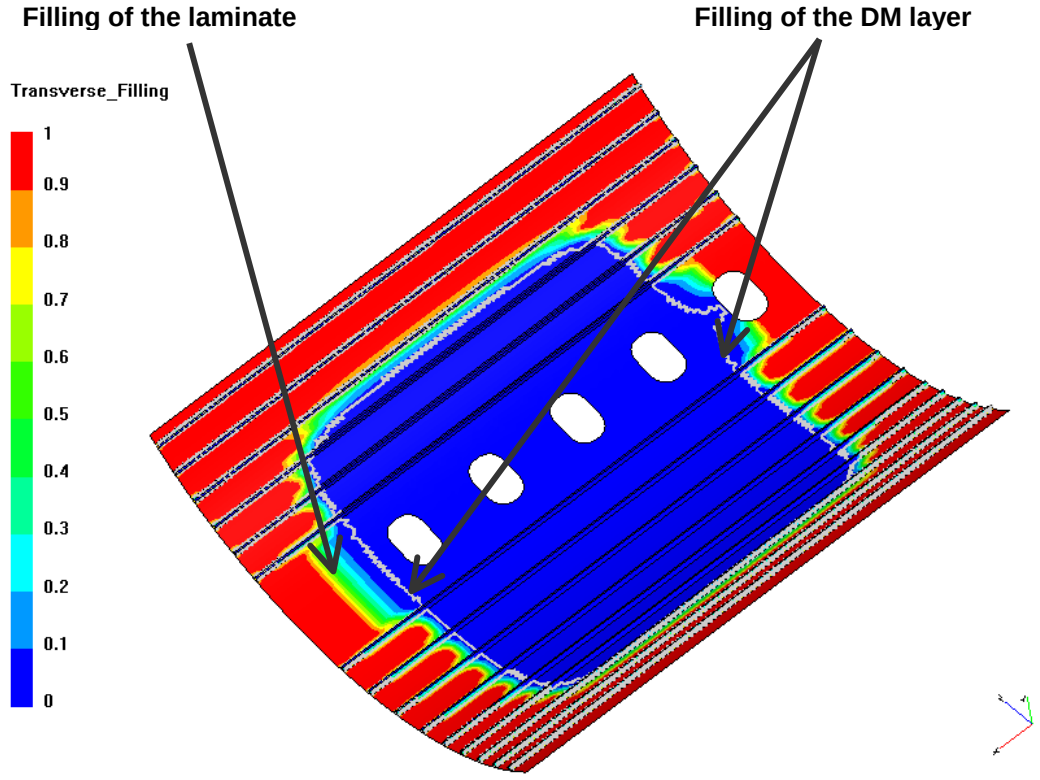

Figure 10. DM-RTM filling simulation of an aeronautical test part: in-plane filling of the DM layer and transverse flow through the laminate can be observed.

Session 8

MONITORING AND CONTROL

INVESTIGATION OF CAPILLARY FLOW ACROSS A BANK OF ALIGNED FIBERS

Valentin Neacsu [1], Johannes Leisen [2], Suresh G. Advani [1]

[1] *Department of Mechanical Engineering and Center for Composite Materials*
University of Delaware, Newark, DE 19716, USA: advani@udel.edu

[2] *School of Polymer, Textile and Fiber Engineering*
Georgia Institute of Technology, Atlanta, GA 30332, USA: jl167@mail.gatech.edu

ABSTRACT: This paper introduces two experimental studies of capillary impregnation across fiber tows. The first experimental technique embeds four to five flow detection sensors into a fiber tow at radial locations from the outside to the center of the tow to track the motion of fluid from outside to the center of the tow with time. The second technique based on Magnetic Resonance Imaging (MRI) is a non-intrusive tracking of the flow front as it impregnates the fiber tow. The techniques are compared and contrasted to identify their advantages and limitations. An analytical model that ignores the backpressure of the entrapped air grossly under predicts the saturation time for the tow as compared with the experiments. In order to explain this discrepancy, we include the effect of entrapped air in the analytic model, which slows down the capillary flow. However, other effects such as non-uniform fiber volume fraction within the tow and the ease with which the entrapped air can escape from the tow could also prove crucial as suggested by some of the experimental results.

KEYWORDS: Magnetic Resonance Imaging (MRI), experimental technique, Liquid Composite Molding (LCM), capillary flow, micro-scale flow

INTRODUCTION

In Liquid Composite Molding (LCM) processes, fiber preforms are placed in a mold and then impregnated with resin. The fiber preform consists of fiber tows woven or stitched together. Each fiber tow is made up of thousands of individual fiber strands grouped together in a bundle. The resin has to impregnate not only the empty spaces between the fiber tows but also the gaps between fibers within each fiber tow. The time to completely saturate fiber tows is usually much larger than the time to fill regions in between the fiber tows. Prior analytical work has investigated various aspects of capillary flow of resin through fiber tows. Nevertheless, analytical models are generally based on many simplifications of the tow geometry, as well as assumptions on the material and process parameters, considered constant in time or uniform within the space domain.

This paper is an abridgment of the work we have done, both analytically [1] and experimentally[2, 3]. Preliminary tests we conducted on large replicas of real fiber tows indicated that the analytical models which do not account for the entrapment of air during the capillary impregnation, underestimate the total fill time. Experimental investigations which we are going to detail below show significant discrepancy between the measured times of impregnation and the values calculated from an analytical

solution. These differences seem to be related to the presence of entrapped air and to whether it can dissolve in the resin and escape outward from within the fiber tow. Our first experimental setup inserted electric sensors inside a model tow that was submerged in a resin and recorded the arrival times of the liquid resin at a limited number of radial locations.
The resin arrived at these radial locations much more slowly than predicted by an analytic model so an amendment to the analytical model, to account for the opposing effect of air on the capillary impregnation is proposed to explain the discrepancy. This phenomenological model was subsequently verified using the experimental technique with embedded electric sensors and with a second non-intrusive experimental method, based on Magnetic Resonance Imaging (MRI). Our MRI setup captured the evolution of the 2D flow front interface, with a series of cross-sectional snapshots at selected time intervals.
A comparison between the two experimental techniques is presented, along with their capabilities and limitations. The experimental results show that non-uniformity in fiber volume fraction within the fiber tow and the ability of the air to dissolve in the surrounding liquid does play a significant role in the impregnation dynamics due to the action of capillary forces.

ANALYTICAL MODEL FOR RADIAL IMPREGNATION INTO FIBER TOWS

Our approach built on other analytical models of impregnation within cylindrical fiber tows [4-8]. We also assumed that the capillary impregnation evolved symmetrically only in the radial direction toward the center of the cylindrical fiber tow (Figure 1), and that longitudinal flow as well as body forces can be neglected.

a)

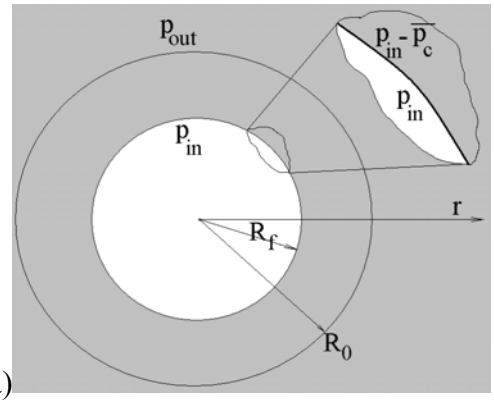

Figure 1. Geometric assumptions of tow impregnation solely by virtue of capillarity

We also derived an equation in finite differences for the more general case, where fiber distribution may vary in radial direction within the porous bundle and liquid parameters may vary in time during the process, as shown below and detailed in [1]:

$$\Delta t = -\frac{\eta(t)\cdot\left[\int_{R_f}^{R_0}\frac{1-V_f(r)}{r\cdot K(r)}dr\right]\cdot R_f}{p_{out}(t)-p_{in}(R_f)+\overline{p_c}(t,R_f)}\cdot\Delta R_f \qquad (1)$$

where t is time, R_f is the flow front radius, Δt and ΔR_f, are finite increments of the time and space coordinates, R_0 is tow's radius, r is the current radial coordinate used for integration, η is liquid's viscosity, V_f is the fiber volume fraction, K is transverse permeability, p_{out} is the pressure of liquid surrounding the tow, p_{in} is the pressure exerted by air opposing the flow, and $\overline{p_c}$ is the average capillary pressure. Some of these parameters can be identified in Figure 1.
If more simplifications are made, such as homogeneity of the porous material (uniform fiber volume fraction) and constant liquid parameters, then a closed form solution can describe the relationship between normalized coordinates time τ and flow front radius ε:

$$\tau = 1 - \varepsilon^2 \left(1 - 2\ln\varepsilon\right) \tag{2}$$

in which $\varepsilon = r/R_0$, r being the location of the resin front and R_0 is the radius of the fiber tow; $\tau = t/t_f^{(0)}$ is the nondimensional time, in which the characteristic time is the analytical fill time $t_f^{(0)}$,. The expression for fill time is given in literature for the ideal case where air does not oppose the capillary flow in any way, the driving pressure remaining constant and equal to the capillary pressure. That expression is

$$t_f^{(0)} = \frac{R_0^2 \cdot \eta \cdot \left(1 - V_f\right)}{4K \cdot \overline{p_c}} \tag{3}$$

where η is the resin viscosity, V_f is the fiber volume fraction, and K is the transverse tow permeability.

Preliminary experimental investigation

To check how well the above analytical model estimates the tow fill time, we conducted a few preliminary experiments by immersing large replicas of fiber tows (cylindrical samples made of aligned fibers) with five embedded electric sensors along the radial direction in a liquid to let capillarity impregnate the sample spontaneously, without any external application of pressure. The details of the experimental setup is described in the next section (also see Figure 5). Other experimental approaches previously carried out, where we looked for inspiration can be found in [9-12].
The results of these preliminary experiments revealed that the dynamics of the capillary impregnation was different from the analytical closed form solution given by Eqs. (2-3), which under predicted the real fill time as shown in *Figure 2* by a large margin. On the other hand, Eqs. (2-3) seemed to estimate the experimental fill time reasonably well in low-fiber volume fraction tows containing a perforated tube at the center that created an easy path for the entrapped air to escape.

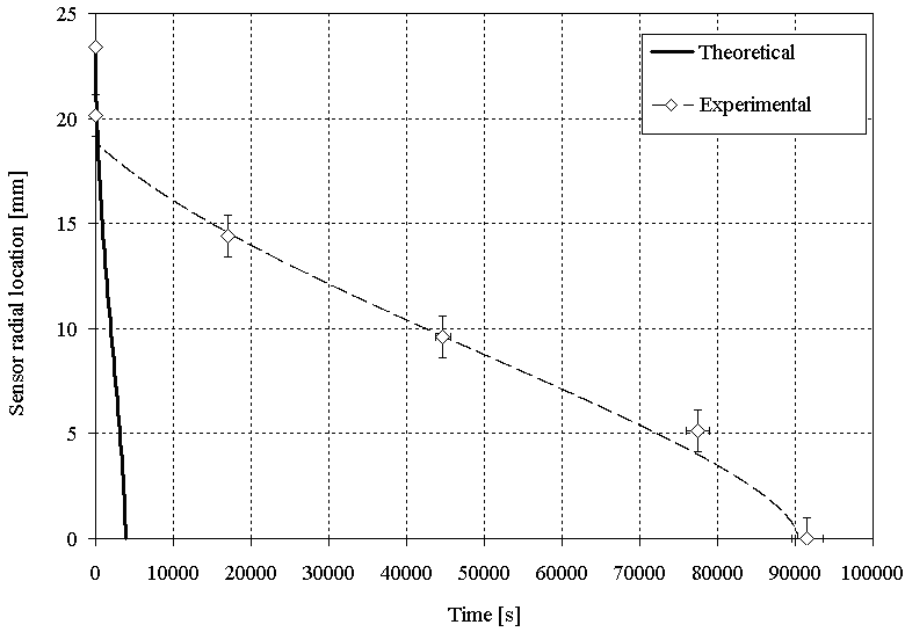

Figure 2. Flow front location vs. time recorded during a preliminary test conducted on a full sample of 70% fiber volume fraction and measuring 47mm in diameter. The dotted curve follows the experimental data points, while the continuous curve represents the analytical estimation, which does not account for the entrapped air effect

These seemed to strongly indicate that air presence and displacement during the capillary impregnation have an opposing effect on the overall dynamics of the process. Although it was observed and measured that during the liquid impregnation air does manage to escape from the sample as emerging bubbles, this was accompanied by a slow-down of the process.

Modification of analytical model

Based on the preliminary experimental findings, we modified the analytical model, to account for the role of air entrapment and displacement. For this purpose, we introduced a correction to account for a gradual loss of air during the inward capillary flow, which has a dual consequence: it lets the air to escape from the porous sample, but at the same time this air displacement slows down the capillary flow front, by exerting a backpressure on it. The proposed model also accounts for the two extreme cases: one, where air escapes outward without exerting any backpressure on the capillary advancement, is equivalent to the situation where air is absent from the tow (e.g. in vacuum assisted processes) and is the only case reflected by the previous simplified analytical model. The other extreme is when the whole quantity of inside air is trapped inside the fiber tow and completely stalls the capillary flow front after a short progression inward.
Without focusing on the exact mechanism of outward air motion, we proposed that there was a pattern for the rate of air loss, uniquely characterized by a scalar parameter δ, which in turn influences the actual fill time of the sample, always greater than the analytical estimation (Figure 3).
In [1], we gave detailed definitions and presented derivations for the rate of air loss and the subsequent fill times, which will not be reproduced here. One important remark is that the model we proposed accounts for both the case where air does not exerts any backpressure and does not slow down the capillary process at all ($\delta=0$) as well as the

other extreme, where air is being trapped inside of the porous sample and completely stops the capillary flow (δ=1) before it reaching the center (Figure 3).

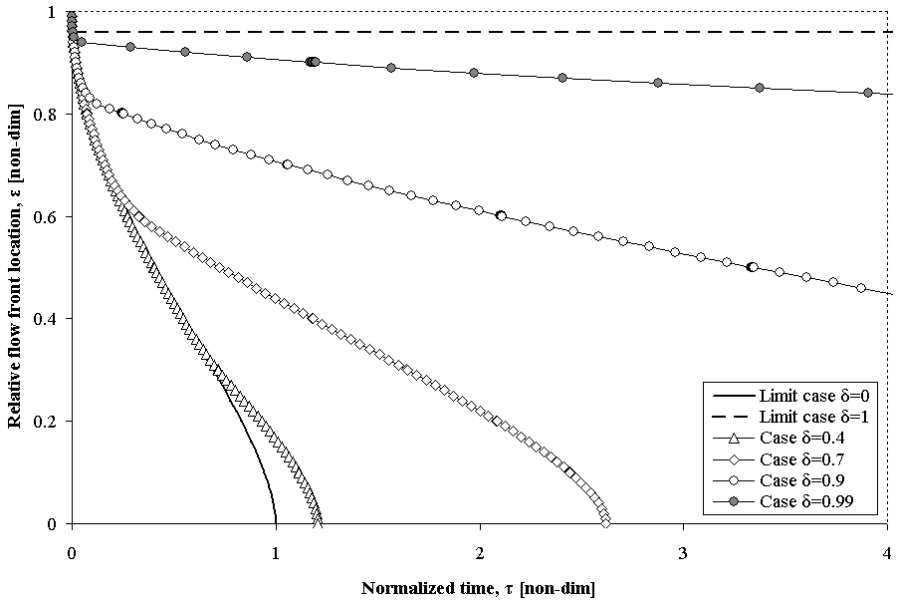

Figure 3. Flow front advancement profile, for several values of parameter δ, in dimensionless coordinates. Case δ=0 (no air effect) is the most favorable case for impregnation, whereas if δ=1 (trapped air), all inside air is compressed until impregnation stops. Any other intermediate value of δ gives a fill time larger than $t_f^{(0)}$

To validate the proposed model and to obtain more insight into what accentuates and what attenuates the opposing role of air displacement on the dynamics of the capillary impregnation, we used two experimental techniques to understand the role of different parameters in the mechanism that slows the impregnation process.
The samples used in both experimental approaches were of two types, as seen in Figure 4. The samples featuring a tube with perforations at the center (Figure 4b) will be referred to as 'hollow', being designed to provide the inside air with an easy escape route, without exerting any back-pressure to oppose the capillary flow front advancing inward. The other samples were 'full', as shown in Figure 4a. A complete description of the samples is provided in [2] and [3]. The two approaches are described in the next two sections.

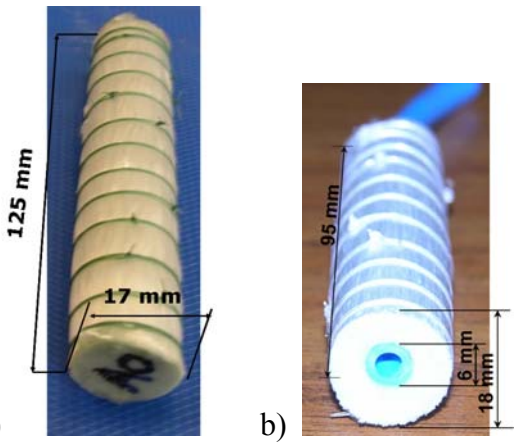

Figure 4. a) 'Full' sample of circular cross section; b) 'Hollow' sample with perforated inner tube, before ends were sealed

USE OF DISCRETE EMBEDDED ELECTRIC SENSORS

The first experimental setup we used, was based on measuring liquid arrival times at the locations of a few hand-made electric sensors inserted at selected radial locations in the samples (Figure 5a & b). The samples were immersed in a bath of liquid. Due to the electric conductivity of the impregnating liquid, each sensor circuit closed as soon as the liquid reached that location. The data acquisition system attached to the setup read the jump in voltage (Figure 5c) and identified that moment as the arrival time for the corresponding sensor. Because the sensors were perceived as possible sources of perturbations for the capillary liquid, their number was limited to five at the most. The sample diameters were approximately 50 mm, a couple of orders of magnitude thicker than the real fiber tows in composite manufacturing. Full descriptions of samples and tests are given in [2].

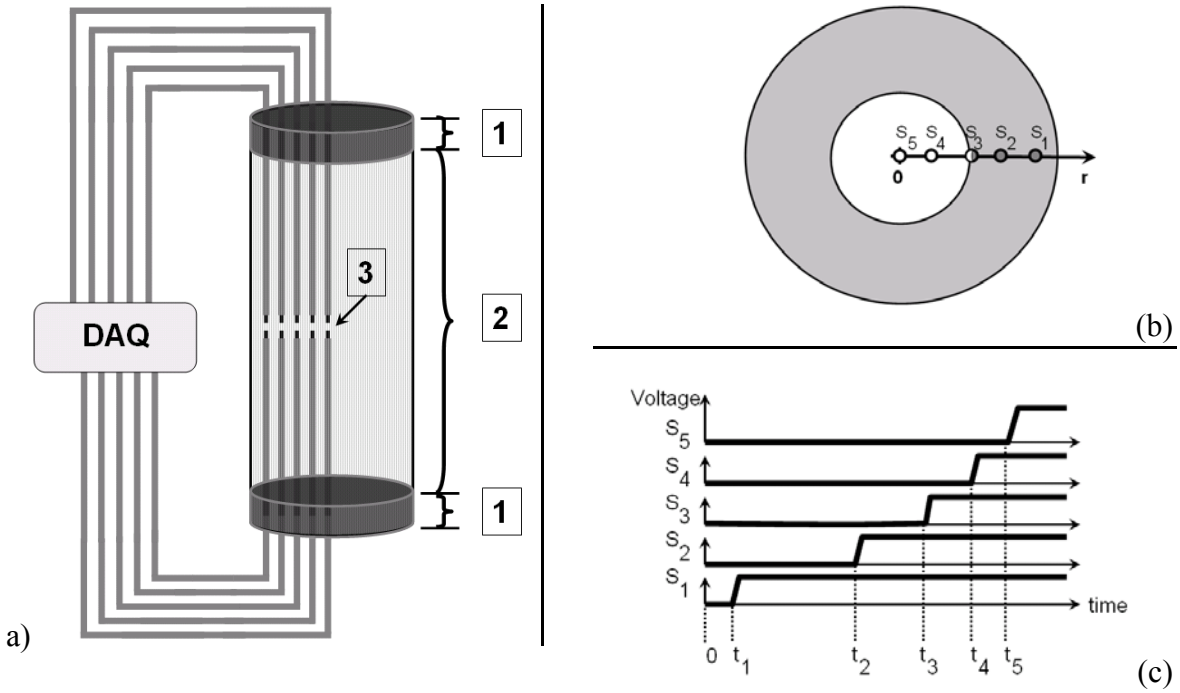

Figure 5 a) Sketch of the setup using electric sensors inserted at radial locations |3|. The cylindrical porous sample |2| and sealed at the ends |1| to minimize longitudinal flow. b) Sensor locations in radial direction S1-S5, shown in cross sectional view. The assumed circular flow front separates the grey (wet) and white (dry) areas. c) Sketch of the electric signals marking the arrival times at sensor locations.

A typical measurement obtained with this technique was presented in *Figure 2* where it is obvious that only few data points were recorded, with relatively significant errors. Among the drawbacks of the technique, its intrusiveness is the most glaring, as sensor wire is much thicker than the individual fibers in the fiber tow sample. Also, the distribution of fibers inside of the samples is perturbed locally by the insertion of the sensors, and this is another cause of concern, as the transverse tow permeability was estimated on the assumption of uniform distribution. In addition to this, not all sensors were identically triggered at the contact of the impregnating liquid, so that in some instances the voltage jumps sketched in Figure 5b were not that sudden, consequently making it more difficult to assess the real arrival time of liquid at the location of that particular sensor. At the same time, we found that the technique is not applicable to

smaller samples, because there is not sufficient room to insert more than one sensor at the center.
In spite of these shortcomings, we were able to use the electric sensors to determine that, arrival times at sensors locations in low-fiber-volume-fraction 'hollow' samples were comparable to those estimated using Eqs. (2-3). Conversely, for a set of 'full' samples made of glass fibers at 45% to 70 % fiber volume fractions, we found that increasing fiber volume fractions V_f are associated with higher values of parameter δ and fill time ratios, which indicate a more inhibiting role of the air escape/dissolution process onto the capillary impregnation. The results presented in Figure 6 show a quadratic trend of fill time ratios vs. V_f, trend well approximated with a R-squared value of 0.98.

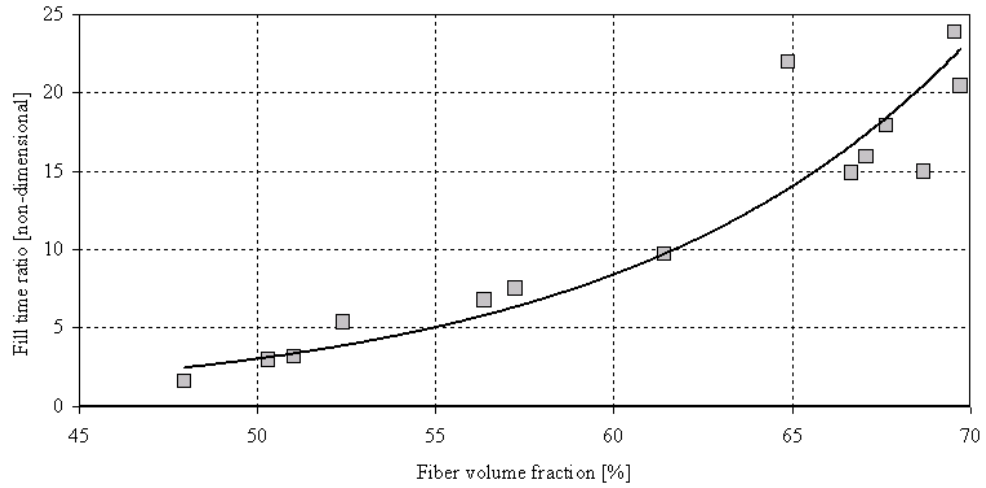

Figure 6. Effect of fiber volume fraction on fill time ratios (calculated by normalizing experimental fill times with respect to the theoretical predictions for the ideal case)

The drawbacks of the technique attracted us to a different approach – Magnetic Resonance Imaging, which is described below.

EXPERIMENTAL APPROACH USING MAGNETIC RESONANCE IMAGING

The primary reason we preferred using Magnetic Resonance Imaging to explore the impregnation dynamics, was due to its ability to yield a two dimensional image of the capillary flow front advancement at a relatively high sampling frequency. Using a Bruker DSX400 MRI spectrometer (by Bruker-Biospin, Rheinstetten/Germany) we were able to record images of the cross-sectional capillary flow front as often as once every 13 seconds. This allowed us to obtain not only a reliable dependence of equivalent flow front radius vs. time, but also to propose a quantification of the irregularity of flow front contour, in connection with the cross-sectional contour of the sample. More technical details on the MRI's applicability to liquid impregnation through porous material have been outlined in [13, 14], while specifics on our experimental study can be found in [3]. A sketch of the experimental setup is shown in *Figure 7*a. The image captured displays dark (dry fibers), grey (wet fibers) and white (surrounding liquid in the test tube) areas, as seen in *Figure 7*b.

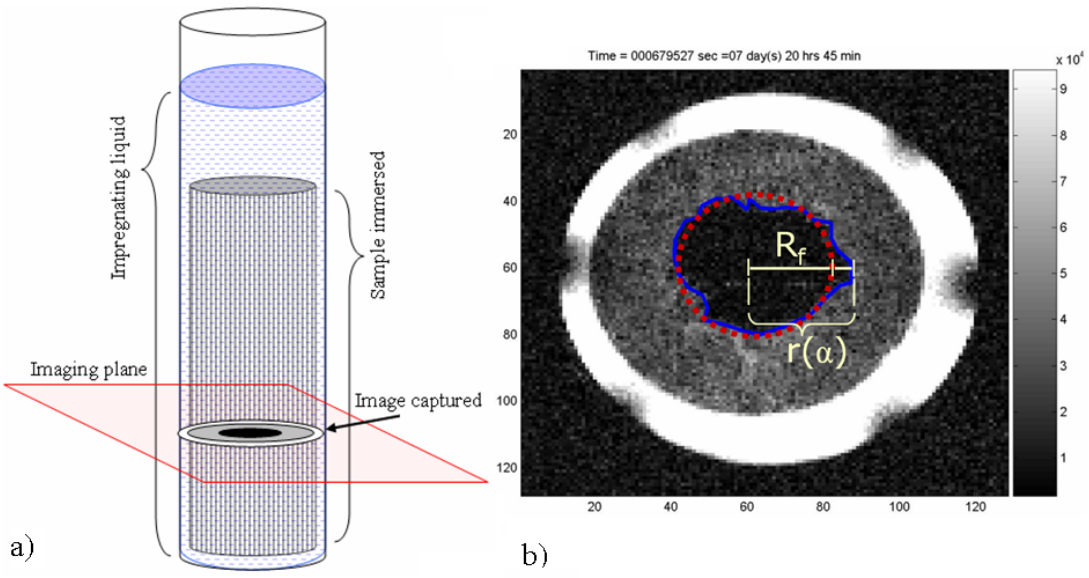

Figure 7. a) Sketch of the MRI setup. b) In addition to the equivalent flow front radius, MRI can also show how much the actual flow front contour (continuous curve) differ from the expected circular pattern (dotted circle).

After data recorded by the spectrometer in digital form are processed, the resulting sequence of frames can serve to generate the flow front advancement vs. time, as seen in Figure *8*a. Each data point on the plot corresponds to a frame recorded, but only selected frames are shown in the inserts in Figure *8*a, superposed on the experimental curve.

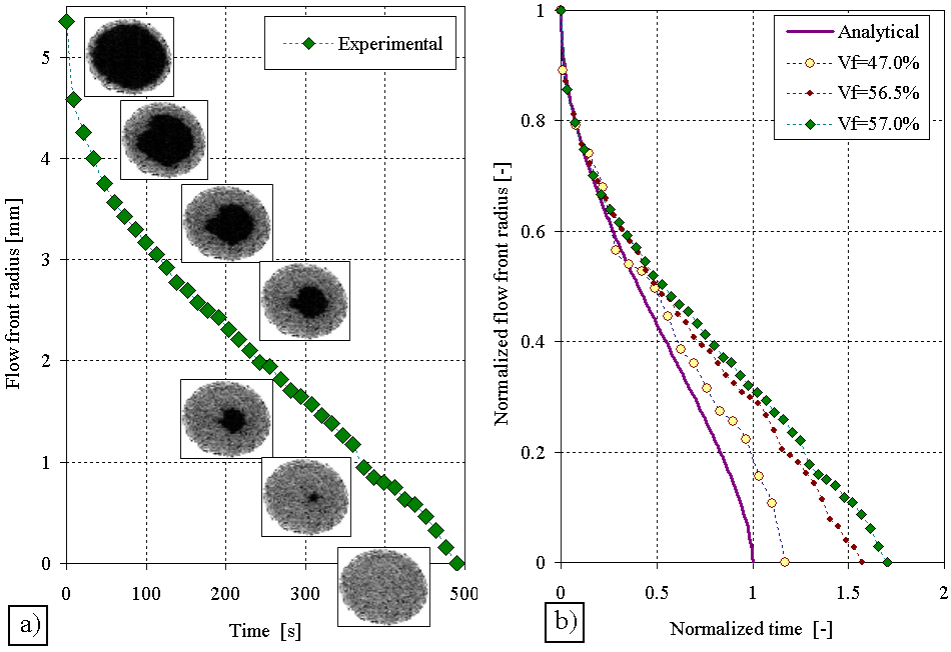

Figure 8a) Typical experimental curve of flow front dependence on time.
b) Experimental and analytical variation of flow front location ε(τ).

We used data recorded experimentally for several samples to generate the profile of capillary impregnation in non-dimensional units, where the flow front location was normalized with respect to the sample radius, and time was normalized with respect to the value of the "ideal fill time" t_f^0. It is important to specify that the value of this

characteristic time was not derived using Eq. (3), but instead the first few experimental points on plots similar to the one in Figure *8* were used to generate a curve fit of the type expressed by Eq. (2). This approach was based on the assumption that at the beginning of the capillary impregnation, the air does not manifest its opposing effect, and therefore the first stage of the impregnation can be safely approximated with Eq. (2).

This allows us to avoid the challenging aspects of correctly evaluating the transverse tow permeability, as required by Eq. (3). In Figure *8*b we have plotted a series of such experimental curves for a set of similar samples of various fiber volume fractions, along with the analytical curve [Eq. (2)], all in non-dimensional coordinates. It is noticeable in Figure *8*b that higher the fiber volume fraction, more significant is the role of the air in opposing the flow and slowing it down by exerting back pressure due to the compressed entrapped air.

Another benefit made possible by the high sampling ratio of the MRI data was that we were able to back-calculate the variation of air pressure inside the sample. As seen in *Figure 9*, a typical profile of the pressure difference $\left(p_{out} - p_{in} + \overline{p_c}\right)$ normalized with respect to capillary pressure $\overline{p_c}$, displays an constant trend at the start of the experiment, and then it decreases as the capillary impregnation progresses. This is an interesting aspect, which confirms the fact that air opposition can be neglected at the beginning, but it becomes significant toward the end of the process. Some oscillations of the pressure might confirm the findings of Young [15], who previously showed that the capillary meniscus moves in subsequent jumps across a bank of aligned fibers.

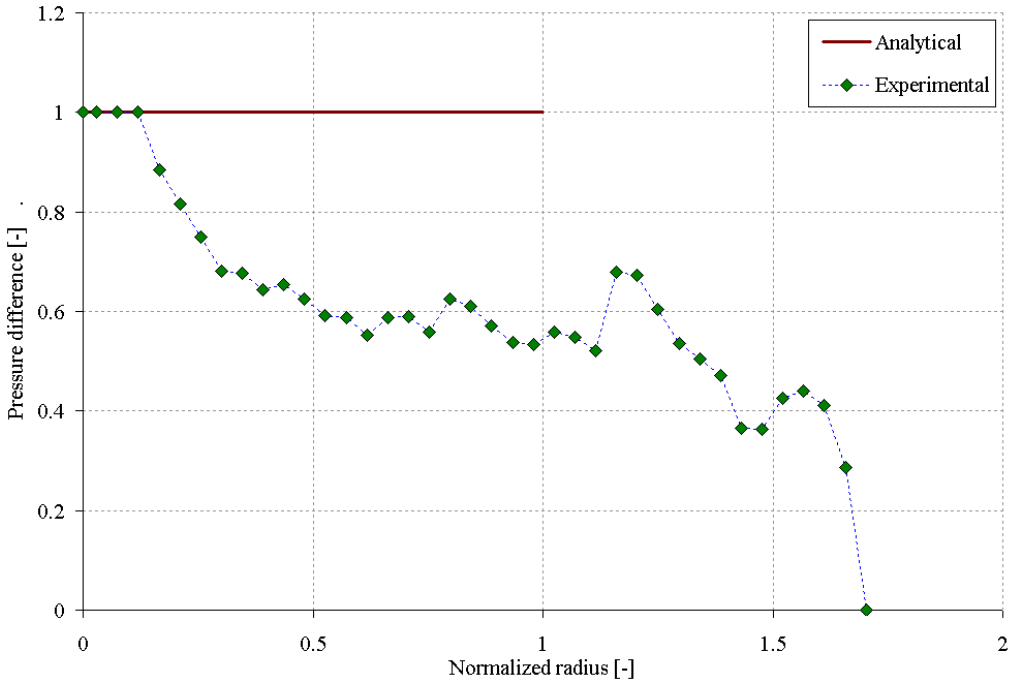

Figure 9. Typical profile of pressure difference driving the capillary flow, as determined indirectly from experimental data (normalized coordinates)

Another interesting finding of our MRI study was that the irregularity of the flow front, which we quantified by means of a parameter, increases during the capillary impregnation due to inherent non-uniformities in fiber distribution within the samples.

Moreover with MRI we were able to compare the dynamics of the capillary impregnation as influenced by the nature of the impregnating liquid. The results in

Figure 10 were already normalized by taking into account the viscosities of the liquids, so under ideal conditions one should not expect the viscosity to influence the solution as much as it does. However, we suspect that for the more viscous liquid (corn syrup), maybe the air dissolution or escape is much less probable as compared to water. Thus, the entrapped air is slowed down more significantly in the corn syrup case, where higher back pressure was caused by the compressed air.

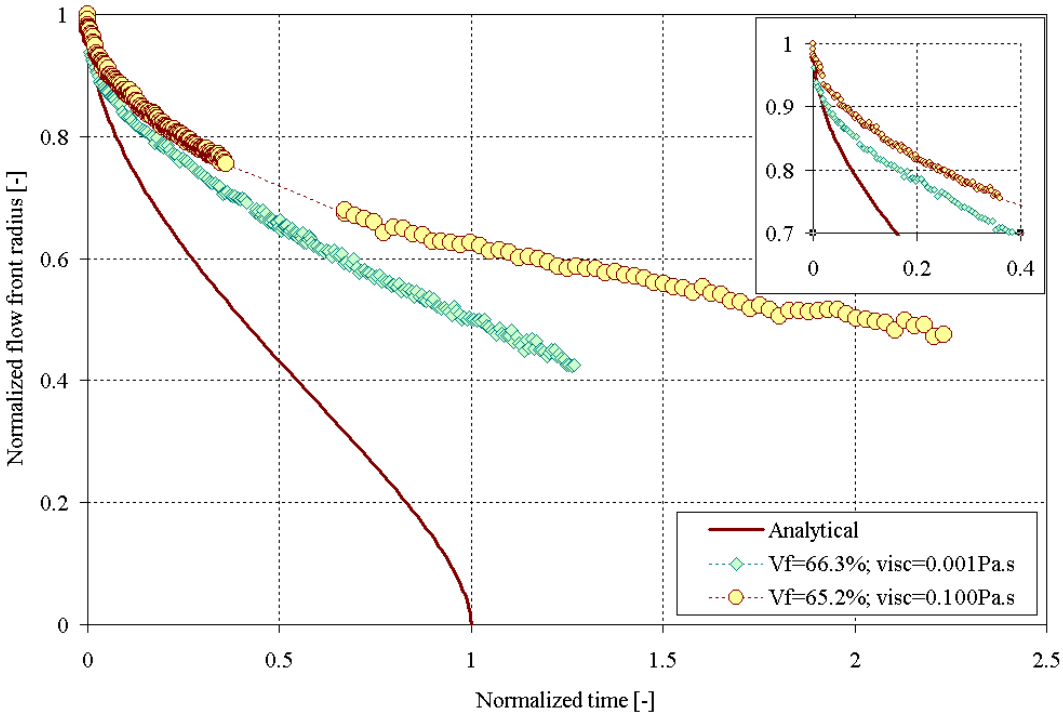

Figure 10. Comparative flow front advancement ε(τ) plotted against normalized time for two similar samples using corn syrup and water, respectively. The discrepancy suggests that the inhibiting effect of air becomes more prominent for the more viscous liquid.

More details on the results obtainable via MRI in capillary impregnation studies may be found in [3].

Our experimental study revealed that the foremost advantage of the MRI technique is that it can generate detailed data on the shape of the flow front in an non-intrusive way at a very high sampling rate, which could reliably recreate the capillary flow behavior within a porous sample. Thus for us, MRI confirmed our previous finding that higher fiber volume fractions intensify the opposing effect by entrapped air displacement, in addition it revealed the unsymmetric behavior of the capillary flow front.

The limitations of the technique include (i) MRI's inability to accommodate larger samples (the maximum diameter was 23mm, much smaller than the ones tested with electric sensors) or (ii) samples containing metallic elements, (iii) restrictions on the choice of testing liquid (necessarily rich in protons) and (iv) our MRI equipment's inability to test under different pressure levels, other then the atmospheric pressure.

CONCLUSIONS

We have shown that the study of capillary impregnation of fiber tows must account for the role of entrapped air. Our experiments, using two different techniques, one using electric sensors and the other using MRI confirmed that the role of entrapped air becomes more crucial with increasing fiber volume fraction. We compared the two procedures, and found that the former is intrusive and can provide a limited number of data values, while the latter yields detailed information related to visualization of capillary flow and indirect estimation of variation of air pressure inside the fiber tow during the process. MRI was also able to reveal the deviation from radial flow as assumed in the model. The experimental findings definitely shed more light on the fact that higher fiber volume fraction tows of large diameters can be difficult to evacuate completely of air and impregnate with resin.

ACKNOWLEDGMENTS

The authors acknowledge support from the US Office of Naval Research through the AMIPC grant N00014-05-1-0832, and from the US National Textile Center.

REFERENCES

1. V. Neacsu, A. Abu Obaid, and S.G. Advani, "Spontaneous Radial Capillary Impregnation Across a Bank of Aligned Micro-Cylinders - Part I: Theory and Model Development", *International Journal of Multiphase Flow,* vol., 2006, pp.
2. V. Neacsu, A. Abu-Obaid, and S.G. Advani, "Spontaneous Radial Capillary Impregnation Across a Bank of Aligned Micro-Cylinders - Part II: Experimental Investigations", *International Journal of Multiphase Flow,* vol., 2006, pp.
3. V. Neacsu, J. Leisen, and S.G. Advani, "Use of Magnetic Resonance Imaging to Visualize Impregnation across Aligned Cylinders Due to Capillary Forces", *Experiments in Fluids,* vol., submitted 2006, pp.
4. C. Binetruy, B. Hilaire, and J. Pabiot, "The Interactions Between Flows Occurring Inside and Outside Fabric Tows During RTM", *Composites Science and Technology,* vol. 57, 1997, pp. 587.
5. Z. Dimitrovova and S.G. Advani, "Analysis and Characterization of Relative Permeability and Capillary Pressure for Free Surface Flow of a Viscous Fluid across an Array of Aligned Cylindrical Fibers", *Journal of Colloid and Interface Science,* vol. 245, 2002, pp. 325.
6. N. Bernet, V. Michaud, P.-E. Bourban, and J.-A.E. Månson, "An Impregnation Model for the Consolidation of Thermoplastic Composites Made from Commingled Yarns", *Journal of Composite Materials,* vol. 33 (8), 1999, pp. 751.
7. K.J. Ahn, J.C. Seferis, and J.C. Berg, "Simultaneous Measurements of Permeability and Capillary Pressure of Thermosetting Matrices in Woven Fabric Reinforcements", *Polymer Composites,* vol. 12 (3), 1991, pp. 146.

8. K.M. Pillai and S.G. Advani, "Numerical and analytical study to estimate the effect of two length scales upon the permeability of a fibrous porous medium", *Transport in Porous Media,* vol. 21, 1995, pp. 1.

9. G.L. Batch, Y.-T. Chen, and C.W. Macosko, "Capillary Impregnation of Aligned Fibrous Beds: Experiments and Model", *Journal of Reinforced Plastics and Composites,* vol. 15, 1996, pp. 1027.

10. S. Chwastiak, "A Wicking Method for Measuring Wetting Properties of Carbon Yarns", *Journal of Colloid and Interface Science,* vol. 42, 1971, pp. 298.

11. S. Amico and C. Lekakou, "An experimental study of the permeability and capillary pressure in resin-transfer moulding", *Composites Science and Technology,* vol. 61 (13), 2001, pp. 1945.

12. M.E. Foley and J.W. Gillespie, "Modeling the Effect of Fiber Diameter and Fiber Bundle Count on Tow Impregnation During Liquid Molding Processes", *Journal of Composite Materials,* vol. 39 (12), 2005, pp. 1045.

13. J. Leisen and H.W. Beckham, "Quantitative Magnetic Resonance Imaging of Fluid Distribution an Movement in Textiles", *Textile Research Journal,* vol. 71 (12), 2001, pp. 1033.

14. J. Leisen, B. Hojjatie, D.W. Coffin, S.A. Lavrykov, B.V. Ramarao, and H.W. Beckham, "Through-Plane Diffusion of Moisture in Paper Detected by Magnetic Resonance Imaging", *Industrial and Engineering Chemistry Research,* vol. 41, 2002, pp. 6555.

15. W.-B. Young, "Capillary impregnation into cylinder banks", *Journal of Colloid and Interface Science,* vol. 273, 2004, pp. 576.

ACTIVE CONTROL OF THE VACUUM INFUSION PROCESS

D.K. MODI, M.S. JOHNSON, A.C. LONG and C.D. RUDD

School of Mechanical, Materials and Manufacturing Engineering, University of Nottingham, Nottingham, NG7 2RD, UK, E-mail: andrew.long@nottingham.ac.uk

ABSTRACT: Heterogeneity in fibrous reinforcements can lead to unforeseen, unpredictable and at times, problematic flow patterns. This necessitates the injection of additional resin into the mould to ensure complete part infusion, creating higher resin wastage. In many cases, resin starts to cure before the infusion is complete, leading to higher part rejections. To address this issue, a new active injection control system is proposed. In addition, a camera-based system is also proposed for flow monitoring in the Vacuum Infusion process. The control system is capable of monitoring resin flow, identifying flow disturbances and taking an appropriate corrective action in real-time, through computer-controlled injection ports. The system has been fully implemented in a computer code and is validated through infusion experiments.

KEYWORDS: Polymer Composites, Vacuum Infusion, Active Control, Image Analysis.

INTRODUCTION

Vacuum Infusion is a low cost process for manufacturing parts with large surface area to volume ratios. The process involves placement of cut reinforcement onto a solid mould bottom half, placement of vent and resin injection lines at pre-determined locations and sealing of the mould using a flexible mould top half. Many times, the reinforcement is also covered with materials to facilitate uniform vacuum pressure, resin flow and part extraction. The sealed mould is evacuated through vent lines which creates a driving potential for resin injection through the injection lines. The quality of manufactured parts, characterised by various mechanical properties, depends on the level of the reinforcement infiltration through resin flow [1]. Incomplete or partial infiltration of reinforcement can lead to dry spots, added salvage costs and many times, complete part rejection [2].

Many research efforts [3-6] have focused either on developing a fundamental understanding of the VI process or on applying current knowledge to design and develop modelling tools which replicate the process. The aim of such approaches is to reduce manufacturing costs, increase the part quality, and improve process reliability.

It is widely known that the reinforcement is heterogeneous in nature [2] and the level of heterogeneity varies with reinforcement architecture [7, 8]. In addition, the influence of heterogeneity depends on the reinforcement permeability. However, in general, the reinforcement is considered homogeneous for ease of modelling [2]. This generalisation, in addition to difficulties associated with reinforcement permeability characterisation, has led to limited success of these approaches.

Another alternative is to employ sensors to collect flow information and use this information for active control of the infusion process. This approach has been reported widely for the Resin Transfer Molding (RTM) process [9-11]. However, very few efforts [12, 13] have been reported for the VI process. Johnson and Pitchumani [12] proposed of producing localised changes in the infiltration rate through changes in resin viscosity. For this, an induction heat source was used. Based on the feedback from flow sensors, the location and the output of this heat source were controlled by a computer. The system was validated with numerical simulations. The system is limited to resin systems with long cure times.

Bender et al. [13] reported an injection system based upon active control of the injection flow rate. For this, the resin supply bucket was placed inside a pressure vessel. A fuzzy logic based controller altered the pressure inside the vessel. The system was validated using numerical simulations and experimental implementation.

The limited number of efforts aimed at controlling the VI process, is mainly due to large number of sensors required for flow monitoring. In addition to cost considerations, part intrusiveness is also a major factor. In this paper, we report the development of a low cost, non-intrusive flow sensing system. This system has been integrated with a flow simulation tool and other control hardware in an actual experimental set-up. Results from actual infusion experiments are also reported.

CONTROL SYSTEM

Design

The on-line control system developed in this work utilizes an image acquisition and analysis system to collect information about the flow progression inside a closed mould with at least one transparent side. This information is used to define the nodal fill-factors (initial conditions) for mould filling simulations. With a pre-defined set of port configurations (injection schemes or boundary conditions) and the initial conditions, mould-filling simulations are performed to predict flow advancement over the next time period. Then, the optimisation algorithm uses a pre-defined cost function to select an optimum injection scheme i.e. from the simulation results, a value of a cost function for each port configuration is calculated and the configuration with the lowest value of the cost function is relayed to the computer controlled injection valves to correct the flow deviations. The strategy is repeated during the entire infusion phase in a series of control steps. Figure 1 shows a flow chart of the system.

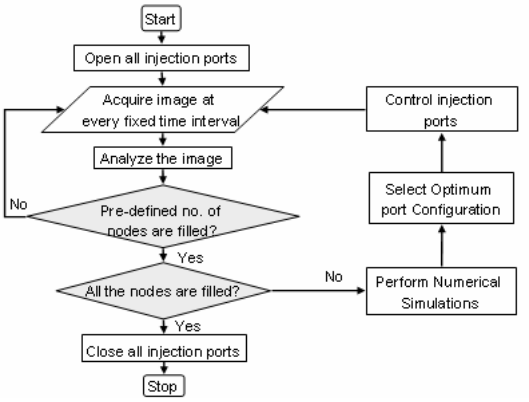

Figure 1 Flow chart of the control system.

Next, the development and implementation of each individual control step is reported for a model case study. The mould (Figure 2), in this case study, had four injection ports located in four corners, while the vent was located in the centre. It was packed with three rectangular layers (Figure 2 Region # 2), of one quarter the mould size, of bi-axial reinforcement (FGE 106, Table 1) sandwiched between two layers (Figure 2 Region # 1) of Continuous Fibre Random Mat (CFRM, Unifilo U750/450, Table 1).

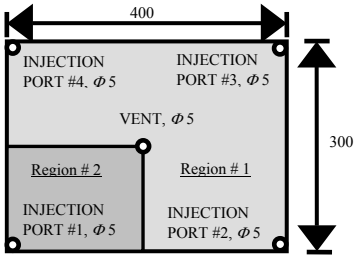

All dimensions are in mm.

Figure 2 Schematic of the mould used in the case study to demonstrate the development and implementation of the control system.

Image Acquisition and Analysis

Top side images, of the mould during the infusion phase, were captured using a web-camera (Fire-i™, Unibrain S.A.). The 640x480 pixels resolution images were captured at a fixed time interval of one second. Analysis of the captured images was performed in MATLAB™ using the native image analysis toolbox. The captured images were processed to select a region of interest. In addition, the images were processed to remove a perspective. Then, they were passed through an averaging and a high-pass filter to convert them into binary images. Note that the relative position of the camera with respect to the mould can vary between experiments. Hence, the entire image acquisition and analysis system was calibrated before the start of any experiment. Then, the stored calibration values were used during the actual infusion experiment.

Numerical Simulations

The flow advancement simulations in this work were carried out using LIMS. LIMS is a finite element/control volume (FE/CV) method based flow simulation tool, developed at the University of Delaware, the details of which can be found elsewhere [14].

Before starting the infusion, a set of sixteen simulation models, corresponding to the 16 individual permutations of the possible port configurations for four injection ports (Table 3 A), was generated. Each port can be in either an open or a closed configuration. In addition, the entire mould filling phase was divided into a number of equal control-steps such that in each step, a pre-defined number of nodes are required to be filled (a filled node lies in the infused region, while an unfilled node is outside the infused region). It is important to distinguish between a time-step and a control-step, which is a set of time-steps.

At the start of any control-step, the current flow front status in the experiment was used to describe the initial conditions (or nodal fill-factors) in all the numerical models. This was done by assigning the fill-factor of each node the same value as that of the corresponding pixel in the matrix of the binary image (Figure 3). Numerical simulations were performed to advance the flow in all models individually until the end of current control-step.

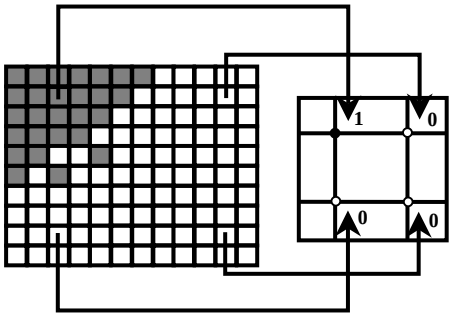

Figure 3 Definition of nodal fill-factors in the numerical model from the captured image.

Control Algorithm Design

To select an appropriate corrective action from the available choices, design of a port configuration selection strategy is necessary. This strategy involves defining a cost function as well as its preferred optimum value (maximum or minimum). Various cost functions such as fill-time, weight ratio of resin wasted via bleeding to the porous volume of the mould, distance between the centroid of an unfilled region and the vent (henceforth, denoted as the centroid scheme) etc. were considered. The centroid scheme, with minimum as the optimum value, was chosen as it indirectly reflects the other cost functions.

Figure 4 shows a schematic of the centroid scheme. Using the simulation results, the centroid of an unfilled region, and hence the value of the cost function (the distance between the centroid and the vent), was calculated for all port configurations. The configuration with the lowest value of the cost function was selected as an optimum injection strategy for the next step.

Hardware Interfacing

The optimum port configuration as selected by the control algorithm is relayed to solenoid valves, which control the resin injection and hence the infusion process. In this work, each injection port was connected to a solenoid valve (Type 6213, Burkert Contromatic) having a response time of 700 milliseconds. These solenoid valves were controlled by a computer

through a digital input/output board (DAQCard DIO- 24) and control modules (SSR series) from National Instruments.

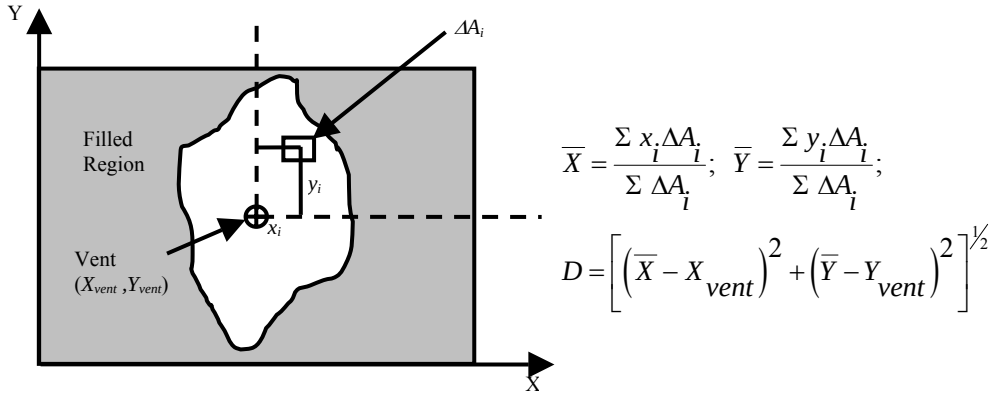

Figure 4 Calculation of distance between the centroid of an unfilled region and the vent. The port configuration with the minimum value of this distance is selected for the next control step.

Experimental Implementation

The experimental programme included four uncontrolled and controlled experiments. In the uncontrolled experiments, all the injection ports were simultaneously opened at the beginning of the infusion and closed at the end of the infusion. For the controlled experiments, the injection ports were computer controlled and the infusion was completed in eleven control steps, resulting in ten control actions. In all experiments, the mould was evacuated to 90 KPa vacuum pressure and the reinforcement layers were infused with hydraulic oil with a viscosity of 0.25 Pa s (at 23 ^{o}C temperature). The numerical model of the mould had 1271 nodes and 1200 quadrilateral elements. Elements in different regions of the mould were assigned different properties (Figure 2, Table 1).

Table 1 Material properties used in the numerical model for active control experiments.

Material	Permeability (m^2)	Fibre Volume Fraction	Thickness (m)
CFRM Unifilo U750/450 (Region 1)	1.00E-08	0.18	0.0015
CFRM Unifilo U750/450 + (-/+) 45 , FGE 106 (Region 2)	2.74E-09	0.412	0.0055

To compare the flow progression in various experiments, all the experiments were recorded with a camera. For quantitative comparison, three parameters were identified and monitored for each experiment. They were: (1) the distance between the vent and the centroid of an unfilled region when resin reached the vent, (2) the unfilled area (as fraction of the mould area) when resin reached the vent, and (3) the amount of resin bled through the vent, as fraction of the mould porous volume (calculated from the amount of resin injected inside the mould and the amount of resin bled through the vent), for complete infusion of the mould.

RESULTS

Results from the uncontrolled experiments show a delayed flow front in the thick region of the preform, which contains three layers of bi-axial reinforcement sandwiched between two layers of CFRM. The unfilled area, when resin reaches the vent, is considerably larger leading to larger resin wastage due to bleeding (Figure 5, Table 2). One can argue that readjustment of the vent position could lead to a reduction in resin wastage. However, as shown in Figure 5, the last point to be filled varies between experiments and it is difficult to predict a suitable vent position. In addition, a number of design factors can influence the selection of suitable vent locations [10]. Relocating vents may also be difficult for variety of reasons such as reworking costs for the mould. In such cases, it is still desirable to fill the mould with the current set-up without a major increase in the production costs or part rejection rates.

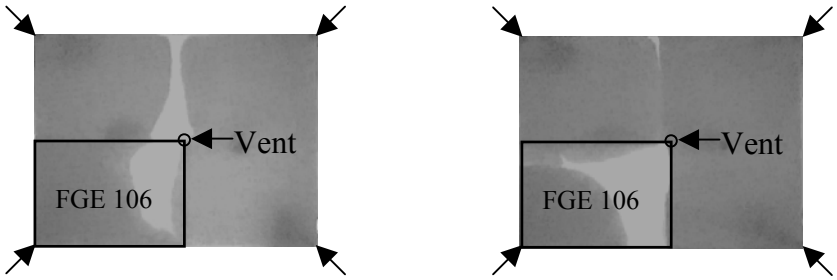

Figure 5 Flow front positions and unfilled region, when resin reaches the vent, in uncontrolled infusion experiments. The injection is from the four corner injection ports.

Table 2 Parameters characterising the efficiency of infusion experiments. Actively controlled experiments show significant improvements in the infusion efficiency as compared to uncontrolled experiments.

	Uncontrolled Experiments				Controlled Experiments		
	Distance (m)	**Area (%)**	**Resin Waste (%)**		**Distance (m)**	**Area (%)**	**Resin Waste (%)**
1	0.070	9.044	13.3	1	0.007	4.076	4.4
2	0.069	14.231	13.5	2	0.028	5.037	6.6
3	0.053	13.915	11.7	3	0.029	1.853	5.3
4	0.081	16.171	20.5	4	0.036	3.406	6.7

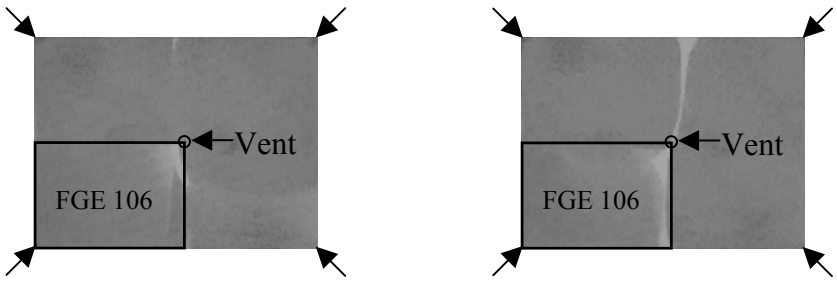

Figure 6 Flow front positions and unfilled region, in the controlled infusion experiments. The control system successfully identifies the flow deviations and implements appropriate corrective action, leading to reduced resin wastage and improved infusion efficiency.

Controlled experiments show considerable improvement in the flow front progression, and a smaller unfilled area when resin reaches the vent, reducing the requirement for resin bleeding as well as reducing resin wastage (Figure 6, Table 2). In addition, the control actions implemented by the system are different from experiment to experiment, which highlights the process variability (Table 3 A, B).

Table 3 (A) Possible port configurations for the mould used in the case study. (B) Port configurations selected by the control system to optimise the infusion process in actively controlled experiments.

(A)

	Injection Gate #			
	1	2	3	4
Port Configuration #				
1	Open	Open	Open	Open
2	Open	Open	Open	Close
3	Open	Open	Close	Open
4	Open	Open	Close	Close
5	Open	Close	Open	Open
6	Open	Close	Open	Close
7	Open	Close	Close	Open
8	Open	Close	Close	Close
9	Close	Open	Open	Open
10	Close	Open	Open	Close
11	Close	Open	Close	Open
12	Close	Open	Close	Close
13	Close	Close	Open	Open
14	Close	Close	Open	Close
15	Close	Close	Close	Open
16	Close	Close	Close	Close

(B)

	Experiment #			
	1	2	3	4
Control Step #				
2	8	8	8	8
3	8	8	8	8
4	4	4	8	8
5	3	11	4	4
6	11	2	2	10
7	2	2	3	9
8	10	1	7	5
9	9	11	3	11
10	1	2	3	11
11	3	2	1	1

CONCLUSIONS

Heterogeneity in fibrous reinforcements can lead to unforeseen, unpredictable and at times, problematic flow patterns. Hence, for full part infusion, it is necessary to continue resin injection, even after it has reached the vent. This results in resin wastage and longer fill-times. In some cases, resin may start to cure before the infusion is complete, leading to higher part rejections.

To address this issue, a new control system, complete with a flow monitoring and analysis system as well as computer controlled injection ports, was developed. Low cost web-cameras were used to capture images of the flow progression, which were then analyzed to identify flow disturbances. Using an infusion process simulation tool, the flow advancement was simulated to identify the optimum corrective action, which was implemented through computer controlled injection ports. All the steps of this control system were performed and implemented in real-time and were repeated a number of times during the infusion stage. Experimental results show that the control system is able to identify flow deviations and take corrective actions, resulting in reduced resin waste, and improved infusion efficiency.

ACKNOWLEDGEMENTS

This work is funded by the UK Engineering and Physical Sciences Research Council (EPSRC) via the Nottingham Innovative Manufacturing Research Centre (NIMRC). In addition, the University of Delaware CCM are thanked for the use of the LIMS code.

REFERENCES

[1] K. Kang, K. Koelling, "Void Transport in Resin Transfer Molding", *Polymer Composites*, Vol. 25, No. 4, 2004, pp. 417-432.

[2] S. Advani, "Flow and Rheology in Polymer Composites Manufacturing", Elsevier Publishers, Amsterdam, Netherlands, 1994.

[3] X. Sun, S. Li, L. Lee, "Mold Filling Analysis in Vacuum-Assisted Resin Transfer Molding. Part I: SCRIMP Based on a High-Permeable Medium", *Polymer Composites*, Vol. 19, No. 6, 1998, pp. 807-817.

[4] A. Hammami, B. Gebart, "Analysis of the Vacuum Infusion Molding Process", *Polymer Composites*, Vol. 21, No. 1, 2000, pp. 28-40.

[5] K. Hsiao, R. Mathur, S. Advani, J. Gillespie, B. Fink, "A Closed Form Solution for Flow During the Vacuum Assisted Resin Transfer Molding Process", *Journal of Manufacturing Science and Engineering*, Vol. 122, No. 3, 2000, pp. 463-475.

[6] J. Acheson, P. Šimáček, S. Advani, "The Implications of Fiber Compaction and Saturation on Fully Coupled VARTM Simulations", *Composites Part A*, Vol. 35, No. 2, 2004, pp. 159-169.

[7] T. Lundstorm, V. Frishfelds, A. Jacovics, "A Statistical Approach to Permeability of Clustered Fiber Reinforcements", *Journal of Composite Materials*, Vol. 38, No. 13, 2004, pp. 1137-1149.

[8] A. Endruweit, A. Long, F. Robitaille, C. Rudd, "Influence of Stochastic Fiber Angle Variations on the Permeability of Bi-Directional Textile Fabrics", *Composites Part A*, Vol. 37, No. 1, 2006, pp. 122-132.

[9] S. Bickerton, H. Stadefld, K. Steiner, S. Advani, "Design and Application of Actively Controlled Injection Schemes for Resin-Transfer Molding", *Composites Science and Technology*, Vol. 61, No. 11, 2001, pp. 1625-1637.

[10] B. Minaie, Y. Chen, A. Mescher, "A Methodology to Obtain a Desired Filling Pattern during Resin Transfer Molding", *Journal of Composite Materials*, Vol. 36, No. 14, 2002, pp. 1677-1692.

[11] D. Nielsen, R. Pitchumani, "Closed-Loop Flow Control in Resin Transfer Molding Using Real-time Numerical Process Simulations", *Composites Science and Technology*, Vol. 62, No. 2, 2002, pp. 283-298.

[12] R. Johnson, R. Pitchumani, "Simulation of Active Flow Control Based on Localised Preform Heating in a VARTM Process", *Composites Part A*, Article in Press (DOI: 10.1016/j.compositesa.2005.09.007)

[13] D. Bender, J. Schuster, D. Heider, "Flow Rate Control during Vacuum-Assisted Resin Transfer Molding (VARTM) Processing", *Composites Science and Technology*, Article in Press (DOI: 10.1016/j.compscitech.2005.12.008).

[14] P. Šimáček, S. Advani, "Desirable Features in Mold Filling Simulations for Liquid Composite Molding Processes", *Polymer Composites*, Vol. 25, No. 4, 2004, pp. 355-367.

VARIATIONS IN THE UNSATURATED FLOW WITH FLOW DIRECTION IN LIQUID COMPOSITE MOLDING

Tonmoy Roy[1] and Krishna M. Pillai [2]

[1] *Department of Mechanical Enginerring.*
University of Wisconsin,Milwaukee, WI 53211
roy@uwm.edu

[2] *Department of Mechanical Engineering.*
University of Wisconsin,Milwaukee, WI 53211
krishna@uwm.edu

ABSTRACT: Liquid Composite Molding (LCM) process includes different technologies used for producing polymer matrix composites. Resin Transfer Molding (RTM), widely used in the industry because of the good dimensional control, consistent quality and fast cycle time, is one such popular LCM technology. In any typical RTM process during mold filling, a thermoset resin is injected/sucked into a mold cavity with a pre-placed preform of fiber mats. The dual-scale nature of these fiber preforms gives rise to the unsaturated flow in RTM process which is characterized by a droop in the injection pressure history due to the delayed absorption of fiber tows (the `sink' effect). In this study, we experimentally investigate the effect of change in flow direction in an anisotropic dual-scale fiber mat on the unsaturated flow. A series of 1-D experiments involving constant flow-rate were conducted for the unidirectional stitched mats. The droop in the inlet pressure history, signifying the strength of sink effect, is found to be strongest for flow along the microchannels aligned with fiber tows. The droop, and hence the sink effect, is observed to weaken progressively for flow directions at 45^o and 90^o to the principal microchannel direction respectively.

KEYWORDS: LCM, RTM, mold filling, unsaturated flow, dual-scale porous media.

INTRODUCTION

Plastics reinforced with carbon or glass fibers form the polymer-matrix composite, which is gaining popularity in the automobile and aerospace industries due to their low weight and high strength. An increase in the fiber volume fraction increases the strength of the composite part. To achieve a high fiber volume fraction, it is essential that the fibers be arranged with predetermined regularity and packed as bundles of fibers. Liquid Composite Molding (LCM) which includes RTM, Vacuum Assisted Resin Transfer Molding (VARTM), Seemann Composites Resin Infusion Molding Process (SCRIMP), has emerged as an important technology for manufacturing polymer composites. In any typical LCM process, reinforcing fibers in the form of fiber preforms are placed in a closed mold, matrix material in liquid form is either injected under pressure or sucked into the mold due to vacuum to infiltrate the fiber mat. When the mold is full, the matrix material is allowed to undergo a solidification process before the final part is removed from the mold. For the thermoset type polymer-matrix

composites, the solidification process is a cross-linking reaction called curing that turns the resin into a hard brittle solid.

RTM is a widely used process for producing polymer matrix composites. A significant amount of work has been done in modeling RTM mold-filling process for optimizing the mold design [1]. Such numerical simulations are essential for predicting the optimum location of resin-inlets and air-vents in the mold, the resin injection pressure, the net clamp-force, and the optimum cooling-circuit design for controlling temperature in the mold during curing. Successful computer simulations are able to improve the mold design in virtual space without the need for the expensive and time-consuming trial-and-error approach to mold design.

PREVIOUS WORK ON UNSATURATED FLOW

In most mold-filling simulations, the resin flow during mold-filling in RTM in porous media created by fiber mats can be modeled by using the continuity equation and Darcy's law [2,3,4,5]. In most flow models, it is assumed that a sharp interface called front exists between the wetted and dry portions of the porous medium during the resin impregnation process and the pores behind the flow front are completely saturated with resin. This assumption leads to the use of the quasi-steady-state approximation for solving the resin pressure behind the moving flow-front in an RTM mold. However, some recent papers [4,5,6,8] show that, the assumption of complete saturation behind the flow-front is often inaccurate for the case when unidirectional, stitched or braided fiber-mats are used. These investigations show that the resin impregnation pattern in these mats is completely different from the pattern in random mats, which is characterized by full saturation behind the front. One idealized model of such fiber-mat architecture is shown in Fig. 1 below.

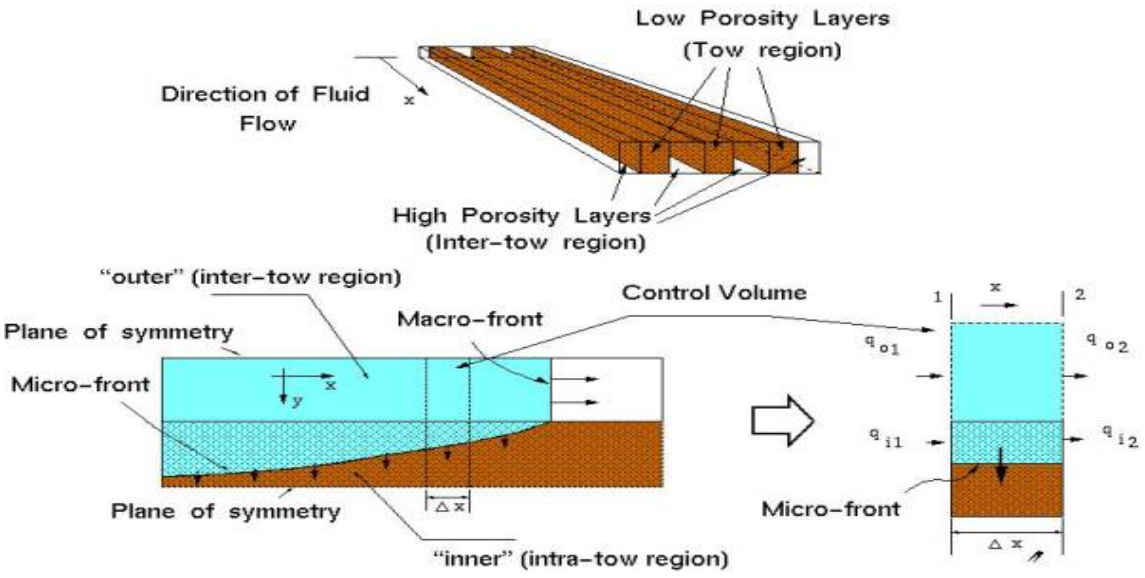

Fig. 1. Schematic of an ideal dual scale media showing intra-tow and inter-tow spaces and flow front propagation along the macro and micro channels.

Here the tows are made of thousands of individual fibers with inter-fiber distances of the order of micrometers, whereas the distances between the tows are the order of millimeters. This order-of-magnitude difference in length scales in the same medium lead to its classification as a `dual-scale' medium (Fig 2 A). Because of this dual-scale nature of fiber mats, when resin is injected into an LCM mold, it quickly passes through the inter-tow channel without impregnating the tows. After the front has passed, resin from the surrounding gap region continues to impregnate the tows. This delayed impregnation of tow leads to the unsaturated flow in LCM process as shown in Fig. 2 (B). It also causes a sink term S to

appear in the macroscopic equation of continuity $\nabla \bullet \mathbf{v} = -S$ for such dual scale porous media [5,11,12]. (**v** is volume averaged velocity.) This delayed impregnation is also behind the appearance of a `droop' in the inlet pressure vs time (inlet pressure history) plot for the constant flow-rate 1-D flow experiment [5,6,9]. Dimensionless parameters `pore volume ratio' and `sink effect index' based on previous flow models for dual scale porous media [5,9] have been successfully used to link the appearance of the inlet pressure droop to the sink effect caused by the dual-scale type microstructure of the fiber mats [8,10].

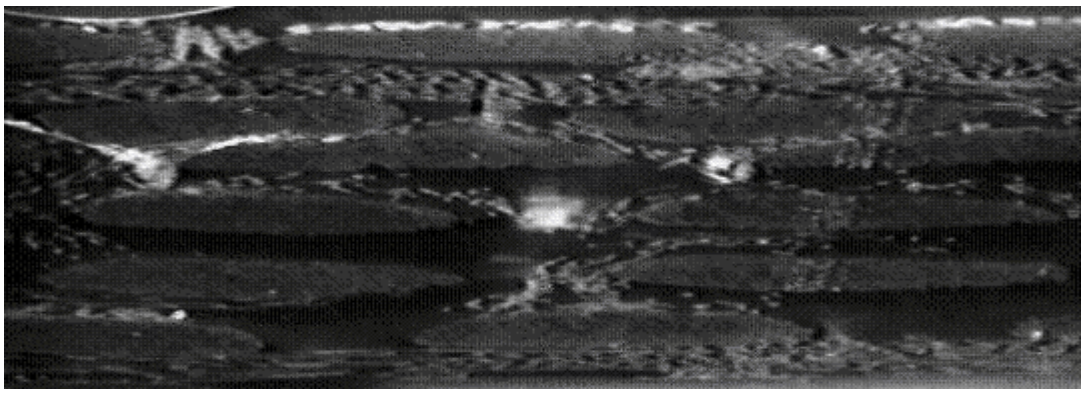

(A)

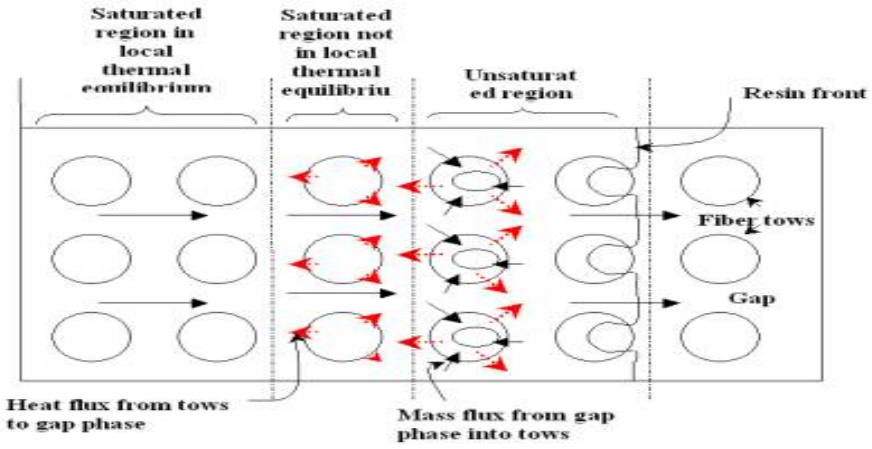

(B)

Fig.2: (A) A typical micrograph of an LCM part made from the directional fiber mats. The elliptical patches are the cross-sections of fiber bundles (or tows) consisting of thousands of a-few-microns-thick fibers. The dark spaces around the bundles are the large gaps surrounding the bundles. (B) Schematic describing the absorption of resin by fiber bundles behind the flow-front and creation of a sink effect

PROPOSED WORK

In this paper our aim is to study variation in the inlet-pressure droop, and hence the sink effect, due to changes in the flow direction within a dual-scale fiber mat. This will be first such study exploring the dependence of the sink effect on flow direction in an anisotropic dual-scale fibrous porous medium.

1-D FLOW EXPERIMENT

Fig. 3(A) shows the schematic of a simple 1-D flow experiment used for detecting the unsaturated flow. (The experimental setup is described in greater detail elsewhere [6,9,10].) In Fig. 3(B), a typical `drooping' inlet-pressure history, a characteristic of the unsaturated flow [6,10], is compared with the inlet-pressure predicted by the conventional physics after assuming full saturation behind a moving resin front. The linearly increasing portion of this theoretical pressure profile is predicted using

$$P_{in} = \left(\frac{Q}{A}\right)^2 \frac{\mu}{k_{sat}\varepsilon} t \quad \cdots\cdots\cdots(1)$$

where P_{in} the inlet pressure, k_{sat} is the saturated permeability of the preform, Q is the constant flow-rate, μ is the viscosity of the liquid, A is the cross-sectional area of flow, and ε is the porosity of the preform. Here Q is measured using a flow meter. The flow meter and Pressure transducer (for measuring ΔP) reading is gathered every after 0.6 seconds using National Instrument Data Acquisition/Lab view system). μ is measured using the Brookfield viscometer. ε is measured using the dipping experiment. In this experiment one sample of the fiber mat is dipped inside a calibrated jar, which is initially filled with water of known volume. Once it is dipped the volume change in the jar is recorded. So this volume is actually the fiber volume without any pores. Once this volume is known pore volume is calculated by subtracting the fiber volume from the total volume. So, porosity is pore volume/total volume. The parameters k_{sat} and $t_{fill\text{-}time}$ are estimated using

$$k_{sat} = \frac{Q\mu L}{A\Delta P} \cdots\cdots(2) \quad t_{fill-time} = \frac{\varepsilon AL}{Q} \quad \cdots\cdots\cdots(3)$$

where ΔP is the pressure drop across a length L under steady-state flow conditions and $t_{fill\text{-}time}$ is the filling time for the fiber mat. ($t_{fill\text{-}time}$ is the time after which the linerly increasing P_{in} in Fig 3(B) becomes the horizontal P_{in} = constant line.)

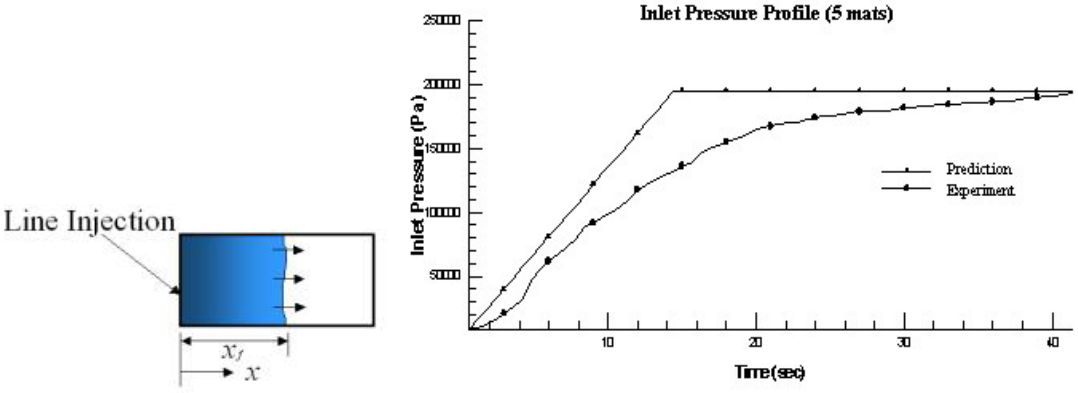

(A) (B)

Fig.3. (A) Schematic of a simple 1-D flow experiment. (B) Typical measured and theoretical inlet-pressure profiles for dual-scale fiber mats [6,8].

A few 1-D flow experiments were conducted using unidirectional fiber mats shown in Fig. 4. The main characteristic of these fiber mats is that the fiber tows are oriented in one direction only. According to the unsaturated flow theory, if these fiber mats are placed such that their tows are in the x-direction with flow taking place in this direction as well, then the

resin will flow easily through the inter-tow channels aligned with the fiber tows and the characteristic inlet-pressure droop (and hence the sink term magnitude S [8]) will be maximum along the x direction. In case of the flow being along the y direction in Fig. 4, which is perpendicular to the orientation of the x direction inter-tow channels, will see no such preferential flows and the inlet-pressure droop is expected to vanish, and hence S can be inferred to be reduced to zero.

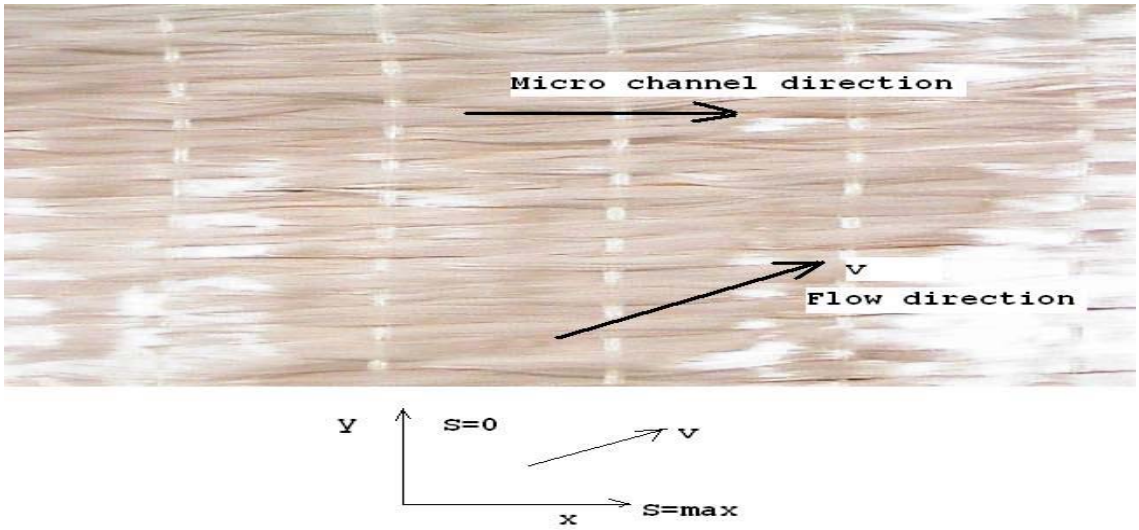

Fig 4: Unidirectional fiber mat and the anticipated directional dependence of the sink effect. (S is the magnitude of the sink term.)

RESULTS AND DISCUSSION

Three experiments were conducted: 1) flow along the x direction; 2) flow at 90^o to the x direction (i.e. along the y direction); 3) flow at 45^o to the x direction. Fig. 5 shows the inlet pressure profile when the flow is along the fibers tows (x) direction. Because of the high-pressure build up inside the mold, local distortions and shifting were observed in the mats, and which caused the inlet pressure profile to be rather tortuous. But the important observation is that there is a significant droop in the inlet pressure profile vis-à-vis the theoretical pressure profile.

In the second experiment, the flow is along the y direction such that preferential flow along inter-tow channels is absent. In such a situation, the flow is likely to behave like a flow in a single-scale porous medium (where no inter-tow channels exist) and the inlet pressure profile is expected to match the theoretical pressure profile. Fig. 6 shows the inlet pressure profile when the fiber tows in the mat are oriented perpendicular to the flow direction. Except for a little shift, which is due to the fiber rearrangement and reorientation, one can see that the inlet pressure plot more or less matches the theoretical pressure profile. But after reaching a maximum, the pressure gradually decreases because of the race tracking along the edges and slow slippage of the mats inside the mold. (Since these fiber tows are very flexible, they start to bow down under high inlet pressure creating some preferential flow path at the edges.)

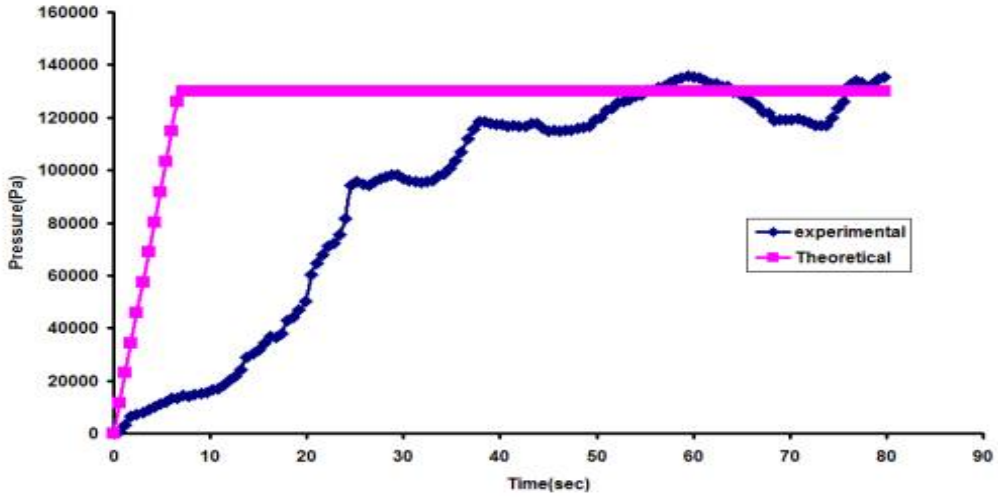

Fig.5. Comparison of the experimental inlet-pressure history with the theoretical prediction for the unidirectional mat when the flow is along its x direction

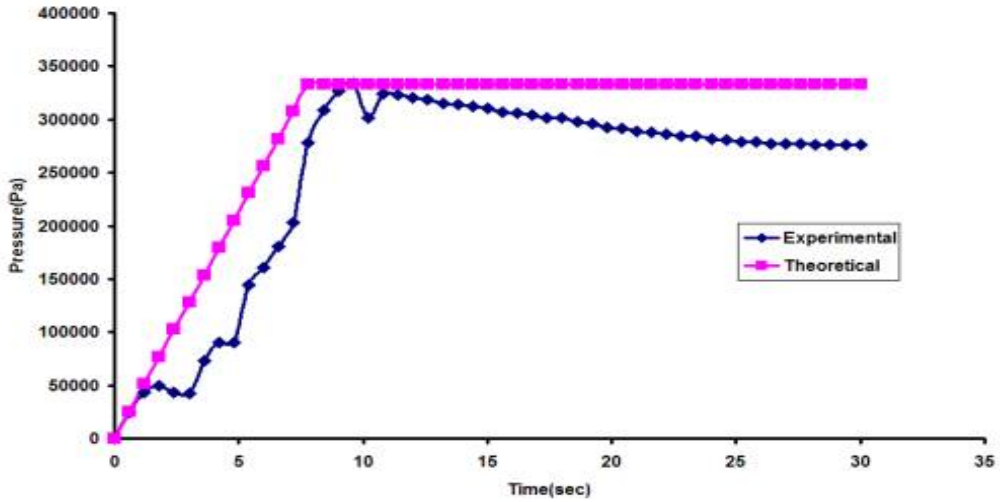

Fig.6. Comparison of the experimental inlet-pressure history with the theoretical prediction for the unidirectional mat when the flow is along its y direction

If these effects after the maximum point are neglected, one can say that the experimental pressure profile follows the theoretical one without the characteristic droop, and one can infer that the sink term S in the macroscopic continuity equation is zero. So clearly the sink effect for flow across fiber tows, as described simplistically in Fig. 2(B), does not work for this particular fiber mat! [A single-scale flow model involving saturated flow in a network of low and high permeability regions (Shih and Lee [13]) is perhaps a better representation of this cross flow.]

As these two above experiments are the two extreme cases of the sink effect (in the first case it's very large and in the second case it is negligible), we conducted another experiment where the flow was oriented at an angle of 45^{o} to the inter-tow channel direction to see if we get some intermediate sink effect. The theoretical and experimental pressure profiles for this case are shown in Fig. 7. It is clear from this figure that the inlet pressure plot has a small droop and a small sink effect can be inferred.

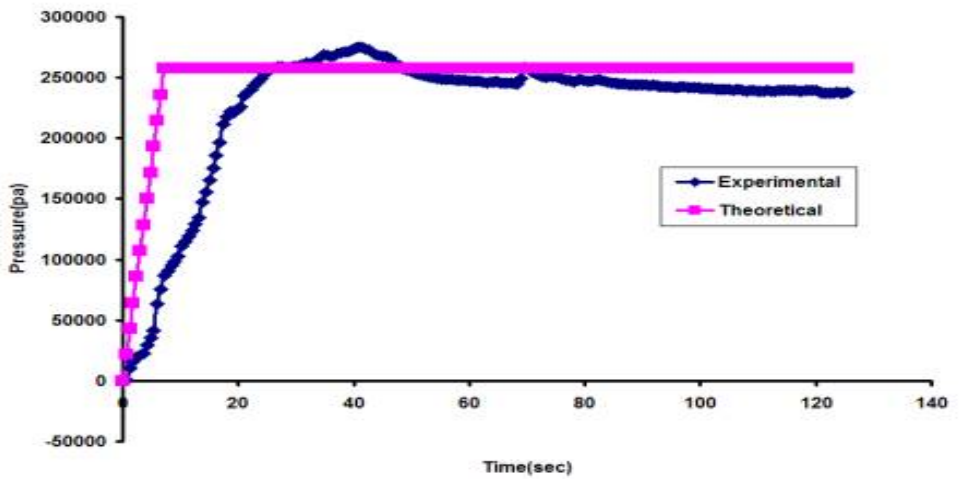

Fig.7. Comparison of the experimental inlet-pressure history with the theoretical prediction for the unidirectional mat when the flow is at 45^0 angle to x direction.

The above-described three experiments are summarized in Table 1. Here the length of the fiber mats, the mold cross sectional area, the test-liquid viscosity, and the porosity are kept constant at 0.254 m, 0.001715 m^2, 0.1875 N-S/m^2 and 0.6129, respectively. As can be seen from the saturated permeability column in Table 1, the permeability along the fiber tow (x) direction is 3 or 4 times more than the permeability across this (or y) direction. So this clearly points to the presence of inter-tow channels along the x direction as such channels are likely to increase permeability along their length.

The drooping of the inlet-pressure profile in case of the dual-scale fiber mats has serious implications as far as governing equations for temperature and cure are concerned. The curing of resin is often an exothermic process where the heat released seriously affects the local flow as a result of temperature and cure dependence of resin viscosities. These observations provide a strong justification for a new set of governing equations for dual-scale fiber mats proposed by Pillai et al. [11,12] where numerous source or sink terms are shown to appear in the governing equations as a result of applying the rigorous phase-averaging method. The current work suggests dependence of such terms on flow direction in an anisotropic dual-scale fiber mat and exploration of such dependence should prove to be a fertile research field in future.

Table 1: Different parameters associated with the three experiments

	Avg.Flow rate Q (m^3/sec)	Saturate pressure ΔP (Pa)	Saturated perm K_{sat} m^2 Eq (2)	Fill time (Sec) Eq(3)
Flow along the fiber	3.8417E-5	135392	7.708E-9	6.9
Flow across the fiber	2.869E-5	333802	2.387E-9	9.3
Flow at 45^0 angle.	3.7386E-5	250000	4.064E-9	7.1

SUMMARY AND CONCLUSION

The effect of fiber-mat orientation on the inlet pressure profile in a 1-D flow experiment was studied successfully. The dual-scale nature of the unidirectional fiber mats gives rise to the drooping inlet pressure profile during injection that deviates significantly from the

theoretically predicted profile. Such a droop is shown to vary with the fiber-mat orientation and appears to be strongest along the direction of the inter-tow channels. Future studies will be directed towards developing a direction dependent sink model for flow in the dual-scale fiber mats in RTM.

ACKNOWLEDGMENTS

The financial support for this work was provided by National Science Foundation of USA through its CAREER research grant (# 0348097). We would also like to thank Owens Corning Inc. for supplying the fiber mats used to conduct the experiment.

REFERENCES

1. Advani, S.G.(ed): *Flow and Rheology in Polymer Composites Manufacturing, Chapter Governing Equationsfor Resin Transfer Molding*,Elsevier,Amsterdam, 1994
2. C.A. Fracchia, J. Castro and C.L. TuckerIII, A finite element/control volume simulation of resin transfers molding. *In Proceedings of the American Society for Composites, Fourth Technical Conference*, Lancaster, PA: Technomic; p. 157-166.
3. M.V. Bruschke and S.G. Advani, RTM filling simulation of complex three dimensional shell-like structures. *SAMPE Quarterly*, **23(1)**, p. 2-11, (1991).
4. Richard S. Parnas and Frederick R. Phelan Jr. Effect of Heterogeneous Porous Media on Mold Filling in Resin Transfer Molding, *SAMPE Quarterly*, June 1990.
5. K.M. Pillai and S.G. Advani, A model for Unsaturated Flow in Woven Fiber Preforms during Mold Fillings in Resin Transfer Molding, *Journal of Composite Materials*, Vol 32, no 19, 1998.
6. B.Z. Babu and K.M. Pillai, Experimental investigation of the effect of fiber-mat architecture on the unsaturated flow in liquid composite molding, *Journal of Composite Materials*, Vol 38, No. 1, 2004.
7. Y.D.Parseval, K.M.Pillai, and S.G.Advani, A Simple Model for the Variation of Permeability due to Partial Saturation In Dual Scale Porous Media, *Transport in Porous Media*, Vol.27, p 243-264, 1997.
8. T. Roy and K.M. Pillai, Characterization of dual-scale fiber mats for unsaturated flow in liquid composite molding, Polymer Composites, Vol. 26, no. 6, p756-769, Dec 2005.
9. J.Slade, K.M.Pillai and S.G. Advani, Investigatioin of Unsaturated flow in woven braided and stitched fiber mats during mold-filling in Resin Transfer Molding, *Polymer Composites*, Vol 22, no 24, p 491-505 Aug 2001.
10. T.Roy, B.Z. Babu and K.M. Pillai, First steps towards quantitative validation of the unsaturated flow theories in Liquid Composite Molding, *Proceedings of ASME International: Summer Heat Transfer Conference*, Las Vegas , July 21-23, 2003.
11. "Governing Equations for Unsaturated Flow through Woven Fiber Mats: Part 1 Isothermal Flows", K. M. Pillai, *Composites Part A: Applied Science and Manufacturing*, v33, p 1007-1019, 2002.
12. “Governing equations for unsaturated flow through woven fiber mats, Part 2: Nonisothermal reactive flows”, K.M. Pillai and M.S. Munagavalsa*, *Composites Part A: Applied Science and Manufacturing*, v 35, p403-415, 2004.
13. C. Shih and L. J. Lee. Effect of Fiber Architecture on Permeability in Liquid Composite Molding. Polymer Composites, 19(5): 626-639, Oct 1998.

MONITORING AND CONTROL FOR LIQUID COMPOSITE MOULDING

Nikos Pantelelis[1] and George Maistros[2]

[1] *National Technical University of Athens, POBox 64078, 15710, Athens, Greece: pande@mail.ntua.gr*

[2] *INASCO Hellas, 17 Tegeas St., Argyroupolis 16452, Athens, Greece: g.maistros@inasco.com*

ABSTRACT: A dielectric monitoring system has been developed for the real-time sensing of composite manufacturing processes. In addition, optimised durable non-intrusive interdigitated dielectric sensors have been designed and manufactured for the sensing of resin arrival, viscosity changes and resin cure. The cure sensors receive the appropriate AC stimuli from the monitoring system while the feedback is recorded and processed by the system providing real-time material state-based information (viscosity, degree of cure etc.). The flow sensors receive DC stimuli for fast and accurate location of resin arrival. A combination of neighbouring flow sensors is capable of providing the flow front direction and velocity, which is a valuable information for flow control. Furthermore the flow sensors can sense the viscosity variations providing a useful indication for the cure evolution until gelation.

KEYWORDS: Dielectric measurements, durable sensors, cure monitoring, flow sensing, control.

BACKGROUND

Several algorithms for the automatic control of the filling phase e.g. [1, 2, 3] and the curing phase e.g. [4, 5, 6] have been presented in liquid composite moulding. However, it seems that there is still a lack of intelligent sensors that could provide more information to the control algorithms. The development of the present flow sensor has been based on the existing platform of the dielectric cure monitoring system VI-DiAMon developed by Inasco Hellas.

The dielectric process monitoring system, as shown in Figure 1, has been successfully compared with an off-the-self high-quality dielectric analyser in static and dynamic tests. The static tests showed the excellent performance of the system over a wide range of impedances and at measurements over the frequency range 0.2 Hz to 100 kHz. The use of this system for room and high temperature cured epoxy resins for everyday production proved its robustness and capabilities to detect the major process milestones: resin arrival, minimum viscosity, gel point and end of cure, as shown in Figure 2.

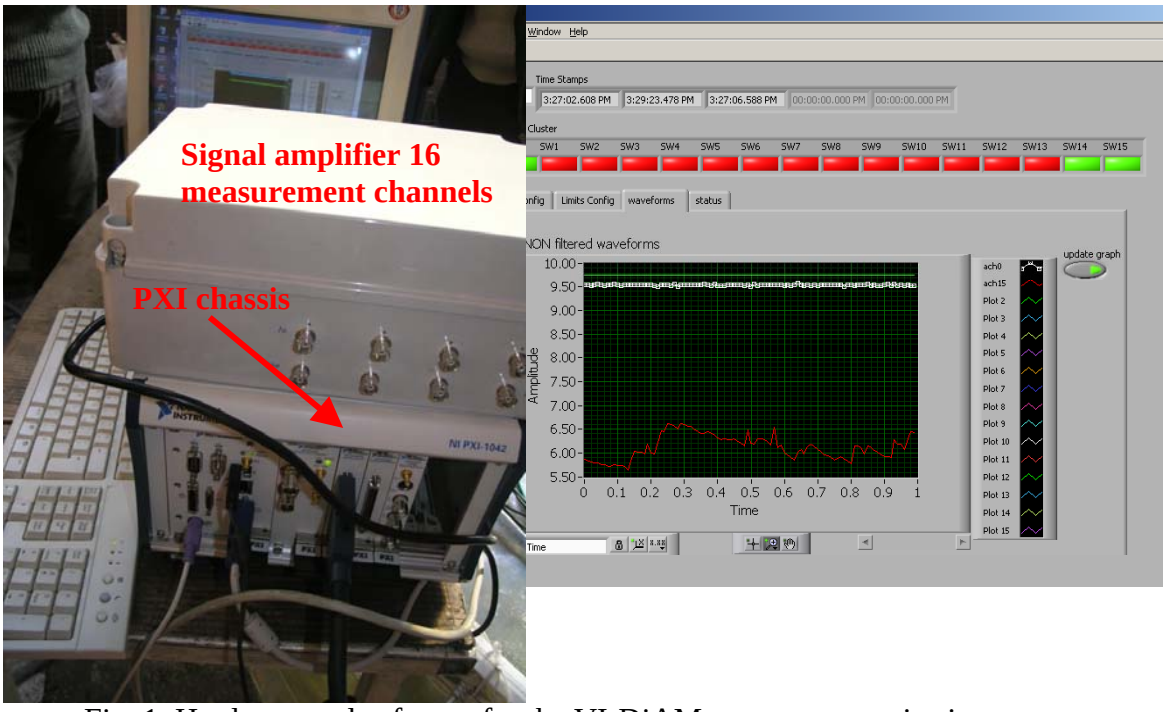

Fig. 1. Hardware and software for the VI-DiAMon process monitoring system

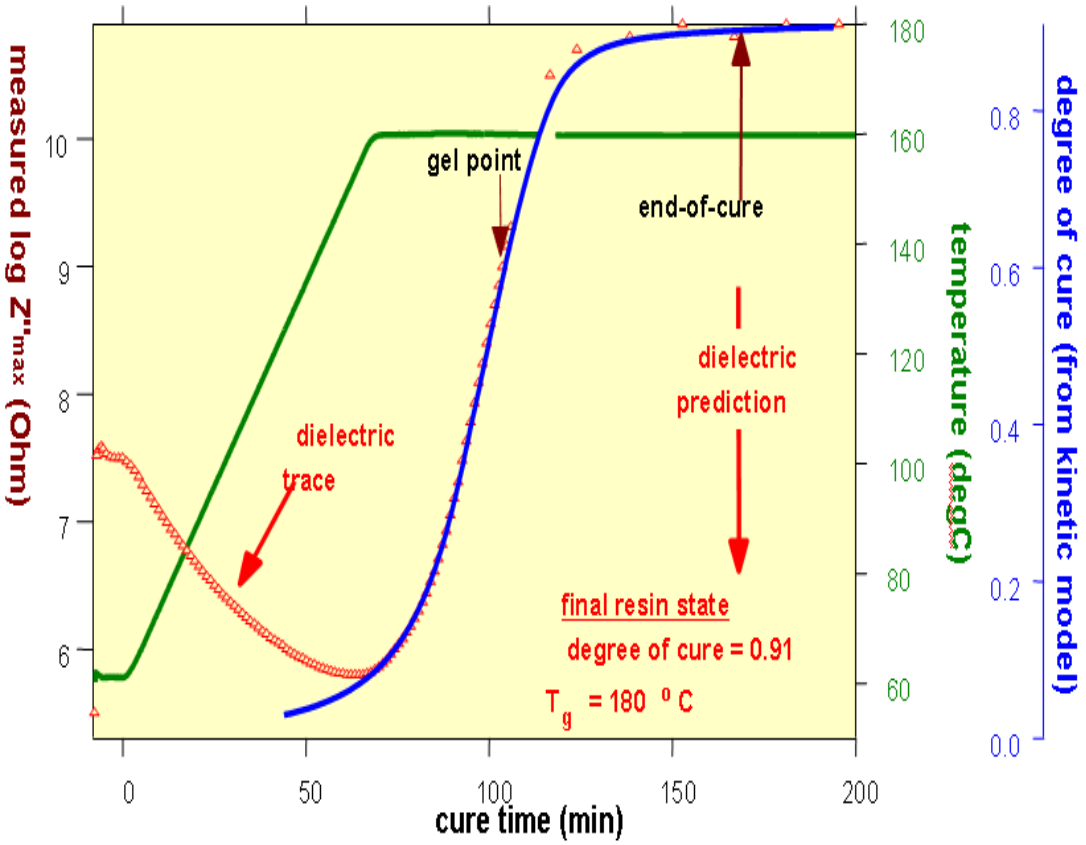

Fig. 2. Evolution of the VI-DiAMon dielectric signal (red line, left vertical axis), the kinetically estimated degree of cure (blue line, right vertical axis) for the RTM6 resin temperature profile (green line, right vertical axis).

In parallel, optimised durable dielectric sensors have been designed and manufactured as shown in Figure 3. Both the cure sensor (see Figure 3, left) and the integrated cure and flow sensor (see Figure 3, right) receive the appropriate (AC or DC) signals from

the monitoring system and their feedback is recorded and post processed by the system providing real-time material state-based information.

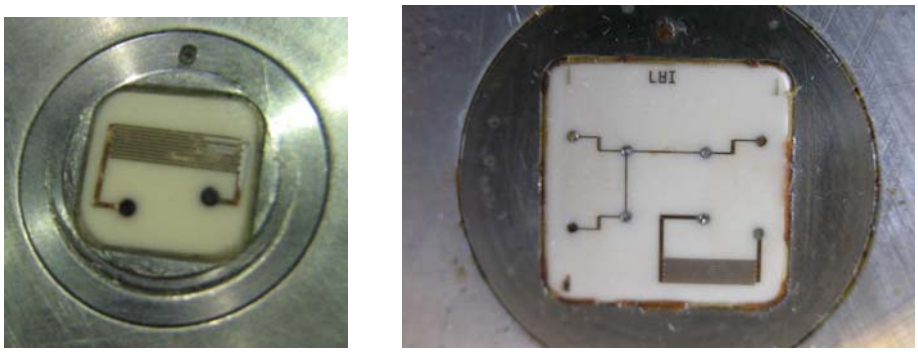

Fig. 3. A durable cure (left) and an integrated (right) dielectric sensors.

FLOW SENSING

In liquid composite moulding techniques there is a real need for sensors that not only inform the production supervisor with resin arrival at some location but also provide as much information as possible of what's happening inside the mould in order to use this information in a real-time control loop. As the installation of such sensors is not an easy task in real production environment, it is very important that one sensor can provide as much information as possible. So the new integrated sensor with flow and cure sensors shown in fig. 3 can provide information on:

- Resin arrival (flow sensor)
- Flow front velocity (flow sensor)
- Flow front direction (flow sensor)
- Viscosity changes (flow sensor)
- Gelation, Vitrification and end-of-cure (cure sensor)

The flow sensor comprises three couples of parallel contacts, which are fed with an appropriate DC signal and from the feedback of each couple resin arrival and viscosity changes can be detected. The hardware can scan the couples every 0.1 s so a very accurate time stamp of the resin arrival at the exact contact spot can be measured. As these contacts are very small the combination of three of them in an orthogonal triangle can provide the accurate calculation of the local velocity and the direction of the flow front using the formulae:

$$U = \sqrt{\frac{\left[\left(x_B - x_A\right)^2 + \left(y_B - y_A\right)^2\right]\left[\left(x_C - x_A\right)^2 + \left(y_C - y_A\right)^2\right]}{\left[\left(x_B - x_A\right)^2 + \left(y_B - y_A\right)^2\right]\left(t_C - t_A\right)^2 + \left[\left(x_C - x_A\right)^2 + \left(y_C - y_A\right)^2\right]\left(t_B - t_A\right)^2}} \quad (1)$$

$$\phi_x = 90^o - \tan^{-1}\left(\frac{\left(t_B - t_A\right)\sqrt{\left(x_C - x_A\right)^2 + \left(y_C - y_A\right)^2}}{\left(t_C - t_A\right)\sqrt{\left(x_B - x_A\right)^2 + \left(y_B - y_A\right)^2}}\right) \quad (2)$$

where x and y are the corresponding coordinates of each flow sensor's switches with respect to a common local (or global) coordinate system and t_i are the corresponding time stamps of resin arrival.

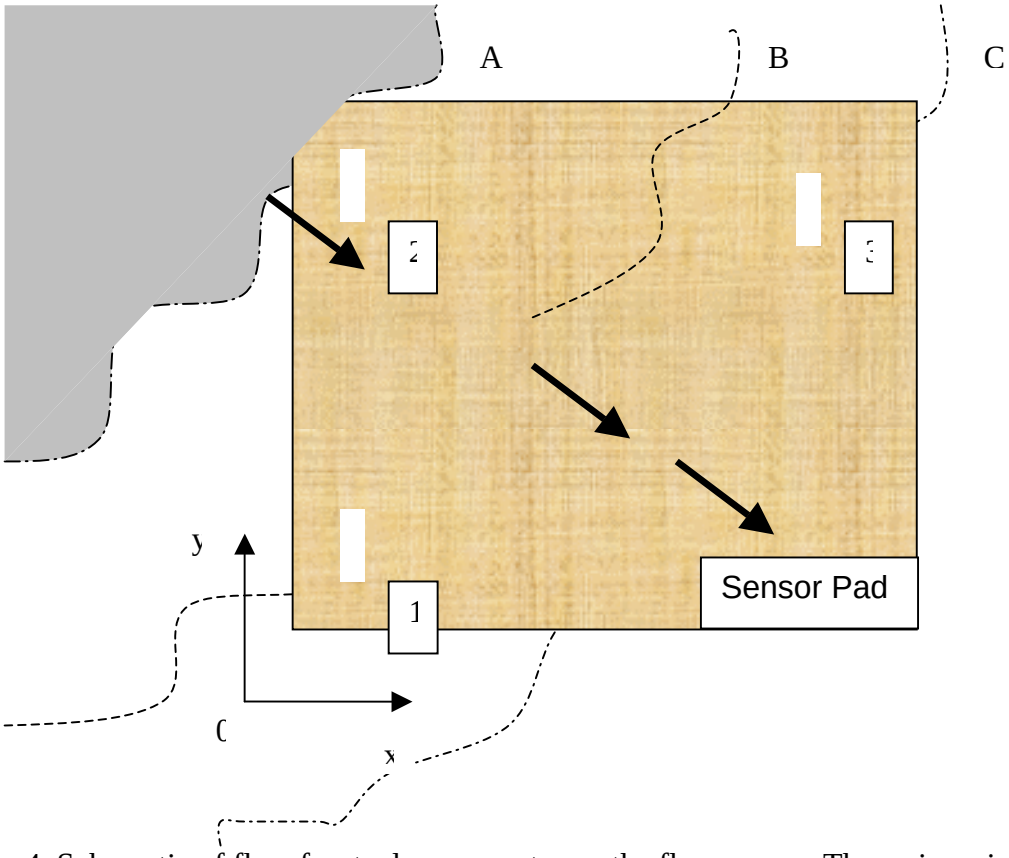

Fig. 4. Schematic of flow front advancement over the flow sensor. The resin arrival time stamps at flow couple locations 2, 1 and 3 are defined by instants A, B and C, respectively.

CONTROL ISSUES

The real-time availability of flow front velocity and direction can reveal valuable information for the current filling pattern and how fast the flow front evolves. Based on this information the supervisor or the automatic control software can make appropriate control actions if these are required. For example, if a dry spot area is expected at a specific region a flow sensor can be installed at an appropriate location in order to sense if there is an on-going formation of the dry-spot or it is a normal filling. In the case of dry-spot formation appropriate measures can be taken to restore the quality of the filling. For the model-based control which is under development for the automatic control of the filling process, the availability of such integrated information is very important for the performance of the control strategy.
Furthermore, the possibility of monitoring viscosity changes with the flow sensors provides a significant advantage as the cure measurements are particularly demanding of CPU and hardware requirements. In contrast, the use of DC-signal for flow sensing is much simpler and faster so various configurations are possible according to the production requirements.

RESULTS

In order to assess the robustness and the accuracy of the flow and cure sensors many trials have been executed with variable fibre volume fraction, type of fibres, type of

fabrics and resins for the two main closed mould liquid moulding processes, RTM and vacuum infusion.

Flow Front Sensing

In the case of vacuum infusion a small composite part with 6 heavy biaxial NCF glass fabrics were infused. As shown in figure 5 the resin enters from a line feeder on the right of the part whereas vacuum was applied on the left. Although the resin flow front seems evident due to the transparent vacuum bag this represents only the flow front at distribution media. Based on the feedback signal from a four-switch flow sensor installed at the bottom of the tool there is a significant time lag between resin arrival at the top and the bottom of the part. In figure 6, the feedback signal of the integrated sensor is shown, while, based on the formulae (1) and (2) the local flow front velocity has a magnitude of 0.28 mm/s speed and an angle of 60^{o} with respect to the local x-axis. The difference on the signal levels over the sensor contact points is due to the variability in the distance of the contacts of the prototype sensor.

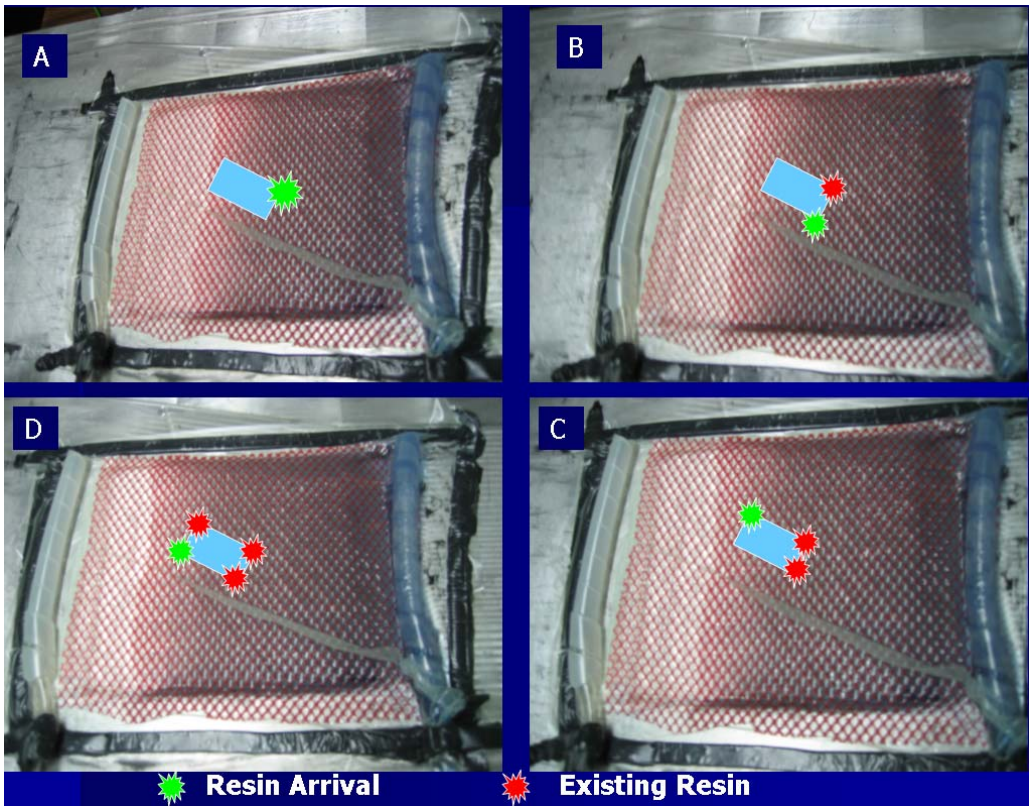

Fig. 5. A: Resin arrival at flow sensor point No 1, B: Resin arrival at flow sensor point No 4, C: Resin arrival at flow sensor point No 3, D: Resin arrival at flow sensor point No 2. The points are located on the sensor as indicated in Figure 6.

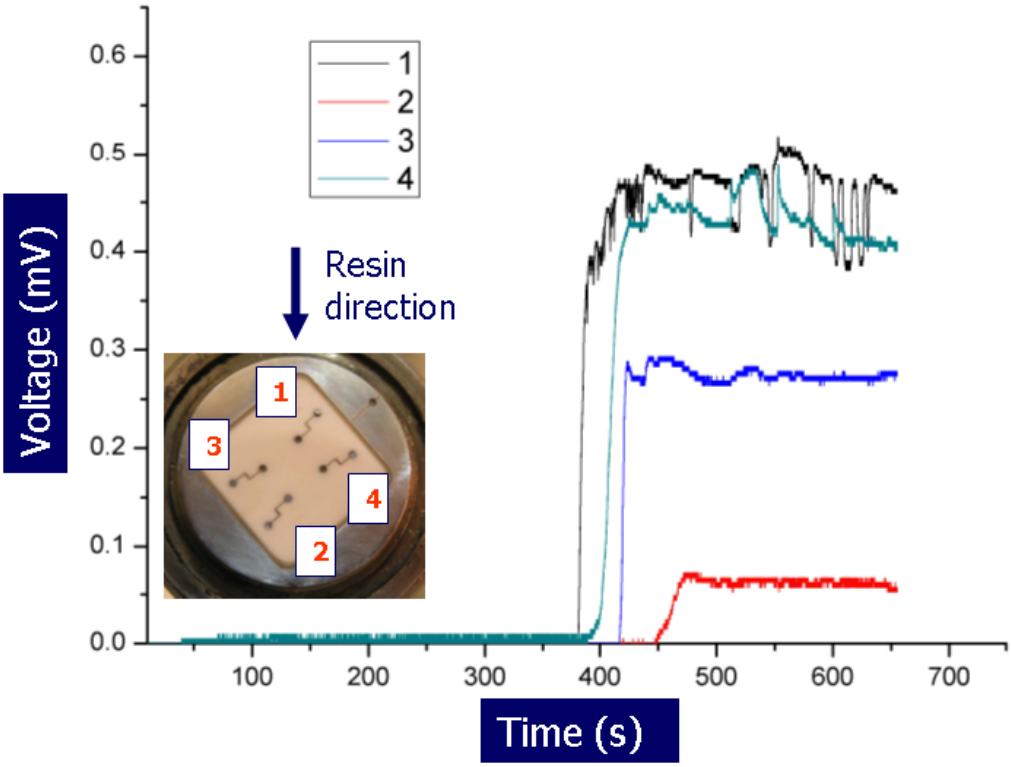

Fig. 6. DC feedback signal monitored at the four switches on a flow sensor during the resin injection.

Viscosity Changes

When the flow front has passed over the flow sensors, they continue supplying important information, such as the resin viscosity changes at the location of the sensor contact points. In case there is no cure sensor involved, this information is particularly useful as it provides a reliable indication of the hardening of the resin up to the gel point. This capability can be seen in fig. 7 at the monitoring the cure reaction of an epoxy single component system (Cycom 890 by Cytec) initially for 20 min at 80°C and then a heating ramp with 1°C/min. As the resin viscosity drops towards the maximum flow point the cure sensor shows a continuous drop of the max imaginary impedance whereas the three flow couples (switches 1, 2 and 3) show a continuous increase of the voltage measurement resulting from the reduction of the apparent resistance of the resin. After the maximum flow point the viscosity starts to rise again so the corresponding feedback signals from the flow sensor decrease while that of the cure sensor increase.

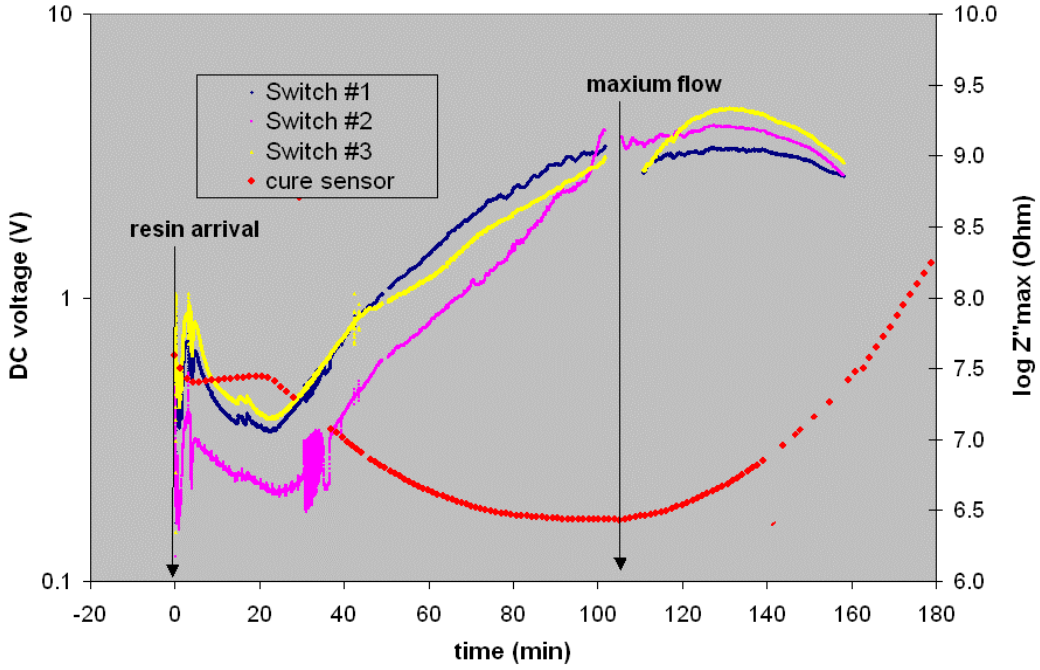

Fig. 7. Feedback signals at three flow sensing (left axis) and one cure sensing (right axis) locations on an integrated sensor during resin injection and isothermal curing of the Cycom 890 Cytec epoxy resin.

In fig. 8 a much faster epoxy resin has been tested using the same integrated sensor during injection and isothermal curing. In this case there is no maximum flow point observed but as the viscosity increases there is a steady decrease of the flow sensors signal in contrast to the continuous rise of the cure signal. As expected the flow sensors signal levels are nullified after gelation, so that vitrification and end-of-cure monitoring can be performed only by the cure sensor.

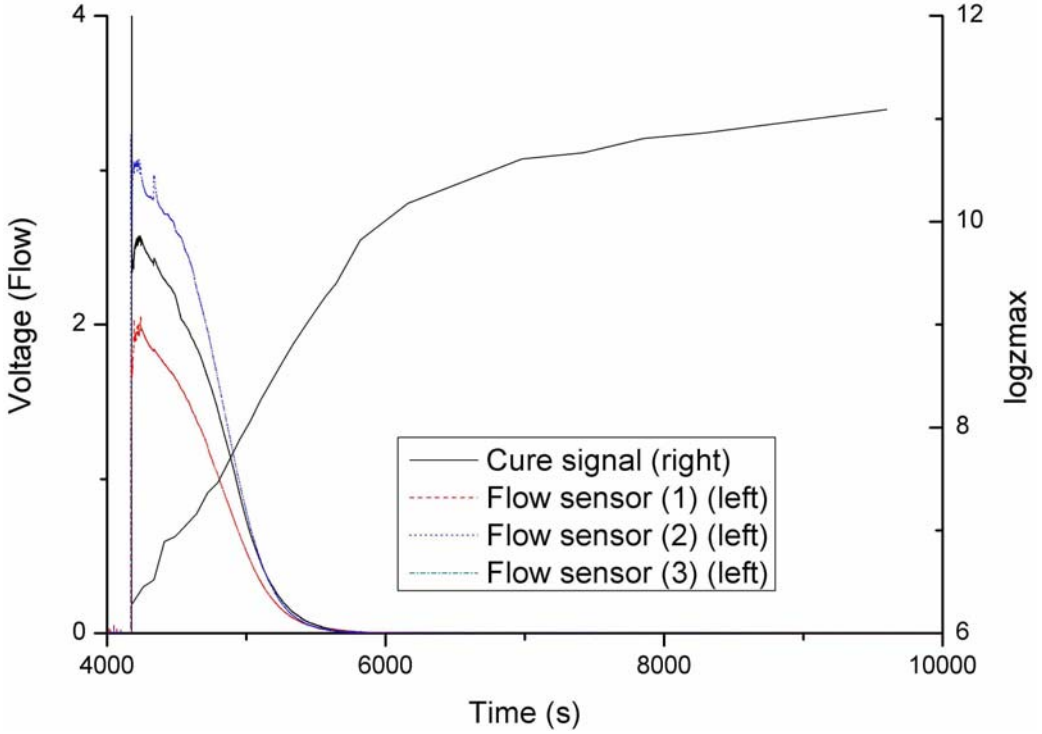

Fig. 8. Feedback signals at three flow sensing and one cure sensing locations on an integrated sensor during resin injection and curing for a fast-reactive two component epoxy system.

For the handling of carbon fibre parts, a non-conductive fabric of appropriate thickness should be used over the cure sensor to avoid short-circuit of the dielectric field. However, the flow sensor is not affected so much by the existence of carbon so a very thin non-conductive fabric is enough to provide robust measurements.

DISCUSSION

Valuable information of the processing status has been provided by the newly developed integrated flow and cure sensor with the relevant hardware and software. The sensor is robust, non-intrusive and durable providing a reliable basis for real-time control.

This information will be combined with a model-based control algorithm developed in parallel within the same project and will provide an intelligent system for the automatic and optimal processing of composite materials.

REFERENCES

1. M. Devillard, K.-T. Hsiao, S. G. Advani, Flow sensing and control strategies to address race-tracking disturbances in resin transfer molding—part II: automation and validation, Composites Part A, 36 (2005) 1581–1589.
2. J. Li, C. Zhang, R. Liang, B. Wang, Statistical characterization and robust design of RTM processes, Composites Part A, 36 (2005) 564–580.
3. D. Nielsen, R. Pitchumani, Intelligent model-based control of preform permeation in liquid composite molding processes, with online optimization. Composites Part A, 32(12), 1789–803.
4. N. Pantelelis, Towards the dynamic optimization for the cure control of thermoset-matrix composite materials, Composites Science and Technology, 65/7-8 (2005), pp. 1254-1263
5. N. Pantelelis, G. Maistros, Online Cure Parameter Identification Using Neural Networks and Dielectric Sensing, in: "2003: Advancing Materials in the Global Economy: Applications, Emerging Markets and Evolving Technologies", Proceedings of the 48th International SAMPE Symposium, Vol. 48, (L.J. Cohen, C-L. Ong and C.P. Arendt, eds.), SAMPE Publishing, pp. 353- 366.
6. G. Maistros, N. Niakas, N. Pantelelis, Intelligent process control for liquid composite moulding, presented at the 12th International Conference in Composites Engineering, Tenerife, August 2005.

ACKNOWLEDGEMENTS

The work has been partially funded by the European Commission under FP6 contract No. AST3-CT-2003-502900 (COMPROME). Special thanks to the partners IAI, Bombardier-Shorts, Technika Plastika, KEMA, KVE, Inasmet, Polyworx and LZH for collaboration and paper clearance.

Session 7

APPLICATIONS

COMPOSITES IN HIGH-END INDUSTRIAL APPLICATIONS

Maarten Labordus, Willem Souren

Lightweight Structures BV
Kluyverweg 1, 2629 HS Delft, The Netherlands
Maarten.Labordus@Lightweight-Structures.com

ABSTRACT: Many high-end industrial applications feature moving parts, which need to be positioned very accurately or need to be transported very fast. Examples are parts in large milling machines, camera cranes, optical instruments in satellites and medical applications. Traditionally, these parts are constructed in metals like steel, or in some cases aluminium. Most high-end industrial applications are designed for high natural frequencies to avoid problems with vibrations. Composites can offer a further step in achieving a higher accuracy or higher speeds. This paper describes the design and production process development of an example of a high-end composite industrial application.

KEYWORDS: Industrial applications, vacuum infusion, flexible tooling, process control, preforming, fibre bridging, degassing

INTRODUCTION

The aim of this study is to demonstrate the technical and economical feasibility of the use of high-end composites, composite design solutions and composite production processes in industrial applications. In some high-end industrial applications, many similarities can be seen with the traditional composite applications from the space or aeronautical industry. Not just specific strength and stiffness requirements are important, but also specific subjects like tolerances, load introductions and joints. Composite materials can offer advantages over metals with respect to a higher internal vibration damping and no risk of Eddy currents in magnetic fields. If designed properly, composite structures do not suffer from fatigue damage which might allow for higher loads or longer design life. For structures performing under temperature gradients, composites can be applied in such a way that for a certain temperature range zero thermal expansion can be achieved which further enhances the accuracy of the application. This paper describes the design and production process development of an example of a high-end composite industrial application. The structure is a highly integrated carbon-epoxy carrier structure. A redesign from the original milled metal structure was made and analysed. It will be demonstrated that composites can offer great advantages and do not have any mayor drawbacks, which would prevent the application in most high-end industrial applications.

DESIGN OF DEMONSTRATOR

The original demonstrator is a milled metal carrier platform. It is a fast moving part which needs to be positioned very fast and very accurately. Several sensors are mounted on the structure, which needs to stay in place within nanometres. Therefore, the structure needs to be very stiff, very light weight and show very high natural frequencies to minimize the risk of vibrations and to ensure the required accuracy of positioning. During the service life, occasional crash loads can be introduced by surrounding structures by attachments on the four corners of the box. After such a collision, the sensors still need to be positioned accurately within nanometres. A redesign in composite will have to meet all these structural and geometrical requirements.

Conceptual design

A conceptual design of the carrier structure consists of a highly integrated carbon epoxy box.

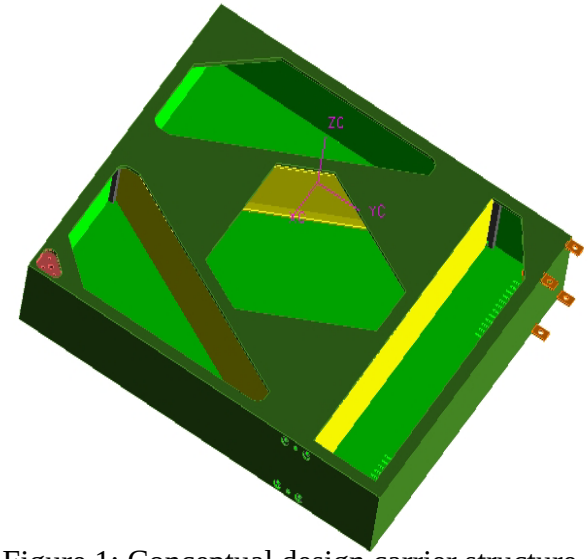

Figure 1: Conceptual design carrier structure

During a brainstorm session, various manufacturing concepts were considered. Since sensors need to be mounted on the outside and the structure was to operate within a limited geometrical volume, it was obvious rigid outer tooling was required. For the ease of manufacturing and to limit the costs of producing the first prototypes, the structure was subdivided in to two separate structures which will have to be assembled afterwards. These to structures are the outer rectangular box, including top flanges and a triangular box which fits in the outer box. A clever geometrical lay-out will ensure an easy assembly by bonding and a proper load transfer after assembly. The substructures will be produced by vacuum infusion in single-sided stiff outer tooling under flexible inner tooling. Any design changes like thickness changes would then still be possible without the need for new tooling. For future series production, pressure infusion in double-sided stiff tooling would be the best option, although the inner tooling would have to be divided in several smaller blocks to allow demoulding.

Conceptual process development

It was decided to use a resin infusion process. This would allow for the use of a room temperature curing epoxy resin systems which would minimize the risk of geometrical inaccuracies due to thermal expansion of the mould. Furthermore, infused laminates based on fabrics allow for better milling with less risk of delamination. Since a high degree of integration is aimed for, conventional tooling can not be used. A dedicated preform method based on folding flat cut-outs was developed to be able to produce accurate performs. The injection strategy for the structure was validated by infusion simulations and simple infusion experiments on flat specimens. The infusion tooling, including the basis infusion strategy is shown in Figure 2. The preform is placed in the rigid outer tooling. A flat metal ring is placed on top of the preform and mould top ensure a good surface definition of the top side of the flange. A preshaped reusable rubber mould is placed in the preform and sealed on the top of the rigid outer mould. Resin is introduced along a channel around the top flange. From there, the resin flows to a central located vacuum outlet. By infusion at a low absolute pressure and curing at a high absolute pressure, in combination with proper degassing of the resin [1], airtight tooling and a very accurate fibre preform, a void free laminate can be produced.

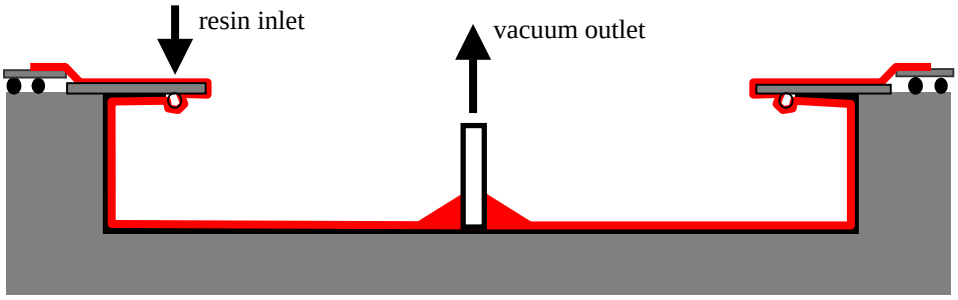

Figure 2: Typical cross-section of infusion tooling

The final mould system, for the triangular box is shown in Figure 3.

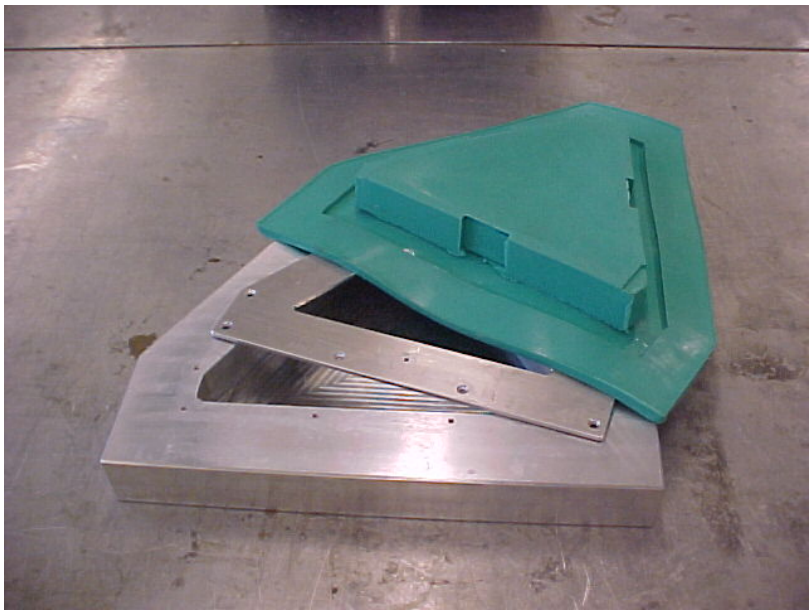

Figure 3: Mould system for triangular box

MATERIAL PROPERTIES

The properties which can be achieved with carbon composites depend on:

- Carbon type:
  - T300 or AS4: E_{f1} = 230 GPa
  - IM7 or T800H : E_{f1} = 276 – 294 GPa
  - M40J : E_{f1} = 377 GPa
- Fibre orientation:
  - Quasi-isotropic: 25 % 0°, 25 % 45°, 25 % 90°, 25 % -45°
  - Ortho-pref 0/90: 37.5 % 0°, 12.5 % 45°, 37.5 % 90°, 12.5 % -45°
- Fibre volume ratio, depending on:
  - Production method (RTM, Vacuum infusion, prepreg)
  - Fabrics or UD
  - Process parameters

Preliminary parameter selection

For the first estimates and calculations, a satin weave material is selected since the drapeability properties of such a fabric are very good which will be advantageous for the production of a box-like structure. The fabric layers are lay-up under 0/90 and +/-45 degree orientations to guarantee a quasi-isotropic laminate. For each layer (200gsm) a thickness of 0.2 mm is assumed. A fibre orientation of ortho-pref 0/90 would be preferable to increase the E-modulus. A minimum amount of 12.5% of +/-45 degree is required to guarantee adequate shear properties. By doing so, it will also be possible to allow holes in the laminate without the need for local thickening of the laminate. To end up with a 2.4 mm ortho-pref laminate, three layers of +/-45 and nine layers of 0/90 degree fabric are needed. For other thicknesses, other fabric arial weights need to be selected. A fibre volume content of 50% is assumed since this can be achieved quite well with infusion processes. By tuning process parameters and selecting optimized fabrics, higher fibre volume contents are also possible. For fibre type, the common T300 from Torayca (supplier Pechiney) or AS4 from Magnamite (supplier Hexcel) are selected. In two steps, fibres with higher moduli are considered. The first step consists of IM7 from Magnamite or the T800H from Torayca. The next step consists of M40J from Torayca. Higher modulus fibres are also available but the processing characteristic diminishes considerably due to increasing brittleness and the prices increases. In the table below, the stiffness properties of quasi-isotropic and orthotropic 0/90 laminates are given for a fibre volume content of 50%. The properties are calculated by using the classical laminate theory.

Table 1: Laminate properties

Carbon type	T300 of AS4		IM7-5000		T800H		M40J	
Fibre orientation	QI	OR 0/90	QI	OR 0/90	QI	OR 0/90	QI	OR 0/90
E_1 [GPa]	44.1	53.8	51.6	63.4	54.5	67.2	68.1	84.7
E_2 [GPa]	44.1	53.8	51.6	63.4	54.5	67.2	68.1	84.7
G_{12} [GPa]	16.8	10.4	19.6	11.8	20.7	12.4	25.8	14.9
ν_{12}	0.31	0.16	0.31	0.16	0.32	0.16	0.32	0.15

Joints

Not only the two substructures need to be joined together, but there will also need to be external parts like sensors attached. These sensors will need to be positioned very accurately. The surface of the composite structure will not guarantee this accuracy, not even when this surface is determined by hard tooling. Therefore, it was decided to use metal inserts in the composite. The position of the holes for the inserts can be determined very accurately by a CNC milling machine. In this way, the high geometrical tolerances can be met in a rather conventional way by metal pick-up points. Several options for joining the composite parts and the metal inserts are considered. Basically, four options for joints in composites are available:

- Form closure
- Pre-stressed bolts
- Bonding
- Close tolerance bolts

Form closure joints are not suitable since this type of joint requires two fitting shapes (for instance a cone in a conical hole) which are pre-stressed together. This requires solid elements which are not available. Pre-stressed bolt are not suitable since the carbon laminate will creep due to the pre-stress. A limited pre-stress up to 15 MPa can be allowed though. This pre-stress should then be applied in two steps to allow creeping of the material prior to the final pre-stressing of the bolts. It requires a rather large number of bolts to pre-stress a reasonable area. The strength of close tolerance bolts can be predicted quite well with existing models. However, the geometrical tolerances, especially after peak loads, are not as good as required. But in combination with glue, better tolerances and stability can be achieved. Pure bonded joints are a good option if the peak loads are limited. The bond line should be thinner than 0.2 mm to avoid tolerance problems. The bonding material is relatively weak material which good cause deformations of the structure in case of thick bond lines. The close tolerance bolts and bonded joints are considered below in more detail.

Close tolerance bolts
In case of a collision of the structure, loads of 3000N are introduced on the joint. For 2 mm laminate thickness, a maximum bolt diameter of 6 mm (D/t=3) can be used for carbon laminates [2]. The nominal stress of 3000 N / 2 mm / 6 mm = 250 MPa will be increased by a factor 2 due to the single lap condition and by a factor of 1,5 due to the stress concentration. The maximum tensile stress is then 250 * 2 * 1,5 = 750 MPa. The design strain under tension is 0.9% for carbon T300. This implies that only 484 MPa is allowed. Therefore, the carbon needs to be thickened locally to 3 mm: 3000 N / 3 mm / 9 mm * 2 * 1.5 = 333 MPa. This still leaves a reserve factor of 1.5 which can be used as material factor.

Bonded joints
The inserts for the structure need to transfer a load of 2500 N. In case of bonded joints, the loads will always have to be transferred by shear forces, rather than perpendicular to the plane. For the inserts under review, the dimensions are 45 mm x 45 mm x 5 mm. The average shear force is: 2500 N / (45 mm x 45 mm) = 1.23 MPa. This seems low at first sight, but one should consider the peak loads at the end of the bond line. These can be estimated by using the method of Volkersen [3]. For an aluminium insert of 5 mm bonded to 2 mm carbon laminate (T300 OR 0/90) with a bond line thickness of 0.2 mm, peak loads of 10.3 MPa are found. By increasing the thickness of the carbon laminates to 6.5 mm, the peak loads decreases to 4.6 MPa. The Volkersen calculation method gives a reasonable estimate in

trends, but the absolute values are not reliable, as practical validation tests have shown. This is caused preliminary by the fact that the not only shear stresses are present in a single lap, but also peel stresses due to the excentricity of the joint. These peel stresses can be of the same order of magnitude as the shear stresses. FE analyses are better suited to study these effects. However, even a FE analysis will not give a complete description of the problem. A singularity at the location of the end of the bond line will cause infinite stresses in the model. In reality, the details of the geometry of the joint (fillets, radii) and plasticity will determine the actual strength. Until now, this can only be determined by practical experiments. The measured tensile strength of epoxy bonding systems like Araldite 2015 or 3M 9323 is around 25 MPa and 42 MPa respectively. Due to a scatter on the strength values, a lower value is used as design value. The 3M 9323 showed a scatter of 1.4 MPa; therefore a design strength of 39 MPa is used. Based on the Volkersen method, a strength reserve of 3.8 MPa is present. The material factor to be used for carbon composites (and joints in carbon composites) is at least 1.5. The conversion factor can be assumed to be 1 since temperature, moisture and creep do not have an influence in these conditions. If we assume that the load factor is already in the loads, we can show that the joint meets the requirements.
The only remaining failure mode can be fatigue. If the load can occur several times in the live of the joint, say a 1000 times, then fatigue should also be considered. To be able to withstand this number of loadings, a bonding strength of 21 MPa is required according to a fatigue analysis based on R = -1 and k = 10. The materials factor of 1.5 should also be applied to this value leading to a minimum required strength of 31.5 MPa, which is still very reasonable.

It should be noted that this analysis is based on several assumptions and uncertainties. The Volkersen method it self has proven to be not very accurate in certain cases. It is also questionable whether the tensile strength can be used for determining shear strength failure. Therefore, the bonded joint should still be subjected to static and fatigue tests. The deformation of the joint is 2500 N / (45 mm x 45 mm) / 967 MPa x 0.2 mm = $2.55 * 10^{-4}$ mm. As long as these deformations are in the elastic region, no problems will occur. If the bond line thickness is smaller less deformation will occur. The outer collision structure will introduce a load of 300N on the joint. The stresses and strains are a factor 1,2 higher. Fatigue might become a load case, which requires a greater interface surface to be able to introduce all loads properly. It might also be advantages to taper the inserts near the ends to lower the stresses locally.

The close tolerance bolts result in a much lighter joint than the bonded joint, which requires a much heavier interface. The tolerance issue can be solved by using a “wet” installation of the bolts; a bonding system will then fill up the fitting tolerance. The bonding system does have a lower bearing strength than the carbon laminate. The bond compression strength will around 150 MPa. The bearing stresses can increase up to 3000N / 3 mm / 9 mm * 2 * 1,25 = 278 MPa. But this value assumes that all loads are taken up by one bolt, and the factor of 2 for a single lap is also very conservative. Based on strength considerations, close tolerance bolt offer a good solution. Whether the geometrical tolerance requirements can also be met has been tested with practical experiments. Several variants of close tolerance bolts with wet installation have been tested on coupon level. On a first set of coupons, the static strength of the joint was measured. On a second set of coupons, the geometrical stability after the occurrence of a peak load of 3000 N was measured. Measurements prior to testing and after testing showed no shift in position of the inserts larger than the required stability.

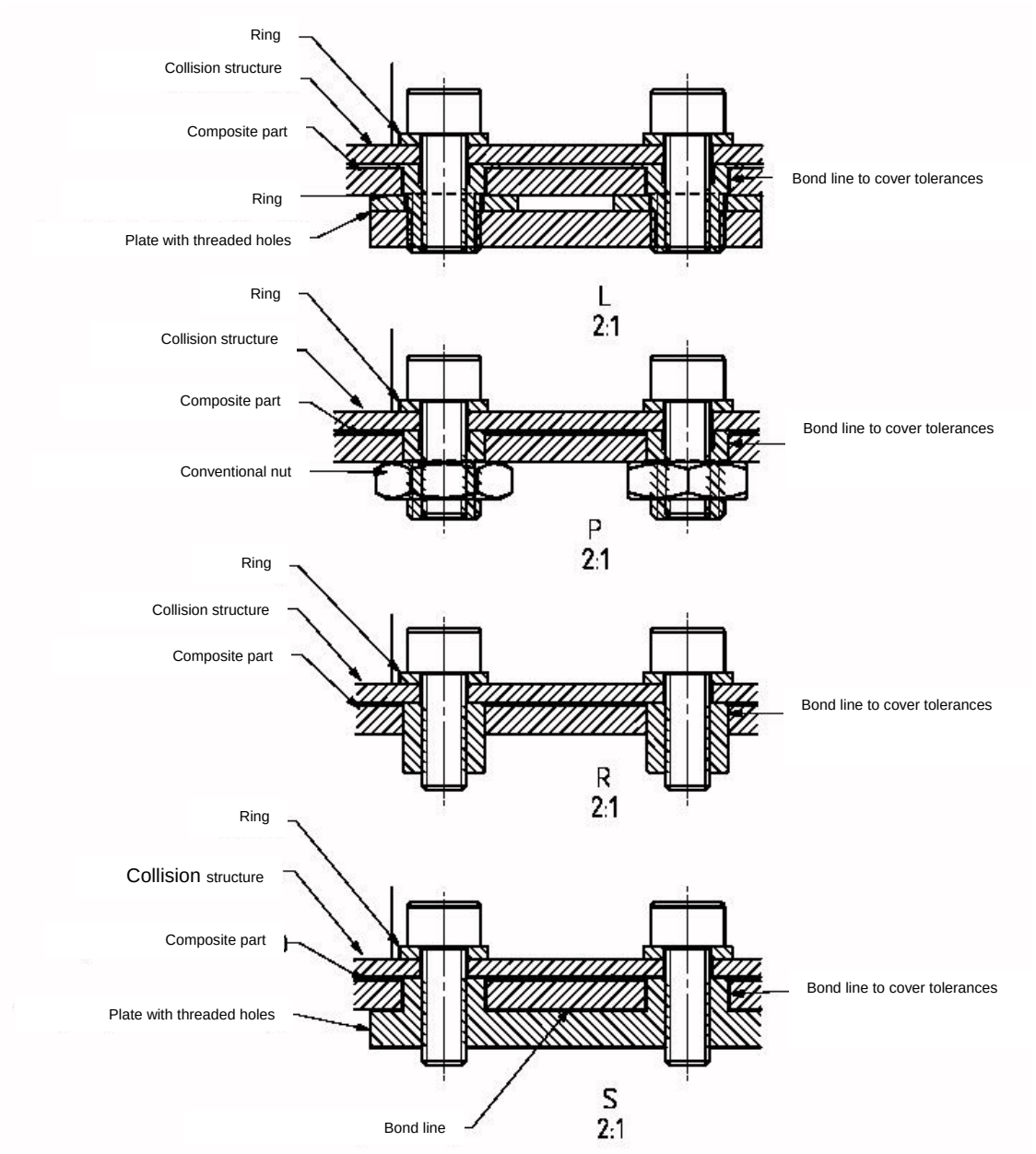

Figure 4: Four options for metal inserts in the composite laminate

PROTOTYPE PRODUCTION

A prototype of the carrier box is produced. The fabrics are preformed and placed inside the stiff outer mould. The metal ring for the definition of the top flanges is attached to the mould. Then, the flexible mould is placed inside the preform and sealed along the sides to the outer mould. Inlet and outlet tubes are fixed in the rubber mould and vacuum is applied. A vacuum of 20 mbar absolute pressure is applied. The air tightness of the mould is checked and the epoxy resin is mixed. The resin is degassed at 5 mbar [1]. Then, the infusion is started. As soon as the resin has reached the vacuum outlet, the pressure is increased to 600 mbar. After a few minutes, the resin inlet is closed and the product is left to cure at room temperature for 24 hours. A subsequent post-cure at elevated temperature is applied prior to demoulding. Both rectangular and triangular box are trimmed and assembled. The assembled structure is shown in Figure 5. The metal inserts still need to be positioned and bonded in.

Figure 5: The assembled carbon carrier structure

ACKNOWLEDGEMENTS

This research was made possible with the financial support of TNO Industry and Technology and the European Space Agency.

REFERENCES

1. Labordus, M, *Avoiding voids by creating bubbles*. Proceedings of the 20th International SAMPE Europe Conference. Paris April 13th-15th, 1999. Centre of Lightweight Structures TUD-TNO
2. *Composite Design Handbook for space structure applications. Volume 2*. European Space Agency. ESA PSS-03-1101.
3. Volkersen, O., *Die Nietkraftverteilung in Zugbeanspruchten Nietverbindungen mit Konstanten Laschenquerschnitten*, Luftfahrtforschung, 15, 1938, pp. 41 – 47

NOVEL FABRICATION METHODS FOR (LOW TEMPERATURE) THERMOFORMABLE COMPOSITES INTENDED FOR MEDICAL APPLICATIONS

*R R Habeb, R A Khan, S Cozien-Cazuc, Y Jing, A J Parsons, G S Walker, I A Jones, C A Scotchford, C D Rudd

Faculty of Engineering, The University of Nottingham, University Park, Nottingham, NG7 2RD, UK

Abstract

A novel SRIM-style process – monomer transfer moulding (MTM, Figure 1) - has been developed for reactive processing of poly-epsilon caprolactone (PCL) composites for bone replacement or fixation. Caprolactone monomer is catalysed using stannous octoate and polymerized in-situ within a closed mould. The material combines the important potentials for low temperature thermoforming with safe resorption in a clinical context. The laboratory scale process also facilitates the introduction of functional additives to control the rate of resorption (Figure 2). The latter can be adjusted to take buffering and tissue regrowth into account. Here we present data on the processing and performance of completely resorpable systems based upon novel, high modulus phosphate glass fibres and on high performance, durable systems based on carbon reinforcements. The first category covers the screening of a range of ternary and quaternary phosphate glasses melt drawing into 15 micron fibres (Figure 3), the screening of coupling agents and fabrication of plane random and unidirectionally reinforced test coupons for durability testing. In the second context, we compare the effectiveness of our reactive processing route with a traditional approach based upon film stacking – very significant enhancements in mechanical properties are highlighted via MTM (Figure 4) and these are investigated by mechanical testing, microstructural characterization and fractography. A single fibre fracture test is applied to assess the relative interfacial bonding efficiencies and a fabrication method is developed to produce in-situ polymerized specimens. Finally, the properties of candidate boneplate materials are examined with respect to in-theatre thermoforming and its impact on structural integrity.

References:

[1] *'Physical and biocompatibility properties of poly-e-caprolactone produced using in-situ polymerisation: novel manufacturing technique for long fibre composite materials',*
T.J. Corden, I.A. Jones, C.D. Rudd, P. Christian, S. Downes, K.E. McDougall,
Biomaterials, 2000, Vol 21, p. 712-724.

*Corresponding author.
E-mail address: rawaa.habeb@nottingham.ac.uk (R.R. Habeb)

[2] *'Monomer transfer moulding and rapid prototyping methods for fibre reinforced thermoplastics for medical applications',*
P. Christian, I.A. Jones, C.D. Rudd, R.I. Camppbell, T.J. Corden,
Composites part A:Applied science and manufacturing, 2001, Vol 32, p. 969-976. .

[3] *'Modelling of the post treatment process of model implants prepared by in-situ polymerised poly(e-caprolactone) using a BF3-Glycerol catalyst system.',*
G. Jiang, I.A. Jones, C.D. Rudd, G.S. Walker,
Polymer, 2003 Vol. 44 No. 6 p. 1809-1818.

[4] *Preparation of poly (ε-caprolactone)/continuous bioglass fiber composite using monomer transfer moulding for bone implant.* Jiang, G.; Evans, M. E.; Jones, I. A.; Rudd, C. D.; Scotchford, C. A.; Walker, G. S.
Biomaterials (2005), 26(15), 2281-2288

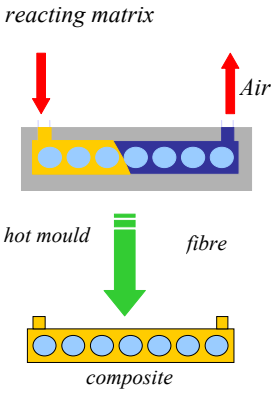

Figure 1 Schematic diagram of process.

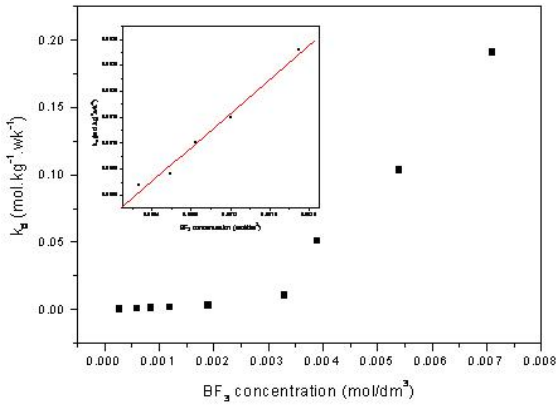

Figure 2 Effect of BF3 loading on PCL Mw
Jiang G. PhD thesis, 2004

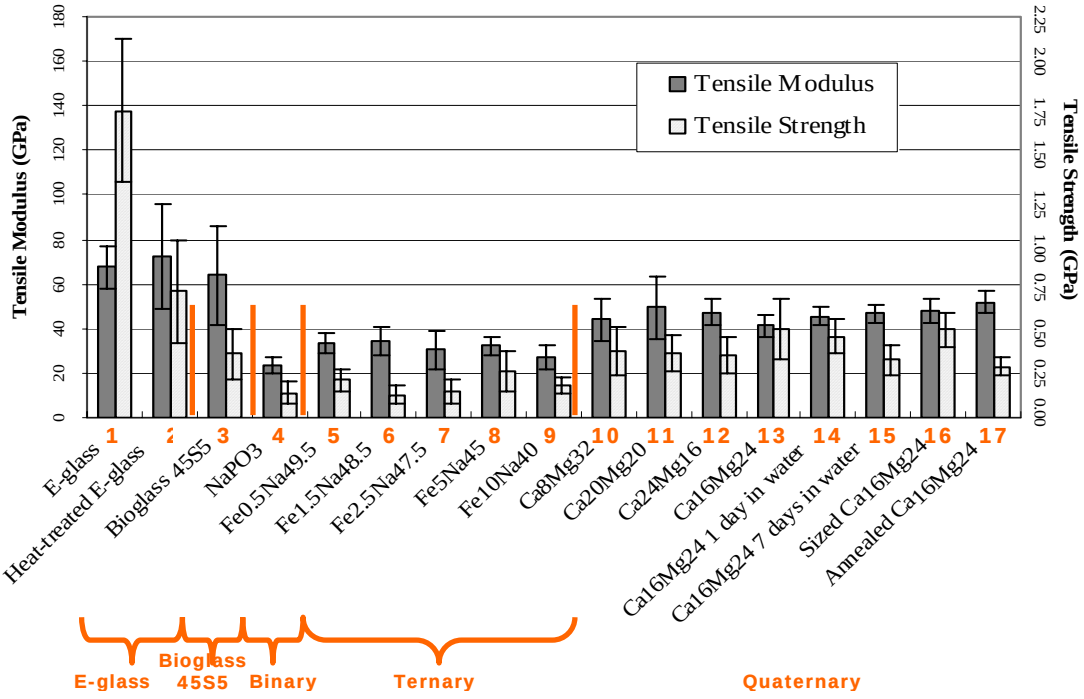

Figure 3 Selected fibre properties.

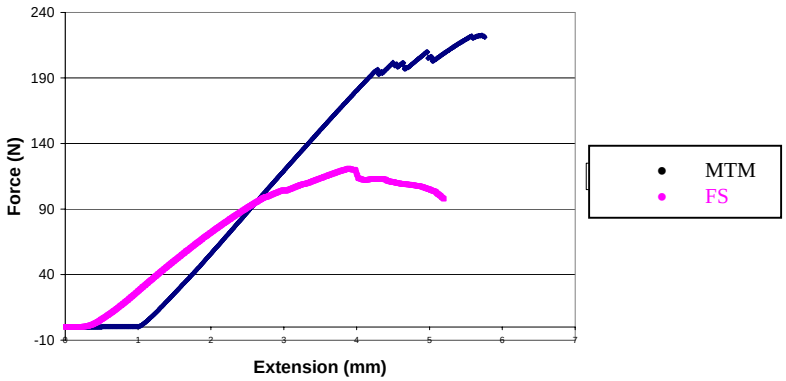

Figure 4 FS vs. MTM properties.

LOW PRESSURE PROCESSING OF HIGH FIBER CONTENT COMPOSITES

V. Michaud, S. Sequeira Tavares, A.Sigg, S.Lavanchy and J.-A.E. Månson

Ecole Polytechnique Fédérale de Lausanne (EPFL)

Laboratoire de Technologie des Composites et Polymères (LTC)

CH-1015 Lausanne, Switzerland

ABSTRACT: The present work proposes a methodology to establish the process window for void-free carbon fiber-epoxy composites, based on prepregs processed under low pressure. The maximal fiber volume fraction that can be attained for a given pressure was measured from prepreg compaction curves. Three different prepregs, and two different stacking sequences were investigated. The curves all exhibited a very similar behavior, for a given stacking sequence, which provided an upper boundary of achievable volume fraction fiber, for a given pressure differential. The stacking lay-up was shown to exert an influence, as well as the fiber modulus. In addition, the role of the initial resin content and of the consumables was evaluated, to show that with a high initial resin content, resin bleed may allow the part to reach the maximal volume fraction fiber. On the other hand, with limited bleeding, high fiber content may be reached by selecting the initial resin content based on the process window.

KEYWORDS: thermoset composites, fiber bed compressibility, low pressure processing

INTRODUCTION

High fiber content composites are currently often produced by autoclave processing of prepreg plies. Using this technique, composite parts having over 65 vol% carbon fibers and less than 0.5% voids are available, mostly for aeronautic or space applications. The increasing use of carbon-epoxy composites, in particular for large structures, such as aeronautic parts or yacht hulls now leads us to explore the feasibility of processing these materials with the same requirements of fiber and void content using vacuum bag processing only, or limited application of pressure.

When an assembly of prepregs with a given stacking arrangement is processed under a given applied pressure (about 0.9 bar for vacuum-bag processing, up to several bars in an autoclave), the externally applied pressure P_{ext} is supported both by the fiber network and the resin, as follows: $P_{ext} = \sigma_{eff} + P$, where σ_{eff} is the effective stress supported by the fiber network, and P the resin pressure. For a given fiber volume fraction (or compressive strain value) σ_{eff} is given by the compressive stress-strain curve of the fiber network [1]. This curve is easily measured during a compression test on the dry fiber bed. When using prepregs, it is tedious and sometimes detrimental to the conservation of the original fiber lay-up to burn or dissolve the matrix to measure this curve. Methods are proposed in the literature to extract the compaction curve of the fiber bed from step-wise compression experiments of the prepregs, by letting the matrix bleed out at each step [2,3]. This curve can then be used to construct a process window for the prepreg compaction, knowing the initial fiber volume fraction or resin

content, and the level of applied pressure, using the approach proposed by Eom et al. [4,5], schematically described in Figure 1. Due to potential shrinkage of the resin during cure, for a given applied pressure during the process, any prepreg with fiber content higher than the intersect of the compaction curve with the pressure value would lead to a composite with voids, since there will be no pressure applied onto the resin during cure to compensate for the shrinkage. This intersection point would thus represent an optimal value, which could be reached either by using a resin content exactly matched to the process pressure, or by using a higher resin content and allowing limited bleeding. The fiber compaction curve thus represents the boundary between a sound composite (above the compaction curve) and one containing porosity (below the compaction curve).

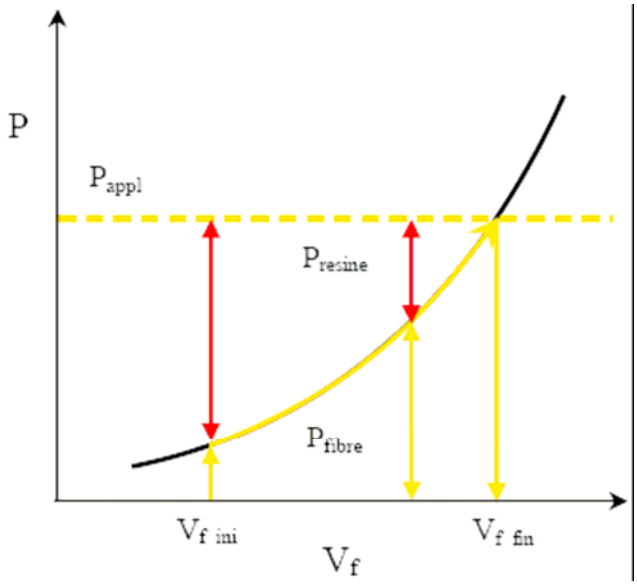

Fig. 1 Schematic view of the process window, the darker arrows represent the value of resin pressure for a given initial fiber volume fraction.

In addition, the influence of humidity in the prepreg could be added, following the methodology proposed by Kardos [6], which indicated, for a given relative humidity content RH in the epoxy based prepreg, that the pressure in the resin should be above P_{min}=4.692 103 exp(-4892/T) (RH), where T is the cure temperature in K. This shifts the boundary line by a fixed amount above the fiber bed compaction curve, for a given value of humidity in the prepreg. The presence of volatils or entrapped air in the resin or between plies may as well be taken into account, if needed.

The present work thus proposes to construct and validate the process window for carbon-epoxy prepregs, with the goal to evaluate the maximal fiber volume fraction that could be reached for a given applied pressure to provide a sound composite. Several carbon-epoxy prepreg materials with fiber modulus ranging from 230 to 390 GPa were evaluated. Processing windows were established, based on the compaction curves of the fiber bed, for various fiber lay-ups. Composite parts were then manufactured with several resin contents, applied pressure, and humidity level to test the validity of the process map. As a consequence, limits in terms of fiber volume fraction can be set to the vacuum-bag production of carbon-epoxy composites, and potential routes to improve this limit will be discussed.

MATERIALS AND EXPERIMENTS

Materials

Three types of prepregs were used, as described in Table 1. The matrix was in all cases epoxy, prepreg A having a different matrix than B and C, and the fibers were carbon fiber of intermediate modulus.

Table 1 Description of the materials

Prepreg	Fiber modulus (GPa)	Fiber density	Resin content (wt%)	Areal weight (g/m^2)
A	390	1.82	26-32	300
B	230	1.8	34	300 or 200
C	242	1.81	34	160 or 200

Compaction experiments

The compaction experiments were performed following the method proposed in Ref.[2]. A compression fixture was designed, schematically presented in Figure 2, with a top piston applying load on the sample placed in the bottom part of the mould, which constrains the sample in the y direction, but not in the x direction, to allow flow of the resin out of the prepregs during the compression experiment.

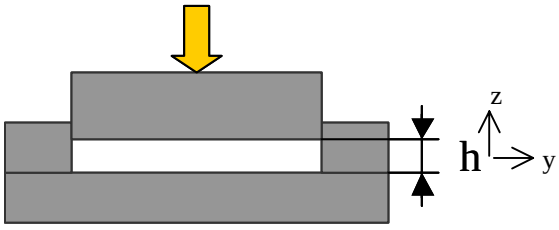

Fig. 2: Schematic of the compression fixture.

The fixture was mounted on a 100kN Interlaken hydraulic press, equipped with a convection oven to heat the assembly up to 100°C. The fixture temperature was monitored by two thermocouples. In a typical experiment, a stack of prepregs, either all aligned in the x direction, or laid at ±45° was placed in the fixture. The sample dimensions were 80 mm wide, 70 mm long, and about 6 mm high at the beginning of test, corresponding to about 16 to 30 layers depending on the fiber areal weight. The sample was then compressed in increasing steps of imposed displacement. The resulting load was recorded with the load cell. The displacement was recorded from the press position corrected for compliance effects. An example of curve is given in Figure 3. At each deformation increment, the load increased strongly, then decreased as the resin flowed out, to a stable position which corresponds to the equilibrium stress-strain curve of the fiber bed. The load curves were fitted as in Ref. [2] with an exponential decay. The number of steps, as well as the test temperature, were optimized for each resin type so as to get a best compromise between a low resin viscosity, and a long enough gel time.

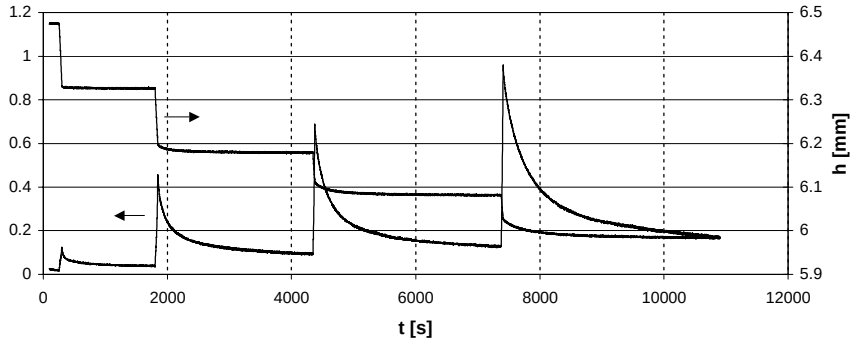

Fig. 3: Typical example of imposed displacement and measured load values with time.

Plate manufacturing

In parallel, several unidirectional plates, 1600 mmx1600 mm were manufactured in an autoclave, either under vacuum only, or using gas pressure up to 5 bars. The preparation of samples was as follows: an aluminum flat plate coated with demoulding agent was used as the base mould. The stack of prepregs was laid on the mould, with intermediate vacuum compaction every three plies, up to about 18 plies. Consumables were then placed on top of the prepregs. Different cases were tested, to investigate the effect of bleeding during cure: (1) a non-perforated film was placed directly on top of the prepreg, followed by a breather ply and vacuum bag, (2) a perforated film P3 (Aerovac) was placed directly on top of the prepregs, followed by a breather ply and vacuum bag, (3) a non-impregnated peel-ply was placed directly on top of the prepreg, followed by a breather ply and vacuum bag. In all cases, the sides of the sample were sealed with sealant tape to ensure that all potential bleeding took place from the top of the prepregs, to simulate the case of large parts. The samples were then cured in the autoclave, under vacuum and in some cases with additional pressure, following the recommended cure schedule for each prepreg type. The fiber volume content in the plates was measured from the final average height of the plates, h, as follows: $V_f = \frac{n m_{of}}{\rho_f h}$, where n is the number of plies in the laminate, m_{of} is the areal weight of each ply, and ρ_f is the fiber density. This was shown to be the most reliable way to compute this value, in order to compare it with the compaction measurements, which are also based on this calculation of V_f. The void content was evaluated using image analysis on optical microscopy photographs of polished cross-sections. To test the influence of humidity, a plate was prepared along the same route, using prepregs which had been initially placed in a climatic chamber at 30° and 70%RH for one week.

RESULTS AND DISCUSSION

Compaction curves

Fig. 4 presents the compaction results for prepreg A, with a fiber orientation of 0° along the mould length, and of ±45°. The points were obtained in a series of several compression experiments. Some scatter is observed in the curves, which most probably results from several causes: there may be some variability between experiments in the fiber alignment, the width of the fiber assembly may slightly vary between experiments (although this is accounted for in the calculation of pressure and fiber volume fraction), and finally, it was shown that the exponential curve fitting used to calculate the

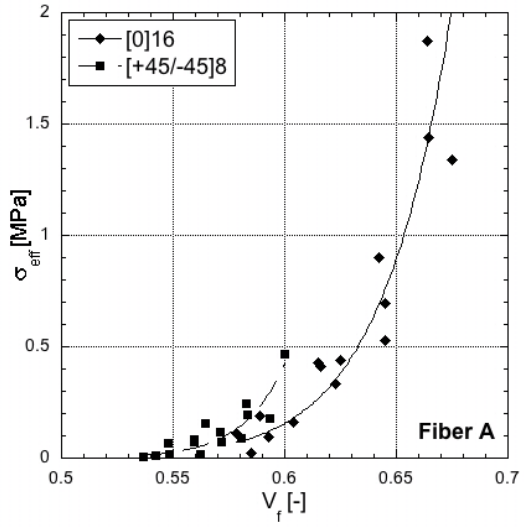

Fig. 4 Compaction results, prepreg A, 0° and ±45

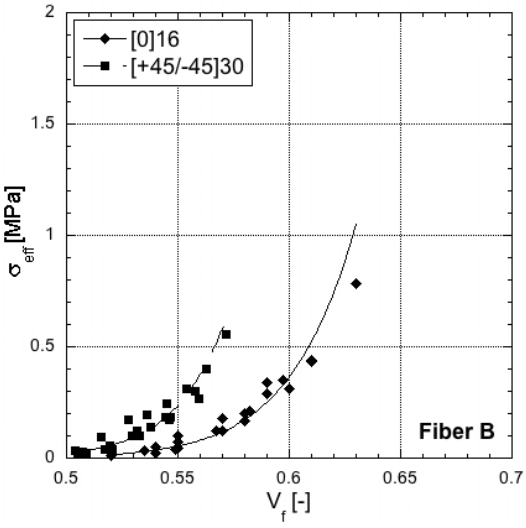

Fig. 5 Compaction results, prepreg B, 0° and ±45°

equilibrium points of the pressure curves sometimes tended to slightly overestimate the final pressure value. This error was estimated to 3%. However, a trend is clearly shown. The curves follow well the power law relation proposed by several authors [7-9], $\sigma_{eff} = k\ V_f^n$, where k is a constant which depends on the fiber bending rigidity. The value of the coefficient n is within the range observed for unidirectional fibers, 20 to 30, as shown in Table 2. As expected and already observed by Eom during compaction of dry glass fibers [5], the fiber lay-up with alternate orientations leads to a stiffer response of the fiber bed. This was however not observed in several other cases [2,3].

The following figures present the compaction results obtained for prepreg B (Fig. 5) and prepreg C (Fig. 6), at 0° and ±45°. Prepreg B follows the same trend as A, whereas C shows more scatter, and a less marked difference between the fiber lay-up type. This may be caused by the fact that these were made from heavy tow fibers, which initially leads to more misalignment in the layers. Finally, Fig.7 presents a comparison of the three prepreg types for the 0° direction. Whereas B and C follow almost exactly the same curve, A shows a better packing, that is a higher fiber volume fraction for a given applied pressure. This may be due to several causes: A fibers have a higher modulus, so they are likely to be more straight and less misaligned during prepreg manufacturing. Also, it is possible that more tension was applied on the fibers during prepreg manufacturing, leading to a denser packing.

Table 2 values of coefficients n for the compression experiments

Prepreg/layup	A 0	A ±45	B 0	B ±45	C 0	C ±45
n	22	31	22	25	20	22

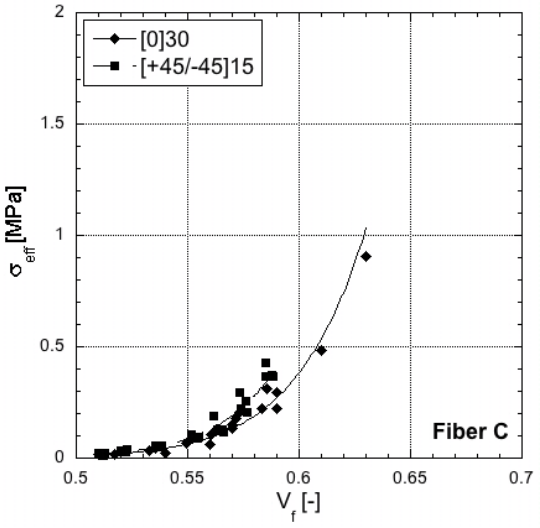

Fig. 6 Compaction results, prepreg C, 0° and ±45°

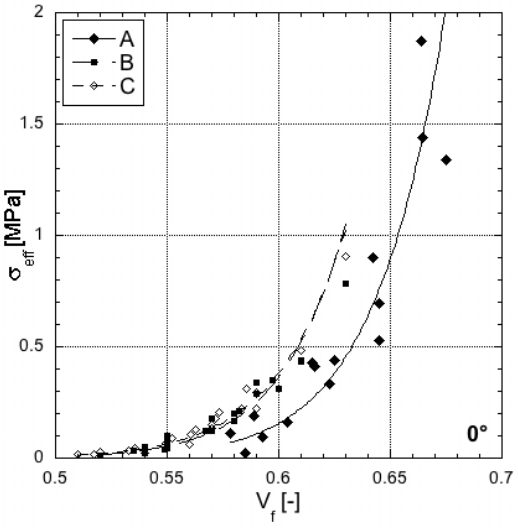

Fig. 7 Compaction results, comparison of all prepregs at 0°

Influence of pressure, initial resin content and consumables

Table 3 presents the various conditions of the plates manufactured, together with the measured final fiber volume fraction and void content. In most cases, the void content was very low, and it is reported as below 1%, to account for the measurement error. The vacuum bag processed samples lead to the highest void content. The samples processed after exposure to humidity in the same conditions as P9 are not reported below. They gave a very high void content, about 4.5±1.6%, indicating that humidity indeed exerts a strong influence on the part quality. However, a reference plate was made with the same prepregs, which were kept during one week in an air-conditioned room at 20°C before manufacturing the plate. This plate also had a final void content of 5.4±1.6%. As a consequence, it seems that the time out of the freezer of the prepreg exerts a much stronger influence than the humidity level. This point needs to be further clarified and taken into account when laminating large structures over several days.

For prepreg A, a study was conducted to test the influence of the release films and initial resin content on resin bleeding. As reported in Fig. 8, the samples with high resin content were subjected to bleeding when the consumables allowed it. The final fiber volume fraction thus varied from 56.8% when no bleeding was allowed, to 62.1% when a dry peel-ply was placed on the material. In the latter case, the final fiber volume fraction was close to that expected from the compaction curve for a pressure differential

Table 3 Conditions of manufactured plates

Sample number	P1	P2	P3	P4	P5	P6	P7	P8	P9	P10	P11
Prepreg type	A	A	A	A	A	A	A	A	B	C	C
Total applied pressure (bars)	5.9	5.9	5.9	5.9	5.9	5.9	2.9	2.9	0.9	0.9	3.9
Initial resin content (wt%)	32	32	32	26	26	26	32	26	34	34	34
Peel-ply type	1	2	3	1	2	3	1	1	2	2	2
Final V_f (%)	56.8	57.7	62.1	63.5	63.1	63.8	57.2	63.6	56	57	59.4
Void content (%)	<1	<1	<1	<1	<1	<1	<1	≈1	1.5	1.3	<1

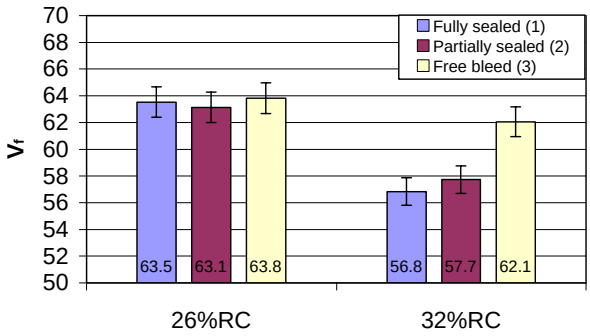

Fig. 8 Role of the consumables and initial resin content on the final fiber content in the plates.

of 5.9 bars, about 63%. The prepregs with the low resin content, calculated to achieve the maximal volume fraction at 5.9 bars (26 wt% resin should lead to V_f=0.65), all indeed had a final volume fraction fiber as expected, whether bleed was allowed or not.

PROCESS WINDOW

As a consequence, a process window can be constructed for each type of prepreg to estimate the risk of void content in the final part, for a given processing pressure, initial resin content and amount of allowed bleeding. An example is given in Fig. 9, for UD plates made from the prepreg A, reporting all samples, assuming that the humidity of the prepregs was negligible. It was verified that except sample P8, all plates had a very low void content. Several manufacturing strategies can thus be deduced, depending on the resin content of the prepregs and the amount of bleeding allowed, based on the consumable type and the resin viscosity profile, to reach the maximal fiber volume fraction for a given pressure differential. Fig.10 reports the process window for prepreg B and C, assuming no humidity, or 70%RH for a cure at 100°C, using Ref.[6]. The points corresponding to plates performed under vacuum only fall very close to the pressure boundary, close as well to their theoretical fiber volume fraction V_f=0.56 based on their initial resin content, and below the boundary with 70%RH. In that region, the curve is flat, and the role of volatils and humidity cannot be ignored anymore. In addition, the exact value of the pressure differential is more difficult to assess, in case of a leak in the mold or the vacuum bag, for example. The process window is however of use to assess the maximal volume fraction that can be achieved with a given prepreg under vacuum bagging, and the risks of a given humidity content.

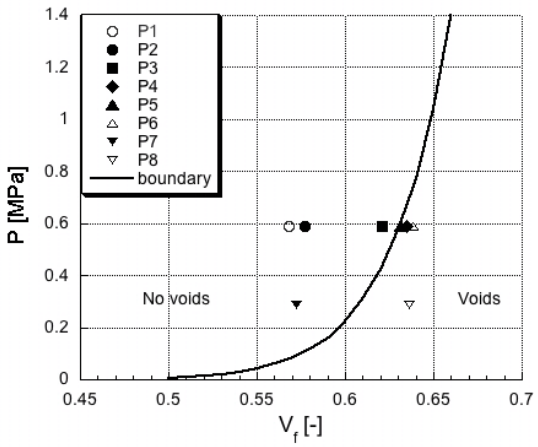

Fig.9 Process window for prepreg A

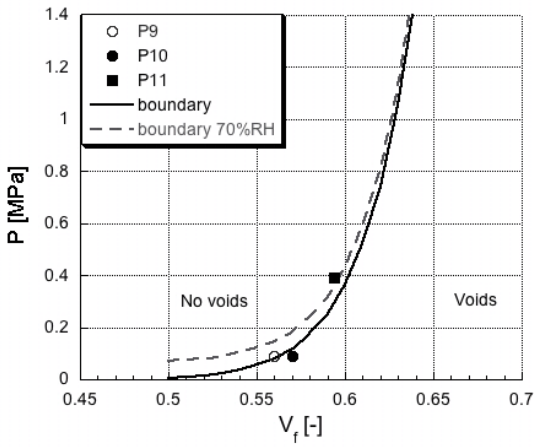

Fig.10 Process window for prepreg B/C

CONCLUSION

The present work showed that process windows for sound processing of carbon-epoxy composites can be established, simply based on compaction curves of the initial prepreg. It is worthy to note that this curve could also be established from the final volume fraction of plates cured with free resin bleed at various applied pressures, if a heated press is not available. Several strategies can be devised based on these guidelines to process the material, depending on the initial resin content and applied pressure during processing. The use of peel-plies and other consumables then allows the amount of resin bleed to be adjusted to reach the maximal fiber fraction. Comparison of prepregs showed that significant differences can be observed, for a given direction, depending on the fiber type and possibly on the prepreg manufacturing route. As a consequence, it should be possible to reach a fiber volume fraction up to 60% with vacuum-bag processing if the fibers are initially well packed during prepreg manufacturing. This does not hold, however, if the fiber orientation is alternated during the lay-up, as is usually done when manufacturing real parts. Again, the choice of prepregs, such as A or C for example rather than B may help achieve higher fiber content and a sound composite.

ACKNOWLEDGEMENTS

This work was funded in part by the Swiss Commission for Technology and Innovation contract n°6972.2, and in part by the Swiss National Fund for Scientific Research contract n°200020-105169. Alinghi SA and Décision SA are thanked for donating prepregs and for fruitful discussions.

REFERENCES

1. V. Michaud and A. Mortensen, "Infiltration processing of fiber reinforced composites: governing phenomena", *Composites part A*, 32 , pp.981-996, 2001.
2. P. Hubert, A.Poursartip, A method for the direct measurement of the fibre bed compaction curve of composite prepregs", Composites Part A, Volume 32, , Pages 179-187 (2001).
3. T. G. Gutowski, Advanced composite manufacturing, John Wiley & Sons Inc. (1997)
4. Y. Eom, L. Boogh, V. Michaud, P. Sunderland and J.-A. E. Månson. "Stress-initiated void formation during cure of three-dimensionally constrain thermoset resin". Polymer Engineering and Science, Vol.41, No.3 (2001).
5. Y.Eom, L.Boogh, V.Michaud and J.A-E. Månson, "A structure and property based process window for void-free thermoset composites", *Polymer Composites*, vol.22, N°1, Pages 22-31(2001).
6. J.L. Kardos, M.P. Dudukovic and R. Davé, "Void growth and resin transport during processing of thermosetting matrix composites", Advances in Polymer Science, Vol.80, K. Dusek, ed, Springer Verlag, Berlin, (1986).
7. Toll, S. and Månson, J.-A.E., ”Elastic compression of a fiber network”, J. Appl. Mech., Vol. 62, 1995, pp. 223-226.
8. van Wyk, C.M., ”Note on the compressibility of wool”, J. Textile Institute, Vol. 37, 1946, pp. T285-T292.
9. C. Servais, V. Michaud and J.A-E. Månson, "The packing stress of impregnated fiber mats", *Polymer Composites,*Vol.22, n°2, April 2001, pp.298-311.

PROCESSING-DEPENDENT MICROSTRUCTURE OF LONG GLASS FIBRE REINFORCED POLYAMIDE 6-6 INJECTION MOULDINGS AND RELATED MECHANICAL PROPERTIES

Eric LAFRANCHE[1], Arnaud COULON[1], Patricia KRAWCZAK[1],
Jean-Pierre CIOLCZYK[2] and Jérôme MAUGEY[2]

[1] *Hutchinson SA, Research Department Rue Gustave Nourry, BP31, F-45120 Châtelette-sur-Loing, France, jean-pierre.ciolczyk@cdr.hutchinson.fr*

[2] *Polymers and Composites Technology & Mechanical Engineering Department Ecole des Mines de Douai, 941 Rue Charles Bourseul, F-59508 Douai, France*

Corresponding Author's e-mail: lafranche@ensm-douai.fr

ABSTRACT: This paper aims at identifying the main parameters that govern the flexural properties of long glass fibre / polyamide 66 injection-moulded parts. The mould geometry has been chosen so as to reproduce some geometrical accidents (e.g. sharp frontal and tangential steps) occurring on industrial moulds. A Taguchi Design of Experiments (DOE) analysis has been devised in order to quantify the processing conditions effects on the flexural strength and modulus. The polymer melt temperature is the main parameter acting on the flexural properties in both flow and transverse directions. The structure/process/flexural properties relationship has then been deduced from a microstructural analysis (local residual fibre length and average orientation, interfacial quality). For optimised injection moulding conditions, leading to the highest flexural strength in the flow direction, a fibre content gradient has been noticed over the part length and width, which is strongly amplified by the presence of a sharp geometrical discontinuity.

KEYWORDS: Long glass fibre, Injection moulding, Microstructure, Polyamide 66

INTRODUCTION

The use of short fibre reinforced thermoplastics in industrial applications is frequently hindered by their rather low mechanical performances, because of the low residual fibre length after processing. In order to overcome this limitation, long fibre reinforced thermoplastics (LFT) have been developed to bring better mechanical properties and to meet the market demand thanks to an improvement of the reinforcement efficiency. At the present time, LFT is one of the fastest-growing sectors of the plastics industry, especially in business areas where high mechanical performances and time stability are required. The automotive applications currently account for over 95% of the worldwide demand. In Europe, an annual growth rate of 10-12% was observed during the 1999-2002 period and car makers forecast further annual growth perspectives of 10% until 2010 for glass reinforced thermoplastics [1,2]. Considering the constraints that such engineering parts have to satisfy, it has become crucial to gain an accurate knowledge of the processing conditions / microstructure / part properties relationship of injection moulded LFT, so as to be able to further optimise their use

potential. However most of the studies on processing-induced fibre orientation and degradation mechanisms carried out up to now were dedicated to short glass fibre injection moulded thermoplastics. Few data is available for LFT injection moulding [3-8], and, in that case, investigations have been usually carried out on very simple (plane) parts, mostly on PP matrices.

As a consequence, this paper aims at contributing to an understanding of how the processing conditions affects the anisotropy and heterogeneity of long glass fibre / polyamide 6-6. An analysis based on a detailed investigation of the injection moulding process at the different elementary stages of plastication and flow will be carried out for this purpose. It will lead to the identification and subsequent optimisation of the main parameters that improve the flexural properties of PA6-6 LFT injection moulded parts.

EXPERIMENTAL

The experiments were carried out on a 2000 kN clamping force injection moulding machine (DK Codim). The machine had an injection gate located in the parting line and a standard 55 mm diameter screw. The prototype injection mould was a rectangular plate of 300 x 120 x 3 mm. The feeding of the cavity was made by a 4 mm thick fan gate over its whole width (unidirectional flow in the longitudinal direction of the plate). This mould was specially designed so as to reproduce some geometrical discontinuities (like frontal and tangential steps) occurring on industrial moulds and to be able to study the effects of such more or less sharp accidents on the flow mechanisms and related part properties (Fig. 1).

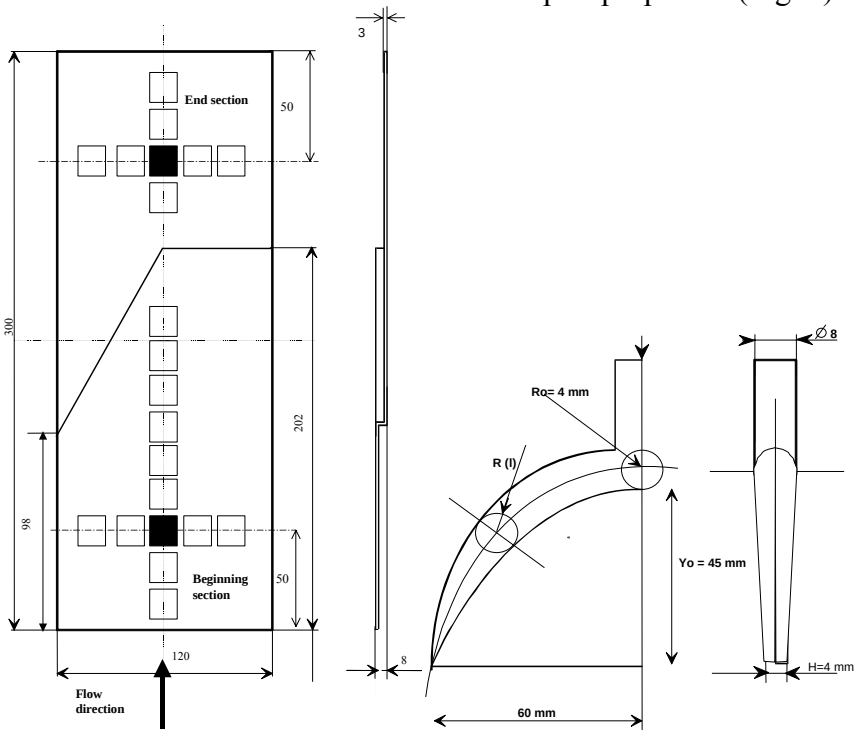

Fig.1: Plastic part and fan gate geometry and cutting pattern of test samples for fibre content (white coupons) and fibre length and orientation (black coupons) determination

A Design Of Experiments (DOE) analysis was devised to identify the main parameters inducing anisotropy and heterogeneity of the moulded part, and then to optimise the injection moulding process of a polyamide 66 (PA66) reinforced by 40 wt% of 10 mm long glass fibres (Ticona). The Taguchi L16 (2^{15}) table used included six factors related to the filling, holding and plastication stages (Table 1) and six interactions between factors. The level of each factor was determined from the material supplier's data sheets. The others processing parameters

(holding time, packing pressure, cooling time …) were kept constant. The output parameters were the flexural mechanical properties (strength, defined as the maximum stress, and modulus). Bending tests were performed according to ISO 178 on a standard tensile machine (Instron) on 5 samples (dimensions 60x25x3 mm) in both flow (longitudinal) and transverse directions at the beginning and at the end of the part according to figure 1.

Table 1. Processing conditions for Taguchi DOE

Parameters (or factors)	**Low Limit**	**High Limit**
Mould Temperature (°C) **MoT**	90	120
Melt Temperature (°C) **MeT**	280	300
Volume flow rate (cm^3/sec) **IS**	83	142
Holding Pressure (Bar) **HP**	277	440
Back Pressure (Bar) **BP**	8	12
Screw rotation speed (cm/min) **SRS**	691	1036

For the fibre length measurements, three 25x25 mm size samples were cut from three injection moulded plates (Fig.1) and then burnt at 530°C during 5 hours. The burning residue was scattered in water by ultrasounds and then dried. The remaining fibres were dropped on a glass slide. A polarizing microscope (Jenapol, CarlZeiss Jena) was used in transmission mode and associated to a CCD camera coupled to a computer to get and record suitable images. These images were then analysed by means of an image processing software package (Visilog® 5.2, Noesis). The analysis of 1000 fibres per sample at least led to the determination of the average fibre length and the distribution of fibre length. The number-average fibre length *Ln*, the weight-average fibre length *Lw* and the corresponding standard deviation on the sample were calculated according to ISO 22314 [9]
Finally, the fibre orientation state of the moulded part were describe by the Advani and Tucker [10] method that uses the notion of orientation tensors, in order to obtain a complete description of the orientation state from a small number of discrete values. Such tensors are defined as the dyadic products of the unit vector $\underline{p}$ averaged over all possible directions, with ψ as weighting function. Using an orientation tensor is equivalent to approximating the orientation distribution function by a finite term number in a Fourier series. The second order tensor $\underline{\underline{a}}_2$, defined by equation 1, was used.

$$\underline{\underline{a}}_2 = a_{ij} = \oint p_i \; p_j \; \psi(\underline{p},t) \; \delta\underline{p} \qquad (1)$$

These tensor values characterize the orientation state with respect to a reference direction (observation direction 1), usually the flow direction ($a_{11}<0.35$ for a perpendicular orientation, $a_{11}>0.7$ for a parallel orientation, $0.5<a_{11}<0.6$ for a random orientation)

MANUFACTURING CONDITIONS EFFECT

The main injection-moulding parameters governing the mechanical properties were identified from a variance analysis [11]. From a general point of view, all parameters that decrease the shear stresses in the melt during plastication and flow increase the mechanical properties [6,7,8,11,12]. Melt and mould temperatures as well as volumetric flow rate thus limit the fibre degradation and increase the part quality whatever the location may be. A strong anisotropy effect was also noticed (properties are on average about 1.3 to 2 times higher in the flow direction than in the transverse one) because of a preferential fibre orientation in the flow

direction. The geometrical discontinuities increase the anisotropy as they increase the shear stresses in the flow and thus the fibre orientations.
In order to establish the processing – mechanical properties – structure relationship, two opposite processing conditions were extracted from the general L16 DOE. The first set of processing conditions was deduced from the experimental and analytical model that leads to the maximum flexural strength in the flow direction. This set up of injection machine is named «maximum combination». The second set of processing conditions was chosen at the opposite experimental levels. It is named «minimum combination». The corresponding machine set-up for these combinations are summarized in table 2.

Table 2. Processing conditions for the Structure/Process/Property analysis

Parameters	Max. Comb.	Min. Comb.
Mould Temperature (°C) **MoT**	120	90
Melt Temperature (°C) **MeT**	300	280
Volume flow rate (cm^3/sec) **IS**	83	142
Holding Pressure (Bar) **HP**	440	440
Back Pressure (Bar) **BP**	8	12
Screw rotation speed (cm/min) **SRS**	1036	691

MICRO-STRUCTURAL ANALYSIS

Fibre content

The average fibre weight content is 41.5wt% and 42wt% respectively for the minimum and maximum combinations. However, the glass weight content measurement highlights a fibre accumulation at the parts end section for both combinations, with a maximum of 51wt% of fibres noticed for the maximum combination (Fig.2). In the transverse direction, the parts beginning section is homogeneous for both combinations, contrary to the end section where the maximum fibre content is observed on the symmetry axis (Fig.3). Such a concentration gradient was also observed by some authors both for short [13,14] and long fibres [15]. It may be attributed to the sweeping towards the parts end of the fibres, which are partially embedded at the interface between the frozen and molten layers and broken by flow-induced shear stresses.
For the minimum combination, the mould and melt temperatures are set at their lower level and the volume flow rate at its higher level. It is possible to suppose that the shear flow in the skin layers is favoured compared to the extensional flow, leading to a higher longitudinal migration at least in the first half part of the plate (Fig. 2). The fibre orientation profile, measured hereafter, is going to confirm this hypothesis.
For the maximum combination, the filling time is 1s higher and the freeze time 3s higher due to a lower volume flow rate and a higher mould or melt temperature. Even if the shear stresses during the filling stage are lower and the frozen outer layers thinner than for the minimum combination, the flow effect during the holding pressure stage is greater, and this induces a higher fibre concentration gradient. An analysis of the glass content of each layer would be required in order to confirm this hypothesis.

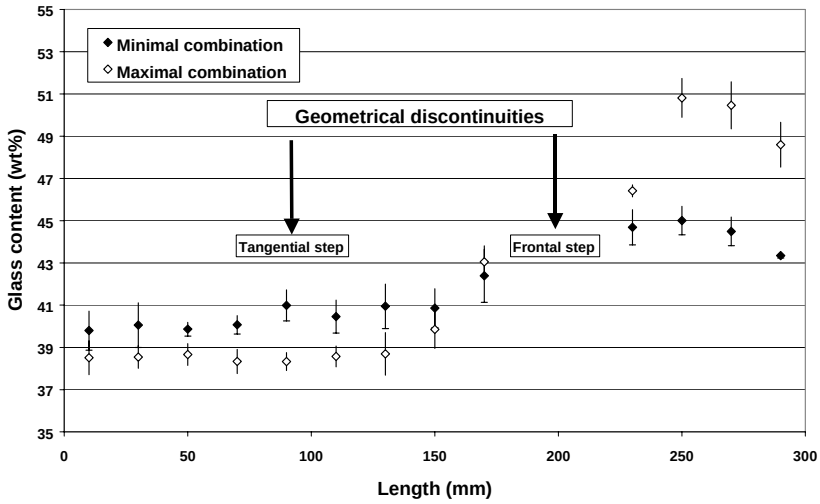

Fig.2: Glass weight content along the mid-axis of the composite plates

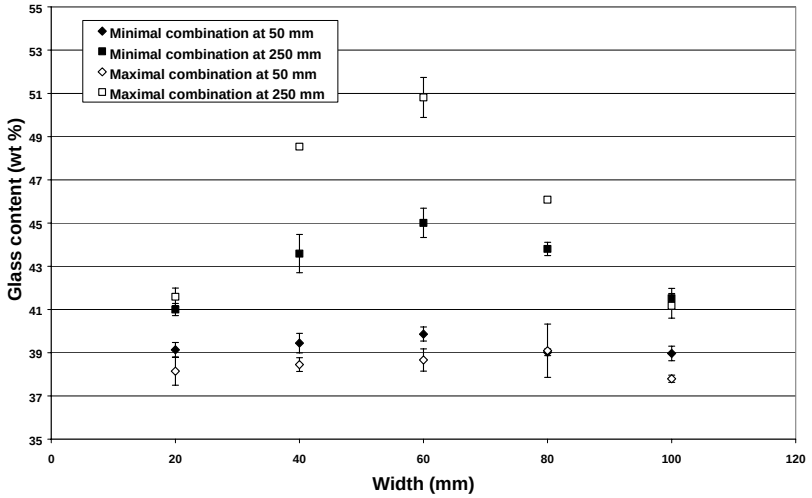

Fig.3: Glass weight content along the width of the composite plates.

Fibre length

The maximisation of the processing conditions allows increasing the whole reinforcement average length (both number- and weight-average) of about 20% (Tab.3.).

Table 3. Fibre length measurements

	Min. comb.		**Max. comb.**	
	Begin.	***End***	***Begin.***	***End***
Number-average length *Ln* (mm)	1.372	1.262	1.503	1.802
Weight-average length *Lw* (mm)	3.114	2.661	3.183	3.839
Standard deviation (mm)	1.573	1.350	1.590	1.917
Polydispersity ratio *Lw/Ln*	2.27	2.11	2.12	2.13
Fibre aspect ratio	91	84	100	120

For the maximum combination, the number-average fibre length in the parts end section is 20% higher compared to the beginning section. This would reveal fibre degradation from the secondary flows during the holding stage of the process. A lower viscosity of the melt favours the pressure transmission.
An important degradation of the reinforcement could be observed for both combinations. Almost half of the fibres have a length less than 1 mm and only 10% of the fibres are longer than 5 mm. The average degradation amount has been evaluated to 80% of the initial average fibre length.
According to the results presented in table 3, most of the degradation occurs in the cavity up stream, in the plasticating unit or in the feeding system (nozzle or gate). An evaluation of the degradation occurring within the plasticating unit has therefore been carried out for the maximum combination in order to understand the fibre degradation mechanism during processing. It appears that the fibre degradation occurs mainly in the compression section where the degradation amount reaches 70% (Fig.4).

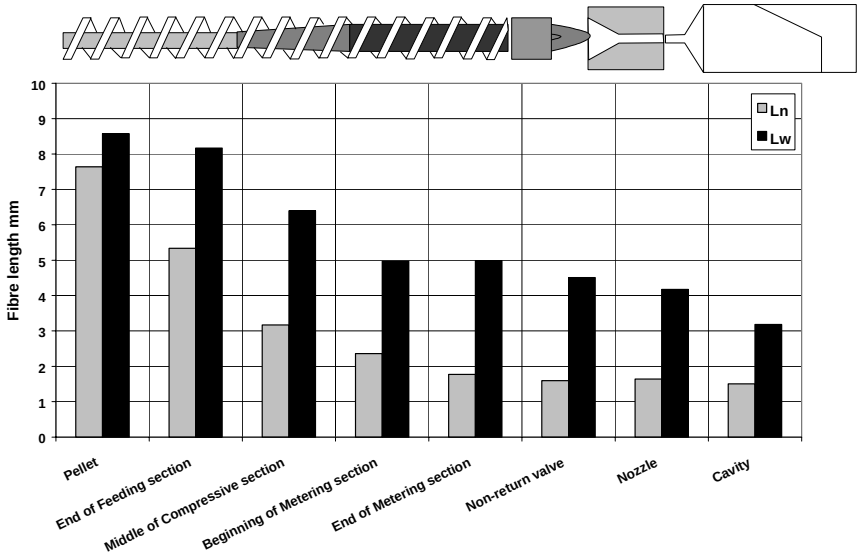

Fig.4: Number- and weight-average fibre lengths along the processing system

Fibre Orientation

The fibre orientations were evaluated as well. The Advani-Tucker [10] tensor values (a11) were plotted through-the-thickness for the two combinations at the parts beginning and end sections (Fig.5).
The orientation profile is symmetric with respect to the plate mid-plane. Seven elementary layers are visible for the maximum combination. There are two skin layers, where the fibres are randomly distributed due to the fountain flow, and two oriented layers due to the shear flow influenced by the injection speed and the non-isotherm effects. Two random intermediate layers resulting from the secondary flows during the holding stage are therefore noticed. Finally, a transversely oriented layer is present in the centre of the parts. The minimum combination shows a 5-layer composite with two thick shear layers. The effect of the holding pressure is similar to that for the maximum combination. At the end of the parts, the a11 tensor value does not change through the thickness due to the sample location on a weld line, which is created there.
The fibre orientation mechanisms seem to be those observed for short fibres at least for fibre length below one millimetre. A the beginning of the cavity, the fibres take a perpendicular orientation in the (1,2) plane due to the divergent flow induced by the fan gate radial

stretching. In the first half of the plate, the flow is unidirectional. The fountain and shear flows influence the fibre orientations as described by GERARD [13]. The geometrical discontinuities disturb the flow and induce a weld line, where the reinforcement is oriented in the flow direction (1).
The thickness of the mould side layer increases from the entry (gate) to the plate end due to cooling. This creates a convergent geometry in the (1,3) plane. This effect is all the more important than the temperature is lower, even for the minimum combination.

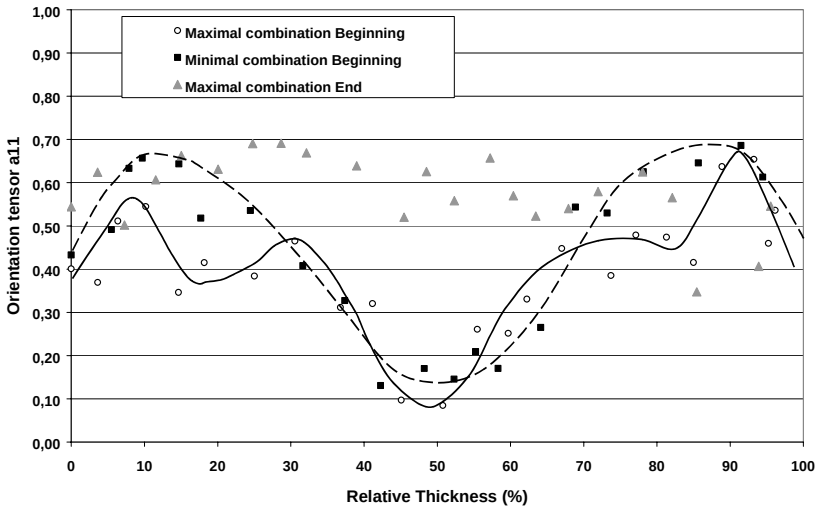

Fig.5: Fibre orientation profiles through-the-thickness of the injection moulded part

Interfacial adhesion evaluation

The quality of the interfacial adhesion were evaluated by observation of the fracture surfaces under Scanning Electronic Microscope (SEM, Phillips). Generally, the samples moulded with the maximum combination are characterised by a better interfacial adhesion. The matrix perfectly covers the fibres and a cohesive fracture is noticed. On the opposite, when the minimum combination is used, the interfacial adhesion quality is poor, the fibres are smooth, the fracture is non cohesive with a matrix/fibre slipping.

CONCLUSIONS

A detailed microstructure analysis of the moulded parts has pointed out some features related to optimised processing conditions:

- ✓ a strong fibre content gradient with higher contents at the end of the parts, which can be attributed to a longitudinal segregation induced by shear stresses in the melt, and is amplified by the presence of sharp geometrical accidents;
- ✓ a higher average fibre length (at least +20% to +40% depending on the location in the part);
- ✓ a 7-layer composite structure with a great effect of the holding pressure.

The analysis of the structure of the parts has also shown that the high flexural properties of the parts moulded with the maximum combination of machine set-up parameters mainly come from the reinforcement content and average length combined to a better interfacial adhesion of the matrix around the fibres.

ACKNOWLEDGMENT

Thanks are due to Ticona for supplying LFT raw materials and to the European Union (European Funds for Regional Development, FERDER) for contributing to funding the equipment.

REFERENCES

1 Marsh G ., Composites on the road to the big time ?, Reinforced Plastics, February 2003, p 33-47.
2 Jacob A., Car makers increase their use of composites, Reinforced Plastics, February 2004, p 26-32.
3 H. Bijsterbosch, R.J. Gaymans, Polyamide 6 – Long glass fiber injection moldings, Polymer Composites, 16, 5, p 363-369, 1995.
4 R. Bailey, B. Rzepka, Fibre orientation mechanisms for injection molding of long fibre composites, International Polymer Processing, VI, 1, p 35-41, 1991.
5 D. O'Regan, M. Akay, The distribution of fibre lengths in injection moulded polyamide composite components, Journal of Materials Processing Technology, 56, 1-4, p 282-291, 1996.
6 R. Hafellner, M. Picher, R. Wörndle, Injection moulding long fibres, Kunststoffe, 90, 3, p 44-48, 2000.
7 M. Metten, M. Cremer, Injection moulding of long-fibre-reinforced thermoplastics, Kunststoffe, 90, 1, p 80-83, 2000.
8 J. L. Thomason, The influence of fibre length and concentration on the properties of glass fibre reinforced polypropylene: 5. Injection moulded long and short fibre PP, Composites Part A: Applied Science and Manufacturing, A33, 3, p 1641-1652, 2002.
9 ISO DIS 22314, Plastics – Glass-Fibre-Reinforced Products – Determination fibre length, 2004
10 S.G. Advani, C.L. Tucker III, Use of tensors to describe and predict fibre orientation in short fibre composites, Journal of Rheology, 31, 8, p 751-784, 1987.
11 E. Lafranche, P. Krawczak, J.P. Ciolczyk, J. Maugey, Injection Moulding of Long Glass Fiber Reinforced Polyamide 66: Processing Conditions / Microstructure / Flexural Properties Relationship, Advances in Polymer Technology, 24, 2 (2005) 114-131
12 L. Cilleruelo, E. Lafranche, P. Krawczak, P. Pardo, P. Lucas, Injection de thermoplastiques PET renforcés de fibres de verre longues, 14émes Journées Nationales sur les Composites, Compiègne, France (22-24 March 2005) 89-98
13 P. Gérard, Maîtrise et optimisation de l'anisotropie et de l'hétérogénéité des composites à matrices thermoplastiques renforcés de fibres de verre courtes en injection, Phd Thesis, University of Lille I - Ecole des Mines de Douai (F), 1998.
14 R. P. Hegler, V. Altstädt, G. W. Ehrenstein, G. Menning, J. Scharschmidt, G. Weber, Influence of material parameters on fibre orientation during processing of short fibre-reinforced thermoplastics, Kunststoffe, 76, 9, p 766-771, 1986.
15 D. O'Regan, M. Akay, The distribution of fibre lengths in injection moulded polyamide composite components, Journal of Materials Processing Technology, 56, 1-4, p 282-291, 1996.

EFFECT OF PACKING PRESSURE AND MOLD TEMPERATURE ON FIBER ORIENTATION IN INJECTION MOLDING OF REINFORCED PLASTICS

Parvin Shokri [1], Naresh Bhatnagar [2]

[1] *Research Scholar, Mechanical Engineering Department, Indian Institute of Technology- Delhi, 110016, India: pashokri@yahoo.com*

[2] *Associate Professor, Mechanical Engineering Department, Indian Institute of Technology- Delhi, 110016, India: nareshb@mech.iitd.ernet.in , narbhat@hotmail.com*

ABSTRACT: Injection molding of fiber reinforced polymeric composites is increasing with demands of complex products possessing superior mechanical properties of high specific strength, high specific stiffness, good fatigue strength and high impact resistance. Complex state of fiber orientation exists in injection molding of short fiber reinforced polymers. The orientation of fibers can vary significantly across the thickness of injection-molded parts and can become a key feature of the finished products. Improving the mechanical properties of molded parts by managing the orientation of fibers during the process of injection molding is the basic motivation of this study. This experimental work reveals the importance of packing pressure and mold temperature in orienting the fibers.

KEYWORDS: Injection Molding, Fiber orientation, Packing Pressure, Mold Temperature, Reinforced Thermoplastics

INTRODUCTION

Injection molding process is capable of producing intricate net shapes without any secondary processing and is thus being widely used in the electronic, automotive, aerospace and various other industries. Recently, the demand is increasing for geometrically complex and precision products, possessing superior mechanical properties. Thermoplastics coupled with fibers, as reinforcement, offer a number of advantages in terms of end-use performance to meet the desired demand. However, their use can also create several processing-related problems. The differential shrinkage between the in-flow and cross-flow directions of fiber-reinforced polymers can make it more difficult to determine the appropriate cavity dimensions and to prevent warpage. Anisotropic behavior of fiber-reinforced polymers can be attributed to the fact that the fibers become oriented during the injection molding process. The orientation of fibers varies significantly across the thickness of injection-molded part and can become a key feature of the finished product. Improving the mechanical properties of molded parts by managing the orientation of fibers during the process of injection molding was concerned in many studies. The effects of different parameters such as melt and mold temperature, flow rate, matrix and fiber properties, volume fraction of fibers, molding geometry, gate type and gate location on the detailed distribution and orientation of fibers in the final products have already been presented in many studies. In spite of all of these investigations still the process offer challenges on a fundamental level to the understanding of the relations between material parameters, processing, structure development, and final properties.

There are confusions in the conclusions of many studies [1, 2, 3, 4, 5] in explaining the state of fiber orientation at core layer of the molded parts. Fischer [1] explained that at the core layer of the part, the melt being pushed forward develops a flattened profile and fibers within this region do not orient without a well-developed shear flow. But Malzahn & Schultz [2] believed on the rotation of fibers at core region and concluded that the complete transverse alignment at the core region develops only after the instant of fill. It can be seen in the study of Gupta & Wang [3] who concluded that the in-plane stretching flow causes the fibers at the mid-plane to align transverse to the flow direction and the authors [3] in contrast to the study of Malzahn & Schultz [2] believed that the fiber orientation is only weakly dependent upon the post-filling stage of injection molding process due to a decreased flow field. Bay & Tucker [4] concluded that if there is significant in-plane stretching, the core is aligned in the principal stretching direction and in the case of no in-plane stretching, the core orientation is generated by the flow just inside the gate and is carried down the cavity with little change and these cores are more likely to have random-in-plane orientation. Another completely different expression can be seen in the study of Folkes & Russell [5] who concluded that the major contribution to the condition of the core comes not from flow induced molecular alignment but from columnar spherulitic growth that is known to occur around fibers in the absence of an externally applied flow field.

Contradictory explanations for the effect of mold temperature on the state of fiber orientation can also be seen in the conclusion of a few related studies [3,4, 6]. Gupta & Wang [3] believed that under isothermal condition, which means replacing the cold-wall temperature with the injection melt temperature; a change in injection speed has no effect on fiber orientation. In other words high mold temperature can eliminate the effect of injection speed; While Bay & Tucker [4] found that the mold wall temperature has little effect on the fiber orientation, even though they believed that the mold temperature could have a large effect on molecular orientation or crystallinity in some polymers. It can also be seen in the study of Vincent et al. [6] that variation in mold temperature did not affect the fiber orientation distribution in the products of their experiments.

In this study, a spiral mold was designed and fabricated to study the effect of packing pressure and mold wall temperature on the final orientation pattern of short fibers in injection molded parts.

EXPERIMENTS

The mold used for this work and the geometry of its products is shown in Fig. 1.

a. Spiral mold cavity plate

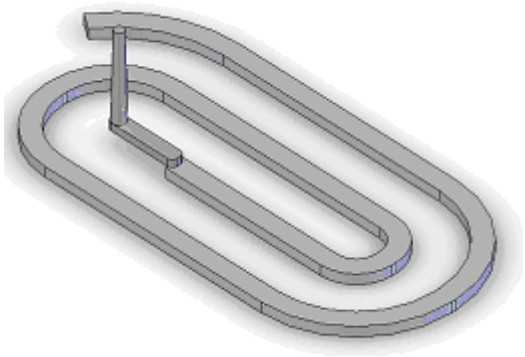

b. The product of spiral mold

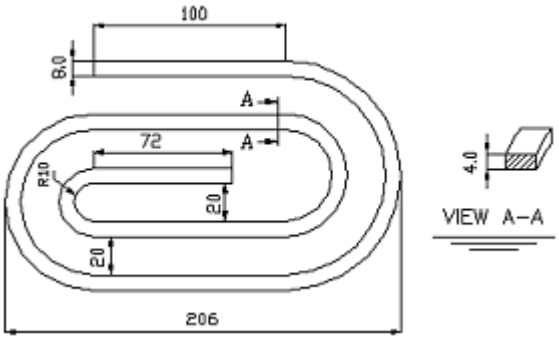

c. Geometry of the product

Fig. 1 Spiral mold and the solid model with geometry of its product

RGF33 NATURAL (TUFNYL, SRF Made), a 33% by weight short glass fiber reinforced in Nylon 66 in natural shade, was used in the experiments of this study. Recommended injection pressure for RGF33 NATURAL is 1000 -1250 Kg / cm^2 (10-12.5 MPa) or sufficient to fill the cavities. For this grade predrying of the granules in a vacuum oven at 100 ºC for 2 hours was done prior to molding as recommended by the supplier. Recommended temperature setting at nozzle was 290ºC for RGF33 NATURAL.

For analyzing the effects of packing pressure and mold temperature on the state of fiber orientation, three different Cases I, II, and III were studied. Injection pressure was set at 70% of maximum available pressure and injection speed was constant for all the Cases of this study. Packing pressure and the mold wall temperature for the three Cases was set according to Table 1.

Table 1 Process conditions

Case	Packing Pressure (%Max Injection pressure)	Mold Wall Temperature (ºC)
I	0%	35
II	40%	35
III	40%	70

The parts were molded on a L&T Demag PFY40-LNC4P injection molding machine of a screw diameter 28 mm, a maximum hydraulic pressure of 16 MPa, a maximum specific melt pressure of 175 MPa at the tip of the nozzle and a clamping force of 40 tons ($4x10^5$ N) for an injection capacity of 60 g.

For analyzing the state of fiber orientation at the core layer, cut-sections parallel to the plane of flow at locations A & B as shown in Fig. 2, were prepared.

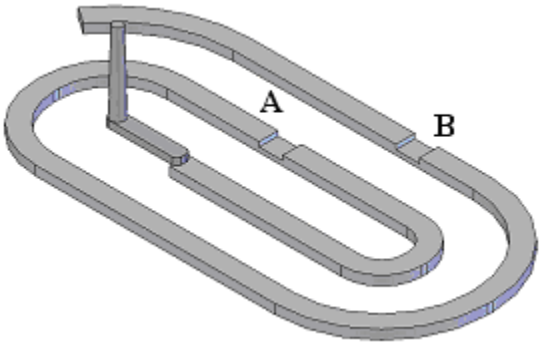

Fig. 2. Cut-sections parallel to the plane of flow at locations A & B for analyzing the state of fiber orientation in the mid-plane (Core layer)

RESULTS

In the first step of this study, the states of fiber orientation at the core layer in the plane of flow for Cases I and II are compared. In Fig. 3a schematic pattern of observed fiber orientation and in Fig. 3b and 3c the micrographs of cut-sections for Cases I & II are shown. Comparing these micrographs shows higher alignment of fibers in the flow direction at the midplane for Case I. However, due to applied packing pressure for Case II, fibers get more transverse orientation. Moreover, as can be seen the fibers follow a specific pattern as depicted schematically in Fig. 3a such that implying random state of fiber orientation at the core layer as understood in earlier works [4, 7], where the specimens were cut at the thickness wise cross section, could not be judged appropriately.

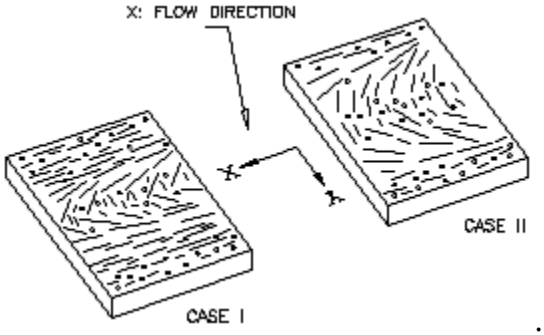

a. Schematic pattern of fiber orientation at location A (Cases I & II)

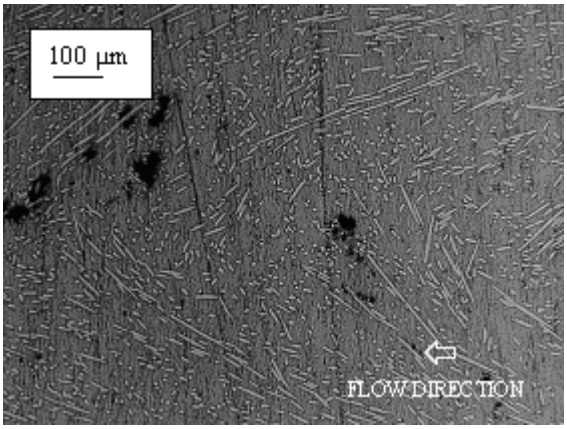

b. Lower degree of transverse orientation of fibers at the centerline (Case I)

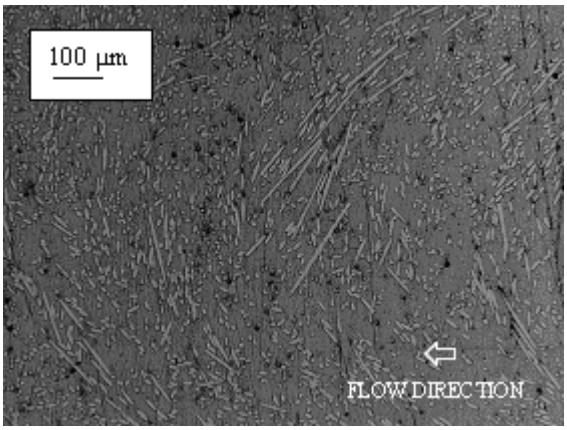

c. Higher degree of transverse orientation of fibers at the centerline (Case II)

Fig. 3 State of fiber orientation in the mid-plane of flow at location A (Cases I & II)

In the second step, for analyzing the effect of mold wall temperature, the state of fiber orientation is compared between Cases II (cold and packed) & III (hot and packed) at locations A & B. Schematic pattern of observed fiber orientation at location A (close to gate) along with related micrographs are shown in Fig. 4.

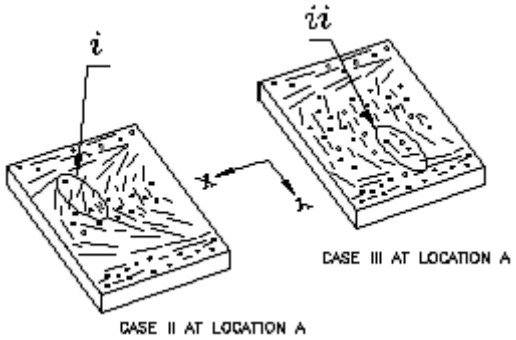

a. Schematic pattern of fiber orientation at location A (Cases II & III)

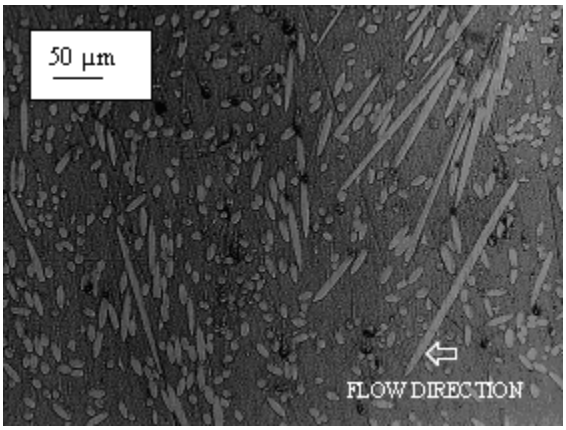

b. Higher degree of in-plane transverse orientation of fibers at location A_i (Case II)

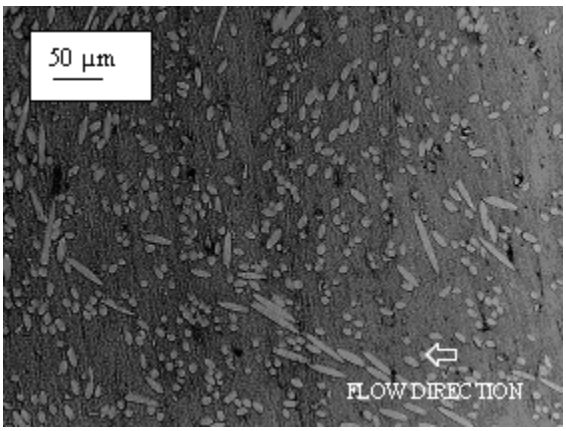

c. Higher degree of out of plane orientation of fibers at location A_{ii} (Case III)

Fig. 4 State of fiber orientation in the mid-plane of flow at location A with higher magnification (Cases II & III)

Comparing these micrographs shown in Fig. 4b and 4c indicates higher circular cut-sections of the fibers in Case III that from top view represents more out of plane orientation of fibers. Since increasing the mold temperature delays heat transfer from the melt to the mold walls, the authors attribute the observed state of fiber orientation to the reduction in the viscosity of melt, which facilitates the rotation of fibers for getting more out of plane orientation during the packing stage. It should be noted that out of plane orientation of fibers could also be considered a kind of transverse orientation of fibers with respect to the flow direction.

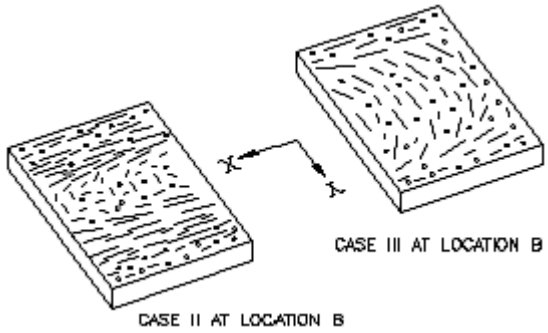

a. Schematic pattern of fiber orientation at location B (Case II & III)

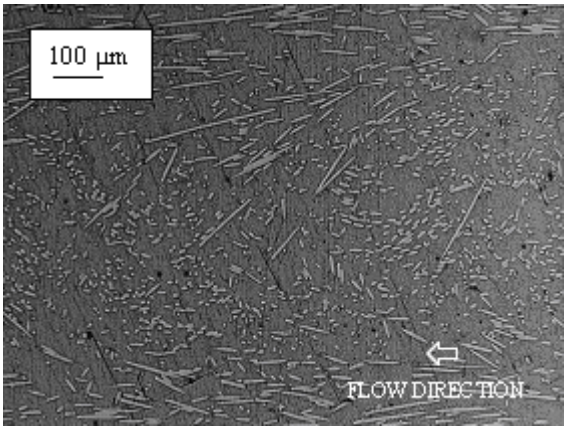

b. Lower degree of transverse orientation of fibers at location B (Case II)

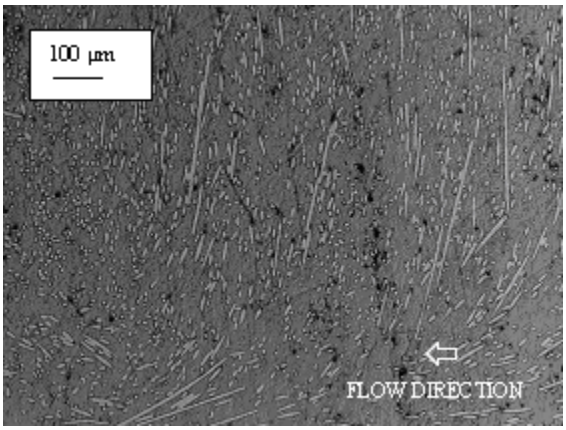

c. Higher degree of transverse orientation of fibers at location B (Case III)

Fig. 5 State of fiber orientation at centerline of mid-plane at location B (Case II & III)

In Fig. 5 schematic pattern of observed fiber orientation at location B for Cases II & III along with the related micrographs are shown. The micrographs shown in Fig. 5b and 5c show higher degree of transverse orientation of fibers at the core layer of Case III which is the product of the hot mold compared to Case II, which is the result of the cold mold. The difference in the state of fiber orientation in these two Cases is quite significant and reveals the importance of mold temperature as an important parameter in orienting the fibers in the final product.

CONCLUSIONS

- Packing pressure increases the degree of transverse orientation of fibers at the core layer.
- Increasing mold wall temperature affects the state of fiber orientation by increasing further the degree of transverse alignment of fibers at the core layer during packing stage.
- Fibers follow specific patterns at the core layer in the plane of flow such that implying random state for expressing the orientation of fibers at the core layer seems incomplete.

REFERENCES

1. J. M. Fischer, *Handbook of Molded Part Shrinkage and Warpage*, Plastic Design Library / William Andrew / Inc., USA, 2002.

2. J. C. Malzahn, and J. M. Schultz, "Transverse Core Fiber Alignment in Short-Fiber Injection-Molding", *Composite Science and Technology*, Vol. 25, 1986, pp. 187.

3. M. Gupta, and K.K. Wang, "Fiber Orientation and Mechanical Properties of Short-Fiber-Reinforced Injection-Molded Composites: Simulated and Experimental Results", *Polymer Composites*, Vol. 14, 1993, pp. 367.

4. R. S. Bay, and C. L. Tucker III, "Fiber Orientation in Simple Injection Moldings. Part II: Experimental Results", *Polymer Composites*, Vol. 13, 1992, pp. 332.

5. M. J. Folkes, and D. A. M. Russell, " Orientation Effects During the Flow of Short Fiber Reinforced Thermoplastics", *Polymer*, Vol. 21, 1980, pp. 1252.

6. M. Vincent, T. Giroud, A. Clarke, and C. Eberhardt, "Description and Modeling of Fiber Orientation in Injection Molding of Fiber Reinforced Thermoplastics", *Polymer*, Vol. 46, 2005, pp. 6719.

7. A. J. Pontes, N. M. Neves, and A. S. Pouzada, " The Role of the Interaction Coefficient in the Prediction of the Fiber Orientation in Planar Injection Moldings", *Polymer Composites*, Vol. 24, 2003, pp. 358.

POSTERS

PREDICTION AND CHARACTERISATION OF THE SHEAR BEHAVIOUR OF VISCOUS WOVEN TEXTILE COMPOSITES

Jinhuo Wang[1], Philip Harrison[2], Andrew C. Long[1] and Michael J. Clifford[1]

[1]*School of Mechanical, Materials & Manufacturing Engineering, University of Nottingham, University Park, NG7 2RD, U.K.* andrew.long@nottingham.ac.uk

[2]*Department of Mechanical Engineering, James Watt Building (South),University of Glasgow, Glasgow G12 8QQ, U.K.* p.harrison@eng.gla.ac.uk

ABSTRACT: The objective of this study is to develop a predictive model of the shear behaviour of textile composites to replace time-consuming material characterisation tests. This paper describes an energy minimisation method (EMM) to reduce experimental inputs for a predictive model developed in previous studies. The algorithm of the EMM is to minimise the summation of the in-plane shear energy dissipated at different regions of the composite sheet. A series of in-plane shear characterisation tests, Picture Frame (PF) tests, were performed. In order to validate the test results, some essential experimental conditions, such as boundary conditions, the direction of the shearing deformation, tow-meander and variability, were investigated. Comparisons between predictions and PF test results show that the implementation of the EMM is promising.

KEYWORDS: predictive modelling, shear behaviour, tow kinematics, Picture Frame test.

INTRODUCTION

Predictive modelling of the shear behaviour of viscous woven textile composites is of interest to many manufacturers as this can potentially decrease the time required to characterise materials and may also facilitate pre-manufacture material optimisation. Both these factors may produce significant reductions in processing costs. The overriding motivation is thus to make viscous textile composite materials more competitive in terms of both cost and functionality.

Multi-Scale Energy Model (MSEM) that predicts the shear behaviour of viscous woven textile composites was developed [1]. In the originally published versions of the MSEM [1, 2], certain experimentally determined input were required in the model. Most of these inputs, such as matrix rheology and fibre volume fraction of the composite are easily obtained. However, a more difficult to determine experimental input is the so-called ‘tow kinematics’ [3]. A tow is a fibre bundle. This term ‘tow kinematics’ refers to the kinematics that reflects different deformations between the tow and the overall material. The tow kinematics had to be obtained from experimental samples, and used as input for the MSEM before predictions could be made [1]. In the current work an energy minimisation algorithm is implemented that predicts the tow kinematics by minimising the energy contributions from tow crossovers, tow

regions and inter-tow regions. Hence the inclusion of the energy minimisation method means that the MSEM requires less experimental input.

Fundamental to the development and evaluation of the MSEM are material characterisation experiments. One of the most popular methods of characterising the in-plane shear behaviour of woven textile composites is the Picture Frame (PF) test [4]. Certain experimental conditions involved in these experiments are analysed. Finally, the MSEM based on the energy minimisation algorithm is evaluated by comparing with PF test results.

PREDICTIVE MODELLING

The role of the MSEM is to predict the shear force – shear angle – shear rate behaviour of viscous textile composites using parameters supplied readily by material manufacturers, such as fibre volume fraction, weave architecture and matrix rheology. The model has been described in detail previously [2] and so only a brief description is given here.

The meso-scale kinematics observed in many types of viscous textile composites have motivated the use of a novel two-phase material model structure to analyse the energy dissipation within viscous textile composites. These kinematics have important consequences for the deformation occurring during shear, both within tow and inter-tow regions, and also between tow crossovers. Namely, the rate of deformation tensor must be derived separately for both the tow and inter-tow regions and a further dissipative energy term must be derived to account for viscous energy loss at the tow crossovers.

The stress-power in the tow region can be calculated using the constitutive equation for a uniaxial ideal fibre reinforced fluid [5]. Within this model appear terms describing the longitudinal and transverse viscosities of the tows. These terms describe the dynamic interaction occurring between fibres and matrix on a micro-scale. Using micro-mechanical modelling principals [6, 7] reasonable predictions for both these viscosity terms can be made from the matrix viscosity and fibre volume fraction within the tows. The stress-power in the inter-tow region and also between crossovers can be calculated using the matrix viscosity. Thus, given the rate of deformation and stress tensor for the tow and inter-tow regions, the stress power generated by these regions can be determined.

The velocity field between crossovers is calculated by analysing the in-plane kinematics of tow deformation during shear. Using the velocity field and matrix film thickness the shear strain rate in the matrix film separating tows at crossovers can be estimated. From these calculations an estimate of the rate of energy dissipation can be determined due to shear between tow crossovers. By combining the energy contributions from both tow and inter-tow shear together with crossover shear, the total rate of energy dissipation during shear of the textile composite can be estimated and from this the resistance to shear deformation can be determined.
The meso-scale kinematics were obtained by measurements in the previous papers [1, 2]. In order for the MSEM to require less experimental input, an energy minimisation method has been attempted to predict the meso-scale kinematics and is described in the following section.

Energy Minimisation Method (EMM)

The actual tow kinematics are determined by minimising the energy generated due to in-plane tow shear, in-plane inter-tow shear and crossover shear. For example, a low degree of in-plane tow shear generates a relatively small amount of energy due to in-plane shearing of tows but a relatively large energy contribution due to in-plane inter-tow shear and crossover shear. Alternatively, a high degree of in-plane tow shear generates a relatively large amount of energy due to in-plane shearing of tows but a relatively small energy contribution due to in-plane inter-tow shear and crossover shear. The amount of energy dissipated by the in-plane tow shear, Eqn (1), is directly related to the longitudinal viscosity of the tows, η_L. The amount of energy dissipated by inter-tow regions, Eqn (2), and crossovers, Eqn (3), is directly related to the matrix viscosity, η_m. The tow angular shear rate, $\dot{\chi}_t$, determines the in-plane shear rate of the tow and inter-tow regions as well as the crossover shear rate. Thus, by increasing $\dot{\chi}_t$ from 0 to $\dot{\theta}$ (material angular shear rate) the minimum energy dissipation during any small angular increment can be determined. In this way the tow angular shear rate corresponding to minimum energy can be determined. The process is demonstrated in Fig. 1. Calculations were made for automotive prepreg (4x4 twill weave, carbon/epoxy) using the following experimental parameters: temperature = 23°C, θ =30°, material shear angular velocity $\dot{\theta}$=0.0026 rad/s, the tow shear angle for this step χ_t = 3°.

$$E_{tow} = \frac{a w_o T \eta_L \dot{\gamma}_t}{2\dot{\theta}\cos\theta} \tag{1}$$

where a is the distance increment of tow regions at small increment of θ, w_o is the initial width of tow regions, T is the thickness of the composite sheet and $\dot{\gamma}_t$ is the simple shear rate in the tow region.

$$E_{inter-tow} = bq\eta_m \dot{\gamma}_m T / \cos\theta \tag{2}$$

where b is the distance increment of inter-tow regions at small increment of θ, q is a factor accounting for weave architecture, $\dot{\gamma}_m$ is the simple shear rate in the inter-tow region and η_m is the matrix viscosity (a function of $\dot{\gamma}_m$).

$$E_{crossover} = \sum cA_e \eta_m^* \dot{\gamma}_f \tag{3}$$

where c is the distance increment of a small element at crossovers at small increment of θ, A_e is the area of the small element, $\dot{\gamma}_f$ is the simple shear rate at this small element at crossovers and η_m^* is the matrix viscosity (a function of $\dot{\gamma}_f$).

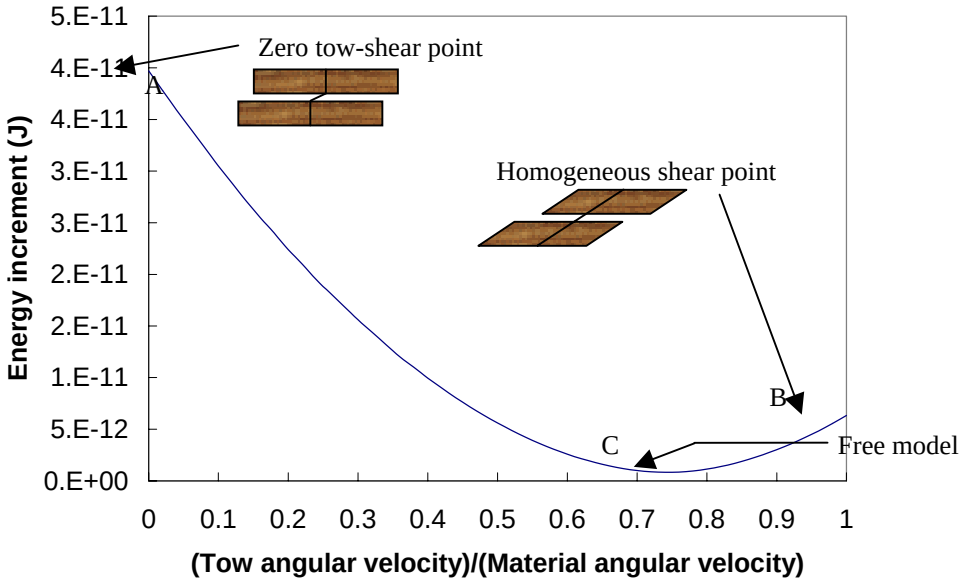

Fig. 1 Schematic of energy minimisation method to predict the tow kinematics.

From Fig. 1, $\dot{\chi}_t$ can be predicted by minimising the total energy increment, which is at point C. Then χ_t can be calculated analytically. By increasing the material shear angle (θ), the corresponding $\dot{\chi}_t$ and χ_t can be determined, which induces a form of χ_t versus θ, i.e. predicted tow kinematics.

CHARACTERISATION TESTS

Material

The material used in this study is a 4x4 twill weave, carbon/epoxy automotive prepreg, provided by Hexcel Composites in the UK, and its material code is 'M47N/42%/280T4X4/CHS-3K/1000mm'. Specimens were cut into a shape with the tows parallel or perpendicular to the outer edges. The thickness of the un-tested sheet is 0.36 mm.

Test Procedure

Picture frame test apparatus comprises of four-bar linkage loaded by a Hounsfield Universal Testing machine through a load cell connected to the crosshead. Four bars are jointed such that the initially square frame becomes a rhombus.

An environmental chamber was used to test materials at elevated temperatures. To minimise heat-up time the picture frame rig and clamps are heated to the required temperature in the chamber prior to mounting the sample. Once samples are clamped within the frame, heat-up times must be sufficiently short to avoid epoxy resin cure during testing.

During the test, a constant displacement rate is applied to the crosshead and the axial picture frame force (F_{pf}) and the displacement (d_{pf}) of the crosshead are measured. If data of shear force versus shear angle is required, then F_{pf} and d_{pf} need to be converted through Eqns (4) and (5).

$$F_s = \frac{F_{pf}}{2\cos\Phi} \tag{4}$$

where Φ is the frame angle, and can be related to the shear angle (θ) through $\theta = \pi/2 - 2\Phi$.

$$\theta = \frac{\pi}{2} - 2\cos^{-1}\left[\frac{1}{\sqrt{2}} + \frac{d_{pf}}{2L}\right] \tag{5}$$

where L is the side length of the picture frame.

Results and Discussions

Effect of boundary conditions

As the test boundary condition is a critical factor in obtaining reliable data [8, 9], two boundary conditions were investigated, clamped (four edges of PF are clamped) and pinned (three pins at each clamping edge provide shear force to material sheet during testing). It had been found that the pinned case is more suitable for Twintex (a 2x2 twill weave, glass/polypropylene thermoplastic composite) [4]. Three tests for each case were performed. Slight wrinkling occurred in only one test for the clamped case, whereas serious wrinkling happened at the start of all tests for the pinned case. This suggests that the clamped case should be used in the PF tests for the automotive prepreg used.

Influence of direction of the shearing deformation

There are two directions of shear deformation, positive and negative. A positive shearing deformation is defined with the warp fibre directions at an angle of + 45^o with the axis of loading, as viewed from the front of the PF apparatus. PF test results for a 1/7 satin weave (glass fibre reinforced Nylon 12) showed that the force required to shear the composite sheet in positive shear was nearly double the corresponding force in negative shear [10]. A theory developed in [11, 12] gives predictions consistent with the results of this test. To investigate its influence, three tests for each case were performed. The results suggest that the direction of shearing deformation for this prepreg has a negligible effect on the PF results, compared to variability of PF tests (see the following analysis).

Influence of tow-meander

Ideally, the tows of specimens in the weft direction are straight and perpendicular to those in the warp direction. However, in practice, the tows are not exactly straight and perpendicular to each other, as shown in Fig. 2(a). In order to investigate the influence of tow-meander, three tests were performed with samples taken directly off-the-roll. From Fig. 2(b), the results for off-the-roll specimens are much higher than those for the case of straightened specimens (i.e. where the material was straightened to improve tow alignment), and show poor repeatability. This suggests that test specimens should be straightened prior to testing in order to reduce the influence of tow-meander on test data.

(a) (b)

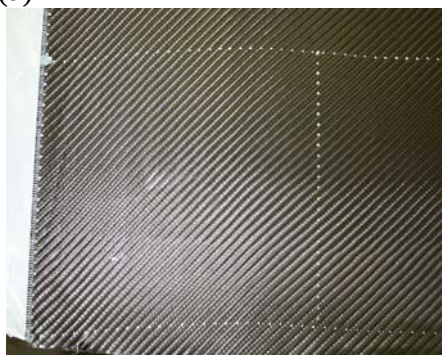

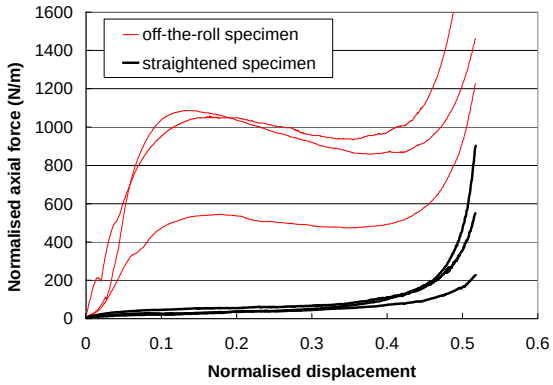

Fig. 2 (a) The profile of tows in the warp and weft direction in the material roll. (b) PF results with the cases of tow-meander and straightened specimens. Note that PF results are normalised by the side length of the picture frame [4], e.g. the normalised displacement equals to the recorded displacement divided by the side length.

Variability of Picture Frame tests

The repeatability of tests can be used to measure the accuracy of the test. The experimental errors involved during the tests may be due to misalignment due to cutting material sheets from the material roll, aligning sheets, clamping of the material, sample misalignment etc. Some PF tests were discarded due to premature wrinkling. Fig. 3 shows the PF results at three normalised crosshead speeds.

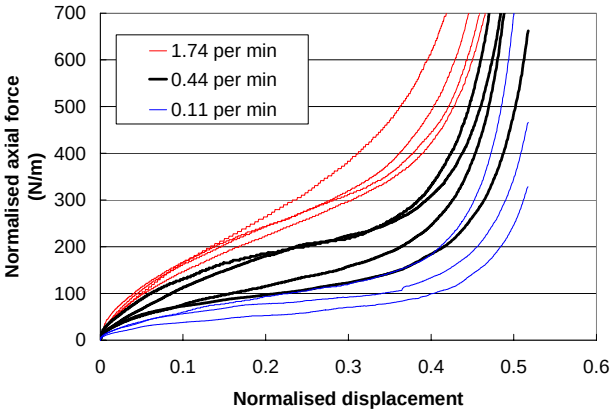

Fig. 3 PF test results at different normalised crosshead speeds to investigate the variability of experiments.

COMPARISONS BETWEEN PREDICTIONS AND CHARACTERISATION

Predictions from the MSEM using the EMM were made to compare with PF results. Within experimental variability, a good agreement between force predictions and experimental results is found (Fig. 4(a)), although the shape of predicted curve of the tow kinematics does not conform to the measurements (Fig. 5). MSEM predictions at a higher rate, 1.74 min^{-1}, were also made to compare with PF test results, shown in Fig. 4(b). The magnitude of force predictions increases rapidly as the rate increases, but the shape remains similar. The discrepancies between predictions and measurements are thought to be mainly due to the accuracy of longitudinal/transverse viscosities used in the MSEM. An suggestion on the improvement of these two viscosities was given by [13]. These problems will be addressed future work.

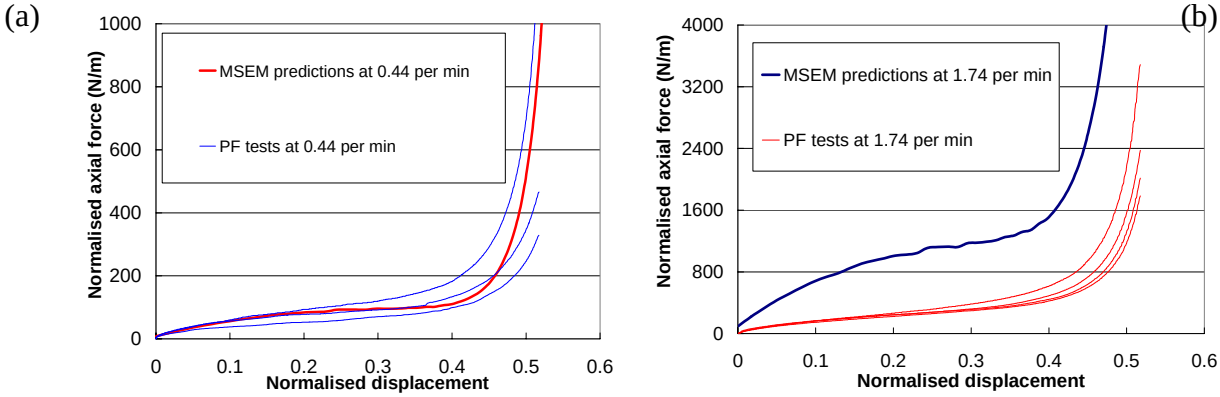

Fig. 4 Comparisons between force measurements from Picture Frame tests and force predictions based on the EMM for automotive prepreg sheet at different normalised displacement rates of (a) 0.11 min^{-1} (b) 1.74 min^{-1}

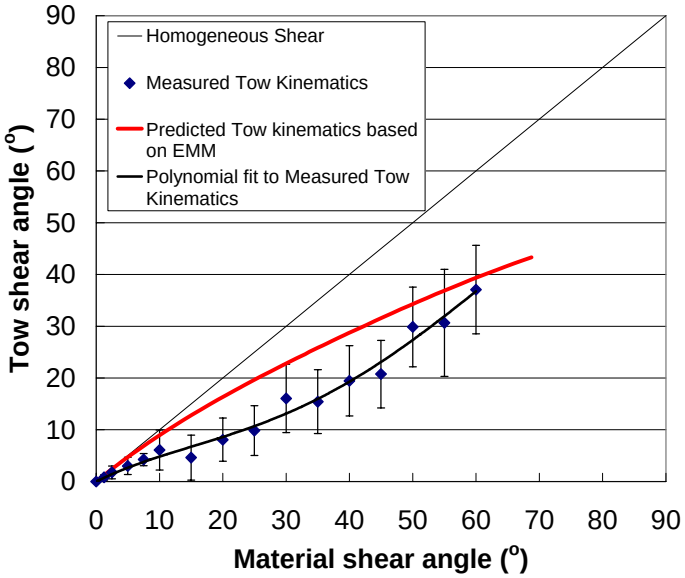

Fig. 5 Comparisons between measurements and predictions of tow kinematics based on the EMM at a normalised displacement rate of 0.11 min^{-1} for automotive prepreg sheet. Measurements were obtained from formed hemispheres. The error bars indicate the standard deviation.

CONCLUSIONS

A predictive model with less experimental input, based on the uniaxial continuum theory for ideal fibre-reinforced fluids but applied to woven textile composites, has been developed. The meso-scale kinematics for tow deformation that in the original MSEM had to be obtained from experimental measurements, such as formed hemisphere, can be predicted by an energy minimisation algorithm.

PF tests have been performed and suggest that the clamped boundary condition should be used for this particular prepreg, and the effect of direction of the shearing deformation for this prepreg can be neglected. The influence of tow-meander is significant, which suggests that test specimens should be straightened prior to testing.

A reasonable agreement between MSEM predictions and PF test results encourages the development of the energy minimisation method.

ACKNOWLEDGEMENTS

We would like to thank the following organisations for their support: EPSRC, Ministry of Defence, University of Cambridge, ESI Software, Ford Motor Company Ltd., Granta Design Ltd, Hexcel Composites, MSC Software Ltd, Polynorm Plastics (UK) Ltd and Saint Gobain Vetrotex.

REFERENCES

1. Harrison, P., Clifford, M.J., Long, A.C., and Rudd, C.D., *A constituent-based predictive approach to modelling the rheology of viscous textile composites.* Composites: Part A, 2004. **35**: p. 915-931.
2. Harrison, P., Clifford, M.J., Long, A.C., and Rudd, C.D., *Constitutive modelling of impregnated continuous fibre reinforced composites: a micro-mechanical approach.* Past Rubber Compos, 2002. **31**(2): p. 76-86.
3. Hivet, G., Dumont, F., Launay, J., Maurel, V., Vacher, P., and Boisse, P. *Optical analysis of woven fabric's shear behaviour*. in *7th International ESAFORM Conference on Materials Forming*. 2004. Trondheim, Norway.
4. Harrison, P., Clifford, M.J., and Long, A.C., *Shear characterisation of viscous woven textile composites: a comparison between picture frame and bias extension experiments.* Composites Science and Technology, 2004. **64**: p. 1453-1465.
5. Rogers, T.G., *Rheological characterisation of anisotropic materials.* Composites, 1989. **20**(1): p. 21-27.
6. Christensen, R.M., *Effective viscous flow properties for fibre suspensions under concentrated conditions.* Journal of Rheology, 1993. **37**(1): p. 103-121.
7. Coffin, D.W., Pipes, R.B., and Simacek, P., *First-order approximations for the effective shearing viscosities of continuous-fiber suspensions.* Journal of Composite Materials, 1995. **29**(9): p. 1180-1196.
8. Milani, A.S., Nemes, J.A., Pham, X.-T., and Lebrun, G. *The effect of fibre misalignment on parameter determination using picture frame test*. in *14th International Conference on Composite Materials (ICCM)*. 14-18th July, 2003. San Diego, California.
9. Peng, X.Q. and Cao, J., *A continuum mechanics-based non-orthogonal constitutive model for woven composite fabrics.* Composites: Part A, 2005. **36**: p. 859-874.
10. McGuiness, G.B. and O'Bradaigh, C.M., *Development of rheological models for forming flows and picture-frame shear testing of fabric reinforced thermoplastic sheets.* Journal of Non-Newtonian Fluid Mechanics, 1997. **73**: p. 1-28.
11. Spencer, A.J.M., *Theory of fabric-reinforced viscous fluid.* Composites: Part A, 2000. **30**: p. 1311-1321.
12. Spencer, A.J.M., *A theory of viscoplasticity for fabric-reinforced composites.* Journal of The Mechanics and Physics of Solids, 2001. **49**: p. 2667-2687.
13. Harrison, P., Haylock, T. and Long, A.C. *Measurement of the Transverse and Axial Viscosities of Continuous Fibre Reinforced Composites*. in *8th International ESAFORM Conference on Materials Forming*. 2005. Cluj-Napoca, Romania.

CORRELATED PERMEABILITY DISTRIBUTION: MOULD FILLING SIMULATIONS VERSUS EXPERIMENTAL RESULTS

F. Desplentere, S.V. Lomov and I. Verpoest

Metallurgy & Materials Engineering Department, Katholieke Universiteit Leuven
Kasteelpark Arenberg 44 3001 Heverlee Belgium
Frederik.Desplentere@mtm.kuleuven.be

ABSTRACT: This paper describes the comparison between the simulation results and experiments for a basic liquid moulding process. In the simulation, the uncertainty valid for the permeability of a textile preform is incorporated in a correlated way. Input data for the meso scale correlated permeability distribution is obtained using surface scanning of textile reinforcements. The Monte Carlo implementation of the scatter of the preform permeability allows generating additional information compared to a conventional deterministic simulation software as there are average filling time, standard deviation on the filling time and number of times a certain element is not filled. Starting from a known injection strategy, the number of times a certain element is not filled can indicate the probability to have good parts. On the other hand, the coefficient of variation for the filling time output together with the average filling allows to find the corresponding macro scale permeability scatter. This information is compared with the widely available experimentally observed scatter obtained with the radial injection set-up. The influence of the different parameters describing the meso scale permeability distribution is also investigated. Good correspondence is found between measurements and simulations.

KEYWORDS: Correlated, permeability, stochastic, mould filling simulation, experiment, textile geometry

INTRODUCTION

Nowadays, the RTM process gains a lot of interest to manufacture composite parts. Depending on the textile and the difficulty of the part to manufacture, it is possible to encounter problems with the mould filling. To lower the amount of bad moulds or injection strategies, one uses mould filling simulations to check the filling behaviour. One of the most important parameters in these models are the preform permeability values. In the past, several measurement set-ups were developed to characterize this parameter in an accurate way for different types of textiles under different process conditions. Every researcher ended up with the conclusion to have a reasonably large scatter for the macro scale permeability values. Up to now, mould filling simulations were performed using average permeability values. As scatter can be quite large for the permeability values, unwanted filling patterns are not seen in a deterministic simulation. To avoid this, one has to take into account the scatter for the meso-scale permeability.

Before, it was already proven that it does not make sense to generate a complete random distribution for the permeability as the resulting macro scale scatter is mainly depending on the size of the regions to which the randomly defined permeability values are assigned [1]. For that reason, a correlated approach is used. Before, there was no information available on the standard deviation and the correlation distance for the permeability on a local scale (meso). Within this paper, a technique is described to find data for the meso scale permeability together with the correlation distance. This information is used as input for the stochastic simulation. The outcome of this study is then compared with well-known data on the scatter for permeability at macro scale. As the technique to find the meso scale permeability information is not that tight, the sensitivity of the different parameters is investigated using the developed simulation tool based on PAM-RTM^{TM} software from the ESI-group (France).

CHARACTERIZING THE MESO SCALE PERMEABILITY SCATTER+CORRELATION

To obtain meso scale permeability data, several approaches were tested. Both direct measurement of the flow fronts and statistical modelling of textile architecture did not result in useful data for the meso scale permeability up to now. The tool presented by S. Lomov in this conference opens new possibilities. Another characterisation of the scatter for the permeability in a textile is making a link with a property which can easily be measured. An example of such a property for a woven fabric or a unidirectional material is the channel width. In case of a thin fabric, optical surface scanning can be used. In case of thick fabrics, X-ray µCT can be used . It is also possible to use this technique for an open channel (for example race-tracking) to define the variability of the channel width together with a correlation for this dimension.
To find the variability together with information about the correlation for thin fabrics, a conventional scanner linked to a desktop computer can be used. It is possible to scan rather large parts of a textile reinforcement (for example 20 x 30 cm). This allows acquiring data in the middle of the textile to avoid too much deformations of the yarn architecture due to cutting and in the regions close to the borders. Of course, it can also be interesting to see what is the influence of the cutting on yarns which are close to the border of the textile. To obtain useful data on the channel dimensions versus position along the channel, the textile has to be scanned with a high resolution to result in accurate information. A resolution of 2000 dots per inch is satisfactory. This corresponds to a measuring resolution of 12.7 µm/pixel. Within a conventional fabric, for example the fabric used in the experiments of Hoes [2], the average channel width between yarns is 0.5 mm. If no measuring errors are taken into account, the maximum relative error that can be made is 2.5% corresponding to this scan resolution.
Formulas (1) and (2) allow to calculate the correlation valid for a property X.

$$\hat{V}_{X,X}(i\Delta z) = \frac{1}{M}\sum_{j=1}^{M-|i.\Delta z|}\left[X(z_j)-\overline{X}\right]\left[X(z_j+i|\Delta z|)-\overline{X}\right] \qquad (1)$$

$$i = 0..M-1$$

$$\hat{R}_{X,X}(i\Delta z) = \hat{V}_{X,X}(i\Delta z)/V_{X,X}(0) \qquad (2)$$

To be able to apply the formulas (1) and (2) to find the correlation distance A for a parameter X for M sample points, the measurement of the channel width should occur at a constant distance Δz. As measurements have to be done by hand, one should avoid to

small Δz. A realistic distance for Δz is the average yarn spacing along a certain direction. Afterwards, a control should be done to check if the correlation distance found is large compared to the distance Δz.

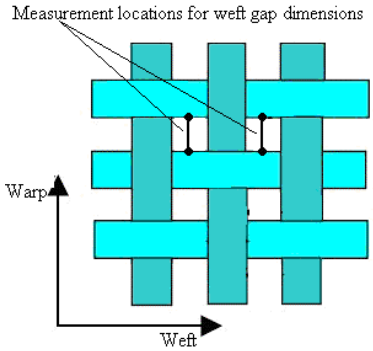

Fig. 1 Measurement location for gap dimensions

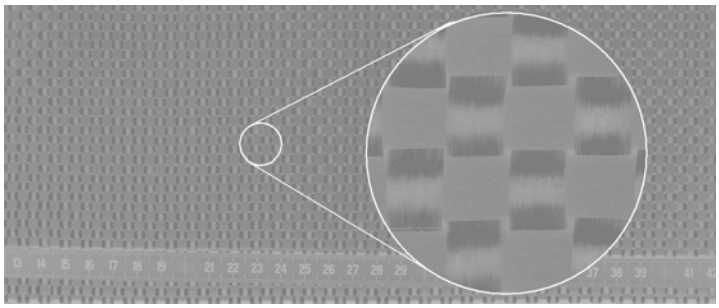

Fig. 2 Example of scanned thin fabric

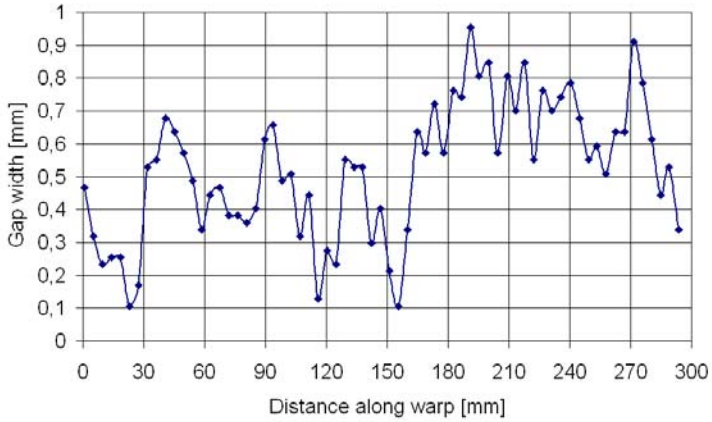

Fig. 3 Example for gap width along warp direction

Fig. 1 shows the measurement locations in case of a plain woven fabric. In Fig. 2 an example is shown of an image acquired with a scanner for the textile used in [2]. For a particular channel, the channel width along the whole scanned length of the fabric is displayed in Fig. 3. From this data, the average value together with the standard deviation can be calculated. This results in a gap width equal to 0.51 ± 0.187 mm (COV = 37%). Using Equations (1) and (2), it is possible to plot the data for the correlation function (Fig. 4). Through this data, a correlation function (Eq. (3)) can be fitted (Least squared error principle) resulting in a correlation distance A to be 1.22 centimetre.

$$R(i \cdot \Delta z) = exp\left(-\frac{i \cdot \Delta z}{A}\right),\ i = 0\ldots M\text{-}1 \qquad (3)$$

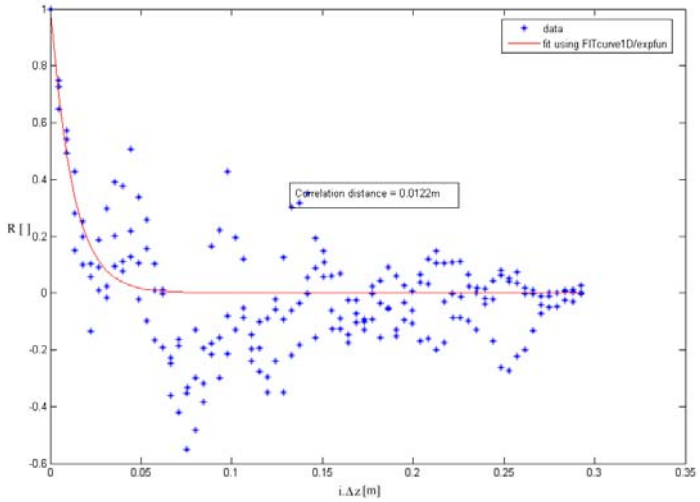

Fig. 4 Correlation function for gap width along warp direction

With this data, the stochastic information for the meso scale permeability can be defined. As permeability depends to the characteristic dimension of a reinforcement in a second order way, the standard deviation for the permeability is twice the standard deviation of the characteristic dimension of the textile reinforcement. In this investigation, a coefficient of variation of 74 % is used along both directions for the meso scale permeability. The correlation distance is kept the same as for the gap dimension as direct relation between the dimension and the permeability is assumed. The average value used for the meso scale permeability in both directions is the average value obtained by the experiments.

DIFFERENT PARTS IN STOCHASTIC SIMULATION

Preparation of the finite element model

To take into account the stochastic effects for permeability in mould filling simulations, the finite element model developed for the deterministic simulation can be used. Within this model, the part can be divided in different master zones depending on the number of textile materials that is used and the part thickness. Before, average data for permeability and other reinforcement parameters is assigned to one master zone. Next to reinforcement data, also information on the boundary conditions (injection, vent,…) can be defined in the usual way. Based on this model, the developed preprocessing program can be used to read the finite element model and to subdivide the different master zones into small sub zones. Within PAM-RTM, only one set of permeability values can be assigned to a zone.

Assigning permeability information

Once the finite element model is available, the meso scale permeability data has to be assigned. This can be done using the covariation decomposition algorithm [3]. To avoid problems with negative permeability values resulting from the normal distribution with a large coefficient of variation, a minimum permeability value has to be defined for each direction. This results in a disturbed normal distribution. To avoid this, the user also has the possibility to use the lognormal distribution. The covariation decomposition

algorithm allows to generate input files for the PAM-RTM™ software in a fast way. For each file, only a new random set of numbers has to be generated and multiplied with the lower triangular matrix resulting from the Cholesky decomposition.

Generation of the input files for PAM-RTM™

Next to the permeability information, also information on the thickness (for thin shell models), the porosity and the viscosity of the matrix material has to be defined. With the preprocessing program, all this information together with the permeability information valid for one of the files out of the Monte Carlo approach is written respecting the order necessary for the input files for PAM-RTM™.
The generated input files can be solved one by one in an automated way.

Post-processing

Once all the input files are solved with the PAM-RTM™ solver, the interesting data has to be filtered out. For each input file, PAM-RTM™ has generated a file containing for each element of the finite element model the time for which a certain element starts to fill and the time when it is completely filled. If the resin never reaches a particular element, this element number is not listed. This indicates an air entrapment in this run of the Monte Carlo approach. All these information is stored in memory to be able to access it in an easy way.
For comparison with experimental results, two additional parts were developed within the post-processing program. First of all, it is possible to read in a file containing the coordinates of sensors placed inside the mould. Based on these sensor coordinates, the scatter for the global permeability can be characterized similar to a technique applied within experiments.
Another additional part, is the possibility to fit the flow fronts with ellipses using least square error algorithm. This allows to find the scatter for the macro permeability in another way.

SIMULATION VERSUS EXPERIMENT

Experimental result

In [2], a new set-up to measure the in-plane permeability using central injection technique is described. Using this set-up, he was able to perform measurements in a fast way enabling to find information about the standard deviation valid for the permeability values for textile reinforcements. The set-up used in this investigation is displayed in Fig. 5. On Fig. 5, also the different sensors used to define the macro-scale permeability are recognizable.

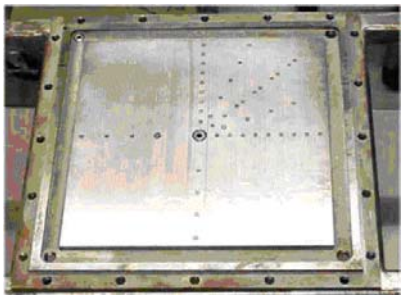

Fig. 5 Sensor based set-up of K. Hoes

For one fiber volume fraction, the obtained data for the permeability on a macro scale is displayed in Table 1.

Table1. Macro scale permeability variation based on sensor approach

Direction	Average value	Standard deviation	COV [%]
Warp	$179 \cdot 10^{-12} m^2$	$40 \cdot 10^{-12} m^2$	22
Weft	$144 \cdot 10^{-12} m^2$	$29 \cdot 10^{-12} m^2$	20

Simulation result

Based on the technique described to characterize the meso scale permeability parameters, Table 2 gives the values used to perform the stochastic simulation.

Table 2. Meso scale input information for the permeability

Direction	Average value [m²]	Standard deviation [m²]	Coefficient of variation [%]	Correlation distance [m]
Warp	$179 \cdot 10^{-12}$	$141 \cdot 10^{-12}$	79	0.0122
Weft	$144 \cdot 10^{-12}$	$114 \cdot 10^{-12}$	79	0.0095

If 150 files were generated using the Monte Carlo approach, the following results (Table 3) were obtained using the information obtained by the sensors. The formulas to obtain the permeabilities along the main axis are given in [4]. Examples of flow front versus time taken from different models within the Monte Carlo approach are given in Fig. 6.
These results show good correspondence to the numbers found during the experiments. In stead of using the sensor approach, also ellipses has been fit through the different flow fronts versus time. With this technique, the center of the ellipse is not forced to be at the injection point. The results for these approach are shown in Table 4. The modeled origin coordinates are 0.15 along both X and Y direction. The values for the permeability also corresponds well to the experimental results.
The influence of the values for the meso scale permeability and the correlation distance is shown in a next paragraph.

Table 3. Simulation result for the macro scale permeability based on sensor approach

Direction	Average value	Standard deviation	COV [%]
Warp	$169 \cdot 10^{-12} m^2$	$44 \cdot 10^{-12} m^2$	26
Weft	$131 \cdot 10^{-12} m^2$	$29 \cdot 10^{-12} m^2$	22

Table 4. Simulation result for the macro scale permeability using the ellipse fitting approach

Direction	Average value	Standard deviation	COV [%]
Warp	$172 \cdot 10^{-12} m^2$	$38 \cdot 10^{-12} m^2$	22
Weft	$139 \cdot 10^{-12} m^2$	$27 \cdot 10^{-12} m^2$	19
Xz	0.151 m	0.006 m	4
Yz	0.151 m	0.006 m	4

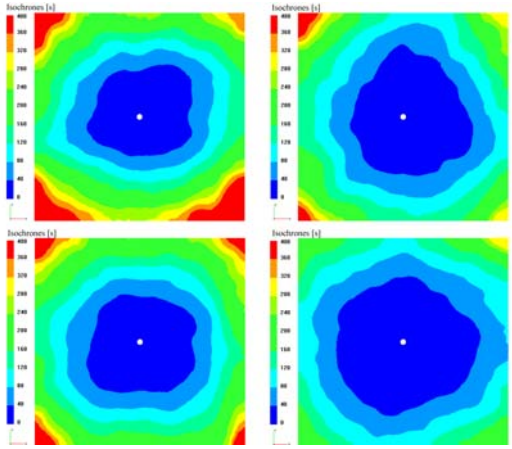

Fig. 6 Examples of flow front positions versus time for different runs from the Monte Carlo approach

INFLUENCE OF DIFFERENT PARAMETERS

To be able to think about the influence of the most important parameters within this stochastic approach, namely the correlation distance and the meso scale scatter for the permeability, an investigation was set up with an average permeability of $200 \cdot 10^{-12}$ m² along both warp and weft direction. First, the meso scale coefficient of variation was changed (Figure 7 left). It seems that the relation between the meso scale coefficient of variation and the macro scale COV is more or less linear for a given correlation distance with this set-up dimensions. If a model is built with doubled dimensions, the macro scale COV does not change. The influence of the correlation distance is shown on Figure 7 right. If the correlation distance would be 0 which corresponds to a complete random distribution, the meso scale coefficient of variation would be zero if the zones to which the permeability values are assigned are small. If a large correlation distance is assumed the limit value for the macro scale coefficient of variation would be 75% (= meso scale coefficient of permeability).

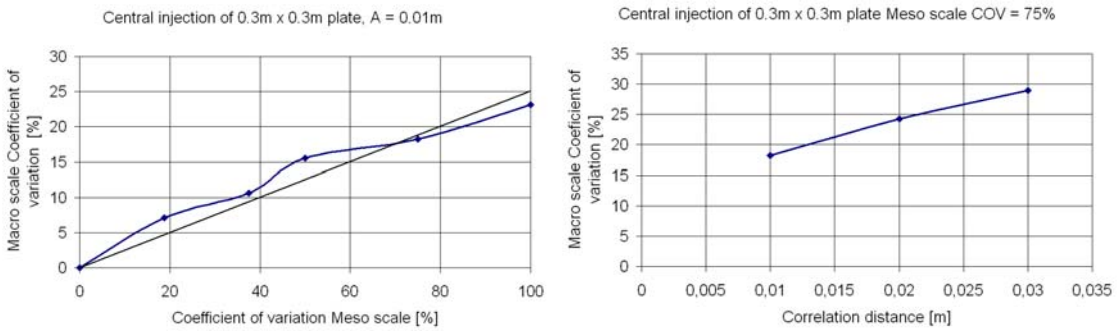

Figure 7. Influences of main parameters on macro scale coefficient of variation for permeability

CONCLUSIONS

With this investigation, it is shown that it is possible to use statistical data within mould filling simulation software in a useful way. Starting from a property which easily can be measured, it is possible to obtain information on the meso scale permeability valid for a certain textile reinforcement type. The investigation on the influences of the different parameters shows the importance of both parameters. Good characterization of the meso scale level coefficient of variation together with the correlation distance is important.

REFERENCES

1. Desplentere, F., S.V. Lomov, and I. Verpoest, *Influence of the scatter of perform permeability on the mould filling: Numerical simulations*, in *Proceedings of the 25th International SAMPE Europe Conference, March 30th - April 1st*. 2004: Paris. p. 331-336.

2. Hoes, K., et al., *New set-up for measurement of permeability properties of fibrous reinforcements for RTM.* Composites Part A: Applied Science and Manufacturing, 2002. **33**(7): p. 959-969.

3. Nicolaï, B., *Modeling and uncertainty propagation analysis of thermal food processes*, in *KUL. Faculteit landbouwkundige en toegepaste biologische wetenschappen*. 1994, KU Leuven: Leuven.

4. Hoes, K., *Development of a new sensorbased set-up for experimental permeability identification of fibrous media*, in *Faculteit Toegepaste Wetenschappen*. 2003, Vrije Universiteit Brussel: Brussels.

NANO ADHESIVE BONDING OF HIGH PERFORMANCE POLYMER FOR AEROSPACE APPLICATIONS

S. Bhowmik[1], H. W. Bonin[1], V. T. Bui[1] and R. Benedictus[2]

[1]*Department of Chemistry and Chemical Engineering, Royal Military College of Canada, Kingston, Ontario, K7K 7B4 Canada*

[2]*Faculty of Aerospace Engineering, Delft University of Technology Kluyverweg 1, 2629 HS Delft, The Netherlands*
Corresponding Author's Email: shantanubhowmik1@rediffmail.com

ABSTRACT: In this investigation, attempts are made to prepare nano adhesive bonding of high performance polymer such as Polybenzimidazole (PBI) (service temperature is –260 ^{0}C to +400 ^{0}C) for its essential applications to aerospace. In order to prepare high performance adhesive, nano adhesive is prepared by dispersing silicate nano particles into the ultra high temperature resistant epoxy adhesive (DURALCO 4703, the service temperature of the adhesive is –260 ^{0}C to +325 ^{0}C) at 10% weight ratio with the matrix adhesive followed by modification of the nano adhesive after curing under high-energy radiation for 6 hours in the pool of SLOWPOKE-2 nuclear reactor with a dose rate of 37 kGy/hr in order to essentially increase the crosslink density within the nano adhesive resulting in much improved cohesive properties of the adhesive. Prior to bonding, the surface of the Polybenzimidazole is ultrasonically cleaned by acetone followed by its modification under low-pressure plasma using nitrogen as process gas under RF glow discharge, in order to essentially increase the surface energy of the polymer leading to substantial improvement of its adhesion characteristics. First, the polymer surfaces are characterized by estimating surface energy and then the polymer surface is characterized by Electron Spectroscopy for Chemical Analysis (ESCA). The thermal characteristics of the basic ultra high temperature resistant epoxy adhesive and the high performance ultra high temperature resistant radiation crosslinked silicate nano adhesive are carried out by TGA and DSC and the physicochemical characteristics of these adhesives are carried out by the studies under solid state NMR. The TGA studies clearly shows that for the basic adhesive, there is a weight loss of the adhesive of about 10% when the adhesive is heated up to 325 ^{0}C resulting in deterioration of cohesive properties of the adhesive over the range of temperatures. However, in the case of the radiation crosslinked epoxy-silicate nano adhesive, there is a perfect 100% retention of weight of the adhesive when the adhesive is heated up to 325 ^{0}C resulting in significant improvement of cohesive properties of the adhesive over the range of temperatures. In order to determine the joint strength, tensile lap shear tests are performed according to ASTM D 5868-95 standard. Considerable increase in the joint strength is observed, more than 15 times when the polymer surface is modified prior to joining. Joints prepared with the unmodified polymer show only a joint strength of 1 MPa and increases up to 15.50 MPa with the surface modified polymer. There is a further massive increase in joint strength up to 25 MPa, when the joint is prepared by nano silicate epoxy adhesive and further modification of the adhesive joint under high-energy radiation results a further significant increase in joint strength up to 30 MPa. Therefore, with all the combinations there is about 30 times increase in joint strength. In order

to simulate with aerospace climatic conditions, the joints are exposed to cryogenic (-80 ^{0}C) and elevated temperature (+300 ^{0}C) for 100 hours and further, thermal fatigue tests of the joints are carried out under 10 cycles by exposing the joint for 2 hours under the above temperatures. When the joint completely kept at ambient condition and the joint strength compared with those joints exposed to aerospace climatic conditions, it is observed that there is no difference in joint strength. Finally, to understand the behaviour of high performance silicate epoxy nano adhesive bonding, the fractured surfaces of the joints are examined by scanning electron microscope. It is observed that the joint essentially fails cohesively within the adhesive even when the joints are exposed to cryogenic, elevated temperature and thermal fatigue conditions. Therefore, this nano adhesive bonding of high performance polymer could be highly useful for structural application in future generation aerospace.

KEYWORDS: High Performance Polymer, High Temperature Resistant Adhesive, Silicate Nano Powder, High Energy Radiation, ESCA, TGA, Lap Shear Tensile Strength

INTRODUCTION

Reinforced polymer laminates especially; the polymers of high temperature resistance have many attributes that are highly desirable properties for applications in aerospace structures. Often in the fabrication processes, polymer sheets are joined by adhesive rather than by welding or riveting. The acceptance of adhesives as a high performance engineering material has grown steadily in the last few decades [1, 2]. Adhesives contribute highly to structural integrity, ease of manufacturing, enhanced performance, improved safety, and cost and time savings. Unfortunately, polymer surfaces are hydrophobic in nature and exhibit low surface energy and therefore, represent challenges for adhesive bonding. Hence, surface modification of polymers is often carried out to enhance their surface energy to overcome technological challenges [3].

However, the main problem with the application of polymer and adhesive for aerospace is high temperatures. This is caused by the aerodynamic friction heating of the structure as it moves through the air. Therefore, to solve the problems, it is necessary to use such high temperature resistant polymeric sheets such as polybenzimidazole (PBI) sheets, which also have excellent cryogenic properties (service temperature ranges from –260 ^{0}C to +480 ^{0}C). The PBI sheet can be joined with another PBI sheet by employing recently developed ultrahigh temperature resistant epoxy adhesive (DURALCO 4703, service temperature ranges from –260 ^{0}C to +350 ^{0}C) as this adhesive retains its cohesive properties even when exposed to cryogenic atmosphere.

In the recent times, research on polymer-clay nanocomposite has become a very important area because it is established that thermoechanical properties of polymer-silicate nanocomposite are far superior to those of conventional polymer or polymeric composites [4-*6*]. Therefore, with this principle, high performance adhesive can be prepared by dispersing silicate nano powder to matrix adhesive and that could open a new dimension on theromechanical properties of adhesive bonding.

In view of this observations, in the present investigation, the surface of polybenzimidazole sheet is modified by low-pressure plasma using a 13.56 MHz RF Glow Discharge for 120 seconds at 100 W of power using nitrogen as process gas, in order to essentially increase the surface energy of the polymer leading to substantial improvement of its adhesion characteristics. The PBI to PBI sheets are joined with an ultra high temperature resistant

epoxy adhesive (DURALCO 4703, service temperature ranges from –260 ^{0}C to +325 ^{0}C) and by dispersing silicate nano powder into the ultra high temperature resistant epoxy adhesive at 10% weight ratio with the matrix adhesive followed by modification of the nano adhesive after curing under high-energy radiation for 6 hours in the pool of SLOWPOKE-2 nuclear reactor with a dose rate of 37 kGy/hr in order to essentially increase the crosslink density within the nano adhesive resulting in much improved thermomechanical properties of the adhesive. The low-pressure plasma exposed PBI surface is characterized by Electron Spectroscopy for Chemical Analysis (ESCA). The physicothermal characteristics of the basic ultra high temperature resistant epoxy adhesive and the high performance ultra high temperature resistant silicate nano adhesive is carried out by TGA. Tensile lap shear tests of the adhesive joints have been carried out to determine the effects of these environments on the joint strength. Finally, in order to understand the failure mode of the joints, the fractured surfaces of the joints after failure under tensile lap shear tests have been examined under scanning electron microscope.

EXPERIMENTAL

MATERIALS

In this investigation polybenzimidazole (PBI) sheets of service temperature ranging from –260 ^{0}C to +400 ^{0}C, tensile strength of 160 MPa and density of 1.3 gm/cc, were used for preparation of adhesive joint by using recently developed ultra high temperature resistant epoxy adhesive, DURALCO 4703, manufactured by Cotronics Corp. Brooklyn, NY, USA of service temperature ranging from –260 ^{0}C to +325 ^{0}C. The mixing ratio of resin to hardener, curing temperature and time of this adhesive are: 1:0.22, 25 ^{0}C and 24 hours, respectively. Silicate nanopowder of 50nm of particle size, manufactured by Glassven, La Victoria, Aragua 2121 United States was used as dispersing nano particles in 10% wt. ratio into the adhesive.

SURFACE MODIFICATION AND SURFACE CHARACTERIZATION OF PBI

Prior to joining, surface modification of the PBI is carried out by RF glow discharge using RF power generator that operates at a fixed frequency of 13.56 MHz. In this investigation, the surface of the polymer was modified under 120 seconds of exposure under 100 W of power. Surface characteristics of PBI are carried out by estimating surface energy of the polymer. Unmodified PBI and modified PBI surfaces are also characterized by ESCA.

PHYSICOTHERMAL CHARACTERIZATION OF ADHESIVE

Physicothermal characteristics of the basic ultra high temperature resistant epoxy adhesive and the silicate nano powder dispersed ultra high temperature resistant adhesive were carried out by TGA. TGA thermograms were obtained on a Universal V2 5H TA Instruments equipment, under a nitrogen atmosphere at a heating rate of 10 ^{0}C /min, and scanned from 25 ^{0}C to 500 ^{0}C.

PREPARATION OF THE ADHESIVE JOINT

The tensile lap shear test samples are prepared using PBI sheets of dimensions 125 × 25 × 6 mm^3 by applying the ultra high temperature epoxy adhesive at an overlap length of 25 mm. Any excess adhesive present at the interface was expelled out by pressing the joint under a load of 10 kg. The tensile lap shear test is performed according to the ASTM D 5868-95

standard, using an Instron Universal Testing Machine under a load cell of 10 kN at a test speed of 5 mm/min at room temperature. Three types of adhesive tensile lap joints were tested: (i) The basic ultra high temperature resistant epoxy adhesive lap joints of PBI-to-PBI,(ii) silicate nano powder with 10% wt. ratio was dispersed into the above epoxy adhesive and (iii) silicate nano powder with 10% wt. ratio was dispersed into the above epoxy adhesive and the joints were irradiated for 6 hours to SLOWPOKE-2 Nuclear Reactor with a dose rate of 37kGy/h. The schematic diagram of the reactor is shown in Fig. 1

DURABILITY TEST

From above three types of joints durability of the joints were carried out on the type (iii) specimens. The joints are exposed to cryogenic (-196 ^{0}C) and elevated temperature (+300 ^{0}C) for 100 hours and further, thermal fatigue tests of the joints are carried out under 10 cycles by exposing the joint for 2 hours under the above temperatures. For each set of environmental conditions, seven joints are tested and the mean value is reported in the result.

RESULTS

ESCA STUDIES ON THE PBI

ESCA wide scan spectra of the unexposed PBI shows the C 1s peak, O 1s peak and a significant concentration of F 1s peak as shown in Fig. 2. However, the PBI surfaces exposed to low-pressure plasma show significant decrease in F 1s peak, and a small increase in N 1s peak as shown in Fig. 3

SURFACE MODIFICATION OF POLYMER UNDER LOW-PRESSURE PLASMA AND WETTABILITY

When the PBI surface is modified by low pressure plasma, polar component of surface energy increases significantly, however, the dispersion component of surface energy remains almost same and therefore, due to the increase in the polar component in surface energy, a considerable increase in total surface energy of PBI is also observed as shown in Fig. 4.

TGA STUDIES ON BASIC ADHESIVE AND NANO ADHESIVE

The results from the TGA on physicothermal characteristics of the epoxy adhesive and the silicate nano epoxy adhesive are shown in Figs. 5 and 6 respectively. It is found that the degradation of the basic epoxy adhesive is a two-stage process: a relatively short stage with a very small percent of weight loss beginning at about 125 ^{0}C, followed by about 8% of weight loss up to 350 ^{0}C, attributed a degradation of the adhesive over the ranges of temperatures up to 350 ^{0}C and thereafter, there is a massive degradation of the adhesive. However, for the silicate-epoxy nano adhesive, degradation of the adhesive occurs in one stage as steady state continues up to 350 ^{0}C and there is no sign of degradation of the adhesive up to 350 ^{0}C. In this case, the percent of weight loss up to 350 ^{0}C is almost negligible as clearly evident from the Fig. 6.

LAP SHEAR TENSILE PROPERTIES OF THE PBI -PBI JOINT

Figure 7 shows the lap shear tensile properties of adhesive joints of PBI when the PBI surface has been modified by low pressure plasma. The figure reveals that the adhesive joint strength of the as received PBI to titanium is 1 MPa and increase to 13 MPa with the modification. It

is observed that there is a considerable increase in joint strength up to 21 MPa, when the joint is prepared by nano silicate epoxy adhesive and further modification of the adhesive joint under high-energy radiation results a significant increase in joint strength up to 30 MPa as shown in Fig. 8.

DURABILITY OF THE JOINTS UNDER LOW TEMPERATURE, ELEVATED TEMPERATURE AND THERMAL FATIGUE CONDITIONS

It is observed that when the best joints i.e., the type (iii) joints are exposed to a low temperature (-196 ^{0}C) as well as an elevated temperature (+300 ^{0}C) for 100 hours, and thermal fatigue conditions with these temperature variations under 10 cycles by exposing the joint for 2 hours at each temperature the joints could retain almost 95 % of the joint strength as shown in Fig. 9.

DISCUSSION

This study examined high performance nano adhesive bonding of PBI to PBI, in the context of its structural applications for aerospace. Fig. 7 indicates that due to surface modification of PBI, adhesive joint strength is significantly high in comparison to the adhesive joint strength of as received PBI. This is possible because due to the increase in surface energy of PBI, essentially contributed to retaining the interfacial strength with the adhesive.

It is well documented by various researchers that thermophysical and thermomechanical properties such as melting, crystallization, thermal conductivity, coefficient of thermal expansion, tensile and breaking strength of epoxy as well as polyolefins improves considerably due to incorporation of silicate nano powder in to the matrix polymer [3-8]. The present investigation of nano adhesive bonding of PBI by dispersing silicate nano powder to ultra high temperature epoxy adhesive also shows a similar trend as there is a considerable improvement of thermophysical and thermomechanical properties of the adhesive. This is because in respect to any adhesive, the thermomechanical properties of silicate are significantly high and therefore, that essentially influence the overall performance of the adhesive.

An earlier investigation on influence of high-energy radiation on polymeric composite reveals that there is a considerable increase on the mechanical strength on the polymeric composite when exposed to high-energy radiation [7], because the exposure under high-energy radiation increases crosslink density within the polymer, essentially affecting the overall behaviour and mechanical properties of the polymer. Therefore, with the exposure under high-energy radiation, mechanical properties of the adhesive joint increase significantly because of increasing crosslink density within the adhesive [7, 8]. Therefore, in this investigation, the joints are essentially exposed to high-energy radiation so as to promote crosslinking within the adhesive by high-energy radiation, and as surface modified PBI to titanium adhesive joints essentially fail cohesively within the adhesive, so it is a clear justification to increase the joint strength up to 30 MPa with the nano adhesive bonding. However, when these PBI - PBI joints are exposed to climatic conditions such as elevated as well as cryogenic temperature related to aerospace and space conditions, the joints could retain the joint strength of about 95% of strength of the joint kept under ambient conditions. However, this could be within the acceptable limit in respect of aerospace applications.

CONCLUSIONS

The present investigation has led to the following conclusions:

(i) Polar component of surface energy leading to total surface energy of the polymer increases significantly due to surface modification of polymer by low pressure plasma

(ii) The adhesive joint strength of PBI to PBI increases considerably from 1 MPa to 13 MPa, when the PBI surface is modified by low pressure plasma.

(iii) There is a significant increase in joint strength up to 21 MPa, when the joint is prepared by nano silicate epoxy adhesive

(iv) When the joints are irradiated for 6 hours in the pool of SLOWPOKE-2 nuclear reactor, there is a further improvement of joint strength up to 30 MPa.

(v) When the joints are exposed to low as well as elevated temperature for 100 hours, and thermal fatigue conditions, the joints could retain about 95% of their the joint strength with respect to the strength of the joint tested under ambient condition.

ACKNOWLEDGEMENTS:

The financial support provided by the Natural Science and Engineering Research Council of Canada for carrying out this work is gratefully acknowledged.

REFERENCES

1. G. Akovali, Z. M. O. Rzaeyand, D. H. Mamedov, *Journal of Applied Polymer Science* (1995) Vol. **58**, pp. 645 – 651.

2. D. S. Bag, V. P. Kumar and, S. Maiti, *Journal of Applied Polymer Science*, (1999) Vol. **71,** pp. 1041 – 1048.

3. J. Behnisch, A. Hollander and H. Zimmerman, *Journal of Applied Polymer Science* (1993) Vol. **49**, pp. 117 – 124.*Applied Polymer Science*, Vol. **71,** pp. 1041 – 1048.

4. T. G. Gopakumar and, D. Page, *Polymer* **43** (2002) 5483.

5. T. Agag, Polymer **42** (2001) 3399.

6. R. A. Void and E. P. Giannels., *Macromolecules* **30** (1997) 8000.

7. H. W. Bonin and V. T. Bui, *J Appl Poly Sci*. **67 (**1998) 37.

8. A. J. Berejka, *Radiation Phys and Chemistry* 63 (2002), 63, 551

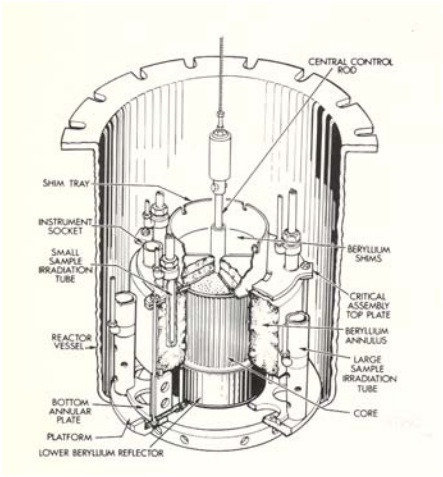

Fig 1. Schematic diagram of SLOWPOKE-2 nuclear reactor.

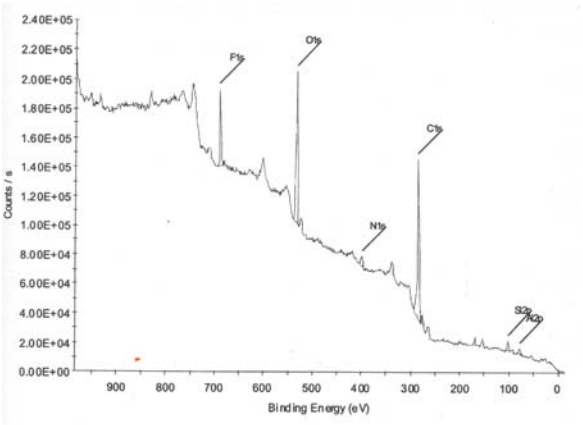

Fig 2. ESCA widescan spectra of unexposed polybenzimidazole surface.

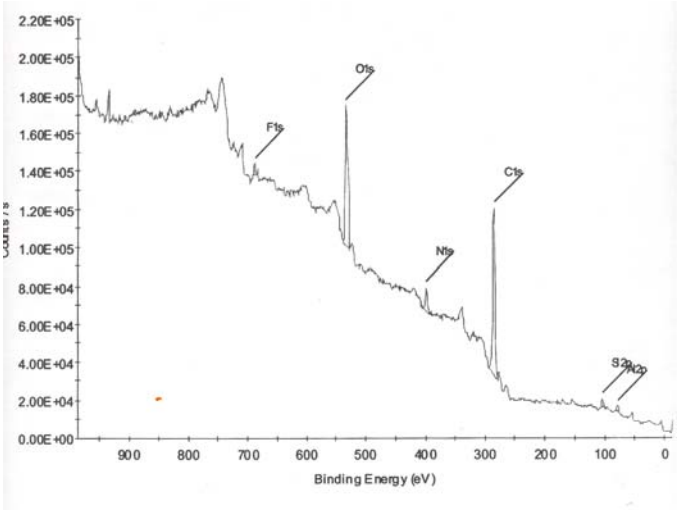

Fig 3. ESCA widescan spectra of polybenzimidazole surface modified by low pressure plasma.

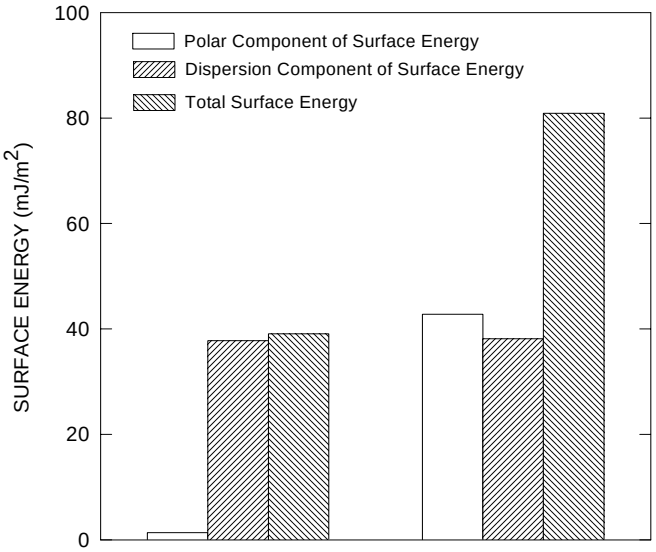

Figure 4. Polar, dispersion and total surface energy of polybenzimidazole when the polymer surface is modified by low-pressure plasma.

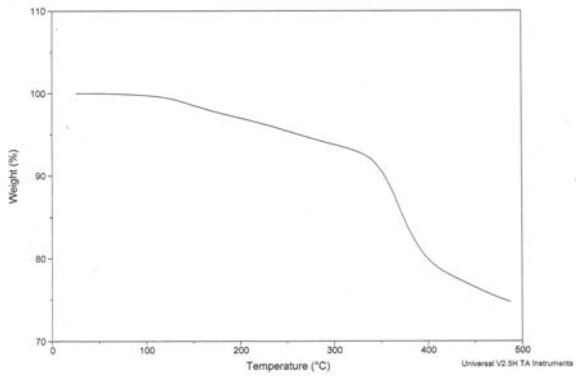

Fig 5. TGA plot of the basic high temperature resistance epoxy adhesive.

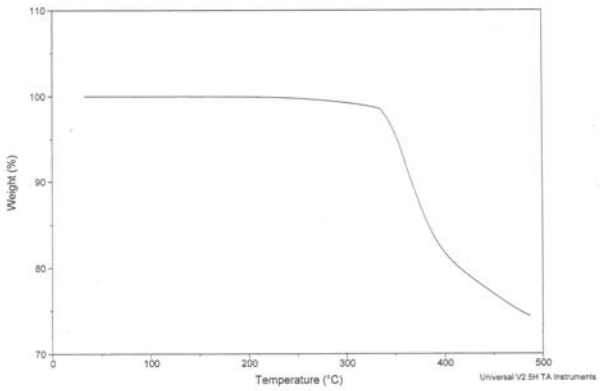

Fig 6. TGA plot of the high temperature resistant epoxy adhesive when silicate nano powder dispersed in to the adhesive in 10% weight ratio.

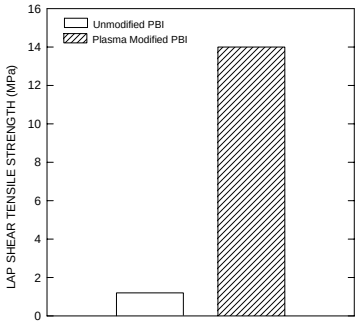

Fig 7. Lap shear tensile strength of adhesive joint of surface modified polybenzimidazole.

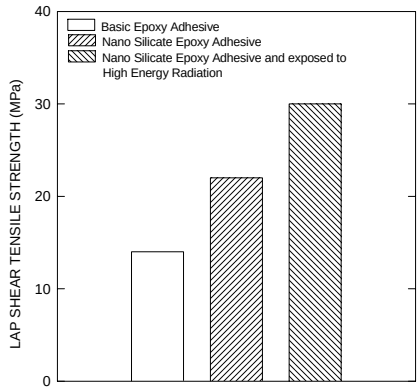

Fig 8. Lap shear tensile strength of the joint prepared with basic epoxy adhesive, nano silicate epoxy adhesive and the nano silicate epoxy adhesive joint exposed to SLOWPOKE-2 Nuclear Reactor for 6 hours.

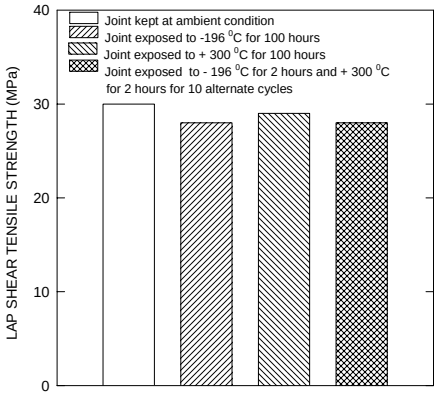

Fig 9. Durability under cryogenic, elevated temperature and thermal fatigue conditions of high performance nano silicate epoxy adhesive joint.

AN ELECTROSTATIC POWDER SPRAY PROCESS FOR MANUFACTURING POLYPHTHALAMIDE HIGH PERFORMANCE COMPOSITE

Chiara Zaniboni [1], Paolo Ermanni [2]

[1] *Centre of Structure Technologies, ETH Zurich, Leonhardstrasse 27, LEO B3, CH-8092 ZURICH, SWITZERLAND: Corresponding Author's e-mail: czaniboni@ethz.ch*

[2] *Centre of Structure Technologies*
ETH Zurich, Leonhardstrasse 27, LEO B3, CH-8092 ZURICH, SWITZERLAND: permanni@ethz.ch

ABSTRACT: The powder impregnation of carbon fiber rovings with low viscosity PA6T/6I polyphthalamide oligomers for the reactive moulding of unidirectional fibre-reinforced thermoplastic composites for high temperature applications was investigated. In order to impregnate the continuous carbon fiber tow with the PA6T/6I oligomer powder an electrostatic powder spray impregnation technique was developed and the material system was characterized. The most pertinent material parameters were determined to establish their influence on the desired powder impregnated prepreg. The oligomers undergo a nonreversible cold crystallization process on heating. The time and temperature interval of this solid state transformation is very sensitive to the applied force field. The definition of a suitable process window with respect to the external forces is necessary to avoid cold crystallization and to effectively impregnate the fibers.

KEYWORDS: Thermoplastic matrix composites, PPA, oligomers, cold crystallization, powder impregnation, reactive processing, in-situ polymerization.

INTRODUCTION

There is a growing interest in the industry in producing high quality thermoplastic composite parts for structural and high temperature applications. In response to this driving force an innovative stamp forming process with a reactive thermoplastic material system is currently being researched and developed aimed at cost-effective processing polyphthalamide PA 6T/6I in the field of continuous-fiber high temperature resistant composites.

Semi-crystalline polyphthalamides (PPA) are semi aromatic high performance engineering thermoplastics that bridge the cost-performance gap between traditional engineering thermoplastics such as polycarbonate (PC), polyamides (PA), polyester (PET, PBT), acetals (POM) and higher-cost specialty polymers such as liquid crystal polymers (LCP), polyphenylene sulfide (PPS) and polyetherimide (PEI). PPA resins and in particular copolyamides based on hexamethylenediamine, therephthalic acid and isophthalic acid (PA 6T/6I) have excellent mechanical properties (e.g. strength, stiffness, fatigue, creep resistance)

over a broad temperature range. PA 6T/6I resin features an excellent stiffness-to-cost ratio and a high strength-to-weight ratio, both of which are superior relative to PBT, PPS, PEI, PET and PA 6,6. Its thermal performance is exceeded only by polyetheretherketone (PEEK) and some LCPs. PA 6T/6I resin has lower moisture absorption than PA 6,6, and its broad chemical resistance is exceeded only by few more costly specialty polymers. This combination of features provides PA 6T/6I resin with the potential to reduce weight, cut costs, and deliver long service life for all types of automotive components, including parts for fuel, transmission, braking, and engine systems [1].

This paper discusses the impregnation of carbon fibers with the low viscosity PA 6T/6I oligomer powder. The most pertinent material parameters were determined to establish their influence on the desired powder impregnated prepreg. The oligomers undergo a nonreversible cold crystallization process on heating. The time and temperature interval of this solid state transformation is very sensitive to the applied force field. The definition of a suitable process window with respect to the external forces is necessary to avoid cold crystallization and to effectively impregnate the fibers.

EXPERIMENTAL

Material

The PPA oligomers (PA 6T/6I, XE 3733 VK) utilized in this work are the intermediates in a two-stage method developed by EMS-CHEMIE AG for the production of partially aromatic polyamides. Because of the typically very high structure-dictated melting viscosities of such polyphthalamides, the polycondensation with a single-stage batch process must be stopped at a very early stage to enable discharging the melt from the autoclaves and processing it into granular material. Limiting the average molecular weight of these polymers to comparatively low values has a very negative effect on their mechanical properties. In order to overcome these problems, the production process of PA 6T/6I at EMS-CHEMIE involves a continuous process for the production of precondensates (prepolymers), in which monomers condensate to oligomers (up to 10 repeating units). In a final reaction stage the precondensates are melt polymerized in a double-or single-screw extruder into high-molecular weight polyphthalamide [2]. The low cost PA 6T/6I precondensates are readily produced especially if compared to cyclic oligomers and allow the development of an in-situ polymerization process for large manufacturing volume applications and reduced production costs [3].

Powder impregnation and reactive processing

The reactive stamp forming process is based on prepreg technologies, reactive processing, and direct stamp forming. In a first stage, carbon fiber rovings are impregnated with the PPA precondensat powder by powder impregnation technique in order to reduce the distance to flow of the low viscosity thermoplastic prepolymer.

The powder impregnation process developed in this work utilize an electrostatic powder spray gun to charge and deposit the PA 6T/6I oligomers powder onto a continuous carbon fiber tow [4] A schematic of the electrostatic spray impregnation process is shown in Figure 1. The process uses a bi-directional fiber tensioner to maintain constant tension in the fiber tow. A pneumatic fiber spreader spreads the fibers, just prior to coating the fibers. An ITWGema EASY 1-L powder coating equipment is used to coat the spread carbon fibers with the

oligomeric powder. The coated fibers are then passed through an infrared heater to melt and adhere the powder to the fibers. The towpreg is then wound onto a take-up mandrel.

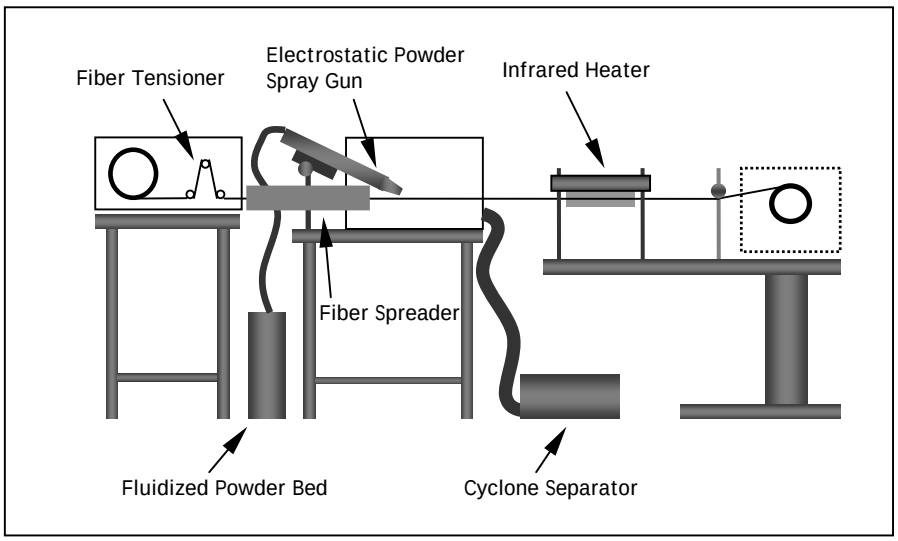

Figure 1. Schematic of electrostatic powder spray impregnation process

In a second stage, the oligomer powder coated prepregs are heated to the melt temperature of the oligomers in a hot press and pressed so that the oligomers, thank to their low melt viscosity, can easily flow and achieve high wetting and impregnation quality of the fibers. Finally, the temperature is raised between the glass transition and the onset of melting in order to induce the oligomers to polymerize in solid state and the so formed polymer to crystallize while the entire mass of material is shaped.

Rheological characterization

Solution Viscosity

Solution viscosity measurements of oligomers were carried out at concentrations of 0.1 g/dL, 0.3 g/dL, 0.5 g/dL und 0.7 g/dL in 98% sulphuric acid in a Paar Physica MC 300 rheometer using Couette geometry. The intrinsic viscosity [η] of oligomers was calculated from the reduced viscosity η_{sp}/c by extrapolation to zero concentration.

Complex Viscosity

The complex viscosity of the PPA oligomers was investigated with a Paar Physica UDS200 rheometer in a parallel plate configuration. All measurements were carried out under nitrogen atmosphere to prevent degradation or absorption of moisture. The oligomer powder was pressed to pills of 20 mm diameter with pressure of 160 MPa and 1 MPa at 140°C.

Thermal Characterization

A Perkin Elmer Pyris 1 DSC instrument calibrated using indium was used to study the melting, cold-crystallization and polymerization behaviour of PPA oligomers. All DSC non-isothermal tests were performed from 80° to 350°C at a constant heating rate of 10°C/min under nitrogen atmosphere to prevent high temperature oxidation.

RESULTS AND DISCUSSION

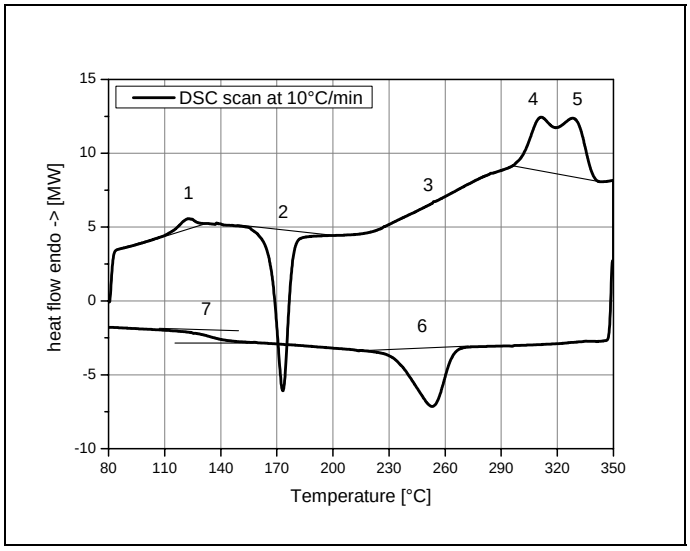

Fig. 2. DSC temperatures scan of PA 6T/6I precondensates from 80°C to 350° C at 10°C/min: a) upper curve is the heating curve b) lower curve is the cooling curve

A typical DSC temperature scan of PA 6T/6I precondensates from 80°C to 350°C at 10°C/min is shown in Fig. 1. The as-received oligomers show seven distinct transitions in the heating (upper curve) and cooling curve (lower curve). Peak 1 represent a glass transition (T_g) step with a strong pronounced enthalpy relaxation [6] where the oligomers undergo softening. The peak temperature and enthalpy are strongly dependent on the thermal history of the sample. On further heating from the glass transition the oligomers are brought to crystallize (peak 2). The cold-crystallization behaviour observed for PA 6T/6I oligomers arises from the short chain lengths and low level of entanglements of the molecules: in the solid state the mobility of the short chain molecules is strongly reduced but above glass transition temperature they can easily rearrange and crystallise in a paraffin-like structure (fully extended chain crystals). The stability of this configuration is further increased in the case of polyamides, which can form hydrogen bonds between the chains [7]. Between 220°C and 305°C peak 3 can be identified as a broad endothermal peak where polycondensation and evaporation of the reaction by-product water take place. Peak 4 between 305°C and 345°C is a double melting peak of the formed polymer. In the cooling curve (lower curve in figure 1) one crystallization peak form the melt can be identified between 280°C and about 210°C and one glass transition temperature at 130° C of the final polymer.

Powder impregnation process window

Cold-crystallization of the low molecular weight PA 6T/6I oligomers was found to be very rapid as shown in figure 3 from the cold-crystallization half time. At a temperature lower than 155°C 50% of crystallization is attained in a time scale of several minutes, while above 155° the half time decreases to seconds. At 180° the oligomers are fully crystalline after few seconds. The cold crystallization of PA 6T/6I oligomers is not a reversible process: once the oligomers are crystallized, they can not be remelted. The powder impregnation process has, therefore, to occur at a temperature lower than 155° in order to fully impregnate the fibers and to avoid cold crystallization.

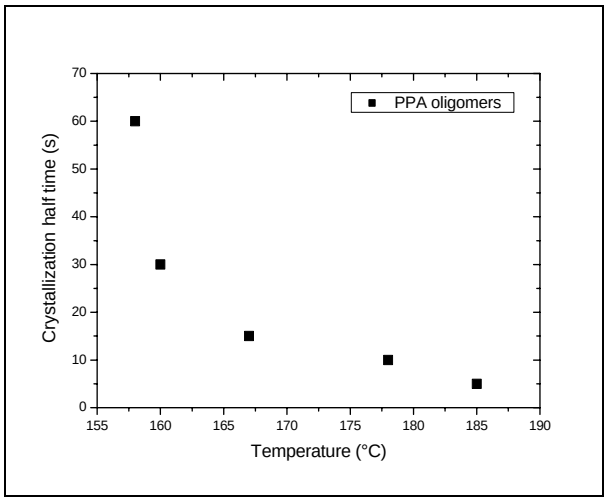

Fig. 3. Crystallization half-time of PA 6T/6I oligomers

The intrinsic viscosity of short chain PA 6T/6I oligomers was found to be very low with [η] = 0.07 dl/g, especially if compared, for example, to low molecular weight PET and PEN oligomers with [η] = 0.2 dl/g [8]. The low molecular weight oligomers begin to soften at 135°C, but they were found to melt only under shear force. In order to measure the complex viscosity at 140°C the oligomer powder was pressed to pills of 20 mm diameter under two different pressures. The complex viscosity values [η*] of the oligomer powder pills (pressed at 140°C with 160 MPa pressure) measured as a function of time at 140°C are very high, [η*] > 10^4 Pa·s, as shown in Figure 4. On the other hand, complex viscosity of oligomer powder pills pressed at 140°C with pressure of 1 MPa show much lower values, [η*] > 10^2. Further investigations were carried out to study the effect of pressure on the cold crystallization process with a torsional resonance rheometer.

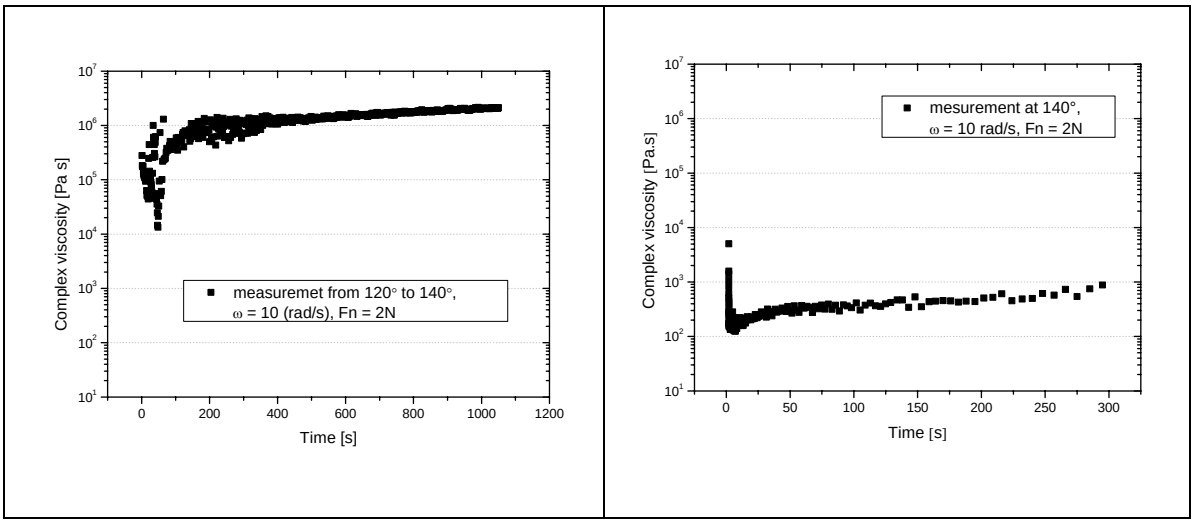

Figure 4. Complex viscosity values versus time for PPA oligomer powder sample pressed at 140°C with different pressure.

The time and temperature interval of cold crystallization was found very sensitive to the applied pressure force: increased applied pressure induces the PPA oligomers to crystallize at lower temperature and with increased crystallization rate [9].
This behaviour could be explained by the increase of orientation of the short oligomer molecules with increasing applied pressure. Pressure could give rise to a more ordered structure as in the case of drawing and cold crystallization in poly(ethylene therephthalate)

fibers [10]. The oligomer segments are shorter than the macromolecules and therefore easier to orient with pressure. The ordered segments are easily arranged into the crystal lattice, making the onset and the end temperature of oligomer crystallization shift to lower values. In other words, the orientation of amorphous phase promotes a substantial increase in crystallization rate.
The low viscosity of the PPA oligomers could not be measured do to the necessity of press the oligomer powder to pills for the rheological measurements. The applied pressure induced partial crystallization of the oligomers that surely affected the measured viscosity values. The low oligomer viscosity was proved during impregnation of the prepregs and has to be taken into account in order not to excessively impregnate the fibers and to maintain the flexibility of the prepreg.

Conclusions

Low molecular weight PPA oligomers begin to soften at 135°C but melt only under shear force. On further heating the oligomers undergo a non-reversible cold crystallization process. This solid state transformation was found to be very rapid: above 155°C crystallization half time of the material is only few seconds. Therefore, an efficient powder impregnation process has to occur at a temperature lower than 155°C in order to preimpregnate the fibers and to avoid solid state transformation. The time and temperature interval of cold crystallization is very sensitive to the applied pressure force: increased applied pressure induces the PPA oligomers to crystallize at lower temperature and with increased crystallization rate. Finally, the very low viscosity of the PPA oligomers was not proved do to the necessity of press the oligomer powder to pills for the rheological measurements. The low oligomer viscosity was proved during impregnation of the prepregs and has to be taken into account in order not to excessively impregnate the fibers and to maintain the flexibility of the prepreg.

ACKNOWLEDGEMENTS

The authors are grateful to GEBERT RÜF STIFTUNG for the financial support and would like to thank EMS Chemie for supplying the PA 6T/6I oligomers, ITWGema for supplying the EASY 1-L powder coating equipment.

REFERENCES

1. H.P. Schmeer, “Polyphthalamid”, *Kautschuk.Gummi Kunstoffe,* Vol. 46, Nr. 10/93, 1993, pp. 799-804.

2. EMS-Inventa AG, U.S. Patent 5,708,125, 1998.

3. Weixia Yan, KeQing Han, LiuLiang Qin, MuHuo Yu, “Study on Long Fiber–Reinforced Thermoplastic Composites Prepared by In Situ Solid-State Polycondensation”, *Journal of Applied Polymer Science,* Vol. 91, 2004, pp. 3959–3965.

4. K. Ramani, D. E. Woolard, M. S. Duvall, “An Electrostatic Powder Spray Process for Manufacturing Thermoplastic Composites”, Polymer Composites, December 1995, Vol.16, No.6.

5. H. G. Kim, R.E. Robertson, “A New Approach for Estimating the Recrystallization Rate and Equilibrium Melting Temperature”, *Journal of Polymer Science*: Part B: Polymer Physics, Vol. 36, 133–141 (1998).

6. N. Pini, C. Zaniboni, S. Busato, P. Ermanni, “Perspectives for Reactive Molding of PPA Matrix for High-Performance Composite Materials”, FPCM7 2004.

7. S. Affolter, A. Ritter., M. Schmid, “Interlaboratory Tests on Polymers by Differential Scanning Calorimetry (DSC): Determination of Glass Transition Temperature (Tg)”, *Macromol. Mater. Eng.*, 286 (2001), 605-610.

8. K. Yao, W. Ray, “Modeling and analysis of new processes for polyester and nylon production”, *AIChE*, J 47 (2) (2001), 401-412.

9. C. Zaniboni, N. Pini, S. Busato, P. Ermanni, “Reactive Processing of Polyphthalamide as Temperature Resistant Matrix for High Performance Composite Materials”, *Theplac* 2005, Lecce, Italy.

10. Supaphol, P.; Apiwanthanakorn, N. “Nonisothermal Cold-Crystallization Kinetics of Poly(Trimethylene Terephthalate)”, *Journal of Polymer Science*: Part B: Polymer Physics, Vol. 42, 4151–4163 (2004).

STRUCTURE AND PROPERTIES OF PP-BASED SANDWICH INJECTION MOLDINGS

Yuji Fujita[1)], Tsutomu Nagaoka[2)], Masaya Kotaki[3)], Hiroyuki Hamada[3)]

[1)] Japan Polypropylene Corporation, 1 Toho-cho, Yokkaichi, Mie 510-0848, Japan
[2)] Kobe Steel, Ltd., 9-12 Kita-Shinagawa 5, Shinagawa-ku, Tokyo, Japan
[3)] Division of Advanced Fibro Science, Kyoto Institute of Technology, Sakyo-ku, Kyoto 606-8585, Japan

ABSTRACT: Structure and mechanical properties of sandwich injection moldings are investigated as well as flow behavior of materials in the process in order to obtain well controlled sandwich injection moldings. It has been found that there are four processes of flow behavior in sandwich injection molding as shown in Figure 1: (1) primary injection process, (2) core material injection process, (3) core material expansion process, and (4) core material break-through process. In the “primary injection process”, only skin material is injected into cavity, and it is followed by core material injection into skin material in the “core material injection process”. In the “core material expansion process”, core material growths with skin material at the flow front, and the core material break through skin material at the flow front in the “core material break-through process”. It has been found that the break-through behavior of core material is dependent on injection conditions such as injection speed and injection pressure, however the primary parameter to the break-through behavior is melt tension of skin material. The occurrence of the core material break-through can be minimized when high melt tension materials are used as skin material as shown in Figure 2.

Well controlled polypropylene (PP)-based sandwich injection moldings with biodegradable polymers in core are molded based on the above results in order to investigate structure-property relationship of the sandwich injection moldings for automotive applications. Two types of compatibilizers are used to improve interfacial adhesion between skin and core parts. Microstructure of PP in skin and at the interface is investigated. Effects of MFR of PP, compatibilizers, and injection molding conditions on mechanical properties of PP-based sandwich injection moldings are discussed. Special attention is given to skin-core adhesion properties and its effect on mechanical properties of sandwich injection moldings. The skin-core adhesion properties are evaluated by modified peel tests. The final goal of this study is to provide the concept to design sandwich injection moldings for target properties based on material selections of skin, core and compatibilizer, and injection molding conditions.

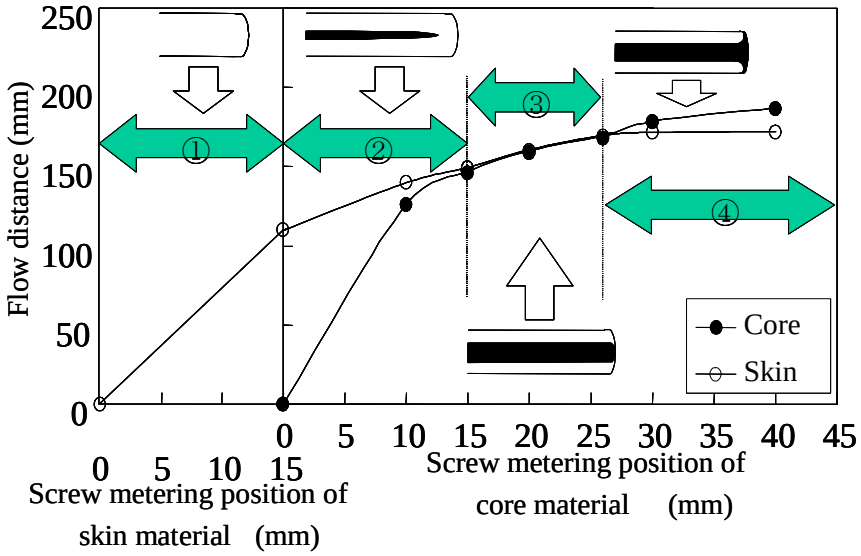

Fig. 1 Four process of flow behavior in sandwich injection molding.

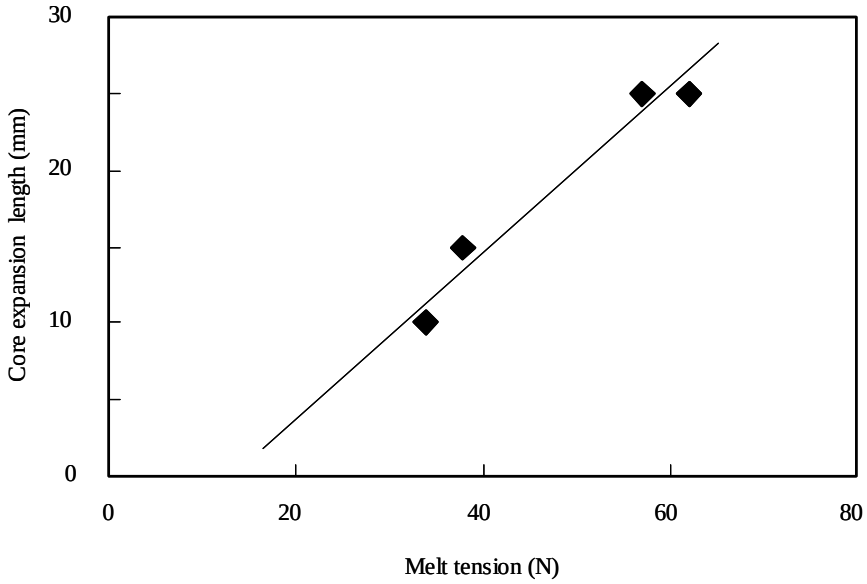

Fig. 2 Relationship between core expansion length and melt tension in sandwich injection moldings.

AUTHOR INDEX